A Confocal Scanning Laser Holography (CSLH) Microscope to Non-Intrusively Measure the Three-Dimensional Temperature and Composition of a Fluid

by

Peter B. Jacquemin
M.Sc., San Jose State University, 1980
B.Sc., San Jose State University, 1978

A Thesis Submitted in Partial Fulfillment
of the Requirements for the Degree of

DOCTOR OF PHILOSOPHY

in the department of Mechanical Engineering

SUPERVISORY COMMITTEE

A Confocal Scanning Laser Holography (CSLH) Microscope to Non-Intrusively Measure the Three-Dimensional Temperature and Composition of a Fluid

by

Peter B. Jacquemin

M.Sc., San Jose State University, 1980
B.Sc., San Jose State University, 1978

Supervisory Committee

Dr. Rodney A. Herring, (Department of Mechanical Engineering)
Supervisor

Dr. Peter Oshkai, (Department of Mechanical Engineering)
Departmental Member

Dr. Harry L. Kwok, (Department of Electrical Engineering)
Outside Member

ABSTRACT

Supervisory Committee

Dr. Rodney A. Herring, (Department of Mechanical Engineering)
Supervisor

Dr. Peter Oshkai, (Department of Mechanical Engineering)
Departmental Member

Dr. Harry L. Kwok, (Department of Electrical Engineering)
Outside Member

The Confocal Scanning Laser Holography (CSLH) microscope non-intrusively measures the three-dimensional (3D) temperature and composition of a solid, fluid, or plasma. A unique reconstruction algorithm uses phase-shift data from the recorded holograms and boundary conditions of the specimen to measure the 3D temperature. The CSLH microscope uniquely combines holography with a scanning confocal microscope to determine the phase-shift in a hologram and to reconstruct the 3D temperature. The confocal aspect of the microscope reduces optical aberrations in the hologram and increases sensitivity to a temperature at a scan position in the specimen. The optical design maintains a stationary focal point on the pinhole aperture within the confocal optics during scanning.

The CSLH microscope uses a focused laser beam instead of a collimated beam to probe the specimen. The advantage of the focused probe beam over the collimated beam is that different phase-shift data is obtained for each scan position of the probe beam. Another advantage is preventing rotational scanning of the laser about the specimen or rotating the specimen, increasing the number of practical applications. This limits the scan angle to the cone angle of the probe beam only.

Reconstruction of the 3D temperature given restricted scanning from a single viewing window places a burden on the reconstruction algorithm to produce low reconstruction error. Three-dimensional reconstruction using methods of tomography prove inaccurate

due to the small cone angle. The result is ill-conditioned reconstruction matrices. A unique low reconstruction error algorithm given a single viewpoint window that specifies a particular scanning geometry and requires boundary conditions is derived for the microscope.

This research involved the design, building, and evaluation of a specific CSLH microscope intended for fluid flow and heat transfer studies in micro-gravity space based experiments. The fluid specimen used to evaluate the microscope sets a benchmark for resolution, sensitivity, and performance. The reconstruction error is primarily due to measurement error, residual optical aberrations affecting holograms, and vibrations since the reconstruction algorithm error is negligible. Additional knowledge gained includes the understanding of sensitivity to optical alignment as well as methods to accurately determine the phase-shift in a varying fringe contrast hologram. A significant trade-off is that as the cone angle of the probe beam increases, the reconstruction error decreases but the optical aberrations increase. One of the more difficult challenges during scanning is to maintain a fixed focal point on the confocal apertures as the beam is tilted off the optical axis centerline.

Further recommended advancements for the microscope are improving the optical lenses to provide pupil planes that are stationary during scanning and the miniaturization of the microscope using diffraction grating lenses instead of glass lenses for more practical applications. Determining the internal temperature of a flame by passing a focused laser beam through the flame is an example of a practical application. The CSLH microscope is uniquely capable of non-intrusively measuring the 3D temperature of a specimen given a single viewpoint window for scanning with applications in the physical and biological sciences.

TABLE OF CONTENTS

List of Figures

List of Tables

Abbreviations and Terminology

2D	Two-Dimensional
3D	Three-Dimensional
AR	Anti-Reflective or Anti-Reflection
BC	Boundary Condition
BE	Beam Expander
BFL	Back Focal Length
BK7	Low dispersion high Abbe number common crown optical glass
BPF	Band-Pass Filter
BSM	Beam Steering Mirror
CAT	Computed Axial Tomography
CCD	Charge Coupled Device
CFD	Computational Fluid Dynamics
CPU	Central Processing Unit
CSA	Canadian Space Agency
CSLH	Confocal Scanning Laser Holography
CSLM	Confocal Scanning Laser Microscope
CT	Computed Tomography
DC	Direct Current or Bias Shift
DPSS	Diode Pumped Solid-State
EFL	Effective Focal Length
FC	Fringe Contrast
FFT	Fast Fourier Transform
FL	Focal Length
FS	Fringe-Spacing
FV	Fringe Visibility
HPF	High-Pass Filter
HVAC	Heating Ventilation and Air Conditioning
LHS	Left-Hand Side
LPF	Low-Pass Filter
LSB	Least Significant Bit
LSE	Least-Square Error

MSB	Most Significant Bit
NA	Numerical Aperture
OPL	Optical Path Length
PID	Proportional-Integral-Derivative
PIV	Particle Image Velocimetry
PL	Path Length
PSF	Point Spread Function
RHS	Right-Hand Side
RMS	Root-Mean-Square
SBR	Signal-to-Background Ratio
SNR	Signal-to-Noise Ratio
SP	Scan Position
SSE	Sum-Squared Error
STLH	Scanning Transmission Laser Holography
WFE	Wavefront Error

Acknowledgements

I would like to thank the following persons who contributed to this thesis:

Rodney Herring, for creating the conceptual CSLH microscope and for his holography expertise and guidance.

Peter Oshkai, for expert advice on fluid dynamics.

For the informative discussions with the advanced microscope research group at UVIC; Elaine Humphrey, Adam Scheutze, Kathryn Gomery, George Sawicki, Barbara Sawicki, Reston Nash, and Mike Fryer.

Stefan Atalick, Rob McLeod, and Songcan Lai for laying out the groundwork for the CSLH microscope and for developing the initial Zemax simulations.

Ian Soutar, for his expert instrumentation technical support and for his assistance with LabVIEW programming.

For the support from the adaptive optics group and the sharing of optics knowledge; Rodolphe Conan, Olivier Lardiere, Shaun Bowman, Peter Hampton, and Colin Bradley from the University of Victoria, and Jean-Pierre Veran and Glenn Herriot from HIA-CNRC.

~ Their contributions are very much appreciated ~

1 Introduction

Herring [1] designed and published the CSLH microscope in 1997 to non-intrusively measure the three-dimensional temperature and composition of a solid, fluid, or plasma (flame) specimen. The microscope was intended for science experiments [31-34] in a low vibration micro-gravity space environment, such as the study of Marangoni convection and heat transfer of a fluid specimen. To prevent the scan mechanism from inducing vibrations the specimen is kept stationary and is not rotated. Scanning is restricted to a single viewpoint window since the laser and camera do not rotate about the specimen. Specimen vibrations are minimized because of the rotation restriction and disturbance to fluid motion is negligible, which provides undisturbed measurement of minute fluid dynamics and heat transfer. Non-intrusive three-dimensional measurement in a vibration isolated microscope of this type was not achieved until now.

The temperature and composition of a specimen is determined from the index-of-refraction based on the optical properties of the specimen. A single laser provides a measurement of either temperature or composition and two lasers with widely separated wavelengths can provide for both temperature and composition. The CSLH microscope built for this research measures temperature only.

The CSLH microscope can be configured to operate in either transmission mode or reflection mode. In transmission mode, as configured for this research, the microscope measures the index-of-refraction given the thickness of a transparent specimen. In reflection mode the microscope can operate as a profilometer measuring the thickness of an opaque specimen given the index-of-refraction.

The design of a proof-of-concept CSLH microscope which scans from a single view point was analyzed, simulated, built, and evaluated to characterize its limitations and assess its performance. Research on the CSLH microscope led to the publishing of its design and simulations in journals [2-5]. Validation of the design includes theory, principles of physics, characterization with and without the specimen, limits of operation, and performance evaluation.

A focused beam rather than a collimated beam was used to probe the specimen because different data is recorded onto a hologram at each scan position. A collimated beam is undesirable because it will produce the same hologram for any scan step along the beam path (also defined as the optical propagation axis). A collimated beam will

provide information along a plane that is perpendicular to the beam path, but information will not differ along the depth axis (also defined as the optical propagation axis).

A focused laser beam in this configuration is considered a non-intrusive probe due to the undetectable energy loss to the specimen. Since the specimen does not absorb the laser wavelength, the laser will not impart any thermal energy. In comparison, a typical intrusive sensor such as a thermocouple probe will physically obstruct the flow and affect heat transfer since it is a heat sink with thermal mass. The non-intrusive laser of the CSLH microscope, which propagates entirely through the specimen, is focused to a small probe within the specimen. Following the confocal optics the re-collimated object and reference beams are combined to form a hologram.

The CSLH microscope uniquely combines confocal microscopy with digital holography to maximize the sensitivity of phase-shift measurements in a hologram to the laser that probes the specimen. A change in temperature or temperature gradient in the specimen produces a change in refractive index, which causes a fringe translation in the hologram. A phase-shift is represented by a fringe translation with a fringe translation of one fringe spacing being a 2π radian phase-shift.

A hologram is recorded for every scan position and the phase-shift information in each hologram is used as input data for the reconstruction algorithm. Scanning the focused probe beam within a fluid-cell that contains the fluid specimen produces multiple holograms. A unique low error reconstruction method was derived to accurately determine the three-dimensional temperature from the scanned holograms as part of this research.

The reconstruction process for the holograms is as follows: 1) Data collection of holograms formed by beam interference, 2) Obtaining phase-shift data from the holograms at the marginal rays of the beams, and 3) Reconstructing the 3D refractive index from the phase-shift data. Steps to reconstruct the index-of-refraction are shown in figure 1.1 below:

Figure 1.1: Reconstruction Process

Three different methods to determine the phase-shift in a hologram were explored and the method that produced the lowest error was selected based on a simulation study. The refractive index output array from the reconstruction algorithm was then

converted to a three-dimensional internal temperature array based on the optical properties of the fluid specimen.

The reconstruction error is primarily due to the cumulative phase-shift error from multiple holograms, optical aberrations in a hologram, spatial resolution of a fringe by the camera, and optical jitter produced from the mechanical vibrations of the pneumatically isolated optics table. Other possible error sources are scan positioning, optical and mechanical misalignment, and errors in determining a phase-shift given non-uniform fringe contrast from the optical aberrations in a hologram.

The CSLH microscope measures the internal temperature of a fluid specimen with minimal intrusion and complexity. Temperature measurements from the CSLH microscope are compared to a precision temperature (±0.05°C) needle probe thermocouple in order to validate the concept and prove the principles of physics and operation. Minimal complexity is based on selecting a Cargille Labs homogeneous reference refractive index fluid with known optical properties that closely matches the index-of-refraction for BK7 glass. All of the lenses and prisms in the microscope are BK7 glass.

A homogeneous silicone oil fluid specimen with known optical properties is used in the process of characterizing and validating the CSLH microscope. The known parameters of the fluid are the index-of-refraction to temperature and wavelength, which is contained in a polished glass rectangular fluid-cell cuvette. Steady-state conditions with constant temperature gradients of the fluid specimen provide a means to characterize the CSLH microscope.

The polished glass fluid-cell cuvette is 5x5 mm for the base and 40 mm high. The fluid-cell is shown in figure 1.2 below:

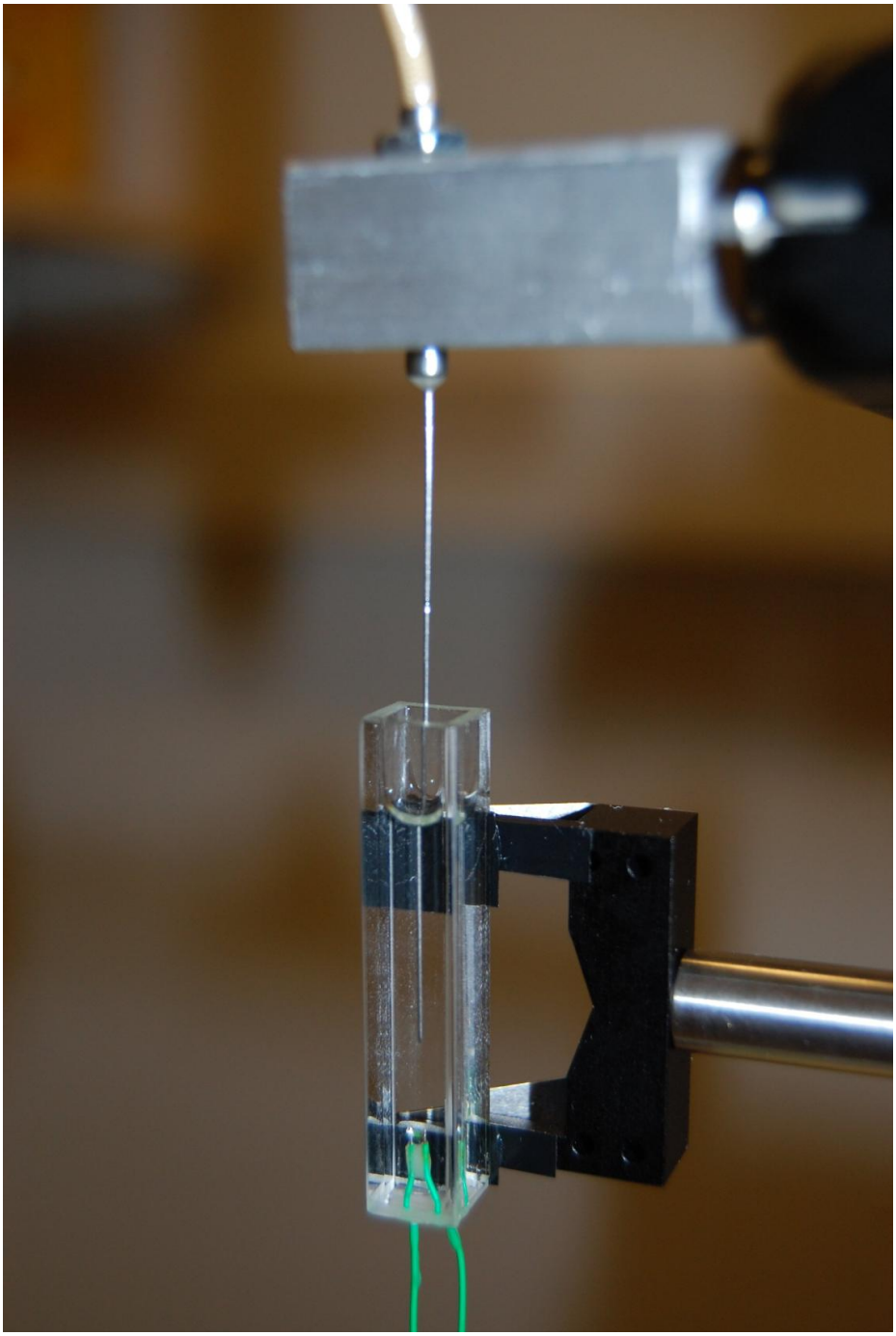

Figure 1.2: Fluid-Cell with Fluid Specimen, Needle Probe Thermocouple, and Heater

The focused laser probe propagates through the 5 mm depth while the side walls are used for observation, alignment, and measuring the boundary condition temperatures. A needle probe thermocouple is used to measure the boundary condition temperatures. A base centered point source heater is placed part way up from the bottom of the fluid-cell

to produce a radial thermal gradient for temperature measurement. The relatively low temperature difference of the heater relative to the ambient wall temperature provides radial heat diffusion by conduction with steady-state heat transfer conditions for measurement.

The microscope can measure a ±0.02° temperature difference given a 350 µm blur spot diameter at the focal point of the probe beam in the specimen. The temperature sensitivity is based on the average temperature difference throughout the fluid-cell. The reconstructed error is 1°C RMS for 128 temperature values in the three-dimensional 8 deep x 4 wide x 4 high computational domain cells of the fluid. The reconstruction error is due to 128 measured phase-shift values from 64 scanned holograms and 64 measured boundary condition values. The boundary condition values are measured at the side walls of the fluid-cell using the thermocouple. The measurement error of the thermocouple is ±0.05°C which is the most accurate repeatable measurement possible.

A recommended advancement for the CSLH microscope is maintaining stationary pupil planes during scanning by improving the optical lens design of the periscope relay lenses. This will reduce the movement of the focal point on the confocal optics pinhole apertures when steering the beams off the optical axis for scanning.

The object and reference beams projected to the camera were converged at a 0.25° angle, which produced the benefit of large fringe-spacing for imaging by the camera detectors, but it also increased the wavefront error of the beams due the longer path length. The path length from the projector optics that converges the two beams to completely overlap one another at the camera exceeds the path length of the microscope optics. A shallow beam convergence angle is required to provide a desired fringe spatial resolution at the camera. The CSLH microscope layout on the optics table is shown in figure 1.3 below:

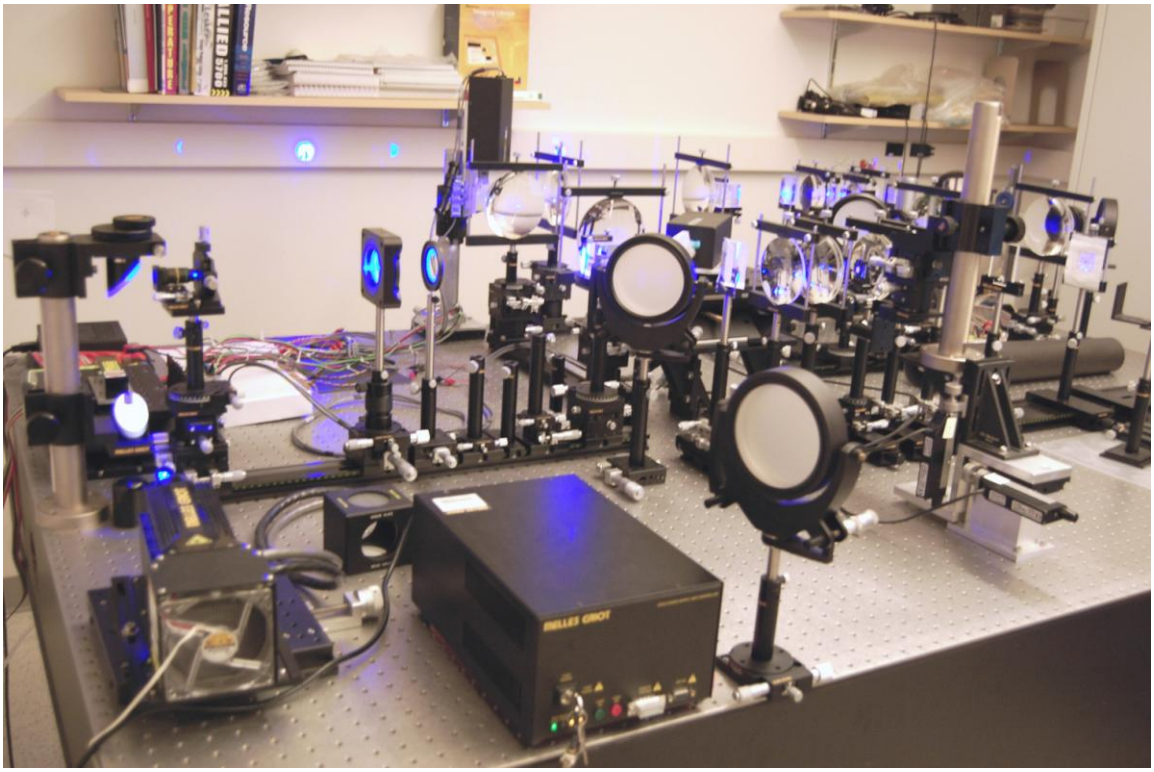

Figure 1.3: CSLH Microscope Layout on the Optical Table

The 457 nm blue laser is on the front left-hand-side corner of the optics table and the fluid-cell specimen is located near the back right-hand-side corner of the optics table. The hologram imaging camera is slightly out of view on the front right-hand-side corner of the optics table. The CSLH microscope used in this research covers a 5'x8' (150x250 cm) surface area of an optics table due to the complex optical design with a wavefront beam splitter section, beam steering mirror section for scanning, telecentric lens and optical loop, confocal optics section, and beam convergence optics. Slight modifications or redesign of the CSLH microscope would be required to accommodate different types of biological and materials science specimens, but the overall size would remain the same.

The proof-of-concept experiments in this research show successful operation of the design and provide a report on the performance of a unique microscope using a new method of microscopy. The favorable results demonstrate potential for further development in a space experiment. This new capability opens possibilities for digital imaging with low error reconstruction given a limited viewing angle restriction. The research presented in this thesis may lead to greater insights into the physics of nature and the exploration of fluid science using these new capabilities.

1.1 Scanning Aspects of the CSLH Microscope

Scanning with the CSLH microscope is accomplished by translating the focal point of the probe beam in the fluid specimen while a hologram is recorded at every scan position. The focal point of the probe beam within the specimen is translated by two precision galvanometer beam steering mirrors in the *xy*-axis. The optical lenses surrounding the specimen are moved along the optical propagation *z*-axis by a precision translation stage. Rectilinear scanning from a single viewpoint window or scanning through a limited viewing angle occurs by mounting the specimen to the optics table so that it is stationary during scanning. Minimizing vibrations of the specimen and accurate temperature measurements taken by the microscope are important conditions for obtaining reliable data from a micro-gravity space experiment; however, the limited viewing angle scanning condition places a burden on the reconstruction algorithm to produce a sufficiently low three-dimensional temperature error.

1.2 Confocal Aspects of the CSLH Microscope

The confocal feature of the CSLH microscope increases the phase-shift or fringe translation sensitivity in a hologram by placing a virtual aperture over the focal point of the beam probing the specimen, which reduces optical aberrations affecting the hologram. The focal point that is optically conjugate to the focal point in the specimen is formed by the confocal optics where the pinhole aperture is placed at this secondary focal point. Reducing optical aberrations reduces both the variations of fringe contrast and uneven fringe spacing across the hologram. The pinhole aperture blocks out most of the aberrated rays as a high frequency spatial filter, but the remaining spherical aberrations from the low f/# telecentric lens and the confocal optics are still transmitted through the pinhole aperture to the hologram.

Reducing optical aberrations with the pinhole aperture also reduces the transmitted beam intensity on the hologram. For example, the confocal pinhole aperture can reduce the 350 μm blur spot size of the focused beam in the specimen to 275 μm diameter spot and attenuate the beam by 75%. The spatial resolution is defined at the focal point of the probe beam in the specimen and at the hologram image plane for the camera. The optical resolution is defined by the 275 μm diameter blur spot size in the specimen. The detector spatial sampling resolution of the camera is defined by the number of detectors to image a fringe or the number of camera pixels per fringe-spacing.

A feature of the CSLH microscope is that the focal point on the confocal pinhole aperture remains stationary during scanning due to an optical loop that reverse propagates the beams back through the beam scanning section. Accurate pupil plane alignment in order to maintain a stationary focal point on the confocal pinhole apertures as the beams are scanned off the optical axis becomes critical. The alignment of the optics showed that a ±5° scan angle produces a change in pupil plane distance, which caused movement of the focal point on the pinhole aperture resulting in an uncompensated error.

1.3 Holography Aspects of the CSLH Microscope

The CSLH microscope uses principles of holography to measure both the amplitude and phase of an optical wave as the phase-shift is sensitive to a change in refractive index. An imaging microscope, in comparison, will measure only the amplitude or intensity of an optical wave.

The laser is split into an object beam that passes through the specimen and a reference beam that bypasses the specimen. Converging the two collimated beams to overlap one another produces a hologram within the overlapped region. An ideal hologram consists of constantly spaced fringes from the interference of the two coherent beams along with a constant fringe contrast across the hologram.

The phase-shift in a hologram occurs from a change in velocity of a light wave as it propagates through a medium, such as the specimen. The change in velocity is due to the index-of-refraction in the medium, which retards the phase of a wave as it passes through the medium relative to a reference wave bypassing the specimen. The object beam passing through the medium interferes with the reference beam in order to produce fringes in a hologram. The fringes in the hologram of the CSLH microscope translate as a phase-shift due to the cumulative or integrated index-of-refraction along the path length of the medium or specimen.

The CSLH microscope is designed with side-by-side propagating object and reference beams, which provides similar aberrations for the two beams at any point along the path length of the microscope. This provides some degree of isolation of the specimen relative to the optical aberrations of the lenses. The remaining optical aberrations that affect a hologram are compensated for by taking a reference hologram while the specimen is at constant temperature. Compensation using a reference hologram effectively removes the effects of optical aberrations from the specimen

measurements since the optical aberrations are constant for the specimen at either a constant or an elevated temperature.

A hologram image processing algorithm using a Fourier transform is used to determine the phase-shift of the overlapped beams at the camera for any point in the pupil.

1.4 Tomography and Reconstruction Aspects of the CSLH Microscope

Standard tomography uses rotational scanning of 180° to 360°about the specimen and records the integrated path length absorption through the specimen for each scan position. The scanned images that record the through-the-thickness properties of the specimen are combined by a reconstruction algorithm to reproduce an image of the interior object or specimen. Since the focused laser beam that probes the specimen passes through the entire depth of the specimen then some form of a tomography algorithm is required to reconstruct the three-dimensional temperature from the scanned holograms.

The phase-shift in a hologram is sensitive to the through-the-thickness cumulative effects of index-of-refraction in a specimen for a particular ray. The path length of the marginal rays of the focused probe beam in the specimen provides a diagonal path length in relation to the optical propagation axis. Placing a rotational scanning restriction on the CSLH microscope limits the scan angle to the 28° cone angle of the beam probing the specimen. The limited viewing angle restriction necessitated the derivation of the reconstruction algorithm.

Methods of limited viewing angle tomography were explored [37-40] after the discovery that the ill-posed condition requires a-priori information or extrapolated data in order to reconstruct. Standard methods of limited viewing angle tomography address the ill-posed condition as a result of insufficient information or correlated data. Additional information, extrapolated data or independent measurements are typically required to enable reconstruction and to reduce reconstruction algorithm error given scanning restrictions. Whether the approach to reconstruction is deterministic or statistical, supplying the missing data or information is necessary to prevent a reconstruction matrix singularity.

The pursuit of standard methods of tomography was abandoned and examining the fundamental principles of optics and reconstruction was explored instead. Defining a scanning geometry that eliminated correlated measurements from computational grid-

cell to grid-cell or scanning steps reduced the condition number of the reconstruction matrix. A more distributed scanning geometry of the CSLH microscope can change the reconstruction matrix from a singular state to an ill-conditioned state, but it will not reduce the reconstruction error to an acceptable level. Methods of singular value decomposition, eigenvalue decomposition, and matrix pivoting for Gaussian elimination to pseudo-inverse the reconstruction matrix still produced excessive error.

A unique limited viewing angle tomography algorithm named the “wily” reconstruction algorithm was derived for the CSLH microscope. The need for the “wily” reconstruction algorithm is due to the limited angle scanning which produces a sparse reconstruction matrix. A general scanning method of moving the focal point of the probe beam within the specimen produced an indeterminate condition for reconstruction because of a non-invertible singular reconstruction matrix. Reconstruction is impossible with a singular reconstruction matrix that produces a zero determinant. A degenerate or ill-conditioned reconstruction matrix with a high condition number produces an unacceptably large reconstruction error. A more complex scanning geometry produced an ill-conditioned matrix with an excessively high reconstruction error, which was due to correlated data from over-sampling and insufficient independent information.

Introducing boundary conditions converted the matrix from an ill-conditioned state to an invertible state with low condition number even though the matrix is extremely sparse due to the shallow cone beam angle. The “wily” matrix reconstruction algorithm operates with a specific scanning geometry and with boundary conditions as a-priori information in order to reconstruct the three-dimensional index-of-refraction with negligible error.

The “wily” matrix reconstruction algorithm reduces reconstruction error to a negligible value by:

1) Specifying a particular scanning geometry in order to produce independent phase-shift measurements, and 2) defining boundary conditions along the side walls of the fluid-cell as additional information. The independent phase-shift measurements are based on the non-correlated optical path length equations through the fluid-cell computational domain. The reconstruction matrix is quite sparse due to the shallow scan angle, but yet is invertible with a low condition number. Since this matrix is surprisingly invertible matrix then I have called it the “wily” reconstruction method. Defining a specific scanning geometry provides independent hologram measurements such that the phase-shifts in the holograms are sufficiently uncorrelated. Defining boundary conditions will

convert the sparse reconstruction matrix from a singular or degenerate condition to an invertible matrix with a low condition number.

In a general way the unique “wily” reconstruction method allows tomography for ordinary optical microscopes since the beam has a normal angle of incidence to the specimen. The CSLH microscope has the same incident angle to the specimen as an ordinary visible light microscope, but has a fixed 0.24 numerical aperture due to the large 28° cone angle of the beam focused within the specimen.

1.5 Challenges and Trade-Offs of the CSLH Microscope

The biggest challenge of achieving low reconstruction error was the restricted scanning from a single viewpoint window [2,3] which limited the rotational scan angle to the cone angle or the numerical aperture of the beam probing the specimen. This scan angle was restricted to the 28° cone angle or an f/2 f-number for the focused beam. Restricting rotational scanning to a single viewpoint window increased the reconstruction error due to the limited viewing angle scanning geometry. Increasing the cone angle of the focused beam will reduce the sparseness of the reconstruction matrix, which provides the benefit of reducing the reconstruction error.

The fundamental trade-off is that as the cone angle of the probe beam is increased the reconstruction error decreases, which also creates the negative consequence of increased optical aberrations. Increasing the optical aberrations increases the blur spot size of the probe beam focal point, which decreases optical scanning resolution in the specimen. In addition, optical aberrations affect the hologram by increasing fringe contrast variations across the hologram, which also increases the error in determining a phase-shift. Ideally, only the crossing rays through the focal point of the beam probing the specimen will contribute to the formation of a hologram with uniform or constant fringe contrast. Constant fringe contrast across a hologram will provide for more accurate determination of the phase-shift. A compromise was reached by selecting the f/2 for the optics to focus the probe beam in the specimen.

1.6 Ground Based and Space Based Environments

A micro-gravity experiment requires lower vibration levels than a ground experiment; therefore, the sensitivity of the CSLH microscope is increased to more accurately resolve temperature and composition at a lower background noise level. Increased

microscope sensitivity increases the requirement for accurate optical alignment, lower optical aberrations, lower noise cameras and sensors, and lower noise data acquisition.

Holography is particularly sensitive to minute vibrations and requires vibration isolation since small fringe-shift displacements are approximately λ/80 waves on a hologram. Fringe-shift resolution or small fringe-shift displacements are in the order of the wavelength of the laser which necessitates a vibration isolated optical table.

The benefit of a rotational scan mechanism is a significant reduction in three-dimensional reconstruction error, therefore, rotational scanning is typically found in tomographic reconstruction scanners or the Computerized Axial Tomography (CAT) scanners used in medical radiology.

1.7 Optical Resolution of the CSLH Microscope

The optical resolution of the CSLH microscope is affected by the:

- Wavelength and coherence length of the laser
- Focal length of the optics and numerical aperture at the specimen
- Beam coherence degradation and increasing wavefront error over path length
- Beam de-collimation from optical aberrations of the lenses
- Beam convergence angle and path length to overlap the beams and form a hologram, which defines the fringe-spacing
- Detector sampling of a fringe by the camera
- Spatial sampling resolution (> 8 pixels/fringe) which decreases the error in determining the phase-shift in a hologram especially since the fringe contrast is non-uniform across the hologram
- Focal point diameter or blur spot size of the probe beam in the specimen based on the f-number or f/# focal ratio of the telecentric lens that focuses the object and reference beam in the specimen region
- Misalignment of the overlapped beams on the hologram that coincides the marginal rays for the two beams

1.8 Limitations and Performance of the CSLH Microscope

A limitation of determining the temperature is that the phase-shift between scan positions must be less than 1 fringe spacing or 2π radians, which sets the maximum temperature differential between scan positions. Phase-unwrapping using two lasers with closely separated wavelengths can increase the temperature range and also extend

the capability to measure both weak phase object and strong phase object specimens. A weak phase object is a specimen with a low temperature gradient and a strong phase object is a specimen with a high temperature gradient such that the phase-shift between scan positions exceeds 2π radians. Phase unwrapping using two lasers will provide a phase-shift or temperature dynamic range that is independent of the scan step distance. The heated fluid contained in the fluid-cell is a weak phase object specimen and only a single laser is used. Phase-unwrapping is not possible with the CSLH microscope in this research and the only other option is to reduce the scan step size in the computational domain grid-mesh of the fluid.

Other limitations of the CSLH microscope are the camera radiometric sensitivity, dynamic range, minimum exposure time, and frame rate. The hologram fringe intensity is attenuated over the long path length distance from the confocal optics to the hologram image plane at the camera. The camera radiometric sensitivity and dynamic range is critical due to the attenuation from the increasing wavefront error and beam de-collimation.

The research on this proof-of-concept CSLH microscope establishes a benchmark for resolution, sensitivity, and performance. The optical resolution is based on the blur spot size of the probe beam focal point in the specimen. The blur spot size at the focal point in the specimen is also affected by coma aberrations since the beams are initially tilted in order to produce side-by-side parallel propagating object and reference beams through the specimen. The spatial resolution depends on the spatial imaging resolution of the hologram fringes with the camera, the phase-shift error from the hologram, and the reconstruction algorithm error. The wavefront error increases with overall path length and when the path length exceeds the coherence length of the laser then the fringe contrast or fringe visibility significantly decreases. Beam de-collimation is reduced by placing an iris diaphragm following the beam expander that truncates the beam for uniform aperture illumination; however, the iris diaphragm introduces a diffraction source that will produce a bell-shaped varying fringe contrast across the hologram, Hecht [41].

The sensitivity is based on the refractive index-to-temperature slope and the fringe phase-shift-to-temperature slope. The dynamic range sensitivity of the microscope is the resolvable temperature to maximum temperature range given a weak phase object specimen. The performance is the capability of the microscope to resolve an average change in temperature in the specimen and the reconstructed three-dimensional temperature error at any specific point in the specimen.

The overall reconstruction error is primarily due to measurement error, the effects of aberrations, and vibrations. The three-dimensional reconstruction algorithm requires a particular scanning geometry through the fluid-cell, phase-shift data for every scan position, and boundary conditions in order to accurately reconstruct the three-dimensional temperature.

Scanning is 625 μm/step from scan position to scan position and the positional resolution of the motorized translation stages is 0.1 μm. The discrete grid-cell volume is assumed to have a constant index-of-refraction and temperature. A diagram of the computational domain at a single elevation plane is shown in figure 1.8.1 below:

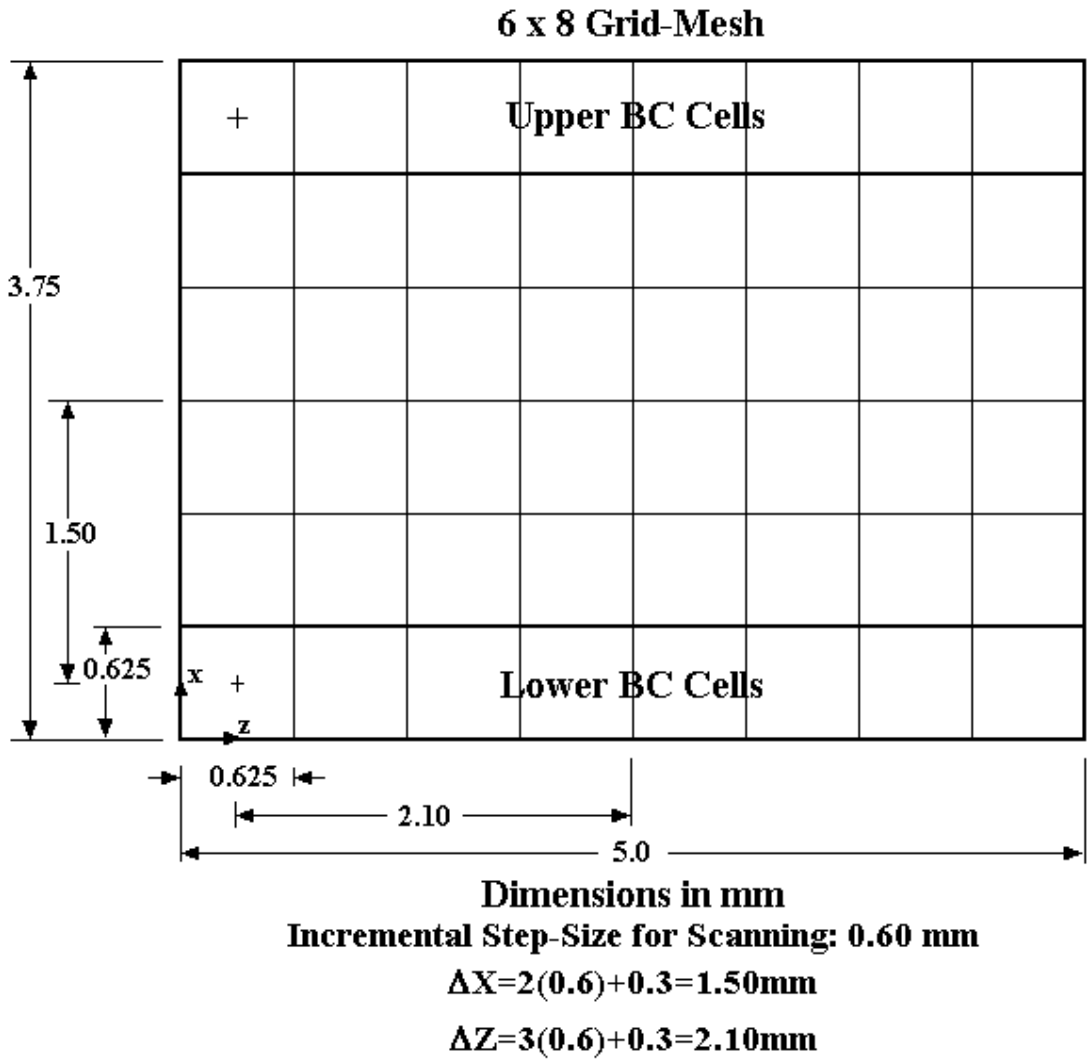

Figure 1.8.1: Computational Domain for a Plane along the Depth and Width of the Fluid-Cell

There are 4 vertical elevation planes in the *y*-axis with a spacing of 625 μm to complete the three-dimensional computational domain volume. A phase-shift is

determined at the two coincident marginal rays for each hologram. Scanning the thermocouple through the boundary grid-cells also contributes to the reconstruction error due to measurement error and the assumption of constant temperature for each grid-cell. The continuous temperature gradients from the heated fluid are approximated by the discrete grid-cells through the computational domain region of the fluid-cell.

1.9 Dissertation Outline and Overview of the Appendices

The CSLH microscope is described in the background section of the thesis along with defining the basic theory of operation. The section describing the CSLH and Scanning Transmission Laser Holography (STLH) microscopes provides more information on the reference hologram, descriptions of the optical sections and lenses, image processing of the hologram, and description of the reconstruction method. The STLH microscope is a simplified version of the CSLH microscope. The STLH microscope was used to evaluate the accuracy in optical alignment by providing a baseline for performance and to provide holograms under conditions of minimal optical aberrations. The section describing the development of the CSLH microscope defines more detailed principles of operation and explains the derivation of the reconstruction algorithm. This section also includes the optical layout and the optical component configuration. The error analysis section examines the effects of wavefront error on the ability to detect a fringe-shift in a hologram, fringe-shift resolution at relatively low spatial sampling of the fringes, and fringe contrast sensitivity to wavefront error. The reference data and experiments section addresses the recording of a reference hologram, the fringe sensitivity to a change in temperature experiment, and the CSLH microscope temperature reconstruction experiment. The CSLH microscope is characterized for operational limits and performance in the following section of the thesis. Conclusion, recommendations to improve the performance of the CSLH microscope, and applications follow to close the dissertation.

The appendix includes sections addressing hologram image processing, computational fluid dynamics modeling of the fluid-cell, calibration, and vibration measurements. A mathematical approach to hologram image processing is presented in the appendix section “Digital Band-Pass Filter (BPF) Algorithm Analysis to Improve Phase-Shift Detection”. Only the algorithm derivations and their filtering performance to a waveform containing three discrete frequencies are presented. The extensive

appendix shows careful adherence to experimental process given the multi-disciplinary aspects of the microscope with complex interfaces involving:

- Optical analysis, simulation, and design (physical ray tracing optics and wave optics)
- Optical instrumentation (optical-mechanical alignment, calibration, and computer control)
- Feedback control for actuators and translators
- Mechanical design of support structures
- Electronics design for sensor signal amplification
- Vibration isolation and optical jitter suppression
- Fluid dynamics simulation of the heated fluid in the fluid-cell
- Digital signal processing of hologram images to isolate the spatial frequency of the fringes
- Alignment and calibration
- Wavefront sensing as the microscope is an interferometer with no specimen
- Near real time sensor data acquisition
- Computer control for experiments through LabVIEW
- Vibration measurement and assessing the pneumatic vibration isolator for the optics table

The appendix also provides background information, analysis, simulations, calibration information, and details of the setup for experiments so that this research can easily be applied to other applications.

2 Other Three-Dimensional Scanning and Imaging Methods

Other methods for scanning and imaging in three-dimensions are: Particle Image Velocimetry (PIV) typically used for the study of fluid dynamics and tomography, typically used in medical CAT scanning with an x-ray source.

2.1 Particle Image Velocimetry (PIV)

Particle Image Velocimetry (PIV) tracks a tracer in a fluid frame-by-frame using a high speed camera. The PIV tracker can measure the velocity of the flow of particles in fluids in three-dimensions. A tracer in the fluid is a reflective neutrally buoyant micro-particle that is added to the fluid. A pulsed laser illuminates the particles for imaging on the high-speed camera. Tracer particles can be added to a gas, vapour, or liquid. In the case of a gas or vapour, oil is typically used for a tracer. In the case of a liquid, neutrally buoyant fluorescent particles are typically used. The tracer particles introduce an intrusive variable to the flow dynamics, but are considered to have a negligible effect on the flow for most applications. PIV imaging typically uses a flood beam to illuminate the tracer particles within a volume. An off-axis high speed camera tracks the tracer particles and frame by frame the velocity of the tracers is determined from the change in position. Closely spaced tracers can produce an ambiguity or velocity error if the tracker misidentifies the tracer from frame-to-frame.

2.2 Standard Tomography and Methods for Reconstruction

Tomography scans slice-by-slice through an object in very small steps so that accurate reconstruction of the interior object is possible. Computed Tomography (CT) or Computed Axial Tomography (CAT) scanning are non-intrusive measurement methods of producing 2D images from 3D information by scanning the patient or specimen about a fixed rotation point. Common scanned x-ray or gamma-ray medical images are mathematically reconstructed using the measured line integrals for beam absorption in transmission mode operation. In ultrasound imaging the emission source is an acoustic beam that is reflected off and scattered by the object. The collected image information is through reflection mode operation. Ultrasound head units co-locate the emitter with the sensor and scanning is typically done by hand motion of the head.

There are several tomographic methods used for image reconstruction [7] such as: filtered back-projection, convolution back-projection, Fourier transform method, algebraic

iterative convergence method, and geometric ray tracing. Computed tomography typically utilizes a collimated beam that is rotationally scanned about a central pivot point within the patient. Tomography scanning angle steps of 22.5º swept over a 360º arc are shown in figure 2.2.1 below:

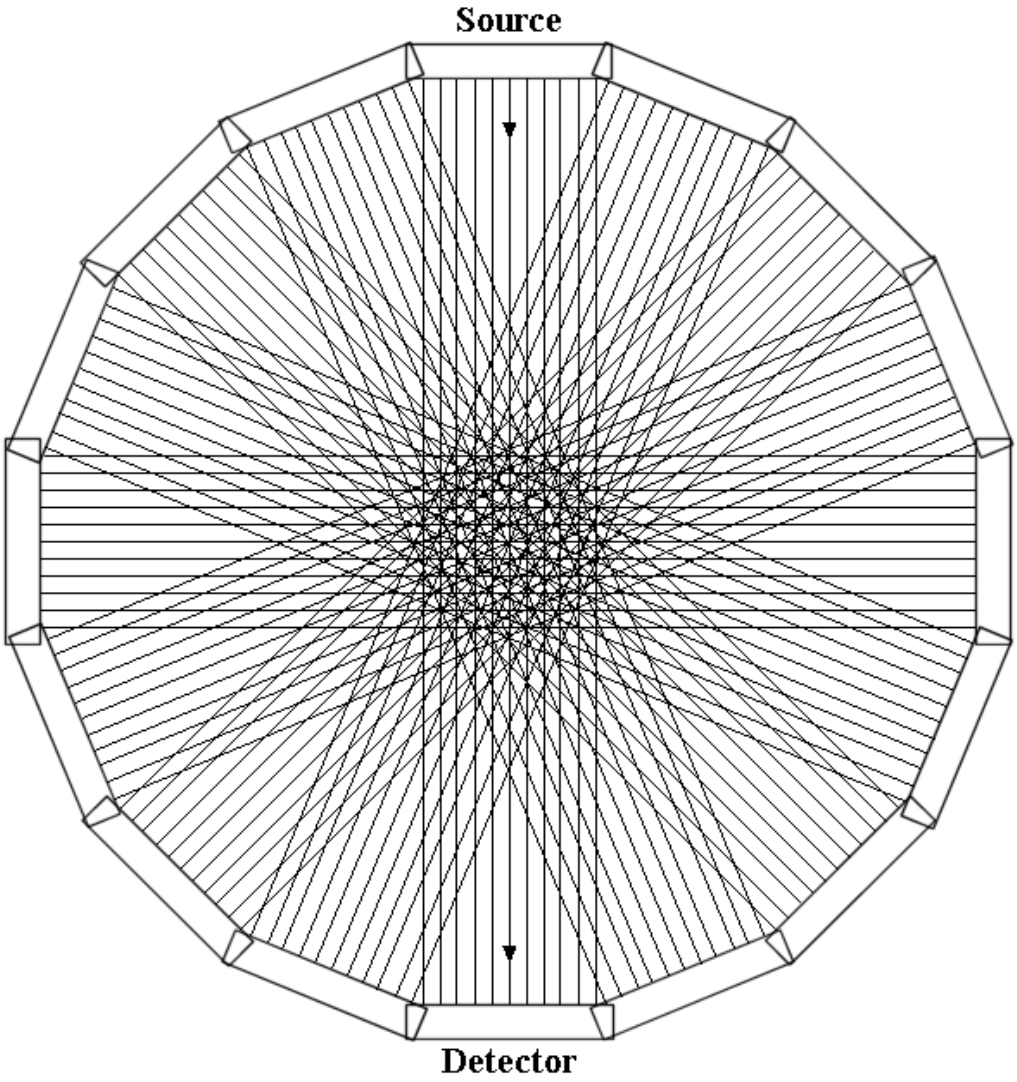

Figure 2.2.1: Tomography Scanning Configuration about a Fixed Central Point

The pivot center is a central point in the patient or a target point since the region for accurate reconstruction is the area of highest ray crossing density or the region near the pivot or center-of-rotation. Typical CT scanning is in steps of 5º or less as the rotation is between a 180º to 360º arc. Limited viewing angle tomography occurs when accessibility is limited or when scanning volume is reduced in order to save time. In situations where the scan mechanism is obstructed by a physical object the scanning can be restricted to limited viewing angles. Limited viewing angle tomography will produce errors in certain

planes or regions due to viewing angle restrictions. The error in three dimensions will be in the form of an ellipsoid and its orientation must be determined in order to properly interpret the image.

The limited viewing angle for the CSLH microscope is 28° which will produce substantial reconstruction error when applying a standard tomography reconstruction method. The “wily” reconstruction matrix was derived using a geometric ray tracing line integral method as a deterministic method that is potentially more accurate than achieving reconstruction using a statistical approach.

The fundamental difference between the “wily” reconstruction algorithm and standard methods of tomography is that standard methods of tomography require a fixed point of rotation, typically about the center of the object, and the “wily” does not as the source or probe is scanned three-dimensionally through the specimen. Because of this difference the “wily” reconstruction method cannot be used for standard methods of tomographic reconstruction.

3 BACKGROUND

A history on the diffraction properties of light that leads to wave theory is explained in this section. Wave theory led to the development of Fresnel zone plates that are used in holography for reconstruction. The phase-shift of a light wave propagating in glass is also discussed since the fluid-cell affects the optical phase-shift of the object beam. The microscope generation of a 1-D hologram is discussed as the line scan camera is used to record a one-dimensional hologram. The restriction of scanning from a single viewing window for a convergent focused beam is presented to show the collection of different information for scanning along the optical path or longitudinal axis. The convergent focused beam in the fluid-cell is compared to a collimated beam of constant diameter in terms of collecting different information from scan-to-scan step. A short description of confocal microscopy and holography as they relate to the CSLH microscope concludes this section.

3.1 Background

In the 17^{th} to 18^{th} century Sir Isaac Newton pioneered the theory of light as a particle and Huygens delved into the theory of light as a wave. At the time fine lines in glass were used as a diffraction grating to disperse light into a spectrum. Diffraction of light can only be described with wave theory and scientists such as Fresnel, Fraunhofer, Kirchoff, and others supported the wave theory. James Clark Maxwell showed that light is a component of both electric and magnetic fields as the electric and magnetic fields are orthogonal propagating waves.

The invention of holography is attributed to Dennis Gabor [8-11] who invented the method of “Image Formation by Reconstructed Wavefronts” in 1948. He received the Nobel Prize in physics in 1971 for his pioneering research in wavefront reconstruction. Gabor used an incoherent mercury-arc lamp source that pre-dated the invention of the laser in his experiments. This experimental setup did not permit him to fully substantiate the theories of diffraction and interference that requires a coherent laser source. Gabor explored optical reconstruction as a means to improve the resolution in electron microscopes. Electron microscopes have shorter wavelength beams than optical sources but are limited in resolution by the electron-optics lenses that produce significant spherical and geometric aberrations. Images from an electron microscope could have higher resolution given a hologram containing the conjugate geometrical aberrations

found in the electron microscope. G.L. Rogers of Dundee, Scotland [12,13] was fascinated with Gabor's papers and coined the term "holography", applying it to his new photographic procedure which produced recorded images in three-dimensions or holograms. Gabor used Fresnel zone plates in the late 1940's to develop holography and reconstruction. A zone plate consists of radial symmetric rings known as Newton's rings or Fresnel zones, which alternate between opaque and transparent. The phrase "Newton's Rings" was coined by Lord Rayleigh in 1871. Light is diffracted by the rings and converged to a central focal point. A zone plate is shown in figure 3.1.1 below:

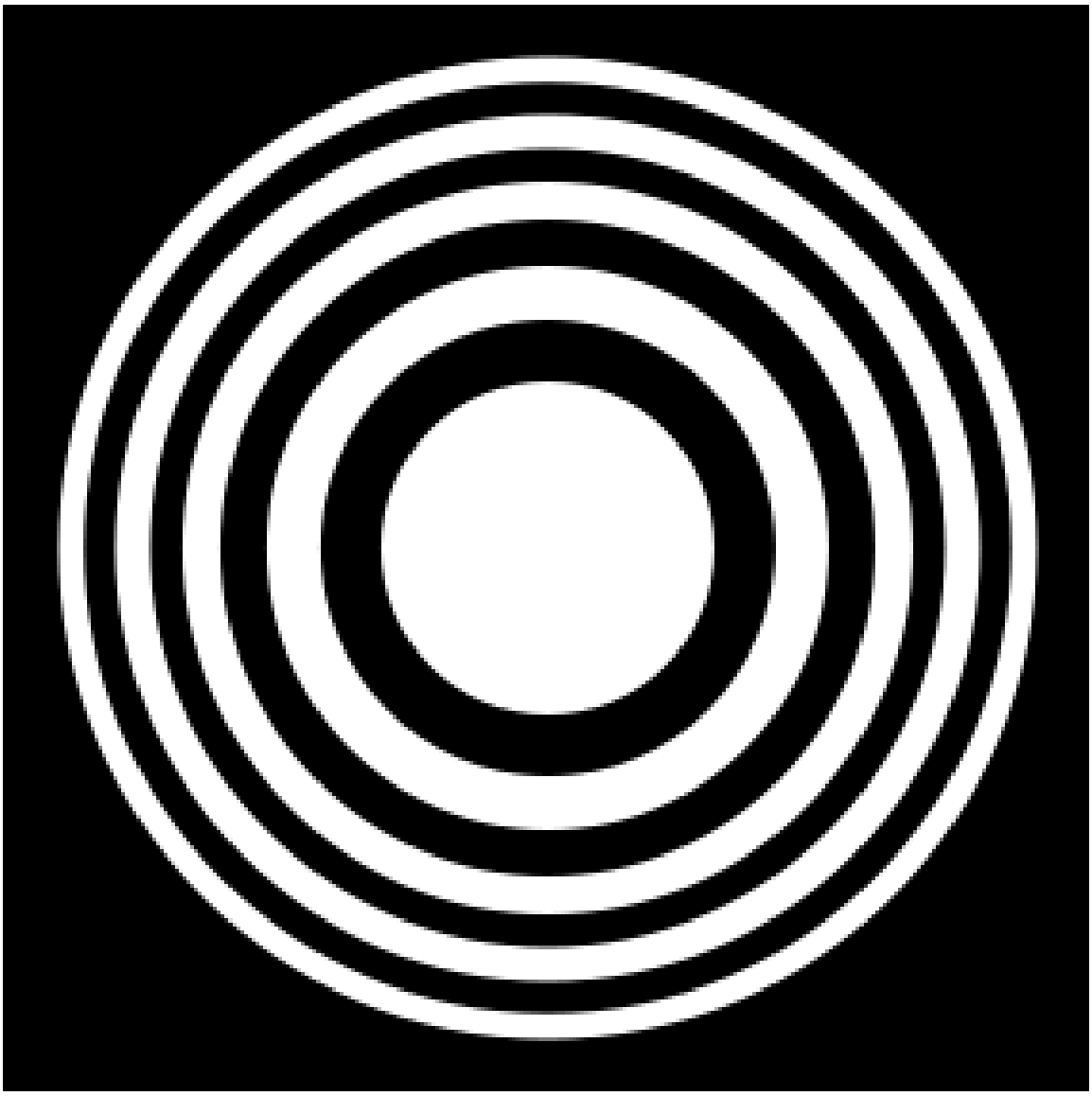

Figure 3.1.1: Binary Zone Plate with Alternating Light and Dark Rings

The high contrast edges create high spatial frequency components in the Fourier transform of the zone plate, which is typically illuminated uniformly with a coherent

beam. Rogers suggested a zone plate with edges that gradually vary in opacity. A zone plate that gradually varies in opacity with a sinusoidal waveform produces a single focal point and is equivalent to a converging lens. A sinusoidal varying opacity zone plate is shown in figure 3.1.2 below:

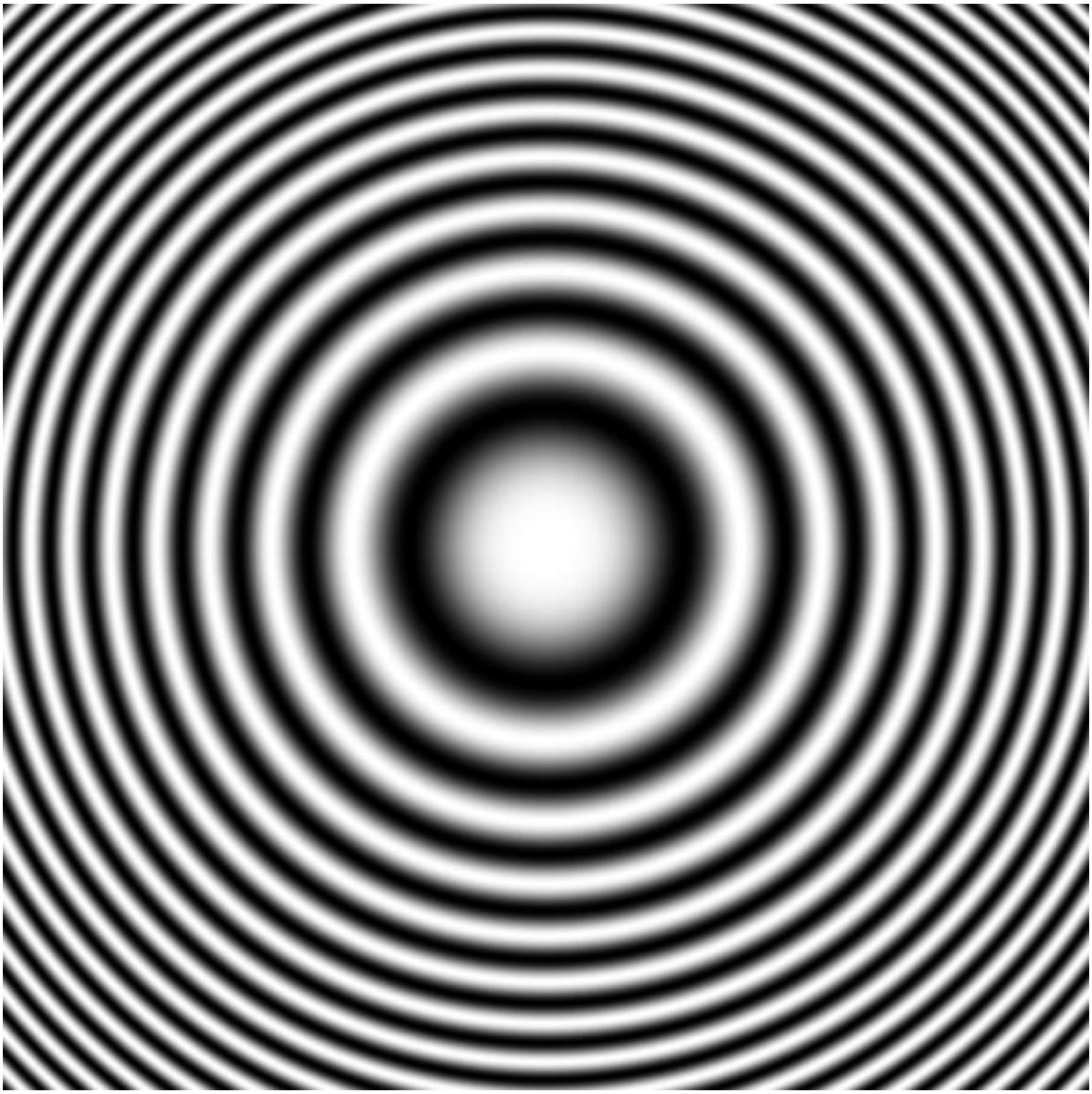

Figure 3.1.2: Gradient Edges Zone Plate with Sinusoidal Variation

Gabor's idea was to design an optical system using holography to correct the aberrations created by the electron lenses and produce a nearly aberration free image. The idea of producing a zone plate to improve resolution is possible since the emission source generates coherent electron beam waves. A diffraction pattern on an emulsion plane or a Fresnel zone plate can represent electron microscope lens aberrations, which has been used by Tonomura [21] to improve the resolution of an image for an electron

microscope. The zone plate incorporates the conjugate aberrations of the electron microscope optics for image enhancement.

An image produced by the electron microscope is enhanced by the holography optics since the spherical and geometric electron-optic aberrations would be corrected. A technical challenge for Gabor was obtaining the precise alignments for the zone plate. Alignments included the accuracy of the emulsion process that defines the resolution of the opacity along with positional registration into the holography optics. Even the surface quality of the glass zone plate can affect the wavefront correction for reconstruction. A phase-shifting zone plate is placed at a pupil plane in order to reconstruct a higher resolution image using a holography microscope in order to attain the diffraction limited resolution of the electron microscope. An optical transfer function representing the electron optics spherical aberrations and defocus requires a precise mathematical model to accurately produce a zone plate and reconstruct an image.

Frits Zernike [14-16] received the Nobel Prize in 1953 for the phase contrast method and microscope that could measure the index-of-refraction or thickness of a specimen. Resolution enhancement using methods of holography for image reconstruction has been developed since the 1960's with the advent of coherent laser sources and electron beam emission sources. Electron microscopes configured in holography mode operation have recently been explored by Tonomura [20-23] and Lichte [24-25] for high resolution sub-atomic level measurements since the resolution of a hologram is higher than that of an electron microscope configured in imaging mode. Holography mode configuration can detect a minute phase-shift which can yield greater discernable information of a specimen.

The concentric circular rings on a CSLH microscope hologram is due to Fresnel diffraction off the optical components. Fresnel diffraction is the near field out-of-focus condition where the distance from a point source radiator to a pupil plane is short and the wavefront has a spherical curvature. On the other hand, Fraunhofer diffraction is the far-field in focus condition where the distance from a point source radiator to a pupil plane is sufficiently long that the wavefront is assumed planar with no curvature and the source considered to be at an infinite distance. Spherical aberrations of the optical components, aperture functions of the lenses, and in particular the diffraction from an iris diaphragm beam stop will contribute to de-focus of a focal point which generates Fresnel fringes. The Huygens-Fresnel principle considers the generation of multiple sources from wave diffraction and wave refraction as shown in figure 3.1.3 below:

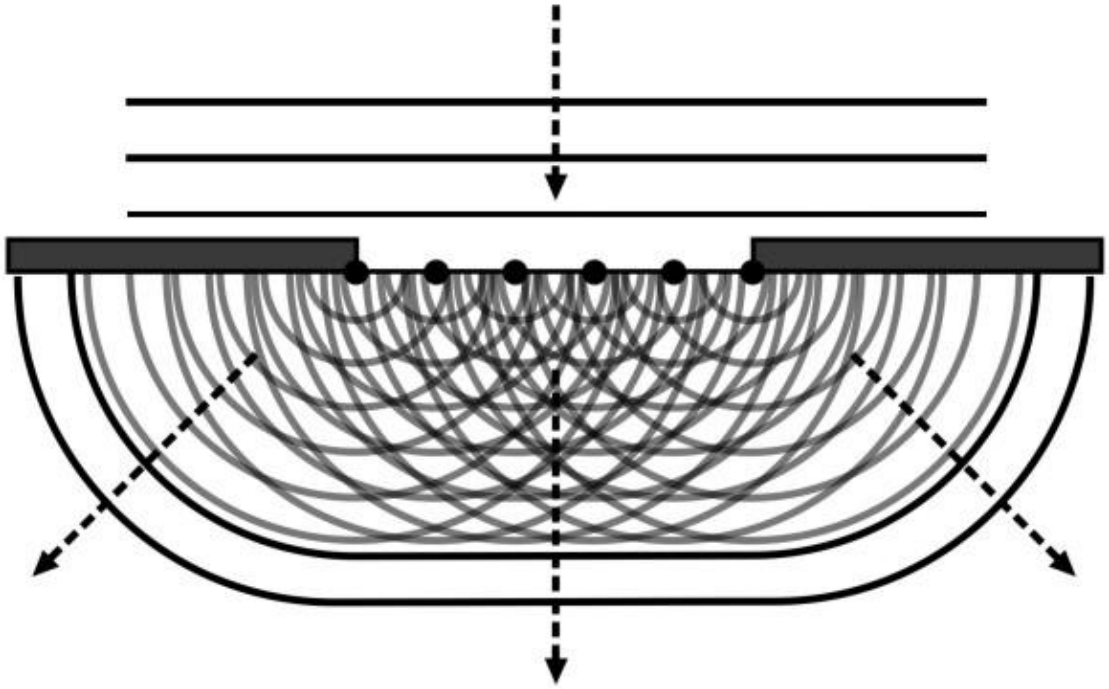

Figure 3.1.3 Huygens-Fresnel Principle for Multiple Sources of Refraction and Diffraction

Focusing lenses and optical prisms, such as a Fresnel biprism and optical wedge, produce wave refraction. An edge of a prism, such as the apex of a Fresnel biprism, and aperture beam stops, such as an iris diaphragm, produce wave diffraction. The optical components of the CSLH microscope produce additional sources other than the laser source primarily based on properties diffraction. The wave interference in a hologram from de-focus of a blur spot reflects a change in ray angle or convergence angle for a subset of optical rays that can produce a few fringes within the overlapped beam region. Another interpretation for de-focus is the variation in optical path length for rays across the beam at a defined focal plane.

An aberration free hologram for the CSLH microscope would not have curved or circular fringe lines, but instead the fringe lines would be straight which would represent constant spaced fringes across the hologram.

3.2 Phase-Shift in Optical Glass

The phase-shift (φ) in optical glass produces wave retardation as the beam exits the glass at the same wavelength as when it entered the glass. The wave retardation becomes a phase-shift or fringe translation in a hologram. The effect of a change in

refractive index from air to glass back to air on phase-shift is shown in figure 3.2.1 below:

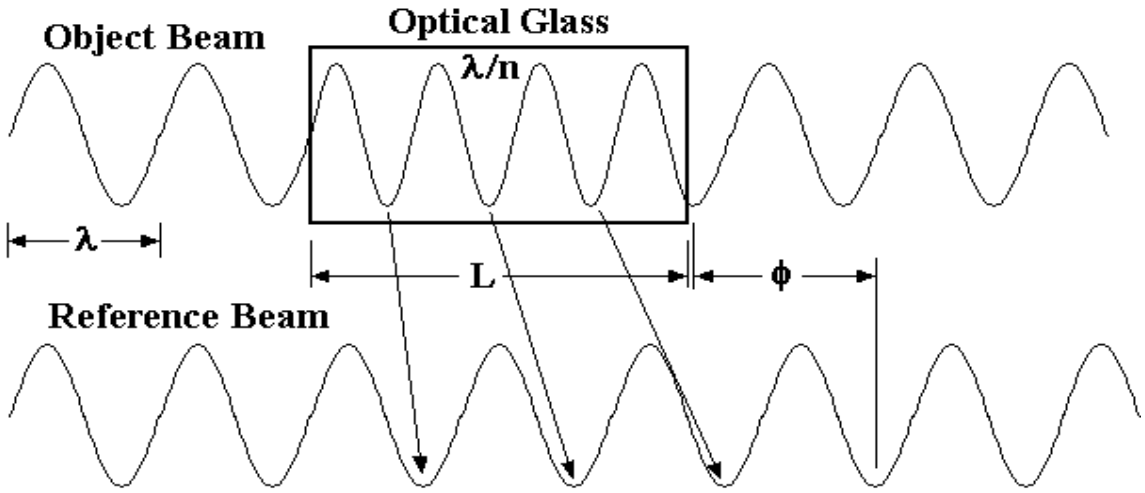

Figure 3.2.1: Object Beam Propagation and Wave Delay through Optical Glass

The wavelength is shortening as the wave propagates through glass of constant refractive index (**n**) and the wavelength is λ/**n** within the glass. The wave returns to the same wavelength as the source or reference when it exits the glass; therefore, the glass retards the wave with a phase-shift (φ).

Snell's Law for Refraction: $\frac{\sin\theta_1}{\sin\theta_2} = \frac{v_1}{v_2} = \frac{n_2}{n_1} = \frac{\lambda_1}{\lambda_2}$ (3.2.1)

Velocity or Speed-of-Light in Medium: $v = f \cdot \lambda$ (3.2.2)

Change in Velocity: $dv = f \cdot d\lambda + \lambda \cdot df$ (3.2.3)

Constant Carrier Frequency: $dv = f \cdot d\lambda + \lambda(0) = f \cdot d\lambda$ (3.2.4)

$$f = f_1 = f_2 = \frac{dv}{d\lambda} \quad (3.2.5)$$

$$\frac{v_1}{\lambda_1} = \frac{v_2}{\lambda_2} \quad (3.2.6)$$

$$\frac{v_1}{v_2} = \frac{\lambda_1}{\lambda_2} \quad (3.2.7)$$

The wavelength to refractive index relationship is given as $n_{air} \cdot \lambda_{air} = n_{gls} \cdot \lambda_{gls}$ (3.2.8)

$$\lambda_{gls} = \frac{n_{air}}{n_{gls}}\lambda_{air} = \frac{1}{n}\lambda = \lambda / n = \frac{0.457\mu m}{1.5} = 0.305\mu m \quad (3.2.9)$$

$\lambda_{air} = 0.457 \mu m$ is the wavelength for the blue laser

$n_{gls} = 1.5$ is the approximate index-of-refraction for BK7 glass at the laser wavelength

The phase-shift (φ) of the Object Beam relative to the Reference Beam is approximately 1.25 waves as seen in the figure above.

Let the Optical Path Length (*OPL*) of the Reference Beam be Length (*L*) or

$OPL_{ref} = L = const$ since

the Index-of-Refraction for air is $n = 1$.

The *OPL* for the Object Beam passing through the optical glass can be over finite Path Length's

(*ΔPL*'s) for a given index-of-refraction (n_k) thus,

$$OPL_{obj} = \int_0^L n \cdot dl = \sum_k n_k \cdot \Delta PL_k \quad \text{where} \quad L = \sum_k \Delta PL_k \tag{3.2.10}$$

The relationship of measured phase-shift to *OPL* is given as

$$\Delta OPL = OPL_{obj} - OPL_{ref} = \lambda \cdot \Delta\phi + 2\pi n \cdot \lambda = (2\pi n + \Delta\phi)\lambda \tag{3.2.11}$$

with the phase unwrapping parameter: $n = 0,1,2,3,4,\ldots$

The measured phase-shift on the hologram is given as $\Delta\phi = \phi_{obj} - \phi_{ref}$ (3.2.12)

Therefore, the measured phase-shift on the hologram can be related to index-of-refraction.

A lens will delay the phase differently for rays within aperture or pupil plane because as the rays refract and change direction through the lens. Redirecting the rays causes a phase-shift, which is a function of the refractive index times the distance along the path length. The phase-shift is radially symmetrical about the center of a standard lens given an on-axis incident beam.

3.3 Microscope Generation of a Hologram

The hologram is represented by a wave equation:

$$I(x) = I_{offset} + I_{peak} e^{i(k_x(x - x_0) + \phi)} \tag{3.3.1}$$

Spatial Frequency: k=1/Fringe-Spacing or

Spatial Frequency: $k_x = 1/fs$ (3.3.2)

Fringe-Spacing: $fs = 209.5 \mu m / wave$ of a fringe is assumed constant or

$fs = 209.5\mu m / \ fringe$

The fringe-spacing is constant due to the constant wavelength of the laser and the constant beam convergence angle that is provided by an optical wedge.

Displacement or Position: x (μm) from the pixel or detector value on the camera

Intensity Offset: $I_{offset} = (I_{\max} + I_{\min})/2$ is the bias intensity midway of the dynamic range

or $I_{offset} = (1024 + 0)/2 = 512$

Intensity Peak: $I_{peak} = (I_{\max} - I_{\min})/2 = (1024 - 0)/2 = 512$ (3.3.3)

Phase-Shift: $\phi = \phi(x)$ where x is a reference point along the camera x-axis

The wave equation for a hologram is shown in figure 3.3.1 below:

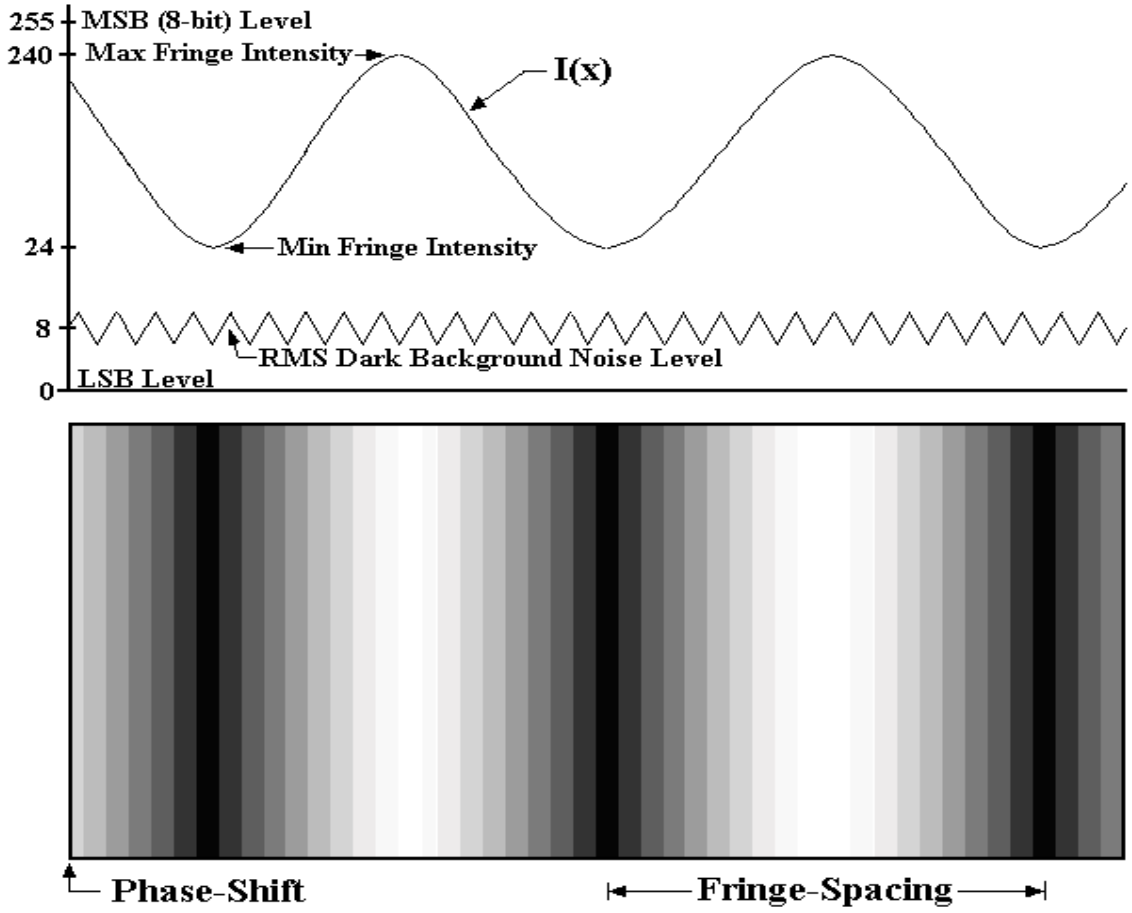

Figure 3.3.1: Interference of Object Wave to Reference Wave to Produce a Hologram

An 8-bit dynamic range analog-to-digital sampling conversion for the intensity is shown in the figure above. The 8-bit dynamic range represents an intensity level of 1 to 256 or 0 LSB (Least Significant Bit) to 255 MSB (Most Significant Bit). The RMS

background noise is threshold removed with a Signal-to-Noise Ratio (SNR) of

$$SNR = \frac{I_{\min}}{I_{noise}} = \frac{24}{8} = 3 \tag{3.3.4}$$

$I_{noise} = 8$ is the assumed noise threshold that is scaled to the range of the 8-bit data acquisition system

Intensity Offset: $I_{offset} = (I_{\max} + I_{\min})/2 = (240 + 24)/2 = 132$ (3.3.5)

Intensity: Peak: $I_{peak} = (I_{\max} - I_{\min})/2 = (240 - 24)/2 = 108$ (3.3.6)

Fringe Contrast: $FC = \frac{I_{\max} - I_{\min}}{I_{\max} + I_{\min}} = \frac{I_{peak}}{I_{offset}} = \frac{108}{132} = 81.8\%$ (3.3.7)

This assumes that the two interfering beams have the same intensity and therefore the high fringe contrast is a measure of the degree of coherence. If one of the beams has a lower intensity than the other beam then the FCR will decrease by the following equation:

$$FC = 2\frac{\sqrt{I_{obj} \cdot I_{ref}}}{I_{obj} + I_{ref}} \tag{3.3.8}$$

The hologram image at the bottom of the figure above shows the intensity variation from fringe interference which produces alternating dark-to-light lines. The fringe spacing is the period of the wave from dark-to-dark minimum intensity lines or light-to-light maximum intensity lines. Determining the fringe-spacing or the period of the fringe waveform from the maximum intensity peaks is more accurate than using the minimum intensity valleys since valleys are at a lower SNR than the peaks.

The phase-shift (ϕ) can thus be determined by: 1) Determining the peak in the waveform using a Least-Square Error (LSE) polynomial curve-fitting algorithm and then finding the intercept of the wave along the *x*-axis reference point, 2) Comparing a reference waveform to the measured waveform and applying a LSE correlation algorithm as the reference wave is swept over a phase-shift of 2π radians, or 3) Taking the Fourier transform of the waveform and using the Power Spectrum to determine the spatial frequency (k_x). The phase-shift is then determined by the arc-tangent relationship of the real part relative to the imaginary part of the Fourier transform at the spatial carrier frequency of the hologram. The main errors in determining the phase-shift from the

holograms are: 1) Number of samples per fringe, 2) Fringe stability on the camera, and 3) Hologram or fringe pattern waveform distortion due to optical aberrations and coma.

3.4 Scanning from a Single Viewpoint or Viewing Window

Scanning from a single view port or viewing window for the microscope is represented by a focused laser entering and exiting a specimen region as shown in figure 3.4.1 below.

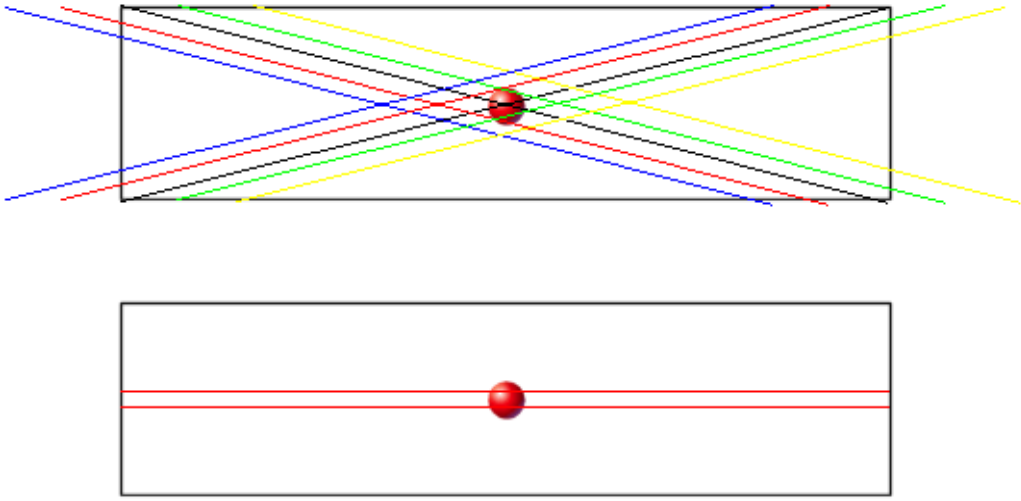

Figure 3.4.1: Comparison of a Scanning a Convergent Focusing Beam to a Collimated Beam

The beam passes through a high index-of-refraction ball and then exits the specimen region to form a hologram with the reference beam at the camera. The upper image of figure 3.4.1 shows a focused beam that is scanned longitudinally along the optical propagation axis with various rays of the focused beam passing through the ball. A focal point is centered at the ball and small diversions from this focal point show the marginal rays to pass through the ball. If the focal point is far from the ball center then the marginal rays will miss intersecting the ball. By stepping the focal point along the optical propagation axis a different hologram will be produced for each scan position.

The lower image of figure 3.4.1 shows a collimated beam passing through the ball that will produce the same hologram for any position of the ball along the optical propagation axis. The phase-shift at the perimeter of the beam where the marginal rays lie will reduce reconstruction error more significantly than the phase-shift at the chief central rays. Using the chief central ray for reconstruction is pointless because the same measurement occurs at every scan position along the optical propagation axis. The

hologram measures the cumulative or sum total refractive index along the path length of the specimen for both the focused and collimated laser beams. The objective is to determine the refractive index of the ball and its position along the optical propagation axis. This is the CSLH microscope configuration for scanning from a single viewpoint window as a beam enters one side of a specimen and exits the other side with no rotational scanning.

3.5 Confocal Microscopy

An optical microscope imaging in reflection or transmission mode is sensitive to the absorption, reflection, and scattering of an illuminated specimen. In transmission mode a specimen can behave like a spectral filter as it absorbs light energy, which is the situation for optical spectroscopy. A typical confocal microscope uses point source illumination on the specimen and then refocuses the beam past the image plane where a pinhole aperture is placed over this optically conjugate focal point. This reduces the aberrations from the optics and sharpens the image at a reduction in the depth-of-field focus range. Scanning plane-by-plane down the optical axis will produce multiple images that can be combined into a composite image with a nearly infinite depth-of-field. Confocal microscopes can produce sharper higher contrast images with greater depth-of-field than ordinary optical microscopes that illuminate the entire specimen since scattered light is reduced in the final image.

Typical scanning confocal microscopes are used in fluorescence microscopy. A molecule or protein is stained or marked with a fluorophore, which fluoresces at a specific wavelength when illuminated by the source in the microscope. The pinhole aperture and dichroic beam splitter admits a single wavelength from the fluoresced wave and images the specific features of interest at the camera. The concept for a confocal imaging microscope is shown in figure 3.5.1 below:

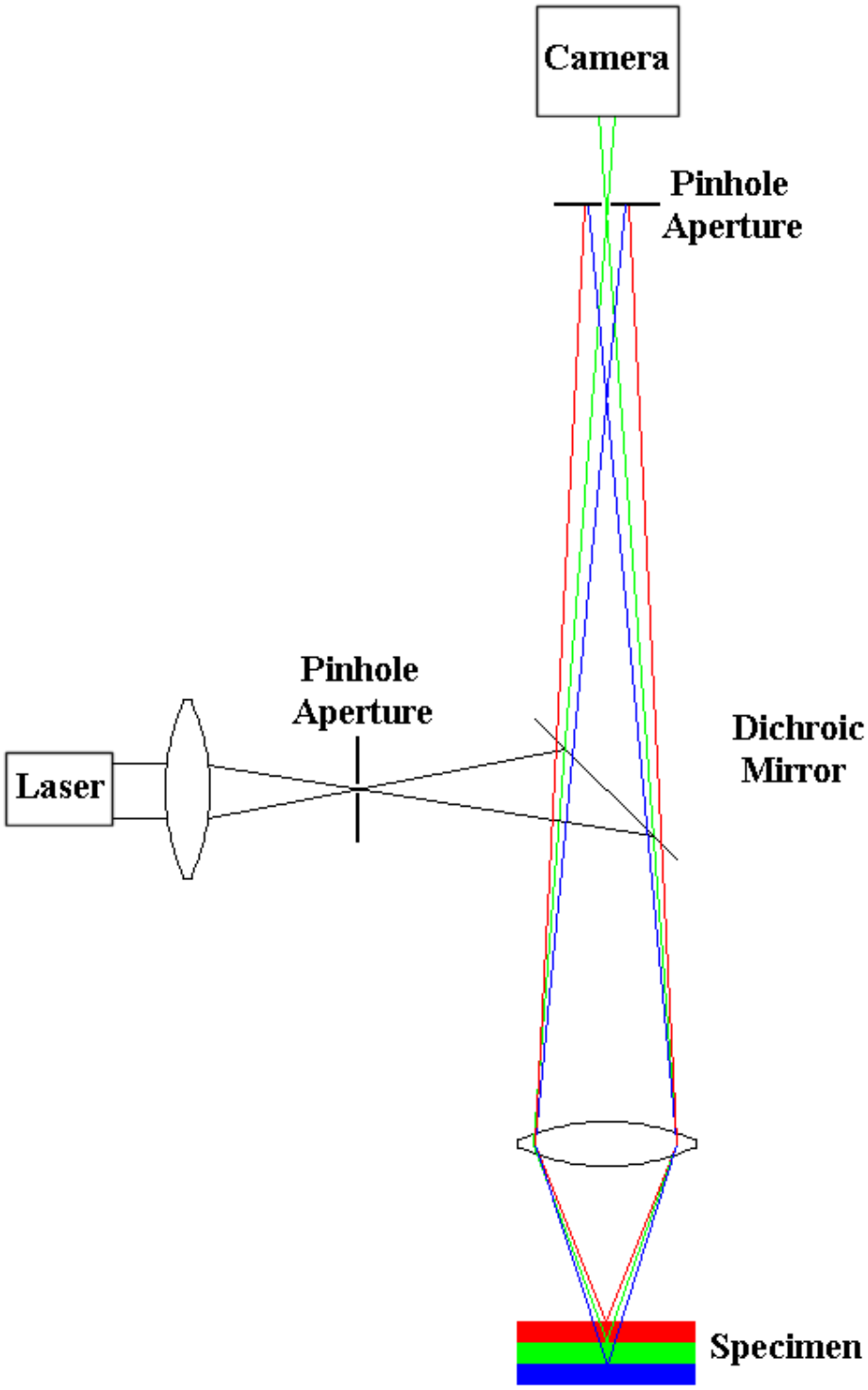

Figure 3.5.1: Confocal Microscope Showing Re-Focusing Pinhole Aperture Stop for Out-of-Focus Rays

This figure shows a thick specimen with three focal regions where the out-of-focus rays from the upper and lower regions are blocked by the pinhole aperture. The central

region is optically conjugate to the pinhole and these rays will pass through the pinhole. In general, the focal depth is reduced as the out-of-focus rays are blocked out. Only the rays representing the wavelength of green light would pass through the pinhole as seen in the figure above. Since the specimen is illuminated at a single point then scanning over the surface is required to produce a 2D image. In a particular way, a confocal microscope that uses a white light source becomes monochromatic because the focal length changes with wavelength and the pinhole aperture admits only a single focal point. The confocal aperture will block the out-of-focus rays as the pinhole will admit only the rays for a single focal length that represents a particular wavelength. In essence, the confocal microscopy method places a virtual aperture at the focal point of the beam within the specimen.

In 1991 Dixon [17] produced a Confocal Scanning Laser Microscope (CSLM) that was able to maintain a stationary confocal re-focusing point during scanning. This was accomplished by returning the scanned laser beam back through the rotational scan mirrors. Before returning to the laser source a beam splitter redirected the back propagating beam to the projector lens. The projector lens focused the beam to a confocal pinhole aperture followed by other optics to re-focus the beam at a camera. A stationary confocal aperture to the focal point in the specimen was thus achieved during scanning. Dixon's Confocal Scanning Laser Microscope (CSLM) incorporated polarizer lenses to convert from reflection to transmission mode imaging along with periscope lenses to reduce excessive beam translation when scanning. Dixon's rotating mirrors or beam steering mirrors were used to scan the beam over the *xy*-axis. The specimen was attached to a *z*-axis translation stage for scanning along the optical propagation path. The key feature of this 3D scanning confocal microscope was the stationary focal point at the confocal apertures during scanning of the specimen. The Dixon's CSLM is similar to the CSLH microscope with the optical loop that reverse propagates a beam back through the beam steering mirror section and then splits the beam off to the projector lens. The dissimilarities between the two microscopes are that the laser source is initially split into an object and a reference beam that propagate side-by-side through the same optical components. At the projector optics the two beams are converged to overlap one another and form a hologram at the camera.

3.6 Holography

Holography is a form of photography that allows the image to be recorded in three dimensions. Holography takes its name from the Greek word “holos”, which means “whole” and “grafe”, which means “write”. Holography can also be described as a complete record or a whole picture. Holography preserves both the amplitude and phase of light while imaging preserves only the amplitude [18,19]. Since the phase of a light wave is recorded in a hologram the potential for higher resolution measurements is possible when compared to the detected energy of a focused beam point spread function. Conventional photography records only the intensity or amplitude squared as the phase information is lost for any point in the emulsion plane. A hologram can be used to project a three-dimensional image of an object. Mathematically, the intensity is the wave times its complex conjugate to produce a magnitude for any point in the focal plane. Aberrations that affect an imaging system also affect a hologram however, since the wavefront properties in the beam are altered.

A hologram contains complete information allowing the reconstruction of the object image. Holography does not require a focal point, but it does require the interference of two coherent beams that are overlapped to form a hologram. The two beams are split from a single coherent source by either amplitude splitting or wavefront splitting. Amplitude splitting directs the output beams on perpendicular paths and the sum of the two output beam intensities is equal to the intensity of the input beam. Wavefront splitting or phase splitting splits a single beam in half as two back-to-back D-shaped beams. Wavefront splitting also directs the two output beams on side-by-side parallel paths. The CSLH microscope wavefront splits the beam and the gap or distance between the two D-shaped beams provides the limit to beam steering angle which translates the probe within the specimen. Wavefront splitting is preferred over amplitude splitting because side-by-side propagating beams will propagate through the same optical lenses, which will introduce common aberrations to each of the beams. The other advantage of wavefront splitting is that the total beam path length of the microscope is not as critical as amplitude splitting when considering the coherence length of the laser.

The refractive index of the specimen in the CSLH microscope produces changes in the optical path length, which creates a shift in the fringes of the hologram. The fringes are constantly spaced which produces a single spatial carrier frequency. The fringe spacing is a function of the wavelength of the laser and the convergence angle of the

overlapping beams at the camera. The phase-shift cannot exceed the fringe-spacing displacement from scan point to scan point because the number of 2π radian phase-shifts due to a fringe-shift displacement would be unknown. A 2π radian phase-shift is equivalent to the spacing of one fringe or the fringe-spacing. The phase-shift equation is $\phi = 2\pi \cdot n + \Delta\phi$ as *n* is the unknown variable. If the phase-shift is less than 2π radians or 1 wave between scan steps then *n*=0, which is the case for a weak phase object with a relatively low phase-shift gradient. The phase-shift is sensitive to a change in refractive index as produced in the hologram of the CSLH microscope. Holographic reconstruction of the specimen is possible due to scanning in three-dimensions.

The CSLH microscope hologram is sensitive to the following sources:

1) Strong phase object with high phase-shift gradient from scan position to scan position
2) Coherence length and wavefront error of the laser
3) Optical aberrations that introduce phase-shifts in the hologram (particularly from off-axis scanning)
4) Fringe contrast and contrast uniformity across the hologram
5) Phase-shift sensitivity to a change in temperature
6) Vibrations that affect fringe stability
7) Alignment and pupil geometry
8) Macro dust particles

4 Description of the CSLH & STLH Microscopes

The Confocal Scanning Laser Holography (CSLH) microscope features an optical loop that is designed to place a stationary focal point at the confocal plane during scanning. The CSLH microscope is divided into the following component sections: 1) Laser Optics, 2) Cube Beam Splitter, 3) *xy*-Scan Mirrors, 4) Optical Loop, 5) Projector Lens, and 6) Line Scan Camera. A block diagram of the CSLH microscope is shown in figure 4.1 below.

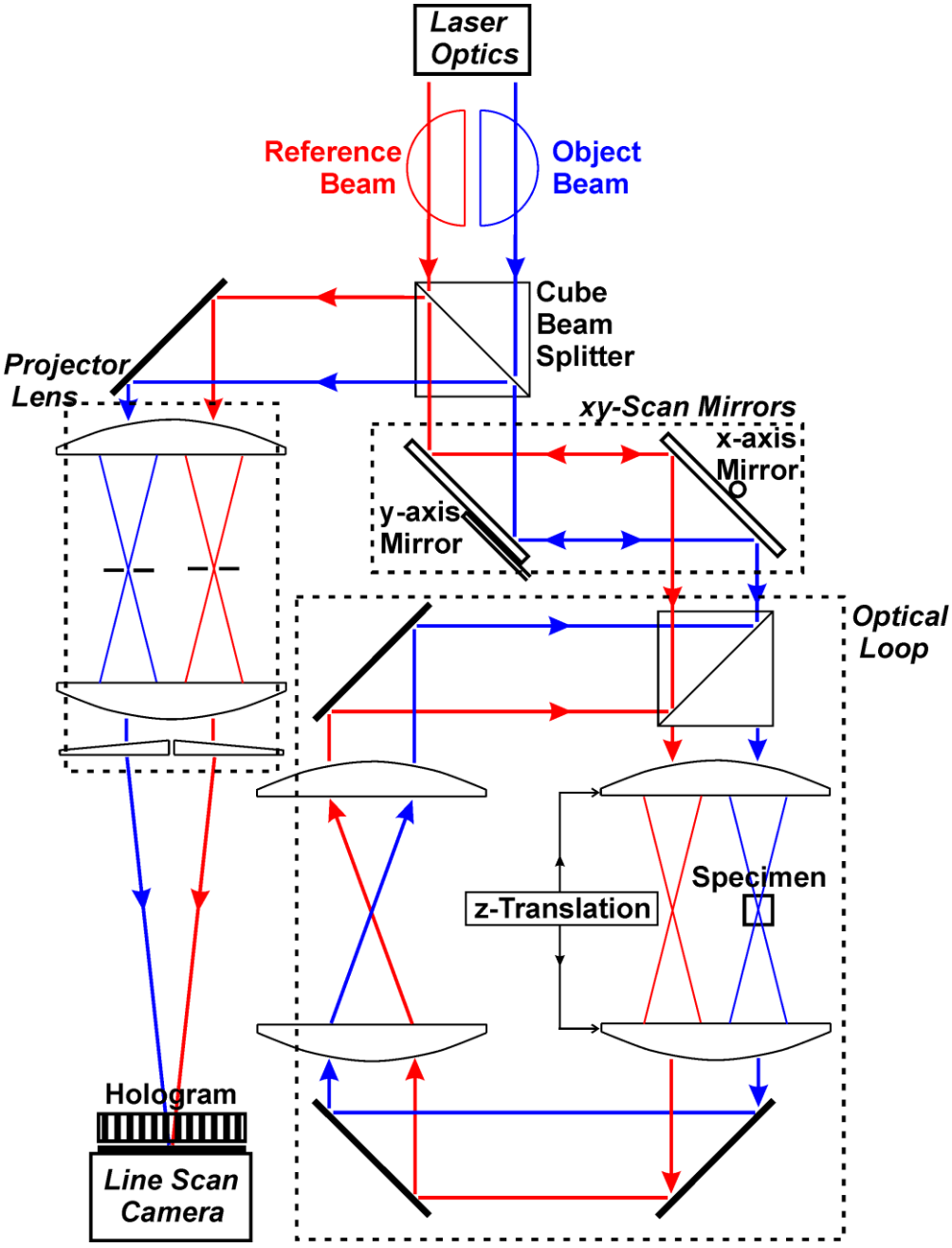

Figure 4.1: Block Diagram of the CSLH Microscope

The laser optics section expands the laser beam source and splits it into two coherent back-to-back “D” shaped beams. The object and reference beams enter the cube beam splitter and then pass into the *xy*-Scan Mirror section. The *xy*-Scan Mirror section includes two Cambridge Beam Steering Mirrors (BSMs) along with two periscope lenses to control the pupil planes, which are not shown in the figure. The beams enter an optical loop and the object beam is focused within the specimen. The optical lens that focuses both the object and reference beams in the specimen region is called the telecentric lens. A *z*-axis translation stage on the telecentric lens moves the focal point in the specimen along the optical propagation axis. A re-focusing lens pair is the periscope lens that inverts the image in conjunction with the telecentric lens in the optical loop and places a pupil at the cube beam splitter. The beams then exit the optical loop by the reflecting surface of the cube beam splitter and reverse propagate back through the *xy*-Scan Mirror section. The reverse propagating beams then enter the first Cube Beam Splitter, which reflects the beams into the Projector Lens. The Projector Lens consists of a Confocal Lens with pinhole apertures and optical wedges to converge the beams. The converging beams completely overlap one another at the Line Scan Camera and the wave interference of the two coherent beams produces a fringe pattern or hologram as seen by the dark and light lines or bands in the hologram image.

Scanning with the CSLH microscope produced off-axis aberrations from the BSMs and the entrance and exit pupils were not stationary as anticipated. This caused movement of the focal points at the pinhole apertures of the confocal lens. The optical aberrations from the lenses in the CSLH microscope over a long path length also affected the wavefront error of the beams that formed a hologram. The holograms showed high contrast fringes with a dish shaped fringe contrast profile. If the optical aberrations could be removed then the fringe contrast profile would be constant. The complexity of the optics with f/2 f-number telecentric and confocal lenses along with a long path length to the camera produced significant aberrations and wavefront error. The reduction in both path length and complexity was possible if *xy*-axis stage translators were placed on the fluid-cell instead of using the beam steering mirrors. The beam steering mirrors also introduced off-axis coma and maintaining stationary pupils required a higher degree of alignment accuracy.

A shorter path length Scanning Transmission Laser Holography (STLH) microscope was built and evaluated as a simplified holography microscope that was used as a benchmark for comparison to the CSLH microscope. This diagnostic STLH microscope

was a scaled down version of the CSLH microscope and eliminated the optical loop, two cube beam splitters, two beam steering mirrors, three long focal length periscope lenses, and the confocal lens. By eliminating these optical components the path length was decreased by more than a factor of two. Furthermore, precise alignment for stationary pupil planes was no longer critical. The telecentric lens still produced a dish shaped hologram, but the curvature of the dish shape was less severe than the cumulative effects of the telecentric lens and the confocal lens in the CSLH microscope. The other benefit was that the wavefront error at the camera was decreased due to the shorter path length. This diagnostic STLH microscope provided a means to isolate and evaluate the on-axis resolution of the telecentric lens and hologram contrast uniformity. It also provided a means to refine LabVIEW computer programs that control translators, beam steering mirrors, and image acquisition in dynamic control loops. The STLH microscope also provided an opportunity to refine optical alignment since there are fewer degrees of freedom due to the reduced complexity. Reference holograms and data holograms were collected with the STLH microscope to assess the “wily” reconstruction algorithm. Since optical aberrations could not be optically compensated at the hologram then a reference hologram provided a means to compensate the effect of optical aberrations by an adjustment to the phase-shift. Designing custom wavefront correctors to compensate the optical aberrations is the only other method, but this approach is costly and it is difficult to define a precise lens prescription. A reference hologram is recorded for every scan position with the fluid at constant temperature. The temperature is then elevated to produce a steady-state thermal gradient for data hologram collection. The CSLH microscope was built and evaluated in a similar manner to the STLH microscope. A description of the CSLH microscope design and significant physical relationships is provided in the following sub-sections.

4.1 Laser Coherence

The monochromatic laser is both temporally and spatially coherent up to the coherence length of the laser. Temporal coherence length is significantly longer than the spatial coherence length. Spatial coherence is represented by the wavefront error of the pupil at a particular path length. The wavefront error increases over path length due to spatial aberrations, such as spherical aberrations, that decreases the fringe contrast in a hologram. Temporal coherence is the time varying wavelength error or the temporal variations in wavelength, such as chromatic aberrations, that is generated by the

resonating laser cavity. The coherence length of the laser is the path length that reduces the fringe contrast to 50% which reduces the ability to discern a phase-shift or fringe translation in a hologram. The path length or distance from the beam splitter to the image plane of the hologram must be less than the spatial coherence length of the laser in order to produce fringes. Mechanical vibrations will cause the fringes to move in a hologram, which is effectively an optical jitter that defines the stability of the fringes.

An interferometer is used to measure the spatial coherence length of a laser and the microscope converts to an interferometer with no specimen or with a constant refractive index phantom specimen. As an interferometer the microscope can be used to measure the wavefront error from the optical aberrations or to record the reference hologram for each scan position of the probe beam in the specimen.

4.2 Reference Hologram

A reference hologram was taken with the specimen at constant temperature to record the optical aberrations of the CSLH microscope. This allowed the removal of optical aberrations from the holograms of the specimen during their reconstruction. The hologram has a constant or uniform fringe contrast given ideal optics. Spherical aberrations of the lenses will produce a bell-shaped hologram where the fringe contrast is lower for the marginal rays of the beam and higher for the chief ray that is central to the beam. The peak intensity of the fringes varies across a hologram as a bell-shaped curve due to diffraction and non-uniform aperture illumination, Hecht [41]. The iris diaphragm on the CSLH microscope is adjusted to produce near uniform aperture illumination which produces a constant fringe contrast across the hologram. The introduction of focusing and re-collimating optics along with the refractive effects of a $5\,mm$ thick specimen affects the fringe contrast across the hologram. The hologram represents the pupil function of the overlapped beams at the camera. Near field diffraction sources occur in the CSLH microscope from the apex of the Fresnel biprism at the wavefront splitter and the iris diaphragm aperture stop, for example. These near field out-of-focus Fresnel diffraction sources produce non-uniform fringe contrast due to phase cancellation and reinforcement in the hologram. Diffraction is a part of the optical aberrations and the geometric aberrations of the lenses tend to dominate the diffraction.

The peak intensity is higher at the extreme ends of a CSLH microscope hologram in comparison to the center of the because of the relative optical path length through the optical components that produces a phase-shift. A spherical lens has a longer optical

path length for a chief ray that will retard the phase more than the perimeter marginal rays that propagate through thinner sections of glass. The phase-shift for the central chief ray is different than the marginal perimeter rays due to the different lens thickness along the optical path. The fringe contrast for various lens configurations is shown in figure 4.2.1 below:

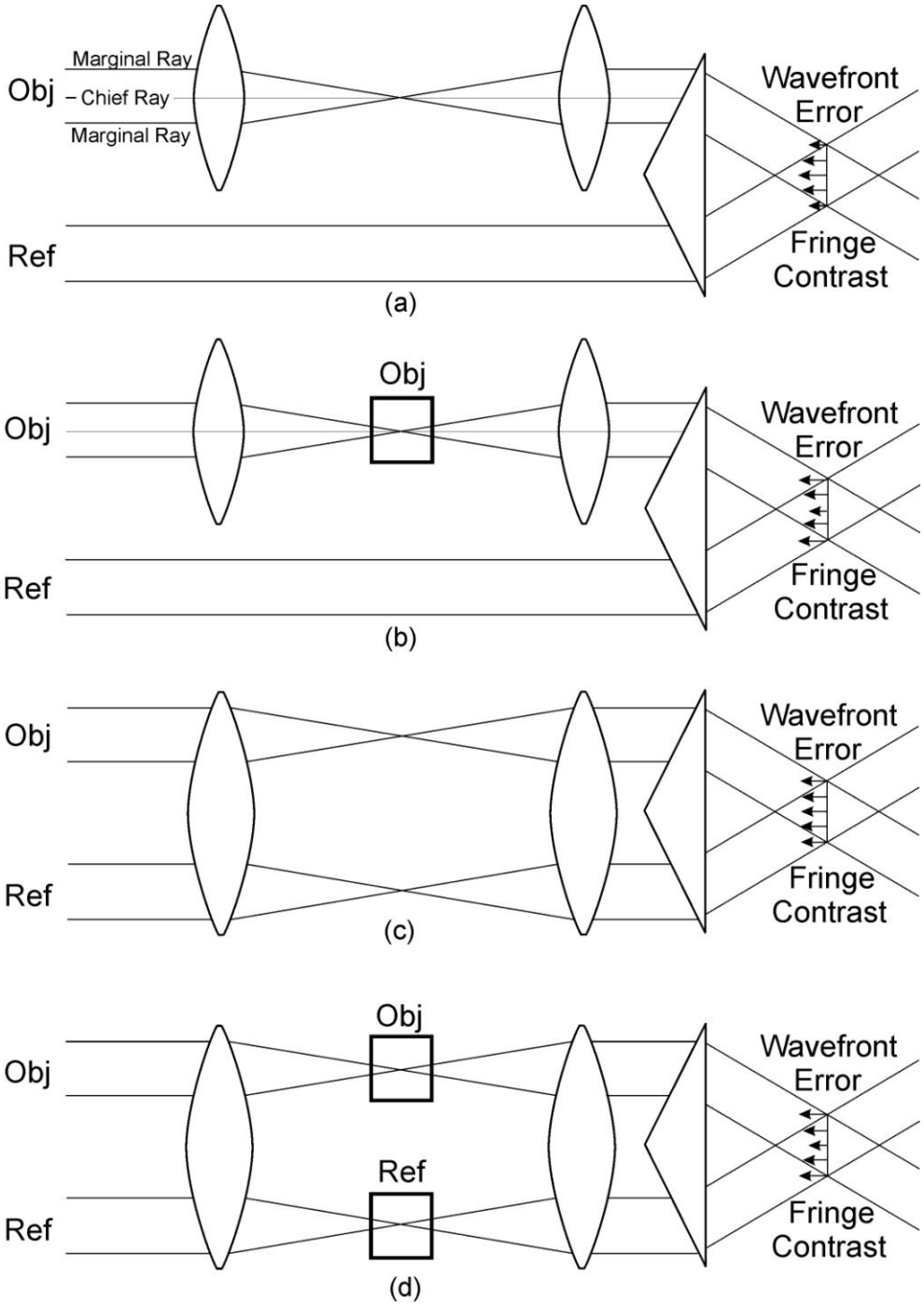

Figure 4.2.1: Fringe Contrast for Various Lens Configurations

A bi-convex focusing and re-collimating relay lens with the chief ray propagating through the lens center produces a bell shaped fringe contrast in the hologram as seen in figure 4.2.1a. A specimen with dominant aberrations is placed at the focal point converts the bell shaped fringe contrast to a dish shaped fringe contrast as seen is figure 4.2.1b. Both the reference beam and the object beam that propagate through the same lens will produce a flat fringe contrast due to the ray crossing at the focal point as seen in figure 4.2.1c. At the focal point the marginal rays flip over so that the marginal rays of the beam have the same optical path length or phase-shift as the chief ray after passing through a symmetrical set of lenses. A specimen is placed at the object beam focal point and a phantom specimen is placed at the reference beam focal point will produce a dish shaped fringe contrast across the hologram as seen in figure 4.2.1d. Figure 4.2.1d is the telecentric lens configuration of the CSLH microscope. A flat fringe contrast across the hologram is desired to more accurately determining a fringe translation or phase-shift.

Complete beam overlap at the camera coincides or aligns the dish shaped wavefronts for the object beam and the reference beam. The marginal rays of the aligned superimposed beams at the camera are necessary for minimizing reconstruction error. The reference hologram compensates for most of the optical aberrations that affect the fringe contrast across the hologram.

4.3 Wave Splitting to Amplitude Beam Splitting Difference

The CSLH microscope uses two Fresnel biprisms to wavefront split a laser source into an object beam that passes through the specimen and a reference beam that bypasses the specimen. Recombining the two beams by converging them to overlap one another produces a hologram with fringes occurring only in the overlapped region of the two beams. Wavefront splitting by means of two identical back-to-back Fresnel biprisms produces two side-by-side parallel beams that propagate through common optical components. The nearly identical optical aberrations for each of the beams will symmetrically overlay one another when the beams are completely overlapped at the hologram image plane. The overlaid beams produce a fringe pattern from the common optical aberrations of the two beams, which reduces the error in determining a phase-shift or fringe translation in the hologram. Common aberrations of the two beams will maximize the fringe contrast and increase the uniformity of fringe contrast across a hologram. Aberration free optics would produce a constant fringe contrast across the hologram, which would minimize the error in determining the phase-shift.

A camera is placed at the hologram image plane to detect the fringes. The desired spatial sampling resolution is greater than 8 camera detectors or samples per fringe so that a phase-shift of λ/20 waves can be resolved. The spherical aberrations from the low f/# or high numerical aperture focusing lenses produce a dish shaped hologram based on the wavefront error across the pupil plane for each of the beams.

Wavefront splitting is preferred over amplitude splitting because a wavefront splitter will have the same wavefront for each of the beams as the source. An amplitude splitter uses an optical surface to split the beams which will impart a wavefront distortion to one of the beams. Introducing wavefront error to one of the beams does not occur when using the Fresnel biprism as a wavefront splitter. Typical optical amplitude splitters are an optical cube that is diagonally split and then the two pieces joined together with cement or a pellicle membrane beam splitter. Either cube or pellicle beam splitters will direct the output beams in orthogonal or perpendicular directions. The object and reference beams will then propagate through different lenses and optical components. The resultant hologram would then represent the relative phase-shift from the optical path length difference of the two beams.

4.4 Description of the Telecentric Lens and Confocal Optics

The telecentric lens focuses two side-by-side parallel beams in the specimen region and then re-collimates the object beam and the reference beam. The confocal optics also focuses and re-collimates the two beams, but instead of a specimen has a pinhole aperture placed at the secondary focal point. The low f/# or the high numerical aperture of the telecentric and confocal lenses produce high optical aberrations that affect a hologram. Optical aberrations produce a dish shaped non-uniform fringe contrast and uneven fringe spacing across the hologram. The advantage of propagating side-by-side beams through common optical components is the optical aberrations will be common to both beams, which is important for the fringe contrast across the hologram.

4.5 Marginal and Chief Ray Differences to Phase-Shift and Reconstruction

The marginal rays at the edges of the focused probe beam reduce reconstruction error rather than the chief central ray because the marginal rays represent the maximum angle for the probe beam. The marginal rays propagate through more computational cells due to their diagonal path than the chief ray that propagates straight through the specimen along the optical axis beam path. The phase-shift is determined at the

marginal rays in the hologram as there are two marginal ray locations for each hologram recorded by the line scan camera. There is only one chief ray location for each hologram and the phase-shift at this location is not important as the integrated index-of-refraction for a chief ray remains constant, being similar to a collimated beam for scanning along the optical axis or beam path. Since the optical path length for the chief ray is constant, the phase-shift will also be constant and the phase-shift at the chief ray is thus ignored. The marginal rays at the edges of the cone beam however, are important and are located at the ends of the hologram. The ends of the hologram on the line scan camera would be pixel 1 and pixel 8192 for a hologram that completely fills the camera. The hologram is sampled by 256 detectors in order to record at least 8 fringes. This spatially sampled image data is used to accurately determine the phase-shift at the marginal rays where they are found on the camera.

4.6 Detector Sampling a Fringe on the Hologram and Spatial Resolution

The CSLH microscope has a high numerical aperture or low f-number beam to probe the specimen in comparison to an electron microscope that uses a low numerical aperture beam. Electron microscopes require only 3 detector samples to image a fringe and the Nyquist sampling limit is 2 detector samples per cycle of a fringe. One detector on the camera is equivalent to one pixel, which is a sample used for signal processing and phase-shift determination. The fringe-spacing or fringe-separation distance is equivalent to one cycle which is equivalent to one wave of a fringe. The electron microscope fringe contrast across the hologram is quite uniform representing a nearly ideal theoretical condition because of the low numerical aperture. A uniform fringe contrast across the hologram allows for a lower spatial sampling rate of a fringe. The CSLH microscope, on the other hand, requires at least 8 detector samples per fringe spatial resolution to compensate for the dish shaped fringe contrast across the hologram. This higher spatial resolution is necessary to accurately determine the phase-shift to less than λ/20 waves rms given the optical aberrations that produce wavefront error on the hologram. Higher spatial resolution also requires an increased path length to the camera. The reason that the CSLH microscope requires higher spatial resolution than the electron microscope is because the higher numerical aperture of the CSLH microscope produces larger aberrations.

4.7 Beam De-Collimation and the Phantom Specimen

A shift in focal plane within the focusing optics will increase beam re-collimation error and change the size of the re-collimated beam. The beam size for both the object beam and the reference beam are to remain the same throughout the optics of the CSLH microscope so that the marginal rays of each beam will coincide where the two beams are completely overlapped at the hologram image plane. The specimen is placed in the focal point region of the object beam and the focal point of the reference beam bypasses the specimen. In order to minimize the relative focal plane shift of the object beam focal point to the reference beam focal point a constant refractive index phantom specimen or reference specimen is placed in the focal point region of the reference beam. The purpose of the phantom or reference specimen is to provide an equivalent focal point distance of the object beam to the reference beam so that the relative focal plane shift for the two beams is zero.

4.8 Creating and Recording a Hologram

The hologram is produced by a coherent wave that is reflected off an object to an emulsion surface and then directing the same coherence source to overlap the object beam at the emulsion surface [26,27]. The superimposed or overlapped beams produce wavelet fringes based on the coherence or wavefront quality of the source. The source beam at the hologram emulsion plane has either a spherical wavefront for the near-field Fresnel diffraction region or a planar wavefront for the far-field Fraunhofer diffraction region. Holography is typically a far-field Fraunhofer diffraction situation. When a laser source re-illuminates the hologram film in the same geometry as the recording of the hologram the viewer perceives a three-dimensional representation of the object in the hologram. The perceived object is called the reconstructed image. A configuration to record a hologram is shown in figure 4.8.1 below:

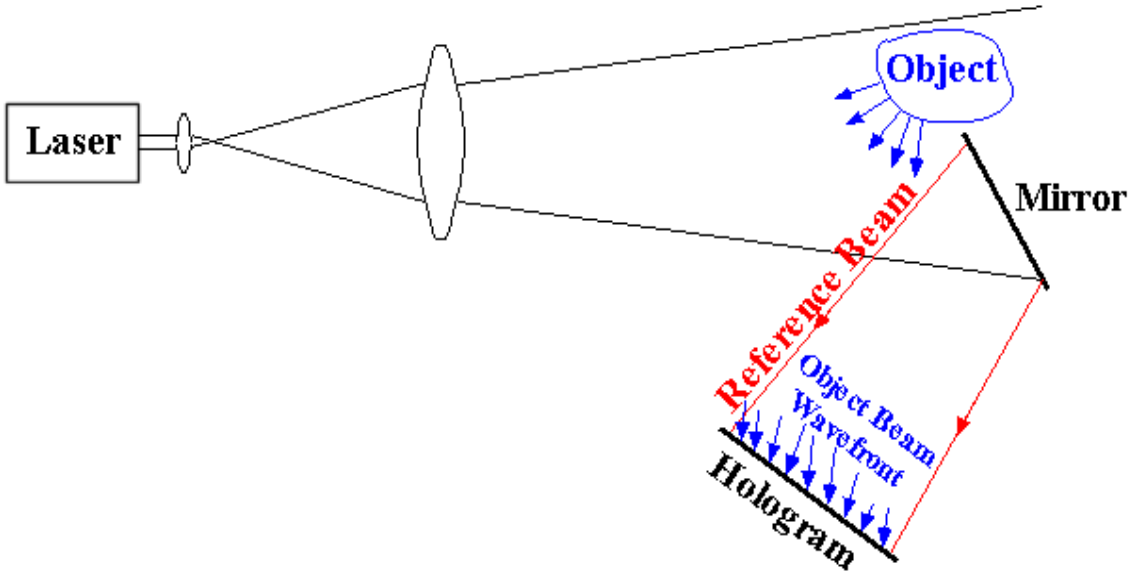

Figure 4.8.1: Recording a Hologram Example

A photographic film can be used to record a hologram or a camera for digital recording of a hologram instead. The object is reconstructed three-dimensionally by illuminating the encoded photographic film transparency with a laser in the same geometry as the recording process. A hologram can be reconstructed if the spatial resolution or grain resolution of the film exceeds the line spacing of the fringes.

We perceive three dimensions by stereoscopic vision as we observe an object from slightly different viewing points through each eye. The projections of the scene into our eyes are slightly different due to the parallax effect (eye separation) which gives us the ability to determine depth, perspective, and distance. This effect is recreated in a hologram when a coherent laser that illuminates the hologram emulsion creates a wave interference pattern. The photographic emulsion plate or hologram is perceived in three dimensions because the phase of the wave is preserved through diffraction and interference.

The creation and recording of a hologram on an emulsion film is achieved by combining the source reference (*ref*) wave with an object (*obj*) wave. The photographic film is sensitive to the constructive and destructive interference of light. The object wave and the reference wave are represented by the following equations.

$$U_{obj} = A_{obj} e^{i\phi_{obj}} \tag{4.8.1}$$

$$U_{ref} A_{ref} e^{i\phi_{ref}} \tag{4.8.2}$$

Where: $\phi = \vec{k} \cdot \vec{r} + \theta$ (4.8.3)

Spatial Frequency or Wave Number: $\vec{k} = k_x \cdot \vec{e}_i + k_y \cdot \vec{e}_j + k_z \cdot \vec{e}_k$ (4.8.4)

Position: $\vec{r} = r_x \cdot \vec{e}_i + r_y \cdot \vec{e}_j + r_z \cdot \vec{e}_k = (x - x_0)\vec{e}_i + (y - y_0)\vec{e}_j + (z - z_0)\vec{e}_k$ (4.8.5)

Phase-Shift: θ

$$\cos(\gamma) = \hat{r}_{obj} \cdot \hat{r}_{ref} \quad (4.8.6)$$

The angle γ represents beam convergence angle or the angle between the object beam and the reference beam that converges the two beams for overlap.

The position vector $(\vec{r})$ is with respect to a reference point in a global coordinate frame. The origin of the global reference frame is (x_0, y_0, z_0). The two wave vectors (U_{obj}, U_{ref}) define the wave properties for any position vector point (x, y, z). The waves combine to form constructive and destructive interference at all points where the two beams overlap. The interference plane at *z = constant* detects or records the interference fringes of the two waves. The object to reference beam convergence angle (γ) that overlaps the two beams is shown in figure 4.8.2 below:

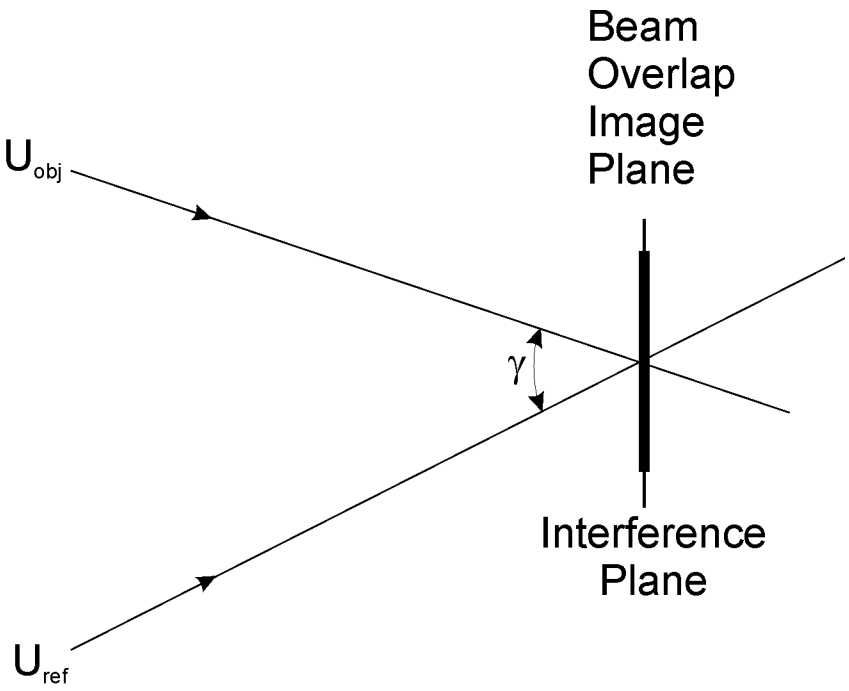

Figure 4.8.2: Wave Vector Crossing

The beam overlap image is the intersection area of the two beams on the interference plane. Figure 4.8.2 above shows the beams as convergent direction vectors U_{obj} and U_{ref} where the coherent beams will produce interference fringes at the region of overlap. If the crossing point for the beams is at the interference plane, the overlapped beams will

form a circle since the two beams have the same diameter. The fringe-spacing or the period of the fringes is a function of the wavelength of the laser and the convergence angle (γ) of the overlapping beams. Fringe-spacing increases as the convergence angle (γ) decreases. The fringe-spacing defines the spatial carrier frequency found in the hologram. Fringe-spacing can also be affected by optical distortions that change the wavefront as the wave propagates to the camera for imaging. The phase-shift is contained within the Fourier transform of the hologram at the carrier frequency. The angle of the reference wave with respect to the interference plane is duplicated for reconstruction of the object image. Overlapping waves create interference fringes, which are represented by the addition of two wave vectors as follows:

$$U = U_{obj} + U_{ref} = A_{obj} e^{i\phi_{obj}} + A_{ref} e^{i\phi_{ref}} \tag{4.8.7}$$

$$U = A_{ref}\left(1 + \frac{A_{obj}}{A_{ref}} e^{i(\phi_{obj} - \phi_{ref})}\right) e^{i\phi_{ref}} \tag{4.8.8}$$

The intensity at the emulsion film or the hologram is:

$$I = U \cdot U^{*} = A_{ref}\left(1 + \frac{A_{obj}}{A_{ref}} e^{i(\phi_{obj} - \phi_{ref})}\right) e^{i\phi_{ref}} \times A_{ref}\left(1 + \frac{A_{obj}}{A_{ref}} e^{-i(\phi_{obj} - \phi_{ref})}\right) e^{-i\phi_{ref}}$$

$$I = A_{ref}^{2}\left(1 + \left(\frac{A_{obj}}{A_{ref}}\right)^{2} + 2\left(\frac{A_{obj}}{A_{ref}}\right)\cos(\phi_{obj} - \phi_{ref})\right) \tag{4.8.10}$$

The first term is due to the amplitude of the reference wave and the second term is due to the relative amplitude or intensity of the object wave to the reference wave. The third cosine term is the phase-shift in the hologram that represents the path length retardation or delay of a wave propagating along a ray path and interfering with another wave at the emulsion plane. The phase information of the object is contained within this cosine term. Fringe contrast or fringe visibility factor is a peak-to-valley fringe intensity ratio and the maximum occurs when the object wave amplitude is equivalent to the reference wave amplitude or $A_{obj} = A_{ref}$. In this case the intensity at the photographic hologram film becomes:

$$I = 2A_{ref}^2 (1 + \cos(\phi_{obj} - \phi_{ref})) \tag{4.8.11}$$

The film transparency is illuminated by the reference beam where the intensity gain (*m*) represents the recorded transfer function. Variations in slope will affect the reconstructed image because it will introduce errors in the interference of a coherent laser source that interacts with the hologram. The recorded hologram (U_{recrd}) is then given as:

$$U_{recrd} = I^{-m/2} \cdot U_{ref} \tag{4.8.12}$$

$$U_{recrd} = A_{ref} (A_{obj}^2 + A_{ref}^2 + 2A_{obj} A_{ref} \cos(\phi_{obj} - \phi_{ref}))^{-m/2} \cdot e^{i\phi_{ref}} \tag{4.8.13}$$

If the photographic process is controlled such that $m = -2$ then

$$U_{recrd} = A_{ref}^3 \left(1 + \left(\frac{A_{obj}}{A_{ref}} \right)^2 + \left(\frac{A_{obj}}{A_{ref}} \right) \left(e^{i(\phi_{obj} - \phi_{ref})} + e^{-i(\phi_{obj} - \phi_{ref})} \right) \right) \cdot e^{i\phi_{ref}}$$

This equation shows a conjugate wave that emanates from a fictitious but identical object placed in a different plane.

4.9 Reconstructing a Hologram

The hologram uses a carrier frequency to store information. Illuminating the hologram with a coherent laser in the same configuration as the recording process reproduces or reconstructs an image of the object. The interaction of the laser with the hologram produces a zero-order image along with two first-order off-axis images that are phase-conjugated with one another. A one-dimensional reconstruction configuration is shown in figure 4.9.1 below:

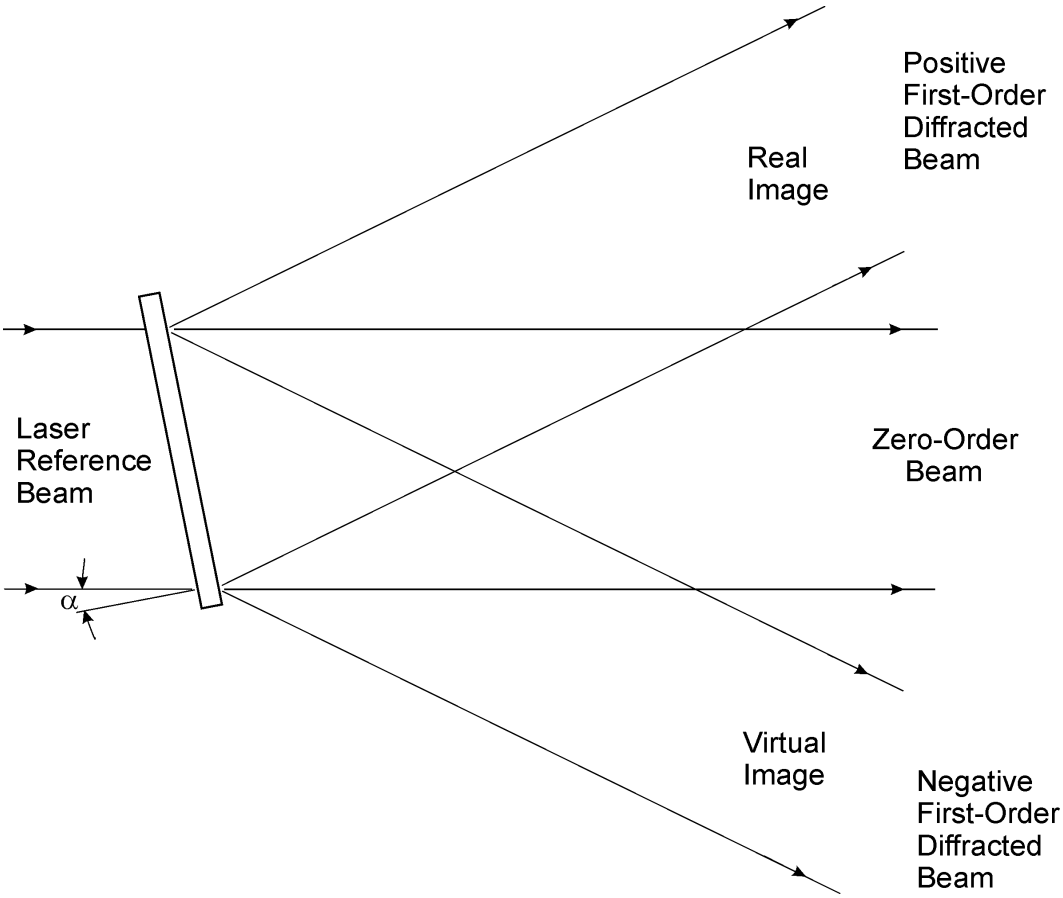

Figure 4.9.1: Illuminating the Hologram to Reconstruct an Image of the Recorded Object

The hologram is similar in effect to a diffraction grating. Fringe lines in the emulsion film diffract the beam as a series of point source radiators. The angle α is the incident angle of the laser to the normal direction vector of the hologram and is duplicated for reconstruction. As angle α is varied the frequency of the carrier wave will also vary resulting in the amplification of the reconstructed images from π to 2π or –π/2 to +π/2, for example so that amplified phase images and amplified amplitude images can be observed.

The zero-order beam is predominantly the laser intensity with the hologram film behaving like a weak phase plate or zone plate since the hologram film is nearly transparent. Laser interaction with the hologram also creates two first-order diffracted beams that have a positive and negative angle to the zero-order beam. A first-order real image is off-axis from the laser line-of-sight axis. A first-order virtual image is off-axis in the other direction from the laser line-of-sight axis. Finally, a zero-order image is formed on-axis to the laser line of sight. This first-order diffracted beam imaging is also known

as the side-band Fresnel reconstruction method or the Fraunhofer hologram reconstruction method.

The object and reference wave for reconstruction is given as:

Folded-In Reference Wave in the Hologram: $U_{ref} = A_{ref} e^{i\phi_{ref}}$ (4.9.1)

Diffracted Fresnel Wave in the Hologram: $U_{obj} = A_{obj} e^{ikx} = A_{obj} e^{i\phi_{obj}}$ (4.9.2)

Where: $\vec{k}$ is the wave number or the spatial carrier frequency. Note that the wavelength of the laser in the hologram emulsion is smaller than the wavelength in air. The reconstruction (*recr*) of the object given an illumination reference wave is:

$$U_{recr} = U_{obj} + U_{ref} = A_{obj} e^{ikx} + A_{ref} e^{i\phi_{ref}} \tag{4.9.3}$$

The intensity of the waves is given as:

$$I_{recr} = U_{recr} \cdot U_{recr}^{*} = \left| A_{obj} e^{ikx} + A_{ref} e^{i\phi_{ref}} \right|^2 \tag{4.9.4}$$

$$I_{recr} = \left(A_{obj} e^{ikx} + A_{ref} e^{i\phi_{ref}} \right) \cdot \left(A_{obj} e^{-ikx} + A_{ref} e^{-i\phi_{ref}} \right) \tag{4.9.5}$$

$$I_{recr} = A_{ref}^2 \left(1 + \left(\frac{A_{obj}}{A_{ref}} \right)^2 + 2 \left(\frac{A_{obj}}{A_{ref}} \right) \cos(\vec{k} \cdot \vec{x} - \phi_{ref}) \right) \tag{4.9.6}$$

This equation is similar to hologram recording since the reference amplitude, relative object amplitude, and cosine term are virtually the same. The third term in the equation represents the phase-shift of the wave interfering with the wave in the hologram surface, which is similar to the equation for hologram recording. The reconstruction of the object image follows the same configuration setup and alignment as the hologram recording. The reconstruction intensity equation can then be re-arranged to show the zero-order and first-order diffracted beams as follows:

$$I_{recr} = U_{recr} \cdot U_{recr}^{*} = \left| U_{obj} + U_{ref} \right|^2 \tag{4.9.7}$$

$$I_{recr} = (U_{obj} + U_{ref}) \cdot (U_{obj}^{*} + U_{ref}^{*}) \tag{4.9.8}$$

$$I_{recr} = U_{obj}U_{obj}^{*} + U_{ref}U_{ref}^{*} + U_{obj}^{*}U_{ref} + U_{obj}U_{ref}^{*} \tag{4.9.9}$$

$$I_{recr} = A_{obj}^{2} + A_{ref}^{2} + U_{obj}^{*}U_{ref} + U_{obj}U_{ref}^{*} \tag{4.9.10}$$

$$I_{recr} = \frac{1}{U_{ref}}\left(U_{ref}^{2}U_{obj}^{*} + (A_{obj}^{2} + A_{ref}^{2})U_{ref} + A_{ref}^{2}U_{obj}\right) \tag{4.9.11}$$

The first term $U_{ref}^{2}U_{obj}^{*}$ represents the First-Order Negative Peak

The second term $(A_{obj}^{2} + A_{ref}^{2})U_{ref}$ represents the Zero-Order Peak at the Origin

The third term $A_{ref}^{2}U_{obj}$ represents the First-Order Positive Peak

The first-order diffracted peaks of the object are conjugate to one another. The zero-order peak of the reference beam has the highest intensity because of the higher multiplication factor $(A_{obj}^{2} + A_{ref}^{2})$.

4.10 Interferometry

Both interferometry and holography employ wave interference of two coherent beams. The difference between the two methods is that holography preserves the absolute phase and interferometry preserves only the relative phase. Michelson type of interferometers preserve just the relative phase in situations where the difference between reference beam and object beam can be phase-shifted by order of $2\pi n$ (n=0,1,2,3,…). Holography preserves the absolute phase where n=0 and the object beam with no specimen has an identical Optical Path Length (*OPL*) to the reference beam. The absolute phase of holography is preserved when $OPL_{obj} = OPL_{ref}$ meaning the beam optical path lengths are equal.

The Michelson interferometer is a common approach to producing interference fringes by using beam splitters and beam combiners that split and then overlaps the two coherent beams. Interference occurs when the path length difference between the reference beam to the object beam is less than the coherence length of the source. The interference fringe pattern consists of intensity minima and maxima at constant fringe-spacing or spatial carrier frequency. The ratio of the intensity maxima to minima difference divided by the intensity maxima to minima sum produces the Fringe Contrast (*FC*) or Fringe Visibility (*FV*), defined by the following formula:

$$FV = \frac{I_{\max} - I_{\min}}{I_{\max} + I_{\min}} = \frac{\frac{I_{\max}}{I_{\min}} - 1}{\frac{I_{\max}}{I_{\min}} + 1} \tag{4.10.1}$$

Where $I_{\max}$ & $I_{\min}$ are the intensity maximum and minimum in the hologram.

As the path length difference of the object beam to the reference beam increases then the *FV* decreases, this means that the peak-to-valley intensity range is also decreasing. The path length where the waves become incoherent and the peaks-to-valleys indistinguishable is known as the coherence length (L_c). The coherence length is the path length difference of object beam to reference beam, or the path length distance that the wave of the laser remains coherent, which typically corresponds to an *FV*=50%. The intensity ratio is $\frac{I_{\max}}{I_{\min}} = 3$ for *FV*=50%. An intensity ratio of $\frac{I_{\max}}{I_{\min}} = e = 2.72$ produces *FV*=46.2%, for example.

Another way to define coherence length is by the following formula which shows that a small change in wavelength, which is based on a narrow distribution line frequency, produces a long coherence length.

$$L_c = \frac{\lambda^2}{\Delta\lambda} \tag{4.10.2}$$

The central wavelength of the laser is λ and the spectral width of the source over the emissive area is $\Delta\lambda$. Spatial coherence is the wavefront error over the emissive area or the aperture of the laser. If the laser is stable with no variations in wavelength, the coherence length would be infinite. The Diode Pumped Solid-State (DPSS) laser used for the experiments is designed to emit a coherent beam from a point source. The collimated output beam is small at 0.1 mm in diameter with a beam waist extending out to the $1/e^2$ encircled energy. A point source radiator will have a lower spatial wavefront error and a correspondingly higher coherence length than a large surface area radiating source. In general, DPSS lasers have smaller area sources for radiation than gas pumped lasers. The coherence length for the blue 457 nm/wave DPSS laser is specified at $L_c = 5m$.

The CSLH microscope preserves the absolute phase by propagating the object beam and the reference beam through the same optical components to the camera, which is placed where the beams overlap. Wavefront splitting the beams and propagating the two beams through the same optical components provides a nearly identical *OPL* for the object and the reference beam. Some constraints with this wavefront split configuration in comparison to the amplitude splitting configuration are:
1) The scanning displacement is limited to the spacing between the split beams, and
2) Focusing the reference and object beams is through a telecentric lens configuration that is off the optical axis centerline.

The off-axis chief rays in the telecentric lens introduce geometrical aberrations, such as coma, that cannot be corrected at the focal point of the telecentric lens even when designing aspheric lenses. The geometric aberrations for beams that are propagating side-by-side through the same lens means that the marginal rays of a single beam pass through a different radius-of-curvature, which cannot be corrected. However, the off-axis coma aberration is corrected at the exit of the telecentric lens by a Fresnel biprism, which is symmetrical to another Fresnel biprism at the entrance of the telecentric lens.

The advantage of this wavefront splitting approach is that the optical aberrations can be compensated to some degree by recording a reference hologram, which records the phase-shifts due to the optical aberrations. Compensation is then accomplished by subtracting the phase-shifts due to the microscope optics from the phase-shifts that are due to the microscope optics plus the specimen.

4.11 Wavefront Error and Coherence Length

As the coherence of a laser increases due to its emission properties the coherence length also increases and the wavefront error decreases. A longer coherence length means that a laser produces discernable fringes from interference over a longer path length. These discernable fringes appear within a hologram. The wavefront error occurs through a cross-section of the laser beam at any point along the optical axis. An example wavefront error over a line across the aperture of the laser is shown in figure 4.11.1 below:

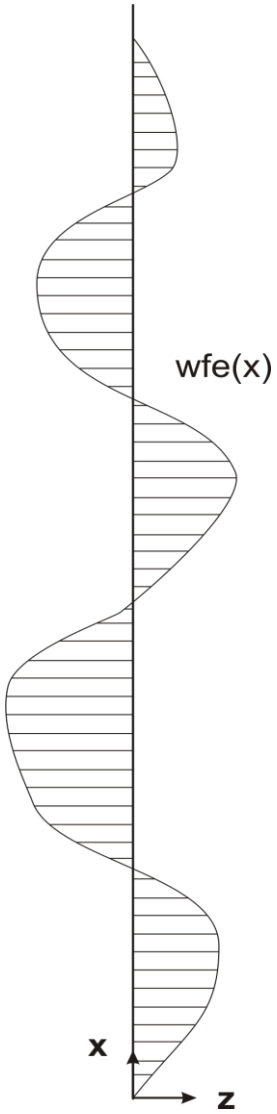

Figure 4.11.1: Wavefront Error Across a Pupil or an Aperture

The Wavefront Error (*wfe*) is a continuous function along the *x*-axis where a discrete value of wavefront error is sampled along the *z*-axis. The cross-sectional area of the circular laser beam used in the wavefront error equation is given below:

$$A_p = \int\int dx \cdot dy = \sum_{j=1}^{m}\sum_{i=1}^{n} \Delta x_i \cdot \Delta y_j = n\Delta x \cdot m\Delta y \quad \text{in Cartesian coordinates} \tag{4.11.1}$$

$$A_p = \int\int r dr \cdot d\theta = \frac{\pi}{4} D_p^2 \quad \text{in Polar coordinates} \tag{4.11.2}$$

Where: D_p is the diameter of the circular Aperture Beam.

Over the cross-sectional area (*x,y*) Cartesian or (*r,θ*) Polar coordinates of the beam the wavefront error (*wfe*) variance is given as:

In Cartesian Coordinates the Wavefront Error Variance:

$$\sigma_{wfe}^2 = \frac{1}{A_p}\int\int (wfe(x,y) - wfe_{mean})^2\, dx \cdot dy \quad \text{Continuous} \tag{4.11.3}$$

$$\sigma_{wfe}^2 = \frac{1}{A_p}\sum_{j=1}^{m}\sum_{i=1}^{n(j)} (wfe(i,j) - wfe_{mean})^2\, \Delta x \cdot \Delta y \quad \text{Discrete Sampled Data} \tag{4.11.4}$$

$$\begin{aligned} \Delta x &= x - x_0 = r \cdot \cos\theta \\ \Delta y &= y - y_0 = r \cdot \sin\theta \end{aligned} \tag{4.11.5}$$

$$r = \sqrt{\Delta x^2 + \Delta y^2} \tag{4.11.6}$$

$$\theta = \tan^{-1}\left(\frac{\Delta y}{\Delta x}\right) \tag{4.11.7}$$

In Polar Coordinates the Wavefront Error Variance:

$$\sigma_{wfe}^2 = \frac{1}{A_p}\int\int (wfe(r,\theta) - wfe_{mean})^2\, r dr \cdot d\theta \quad \text{Continuous} \tag{4.11.8}$$

$$\sigma_{wfe}^2 = \frac{1}{A_p}\sum_{t=1}^{\theta(t)}\sum_{s=1}^{r(s)} (wfe(s,t) - wfe_{mean})^2\, r(s) \cdot \Delta r \cdot \Delta\theta \quad \text{Discrete Sampled Data} \tag{4.11.9}$$

The Wavefront Error (μm) is as follows:

$$wfe = \lambda\sqrt{\sigma_{wfe}^2} \tag{4.11.10}$$

The Coherence Length (L_c) is then:

$$L_C = \frac{\lambda^2}{\Delta\lambda} = \frac{\lambda^2}{wfe} = \frac{\lambda^2}{\lambda\sqrt{\sigma_{wfe}^2}} = \frac{\lambda}{\sqrt{\sigma_{wfe}^2}} \tag{4.11.11}$$

The coherence length can be viewed as an inverse relationship to the wavefront error. No references were found proving this relationship. Since coherence length and wavefront error are often mentioned in holography references, but are not mathematically linked, then the relationship derived above was determined from principles and logical deduction.

4.12 Confocal Holography

Confocal holography was primarily researched by Herring et. al. [1-5,33-36] to attain high-resolution three-dimensional imaging of specimens and measurement of their properties, such as temperature and composition. A method to combine confocal microscopy with holography was first conceived by Herring [1] which wavefront splits a common laser source into two beams and then propagates the two side-by-side beams through a Dixon [17] like Confocal Scanning Laser Microscope (CSLM). The advantage of the wavefront splitter approach is that the propagation of both the reference beam and the object beam is through common optical components. Thus the geometric optical aberrations that are common to both beams will be combined at the camera and the fringe contrast or the fringe visibility will be maximum since $I_{obj} \cong I_{ref}$ for all points across the overlapped region of wave interference.

The confocal aspect is to aperture the focal point in the specimen by creating a conjugate focal point and placing a pinhole aperture at this focal point, which is downstream from the specimen. The beam aberrations from the high Numerical Aperture (NA) and low f/# focusing lenses can then be blocked by the pinhole apertures. This will sharpen the image for higher resolution at the scan point of the focused beam in the specimen and reduce the depth-of-focus. Confocal apertures are less effective on large f/# focusing lenses because the optical aberrations are lower.

The CSLH microscope as designed by Herring is one of the most complex optical microscopes built and has the advantage of preserving the absolute phase information from measured holograms. The absolute phase is preserved by the side-by-side propagating beams through the same optical components having an equivalent optical path length. A fringe-shift in a hologram is proportional to a change in index-of-refraction within the specimen. This refractive index can then be split into interior temperature profiles and internal composition profiles given two laser sources that are sufficiently separated in wavelength. The large separation in wavelength from the blue to red lasers provides an independent measurement for temperature and composition from the refractive index. The scanning geometry and confocal feature of this CSLH microscope provides a means to reconstruct the internal temperature from a hologram that measures the cumulative Optical Path Length (*OPL*) effects along the entire path length through the specimen.

This CSLH microscope demonstrates uniqueness in two different ways: 1) A microscope of this complexity that combines holography with confocal microscopy has never been built. This design is similar to the Dixon [17] scanning confocal microscope in that the confocal re-imaging focal point is stationary during three-dimensional scanning; however, the CSLH microscope differs from the Dixon scanning confocal microscope as the projector lens converges two beams to produce wave interference that forms a hologram. 2) The CSLH microscope has a unique capacity to reconstruct the internal three-dimensional properties within the specimen given a focused scan beam and a single view port window restriction. The single view port or viewing window limits the viewing angle scanning geometry to that of the cone beam angle of the focused beam within the specimen. Dr. Herring imposed the single view port window with no rotational scanning for micro-gravity space-based experiments and other restricted scanning angle applications. In general, the uniquely derived “wily” reconstruction method allows tomography for ordinary microscopes as the beam has a normal incident angle to the specimen. This is the same configuration for the CSLH microscope because of the rotational scanning restriction. Directing a beam from a single window as a focused cone beam with a high index-of-refraction sphere in the specimen region will produce a hologram as shown in figure 4.12.1 below:

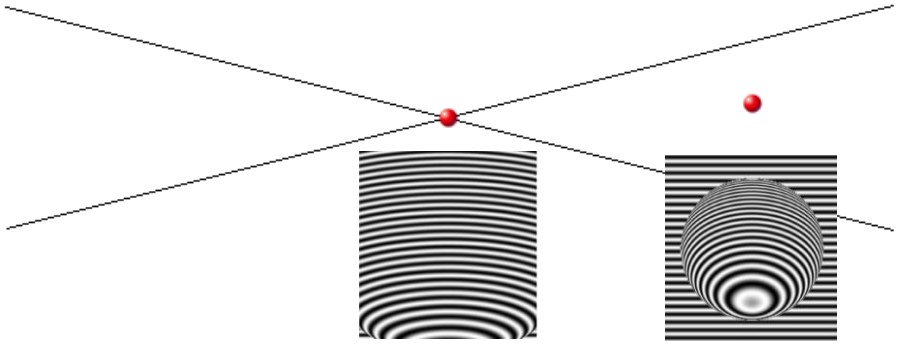

Figure 4.12.1: High Refractive Index Ball and Corresponding Fringe Pattern for Two Scan Positions

The holograms were produced by a high resolution 512x512x512 array computational grid and 1 million rays for the focused cone beam simulation. The ball is shown in two different positions. When the ball is centered at the focal point all of the rays pass through the ball and the curved lines represent the curvature of the ball since all of the rays pass through the same thickness. When the ball is moved away from the crossing point of the beam or the focal point then only a portion of the rays will pass through the ball. There is a significant phase-shift in the fringes when the rays intercept the edges of

the ball. The fringe pattern shows the effect of rays that pass through the central region of the ball that is thicker than the rays that pass through the edges of the ball.

The generation of a hologram by the simulation program takes over one day of computer run time. A large phase-shift occurs at the edge from the relatively high refractive index ball (Δn=1x10^{-4}). The ball is considered a strong phase object as there are a significant number of waves that have shifted at the edge of the ball over a small displacement. Phase unwrapping is possible if the computational grid resolution is increased along with an increase in the number of focused beam rays.

The number of rays in the focused beam is infinite and the hologram is imaged with a line scan camera at 1x8192 pixel resolution. The computational grid resolution in the fluid-cell is 8x6x4 array. The reconstruction algorithm uses a 32x32 array to solve for 8x4=32 unknown index-of-refractions in a cross-sectional plane or slice through the fluid-cell. The cross-sectional planes or slices are scanned in 4 steps along the vertical *y*-axis to produce a three-dimensional reconstruction of the index-of-refraction. The index-of-refraction can then be converted to a 3-D temperature profile or distribution through the fluid-cell.

4.13 Interference Waves

Interference of intersecting waves from a coherent source can produces a diamond shaped pattern as in the ripples of water waves from two stones thrown into a pond. Young's double-slit experiment is a single dimensional case where two slits produce a wave pattern from a single coherent source. The two slits create a wave interference pattern as shown in figure 4.13.1 below:

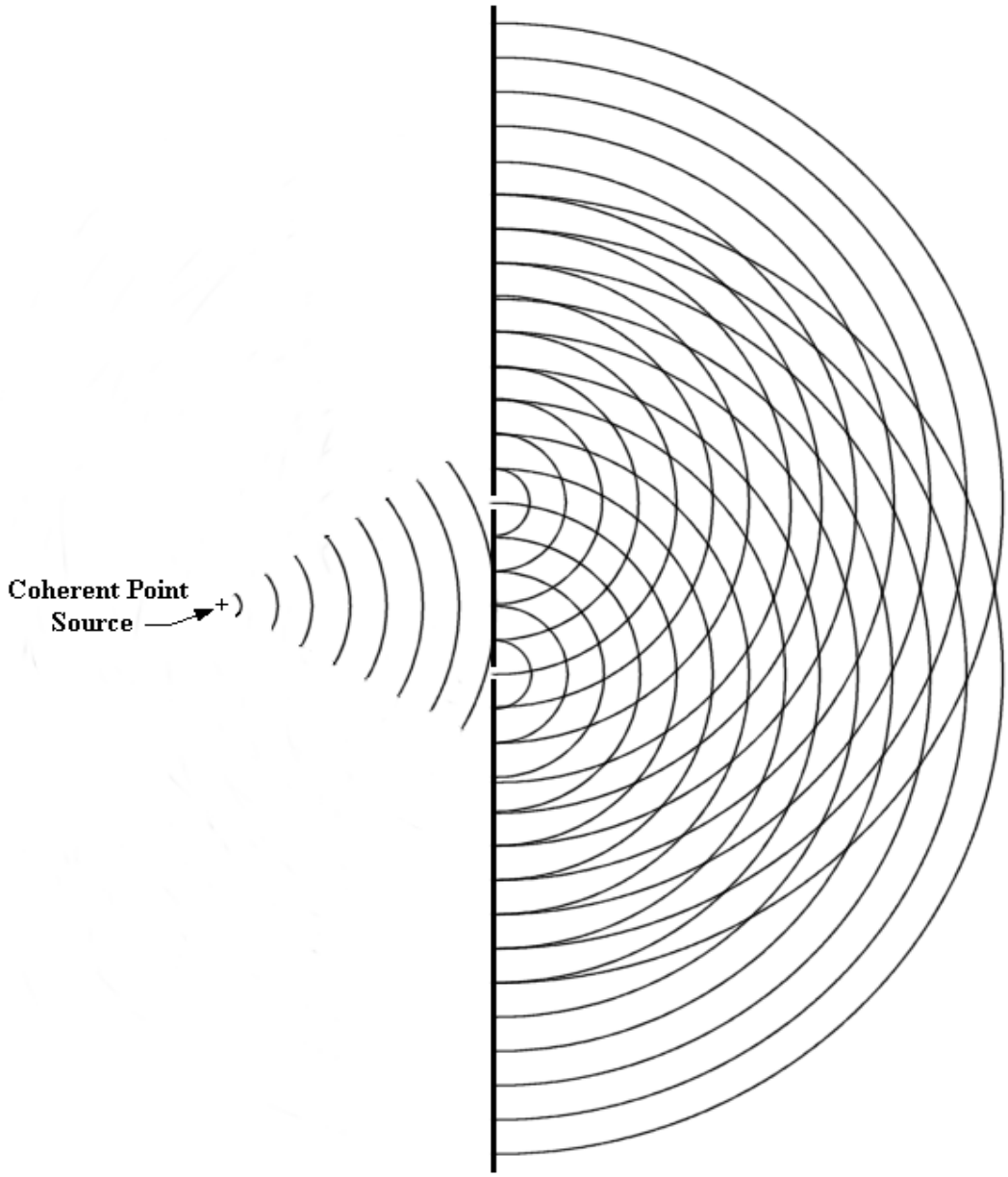

Figure 4.13.1: Young's Interference Fringes from Wave Cancellation and Reinforcement

The intersecting lines show either the reinforcement or cancellation of the coherent waves emitted from the slits. If a vertical detector plane is placed in the field of emission then a fringe pattern would be imaged on the detectors of a camera. The back-to-back Fresnel biprisms in the CSLH microscope wavefront splits a coherent beam into two separate beams that propagate as plane waves in parallel. One of the beams can be designated the reference beam and the other the object beam. Overlapping the object beam onto the reference beam with a Fresnel biprism is shown in figure 4.13.2 below:

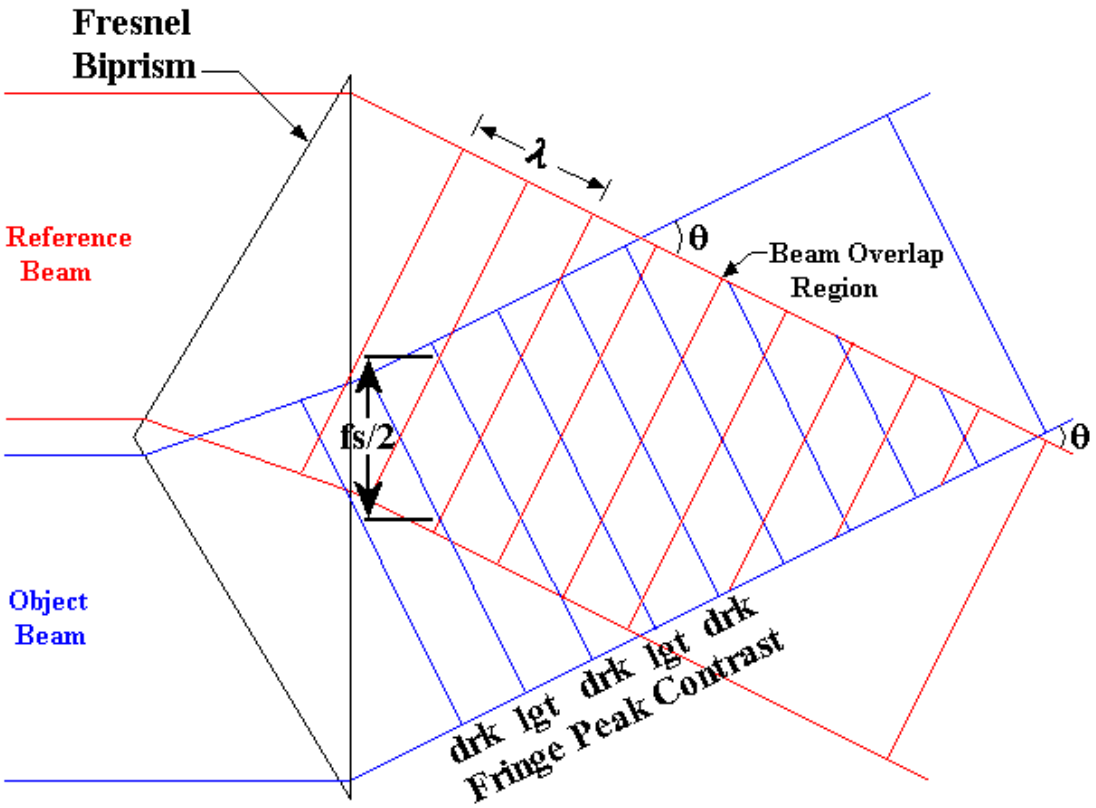

Figure 4.13.2: Interference Pattern Fringes due to Beam Overlap

The biprism tilts the wavefront of the two beams so that the waves cross one another. Fringes occur in the region of beam overlap. A camera can be placed in the region of overlap to detect the fringes. The dark and light contrast region produces the fringe lines from wave reinforcement and cancellation and the pattern has a diamond shape. The height of two diamonds is the fringe-spacing (*fs*) that represents a displacement from either dark-to-dark or light-to-light. The fringe-spacing equation is as follows:

Fringe-Spacing: $fs = \dfrac{\lambda}{\sin(\theta/2)}$ (4.13.1)

Given:

Beam crossing angle or wavefront overlap angle: θ=1°

Wavelength: λ=0.457μm

$$fs = \frac{\lambda}{\sin(\theta/2)} = \frac{0.457\,\mu m}{\sin(1/2)} = 52.4\,\mu m/wave \text{ of a fringe or } 52.4\,\mu m/fringe \quad (4.13.2)$$

Given:

Beam crossing angle or wavefront overlap angle: θ=0.25°

$$fs = \frac{\lambda}{\sin(\theta/2)} = \frac{0.457\,\mu m}{\sin(0.25/2)} = 209.5\,\mu m/wave \text{ of a fringe} \quad (4.13.3)$$

Camera Detector Spacing: Δs = 7 μm/pixel

Number of Pixel Samples per fringe: $num_{smpls} = \frac{fs}{\Delta s} = \frac{209.5\mu m}{7\mu m} = 30\ pixels/\ fringe$

The minimum required is $16\ pixels\ /\ fringe$ sampling resolution in order to accurately determine the phase-shift in the hologram.

The purpose of the simple interferometer is to examine fringe contrast at a long path length, which represents the path length of the CSLH microscope.

Wavefront propagation is shown by the wave equation below:

Intensity: $\vec{I}(x,y,z,t) = I_o e^{i(\vec{k}\cdot\vec{r}-\omega\cdot t)}$ (4.13.5)

Where:

Wave Number: $\vec{k} = k_x \cdot \vec{e}_i + k_y \cdot \vec{e}_j + k_z \cdot \vec{e}_k$ (4.13.6)

Position: $\vec{r} = (x - x_o)\cdot\vec{e}_i + (y - y_o)\cdot\vec{e}_j + (z - z_o)\cdot\vec{e}_k$ (4.13.7)

Steady-State: $t = 0$

Fixed Cross-Sectional Plane: $z = z_o$

Object Wave Position Vector: $\vec{r}_{obj} = (x_{obj} - x_o)\cdot\vec{e}_i + (y_{obj} - y_o)\cdot\vec{e}_j + (z_{obj} - z_o)\cdot\vec{e}_k$

Reference Wave Position Vector: $\vec{r}_{ref} = (x_{ref} - x_o)\cdot\vec{e}_i + (y_{ref} - y_o)\cdot\vec{e}_j + (z_{ref} - z_o)\cdot\vec{e}_k$

Relative Object to Reference Wave Position Vector:

$$\Delta\vec{r} = (x_{obj} - x_{ref})\cdot\vec{e}_i + (y_{obj} - y_{ref})\cdot\vec{e}_j + (z_{obj} - z_{ref})\cdot\vec{e}_k \quad (4.13.10)$$

Let $x_{ref} = y_{ref} = z_{ref} = 0$ since wavefront perturbations are relative to the reference wavefront.

Then the wave equation is simplified to: $\vec{I}(x,y) = I_o e^{i(k_x \cdot x_{obj} + k_y \cdot y_{obj})}$ (4.13.11)

Given spatial frequencies f_x, f_y then the spatial wave numbers are:

$k_x = 2\pi f_x$ and $k_y = 2\pi f_y$ (4.13.12)

Then

$$\vec{I}(x,y) = I_O \cos(2\pi f_x \cdot x_{obj} + 2\pi f_y \cdot y_{obj}) + i \cdot I_o \sin(2\pi f_x \cdot x_{obj} + 2\pi f_y \cdot y_{obj}) \quad (4.13.13)$$

or

$$\bar{I}(x,y) = I_x + i \cdot I_y \tag{4.13.14}$$

Vectors x_{obj} , y_{obj} are random variables represented by Gaussian statistical probability density functions. These equations are used to evaluate the fringe contrast variation in a hologram given a random variable for the wavefront error in terms of λ/50 waves, for example. If the wavefront error is too high then a small change in index-of-refraction of fringe-shift will not be detected. This is further explained in the error analysis section.

4.14 The “wily” Matrix Reconstruction Method

The “wily” reconstruction method does not assume a proportional relationship of index-of-refraction to phase-shift since it is possible that only a portion of one ray will propagate through a grid-cell for only one of all the scan positions. This implies a high error in determining the index-of-refraction for that particular grid-cell. Instead a path length “wily” matrix is derived for the marginal rays which are propagated through the grid-cell volumetric domain. The “wily” matrix includes cross-coupling terms for the phase-shift vector. The cross-coupling occurs because the index-of-refraction is a function of more than a single phase-shift value. The 32x32 “wily” reconstruction matrix represents a phase-shift to index-of-refraction relationship for all scan positions of the marginal rays at a single elevation plane in the specimen. The marginal rays of the focused cone beam provides two phase-shift measurements from a single hologram as a hologram is acquired and recorded for each scan position. The rows of the “wily” matrix represent the phase-shift for 16 scan positions at 2 phase-shifts per scan position. The columns of the matrix represent a pointer to a grid-cell in the computational domain.

The reconstruction matrix was typically found to be non-invertible due to the scanning restriction with no rotations. Neither the fluid-cell specimen nor the laser system can be rotated. The fixed viewing window to the fluid-cell produces a reconstruction matrix that is ill-conditioned with a high condition value because of correlated information or too little information. Inverting an ill-conditioned matrix produces an unacceptable reconstruction error. A matrix with zero-determinant cannot be inverted. The zero determinant matrix typically occurs from too little information of a sparse matrix. Scanning from a single viewport window with the scan angle being the cone angle of the beam in the fluid-cell produces a sparse matrix. The limited viewing angle tomography configuration of the

CSLH microscope is an ill-posed condition, which is either non-solvable or subject to large reconstruction error.

The approach of two scan positions per computational cell was found to produce an ill-conditioned reconstruction matrix with large reconstruction errors. The reconstruction errors produced by the ill-conditioned matrix were unacceptable as the reconstructed temperature error was well over 1º C based on our simulations. Changing from two scan positions per computational cell to only one scan position per computational cell reduced the correlation of phase-shifts from scan position to scan position. Non-correlated holograms provided independent measurements to the reconstruction algorithm and the reconstruction matrix are derived from marginal ray tracing through the fluid-cell was invertible with an acceptably low condition value. The extremely sparse matrix is invertible producing negligible reconstruction error.

The creation of the “wily” matrix made reconstruction possible which was previously thought impossible. The reason reconstruction was previously thought impossible is that a small angle difference in two line equations can be approximated by a single equation. Lai [5] explored reconstruction algorithms and the small differences in line equations by using a double precision math kernel in his numerical simulations. In comparison, Lai’s reconstruction algorithm uses a propagation method given boundary conditions from grid-cell to grid-cell of the scanned fluid-cell. A marginal ray of the cone beam is propagated iteratively through the grid-cells and the measured phase-shift is considered proportional to the index-of-refraction for each computational grid-cell. In Lai’s publication the computational array is 4x4 given 16 measured phase-shifts and 16 unknown index-of-refraction values.

Various approaches to scanning geometry and grid-mesh size were explored and three of the approaches are shown in figure 4.14.1 below:

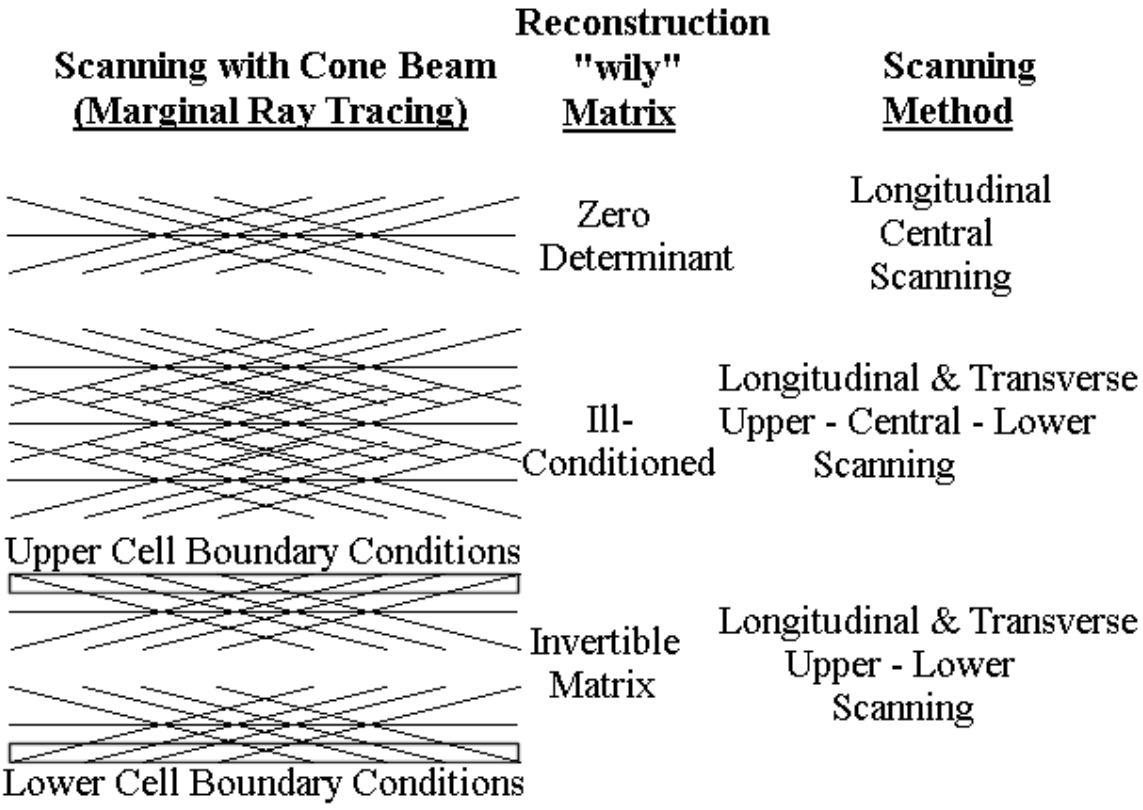

Figure 4.14.1: Three Methods of Scanning

The first method is a direct longitudinal scan along the optical propagation *z*-axis. The reconstruction matrix for this longitudinal central scanning configuration produces a zero determinant.

The second approach is upper, central, and lower scanning in the transverse direction along the *y*-axis. The second method uses two scan positions per grid cell. This approach produces an ill-conditioned reconstruction matrix and the reconstructed refractive index error from simulation studies is unacceptable. The ill-conditioned matrix was inverted using pseudo-inverse and singular value decomposition techniques. All methods produced an index-of-refraction with large error with respect to a reference profile.

The third approach, using the “wily” matrix used upper and lower transverse scanning along the *y*-axis with Boundary Condition (BC) values along the walls of the fluid-cell. It was assumed that the BCs could be measured non-intrusively as the interior region is the computational domain for reconstruction. There is only one scan position per grid-mesh cell and the rays are evenly distributed throughout the fluid-cell. A portion of the rays are seen to propagate through the BC region and the remaining portion of the rays

propagate through the interior computational domain. The distribution of the scan positions provides independent non-correlated hologram measurements and incorporating the BCs provides additional information. The determinant of the Path Length (*PL*) matrix for reconstruction is non-zero. This *PL* matrix is sparse as it does not contain even a single diagonal of non-zero elements and yet is invertible. Given a scanning geometry with evenly distributed scan positions and defined BCs we can now produce the reconstructed refractive index with negligible error. The derived "wily" reconstruction algorithm produces the internal 3D index-of-refraction values with a reconstruction error of < $1x10^{-10}$ RMS based on our simulations. This shows that the reconstruction algorithm error is significantly less than the measurement error which is 7×10^{-6}.

Some sources that contribute to reconstruction error are given as follows:

1) Algorithm instability as singularities are encountered from a sparse matrix and ill-conditioning
2) Thermocouple measurement error as the thermocouple is a reference for the interior computational domain and the boundary conditions
3) Phase-shift error from the measured holograms as a hologram is subject to waveform distortions from optical aberrations and signal-to-noise ratio
4) Camera radiometric dynamic range is reduced at the 457nm (blue laser) wavelength as the camera is most sensitive at 633nm (red laser) wavelength
5) Fourier transform algorithm error to determine the phase-shifts in a hologram due to inconsistencies of amplitude in the fringe pattern waveform
6) Ground vibrations transmitted through the isolated optical table that affect the holograms

4.15 Refractive Index Reconstruction by Longitudinal Scanning

A longitudinal scanning approach along the *z*-axis is assessed for index-of-refraction reconstruction. The focused scan beam with f/2 optical f-number or slope of *m*=1/4 is shown in figure 4.15.1 below:

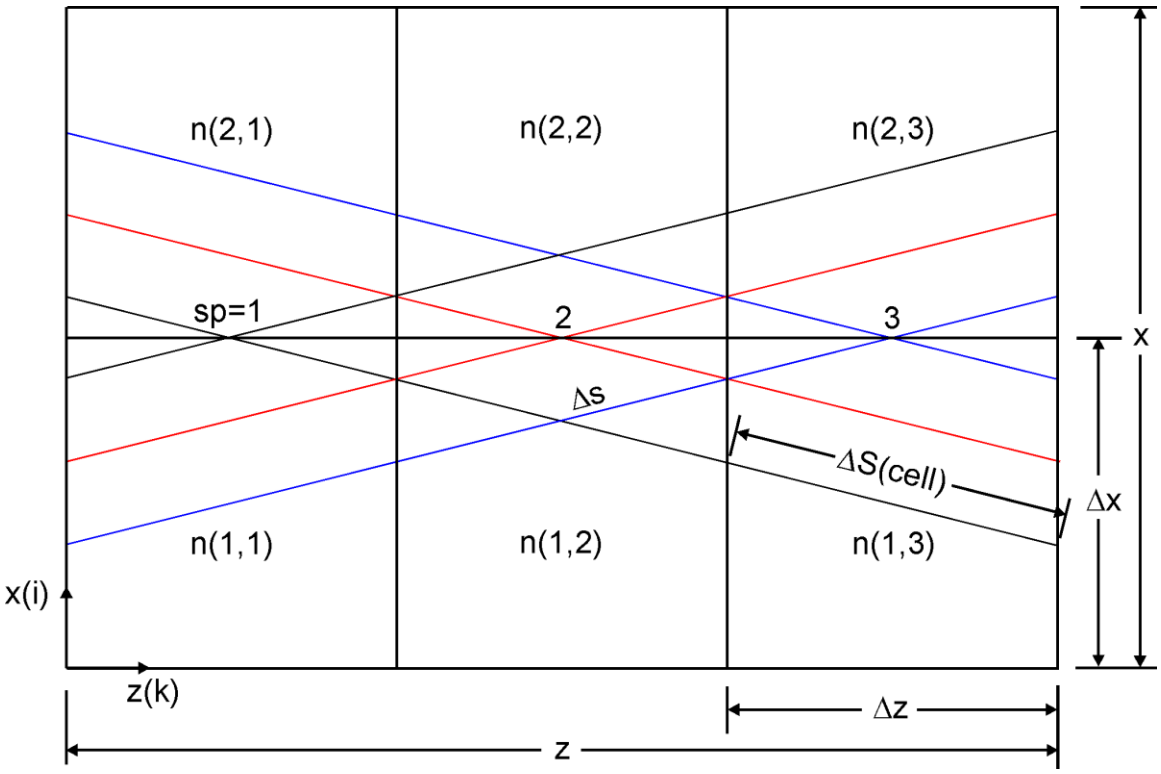

Figure 4.15.1: Longitudinal Scanning of a Fluid-Cell

The figure shows three scan positions $(sp = 1,2,3)$ of the focused cone beam along the optical propagation axis or *z*-axis. The marginal rays of the cone beam are represented by the negative and positive slope lines. The Optical Path Length (*OPL*) vector in microns is given by the following equation:

$$OPL = [PL] \times \vec{n} = \lambda \cdot \Delta\vec{\phi} \qquad (4.15.1)$$

Given:

Path Length (*PL*) Matrix: 6x6 array defining a path length for each ray through the cells

Index-of-Refraction: $n(i,k)$ that is converted from an array to a vector

Wavelength of the Laser: λ=0.457 μm/wave (scalar constant)

Measured Phase-Shift: $\Delta\phi(sp,r)$ (waves) that are converted from an array to a vector

Units are $\dfrac{\Delta\phi\ (radians)}{2\pi\ (rad\ /\ wave)} \equiv (waves)$

Scan Position: *sp*=1,2,3

Marginal Rays with Negative Slope: *r* = 1

Marginal Rays with Positive Slope: *r* = 2

The Index-of-Refraction vector is given below, which is the unknown parameter to reconstruct:

$$\vec{n} = \begin{bmatrix} n(1,1) \\ n(1,2) \\ n(1,3) \\ n(2,1) \\ n(2,2) \\ n(2,3) \end{bmatrix}$$

Dimensional Parameters for the diagonal path length of the marginal rays are:

$$\Delta s_{cell} = \sqrt{1+m^2} \times \Delta z \qquad \text{Where: } \Delta z = 625 \mu m / cell \tag{4.15.2}$$

$$\Delta s = \sqrt{1+m^2} \times z \qquad \text{Where: } z = 3 \cdot \Delta z \tag{4.15.3}$$

The Path Length (*PL*) for each Scan Position (*sp* = 1,2,3) and Slope (*r* = 1,2) is shown in the following matrix.

$$PL = \begin{bmatrix} 0.5 & 1 & 1 & 0.5 & 0 & 0 \\ 0 & 0.5 & 1 & 1 & 0.5 & 0 \\ 0 & 0 & 0.5 & 1 & 1 & 0.5 \\ 0.5 & 0 & 0 & 0.5 & 1 & 1 \\ 1 & 0.5 & 0 & 0 & 0.5 & 1 \\ 1 & 1 & 0.5 & 0 & 0 & 0.5 \end{bmatrix} \times \Delta s_{cell} \tag{4.15.4}$$

The determinant of the sparse Path Length (*PL*) matrix is:

$$|PL| = 0$$

Thus, the inverse of the Path Length (*PL*) matrix is not achievable and reconstructing the Index-of-Refraction from this method of longitudinal scanning is not possible. The longitudinal scanning method must be abandoned since a zero determinant matrix implies that insufficient information is available. The workaround to this problem is to introduce additional information such as Boundary Conditions (BCs) and configure an improved scanning geometry.

5 Development of the CSLH Microscope

The development of the CSLH microscope consists of the “wily” reconstruction derivation, optical design configuration, and alignment of the optics. The Scanning Transmission Laser Holography (STLH) microscope is a simplified version of the CSLH microscope that was used in the development process to validate the CSLH microscope.

5.1 The “wily” Reconstruction Algorithm

The development of the CSLH microscope required the “wily” reconstruction algorithm, which uses upper and lower scanning of the fluid-cell along with upper and lower Boundary Conditions (BCs) along the walls. Scanning through the grid-mesh structure of the fluid-cell is shown in figure 5.1.1 below:

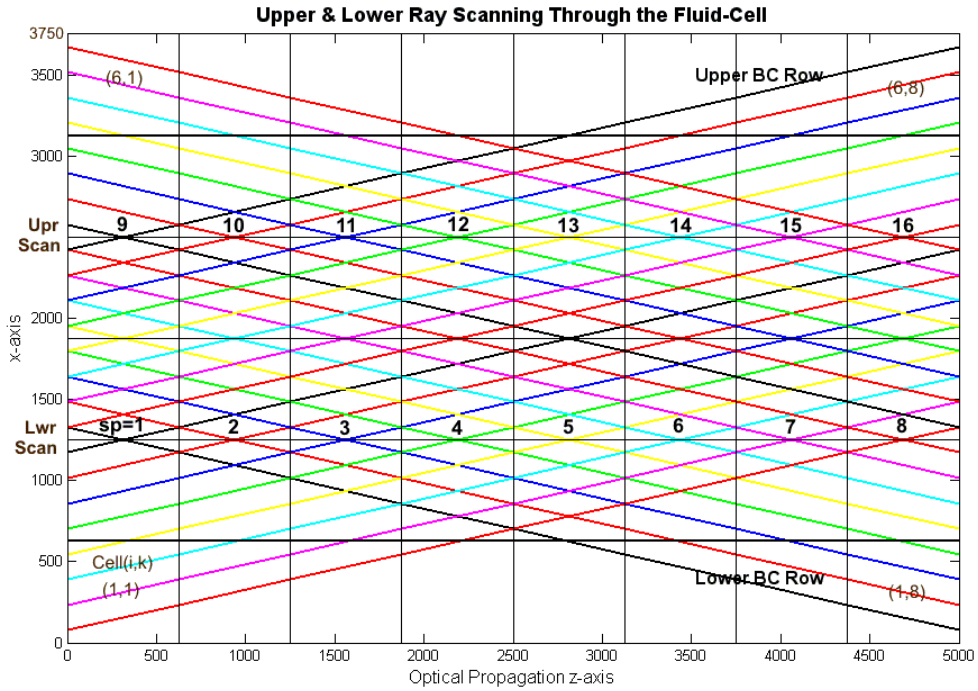

Figure 5.1.1: Upper and Lower Scanning Geometry of the Marginal Rays through a Fluid Cell

The scan angle for the STLH and CSLH microscopes is 28º, which represents the cone angle of the focused beam in the specimen and a sparse reconstruction matrix. A 28º rotation angle represents a marginal ray slope of m=±1/4 as seen in figure 5.1.1 above. The reconstruction matrix rows are represented by the scan position $(1 \le sp \le 16)$ and marginal ray slope (r=1 for Negative Slope Marginal Rays and r=2 for

Positive Slope Marginal Rays) rays that pass through the specimen. The matrix columns are represented by the index-of-refraction $(i\ ,k)$ cell within the $(1 \le i \le 6, 1 \le\ j \le 4, 1 \le k \le 8)$ computational grid-mesh. The i index represents the number of cells across the fluid-cell specimen in a horizontal axis. The j index represents the number of cells in the vertical axis. The *k* index represents the number of cells down the fluid-cell specimen along the optical propagation horizontal axis. The sparse 32x32 $(row \times col)$ reconstruction transformation matrix has a scanning to refractive index cell registry $((sp, r) \times (i, k))$.

The computational grid in the fluid-cell is 4 cells wide x 8 cells deep along the *z*-axis or the optical propagation axis for any of 4 vertical positions. The 4x8 grid-cell computational domain is represented by a horizontal plane. The "wily" reconstruction matrix uses 32 measured phase-shifts from 16 holograms (based on 16 scan positions) to determine 32 unknown index-of-refraction values in a rectilinear grid with constant index-of-refraction for each grid-cell. The lower scan line is for scan positions $sp = 1\ to\ 8$ and the upper scan line is for scan positions $sp = 9\ to\ 16$.

The lower scan line is at *x*=1250μm for scan positions 1 to 8 at the center of the cells. The upper scan line is at *x*=2500μm for scan positions 9 to 16 at the center of the cells. The depth of the fluid-cell is *z*=5000μm and the width of the fluid-cell is *x*=3750μm. The lower BCs are defined as cells(row 1, cols 1 to 8) or (1, 1 to 8) in figure 5.1.1 above. The upper BCs are defined as cells(row 6, cols 1 to 8) or (6, 1 to 8) in figure 5.1.1 above.

The scan position increments along the optical propagation *z*-axis is $\Delta z = 625\ \mu m / step$ where the crossing point of the marginal rays or the focal point of the cone beam is a scan position location. The negative slope and positive slope of the marginal rays for the focused ray cone beam represents a line equation. The Optical Path Length (*OPL*) for the index-of-refraction over a line or path length is defined as:

$$OPL = \int n \cdot dl \tag{5.1.1}$$

The Optical Path Length (*OPL*) for the scan position and slope of a marginal ray in terms of the grid-mesh is defined as:

$$OPL(sp, r) = \sum n(i, k) \cdot PL(i, k, sp, r) \tag{5.1.2}$$

Given:

Scan Position: $sp = 1\ to\ 16$

Marginal Rays with Negative Slope: $r = 1$

Marginal Rays with Positive Slope: $r = 2$

Grid-Mesh Cell Refractive Index: $n(i,k)$

Slope of the Marginal Rays: *m*=±1/4 where the focusing cone beam is f/2 focal length to diameter ratio in the specimen.

Diagonal displacement for a ray that passes through the front and back of a cell:

$$\Delta s = \sqrt{1+m^2}\cdot\Delta z = 644.235\,\mu m/cell \tag{5.1.3}$$

Path Length: $PL(i,k,sp,r)$

The general equation for optical path length again is:

Optical Path Length: $OPL(sp,r) = \sum n(i,k)\cdot PL(i,k,sp,r)$ (5.1.4)

The OPL for the first scan position of a negative slope marginal from the figure above is given as:

$$\begin{aligned} OPL(1,1) = {} & n(3,1)\cdot PL(3,1,1,1) + n(2,1)\cdot PL(2,1,1,1) + n(2,2)\cdot PL(2,2,1,1) + n(2,3)\cdot PL(2,3,1,1) \\ & + n(2,4)\cdot PL(2,4,1,1) + n(2,5)\cdot PL(2,5,1,1) + n(1,5)\cdot PL(1,5,1,1) + n(1,6)\cdot PL(1,6,1,1) \\ & + n(1,7)\cdot PL(1,7,1,1) + n(1,8)\cdot PL(1,8,1,1) \end{aligned} \tag{5.1.5}$$

$$\begin{aligned} OPL(1,1) = {} & n(3,1)\cdot\Delta s/2 + n(2,1)\cdot\Delta s/2 + n(2,2)\cdot\Delta s + n(2,3)\cdot\Delta s + n(2,4)\cdot\Delta s + n(2,5)\cdot\Delta s/2 \\ & + n(1,5)\cdot\Delta s/2 + n(1,6)\cdot\Delta s + n(1,7)\cdot\Delta s + n(1,8)\cdot\Delta s \end{aligned} \tag{5.1.6}$$

Given: $n(1,5)$, $n(1,6)$, $n(1,7)$, $n(1,8)$ for the Lower Row BCs as known values based on measured temperatures.

The *OPL* path length is defined for 16 scan positions over a negative and positive slope for a total of 32 measured phase-shifts along with 32 unknown index-of-refractions for the interior computational domain. There are 16 scan positions providing 16 holograms and 2 phase-shift values are obtained from a single hologram at the marginal rays. The interior computational domain refractive index is given as *n*(2:5,1:8) for *i*=2 to 5 and *k*=1 to 8.

The refractive index or temperature is assumed constant for each cell in the grid for computational discretization. This is a similar assumption found in the grid-mesh spacing for computational fluid dynamics. The three-dimensional grid-mesh is 6x8x4 cells which

includes the boundary condition cells. Three-dimensional reconstruction requires 64 holograms and 64 boundary conditions and the “wily” reconstruction matrix is a 32x32 sparse element array over 4 vertical planes. The 32x32 sparse “wily” path length matrix from the marginal rays that are scanned through the fluid-cell is shown in figure 5.1.2 below:

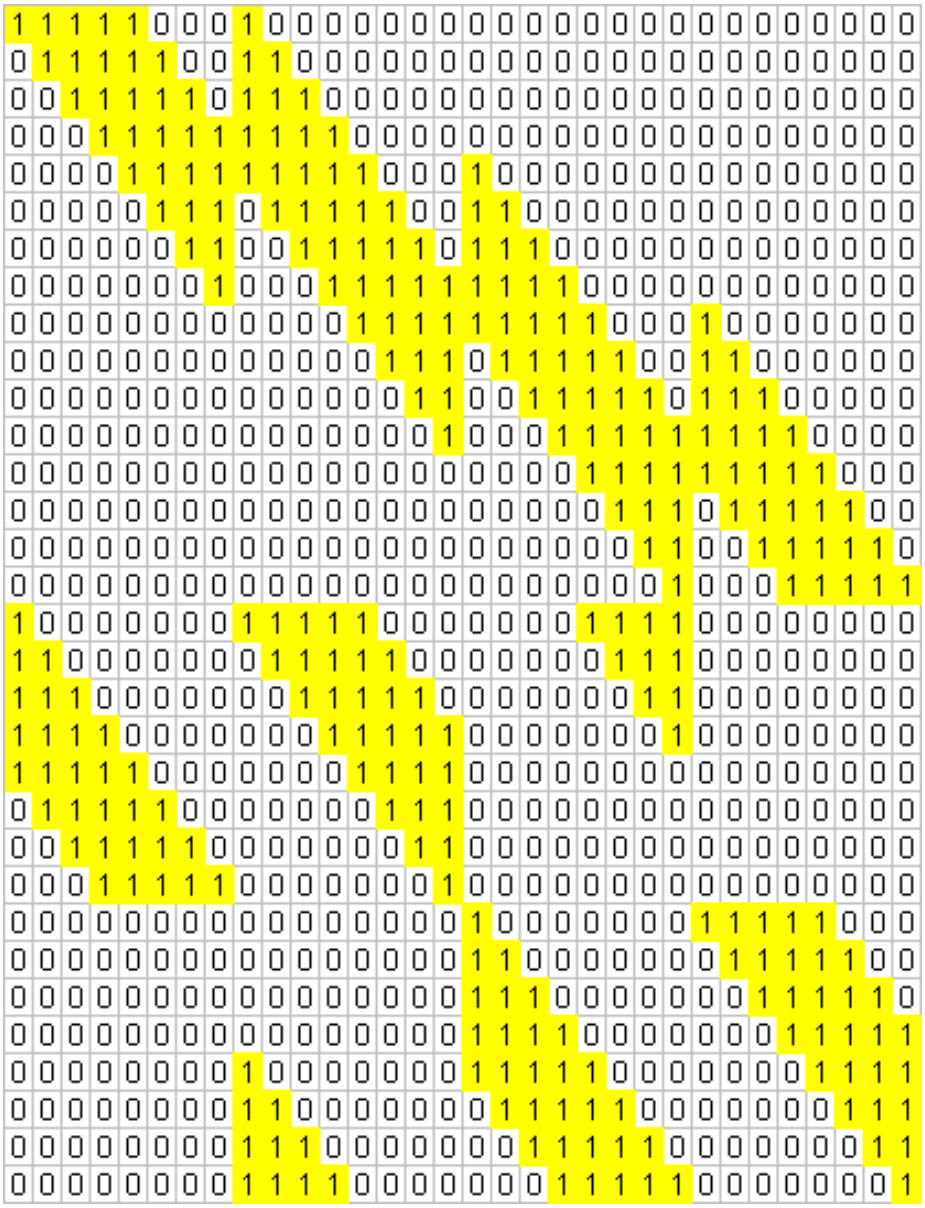

Figure 5.1.2: The “wily” Matrix

The “1” values in the matrix signify a non-zero value at the array index. Each row of the “wily” matrix is represented by the scan position and slope (*sp,r*) that is converted to a (32x1) vector. Each column of the “wily” matrix is represented by the index (*i,k*) of the grid-mesh that is converted to a (1x32) vector. Notice that there is not a single diagonal

across the matrix that does not contain at least one zero value and yet this matrix has a non-zero determinant. The *xyz*-scanning registry converts the 64x8192 hologram array into scan positions for the reconstruction algorithm. Each line from 1 to 64 is represented by a *xyz*-coordinate where $x(i), y(j), z(k)$. The *xyz*-scanning registry is shown in table 5.1.1 below:

Array Line to Scan Position (sp) Index								
Line No.	**Vertical Y**	**Horizontal X**	**Optical Z**		**Line No.**	**Vertical Y**	**Horizontal X**	**Optical Z**
1	1	1	1		33	3	1	1
2	1	1	2		34	3	1	2
3	1	1	3		35	3	1	3
4	1	1	4		36	3	1	4
5	1	1	5		37	3	1	5
6	1	1	6		38	3	1	6
7	1	1	7		39	3	1	7
8	1	1	8		40	3	1	8
9	1	2	1		41	3	2	1
10	1	2	2		42	3	2	2
11	1	2	3		43	3	2	3
12	1	2	4		44	3	2	4
13	1	2	5		45	3	2	5
14	1	2	6		46	3	2	6
15	1	2	7		47	3	2	7
16	1	2	8		48	3	2	8
17	2	1	1		49	4	1	1
18	2	1	2		50	4	1	2
19	2	1	3		51	4	1	3
20	2	1	4		52	4	1	4
21	2	1	5		53	4	1	5
22	2	1	6		54	4	1	6
23	2	1	7		55	4	1	7
24	2	1	8		56	4	1	8
25	2	2	1		57	4	2	1
26	2	2	2		58	4	2	2
27	2	2	3		59	4	2	3
28	2	2	4		60	4	2	4
29	2	2	5		61	4	2	5
30	2	2	6		62	4	2	6
31	2	2	7		63	4	2	7
32	2	2	8		64	4	2	8

Table 5.1.1: Scanning Sequence to *xyz*-axis Index

There are a total of 64 holograms required for reconstruction consisting of four elevation planes. Each scan plane is along the 5mm depth of the fluid-cell (or optical

propagation *z*-axis) and across the 5mm width of the fluid-cell (or *x*-axis). The elevation plane is a constant or fixed vertical distance from the heater along the *y*-axis. The vertical displacement to the heater is 0.5, 1.1, 1.7, and 2.3 mm in 0.6 mm increments or steps for *y*-axis scanning.

The Lower Ray Scanning follows the sequence:
k = 1 to 8 for *i* = 1 and all *j*
The Upper Ray Scanning follows the sequence:
k = 1 to 8 for *i* = 2 and all *j*

The three-dimensional volume of the fluid-cell is subdivided into grid-cells or cells where $x(i), y(j), z(k)$. The fluid-cell is comprised of vertical planes or slices along the *y*-axis. Each slice of index *j* is a plane along the *xz*-plane. The *z*-axis is the optical propagation axis and the Boundary Conditions (BC's) are found along the extremes of the *x*-axis where index pointer *i*=1 (Lower BC) and index pointer *i*=6 (Upper BC). The *xz*-plane is a 6x8 array with *i*=1,6 representing the BCs and *i*=2 to 5 representing the interior computational domain for reconstruction. The "wily" 32x32 $(row \times col)$ or $((sp, r) \times (i, k))$ matrix has a row registry that is shown in table 5.1.2 below:

"wily" matrix rows						
row	***sp***	***r***		**row**	***sp***	***r***
1	**1**	**1**		**17**	**1**	**2**
2	**2**	**1**		**18**	**2**	**2**
3	**3**	**1**		**19**	**3**	**2**
4	**4**	**1**		**20**	**4**	**2**
5	**5**	**1**		**21**	**5**	**2**
6	**6**	**1**		**22**	**6**	**2**
7	**7**	**1**		**23**	**7**	**2**
8	**8**	**1**		**24**	**8**	**2**
9	**9**	**1**		**25**	**9**	**2**
10	**10**	**1**		**26**	**10**	**2**
11	**11**	**1**		**27**	**11**	**2**
12	**12**	**1**		**28**	**12**	**2**
13	**13**	**1**		**29**	**13**	**2**
14	**14**	**1**		**30**	**14**	**2**
15	**15**	**1**		**31**	**15**	**2**
16	**16**	**1**		**32**	**16**	**2**

Table 5.1.2: The "wily" Matrix Scanning Registry for the Rows

The "wily" 32x32 $(row \times col)$ or $((sp, r) \times (i, k))$ matrix has a column registry that is shown in table 5.1.3 below:

"wily" matrix columns (cols)						
col	***i***	***k***		**col**	***i***	***k***
1	**1**	**1**		**17**	**3**	**1**
2	**1**	**2**		**18**	**3**	**2**
3	**1**	**3**		**19**	**3**	**3**
4	**1**	**4**		**20**	**3**	**4**
5	**1**	**5**		**21**	**3**	**5**
6	**1**	**6**		**22**	**3**	**6**
7	**1**	**7**		**23**	**3**	**7**
8	**1**	**8**		**24**	**3**	**8**
9	**2**	**1**		**25**	**4**	**1**
10	**2**	**2**		**26**	**4**	**2**
11	**2**	**3**		**27**	**4**	**3**
12	**2**	**4**		**28**	**4**	**4**
13	**2**	**5**		**29**	**4**	**5**
14	**2**	**6**		**30**	**4**	**6**
15	**2**	**7**		**31**	**4**	**7**
16	**2**	**8**		**32**	**4**	**8**

Table 5.1.3: The "wily" Matrix Computational Grid-Cell Registry for the Columns

The table 5.1.3 above represents the interior computational domain column registry with the transfer of index values to the fluid-cell grid-mesh as shown in table 5.1.4 below:

Computational Grid-Cell Registry *i*	**Fluid-Cell Grid-Mesh *i***
1	2
2	3
3	4
4	5

Table 5.1.4: Transfer from Computational Domain Column Registry to Scanning in Fluid-Cell

The "wily" matrix rows and columns relate scanning to index-of-refraction tables 5.1.1 to 5.1.4 above are used for transformations in the "wily" matrix algorithm.

The derived "wily" matrix reconstruction equations are given by:

$OPL_{obj} = [wily] \times \vec{n}_{obj} + OPL_{BC} = \lambda \vec{\phi}_{obj}$ for the Object Hologram (5.1.7)

at Elevated Temperature

$OPL_{ref} = [wily] \times \vec{n}_{ref} = \lambda \vec{\phi}_{ref}$ for the Reference Hologram (5.1.8)

at Constant Temperature

$|OPL_{ref}|$ is determined from the index-of-refraction of the fluid at the wavelength of the laser and room temperature along with the path length dimension of the fluid-cell for the marginal rays of the cone beam. A phantom fluid-cell for the reference beam at constant room temperature provides a constant index-of-refraction. The magnitude of the OPL_{ref} vector for the reference beam is constant since the index-of-refraction is constant and the path length for the marginal rays through the fluid-cell is constant.

$[wily]$ is the 32x32 path length matrix

OPL vector is the Optical Path Length through the specimen

The boundary condition *OPL* is based on the temperature measurements along the side walls of the fluid-cell which are converted as follows:

$n_{BC} = \frac{dn}{dT}(T_{BC} - T_{25}) + n_{25}$ and the fluid properties define $\frac{dn}{dT}$ along with n_{25} at 25°C.

$OPL_{BC} = PL_{BC} \times n_{BC}$ given the Path Length (*PL*) of the BC cell (5.1.9)

Relative Optical Path Length (Δ*OPL*):

$\Delta OPL = OPL_{obj} - OPL_{ref} = [wily] \times \vec{n}_{obj} + OPL_{BC} - [wily] \times \vec{n}_{ref} = \lambda \vec{\phi}_{obj} - \lambda \vec{\phi}_{ref}$ (5.1.10)

$\Delta OPL = [wily] \times (\vec{n}_{obj} - \vec{n}_{ref}) + OPL_{BC} = \lambda (\vec{\phi}_{obj} - \vec{\phi}_{ref})$ (5.1.11)

$\Delta OPL = [wily] \times \Delta \vec{n} + OPL_{BC} = \lambda \cdot \Delta \vec{\phi}_{meas}$ (5.1.12)

$\Delta \vec{n} = \vec{n}_{obj} - \vec{n}_{ref}$ Relative index-of-refraction (5.1.13)

$\Delta \vec{\phi}_{meas} = \vec{\phi}_{obj} - \vec{\phi}_{ref}$ Relative measured phase-shift of object to reference hologram

The reconstructed (*rec*) index-of-refraction of the object (*obj*) from measured phase-shift

$\vec{n}_{rec} = [wily]^{-1} \times (\lambda \vec{\phi}_{obj} - OPL_{BC})$ (5.1.15)

Where: $\vec{\phi}_{obj} = \Delta \vec{\phi}_{meas} + \vec{\phi}_{ref}$ (5.1.16)

$\vec{\phi}_{obj}$ represents the object or specimen phase-shift at elevated temperature

$\vec{\phi}_{ref}$ represents the reference hologram at constant room temperature

The measured phase-shift difference:

$$\Delta\vec{\phi}_{meas} = \vec{\phi}_{obj} - \vec{\phi}_{ref} \tag{5.1.17}$$

The phase-shift difference between the object hologram at an elevated temperature and the reference hologram at constant room temperature must be less than 1 fringe spacing between the sample positions. If the phase-shift between measurement points or scan positions is greater than 1 fringe-spacing or 2π radians then reconstruction becomes indeterminate since the number of cycles or waves is unknown. By subtracting out the reference hologram most of the aberrations due to the optics will be removed when determining the phase-shift.

The reconstructed index-of-refraction error with respect to thermocouple measurements:

$$\Delta\vec{n}_{error} = \vec{n}_{rec} - \vec{n}_{obj} \tag{5.1.18}$$

$$\Delta\vec{n}_{error} = \left[wily\right]^{-1} \times (\lambda \cdot \Delta\vec{\phi}_{meas} - OPL_{BC}) - \vec{n}_{obj} \tag{5.1.19}$$

Where: $\vec{n}_{obj}$ is the index-of-refraction based on the measured thermocouple temperature

This reconstructed index-of-refraction difference or error defines the overall performance of the microscope to resolve an index-of-refraction or temperature relative to the thermocouple measurements. The phase-shift $(\vec{\phi}_{obj} = \phi_{obj}(sp, r))$ due to the specimen in the object beam is determined from the Fourier transform at the carrier frequency and the arc-tangent of the imaginary part to the real part ratio. The carrier frequency is based on the average fringe-spacing in the hologram. At least 6 fringes at 256 samples were recorded for the Fourier transform. The peak in the power spectrum is represented by the constant fringe-spacing in the hologram.

The equation for OPL_{BC} is given as follows.

$$OPL_{BC}(sp, r) = n(i, k) \times PL(i, k, sp, r) \tag{5.1.20}$$

Given:

$i = 1$ Index for Lower BC row

$i = 6$ Index for Upper BC row

$k = 1\ to\ 8$ Index along the optical propagation *z*-axis or longitudinal scanning axis

$sp = 1\ to\ 16$ Scan Position index for Upper and Lower transverse scanning

$r = 1\ to\ 2$ Index for Negative Slope $(r = 1)$ Marginal Rays and

Positive Slope $(r = 2)$ Marginal Rays

The OPL at the BCs: $OPL_{BC}(sp,r) = PL(i,k,sp,r) \times n(i,k)$ (5.1.21)

$$OPL_{BC}(1,1) = PL(1,5,1,1) \times n(1,5) + PL(1,6,1,1) \times n(1,6) + PL(1,7,1,1) \times n(1,7) + PL(1,8,1,1) \times n(1,8)$$
$$OPL_{BC}(2,1) = PL(1,6,2,1) \times n(1,6) + PL(1,7,2,1) \times n(1,7) + PL(1,8,2,1) \times n(1,8)$$
$$OPL_{BC}(3,1) = PL(1,7,3,1) \times n(1,7) + PL(1,8,3,1) \times n(1,8)$$
$$OPL_{BC}(4,1) = PL(1,8,4,1) \times n(1,8)$$
$$OPL_{BC}(5,1) = 0$$
$$OPL_{BC}(6,1) = 0$$
$$OPL_{BC}(7,1) = 0$$
$$OPL_{BC}(8,1) = 0$$
$$OPL_{BC}(9,1) = 0$$
$$OPL_{BC}(10,1) = 0$$
$$OPL_{BC}(11,1) = 0$$
$$OPL_{BC}(12,1) = 0$$
$$OPL_{BC}(13,1) = PL(6,1,13,1) \times n(6,1)$$
$$OPL_{BC}(14,1) = PL(6,1,14,1) \times n(6,1) + PL(6,2,14,1) \times n(6,2)$$
$$OPL_{BC}(15,1) = PL(6,1,15,1) \times n(6,1) + PL(6,2,15,1) \times n(6,2) + PL(6,3,15,1) \times n(6,3)$$
$$OPL_{BC}(16,1) = PL(6,1,16,1) \times n(6,1) + PL(6,2,16,1) \times n(6,2) + PL(6,3,16,1) \times n(6,3) + PL(6,4,16,1) \times n(6,4)$$
$$OPL_{BC}(1,2) = 0$$
$$OPL_{BC}(2,2) = 0$$
$$OPL_{BC}(3,2) = 0$$
$$OPL_{BC}(4,2) = 0$$
$$OPL_{BC}(5,2) = PL(1,1,5,2) \times n(1,1)$$
$$OPL_{BC}(6,2) = PL(1,1,6,2) \times n(1,1) + PL(1,2,6,2) \times n(1,2)$$
$$OPL_{BC}(7,2) = PL(1,1,7,2) \times n(1,1) + PL(1,2,7,2) \times n(1,2) + PL(1,3,7,2) \times n(1,3)$$
$$OPL_{BC}(8,2) = PL(1,1,8,2) \times n(1,1) + PL(1,2,8,2) \times n(1,2) + PL(1,3,8,2) \times n(1,3) + PL(1,4,8,2) \times n(1,4)$$
$$OPL_{BC}(9,2) = PL(6,5,9,2) \times n(6,5) + PL(6,6,9,2) \times n(6,6) + PL(6,7,9,2) \times n(6,7) + PL(6,8,9,2) \times n(6,8)$$
$$OPL_{BC}(10,2) = PL(6,6,10,2) \times n(6,6) + PL(6,7,10,2) \times n(6,7) + PL(6,8,10,2) \times n(6,8)$$
$$OPL_{BC}(11,2) = PL(6,7,11,2) \times n(6,7) + PL(6,8,11,2) \times n(6,8)$$
$$OPL_{BC}(12,2) = PL(6,8,12,2) \times n(6,8)$$
$$OPL_{BC}(13,2) = 0$$

$$OPL_{BC}(14,2) = 0$$
$$OPL_{BC}(15,2) = 0$$
$$OPL_{BC}(16,2) = 0$$

The defined OPL_{BC} array is used in the “wily” reconstruction algorithm. The BC index-of-refraction values are converted from the measured temperatures at the BCs.

5.2 Reconstruction Algorithm Simulation

The reconstruction algorithm uses a reference temperature profile given a point source heater at the bottom of the fluid-cell cuvette. The temperature is converted to index-of-refraction based on the optical specifications of the fluid.

The Cargille Labs Fused Silica Matching Liquid #19571-06350 at the highest available viscosity of 80 centistokes has a 1.4587 index-of-refraction at 589.3 nm wavelength and 25ºC. See the appendix for more information on the fluid and optical properties of the fluid. A Cauchy equation converts the 1.4587 index-of-refraction at 589.3 nm wavelength to a 1.4688 refractive index at 457 nm wavelength. The change in refractive index of the fluid with respect to temperature is specified as $\frac{dn}{dT} = -3.65 \times 10^{-4}\, 1/^{o}C$ from 15 to 35°C. A reference index-of-refraction profile for the reconstruction simulation is shown in figure 5.2.1 below:

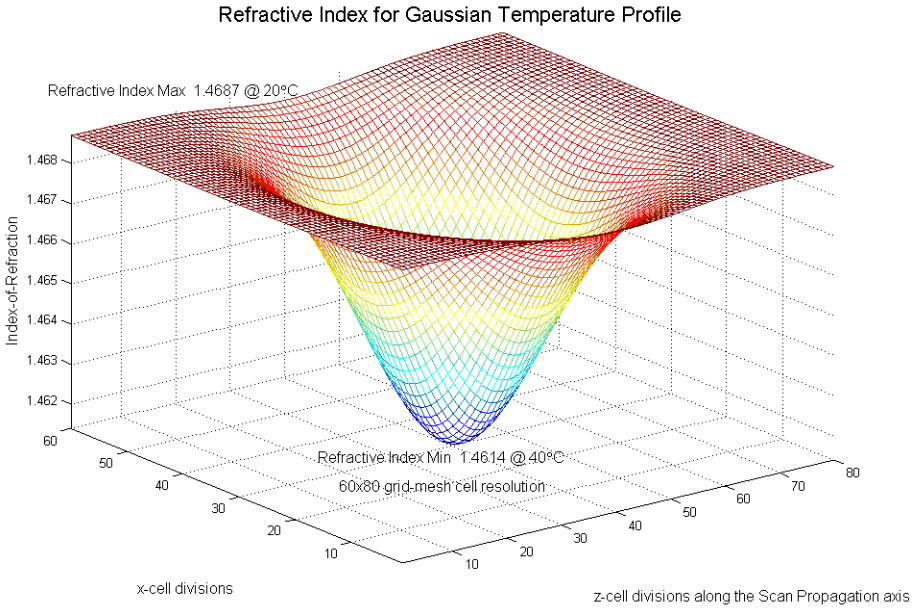

Figure 5.2.1: Reference Gaussian Profile Refractive Index due to a Point Source Heater Centered in the Fluid-Cell

The 60x80 grid-mesh resolution is reduced to a 6x8 computational cell resolution by averaging the values in each cell. The 6x8 array for index-of-refraction includes the boundary conditions for the “wily” reconstruction algorithm. The reconstruction computational domain is 4x8 for the internal cells. The refractive index reconstruction error is $1x10^{-14}$ for any point in the array, which shows the reconstruction error to be insignificant as compared to the measurement error. De-centering the heater will produce a reconstructed profile that is offset or displaced from the reference profile. The reconstruction error sensitivity to an offset or de-center of the heater is shown in figure 5.2.2 below:

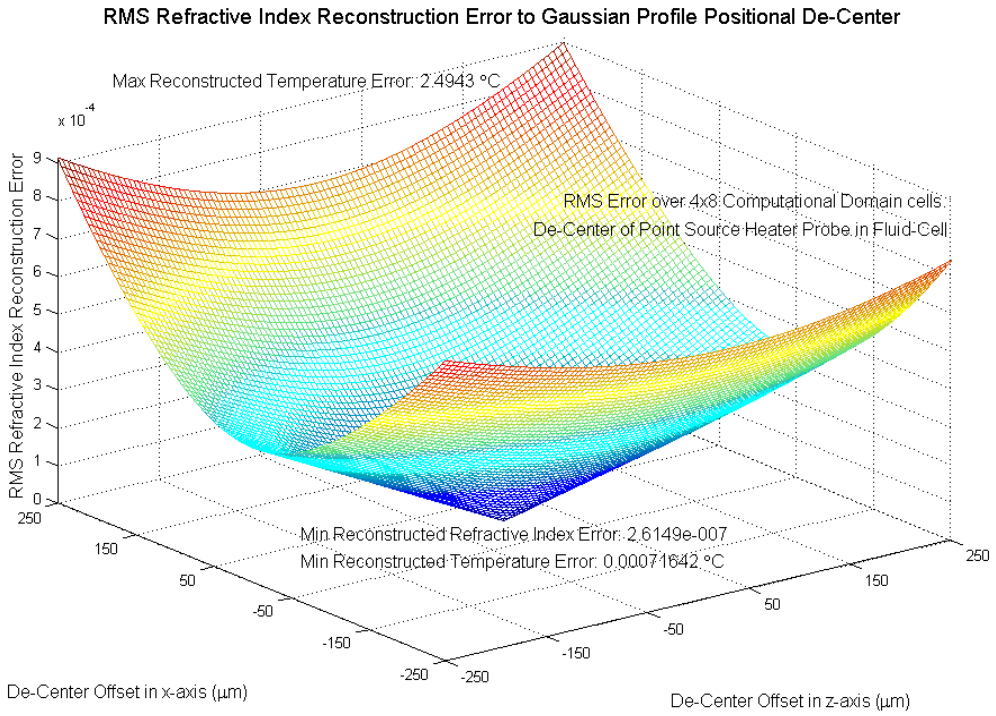

Figure 5.2.2: “Wily” Reconstruction Error Sensitivity to Point Source Heater De-Center

This plot shows an RMS Reconstruction Error of $2.6x10^{-7}$ for the 4x8 computational domain and a centered heater. The corresponding reconstructed temperature error is 0.0007ºC for a centered heater. As the heater position is moved to 250 µm off-center then the reconstructed temperature error rises to 2.5ºC.

5.3 CSLH Specimen

The CSLH microscope is designed to measure the three-dimensional index-of-refraction (or temperature/composition or both) of specimens that consist of a fluid, solid, vapor, gas, or plasma. A simplified CSLH microscope built by Atalick [36] was used to

measure the temperature of a flame or plasma. The CSLH microscope can be configured to measure semi-transparent objects in transmission mode or opaque objects in reflection mode as a profilometer.

The specimen selected for the CSLH microscope in this research is a simple silicone oil based fluid because it has known optical properties, which make it suitable to characterize this complex microscope. A biological specimen would introduce more unknown variables and can be considered once the physical parameters and performance characteristics are known for the microscope. Physical parameter assessment and proof-of-concept evaluations need to be considered first before exploring the interactions with biological specimens. A fluid with known refractive index properties was selected so that relationships of refractive index to wavelength and temperature could be established for the microscope. These parameters are important to determine temperature to phase-shift sensitivity and reconstruction error. This also allows for comparison to an absolute temperature measured with an independent thermocouple. The other means to obtain an independent temperature measurement is by the phase-shift in the holograms, boundary conditions, and the reconstruction algorithm since the specimen's refractive index is known.

The fluid-cell has a point source heater for radial diffusion rather than side-to-side Peltier wall heaters that would provide only a 2D thermal gradient. The fluid-cell with wall heaters was simulated on Matlab using modified Navier-Stokes equations from Antar [29]. The fluid dynamics simulation for convection and heat transfer is shown in the appendix. Wall heating excites convection currents, which are not desirable since the intention is to measure only steady-state diffusion heat transfer. The fluid dynamics simulation on Matlab was written from first principles finite difference equations with routines for convergence of the non-linear partial differential equations. At the time math models were written for surface heating, but not for a point source heater. Even Computational Fluid Dynamics (CFD) programs such as FEM Lab and COMSOL did not provide analytical models for a point source heater. Deriving mathematical models and transport equations for a thermally diffusing point source heater was beyond the scope and resource limitations of the research. Because of the modeling complexity a fluid dynamics response to a wall heated fluid-cell is reported in the appendix. The results of my CFD simulation shows no convective flow with wall heaters given a small temperature gradient of the Peltier heaters. This provides some confidence that the re-circulation and convective flow characteristics are minimized due to the low Reynolds

number and relatively high Prandtl number since the reference refractive index silicone oil has a relatively high viscosity.

5.4 Scanning Transmission Laser Holography (STLH) Microscope Optical Layout

The STLH microscope is a simplified version of the CSLH microscope that was built to align optical components and to produce holograms with lower aberrations for proof-of-principle experiments. The STLH microscope also provided a test bed to align groups of optical components into lenses, such as the telecentric lens, confocal lens, periscope lens, and projector lens. The STLH microscope also provided a means to test the camera, beam steering mirrors, translation stages, and data acquisition through a LabVIEW controller. Custom LabVIEW programming provided an interface to camera frame grabbers (CameraLink, Firewire, and USB), Newport XPS-C8 motion controller for translation stages (Ethernet Link), beam steering mirror controls (analog outputs through a data acquisition board), and temperature measurement (analog inputs through a data acquisition board). The data acquisition board interface to LabVIEW also provided beam steering mirror calibration, thermocouple calibration, and thermocouple data acquisition. The STLH microscope was also used to provide a benchmark for reconstructing the temperature in comparison to CSLH microscope reconstruction. The reconstructed temperature of both the STLH and CSLH microscopes was also compared to the thermocouple measurements considering scanning positional errors with each setup or configuration.

The main differences between the STLH microscope and the CSLH microscope are: 1) Translation (along the *xy*-axis) of the fluid-cell rather than using the two beam steering mirrors, 2) Elimination of the confocal lens and optical loop, 3) Elimination of three periscope lenses, 4) Elimination of two cube beam splitters, 5) Elimination of a quarter-wave plate and polarizing lens, and 6) Shorter path length. The STLH has a shorter path length than the CSLH microscope with fewer lenses that reduces optical aberrations and wavefront error. As a result the STLH microscope was easier to align due to the simpler optical path. The STLH microscope retained the telecentric lens and the optical wedges that are used to overlap the beams. The 11m path length of the CSLH was reduced to about 6m for the STLH microscope. An optical diagram of the STLH microscope that was used to characterize sensitivity and provide three-dimensional measurements is shown in figure 5.4.1 below:

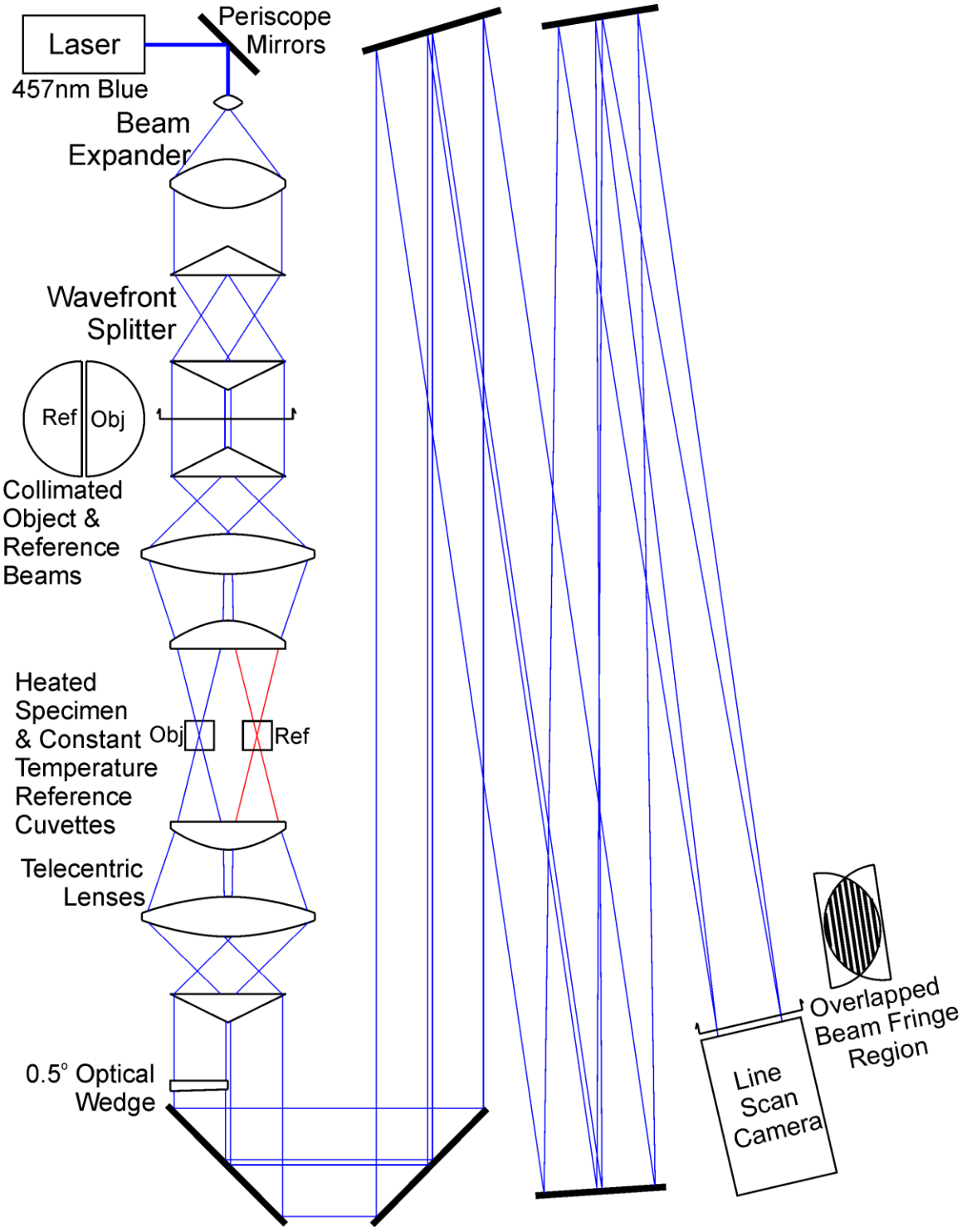

Figure 5.4.1: STLH Microscope Optical Layout

The microscope begins with a 457 nm blue light laser source of 0.1 mm diameter to the $1/e^2$ beam waist power point. The laser has an effective beam spread out to 1 mm aperture or diameter. The laser beam is reflected by two periscope mirrors to elevate the

beam to a height of 300 mm above the optics table. Following the beam elevating periscope mirrors is a Keplerian Beam Expander (BE) that expands the beam diameter from 1 to 37 mm. The Keplerian BE has a short focal length objective lens that focuses the 1 mm beam into a 100 µm diameter pinhole aperture. The pinhole aperture is a spatial filter that removes the high frequency components of the focused beam Point Spread Function (PSF) from the 10.8 mm short focal length objective lens. The spatial filter is precisely aligned to transmit >90% of the beam energy and to reduce spherical aberrations along with the higher-order aberrations of the objective lens. The expanding beam rays from the spatial filter are then collimated to a 37 mm diameter using a 400 mm focal length achromatic doublet re-collimating lens. The aberrations from the collimating lens are typically considered to be negligible for the experiments.

Following the collimating lens of the beam expander is an iris diaphragm that truncates the beam to 35 mm in diameter for uniform aperture illumination before entering the wavefront splitter. The 35 mm aperture beam then enters two Fresnel biprisms to wavefront split the beam into two separate back-to-back D-shaped beams that are separated by 4 mm. See the “Collimated Object & Reference Beams” in figure 5.4.1 above. The wavefront splitter provides equivalent coherence and wavefront error for both the object and reference beams.

The telecentric lens follows the wavefront splitter and focuses the beams in the fluid-cell region. The telecentric lens focuses both the object and reference beams and then re-collimates the beams at the output. The telecentric lens has a short focal length f/2 f-number producing a 28° cone beam in the specimen region, which is beneficial for reconstruction and detrimental for aberrations. The two side-by-side D-shaped beams that pass through the specimen region are designated the object beam that passes through the specimen and the reference beam that bypasses the specimen. The reference beam that bypasses the heated fluid specimen passes through a phantom fluid-cell. The constant temperature or constant refractive index phantom fluid-cell provides the same focal length for the two beams in the telecentric lens. The focal point of the object beam in the heated fluid-cell and the focal point of the reference beam in the phantom fluid-cell move in tandem during scanning. This provides equivalent reference beam to object beam size at the output of the telecentric lens where both beams are equally re-collimated as well. If the phantom fluid-cell is removed then one of the beams will not re-collimate. This is due to the shift in focal point which is compensated and balanced using the phantom fluid-cell along the reference beam. The

telecentric lens is mounted to an optical rail carrier and is translated in the *z*-axis along the direction of optical propagation. The telecentric lens is a symmetrical arrangement of optical components about the central specimen fluid-cell and phantom fluid-cell. The telecentric lens consists of two Fresnel biprisms, two bi-convex lenses, and two plano-convex lenses.

The telecentric lens produces a combination of spherical aberrations and coma at the focal point in both the specimen fluid-cell and the phantom fluid-cell due to the geometry of side-by-side propagating beams. Although the coma from the incident beam is corrected by the Fresnel biprism at the output of the telecentric lens the higher order optical aberrations remain due to the side-by-side beams that are propagating off the center of the lens. The aberrations at the output of the telecentric lens prevent the output beams from being fully re-collimated. This causes the two beams to gradually expand along their relatively long path length from the telecentric lens output to the camera. The two D-shaped beams gradually degrade to ellipses over a 1 m path length and the divergence from de-collimation becomes quite noticeable over a 2 m path length. A reference hologram is taken with the specimen fluid-cell at constant temperature to compensate for the phase-shift in a hologram that is generated by the aberrations of the optics.

Either the object beam or reference beam that exits the telecentric lens enters a shallow angle optical wedge which converges the two beams to overlap their marginal rays at the camera. The 0.5° or 1° optical wedge converges the beams over a long path length of about 4 m until the complete overlap of the beams at the camera. The shallow angle wedge and long path length is required to provide a fringe-spacing that will be sampled by at least 16 detectors of the camera. This spatial sampling resolution of >16 pixels/fringe specification is required to determine a fringe-shift in the hologram to within 0.008 waves of a fringe or λ/125 waves. Slight beam divergence or de-collimation along the path length increases the sampling resolution and reduces the irradiance or light energy subtended by a detector on the camera. Fringes are shown in the “Overlapped Beam Fringe Region” next to the “Line Scan Camera” in figure 5.4.1 above.

Both the STLH and CSLH microscopes scan in the *z*-axis by translating the telecentric lens assembly of optical components. The main difference between the STLH and CSLH microscopes is that the STLH microscope moves the fluid-cells using *xy*-axis translation stages mounted to the fluid-cells and the CSLH microscope fixes the fluid-

cells to the optics table and uses the *xy*-axis beam steering mirrors to translate the beams.

The ability to measure a fringe depends on the quality and specifications of the camera. A high resolution wide field camera was selected to image the overlapped beams. The hologram and camera specifications reduced camera selection to either a Basler or Dalsa line scan camera. A Dalsa Piranha P2-23-08k40 CCD line scan camera with 1x8192 pixels at 7 μm/pixel was selected. This $10,000 camera has a 57 mm detector width that is sufficient to image a slightly de-collimated or diverging beam over a long path length. The Dalsa camera has a 40MHz pixel sampling rate and a maximum line scan rate of 1kHz. The radiometric dynamic range is specified at 390:1 given a 0dB nominal gain setting and 496:1 given a -10dB minimum gain setting. The radiometric resolution is set to 10 bit or 0 to 1023. The desired spatial resolution is >16 pixels/fringe as established by the fringe-spacing of the projector optics.

The Dalsa Piranha line scan camera is insensitive to low level light in comparison to a typical 2000x3000 pixel array CCD camera. The area array CCD camera would be better for radiometric sensitivity than the Dalsa line scan camera, but the Dalsa line scanner has 8192 pixels at 7 μm/pixel for greater spatial resolution. The Piranha line scan camera required a flood light illumination source to raise the low level background intensity to a detectable level above the noise floor. This prevented clipping of the low level fringe valleys by radiometrically setting the threshold, which was not achievable by changing the configuration settings of the camera. The responsivity of the camera peaks at 12 nJ/cm^2 and 658 nm wavelength using default operating parameters. The responsivity of the camera is about 50% of the peak at 5 nJ/cm^2 and 457 nm wavelength. The radiometric dynamic range is relatively low at 390:1 due to the type of detectors and responsivity to laser wavelength. The sensitivity of camera was increased by manually setting the exposure time to 1,000 μsec (maximum) and the radiometric dynamic range increased, but still the flood light background source was needed to bias the signal and eliminate low level clipping. The low-level radiometric threshold level of the camera was manually set to a minimum threshold at SNR > 5. In particular, the six Fresnel biprisms of the CSLH microscope and four Fresnel biprisms of the STLH microscope produced significant back reflections and loss of intensity along the optical beam path.

Setting the camera to maximum exposure time meant that scanning at a constant rate would produce smearing of the image across the detectors and the spatial

resolution would be compromised. A step-stare image grab scanning method was used instead of a constant rate scanning method as the actuators increment by moving and stopping in order for an image to be acquired by the camera. A concern with the step-stare image acquisition mode was that the transient accelerations placed on the optical components would create mechanical vibrations. This was tested by increasing a dwell time between scan commands that would allow for the settling of the vibrations. Increasing the loop time delay in LabVIEW from 500 msec to 1500 msec showed no discernable change in the fringe-shift or phase-shift of a hologram. Since increasing the loop time did not improve fringe stability in the holograms then the loop delay was reset to 100 msec settling time following frame grabbing for the experiments.

The Cambridge galvanometer beam steering mirrors have significantly faster response times than the Newport translation stages so the settling time vibrations are primarily due to the Newport *z*-axis translation worm drive stage that supports a rail carrier and the telecentric lens. The 625 μm/step increment for the *z*-axis translation stage moves the focal point along the optical propagation axis and this translation increment is represented by an approximate 30° rotation of the worm drive.

The Newport XPS-C8 motion controller provided *xyz*-axis translation scanning. The control for the three translation stages is through an adjustable Proportional Integral Derivative (PID) low transient settling time and fast response drive. The PID gains needed to be manually adjusted to tune the stages for optimal response since the automatic calibration and tuning of the controller produced an unstable output. Manual tuning caused an increase in the transient settling time in order to achieve a stable 0.1 μm or 100 nm positional resolution. The positional resolution of the translation stages is substantially less than 625 μm/step increment for scanning the fluid-cell. A LabVIEW program provided Newport translation stage control and image acquisition was obtained through a National Instruments PCI-1428 frame grabber and base link cable connection to the camera. The near real-time LabVIEW program stored the three-dimensionally scanned holograms in a 64x8192 array. A LabVIEW program for the CSLH and STLH microscope image acquisition, beam steering mirror, and translation stage control is found in the appendix.

The three-dimensional reconstruction is accomplished plane-by-plane or slice-by-slice along the *y*-axis for each elevation plane. This scanning method provides the 64 holograms that are required for three-dimensional reconstruction. Scanning and camera frame grabbing acquisition is by a step-stare grab control as the camera sensitivity and

exposure time limitations did not allow for constant rate scanning and frame grabbing. The worm drive actuators or translators are stepped in 625 μm *z*-axis increments for 8 steps then 1300 μm *x*-axis increments for 2 steps followed by 625 μm *y*-axis increments for 4 steps. The *zxy*-axis scanning sequence is along the *z*-axis for 8 steps then reset *z*-translator to origin, then along the *x*-axis for 2 steps then reset *x*-translator to origin and *z*-translator to origin, and finally along the *y*-axis for 4 steps. Reconstruction is determined from *xz*-axis scanning along a single *y*-axis elevation plane.

The STLH microscope with a shorter beam path than the CSLH microscope is advantageous when optical aberrations that cause de-collimation and wavefront error are considered. The pupil planes of the STLH microscope are stationary, but are not stationary on the CSLH microscope due to the off-axis scanning configuration. Optical aberrations or wavefront error at the pupil plane means that perfect re-collimation of the beam is not possible and these wavefront errors increase over the path length as the pupil gradually increases in size. The beam steering mirrors of the CSLH microscope tilts the beams off-axis for scanning in the *xy*-axis plane, which contributes to coma aberrations. These aberrations are compensated for by recording a reference hologram.

5.5 Confocal Scanning Laser Holography (CSLH) Microscope Optical Layout

The Confocal Scanning Laser Holography (CSLH) microscope with the beam steering mirrors and optical loop is designed to maintain a stationary focal point at the confocal apertures during scanning. This means that the confocal apertures do not have to be moved during scanning and that a constant virtual aperture is placed over the focal point of the beam in the fluid-cell. The CSLH microscope is large and it uses up almost the entire 1.5x2.5 sq m (5’x8’) Newport optical table. An optical layout of the CSLH microscope in transmission mode configuration that begins with a 457 nm wavelength blue laser and a 658 nm wavelength red laser is shown in figure 5.5.1 below:

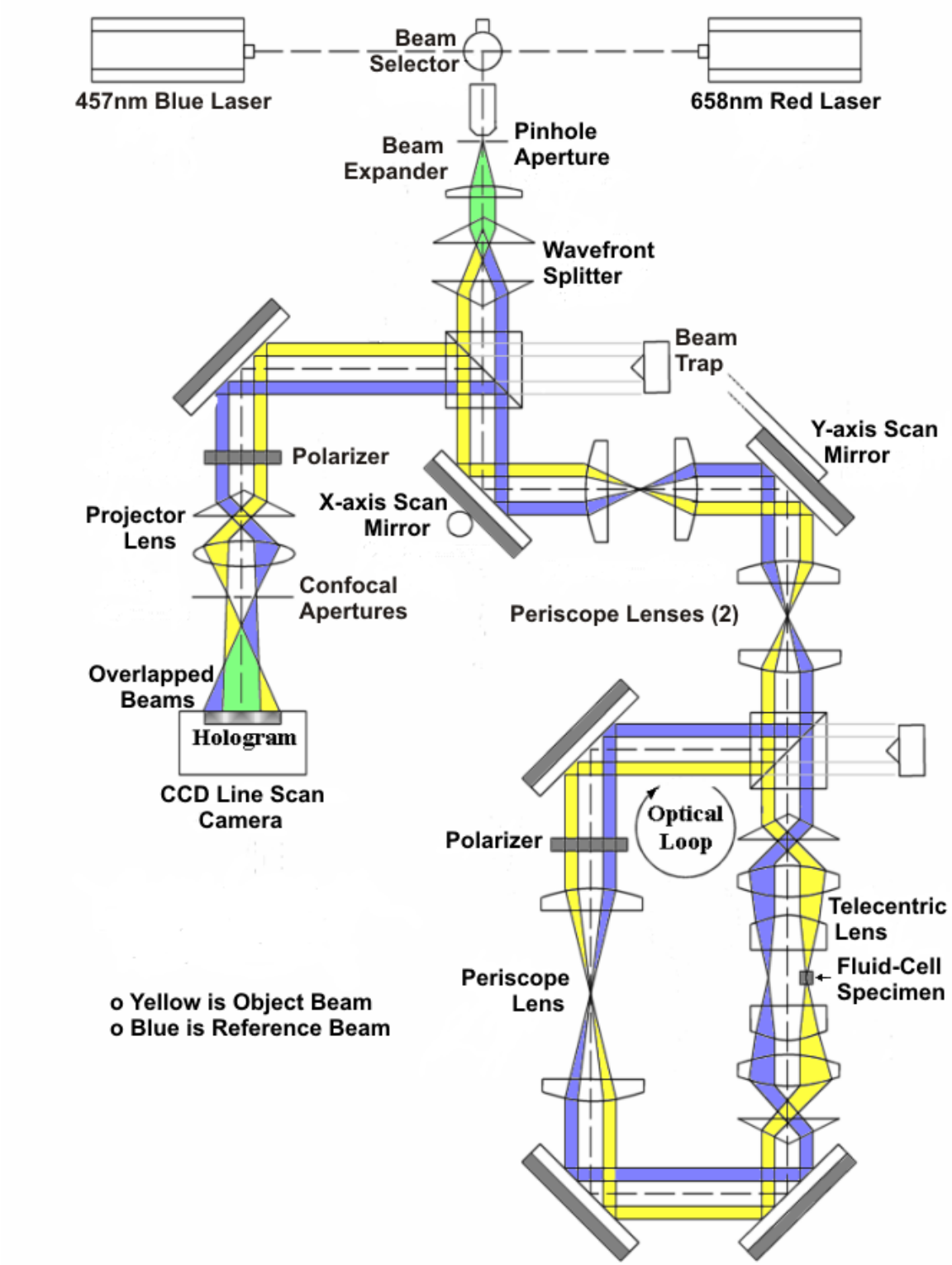

Figure 5.5.1: CSLH Microscope Optical Layout for Transmission Mode Scanning through the Specimen

The Confocal Scanning Laser Holography (CSLH) microscope has a red 658 nm wavelength laser and a blue 457 nm wavelength laser that can be used to determine both the Temperature (*T*) and the Composition (*C*) of the specimen. The lasers are sufficiently separated in wavelength so that the temperature from the refractive index measurements and the composition from the refractive index measurements are considered independent.

A change in Refractive Index is given as:

$$\Delta n = \left(\frac{dn}{dT}\right)_C \cdot \Delta T + \left(\frac{dn}{dC}\right)_T \cdot \Delta C \qquad (5.5.1)$$

Where: $\left(\frac{dn}{dT}\right)_C$ derivative or gradient is at constant Composition (*C*) for the blue laser.

and $\left(\frac{dn}{dC}\right)_T$ derivative or gradient is at constant Temperature (*T*) for the red laser.

The condition for constant composition pertains to the blue laser as the refractive index is a function of temperature. The condition for constant temperature pertains to the red laser as the refractive index is a function of composition.

Abe and Iwasaki [28] have shown that the temperature and composition of a specimen can be independently determined simultaneously in a single experiment when using two lasers of sufficiently separated wavelength. Abe and Iwasaki performed their micro-gravity free fall drop experiments on non-azeotropic binary mixture vapor bubbles. One of their objectives was to measure Marangoni surface tension effects with heat transfer convection and fluid dynamics transport on a bubble in micro-gravity. The research of this thesis is limited to determining only the internal temperature by using the blue laser and not the red laser.

A flip-in mirror beam selector in figure 5.5.1 above is used to select either the red or blue laser. The rotating flip-in mirror is part of a periscope pair of mirrors to elevate the beam to 300 mm above the optics table. Only the blue laser is set up and aligned for the temperature measurement experiments.

The beams propagate from the wavefront splitter to the first cube beam splitter and then pass through the *xy*-axis Beam Steering Mirrors (BSMs) section. The two beam steering mirrors are for *xy*-axis scanning and three periscope lenses are used to set a pupil near the cube beam splitters and also to reduce beam walk on optical components.

The BSM section includes two periscope lenses that reduce beam translation or beam walk on the cube beam splitters from the rotations of the BSMs. The BSM mirrors tilt the beams off-axis to as much as ±2°. This translates the focal point ±2.8 mm in the *x*-axis horizontal direction and *y*-axis vertical direction within the specimen. The periscope lenses also establish near stationary pupil planes, which is important for reverse beam propagation through the BSM section and then to the confocal lens. Coincident pupil planes reduce the movement of the focal point on the confocal apertures for off-axis beam scanning.

The beams then exit the BSM section and enter a second cube beam splitter which is part of an optical loop. The optical loop consists of a telecentric lens and another periscope lens. The telecentric lens comprises two Fresnel biprisms, two bi-convex lenses, and two plano-convex lenses as similarly found in the STLH microscope. A specimen and phantom fluid-cell is centered in the telecentric lens where the beams are focused. The object beam that is passing through the specimen fluid-cell is shown in the figure above. A phantom fluid-cell is used to match the phase delay and image distortions of the reference beam to the object beam. This phantom fluid-cell is placed at the focal point of the reference beam, which is not shown in the figure above. The specimen and phantom fluid-cells places the focal points of both the object and reference beams in the same cross-sectional plane within the telecentric lens. These co-planar focal points of the object beam and reference beam means that both output beams of the telecentric lens will have the same size and collimation error. Both the object and the reference beams propagate through individual fluid-cell cuvettes. The reference beam propagates through the phantom fluid-cell at constant room temperature and the object beam propagates through the heated specimen fluid-cell. The phantom fluid-cell is at constant temperature and constant refractive index so that a co-planar focal point to the focal point in the specimen fluid-cell is maintained along the optical propagation axis.

The telecentric lens then re-collimates the beams for propagation to the periscope lens. A single translation stage is used for *z*-axis scanning by moving the telecentric lens, which has optical lenses and biprisms mounted to a component carrier rail. The optical loop has a third periscope lens that inverts the image in conjunction with the telecentric lens and also reduces the beam translation or beam walk at the second cube beam splitter. This periscope lens is also used to establish a stationary pupil near the

cube beam splitter during scanning. All three periscope lens have two large 130 mm diameter by 200 mm focal length plano-convex lenses. The beams exit the periscope lens and then reflect off the second cube beam splitter for reverse propagation back through the BSM section. This is done so that the beams exiting the BSM section will no longer tilt or have an angular displacement. Following the BSM section the reverse propagating beams reflect off the first cube beam splitter. The nearly stationary beams then enter the projector optics section. The projector optics section consists of the confocal lens and a wedge prism. The confocal lens is another telecentric lens except that pinhole apertures replace the fluid-cells. The pinhole apertures of the confocal lens effectively place a virtual aperture over the focal point in the specimen. The intent is to have stationary confocal apertures throughout scanning as the focused rays pass through the pinhole apertures. The pinhole apertures remove stray rays and some of the optical aberrations for ±1° rotation of the *x*-axis BSM and ±1.4° rotation of the *y*-axis BSM. If the pupil planes are properly aligned then minimal motion of the focal point at the pinhole apertures will occur as the beams are tilted off-axis during BSM scanning. The wedge prism of the projector optics section applies a shallow convergence angle to one of the beams for overlap. The overlapped beam region forms a fringe pattern from the interference of the coherent beams. The hologram is imaged by the CCD line scan camera. The path length of the CSLH microscope is over 11 meters including the projector lens path length that overlaps the object beam onto the reference beam at the line scan camera.

The result is that the marginal rays for both the object and reference beams overlap one another at the camera and remain stationary during scanning. The marginal rays represent the edge rays of the 28º cone beam or the f/2 focused beam in the specimen region. The fringes generated by these marginal rays are used for determining the phase-shift in the holograms, which is important for 3D refractive index reconstruction.

The polarizing lenses as seen in the optical layout of the figure above are used to conveniently convert the microscope from transmission mode to reflection mode operation. The CSLH microscope is used exclusively in transmission mode configuration for characterization, measurement, and experiments thus the polarizing lenses have been removed. An aerial photograph of the CSLH microscope with outlined sections is shown in figure 5.5.2 below:

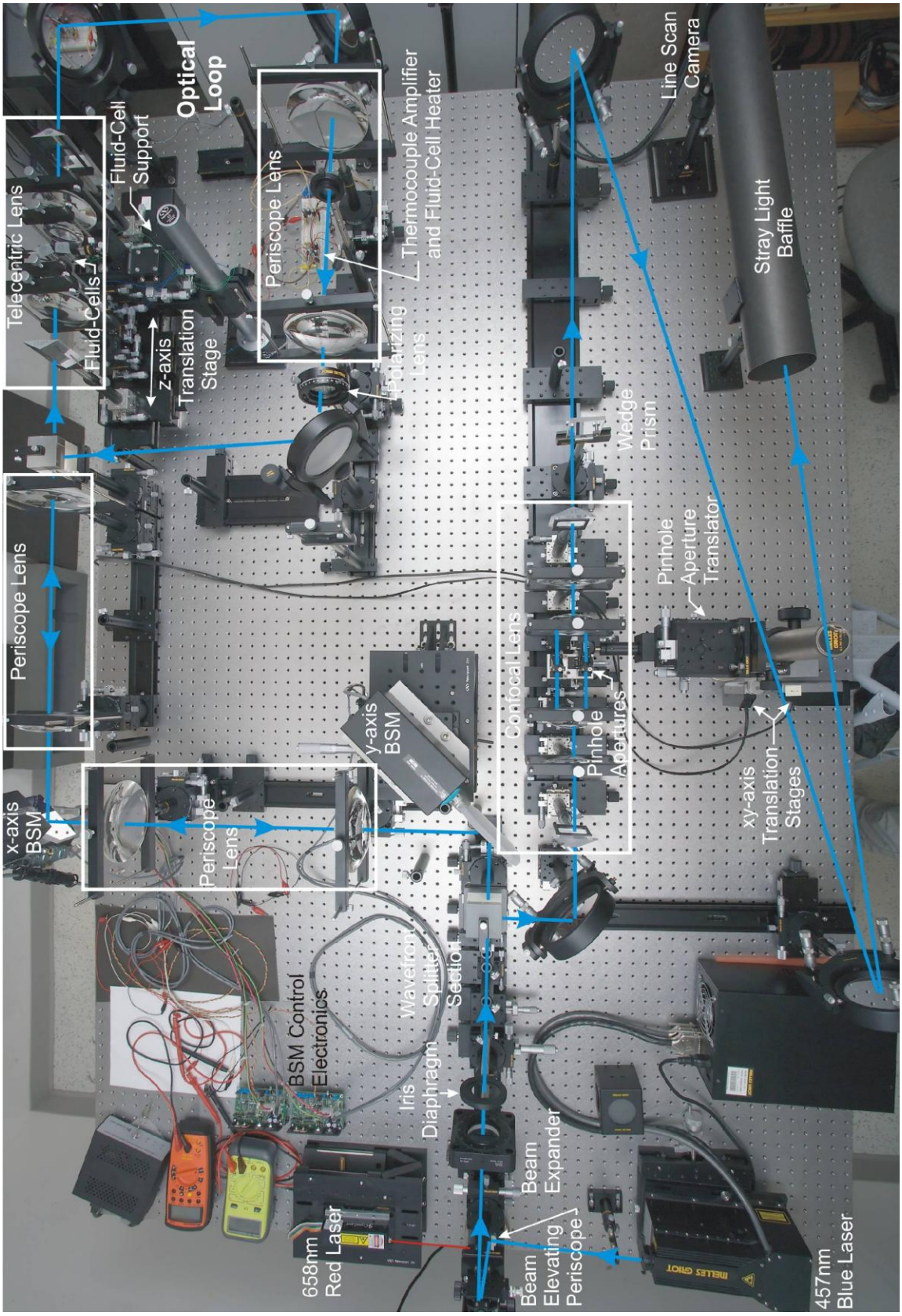

Figure 5.5.2: The CSLH Microscope Aerial View

Scanning in the *xy*-axis is provided by the two Cambridge galvanometer Beam Steering Mirrors (BSMs) and scanning in the *z*-axis is provided by a Newport translation stage that supports the telecentric lens. The optical component rail carrier that supports the telecentric lens is mounted to the *z*-axis translation stage. Control for the *xy*-axis BSMs is provided by a National Instruments data acquisition board that includes analog outputs. BSM calibration is shown in the appendix. Control for the *z*-axis translation stage is provided by the Newport XPS-C8 Motion Controller. The Newport Motion Controller also controls two *xy*-axis translation stages that can move the pinhole apertures in the confocal lens, if necessary. This configuration minimizes vibrations from the translation and rotation actuators as the fluid-cells are stationary being fixed mounted to the optical table. LabVIEW provides overall control for the BSMs, translation stages, and image acquisition frame grabbing for the camera. LabVIEW also provides hologram array data storage.

The frame rate for the camera is determined from the step-to-step scan time for a step-stare configuration that allows for a settling delay before the hologram image is acquired. The step-stare sequence timing is shown in table 5.5.1 below:

Dwell Time Function	**Time (µsec/step)**
Slew	20000
Settling	5000
Stare	1000 (Max.)
Frame	**26000**

Table 5.5.1: Step-Stare Scanning Timeline

The step-stare scanning frame rate is determined from the frame time as follows:

$$Frame\ Rate = \frac{1}{Frame\ Time} = \frac{1}{26000\ \mu\sec} = 38\ frames/\sec \qquad (5.5.1)$$

Given: 1 frame = 1 line scan since the camera scans at 1 line/frame

The timing is based on LabVIEW control of Cambridge Technology beam steering mirrors, Newport translation stages, and the Dalsa line scanning camera frame rate. LabVIEW software holds the process until the translation stage feedback settles within error limits before continuing with loop execution, which is accounted for in the

$5 msec/step$ setting time. The Newport translation stage rotates a worm gear drive shaft over a 30° angle for a 625µm/step displacement of the stage. This small step displacement produces a small vibration due to the start and stop transient of the step-stare control, which is reported in the appendix. Screen shot pictures of the LabVIEW program code and photographs of the CSLH microscope are found in the appendix.

The CSLH microscope uses the Newport *xy*-translation stages to move the pinhole apertures in the confocal lens and track the movement of the focused object beam and focused reference beam onto the pinholes. The tracking displacement of the pinhole apertures is based on the deflection angles of the BSMs that scan the beam in the specimen and the 80 mm focal length of the confocal lens optics. The reason for placing translation stages on the confocal apertures is because the exit pupil plane is not the same distance as the entrance pupil plane for the periscope lenses. Paraxial ray tracing through an ideal lens shows the entrance and exit pupil plane distances to be equivalent, but ray tracing with Zemax using the Melles-Griot lenses for our experiment shows the exit pupil plane distance to be longer than the entrance pupil plane distance. Since the beams are both forward and reverse propagating through the periscope lenses in the BSM section this will produce a displacement error of the focal point at the confocal lens. The idea of reverse beam propagation through the BSM section was to establish a stationary focal point at the confocal pinhole apertures, which is not the case. After much alignment and re-alignment it was decided that an *xy*-axis translator stage should be placed at the pinhole apertures. An optical solution is to upgrade the optics to custom precision lenses as designed for the Zemax sequential and non-sequential mode simulations. The *xy*-axis translation stage will not introduce any vibrations that will adversely affect the specimen since it is not attached to the fluid-cell. The synchronized control of the pinhole aperture translation stages to the BSM angular deflections or rotations is provided by a LabVIEW program. The LabVIEW program also provides image acquisition from the line scan camera and stores a 64x8192 hologram array for all four of the scanned elevation planes in the fluid-cell.

The wavefront splitter produces two back-to-back D-shaped beams. Zemax simulated D-shaped object and reference beams are shown in figure 5.5.3 below:

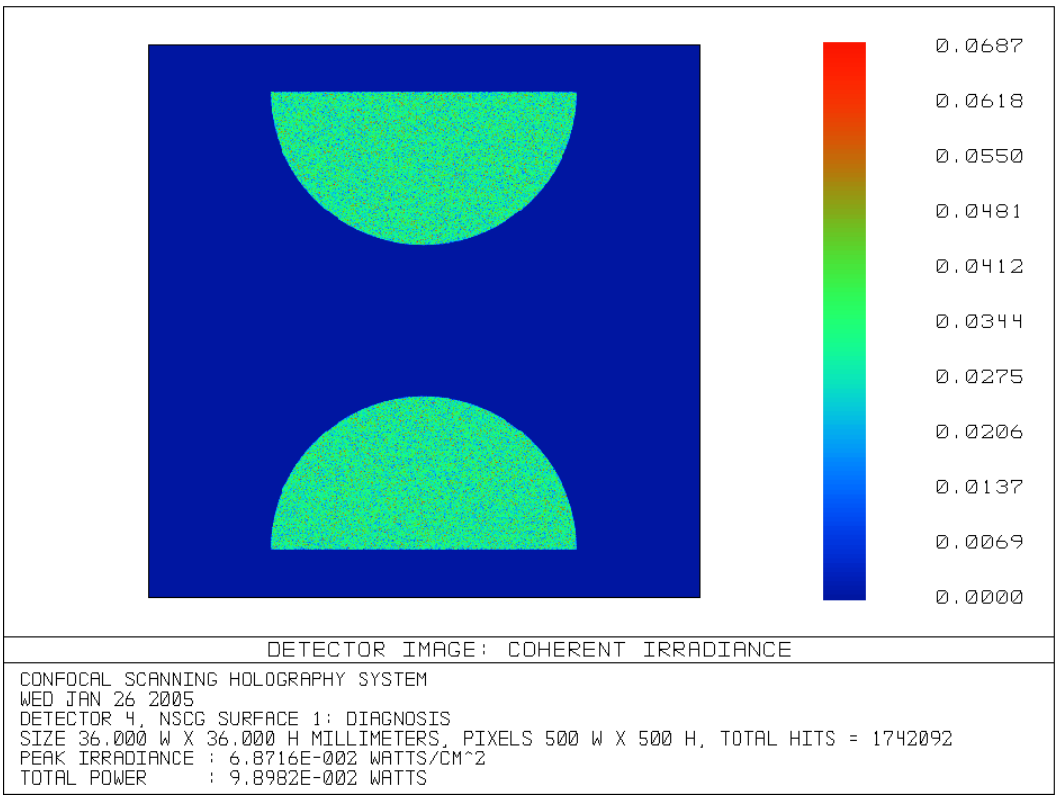

Figure 5.5.3: Wavefront Split Beams as Simulated with Zemax

As the beams propagate the wavefront error accumulates and the high spatial frequencies cause the edges of the beam to smooth out into gradients. This is particularly noticeable at the corners of the D-shape as seen in Zemax figure 5.5.4 below:

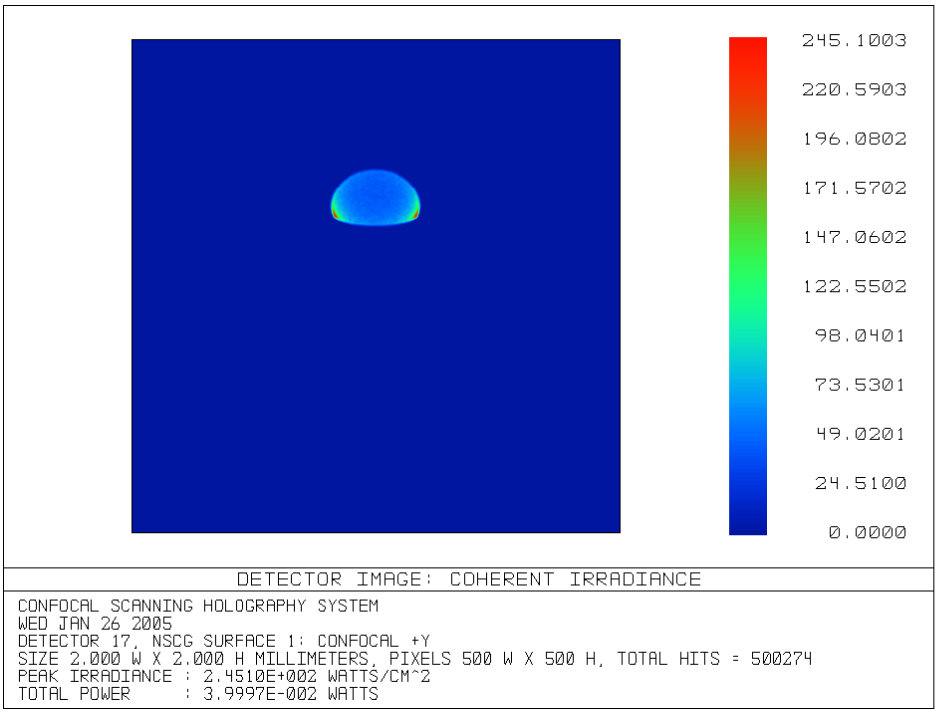

Figure 5.5.4: Degradation of Beam Shape over Path Length

As the beams propagate further along a path the D-shaped beams lose more edge definition and degrade to ellipse shapes as shown in figure 5.5.5 below:

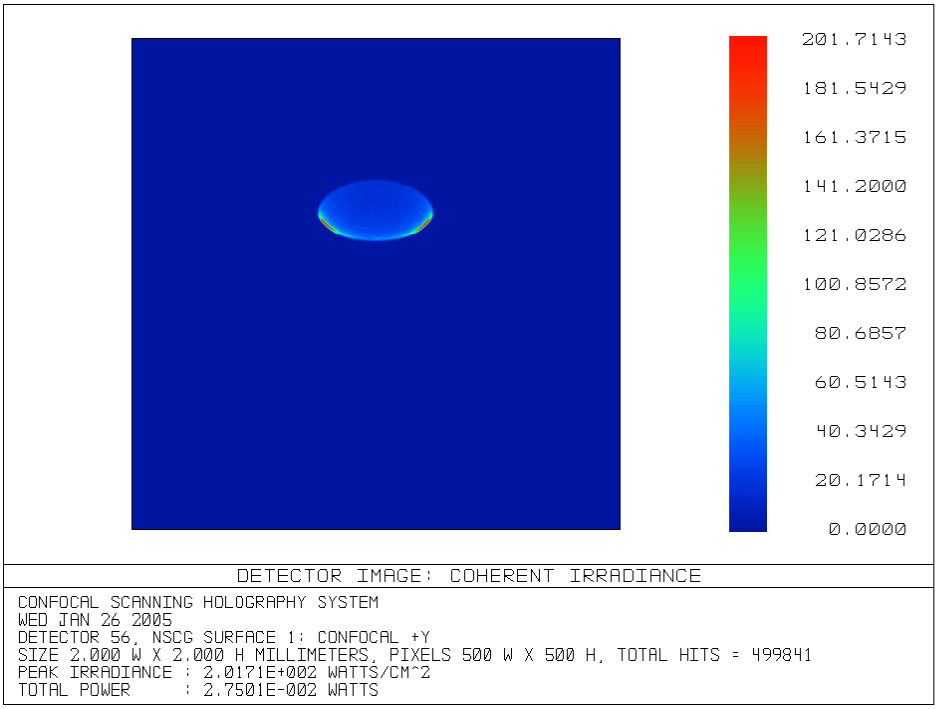

Figure 5.5.5: Further Degradation of Beam Shape over Path Length to an Ellipse Shape

The corners are rounding and the edges smoothing out as the beam is losing definition and detail. The optical result is a low-pass spatial filter with reducing cut-off frequency over path length. The CSLH microscope has been modeled in Zemax for non-sequential mode ray tracing as shown in figure 5.5.6 below:

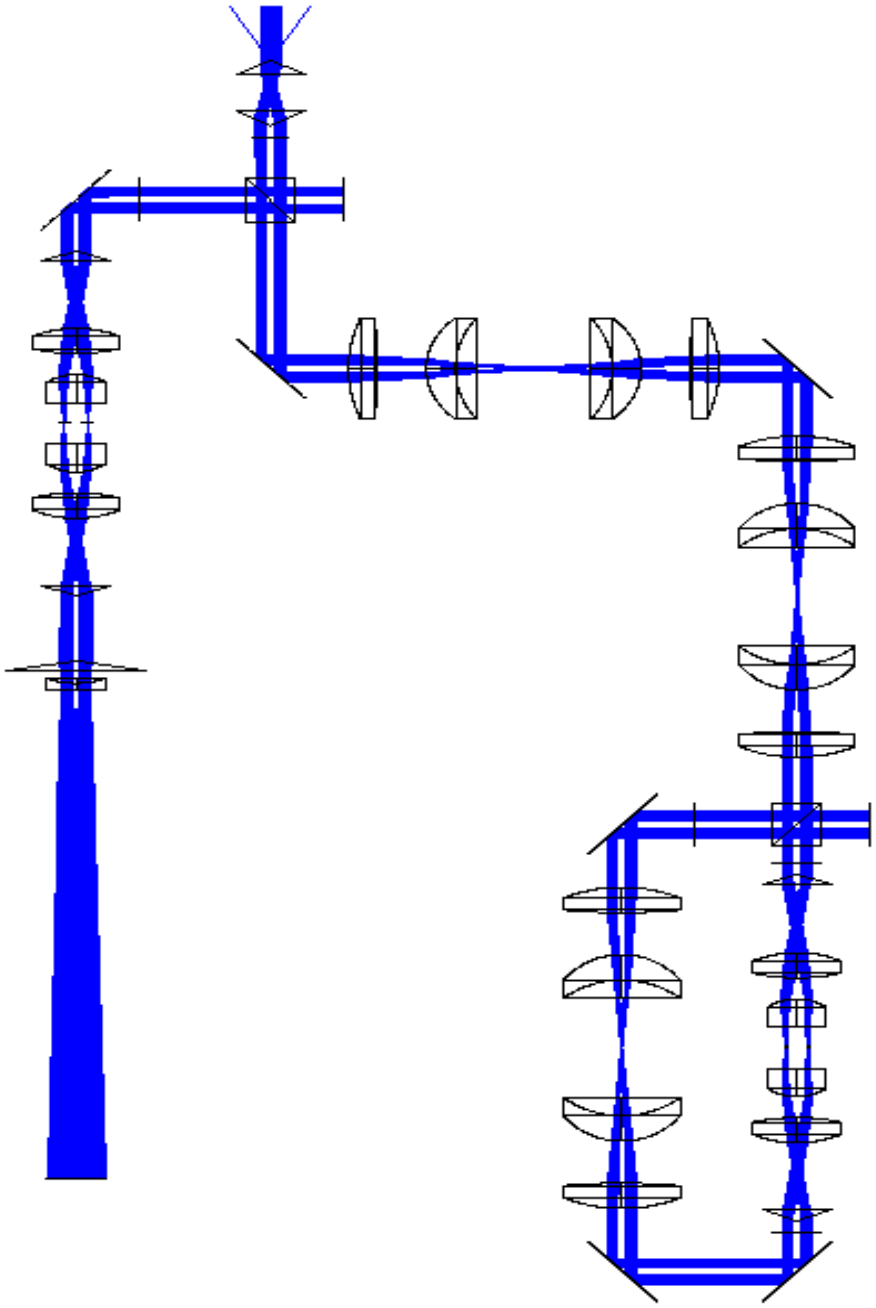

Figure 5.5.6: CSLH Microscope Layout using Zemax

This Zemax simulation uses 10 million rays to show the effect of beam tilt by BSM rotations on the field-of-view. The confocal lens is a duplicated telecentric lens except

that the confocal apertures have replaced the fluid-cells in the specimen. The projector optics also have a Fresnel biprism to overlap the two beams followed by a plano-concave lens to expand the beams so that the 57 mm wide line scan camera can be completely filled with the fringes of a hologram. Complete beam overlap coincides the marginal rays of the object beam to the reference beam at the camera.

The object and reference beams are focused in the specimen region of the telecentric lens as shown in figure 5.5.7 below:

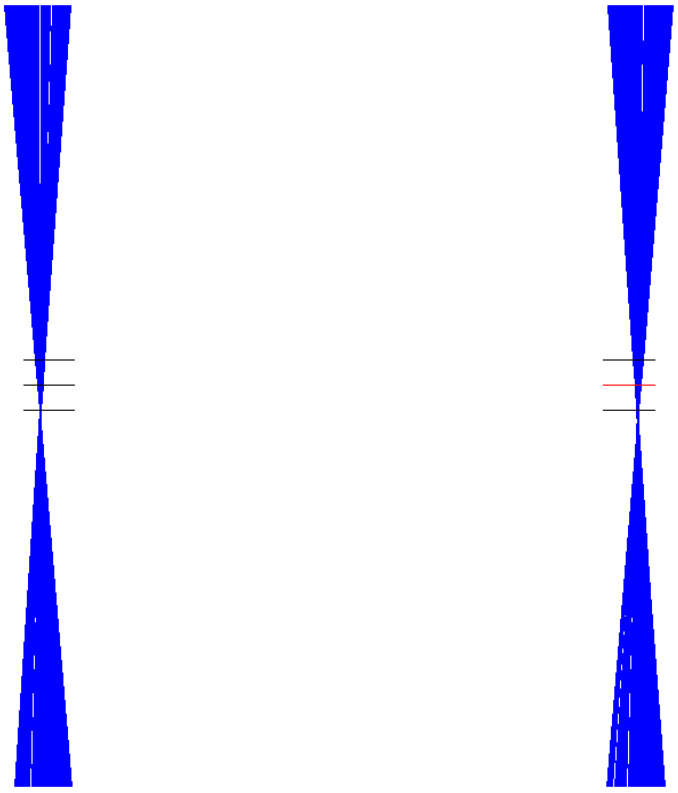

Figure 5.5.7: Object and Reference Beams Focusing at Specimen Region

This is the on-axis condition with no tilt in the beams from the beam steering mirrors. The three horizontal lines are detectors for imaging the blur spot size along the beam path. This also provides a means to verify the convergence angle of the beams or cone beam angle. The focal point is not centered on the Zemax imaging planes and there is a slight tilt that converges the two beams. This is due to the telecentric lens biprism that tilts the beams into the bi-convex and plano-convex lenses, which introduces a geometric aberration. As a result the side-by-side beams propagate nearly parallel off the optical centerline. This geometric condition that produces the slight convergence angle of the beams cannot be corrected even when optimizing the design with custom aspheric lenses. For each beam entering the telecentric lens the incident angle to the

lens is different for the upper and lower marginal rays, which cannot be compensated with Zemax merit function lens design optimization.

The telecentric lens introduces the highest optical aberrations primarily due to the short 80 mm back focal length high focusing power of the lenses. Geometric aberrations are produced by the biprism of the telecentric lens that introduces an incident beam angle to the first bi-convex lens. Spherical aberrations are produced by the radius-of-curvature of the lenses and the aberrations increase with shorter focal length or lower f/# or f-number. Coma is an off-axis aberration that is produced by the side-by-side parallel beams that propagate off the optical centerline. These optical aberrations result in a beam that cannot be perfectly re-collimated as the telecentric lens is symmetrical about the focal point in the specimen region. As the nearly re-collimated beams exit the telecentric lens the beams will slightly expand and the wavefront will change along the path length. As the path length past the telecentric lens increases then the D-shaped beams will deteriorate into the shape of ellipses as shown above. Severe aberrations from the optics can produce multiple spatial frequencies in the hologram, which are represented by variable fringe spacing across the hologram. These multiple spatial frequencies and variations of fringe contrast across a hologram can introduce errors in determining the fringe-shift or phase-shift at the marginal rays of the beams. Aberrations across the aperture are most significant at the marginal rays in comparison to chief rays because marginal rays at the beam edges have higher aberrations than chief rays at the beam center where the rays are refracted over a smaller angle.

A beam steering mirror is tilted ±1° to produce a ±2° field angle for the beam entering the fluid-cell specimen. The tilted beams approach the apex of the biprism, which limits the field-of-view or scanning displacement in the fluid-cell as shown in figure 5.5.8 below:

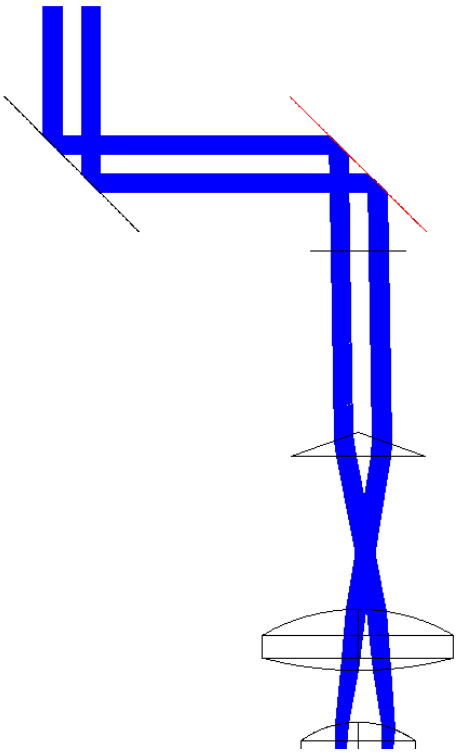

Figure 5.5.8: Tilting Limit to Beams for Scanning and the Effect on the Telecentric Lens

The off-axis coma aberrations increase with scan angle until the field-of-view limit of the biprism is reached. At the maximum field angle of ±2° the beam reaches the apex of the biprism and also approaches the limit of the clear aperture of the cube beam splitter as shown in figure 5.5.9 below:

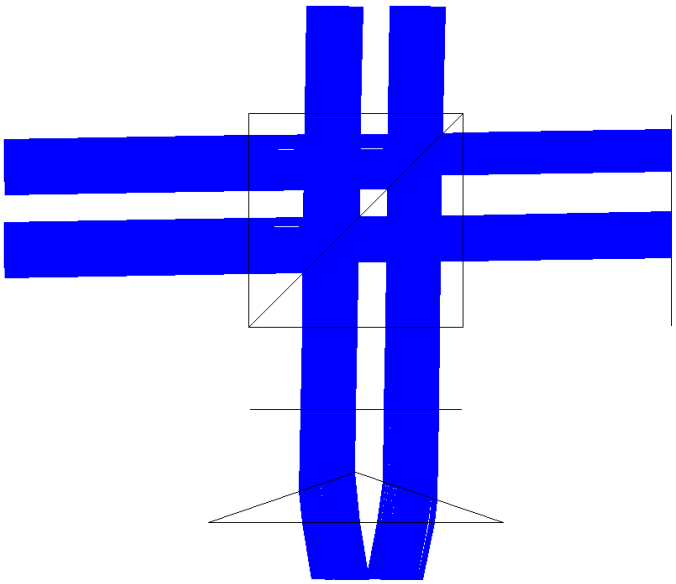

Figure 5.5.9: Scan Displacement Limits for the Microscope

This is a detailed view of the second cube beam splitter at the optical loop entrance (top of cube beam splitter in downward direction) and optical loop exit (left of cube beam splitter in left to right direction). The Fresnel biprism is the initial optical element to the entrance of the telecentric lens. The inside edge of the beam on the left hand side intersects the apex of the biprism, which is the limiting factor for scanning displacement. If the beams are separated further then excessive aberrations occur and the beams de-collimate. The apex of the biprism and the edges of the cube beam splitter limit the scan displacement across the specimen to ± 1.4 mm in the *y*-axis as shown in the figure above. The scanning relationship of angle to displacement for a focal point in the fluid-cell is based on the 80 mm back focal length of the telecentric lens:
y-axis scanning: ±0.75 deg represents ±1.1 mm across the specimen.
x-axis scanning: ±0.50 deg represents ± 0.7 mm across the specimen.
The *xy*-axis represents a cross-section along the *z*-axis or the optical propagation axis. The Cube Beam Splitter is 50.8 mm to a side with a clear aperture of 45 mm in diameter.

The cube grid-cell size is 625 µm/cell for any *xyz*-axis direction. The scanning displacement in the fluid-cell is 625 µm/step at 7 steps in the *z*-axis and 625 µm/step at 3 steps in the *y*-axis. The scanning displacement is also 1250 µm/step at 1 step in the *x*-axis. There are 8 scan positions in the *z*-axis by 2 scan positions in the *x*-axis by 4 scan positions in the *y*-axis. The scanning sequence is *zxy*-axis order. The effective scanning displacement is ±0.625 mm in the *x*-axis by ±0.9375 mm in the *y*-axis of the fluid-cell.

5.6 Telecentric Lens

The telecentric lens is a symmetrical configuration of lenses about the focal point in the fluid-cell specimen region. The telecentric lens focuses the object and reference beam in the specimen region and then re-collimates the two side-by-side beams.. Since the beams propagate through common optics along a similar geometrical path then the aberrations will be the same for each beam. The STLH and CSLH microscope aberrations are primarily due to the short focal length (80 mm back focal length) telecentric lens. Spherical aberrations are produced from the constant radius-of-curvature lenses. Coma aberrations at the focal point are due to the incident beam angle to the first lens and from the parallel beams that are off the centerline of the lenses. The Fresnel biprism introduces an incident beam angle to the first bi-convex lens, which produces part of the coma. The other part of coma aberrations at the focal point in the

specimen is also due to the side-by-side nearly parallel propagating object and reference beams. The ray tracing geometry is different for the marginal rays of each beam.

The telecentric lens optical layout is shown in figure 5.6.1 below:

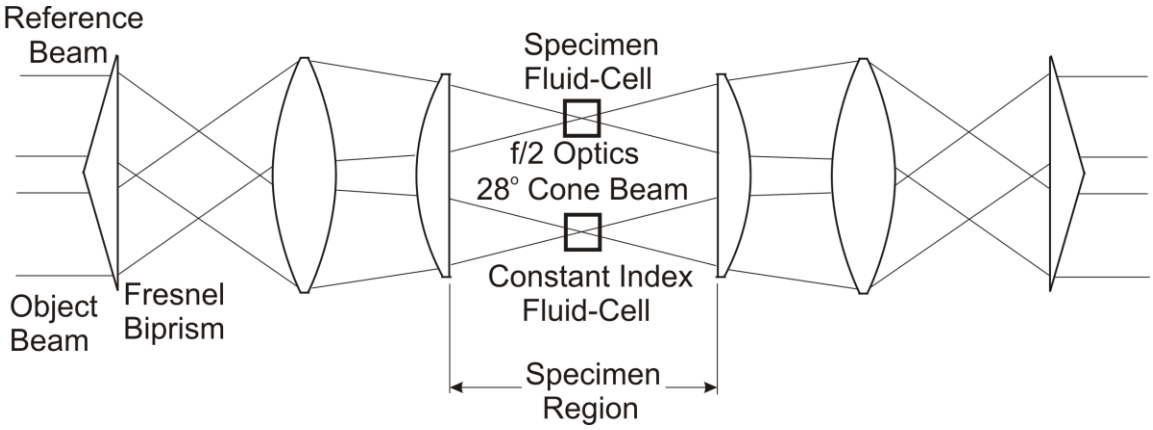

Figure 5.6.1: Telecentric Lens Optical Layout

The symmetry of the telecentric lens about the focal point produces re-collimated output beams that are the same size as the input beams. This means that an angular tilt or scan angle input will produce the same angle at the output but in the opposite direction in relation to the input beam tilt angle. The telecentric lens optical layout shows the f/2 f-number in the specimen region that is produced by the bi-convex and plano-convex lenses. The f/2 f-number is represented by a 28° cone beam (or the 80 mm back focal length) that is focused in the center of the specimen region. The telecentric lens is designed to provide a maximum cone angle for reconstruction at minimum aberrations for a low distortion hologram. The trade-off relationship is the larger the cone angle (that includes the scanning angle), the larger the aberrations.

The large 28° cone beam at a relatively short back focal length is a compromised design that produces an acceptable Point Spread Function (*PSF*) resolution or blur spot size when the re-collimated output beams are re-focused using an ideal paraxial lens. The constant refractive index fluid-cell at the focal point region of the reference beam is held at constant temperature. If the constant index-of-refraction fluid-cell is removed the focal point of the reference beam will shift to the right along the optical axis and the reference beam will not re-collimate to the same size as the input beam. The output reference beam will also converge or diverge due to re-collimation error associated with the shifted focal point.

The specimen fluid-cell is heated and transmits the refractive index information to the object beam. The constant temperature or phantom fluid-cell provides an equivalent

back focal length to the specimen fluid-cell. The phantom fluid-cell provides constant refractive index because it is held to a constant room temperature. The resultant hologram is sensitive to the relative index-of-refraction of the specimen fluid-cell to the phantom fluid-cell.

A Fresnel biprism tilts both the object and reference beams to produce an incident beam angle to the first bi-convex lens. A 140° biprism will tilt the beam to an 11° incident angle to the first lens. Spherical aberrations occur from the curvature of the lenses. Geometric aberrations occur from the off-axis incident angle of the beams to the first lens along with the parallel beams that propagate side-by-side off the optical centerline. Coma aberrations occur from the off-axis incident beam angle, from the beams propagating off the centerline of the lenses, and from the beam scanning angles. An example of a blur spot diagram showing coma is shown in figure 5.6.2 below:

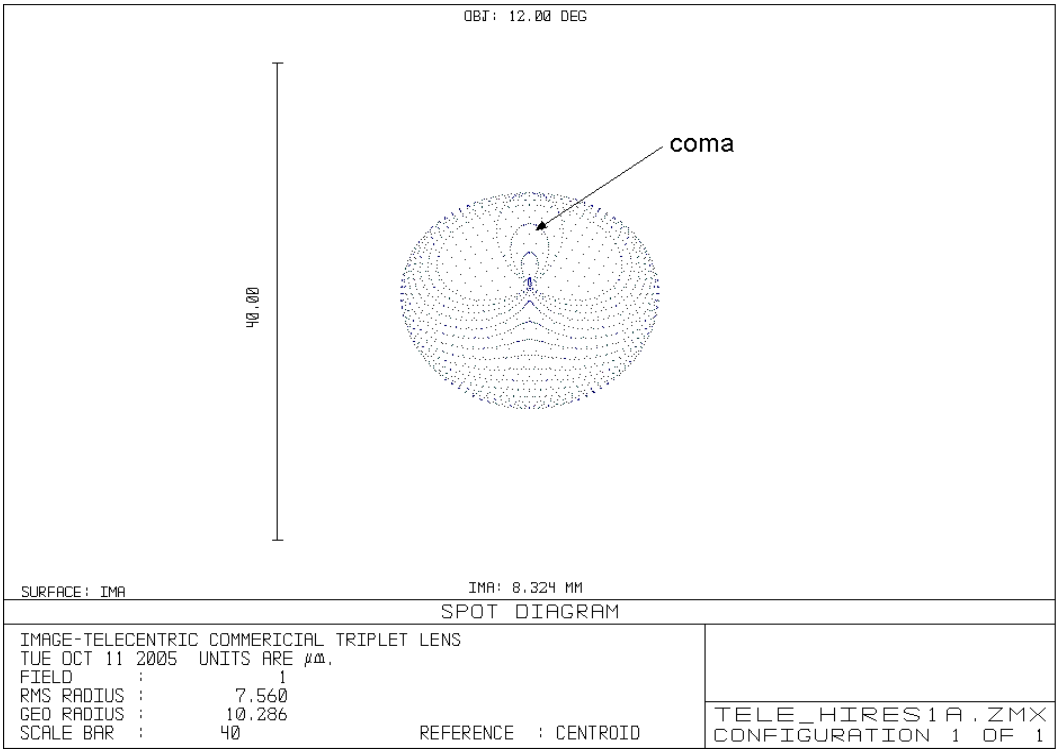

Figure 5.6.2: Zemax Off-Axis Ray Trace Lens Design Showing Coma at a Focal Point

The spots in the diagram show the number of rays that are propagated through the optics and strike at different positions within the focal plane. The coma shows the asymmetrical shift of rays at the focal point as they propagate off-axis through a lens. Whenever a beam is off the axis central line then coma will be introduced into the

aberrations. The first order coma due to the beam tilt of the entrance Fresnel biprism is compensated by the Fresnel biprism at the exit of the telecentric lens and only the residual error of the coma will propagate to the hologram.

Beam steering mirrors that tilt the wavefront of the beam and change the angle of propagation will produce additional coma as the rays propagate through the telecentric lens. The coma that is introduced by the beam steering mirrors, however, is compensated for by the reverse propagation of the beams back through the beam steering mirror section so that only the residual coma error from misalignments is projected into the hologram.

5.6.1 Custom Lens Design

The coma in the focal plane of the telecentric lens was thought to be reduced by designing lenses with either aspherical surfaces or custom spherical lenses. The Zemax optical lens design program showed that the coma at the focal plane of the specimen could not be reduced due to the geometry of the optics. The Zemax software was used to optimize the layout and produce lens prescriptions for custom spherical and aspherical lenses in order to minimize the point spread function blur spot size. An optimized custom spherical lens design by Zemax is shown in figure 5.6.1.1 below:

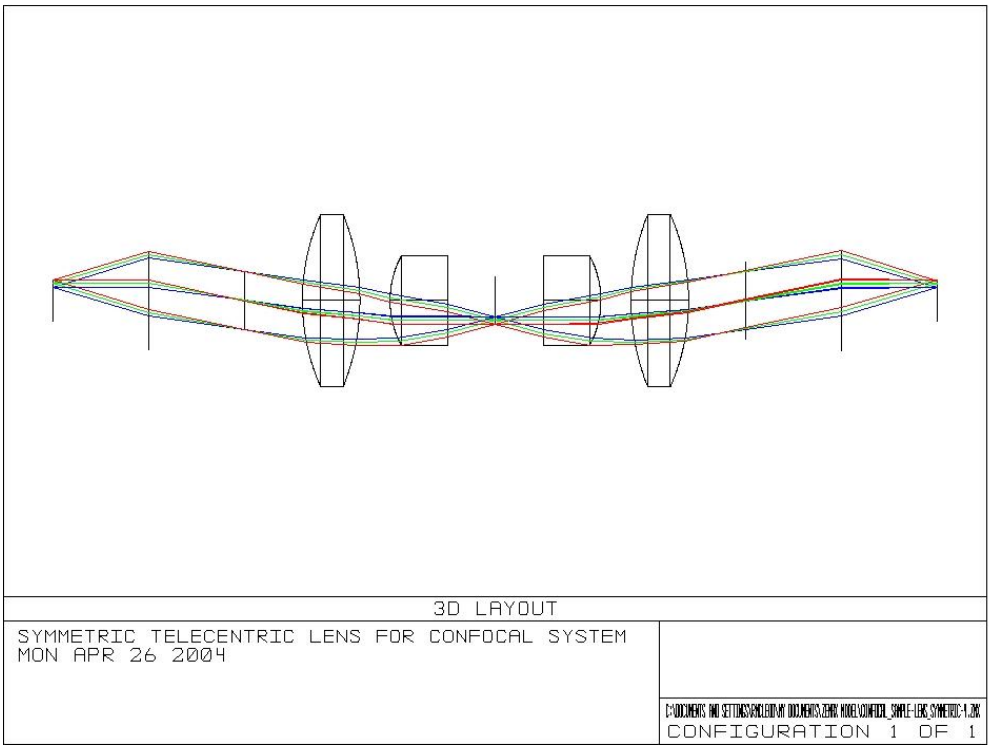

Figure 5.6.1.1: Zemax Custom Spherical Lens Design for the Telecentric Lens

The Zemax layout replaces the Fresnel biprism with an ideal lens that passes all the rays through a pupil plane, shown just before the first lens. The symmetrical pupil plane is duplicated just after the last bi-convex lens where the rays are not crossing one another at this pupil plane. This is due to the geometric aberrations of the layout and the spherical aberrations from the relatively short focal length lenses.

The entrance pupil is represented by the crossing of the ±2° field angle rays to the central on-axis rays. The exit pupil is not as well defined as the entrance pupil due to the aberrations. The rays do not have the same crossing point at the exit pupil plane of the telecentric lens. The crossing point of the rays is between the surface of the last bi-convex lens and the vertical line marking the exit pupil plane as seen in the figure above. Furthermore, the pupil distance varies from marginal ray to marginal ray of the ±2°off-axis rays when they cross the on-axis rays. In other words, the exit pupil is not stationary across the aperture in comparison to the input pupil that is stationary for any field angle. The variation of the exit pupil plane from off-axis rays crossing on-axis rays is aggravated by the periscope lens that reduces beam walk and ideally places a fixed non-varying exit pupil for any scan angle of the beam steering mirrors.

An off-axis geometric aberration is present due to the side-by-side propagating beams through the lenses. This geometric aberration cannot be corrected even when using aspheric lenses and optimizing the design on Zemax. Since only a marginal reduction in blur spot size was gained with custom aspheric lenses then standard spherical lenses were specified at $1/10^{th}$ the cost.

A blur spot diagram for the custom telecentric lens design at the focal point where the re-collimated output beams are focused with an ideal paraxial lens is shown in figure 5.6.1.2 below:

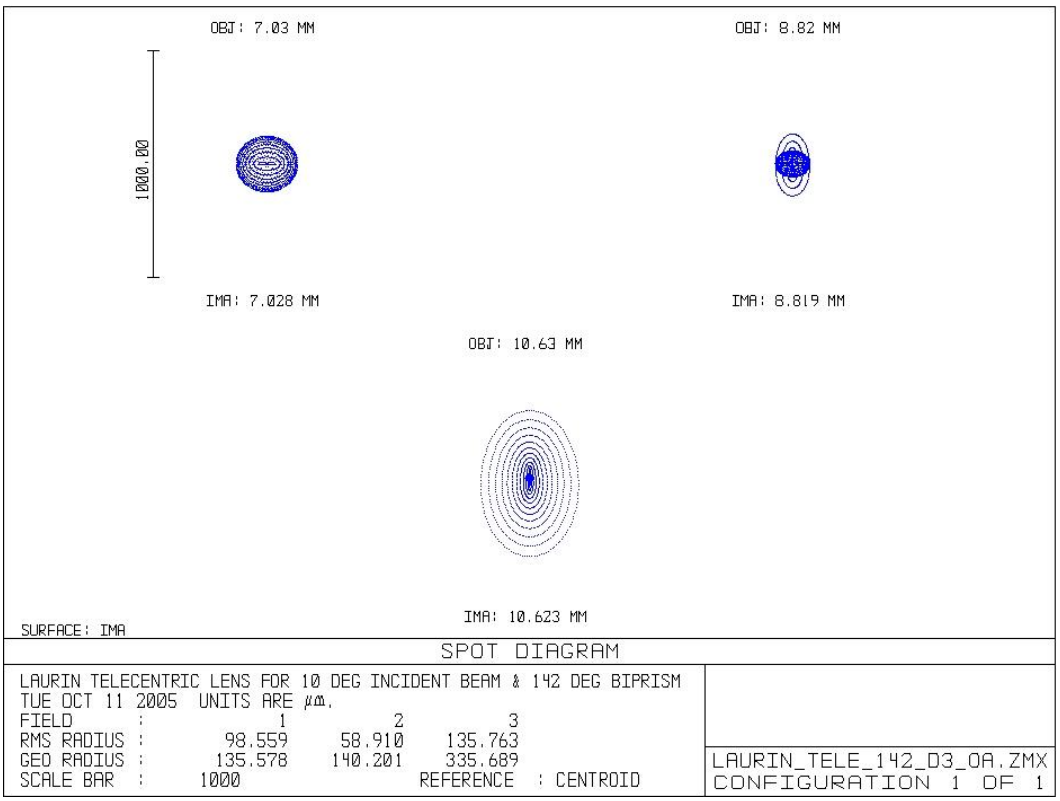

Figure 5.6.1.2: Zemax Spot Diagram for the Custom Spherical Lens Design of the Telecentric Lens

- The first spot in the diagram is the 0° on-axis central ray that has an RMS radius blur spot size of 98 µm.
- The second spot in the diagram is +2° off-axis from the central ray that has an RMS radius blur spot size of 136 µm.
- The third spot in the diagram is -2° off-axis from the central ray that has an RMS radius blur spot size of 59 µm.

5.6.2 Standard Lens Design

Since the geometric aberrations could not be completely corrected in a custom lens prescription then another layout using standard commercial spherical lenses was designed. This layout is shown in figure 5.6.2.1 below:

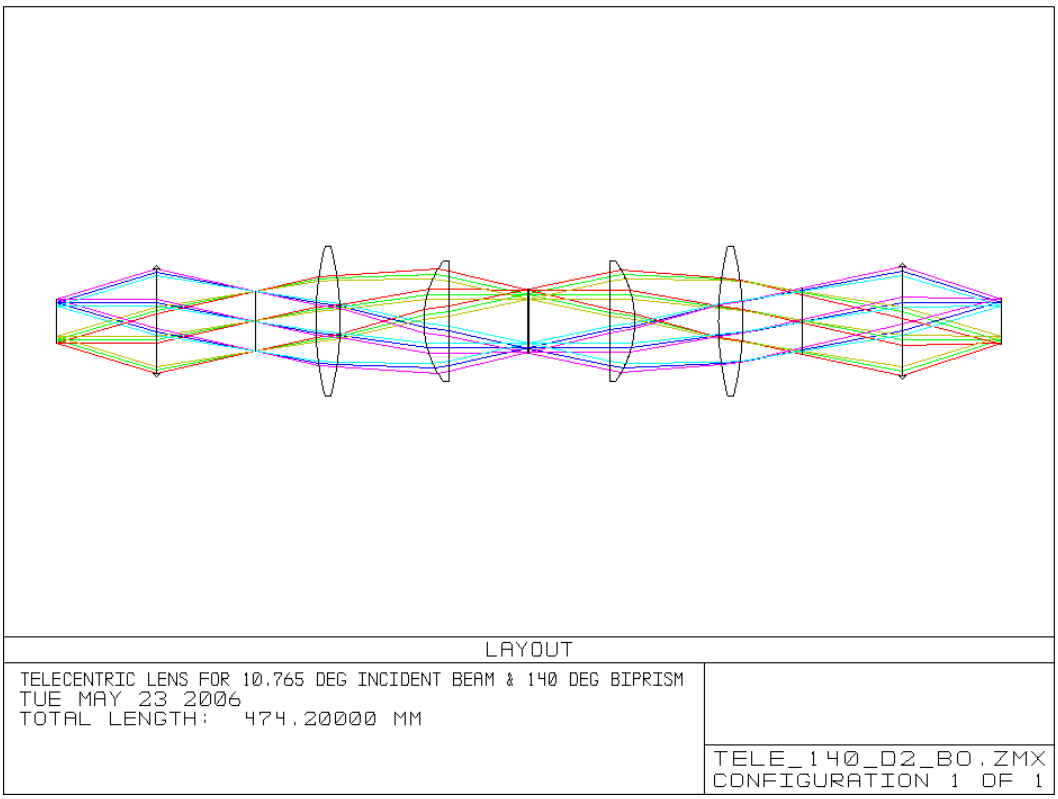

Figure 5.6.2.1: Zemax Standard Commercial Lens Design for the Telecentric Lens

This lens design was first optimized by determining the appropriate focal length for the lenses and then selecting standard Melles-Griot lenses from a catalog. The second Zemax optimization was for lens separation since the lens prescriptions and radius-of-curvatures is a fixed value. There is a nominal degradation in optical resolution of the standard commercial lens design in comparison to the custom lens design because the dominant geometrical aberrations cannot be significantly reduced with minor changes to the radius-of-curvature. Custom lens cost approximately $2,000 per lens and standard commercial lens cost approximately $200 per lens. Standard commercial lenses were purchased for the telecentric lens and the confocal lens. The confocal lens is similar to telecentric lens, but has a larger distance between the two plano-convex lenses in order to fit the pinhole apertures and their holders. The confocal lenses are different in focal length than the lenses for the telecentric lens and all the lenses have anti-reflective coatings. The bi-convex and plano-convex lenses for the telecentric lens and the confocal lens are standard Melles-Griot products with the Fresnel biprisms being custom made by Optikon. The Fresnel biprism is considered ideal in the Zemax simulation as a

30mm entrance pupil is placed just prior to the first bi-convex lens, which produces the proper incident rays into the bi-convex lens.

A Zemax optical resolution spot diagram for the standard commercial lenses of the telecentric lens is shown in figure 5.6.2.2 below:

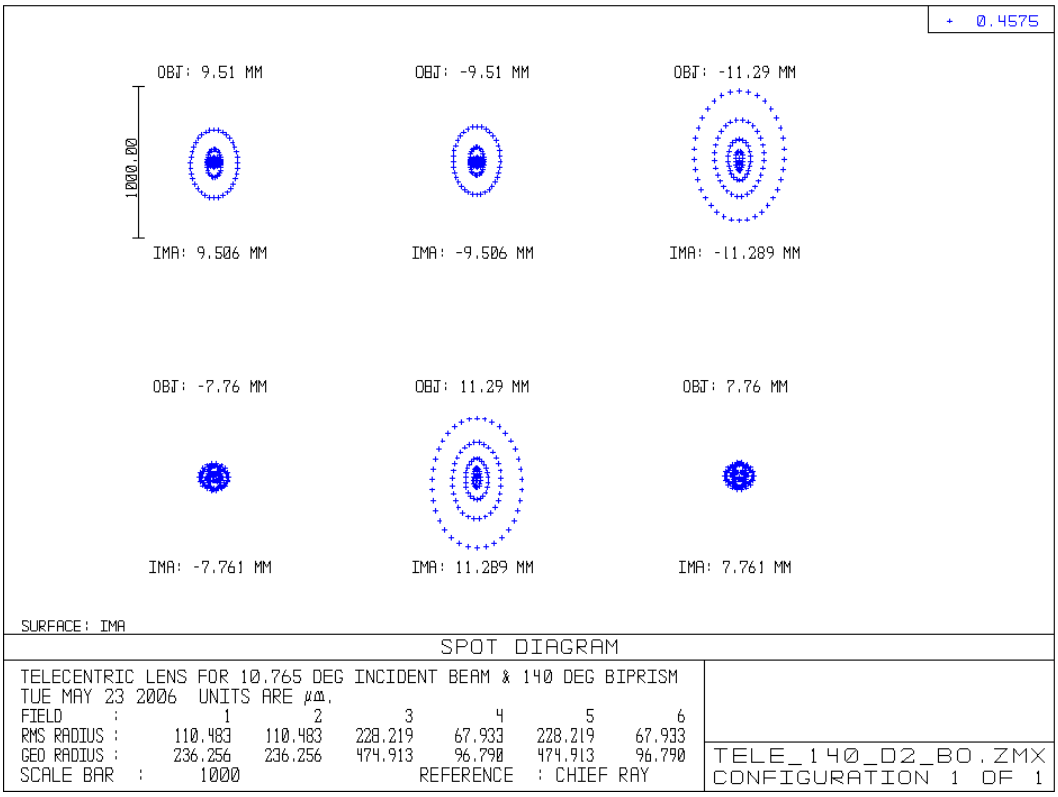

Figure 5.6.2.2: Zemax Telecentric Lens Design Spot Diagram at Various Field Angles

The Zemax spot diagram is taken at the focal plane of the telecentric lens output. Columns 1 and 2 in the upper row show the blur spot size for the on-axis condition of the reference beam and object beam. Column 3 in the upper row shows the blur spot size for the object beam at +2° from the on-axis condition. Column 1 in the lower row shows the blur spot size for the object beam at -2° from the on-axis condition. Column 2 in the lower row shows the blur spot size for the reference beam at +2° from the on-axis condition, Column 3 in the lower row shows the blur spot size for the reference beam at -2° from the on-axis condition.

- The RMS radius blur spot size for either of the two beams is 110 μm at the 0° on-axis condition.
- The RMS radius blur spot size for either of the two beams is 228 μm at +2° from the on-axis condition.

• The RMS radius blur spot size for either of the two beams is 97 µm at -2° from the on-axis condition.

5.6.3 Wavefront Error and Degradation along the Beam Path

An image plane in the specimen region, not located at the focal point, is taken to show the wavefront error. The wavefront error for one of the expanding beams in the specimen region is shown in figure 5.6.3.1 below:

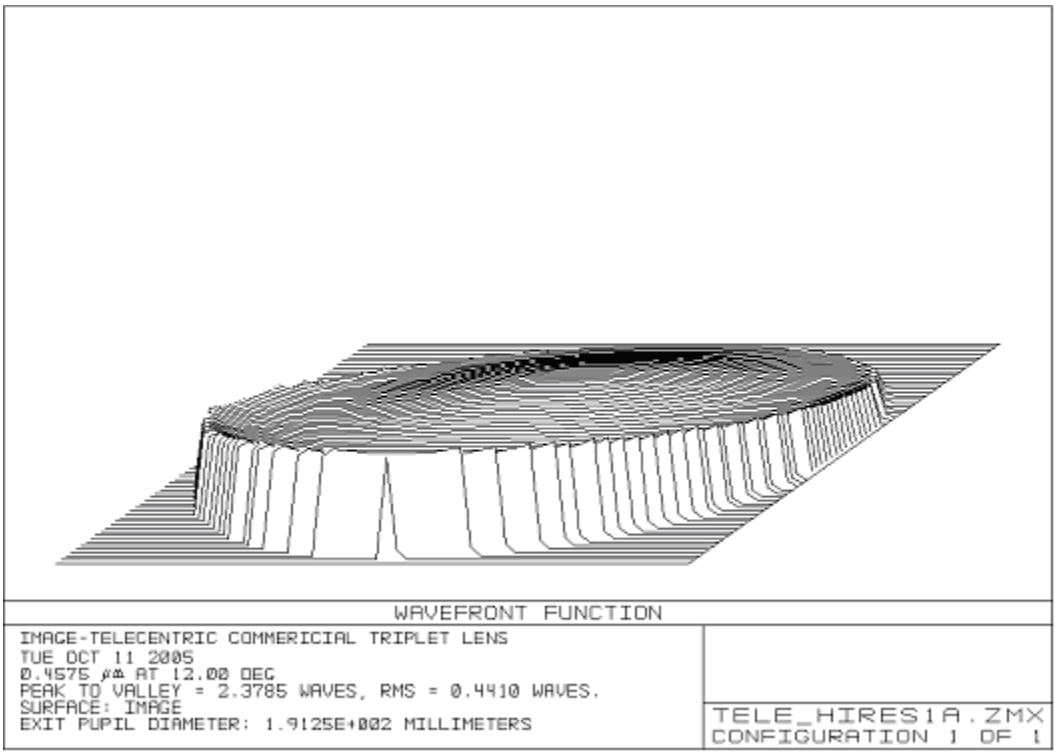

Figure 5.6.3.1: Wavefront Error at an Image Plane or Pupil Plane Near the Focal Point

The first and second lenses of the telecentric lens create a spherical aberration that produces a dish shaped curvature of the wavefront. The tilt in the wavefront is due to the incident beam angle from the biprism. The tilt edge is largest where the rays have maximum optical path length as the rays propagate through air and glass to the image plane or pupil plane. Wave retardation or delay is largest where the glass is thickest. The area of thickest glass is at the optical centerline where the chief ray propagates. The lens edge of thinnest glass is where the marginal rays propagate. The second biprism in the telecentric lens removes the tilt and leaves a wavefront with only spherical aberrations and coma.

The wavefront splitter separates a circular beam into two back-to-back D-shaped beams. Propagating one of the D-shaped beams through the telecentric lens produces an image as shown in figure 5.6.3.2 below:

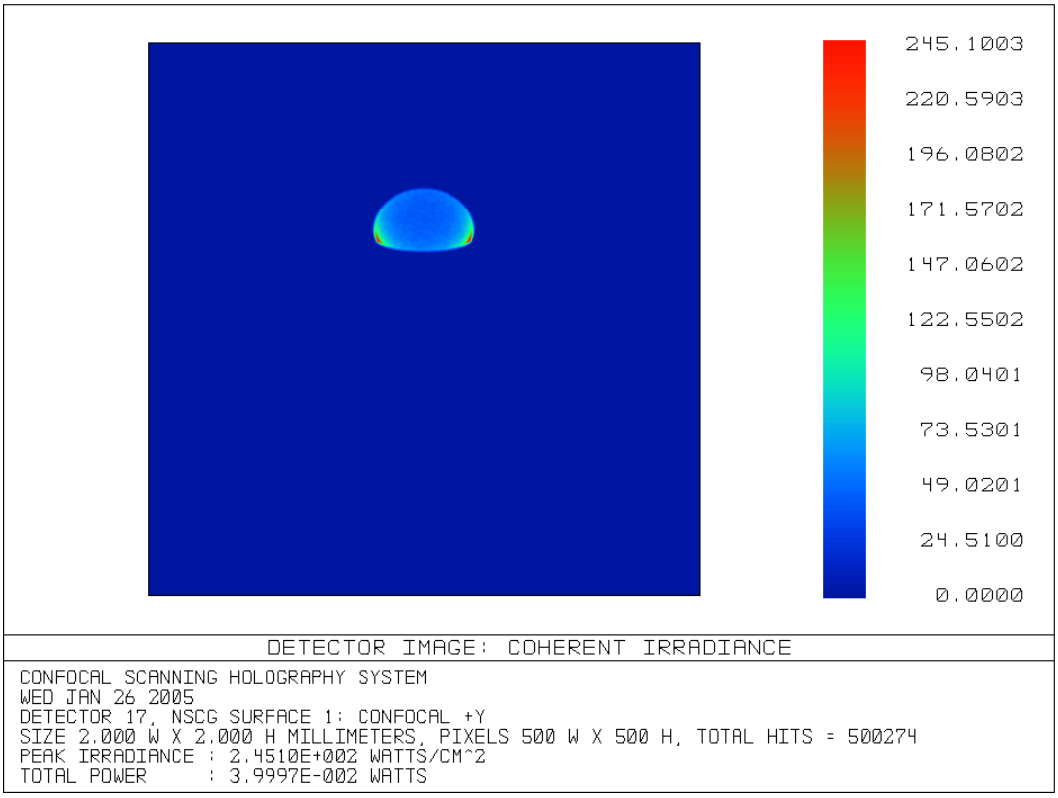

Figure 5.6.3.2: Telecentric Lens Degradation of a D-Shaped Beam from the Telecentric Lens

The image is taken at a pupil plane where the beam is re-collimated at the output and the geometrical aberrations have rounded the edges which indicates a loss of high spatial frequency coherence. The degradation of beam shape is primarily due to the short 80 mm back focal length of the telecentric lens at the specimen region or the f/2 f-number cone beam that introduces spherical aberrations. The off-axis aberrations from the incident beam angle and the beams propagating off the optical center line are also contributors to the degradation of the beam shape.

The Point Spread Function (PSF) at the focal point in the specimen region center is reconstructed back to a D-shaped beam. The aberrations of the telecentric lens introduce a wavefront error that increases with path length. Another pupil plane is selected further down the path of the re-collimated beam. There are no additional optical components along this path and the D-shaped beam distortion is increased. The D-

shaped beam distortion further downstream of the telecentric lens is shown in figure 5.6.3.3 below:

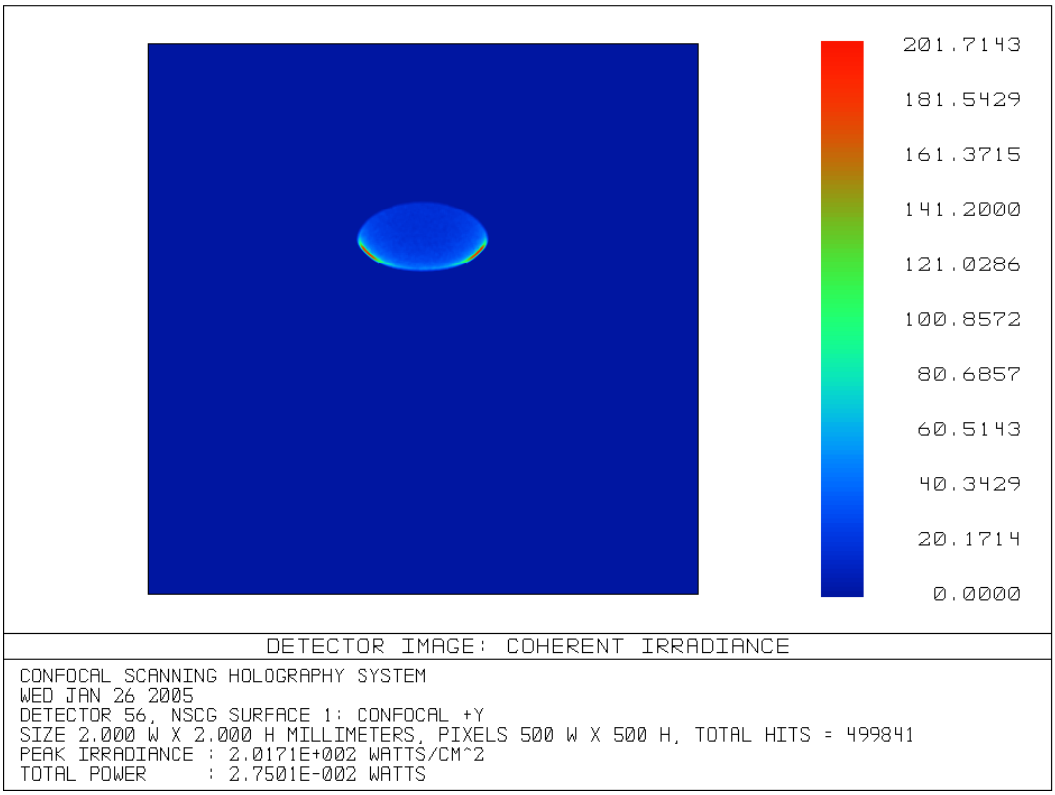

Figure 5.6.3.3: Telecentric Lens Degradation of the D-Shaped Beam at 150 cm Downstream from the Last Telecentric Lens Optical Component

The beam shape has degraded from a distinctive D-shape to more of an ellipse shape. The path length from the projector optics (or the confocal lens) to the camera is from 2 to 4 m. This long path length causes the beam shapes to degrade into ellipses and perfect re-collimation cannot be realized due to the aberrations. The re-collimation error amounts to a beam that expands from 17.5 mm wide at the wavefront splitter to about 60 mm wide at the camera over a 4 m long path length.

5.7 Periscope Lens

The periscope lens provides image inversion along with the reduction of beam translation or beam walk on lenses from the rotations of the beam steering mirrors. The periscope lens with ideal optical lenses effectively translates a pupil plane down the optical axis. Minimal beam walk is desired on the 50x50x50 mm cube beam splitters in order to maximize the field-of-view of the microscope. Negligible beam walk means the location of a pupil remains stationary on a cross-sectional plane along the optical axis.

The periscope lens reduces the beam walk or beam translation by establishing a stationary pupil. The entrance and exit pupil plane distances should be the same for both forward and backward propagating beams in the beam steering mirror section of the CSLH microscope. This is important in order to maintain a stationary focal point on the confocal lens pinhole apertures as the beam steering mirrors rotate for scanning. Optical aberrations, such as coma in particular, will cause beam translation at the pupil plane and therefore the pupil plane is considered to be non-stationary relative to scan angle. It is not possible to maintain a perfectly stationary focal point on the confocal lens pinhole apertures when scanning off the optical axis. A Zemax layout for the periscope lens is shown in figure 5.7.1 below:

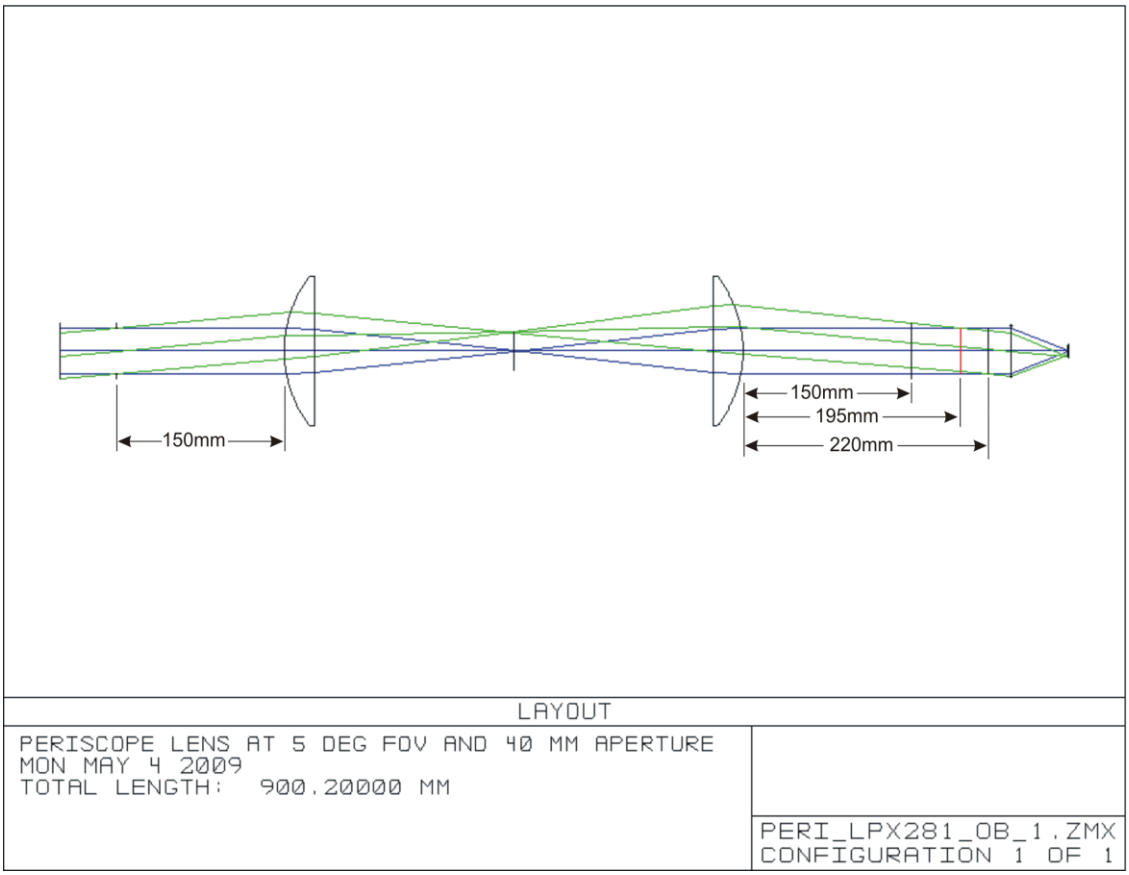

Figure 5.7.1: Focusing and Re-Collimating Plano-Convex Periscope Lens

The periscope lenses are 130 mm in diameter so that the lens apertures can receive the off-axis beams. The off-axis beam translates on the periscope lens aperture from rotations of the beam steering mirrors. A large aperture lens can accept the beam walk from the ±2º rotations of the beam steering mirrors, but the large lens is significantly more costly than lenses under 100 mm in diameter. Melles-Griot plano-convex converging lenses in the Zemax layout are 01LPX281 200 mm focal length by 130 mm

diameter BK7 glass with standard broad-band anti-reflective coatings. The re-collimated output beam size is the same as the input beam size and the output angle is the same as the input angle except in the negative direction in relation to the central axis. The exit pupil distance would equal the entrance pupil distance of 150 mm using ideal lenses and paraxial ray tracing. The aberrations of the lenses causes the exit pupil distance to increase from 150 mm to a range of 195 to 220 mm depending on the selection of marginal ray crossing from the 5º field angle.

The focal length of the lens is relatively large at 200 mm to minimize spherical aberrations, but not sufficiently large enough to establish a fixed or stationary pupil plane. There are two periscope lenses, one located near the two galvanometer beam steering mirrors and another periscope lens placed in the telecentric lens optical loop. The periscope lenses provide beam inversion and also defines pupil plane distances that will minimize translation of the focal point at the confocal lens pinhole apertures during scanning.

5.8 Projector Lens and Phase-Shift Measurements to Wavefront Error Relationship

Interferometers are typically used to measure the phase of optical components or objects such as a fluid specimen or a semi-transparent solid. Given the phase and thickness the index-of-refraction can be determined. Alternatively, given the phase and index-of-refraction the thickness can be determined. Interferometers are commonly used to measure surface flatness or curvature of an optical component given a reference surface. The STLH microscope is similar in principle to an interferometer since it produces a hologram or interference pattern based on either air or a fluid-cell of constant refractive index as a reference. Fringe-shifts in the hologram are due to a phase-shift produced by the specimen. The fringe-spacing is the distance between fringe lines. A phase-shift of 1 wave of a fringe or 2π radians is represented by the fringe-spacing.

Optical aberrations, such as spherical aberrations, coma, and chromatic aberrations create phase-shifts over a pupil or aperture or cross-sectional area of a beam. The phase-shifts over the pupil constitutes a wavefront error and because of this a focused beam cannot be perfectly re-collimated using real lenses. The re-collimated beam shape degrades with path length beginning with the rounding of corners and smoothing of the edges. The “D” shaped beams of the STLH & CSLH microscopes will ultimately degrade to an ellipse shape over a sufficiently long path length. Beam shape transition to an ellipse over path length is represented by the wave mixing of high spatial frequency

components and the coherence of low spatial frequency components. Spherical aberrations, for example, will produce a changing fringe-spacing over the pupil that can be measured in a hologram. Also found in the hologram is fringe contrast over the pupil, which too is a measure of aberrations or wavefront error. Image acquisition with a camera limits the ability to accurately determine wavefront error from the properties of fringes as the number of pixels in the camera resolve a fringe. The camera also has a finite radiometric dynamic range to resolve the fringe contrast along with a low level radiometric sensitivity that can clip the valleys of the fringe pattern waveform or hologram.

The STLH microscope was slightly modified to measure the wavefront error that is primarily due to the aberrations of the optics. A vertical translator was placed on the camera to convert from line scanning to area scanning. The fluid-cell was unheated and at constant room temperature during the wavefront measurements or collection of holograms. The unheated fluid-cell provided a constant refractive index specimen. This configuration allowed for the measurement of wavefront error or phase-shift across the aperture where the beams overlap.

A Zemax projector lens layout was used to demonstrate the effects of spherical aberrations on a hologram as shown in figure 5.8.1 below:

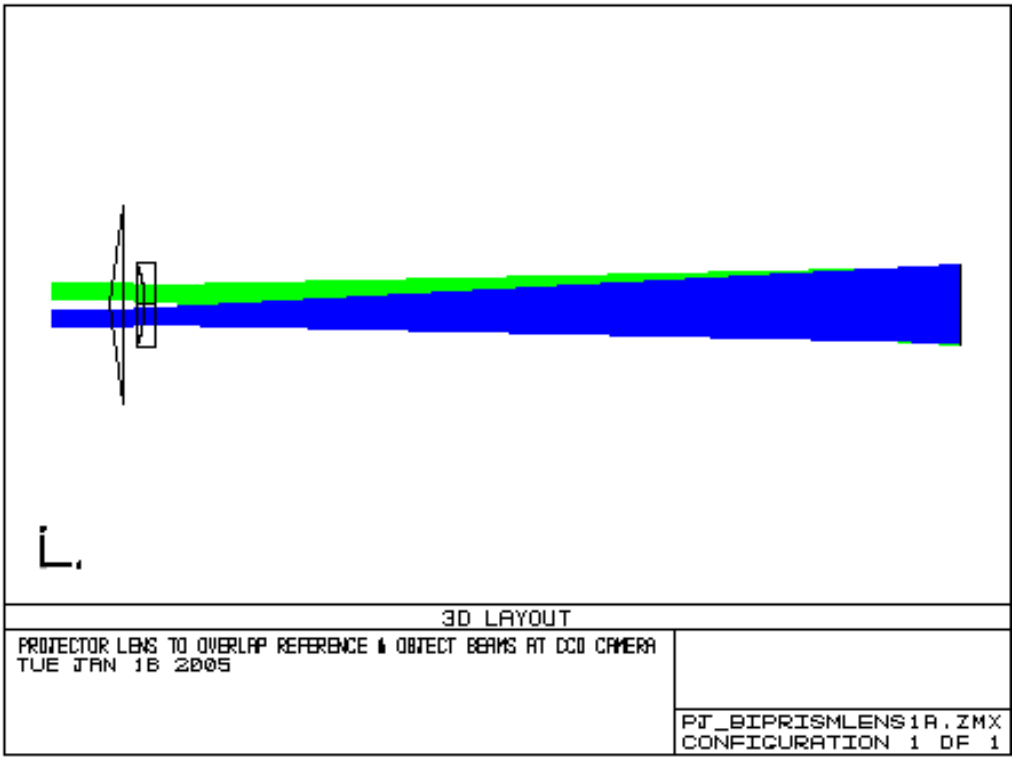

Figure 5.8.1: Zemax Layout for a Projector Lens

A Fresnel biprism tilts two coherent beams for overlap and a plano-concave diverging ray lens expands the size of the beams to fill the line scan camera at the point of complete beam overlap. Complete beam overlap means that interference will occur for the marginal rays at the edges of the beams. The marginal rays are at the top and bottom of the hologram as seen at the camera focal plane in figure 5.8.1 above. The Dalsa line scan camera is 1x8192 pixels at 7 μm/pixel and a width of 57 mm, which the overlapped beams fill. The biprism tilts each of the beams 7.5° to produce a 15° convergence angle and the plano-concave diverging lens introduces spherical aberrations. The path length from biprism to camera is relatively short due to the focal length or radius-of-curvature of the diverging lens.

The objective is to design the projector lens with at least 16 pixels of detector sampling per wave of a fringe and to fill the detector width of the camera. Fringe-spacing is primarily due to the wavelength of the laser, the angle of the biprism that produces a convergence angle for beam overlap, and the plano-concave lens radius-of-curvature. The hologram image plane is placed where the two beams completely overlap one another. The 16 pixels/fringe sampling or 16 samples/wave of a fringe waveform sampling is the minimum required to determine a fringe-shift of less than 3º or λ/100 waves given a constant fringe contrast across the pupil or area of wave interference in the overlapped region.

The biprism in the figure above produces a 16º beam convergence angle and along with a 457 nm wavelength laser the resultant fringe-spacing is 3.3 μm. This fringe-spacing is too small relative to the detector spacing of 7 μm/pixel. The diverging lens expands the beams over the distance to the camera and the fringe-spacing increases from 3.3 μm to 13 μm. This provides fringe sampling of $13\mu m / 7\mu m = 1.9\ pixels\ /\ fringe$, which is less than the minimum required 16 pixels/fringe. Therefore, a different projector lens has been designed for the CSLH microscope that produces a spatial sampling of $30\ pixels\ /\ fringe$.

The Fresnel biprism, which was used to measure the wavefront error, was replaced with an optical wedge in the STLH microscope. A 0.5 º optical wedge was used to increase the number of pixels per fringe, which also increased the path length to complete beam overlap. The fringe-spacing was also increased by the slightly diverging or expanding beams from the telecentric lens. The slightly diverging beams will increase the number of pixels per fringe at the camera. Since the aberrations from the telecentric lens produce a slightly diverging beam following re-collimation the plano-concave lens

can be eliminated. This Zemax projector lens design however, shows the effects of spherical aberrations from a plano-concave lens on a hologram. A Zemax generated hologram from the overlapped beams of the projector lens layout is shown in figure 5.8.2 below:

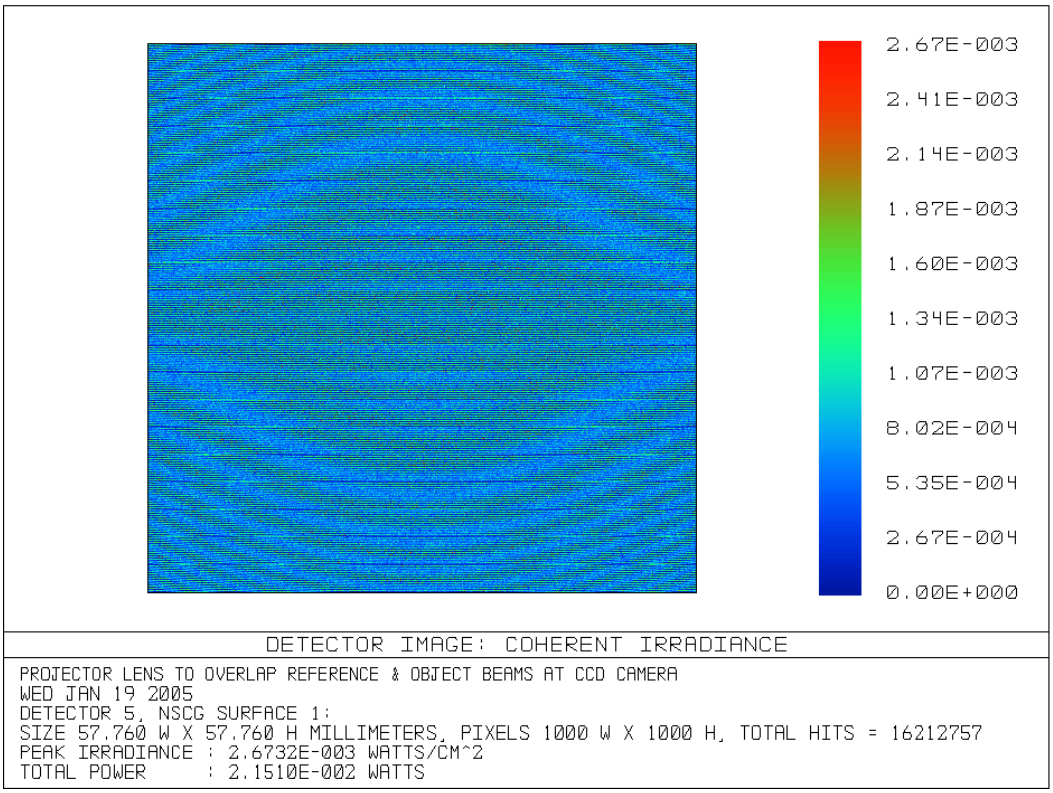

Figure 5.8.2: Fringe Pattern or Hologram at Camera Detector Plane

The curved fringe lines in the hologram represents a phase-shift across the aperture from the spherical aberrations produced by the radius-of-curvature of the plano-concave lens. The hologram was produced at the image plane by the interference of 20 million rays. An aberration free lens would show straight horizontal lines that have constant fringe-spacing across the hologram. Spherical aberrations produce fringes with larger spacing at the center of the hologram resulting in curved fringe lines that represent a phase-shift relative to a straight horizontal line. The outside edges of the plano-concave lens are thicker than the center, which will retard the phase of the wave more than at the center of the lens. The spherical aberrations produce the curved fringe lines which otherwise would be straight. The vertical symmetry across the center is due to the coma from the wavefront tilt of the two beams that are converging to overlap one another.

The line scan camera was placed vertically centered in this hologram to measure the fringes. Constant fringe spacing produces one spatial frequency, which is the carrier

frequency in the hologram. The carrier frequency is important to accurately determine the phase-shift using the Fourier transform method or other methods. Accurate phase-shift determination from a fringe-shift in the hologram also depends on fringe contrast variation across the hologram. Constant fringe contrast is desired, but the fringe contrast is affected by optical aberrations, non-uniform aperture illumination, and macro sized dust particles.

The region of interest for fringe-shift measurements is at the top and bottom edges of the hologram where the marginal rays of both the object and reference beams coincide. This marginal ray region is used to determine the phase-shift that will provide minimum error for refractive index reconstruction. The CSLH microscope lens produces more aberrations than the STLH microscope primarily due to the addition of a confocal lens and three periscope lenses. Both the STLH and CSLH microscopes measure the effects of the specimen as well as the optical aberrations of the lenses as the figure above indicates.

The STLH microscope with a vertical scanning camera was used to examine the effect of phase-shift measurements on wavefront error. A *y*-axis vertical translator micrometer stage was placed on the 1x8192 line scan camera. The 8192 pixel camera width was divided into 16 equally separated points to establish a reference point for the Fourier transform, which read 256 samples at each point. The fluid-cell was scanned in the *x*-axis horizontal direction for 16 steps and scanned in the vertical *y*-axis direction for 12 steps. The Fourier transform method determined the phase-shift at each reference point. This measured phase-shift is shown in figure 5.8.3 below:

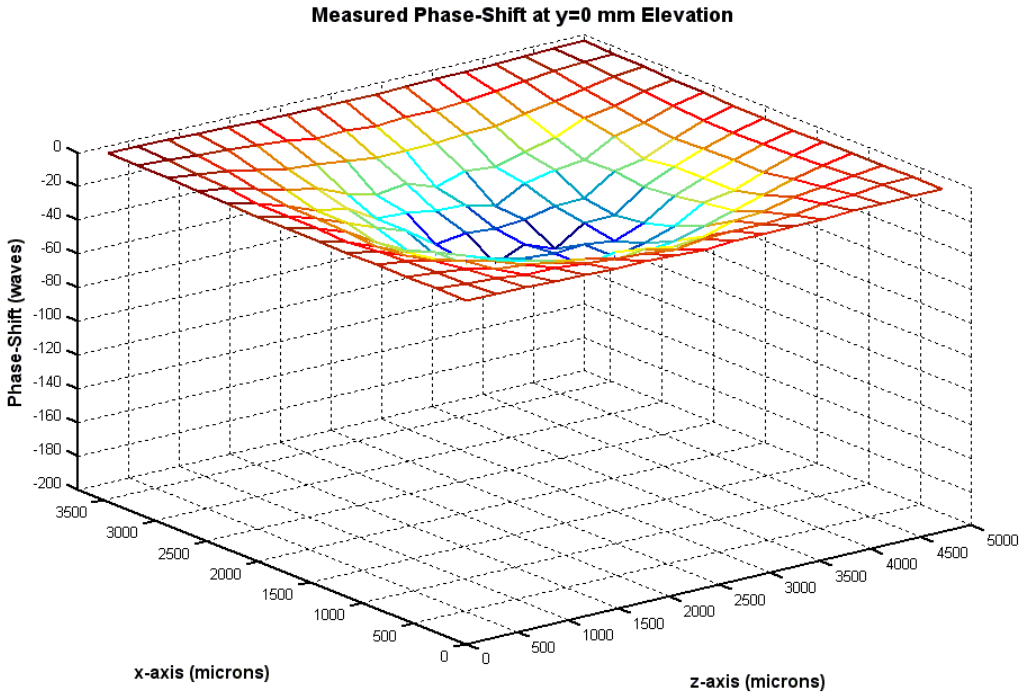

Figure 5.8.3: Measured Phase-Shift for Holograms taken at the Pupil Plane of the Camera

This figure is similar in shape to a wavefront error showing spherical aberrations of the optics along with geometrical aberrations. This demonstrates that the microscope can be used to measure the wavefront error of a beam from the phase-shifts in a hologram.

6 Error Analysis

Error analysis identifies the optical effects that contribute to errors in the hologram followed by image acquisition and data sampling of the hologram. In addition, error analysis includes image processing to determine the phase-shift in the hologram. The "wily" matrix reconstruction algorithm error is found in section 4.2 Reconstruction Algorithm Simulation.

6.1 Phase-Shift Sensitivity to Hologram Sampling and Methods to Determine the Phase-Shift

The phase-shift is related to the change in index-of-refraction, which is represented by a change in the Optical Path Length (OPL) due to the fluid-cell specimen. The projector optics limit the spatial sampling of a fringe on the hologram due to the shallow beam convergence angle and the long path length that completely overlaps the object beam onto the reference beam. The projector optics are designed to provide a particular fringe-spacing on the camera. The camera images the fringes of the hologram at a spatial resolution of at least 8 pixels/fringe. The size of a detector element is 7 μm/pixel and one pixel is equivalent to one sample. The number of discrete samples used in the Fourier transform is defined by a 2^n sampling range. The fringe sampling at the camera is 8x7 = 56 μm/fringe. The minimum spatial resolution is an important factor contributing to the accuracy of determining the phase-shift. The fewer number of pixels per fringe, the less accurate the phase-shift measurement. A simulation at a spatial sampling of 8 samples/wave of a fringe with added noise to a constant amplitude hologram was used to evaluate the phase-shift sensitivity and error. The simulation was evaluated with the hologram at constant spatial frequency or the carrier frequency of the waveform due to constant fringe-spacing.

There are three methods to determine the phase-shift from sampled data:

1) Arc-Cosine Trigonometry Method from estimating the waveform peak using a polynomial curvefit of the sampled data.
2) Least-Square Error (LSE) Waveform Correlation Method from varying the phase-shift of a reference waveform to the hologram sampled data waveform and finding the minimum LSE over discrete phase-shifts.

3) Fourier Transform Method to find the Power Spectrum peak and the corresponding frequency then determining the phase-shift from the Fourier transform real and imaginary components at the corresponding frequency peak.

The challenge when using any of the three methods is to accurately estimate the peak and valley intensity of the fringe pattern waveform from the relatively sparse sampling. The Arc-Cosine trigonometric approach calculates the peak of the waveform in conjunction with the period of the wave using a polynomial curve fit to determine the phase-shift. Unfortunately the peak in the sampled data array does not necessarily represent the peak of the waveform. The estimation of the peak using a low order polynomial curvefit is less than the peak in the waveform, which produces an error in calculating the phase-shift.

The Waveform Correlation method uses all of the data in the hologram and the phase of a reference waveform is varied until a minimum LSE is obtained. This method is generally limited in accuracy to the variation of peak and valley intensity levels across the hologram.

The Fourier Transform method is commonly used in electron microscope holography signal processing. The phase-shift is determined from the complex arguments of the Fourier transform at the spatial carrier frequency. This method is generally more accurate for larger variations in fringe contrast or peak-to-valley intensity.

Factors that affect the fringe-shift or phase-shift are: 1) Spatial sampling of a fringe, 2) Consistency of the spatial frequency from the fringe line spacing, 3) Consistency of the hologram waveform valleys due to noise and background source interference, and 4) Consistency of the hologram waveform peaks due to aberrations of the lenses as the fringe contrast changes over the aperture of both the object beam and the reference beam.

The worst case sparse fringe sampling is assumed to be 8 pixels/fringe or $8 samples / fringe$ spatial sampling. An ideal fringe contrast across a hologram is represented by a cosine function with zero phase-shift, constant peak amplitude, constant valley amplitude, and constant spatial frequency is shown in figure 6.1.1 below:

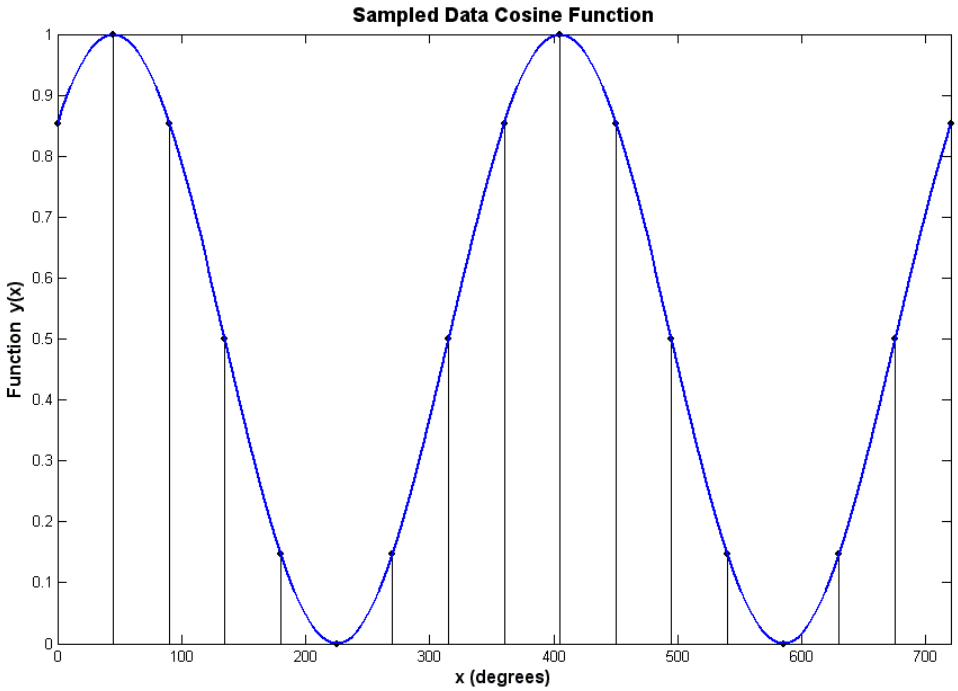

Figure 6.1.1: Line Scan Camera Sampling of Fringes

This figure shows the hologram waveform function with zero phase-shift, which is given as $x(\theta) = 1000 \times (1 + \cos(\theta))$ where the sampled peaks coincide with the function peaks. The axis units are arbitrarily scaled for the simulation. There are 6 peaks or 5 waves and the spatial sampling rate is $8\ samples\ /\ fringe$ where the Nyquist sampling frequency limit is $2\,samples\ /\ fringe$. This sparse spatial sampling rate is considered an absolute minimum to reasonably determine the phase-shift.

The purpose of this simulation is to show the error in determining the phase-shift given an estimate of the peak intensity from sampled data of a cosine waveform. This sparse sampling can accommodate up to a second-order polynomial curve fit to approximate the cosine function waveform. A second-order polynomial curve fit will estimate a peak that is less than the value for the cosine function, introducing an error in determining the phase-shift. A second-order quadratic polynomial can be used to curvefit the sampled data and determine the peak of the waveform given 8 samples/wave or 4 samples over a half-wave. An LSE second-order quadratic polynomial curvefit is applied to 4 data points of a cosine function waveform with a phase-shift that coincides with the peak of the cosine function with that of the sampled data. The LSE quadratic polynomial curvefit to a cosine function is shown in figure 6.1.2 below:

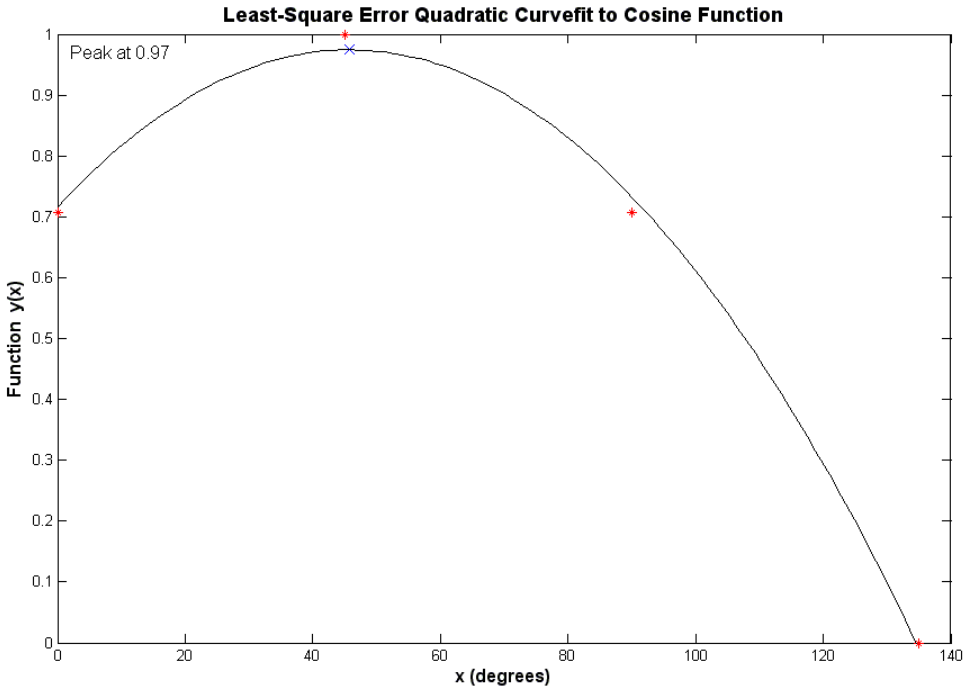

Figure 6.1.2: Second-Order Least-Square Error Polynomial Curve Fitting and Peak Value

The sampled data of the cosine waveform coincides with the peak of the waveform and the error of cubic polynomial curvefit is due to the low order of the polynomial. The sampled data for a cosine waveform is represented by red "*" markers. The LSE second-order quadratic polynomial curvefit is represented by the curve and the peak of the polynomial curve is represented by the blue "x" marker. The ideal minimum error condition occurs with polynomial curvefits having greater than 8th order where the phase-shift error is $\cos^{-1}(1) = 0$. The phase-shift error for the LSE second-order polynomial curvefit is $\cos^{-1}(0.97) = 14.1°$. If the wavefront error is λ/50 waves RMS then the corresponding phase-shift error is 360/50 = 7.2° RMS then phase-shift error. Decreasing the phase-shift error is accomplished by increasing the number of samples per fringe in a hologram. The second-order quadratic polynomial curvefit of the 8 samples/fringe sampled data produces excessive error and does not take into account the average of multiple peaks and valleys of the waveform in the hologram. The waveform correlation method and the Fourier transform method must thus be considered.

The waveform correlation method uses a LSE discrete phase-shifting algorithm to optimally fit the sampled data to a reference cosine function waveform. The reference cosine function waveform uses independent input variables such as amplitude bias, amplitude peak, period of the waveform (based on the fringe-spacing or carrier frequency), and the phase of the waveform relative to a reference point or origin. Since the waveform is constant in all variables except the phase then the LSE Waveform Correlation Method for amplitude bias, amplitude peak, and period of the waveform need only be performed once. The Waveform Correlation Method is then applied to the phase-shift parameter from 0 to 2π radians to LSE match the reference cosine waveform to the sampled data in the hologram. The cosine function waveform is represented by the following sinusoidal function:

$$I(x_{i,}\phi_j) = I_i(\phi_j) = I_{bias} + I_{pk}\cos(2\pi f_x \cdot x_i + \phi_j) \tag{6.1.1}$$

The constant steady-state parameters are:

Intensity Bias or DC Intensity: I_{bias}

Intensity Peak: I_{pk}

Spatial Frequency: f_x

Wave Number: $k_x = 2\pi f_x$ (6.1.2)

The independent variables are:

Displacement: x_i

Phase-Shift: ϕ_j

Measured Hologram Data: $(x_i, I_{data}(x_i))$

The Sum-Squared Error (*SSE*) for correlation is given as follows.

$$SSE(\phi_j) = \sum_{i=1}^{n}(I(x_i,\phi_j) - I_{data}(x_i))^2 \tag{6.1.3}$$

Given: $0 \le \phi_j \le 2\pi$

Where: 2π radians is equivalent to 1 wave of a fringe or the fringe-spacing displacement.

The phase-shift variable ϕ_j is incremented in small steps such that *SSE* produces a minimum value. A halve-the-interval algorithm is used to search for the ϕ_j value solution which has quicker convergence than small step iterations from 0 to 2π radians. Setting a minimum *SSE* phase-shift threshold can prematurely terminate the search for minimum

phase-shift from 0 to 2π radians. The minimum phase-shift error threshold is set to 0.5° or 0.0014 waves. The LSE Waveform Correlation Method algorithm is given a range value for the input variables where a halve-the-interval routine converges on the minimum error solution.

In general, the LSE Waveform Correlation Method works well in simulation evaluations where the measured data maintains a near ideal waveform having minimal distortion. Applying the LSE Waveform Correlation Method to the holograms produced by the STLH and CSLH microscopes was not practical because of distorted holograms from the optical aberrations affecting the hologram. The aberrations are primarily from the telecentric lens, confocal lens, and periscope lenses. The hologram fringe contrast or amplitude peak is dish shaped from marginal ray to marginal ray across the hologram. There are hundreds of fringes in the overlapped region of the beams that the camera images due to the 8192 pixels or 57 mm detector width of the camera.

Attempts to perfectly re-collimate the beam results in a beam with coma like aberrations in the fringes across the hologram. This presents highly undesirable additional fringes or multiple spatial frequencies in the hologram. The compromise is to allow slight beam divergence with no fold over of spatial frequencies into the hologram. This slight beam divergence provides the advantage of increasing the number of detectors per fringe spatial sampling at the expense of lowered irradiance or intensity per detector.

In addition, maintaining a constant beam size through all the lenses and optical components was not possible. Maintaining constant beam size is especially difficult with the optical loop due to alignment of both forward and reverse propagating beams. The output beam size at the projector optics was smaller than desired with every effort made to properly align the microscope and maintain an optical gain of one throughout all of the re-collimating lenses along the beam path.

Optical alignment is critical to achieve perfect beam re-collimation which will reduce the number of frequencies to one dominant carrier frequency in the hologram. Since the hologram waveform is not consistent in peak amplitude or peak image intensity across the aperture or pupil then the Waveform Correlation Method will produce additional error than what is shown in the simulation. Due to the inconsistent peak intensity a reference hologram is used to compensate for the optical aberrations in the hologram or to correct for the variations in peak amplitudes across the beam overlap region.

The standard signal processing approach is to use the Fourier Transform Method to determine the phase-shift of the fringes in the hologram. The phase-shift is determined from the Fourier transform complex variable arc-tangent relationship at the fringe carrier frequency. The peak spatial frequency is the first-order frequency in the power spectrum that produces the maximum power spectrum magnitude. The zero-order peak in the power spectrum represents the non-diffracted beam and is the DC-bias value in the spectrum. The first-order peak frequency is represented by the spatial carrier frequency from the nearly constant fringe-space lines in the hologram. Typically the waveform data is processed with a data window or apodization tapering function before entering the Fourier Transform.

Typical data windowing such as Hanning, Hamming, Bartlet, Blackman, etc. is used to reduce high frequency error or aliasing frequency error at high bandwidth. High bandwidth is at the Nyquist limit frequency where 2 samples/wave occurs for digital signal processing and 3 samples/wave occurs for holography.

Introducing a data window in the spatial or temporal frequency domain is effectively a band-pass filter that attenuates both the low and the high frequencies. Attenuating the high frequencies with a low-pass filter is desirable if the bandwidth is close to the Nyquist frequency limit. The collected fringe spatial frequency data from the camera is well below the Nyquist limit at approximately 30 samples/fringe.

The power spectrums of the measured holograms show negligible frequency content above the fringe spatial carrier frequency and elimination of the data window will not introduce a fringe-shift error. Since determining the phase-shift is from the spatial carrier frequency in the Fourier spectrum and is a low spatial frequency component then introducing a data windowing or apodization tapering function has been found unnecessary based on simulation studies. Data windowing is more critical for holograms that have a large variation in phase-shift across the hologram or a specimen object that has large refractive index gradients.

The Fourier Transform Method uses a power spectrum to determine the spatial frequency from the constantly spaced fringes in the hologram, which defines the dominant spatial carrier frequency in the spectrum. The spatial carrier frequency is constant for all holograms and the power spectrum needs only to be taken once. A Fourier transform is taken for each hologram and both the real and imaginary values (at the spatial carrier frequency) are saved to an array. The phase-shift is the arc-tangent of the imaginary value to real value ratio. The sign of the real and imaginary values defines

the quadrant for the phase-shift so that the range for the phase-shift can be determined from 0 to 2π radians or 1 wave. The 8 samples/fringe of a hologram at phase-shift = 0º is shown in figure 6.1.3 below:

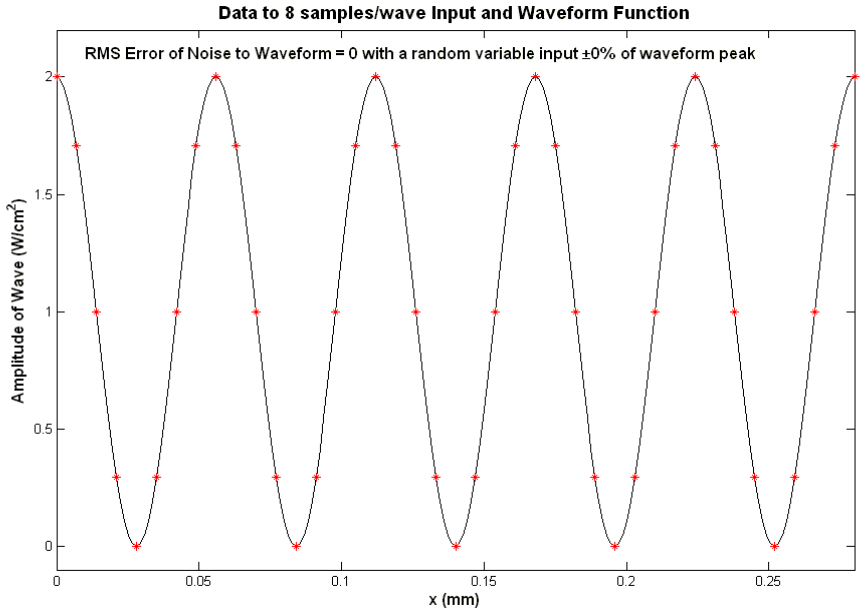

Figure 6.1.3: Sampled Data of Hologram with No Noise and No Phase-Shift

This is the ideal fringe waveform or hologram image with peaks representing light fringe lines and valleys representing dark fringe lines. Noise was added to the signal as a ±5% random variable to the peak value of the amplitude. The signal plus noise waveform is shown in figure 6.1.4 below:

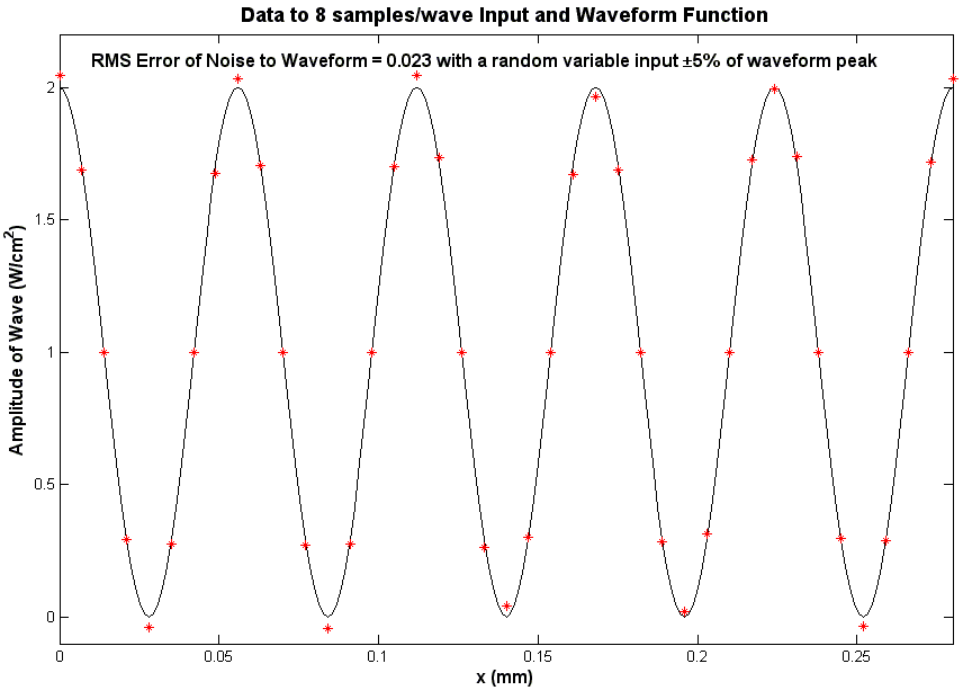

Figure 6.1.4: Sampled Data of Hologram with Noise and No Phase-Shift

The noise in the hologram function represents measurement error that could be attributed to quantization error of the Least-Significant Bit (LSB) in the 10-bit resolution frame grabber. The phase-shift (ϕ) is an input to the hologram function given as

$$I(x,\phi) = I_{bias} + I_{peak}\cos(kx+\phi) \tag{6.1.4}$$

A comparison of the phase-shift error produced by the Arc-Cosine Trigonometry Method, LSE Waveform Correlation Method, and the Fast Fourier Transform (FFT) Method is shown in figure 6.1.5 below:

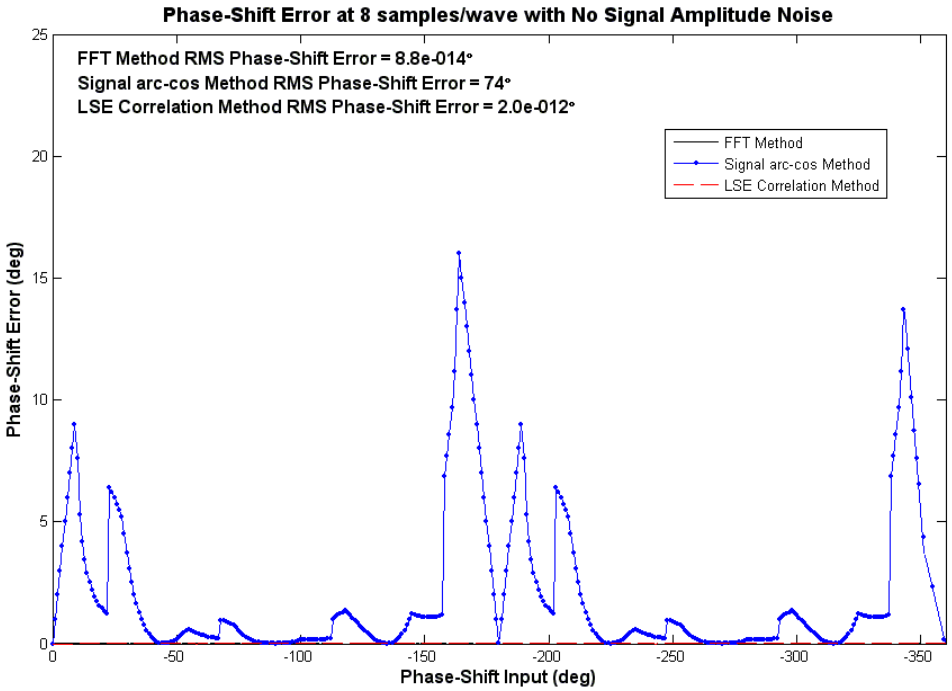

Figure 6.1.5: Phase-Shift Error using Arc-Cosine Method, LSE Correlation Method, and FFT Method with No Noise

Even with no noise the Arc-Cosine Trigonometry Method shows a peak error exceeding 15º. The rising error of the Arc-Cosine Method nearing -360º can probably be reduced by introducing a phase-unwrapping algorithm. The Arc-Cosine Method shows significant 17º phase-shift error at -180º, which is unacceptable. Both LSE Correlation and FFT Methods show an acceptable phase-shift error of less than $1\text{x}10^{-11}$ degrees.

Given:

$\Delta\phi = 2\times10^{-12}$ degrees Phase-Shift Error

λ=0.457μm/cycle Laser Wavelength

$\Delta L = 625\,\mu m$ Computational Grid-Cell Size within the Fluid-Cell

$\frac{dn}{dT} = -3.65\times10^{-4}$ 1/ºC Fluid Refractive Index relative to Temperature Slope

Then

$\Delta OPL = \lambda\cdot\Delta\phi/360 = 0.457\cdot2\times10^{-12}/360 = 2.54\times10^{-15}\,\mu m$ Change in *OPL*

Optical Path Length: $\Delta OPL = \sum_{i=1}^{m} n_i \cdot \Delta L$ (6.1.5)

$\Delta n = \frac{\Delta OPL}{\Delta L} = \frac{2.54 \times 10^{-15}}{625} = 4.06 \times 10^{-18}$ Change in Index-of-Refraction per cell (6.1.6)

$\Delta T = \frac{\Delta n}{\left|\frac{dn}{dT}\right|} = \frac{4.06 \times 10^{-11}}{\left|-3.65 \times 10^{-4}\right|} = 1.11 \times 10^{-14}$ ºC Temperature Resolution per cell (6.1.7)

$\Delta T = 1.11 \times 10^{-14} \times 8 cells = 8.90 \times 10^{-14}$ ºC Resolution through the Fluid-Cell

This small temperature error is due to the phase-shift error from a constant fringe contrast across the hologram and not a hologram affected by optical aberrations and measurement error.

The required temperature resolution due to a measured fringe-shift or phase-shift is 0.01°C, which represents the measurement-to-measurement scan error at a constant temperature within the fluid-cell. Independent measurements of the temperature profile using a thermocouple has a resolution of 0.05ºC error that is primarily due to thermocouple sensor noise, cold junction compensation noise, and amplifier noise. Both the LSE Correlation Method and FFT Method of determining the phase-shift from a sampled hologram at 8 samples/fringe introduces negligible error given a hologram with constant bias amplitude, peak amplitude, and spatial frequency.

The number of samples per fringe or pixels per wave of a fringe in the hologram defines the spatial sampling. In a hologram the period of the interference wave is the same as the fringe-spacing. Since the interference wave of the beams also produces a wave or cycle of fringes in the hologram then the definition of units is provided below for clarification.

1 sample for FFT = 1 pixel on the camera
1 fringe = 1 wave of a fringe = 1 cycle on the hologram waveform

Adding random noise to the signal of the waveform affects the LSE Correlation Method and the FFT Method to determine the phase-shift error which is shown in figure 6.1.6 below:

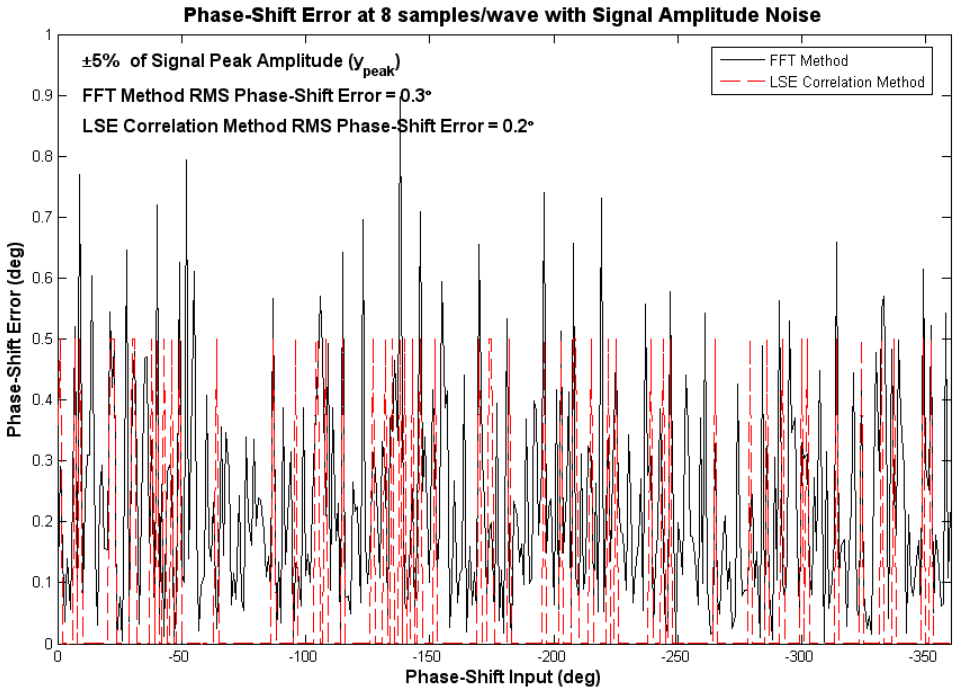

Figure 6.1.6: FFT & LSE Correlation Method of Phase-Shift Determination with Hologram Noise

The hologram has ±5% random variable noise of the peak amplitude or intensity peak added to the waveform which increases the phase-shift error determination from the no noise case. The LSE Correlation Method terminates the halve-the-interval convergence loop when the phase-shift error is less than 0.5°. This means that convergence is possible even with a lower minimum threshold level or setting. The RMS phase-shift error is 0.3º for the FFT Method.

The temperature resolution of the holography microscope is 0.02ºC. Independent measurements using a thermocouple provides a temperature resolution of 0.05ºC. The FFT Method to determine the phase-shift was used for the experiments because of greater accuracy than the LSE Correlation Method when applied to holograms with varying fringe contrast.

6.2 Fringe Contrast Sensitivity to Wavefront Error

The wavefront error and coherence length is a property of the beam quality at the laser source. The blue 457nm wavelength laser has a small beam diameter of 0.1 mm and the emission source is considered to be point source radiator. The fringe contrast is primarily sensitive to wavefront error, which is represented by the coherence length of

the laser. Fringes are produced by the wave interference of the overlapped object and reference beams and the fringe contrast is the intensity peak to intensity valley difference of a fringe in a hologram. In general, a wavefront degrades by an increasing wavefront error, which is measured by a reduction in fringe contrast as the peak-to-valley intensity difference in the hologram diminishes to the level of the background noise over a long path length.

The Melles-Griot Diode Pumped Solid-State (DPSS) 457 nm blue laser model 85-BLS-301 has a coherence length of 5 meters. This means that overall path length of 5 meters the Fringe Contrast (FC) reduces to 50%. The FC is the reduction of peak to background intensity of a fringe and is also a measure of beam's degree of coherence. As the path length increases over 5 m the beam coherence noticeably decreases as the wavefront error increases. The CSLH microscope has a long path length as the object and reference beams are wrapped 4 times over the length of the 2.4 m long optics table. The CSLH microscope optical lenses wrap the beams 1.5 times and the projector optics wraps the beams an additional 2.5 times with a path length distance of 9.6 m from laser to camera. Beam coherence is acceptable at the 9.6 m path length as the laser source was wavefront split following the beam expander and parallel beams are propagated over 9.6 m to form a hologram at the camera. The long path length of the CSLH microscope that exceeds the coherence length of the DPSS laser is not an issue since the fringe contrast remains relatively high and satisfactory for experiments.

Introducing normal focusing optical components will add optical aberrations and wavefront error as the beam coherence is degraded. The aberrations due to optical lenses can be corrected by using a Schmidt wavefront corrector plate, for example, that is found in astronomical telescopes to primarily correct for spherical aberrations. The Schmidt refractor plate is placed at the aperture of the telescope and varies in thickness to slightly more than the wavelength of light. The geometric aberrations of the lenses are conjugated by a wavefront corrector plate to cancel out the optical degradation by producing an equal and opposite phase-shift. Off-axis viewing by the CSLH microscope introduces coma aberrations that cannot be corrected using a Schmidt wavefront corrector plate since off-axis viewing has a variable field angle. Aberrations created by off-axis scanning cannot be compensated using static wavefront correctors or wave plates since the aberrations change with the tilt of the beam from the beam steering mirrors. Off-axis coma is produced by the lenses having an incident beam angle from the Fresnel biprism. The entrance Fresnel biprism, focusing lenses, re-collimating lenses,

and exit Fresnel biprism of the telecentric lens corrects the coma at the exit of the telecentric lens, but not at the focal point of the beams within the telecentric lens.

An entrance Fresnel biprism tilts the two beams and the lenses focus the two side-by-side parallel propagating beams at the center of the symmetrical lens configuration. The entrance biprism introduces a 12° incident beam to the first bi-convex lens and the coma can be seen at the focal point of the beams. The biprism at the end of the telecentric and confocal lens then re-directs the beams along the optical axis following the second bi-convex lens. Coma occurs as a geometric aberration from the side-by-side beams that propagate off the optical axis centerline. The coma at the focal point of the side-by-side propagating beams cannot be completely corrected even when designing with custom aspheric lenses and invoking Zemax optimization tools. The wavefront error at the output of the telecentric or confocal lens prevents the perfect re-collimation of the output beam. Perfect re-collimation is also restricted due to the short back focal length of the telecentric lens that produces an f/2 beam in the specimen region. The FC can be somewhat enhanced by compensating for the transfer function of the camera and employing digital filters. FC signal processing enhancement has not been attempted in this research.

Eliminating the telecentric lens of the STLH microscope leaves the beam expander, Fresnel biprism wavefront splitter, and optical wedge to overlap the object beam onto the reference beam. This simple interferometer configuration is shown in figure 6.2.1 below:

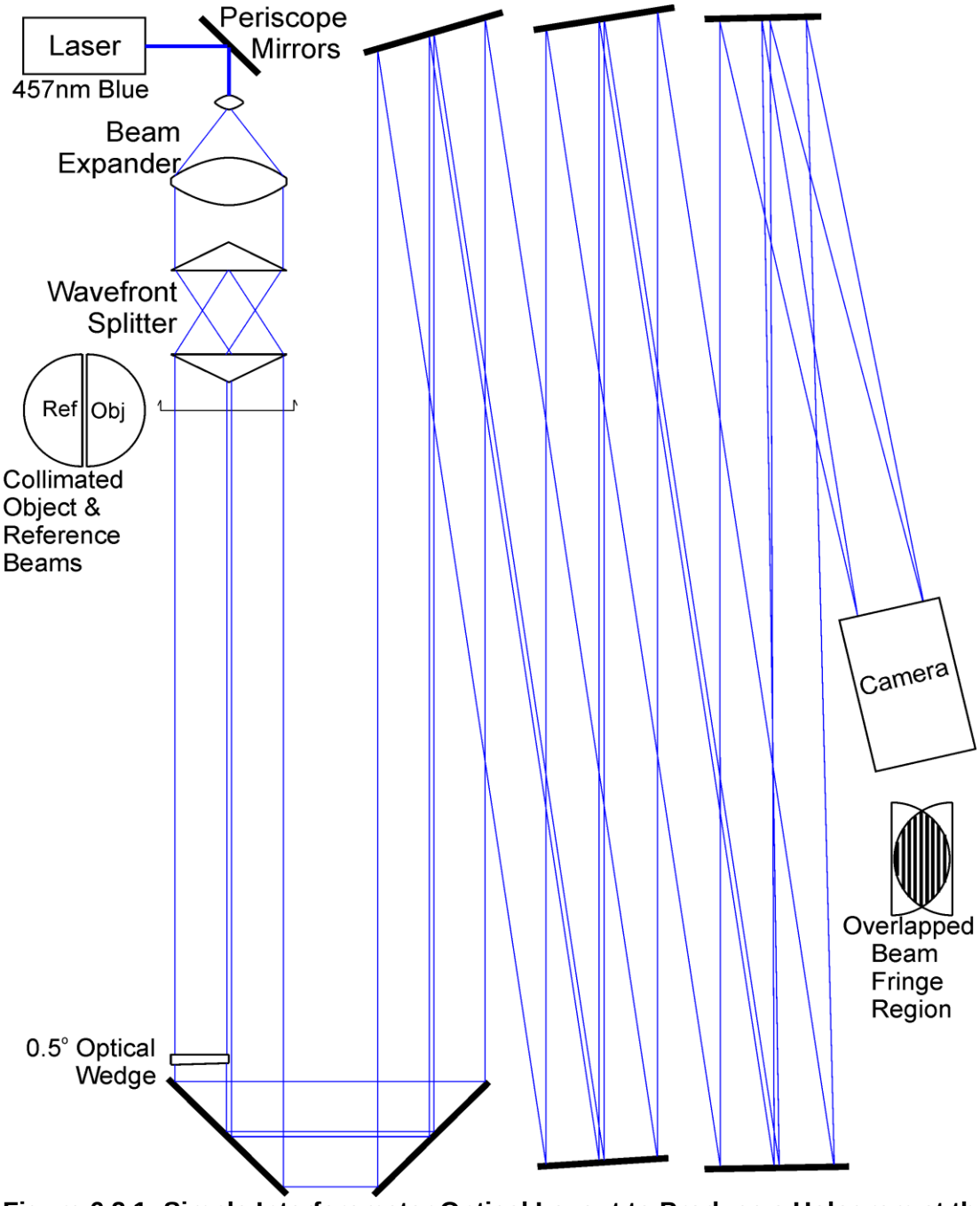

Figure 6.2.1: Simple Interferometer Optical Layout to Produce a Hologram at the Camera

The purpose of the simple interferometer is to examine fringe contrast at a long path length, which represents the path length of the CSLH microscope. The interferometer features minimal optical aberrations that would otherwise introduce wavefront error. The focusing and re-collimation optics of the microscope have been eliminated. This interferometer can provide a beam path length out to 9 m that is based on the distance

from the optical wedge to the camera. The longest beam path length occurs when using either no optical wedge or the 0.5° optical wedge. Beam convergence when removing the optical wedge occurs from the angular tolerance error of the Fresnel biprism pair used in the wavefront splitter. Folding mirrors are moved to vary the beam path length to the camera.

The beam expander produces a 35 mm diameter beam that enters the wavefront splitter. The wavefront splitter is made up of two back-to-back Fresnel biprisms. The beam is split into an object beam and a reference beam. Since the microscope lenses have been removed then designating the object and reference beams is not important because the object beam does not pass through a specimen. An optical wedge is used to converge the beams for interference in the overlap region at the camera.

A wavefront error simulation program was written in Matlab to examine the ability to detect a small change in refractive index of a specimen in the presence of wavefront error.

Wavefront error variable: $\sigma = \lambda / 50\, waves$ and $\sigma = \lambda / 20\, waves$ RMS inputs to the simulation which represents a standard deviation of 1σ and $\bar{x} = 0$ or zero-mean.

The wavefront error path is shown in figure 6.2.2 below:

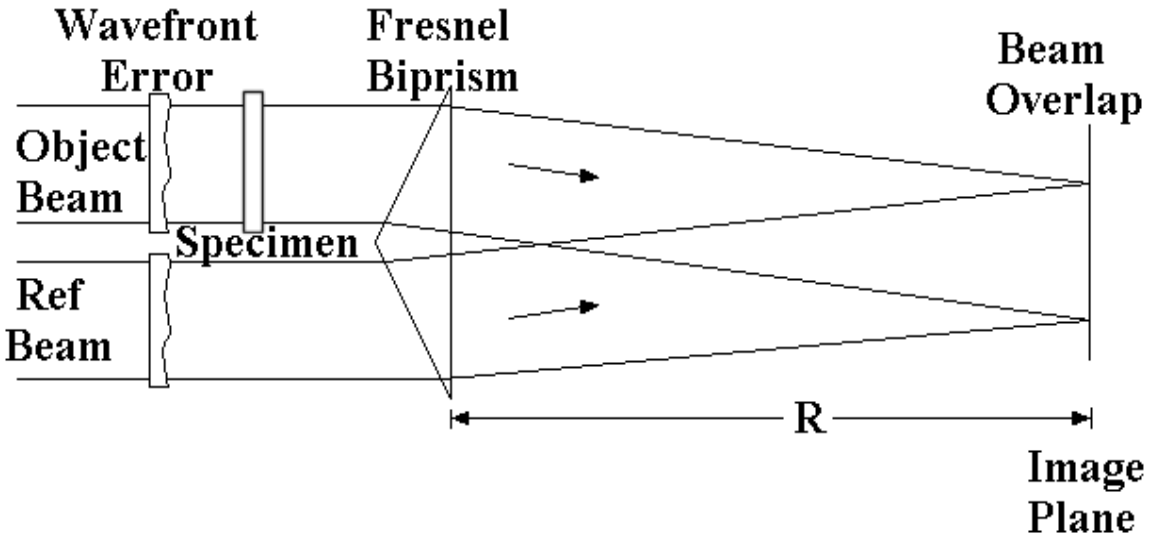

Figure 6.2.2: Wavefront Propagation from Laser to Camera Image Plane

In a Matlab ray tracing simulation of the configuration above the Range (*R*) is calculated based on the angle of the Fresnel biprism and complete beam overlap at the

image plane. The completely overlapped beams with a central computational region box are shown in figure 6.2.3 below:

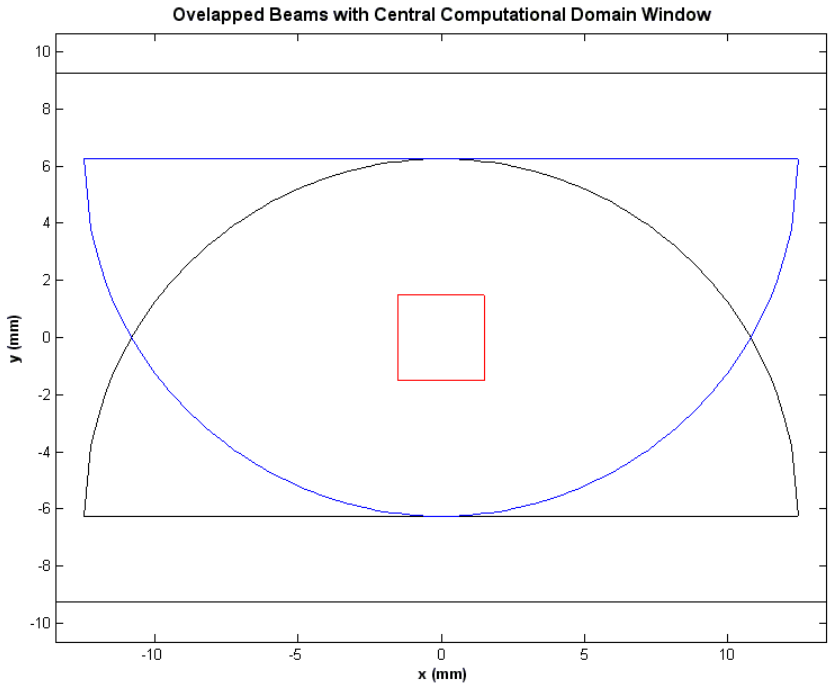

Figure 6.2.3: Completely Overlapped Beams with Computational Region Box

The region of beam overlap is where the interference fringes will appear. The line scan camera is oriented vertically at the center where x=0. The marginal rays of the object beam and reference beam are located at (0, ±6 mm) at the point where 256 samples of the hologram fringes are measured. The marginal rays are important to the "wily" reconstruction algorithm because they prevent reconstruction matrix singularities. The marginal rays are used to determine the three-dimensional index-of-refraction and temperature profile within the fluid-cell. The central box is 3.0x2.88 mm that is represented by a 450x432 array. The fringes are sampled along 450 rows of the 3.0 mm vertical dimension, which comprises around 50 waves. A simulated hologram that is sampled at 8 pixels/fringe over 5 fringes is shown in figure 6.2.4 below:

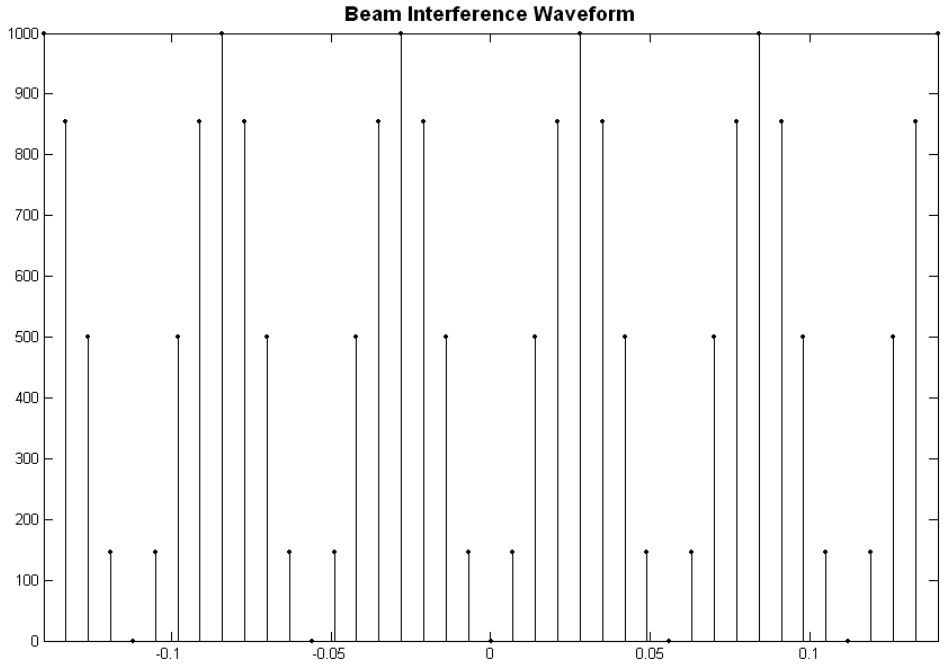

Figure 6.2.4: Hologram Waveform Sampling at 8samples/fringe

The wave combination of the object and reference beam produces a Fringe Contrast (*FC*) that is dependent on the relative intensities of the two beams and the sampling resolution. The fringe contrast is given by the following equation:

Fringe Contrast (*FC*) Equation:

$$FC = \frac{|\vec{a}|^2 - |\vec{a}|^2_{\min}}{|\vec{a}|^2_{\max} - |\vec{a}|^2_{\min}} = \frac{\left(\frac{a_{obj}}{a_{ref}}\right)}{1+\left(\frac{a_{obj}}{a_{ref}}\right)^2}\left(1+\cos(\phi_{obj} - \phi_{ref})\right) \tag{6.2.1}$$

Derived from the following:

Common Coordinate Frame for Wave Interference (x, y)

Beam Convergence Angle: $\theta_{obj} + \theta_{ref}$

Object Beam Rotated Coordinate Frame by θ_{obj}

$$\vec{x}_{obj} - \vec{x}_0 = \begin{bmatrix} x_{obj} - x_0 \\ y_{obj} - y_0 \end{bmatrix} = \begin{bmatrix} \cos\theta_{obj} & -\sin\theta_{obj} \\ \sin\theta_{obj} & \cos\theta_{obj} \end{bmatrix} \cdot \begin{bmatrix} x - x_0 \\ y - y_0 \end{bmatrix} \tag{6.2.2}$$

Reference Beam Rotated Coordinate Frame by θ_{ref}

$$\vec{x}_{ref} - \vec{x}_0 = \begin{bmatrix} x_{ref} - x_0 \\ y_{ref} - y_0 \end{bmatrix} = \begin{bmatrix} \cos\theta_{ref} & \sin\theta_{ref} \\ -\sin\theta_{ref} & \cos\theta_{ref} \end{bmatrix} \cdot \begin{bmatrix} x - x_0 \\ y - y_0 \end{bmatrix} \tag{6.2.3}$$

Temporal Frequency: ω

Spatial Frequency or Spatial Wave Number: $\omega_x = k = \frac{2\pi}{\lambda}$ (6.2.4)

$$\vec{k}_{obj} = \begin{bmatrix} k_{obj}\cos\theta_{obj} \\ k_{obj}\sin\theta_{obj} \end{bmatrix} \tag{6.2.5}$$

$$\vec{k}_{ref} = \begin{bmatrix} k_{ref}\cos\theta_{ref} \\ k_{ref}\sin\theta_{obj} \end{bmatrix} \tag{6.2.6}$$

Object Beam Amplitude: $\vec{a}_{obj} = a_{obj} \cdot \exp(i(\omega \cdot t + \phi_{obj})) \cdot \exp(i\vec{k}_{obj} \cdot (\vec{x}_{obj} - \vec{x}_0))$ (6.2.7)

Reference Beam Amplitude: $\vec{a}_{ref} = a_{ref} \cdot \exp(i(\omega \cdot t + \phi_{ref})) \cdot \exp(i\vec{k}_{ref} \cdot (\vec{x}_{ref} - \vec{x}_0))$ (6.2.8)

Given: $k = k_{obj} = k_{ref}$

$\theta = \theta_{obj} = \theta_{ref}$

Beam Convergence Angle: $\theta_{obj} + \theta_{ref} = 2\theta$ (6.2.9)

Interference of Wave Amplitudes:

$$\vec{a} = \vec{a}_{obj} + \vec{a}_{ref} \tag{6.2.10}$$

$$\begin{aligned} \vec{a} = {} & a_{obj}\exp(i(\omega\cdot t + \phi_{obj}))\cdot\exp(ik\cos\theta\cdot((x-x_0)\cos\theta - (y-y_0)\sin\theta) \\ & + ik\sin\theta\cdot((x-x_0)\sin\theta + (y-y_0)\cos\theta)) \\ & + a_{ref}\exp(i(\omega\cdot t + \phi_{ref}))\cdot\exp(ik\cos\theta\cdot(+(x-x_0)\cos\theta + (y-y_0)\sin\theta) \\ & + ik\sin\theta\cdot(-(x-x_0)\sin\theta + (y-y_0)\cos\theta)) \end{aligned} \tag{6.2.11}$$

$$\vec{a} = \vec{a}_{obj} + \vec{a}_{ref} = (a_{obj}\exp(i(\omega\cdot t + \phi_{obj})) + a_{ref}\exp(i(\omega\cdot t + \phi_{ref})))\cdot\exp(ik(x - x_0)) \tag{6.2.12}$$

Magnitude: $|\vec{a}|$

Intensity: $|\vec{a}|^2 = \vec{a}\cdot\vec{a}^* = |\vec{a}_{obj}|^2 + |\vec{a}_{ref}|^2 + \vec{a}_{obj}\cdot\vec{a}_{ref}^* + \vec{a}_{obj}^*\cdot\vec{a}_{ref}$ (6.2.13)

$$\begin{aligned} |\vec{a}|^2 = {} & (a_{obj}\exp(+i(\omega\cdot t + \phi_{obj}))\cdot\exp(+ik(x-x_0)) + a_{ref}\exp(+i(\omega\cdot t + \phi_{ref})))\cdot\exp(+ik(x-x_0)) \\ & \cdot(a_{obj}\exp(-i(\omega\cdot t + \phi_{obj}))\cdot\exp(-ik(x-x_0)) + a_{ref}\exp(-i(\omega\cdot t + \phi_{ref})))\cdot\exp(-ik(x-x_0)) \end{aligned}$$

$$|\vec{a}|^2 = a_{ref}^2\left(1 + \left(\frac{a_{obj}}{a_{ref}}\right)^2 + \left(\frac{a_{obj}}{a_{ref}}\right)\cdot(\exp(i(\phi_{obj} - \phi_{ref}) + \exp(-i(\phi_{obj} - \phi_{ref})))\right) \tag{6.2.15}$$

$$|\vec{a}|^2 = a_{ref}^2\left(1+\left(\frac{a_{obj}}{a_{ref}}\right)^2+2\left(\frac{a_{obj}}{a_{ref}}\right)\cdot\cos(\phi_{obj}-\phi_{ref})\right) \tag{6.2.16}$$

$$|\vec{a}|_{\min}^2 = a_{ref}^2\left(1-\left(\frac{a_{obj}}{a_{ref}}\right)\right)^2 \tag{6.2.17}$$

$$|\vec{a}|_{\max}^2 = a_{ref}^2\left(1+\left(\frac{a_{obj}}{a_{ref}}\right)\right)^2 \tag{6.2.18}$$

Maximum Fringe Contrast: $FC_{\max}$

$$FC_{\max} = \frac{|\vec{a}|_{\max}^2-|\vec{a}|_{\min}^2}{|\vec{a}|_{\max}^2+|\vec{a}|_{\min}^2} = \frac{2\cdot\left(\frac{a_{obj}}{a_{ref}}\right)}{1+\left(\frac{a_{obj}}{a_{ref}}\right)^2} \tag{6.2.19}$$

If $a_{obj} = a_{ref}$ Then

$$FC = \frac{1}{2}(1+\cos(\phi_{obj}-\phi_{ref})) = \frac{1}{2}(1+\cos(\Delta\phi)) \tag{6.2.20}$$

$$FC_{\max} = 1$$

Fringe Spacing: $fs = \dfrac{\lambda}{\sin\theta}$ (6.2.21)

Intensity: $I(x) = I_{pk}\cos(k\cdot x+\Delta\phi+\phi_0)$ (6.2.22)

Wave Number: $k = 2\pi\omega_x$ (6.2.23)

Spatial Frequency: $\omega_x\,(rad/mm)$

Position: $x\,(mm)$

Relative Object-to-Reference Beam Wavefront Phase: $\Delta\phi\ (rad)$

Initial Offset Phase: $\phi_0\,(rad)$

The initial offset phase can affect the *FC* due to the sampling resolution of the waveform. Given that the object and reference beams have identical intensities the phase-shift ϕ_0 will modulate the *FC*. The sensitivity of *FC* to relative phase of the object-to-reference beams is shown in figure 6.2.5 below:

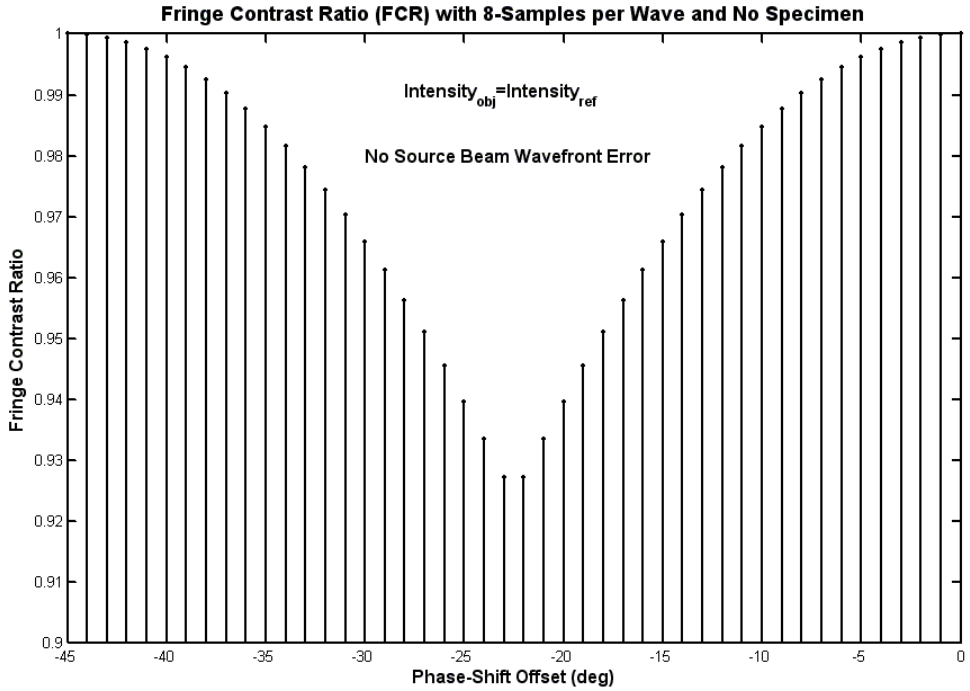

Figure 6.2.5: Fringe Contrast Sensitivity to Phase-Shift given 8 samples/fringe

With no wavefront error the reduction in *FC* is 7% which is negligible relative to determining the phase-shift from sampled holograms. The *FC* is a function of the relative intensity of the object beam to the reference beam. This relationship is shown in figure 6.2.6 below:

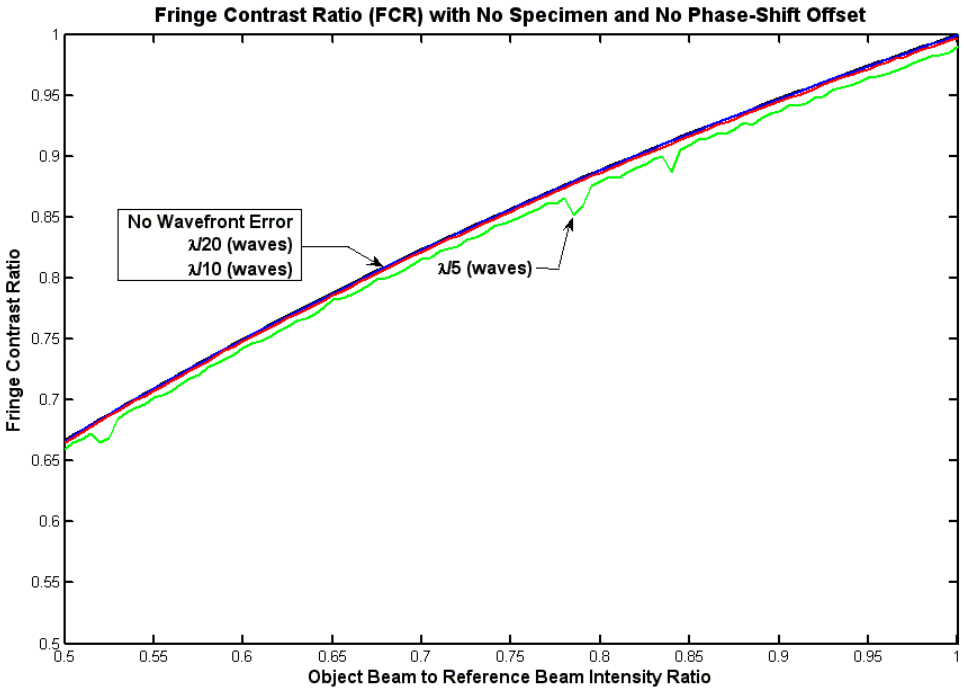

Figure 6.2.6: Fringe Contrast to Relative Intensity of Object to Reference Beam

This figure shows very little sensitivity to wavefront error as fringe contrast is primarily a function of object beam to reference beam intensity ratio. The intensity of the object and reference beams are almost identical since the laser source is wavefront split into two beams and the two beams propagate through identical optics except for the optical wedge prism. The simple interferometer wavefront error from the combined overlapped beams can affect the detection of a phase-shift.

A Matlab simulation uses a 1 mm thick specimen with a constant refractive index difference of 0.1×10^{-3} relative to air and equivalent object beam to reference beam intensity. This specimen introduces an optical path length difference that shifts the phase by -7.9° retardation angle given no offset phase-shift. Hologram sampling with the specimen and no wavefront error is shown in figure 6.2.7 below:

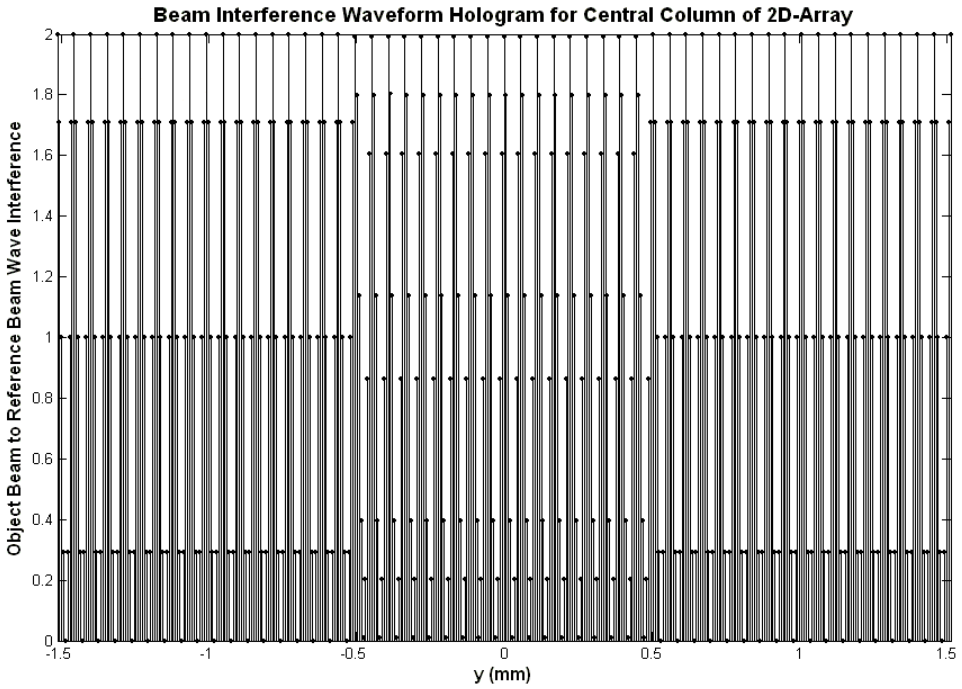

Figure 6.2.7: Sampled Data Hologram at 8 samples/fringe and No Wavefront Error

A distinctive sampling transition can be seen at the boundaries of the specimen. Given a fluid refractive index gradient of $\frac{dn}{dT} = -3.65 \times 10^{-4}$ 1/ ºC from 15-35 ºC then the temperature change would be

ΔT = 0.1x10^{-3}/-3.65x10^{-4} = -0.27 ºC

This is not the absolute resolution of the microscope to detect a change in temperature, but instead a visual example of phase-shift change with respect to sparse hologram sampling. Wavefront error is then applied to both the object and reference beams. The wavefront error is represented by zero mean and 1-σ Gaussian probability density function to a random variable. In addition, the accuracy of the derived algorithms from first principles mathematics produces a guaranteed zero mean. This eliminates the possibility of relative mean value affecting the phase-shift. The 1-σ variable is represented by λ/*n* RMS waves where $n = 50 \ \& \ 20$. The same specimen hologram with λ/50 waves RMS wavefront error for both the object and reference beam is shown in figure 6.2.8 below:

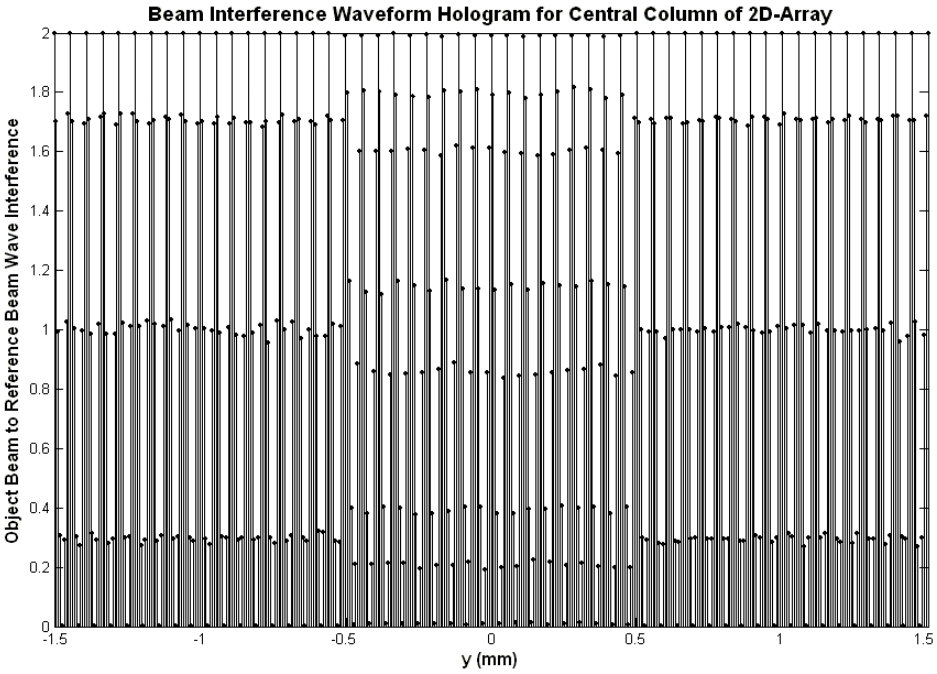

Figure 6.2.8: Sampled Data Hologram at 8 samples/fringe and λ/50 waves RMS

The figure shows the effect of minimal wavefront error on specimen detection within the y = ±0.5 mm region. Increasing the wavefront error to λ/20 waves RMS produces the following sampled data hologram in figure 6.2.9 below:

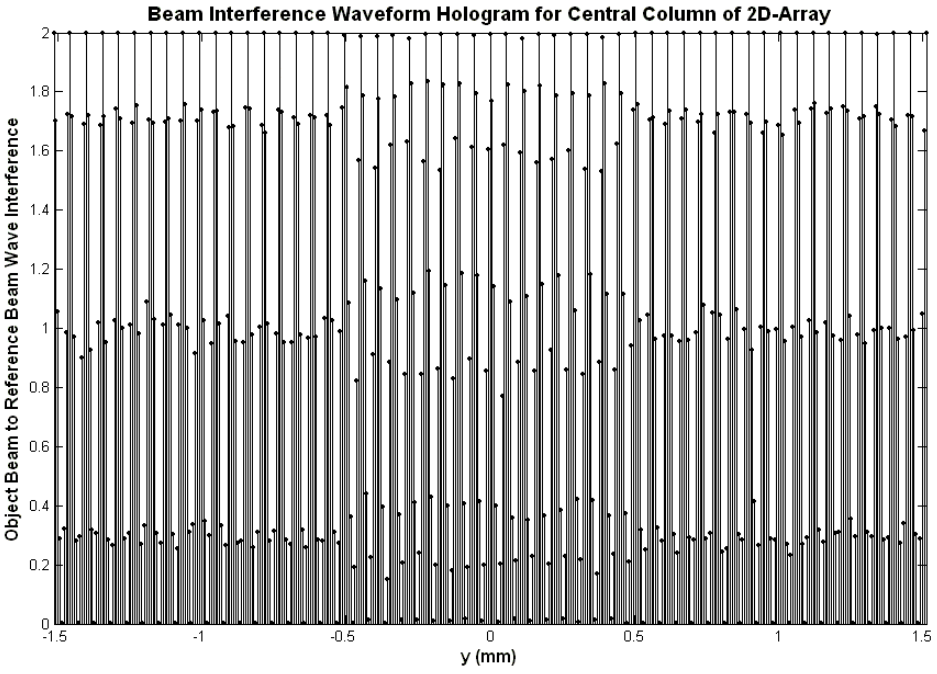

Figure 6.2.9: Sampled Data Hologram at 8 samples/fringe and λ/20 waves RMS

The wavefront error has increased and the phase-shift discontinuity at the specimen is more difficult to discern. As the wavefront error increases then the sensitivity to determine the phase-shift decreases. At λ/10 waves RMS the discernable phase-shift edges diminishes within the wavefront error. Determining the edges of the specimen will have significant error. The sensitivity to phase-shift can be increased by increasing the number of samples per fringe in the hologram or by increasing the refractive index of the specimen. It is increasingly difficult to detect the specimen with a $1x10^{-4}$ change in refractive index at a wavefront error >λ/20 waves. The objective of the CSLH microscope is to resolve a temperature difference of <0.02ºC. This small temperature change represents a change in index-of-refraction of $7.30x10^{-6}$, which is significantly smaller than the $1x10^{-4}$ used in this Matlab simulation. The fringe sampling would thus need to be increased in order to detect a minute refractive index change in the specimen at a wavefront error <λ/20 waves. This means that the wavefront error of the laser should be less than λ/50 waves. The Melles-Griot laser provides a coherence length of 5 meters with a beam divergence angle of <0.7 mrad (full-angle using a beam collimator). The x20 beam expander reduces the divergence angle to <17.5 μrad (half-cone angle) and this divergence angle is reduced even further by using an iris diaphragm. The iris diaphragm aperture is set to 35 mm diameter.

The fringe contrast for the microscope is high given the path lengths used in the experiments. The path length from projector lens to camera was approximately 1.5 meters. Overall, the wavefront quality of the laser provides a stable hologram with relatively high fringe contrast from the overlapped beams and there is sufficient intensity to saturate the detectors on the camera using the STLH microscope. Absorption and stray reflections of the CSLH microscope along the longer path length will not provide for saturation of the detectors. The STLH and CSLH microscopes were found to provide about 32 pixels/fringe sampling resolution. This provided a means to detect a 3° phase-shift or λ/25 waves even with a varying fringe contrast across the hologram. The varying fringe contrast is primarily due to optical aberrations and measurement error and the reference hologram reduces the phase-shift error from a varying fringe contrast.

6.3 Error Propagation from Sources to Overall System Level

The primary contributor to reconstruction error is due to the single viewing window for the laser that scans through the fluid-cell. As a result of this rotational scanning restriction the other error sources that contribute to reconstruction error are:

1) Thermocouple measurement error and position error, although this is an independent measurement that is used for comparison.
2) Measured thermocouple temperature error and conversion to index-of-refraction.
3) Positional accuracy of the thermocouple relative to the scan position of the probe beam in the fluid-cell.
4) Scan position error that produces a phase-shift measurement error in the hologram.
5) Determination of phase-shift from the recorded holograms and the error from a varying fringe contrast.
6) Boundary condition measurement error.
7) Small beam angle (f/2 f-number) for the probe beam in the fluid-cell specimen.
8) Determination of the reference Optical Path Length at constant temperature of the fluid-cell.
9) Phase-shift measurement errors in the reference holograms that are primarily due to spherical aberrations in the telecentric and confocal lenses plus coma from off-axis beam propagation.
10) Measurements of 16 boundary conditions and 16 measured holograms for 32 phase-shift measurements at each of the elevation planes in the fluid-cell.
11) Coherence of the laser that produces ±3° phase-shift error at λ/100 waves RMS.
12) Variations in fringe contrast across the holograms due to optical aberrations and near complete beam overlap at the camera.
13) Fringe line variation and motion due to acoustic and mechanical vibrations (see appendix).

Error sources for the microscope are identified at the lowest level and combine to an overall microscope resolution at the highest level as shown in figure 6.3.1 below:

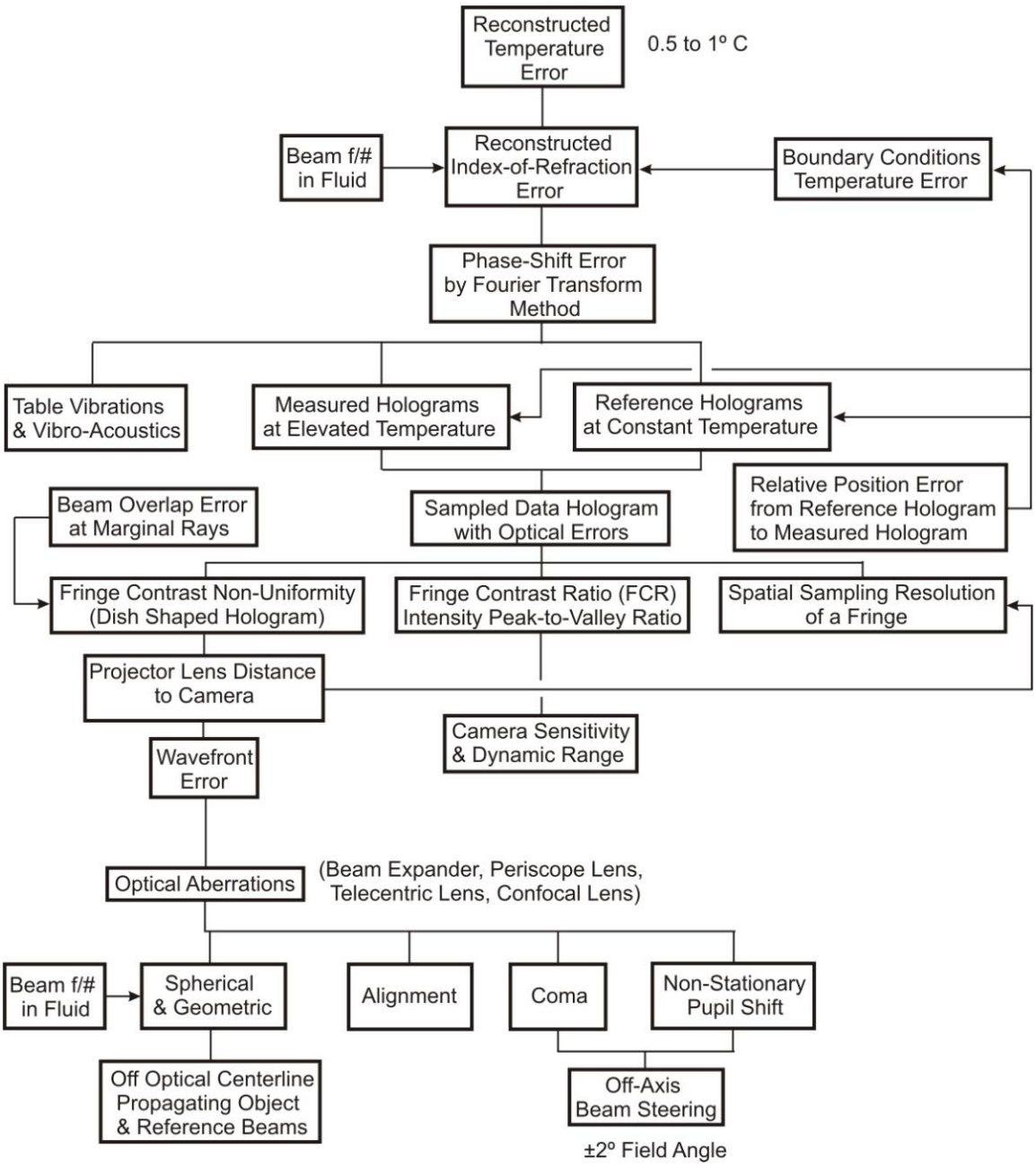

Figure 6.3.1: Source Errors to Overall Microscope Error Flow Diagram

The error flow diagram above shows the error sources along the bottom and their relationship to the microscope as they combine to an overall system error at the top of the diagram. Quantization error, which is not shown, addresses sensor interface to data acquisition, camera interface to image acquisition, and spatial sampling resolution that defines a grid-mesh for the fluid-cell. Spatial quantization is represented by the computational domain and boundary condition grid-mesh cells as each grid-cell is assumed to have constant properties. Temporal quantization is represented by the data

acquisition and image acquisition rates. Quantization resolution is represented by the low level Least-Significant Bit (LSB) detectable amplitude. Quantization occurs for the thermocouple that is used to measure the boundary condition temperatures, image acquisition for the camera, analog output voltage commands for the beam steering mirrors, and position commands for the translation stages. Quantization error also occurs during calibration for the setting of constants.

7 Reference Data and Experiments

The reference data consists of a reference hologram that is used to determine the phase-shift of the marginal rays and to compensate the optical aberrations that affect a hologram. The experiments consist of measuring the microscope phase-shift sensitivity to temperature and reconstructing the index-of-refraction from the holograms using the "wily" matrix reconstruction algorithm.

7.1 Reference Hologram

A reference hologram is the hologram of the specimen fluid-cell at constant room temperature. Both the specimen and phantom fluid-cells are at the same temperature when reference hologram data is acquired. A 16x2 phase-shift array is obtained for a reference hologram that is represented by every scan position of the focused beam in the fluid-cell. The reference hologram can be used to remove the aberrations of the optics since they introduce a constant fringe-shift in the hologram. Two scan positions within the fluid-cell are shown in figure 7.1.1 below:

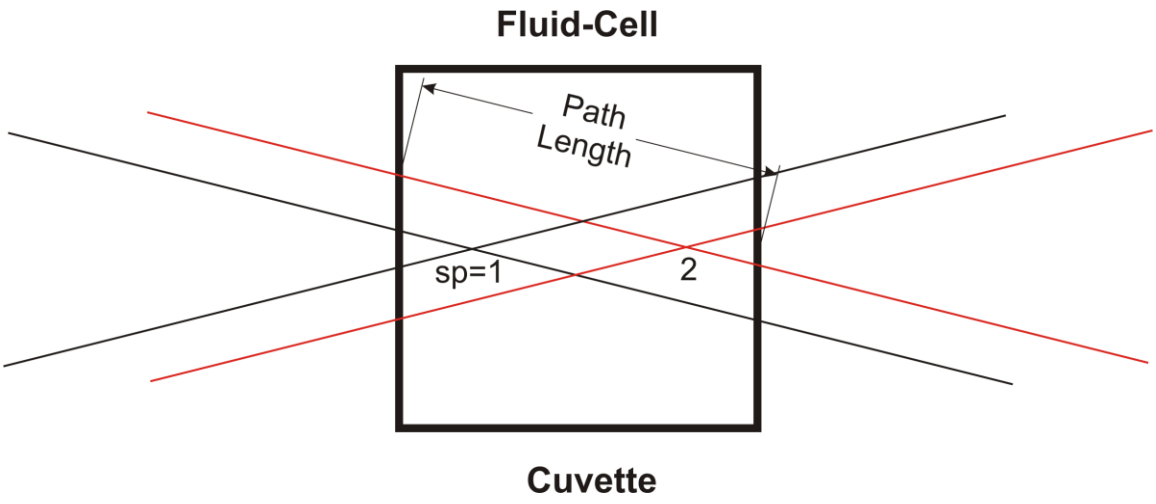

Figure 7.1.1: Two Scan Positions of the Object Beam within the Fluid-Cell

At a constant temperature the refractive index of the fluid is constant. The reference hologram is obtained at constant room temperature. The Path Length (*PL*) for any marginal ray of the beam in the fluid-cell remains constant since the incident marginal ray angles are equal though opposite in slope relative to the optical axis and the cell size is also constant. The index-of-refraction is assumed constant over the region of the cell.

The Optical Path Length (*OPL*) is the refractive index (*n*) times the Path Length (*PL*) and is given by the following equation.

$$OPL = \int n(l)dl = \sum_{i=1}^{m} n_i \cdot \Delta l = n\sum_{i=1}^{m} \Delta l = n \cdot m \cdot \Delta l = n \cdot PL \qquad (7.1.1)$$

for a constant refractive index due to constant temperature.

For any scan position the *OPL* of the reference hologram should remain constant. The removal of optical effects is accomplished by subtracting the phase-shift of the reference (*ref*) hologram from the object (*obj*) hologram. An object hologram is created when the fluid-cell is heated up to an elevated temperature. Increasing temperature causes a decreasing index-of-refraction since the ratio of a change in refractive index to a change in temperature is negative. The refractive index to temperature slope for the Cargille Labs Fused Silica Matching Liquid is $\frac{dn}{dT} = -3.65 \times 10^{-4}\ 1/°C$. The phase-shift is obtained from the *OPL* by following equation: $OPL = \lambda \cdot \Delta\phi$ (7.1.2)

The phase-shift is a function of the index-of-refraction, which can vary through a temperature gradient. The change in phase-shift from experiment condition at elevated temperature to reference condition at constant room temperature is:

$$\Delta\phi = \phi_{obj} - \phi_{ref} \qquad (7.1.3)$$

$\Delta\phi$ is the relative phase-shift that is an input for reconstruction.

ϕ_{obj} is the object beam phase-shift with the specimen at elevated temperature.

ϕ_{ref} is the reference beam phase-shift with the specimen at constant room temperature, which is represented by the reference hologram.

The phase-shift for both the object and reference holograms were referenced to the marginal ray locations on the 1x8192 pixel line scan camera. The negative slope marginal ray was located at pixel 220 and from this location 256 samples were recorded for the Fourier transform. The positive slope marginal ray was located at pixel 7715 and from this location 256 samples were recorded for the Fourier transform. The marginal ray pixel locations are at the LHS and RHS of a single hologram. The Fourier transform was used to determine the spatial line frequency of the fringes and the phase-shift. The number of samples per wave or the number of pixels per wave of a fringe specifies the spatial carrier frequency since the fringes are nearly constantly spaced. When the

number of samples per wave of a fringe is less than 8 then the error in determining a fringe-shift becomes significant.

Scanning was done in the *xz*-plane along the optical *z*-axis and horizontally across in the *x*-axis. Measurements of holograms were taken for 16 steps along the *z*-axis and 12 steps along the *x*-axis. The Fourier Transform Method was used to determine the phase-shift in the hologram for every scan position. A plot of the phase-shift for every scan position given a single negative slope marginal ray is shown in figure 7.1.2 below:

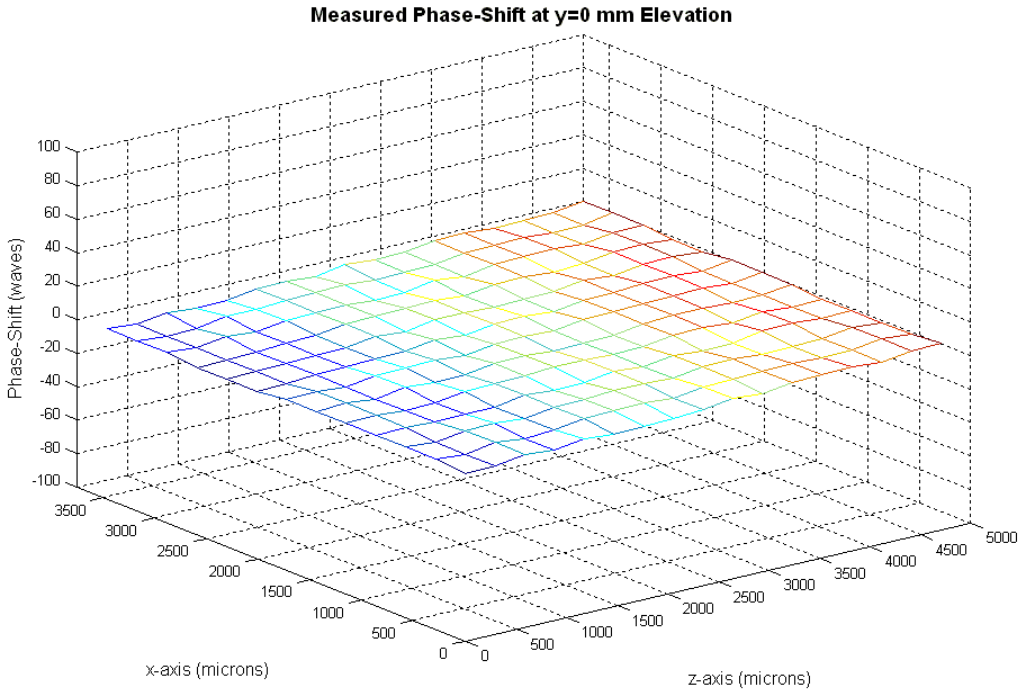

Figure 7.1.2: Phase-Shift for Every Scan Position at Constant Elevation y=0 mm

The RMS phase-shift error is 0.5 waves. There is a slight slope along the *z*-axis and the viewing angle of this plot is rotated to examine the slope as shown in figure 7.1.3 below:

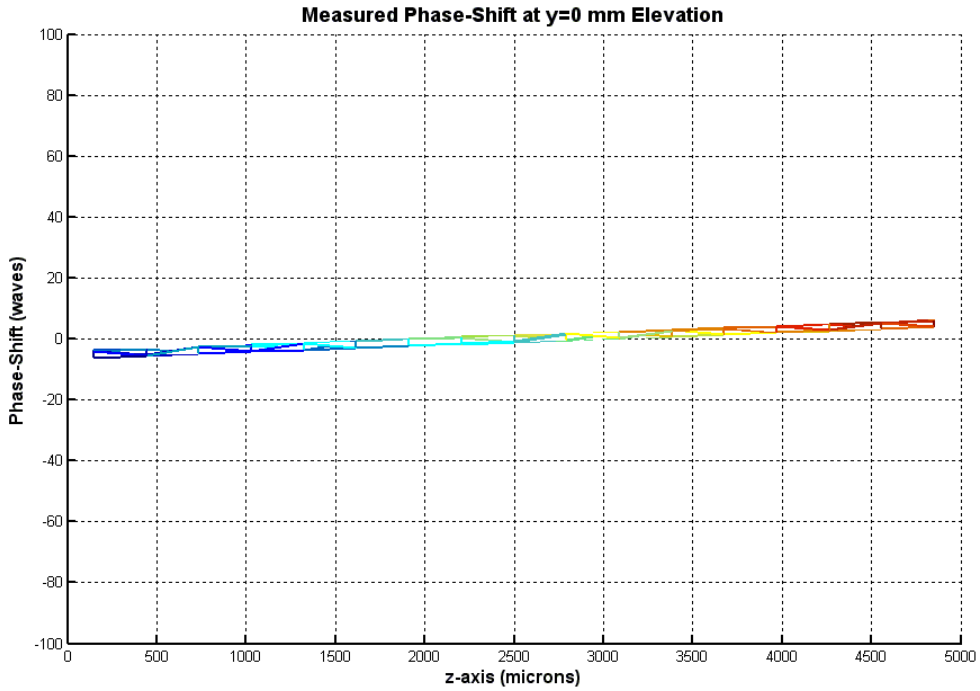

Figure 7.1.3: Rotated View of Phase-Shift for Every Scan Position

The tilt in the beam introduced a phase-shift error of approximately 4º. This slope was probably due to the misalignment of the telecentric lens relative to the optical axis. A misalignment would cause the focal point to translate along the *x*-axis as the fluid-cell is scanned along the *z*-axis. This translation of the focal point along the *x*-axis will introduce an angular shift to the output beam of the telecentric lens. The camera would detect this shift and this error would be included in the phase-shift measurements. The reference hologram can compensate for the misalignment error of the telecentric lens.

The phase-shift $\phi(sp, r)$ for a reference hologram is a function of scan position (*sp*) and slope of the marginal ray (*r*) in the fluid-cell. The reference hologram phase-shift for each scan position and marginal ray slope is shown in table 7.1.1 below:

Phase-Shift (waves)		
sp	*r*=1	*r*=2
1	-4.962	-4.468
2	-4.025	-4.242
3	-2.856	-2.963
4	-1.310	-1.584
5	-0.328	-0.390
6	1.533	1.531
7	2.563	2.787
8	3.771	4.238
9	-4.430	-5.536
10	-4.058	-4.028
11	-2.554	-2.601
12	-1.277	-1.568
13	-0.019	0.176
14	1.292	1.326
15	3.332	2.795
16	4.073	4.083

Table 7.1.1: Reference Hologram Phase-Shift at *y*=0mm Elevation

The scan position is represented by the rows and the slope is represented by the columns in the table. Marginal rays with negative slope (*r*=1) are represented by the first column and marginal rays with positive slope (*r*=2) are represented by the second column. The scanning sequence was done for 8 steps down the *z*-axis at constant *x* in the fluid-cell, then *x* was incremented in the horizontal plane as *z*-axis scanning restarted for another 8 steps at constant *x* in the fluid-cell. See section 4.1 “The ‘wily’ Reconstruction Algorithm” and also the appendix for fluid-cell coordinate frame axis definition. A total of 16 scan positions that are represented by the number of rows in the table were taken. The table above is for a constant elevation plane at *y*=0 mm in the fluid-cell. A reference hologram table is recorded for every elevation along the *y*-axis of the fluid-cell.

It is important that the phase-shift difference from scan step to scan step remains less than one wave otherwise phase-unwrapping would be required. Scanning other *xz*-planes along the *y*-axis produced similar phase-shift values to the values in the phase-shift table at the *y*=0 mm elevation. The reference hologram was used to reduce error from optical misalignment as well as to compensate for the aberrations of the lenses when determining a phase-shift from a marginal ray location in the hologram. The

reference hologram phase-shift values are used in the “wily” matrix reconstruction algorithm to provide for more accurate resolution of the reconstructed index-of-refraction.

The relative Optical Path Length (*OPL*) is given as:

$$\Delta OPL = \lambda \cdot \phi = \lambda \cdot \phi(sp, r) \tag{7.1.4}$$

Where: $\phi(sp, r)$ is the array from the table above.

The absolute *OPL* at constant room temperature is given as:

$$OPL = [wily] \times \vec{n}_{ref} \tag{7.1.5}$$

Given:

Room Air Temperature: $T_{air} = 23.8°C$

Constant Steady-State Temperature in the Fluid-Cell: $T_{ref} = 30.8°C$

The heater was running for 12 minutes in order to produce a near uniform temperature gradient from the center to the walls of the fluid-cell. In a 5 minute warm up the temperature gradient is concentrated at the heater and in an 18 minute warm up the temperature gradient is concentrated at the walls.

Constant Refractive Index: $n_{ref} = 1.4647$ at $\lambda = 0.457\,\mu m$ and T_{ref}

Refractive Index Vector: $\vec{n}_{ref} = n_{ref}$ (32x1 array)

Vector to Array Conversion: $OPL(sp, r) = OPL$

The absolute reference hologram *OPL* for each scan position and marginal ray slope is shown in table 7.1.2 below:

Reference OPL (µm)		
sp	*r*=1	*r*=2
1	4246.20	7548.80
2	5189.80	7548.80
3	6133.40	7548.80
4	7077.00	7548.80
5	7548.80	7077.00
6	7548.80	6133.40
7	7548.80	5189.80
8	7548.80	4246.20
9	7548.80	4246.20
10	7548.80	5189.80
11	7548.80	6133.40
12	7548.80	7077.00
13	7077.00	7548.80
14	6133.40	7548.80
15	5189.80	7548.80
16	4246.20	7548.80

Table 7.1.2: Reference Hologram Absolute Optical Path Length

The phase-shift along the *OPL* is given as: $\phi_{ref} = OPL_{ref} / \lambda$

For example: $\phi_{ref}(3,1) = OPL_{ref}(3,1) / \lambda = 6133.40 / 0.457 = 13{,}421.01\ waves$

7.2 Fringe-Shift Sensitivity to Temperature Experiment

The STLH microscope was used to determine the sensitivity of a fringe-shift in the hologram from a change in temperature of the heated fluid in the fluid-cell. A translation of a fringe over the distance of a single fringe-spacing is represented by a phase-shift of 2π radians or 1 wave of a fringe. The phase-shift resolution is 1/30th of a wave and the maximum is 1 wave from scan position to scan position. If the phase-shift is greater than 1 wave between measurements then the measurement is indeterminate because there could be $n \times 2\pi$ radians wrappings with unknown variable $n = 0,1,2,3,\ldots$. The phase-shift is not resolvable or discernable to less than 1/30th of a wave because the fringe contrast is not constant across the hologram and because the Fourier Transform Method to determine the phase-shift becomes inaccurate.

A calibrated micro-probe thermocouple was used to measure the temperature of the fluid at the focal point of the object beam within the fluid-cell. The focal point in the fluid-cell was located 12 mm directly above a resistive heating element, which was positioned at 3 mm from the bottom center of the fluid-cell. The thermocouple was then elevated

slightly above the focal point so that the hologram fringes could be seen at the camera rather than the tip of the thermocouple. In this configuration the thermocouple was considered to be co-located with the focal point of the laser as both temperature and hologram images were recorded simultaneously using LabVIEW. As the fluid was heated the fringes could be seen to translate or shift across the hologram. Maximum fringe-shift rate was reached in approximately 6 minutes of heating from room temperature to a steady-state temperature in the fluid-cell. The camera display on LabVIEW showed fringe translation at 100 msec frame time. Measurements were sampled every 10-15 seconds and the resulting phase-shift was approximately 45° to 135°. Steady-state conditions are established when the fringe-shift is approximately 90° between 10-15 second intervals. The measurement sample time is controlled by the clicking of a mouse button to simultaneously record a hologram image and the temperature. LabVIEW performs the data and image acquisition and also stores the data into an ASCII text file for Matlab. The LabVIEW temperature measurement and Save Image program simultaneously displays a near real-time hologram at 100 msec frame update. The near real-time hologram display shows the fringes moving in one direction for heating-up and in the opposite direction for cooling-down. The image files and temperature data are then transferred to Matlab and the Fourier Transform Method is used to determine the phase-shift in the hologram. The first hologram represents the reference hologram and the first sampled temperature establishes the reference temperature.

The highest temperature gradient will occur at the heater when it is turned on. In 30 minutes the highest temperature gradient will be at the walls of the fluid-cell and the fluid will have a consistent temperature throughout the volume. The interval from 10 to 15 minutes is the steady-state condition that produces a Gaussian shaped temperature profile with consistent temperature gradients, which is used for the experiments.

The change in fringe-shift was approximately a 100° angle shift per hologram collected at approximately 12 second intervals along with the sampled temperature data from the thermocouple. Hologram image and temperature data was collected for both the heating up and cooling down cycles in order to evaluate the potential differences in slope. A hologram from the Dalsa 1x8192 pixel line scan camera, which had poor sensitivity and required diffuse lighting to raise the background, is shown in figure 7.2.1 below:

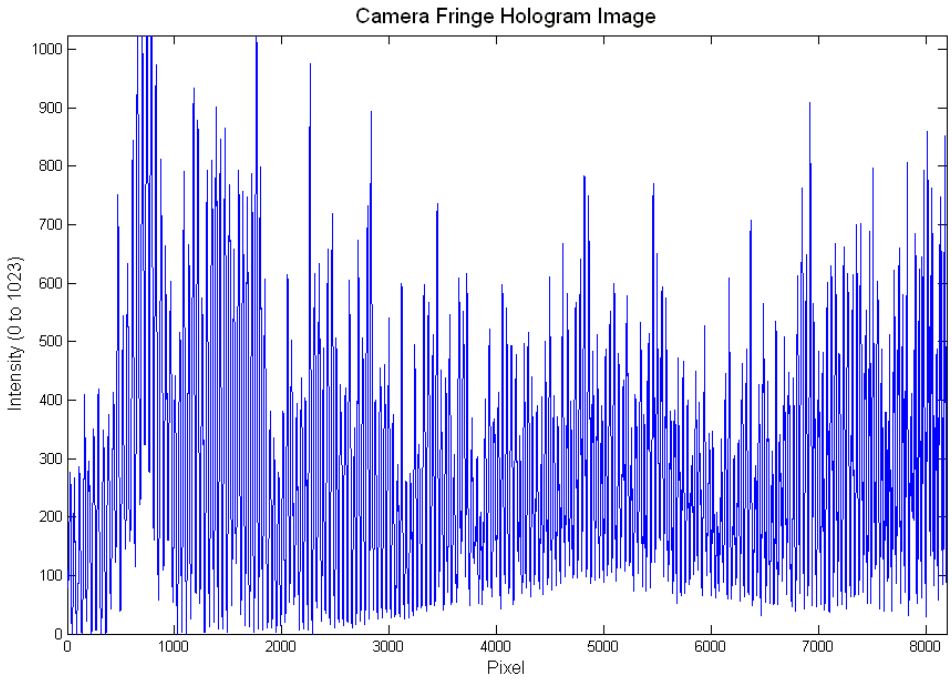

Figure 7.2.1: Hologram of Fringes from Overlapping Object to Reference Beams

The National Instruments PCI-1428 frame grabber was set to an intensity range of 0 to 1023 (10-bit data resolution). The Dalsa Piranha P2-23-08k40 1x8192 pixel Charge Coupled Device (CCD) line scan camera was connected to the frame grabber by a Base Camera-Link cable. The Dalsa line scan camera has a significantly lower radiometric sensitivity in comparison to a Point Gray Research Grasshopper 2000x3000 array CCD camera or the Red Lake Mega-Plus II ES-3200 1200x2000 array CCD camera, both of which have been used in the laboratory. The two-dimensional CCD array cameras have extremely low light level sensitivity and saturate with very little background light. The Dalsa line scan camera requires background lighting to raise the sensitivity above the floor threshold. The peak fringe intensity on the camera is regulated by the optical attenuators, which are the neutral density filters, and the polarizing wave plate.

The peak region as seen on the left-hand side of the figure above is the area where the marginal rays of the object and the reference beams overlap. The average fringe contrast shows a trough dish shape in the central region around pixel 4500, which is primarily due to the spherical aberrations of the lenses. The chief rays pass through the center of the optical axis which is where the minimum of the dish occurs. There is another peak in the right hand region of the hologram in the figure above, which is slightly out of view. The left hand side and right hand side peak regions represent the coincident marginal rays of the completely overlapped object and reference beams.

Since a change in temperature causes the fringes in the hologram to shift evenly then any specific region can be selected to determine the phase-shift to temperature sensitivity, with the central region providing the best results. The trough or dish shape of the hologram can also be due to the non-uniform aperture illumination of the laser beam or the background light illumination source. The background light illumination source was used to bias the intensity level on the hologram and prevent clipping of the low-level signal.

The reference hologram was used to compensate the dish shape in the hologram and establish a reference point since the aberrations due to the optical lenses will produce less error. The reference point or origin in the hologram is arbitrarily defined as pixel 2200. The pixel value range from 2200 to 2752 of the hologram as a close-up view is shown in figure 7.2.2 below:

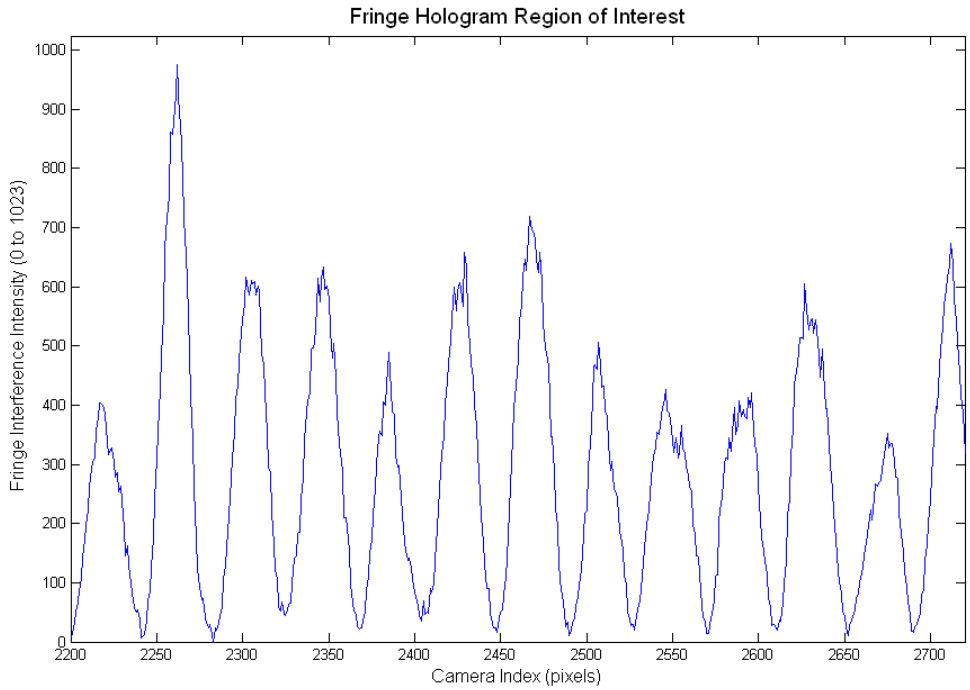

Figure 7.2.2: Hologram Detail for a Temperature Sample

The region start point or origin is at pixel 2200 and then 512 samples at $1\ sample\ /\ pixel$ are collected for the Fourier transform. The waveform that contains a single spatial carrier frequency is mainly harmonic because of the constantly spaced fringes. There are about 12 fringes for the Fourier Transform Method to determine the phase at the origin or pixel 2200. The next measurement interval is 13 seconds to update the previous hologram. This updated hologram is shown in figure 7.2.3 below:

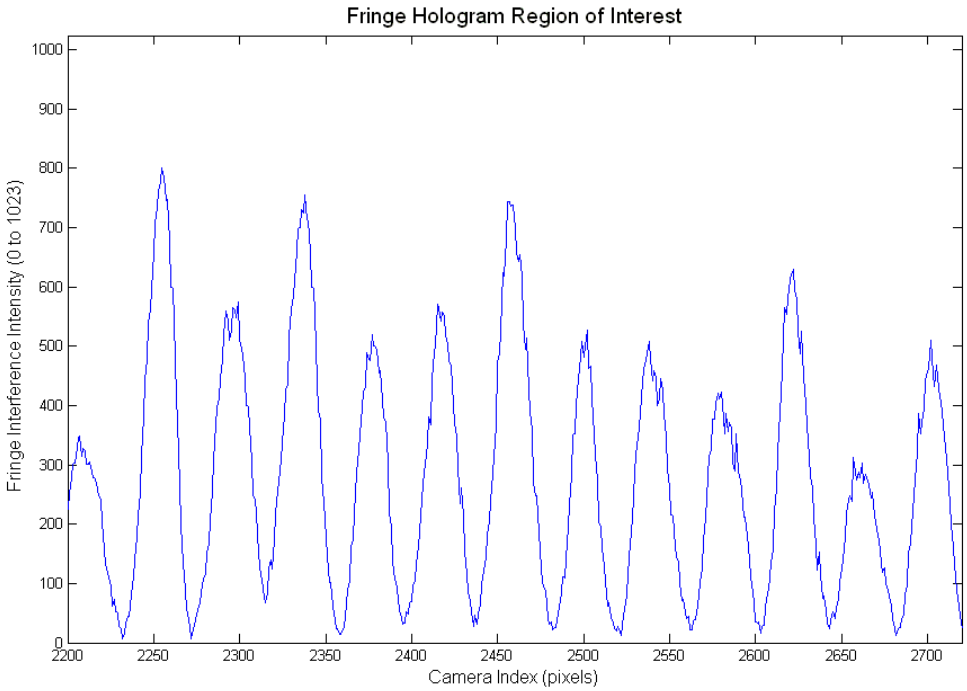

Figure 7.2.3: Hologram Detail Fringe-Shift for the Next Temperature Sample

The phase can be seen to shift from the previous hologram to the updated hologram where the fringe crosses the *x*-axis at pixel 2200. The phase-shift was determined from the Fourier Transform Method as both hologram image and temperature data were simultaneously acquired. The phase-shift sensitivity for a heating up fluid-cell is shown in figure 7.2.4 below:

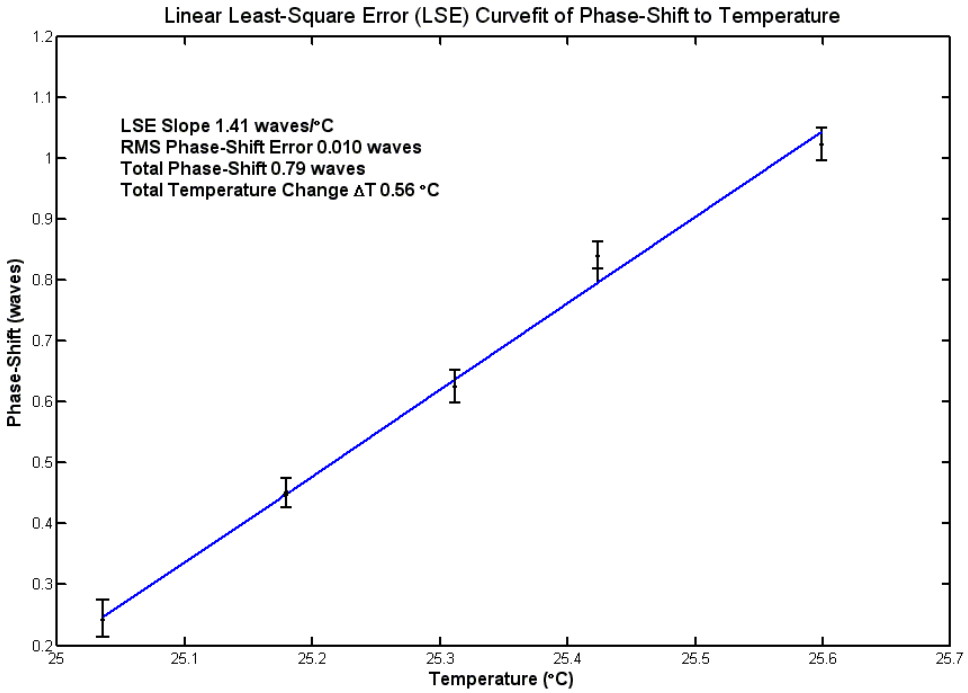

Figure 7.2.4: Phase-Shift Response to a Change in Temperature for a Heating-Up Fluid-Cell

A linear Least-Square Error (LSE) line is plotted through the data in the figure above. Annotated on the graph is the slope and Root-Mean-Square (RMS) error. The STLH microscope sensitivity was determined by the slope at $+1.41 waves/°C$ and the RMS phase-shift error was 0.010 waves. The sensitivity to a change in temperature is $RMS_{error}/slope = 0.010 waves/1.41 waves/°C = 0.0071°C$. The thermocouple resolution is +/-0.1°C with an RMS error of approximately 0.071°C. A plot of temperature to time as the fluid-cell is heated to produce a thermal gradient is shown in figure 7.2.5 below:

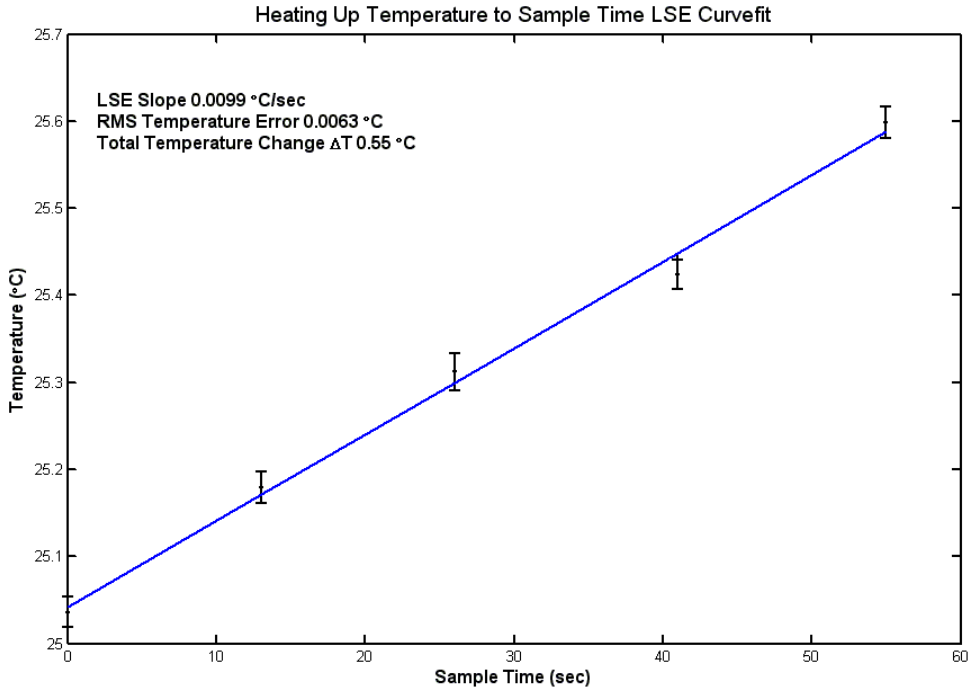

Figure 7.2.5: Temperature-to-Time for a Heating-Up Fluid-Cell

The LSE heating-up slope was 0.01°C/sec for a total temperature change of 0.55°C. The cooling down cycle phase-shift to temperature plot is shown in figure 7.2.6 below:

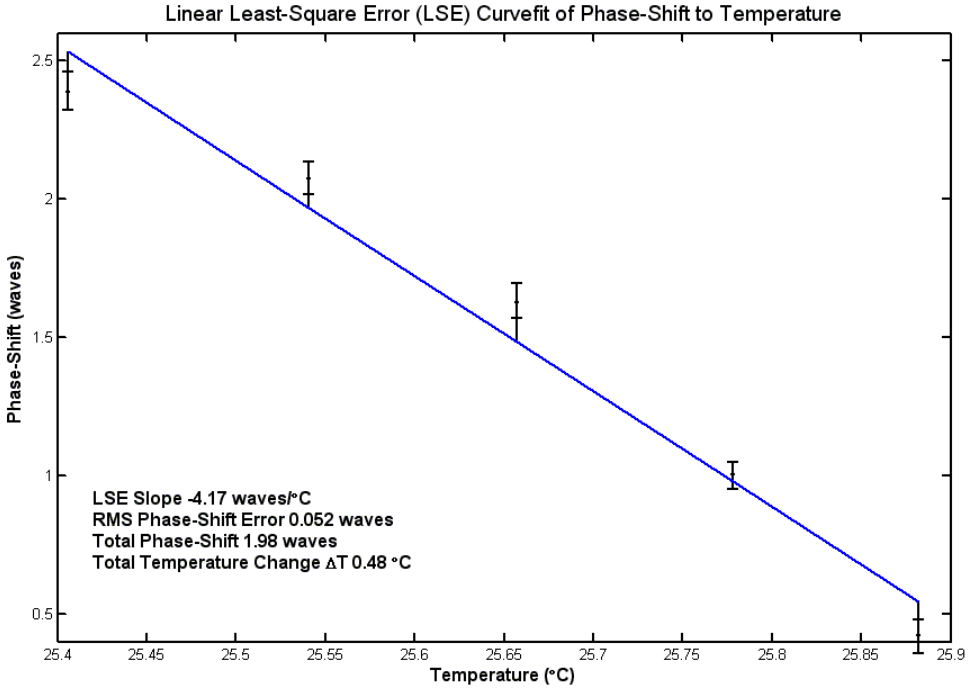

Figure 7.2.6: Phase-Shift Response to a Change in Temperature for Cooling-Down

A linear LSE line is plotted through the data in the figure above. Annotated on the graph is the slope and Root-Mean-Square (RMS) error. The STLH microscope sensitivity is determined by the slope at $-4.17\ waves/°C$ and the RMS phase-shift error is 0.052 waves. The sensitivity to a change in temperature is $RMS_{error}/slope = 0.052\ waves/4.17\ waves/°C = 0.013°C$. The thermocouple resolution is +/-0.1°C with an RMS error of 0.071°C. There is a discrepancy between the heating-up and cooling-down slopes due to the heat capacity of the fluid and heat transfer conditions for the heating and cooling down cycles.

In the heating up cycle the power to the heater was turned on for about 5 minutes to create a more uniform thermal gradient across the fluid-cell. The camera image and temperature data was then collected in approximately 13 second intervals for 5 measurements as the power remained on. The power to the heater stayed on for an additional 2 minutes as data files were manipulated. The power to the heater was then turned off and the temperature was monitored as it dropped down to the same temperature when data was collected for the heating up condition. When the cooling down temperature equaled the start temperature for the heating up cycle then the temperature and hologram image data was collected for the cooling down cycle. As the temperature was steadily dropping the measurements were taken at 18 second intervals on average. A plot of temperature to time as the fluid-cell is cooling down from the disconnected heater is shown in figure 7.2.7 below:

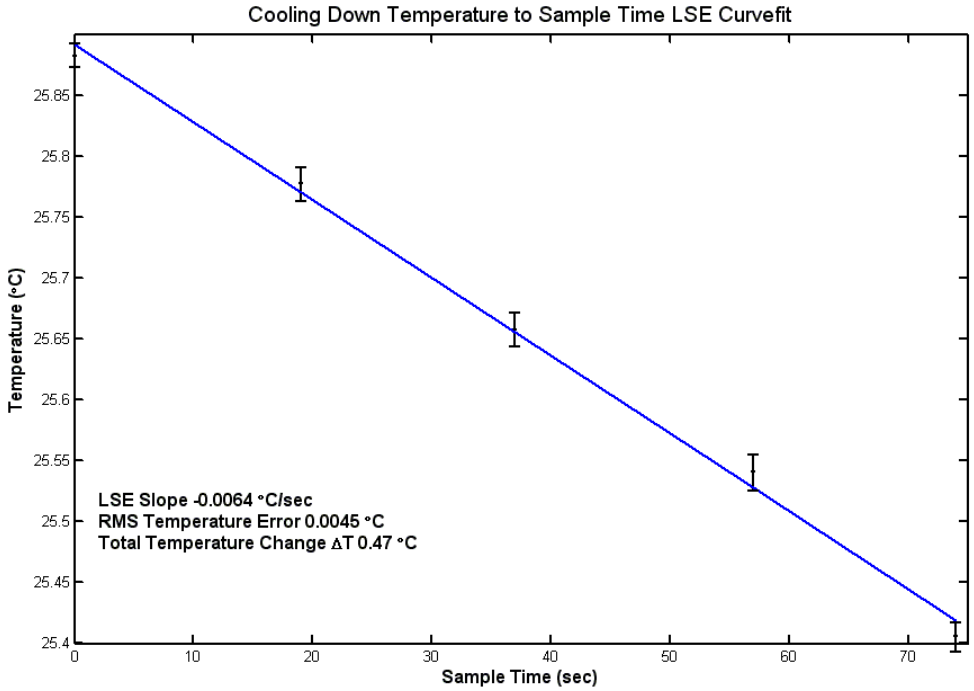

Figure 7.2.7: Temperature-to-Time for a Cooling-Down Fluid-Cell

The LSE cooling-down slope is -0.006°C/sec for a total temperature change of 0.47°C. The heating up and cooling down rates are similar, which is expected due to the constant thermal conductivity of the fluid and steady-state heat transfer.

7.3 STLH Microscope Reconstruction Experiment

The STLH microscope used the *xyz*-translation stages for scanning the fluid-cell. Scanning was done for 8 scan positions along the optical propagation *z*-axis, 2 scan positions in the horizontal *x*-axis, and 4 scan positions in the vertical *y*-axis that produced 64 holograms as recorded by the line scan camera. The scanning order is along the *zxy*-axis respectively. The phase-shifts at the marginal ray regions of a hologram were determined using the Fourier Transform Method. The phase-shifts from the holograms along with refractive index Boundary Conditions (BCs) are used by the "wily" matrix reconstruction algorithm to determine the interior three-dimensional index-of-refraction within the fluid-cell.

The reconstructed index-of-refraction RMS error array is based on the computational grid-mesh indices of $i = 1\ to\ 4$ and $k = 1\ to\ 8$ or a 4x8 array for each of the 4 vertical *y*-axis planes.

The reconstructed index-of-refraction (n_{rec}) is determined from phase-shift measurement (ϕ_{obj}) data using:

$$n_{rec} = [wily]^{-1} \times (\lambda\phi_{obj} - OPL_{BC}) \quad \text{(see section 4.1)} \qquad (7.3.1)$$

Factoring the reference hologram the reconstructed index-of-refraction becomes:

$$\Delta n_{rec} = [wily]^{-1} \times (\lambda(\phi_{obj} - \phi_{ref}) - OPL_{BC}) \qquad (7.3.2)$$

$\Delta n_{rec} = n_{obj} - n_{ref}$ from the object and reference holograms

This reconstruction error represents the resolution of the microscope to determine the temperature or index-of-refraction. Reconstruction is performed in the *xz*-plane at a constant *y*-axis vertical height or elevation. The *y*-axis dimension is represented by the vertical distance from the heater to the focal point of the object beam in the fluid-cell. Given a coordinate system origin at near the top-left-back of the fluid-cell then the vertical distance to the heater for various *y*-values is shown in table 7.3.1 below:

Elevation y (mm)	Vertical Distance To Heater (mm)
0.0	2.3
0.6	1.7
1.2	1.1
1.8	0.5

Table 7.3.1: Elevation Displacements along the Vertical *y*-axis

The elevation column is represented by a unit vector pointing in the downward direction. The vertical distance from focal point to heater decreases as the *y*-elevation increases. Three-dimensional reconstruction is determined for each *xz*-plane along the *y*-axis elevation planes. Reconstruction at *y*=0 mm elevation is as follows:

Elevation at y=0 mm (Furthest distance from focal point to heater)

The measured phase-shift $\phi_{meas}(sp, r)$ that is indexed to a reference scan position (*sp*) and slope (*r*) uses the cumulative number of propagated waves through the fluid-cell for absolute phase referencing in the calculations. The measured relative phase-shift at *y*=0 mm elevation is shown in table 7.3.2 below:

Measured Phase-Shift (waves)	
-0.889	-5.707
-1.485	-5.204
-2.628	-4.493
-3.322	-3.580
-4.349	-1.656
-5.505	-0.895
-5.842	-0.727
-6.486	0.000
-6.772	-1.250
-6.824	-1.490
-6.919	-2.153
-6.946	-2.781
-5.985	-3.644
-3.604	-4.696
-1.800	-5.136
0.000	-5.505

Table 7.3.2: Relative Phase-Shift of Object Holograms to Reference Holograms

Table 7.3.2 above shows 16 scan position (*sp*) rows and 2 slope (*r*) condition columns. The column (*r*=1) represents marginal rays with negative slope and column (*r*=2) represents marginal rays with positive slope. A reference point for the marginal ray that passes through the most number of boundary condition cells is at scan position (*sp*=16) for a negative slope (*r*=1) ray and scan position (*sp*=8) for a positive slope (*r*=2) ray. The relative phase-shift at the negative and positive slope reference points are defined as zero. The reference points are also used to estimate the reference Optical Path Length (*OPL*) since the rays represented by these reference points pass through the greatest number of Boundary Condition (BC) cells. The reference hologram provides the reference *OPL* at *OPL*(16,1) and *OPL*(8,2) reference points.

The reconstructed (interior 4x8 computational domain array) index-of-refraction from the measured hologram phase-shift data is shown in figure 7.3.1 below:

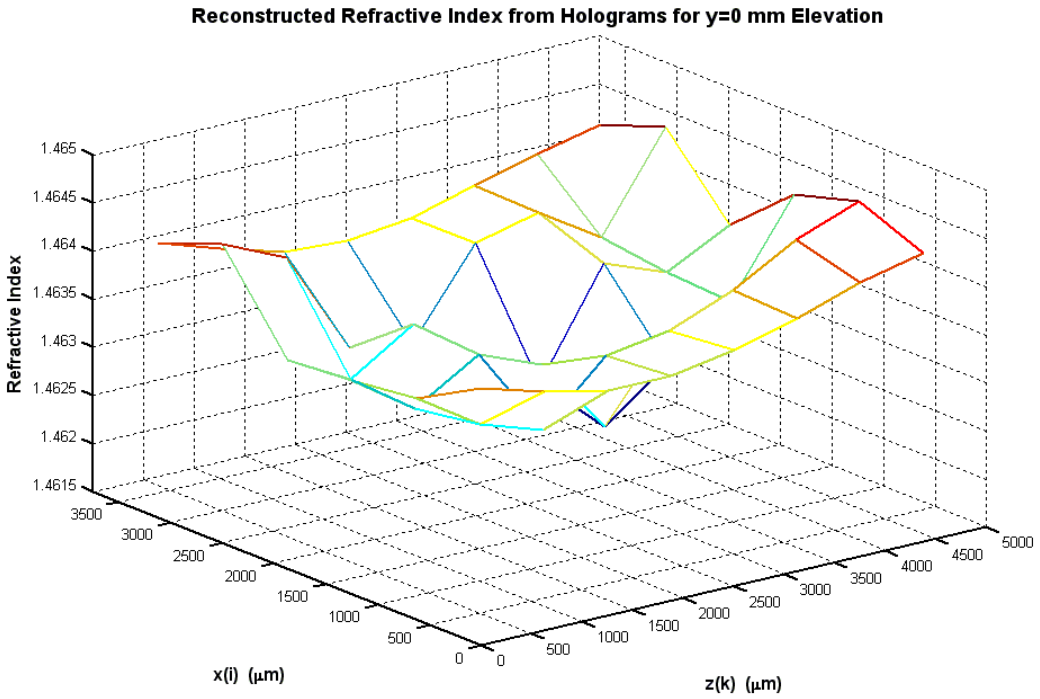

Figure 7.3.1: Reconstructed Index-of-Refraction for y=0 mm Elevation

The boundary conditions are along the edges for x=0 from z=0 to 5000 mm and for x=3750 mm from z=0 to 5000 mm. The 2x8 array boundary conditions are assumed to have no error for reconstruction. The index-of-refraction range is from 1.4620 to 1.4645. The calculated refractive index from the measured thermocouple temperatures along the *xz*-plane in the fluid-cell is shown in table 7.3.3 below:

Index-of-Refraction							
1.45607	1.45589	1.45574	1.45574	1.45585	1.45604	1.45625	1.4564
1.45604	1.45571	1.45545	1.45531	1.45545	1.45574	1.45607	1.45629
1.45596	1.4556	1.45523	1.45498	1.45494	1.45538	1.45585	1.45615
1.45593	1.45556	1.45527	1.45505	1.45509	1.45545	1.45593	1.45622
1.45611	1.45578	1.45552	1.45542	1.45552	1.45578	1.45607	1.45625
1.45625	1.45604	1.45585	1.45582	1.45589	1.45607	1.45625	1.4564

Table 7.3.3: Index-of-Refraction from Converted Thermocouple Temperature Measurements

The reason for showing the index-of-refraction from thermocouple measurements is to compare the thermocouple measurements to the reconstruction method. The index-of-refraction in table 7.3.3 above is a 6x8 array that includes the boundary condition cells. A mesh plot of the index-of-refraction over the *xz*-plane in the fluid-cell is shown in figure 7.3.2 below:

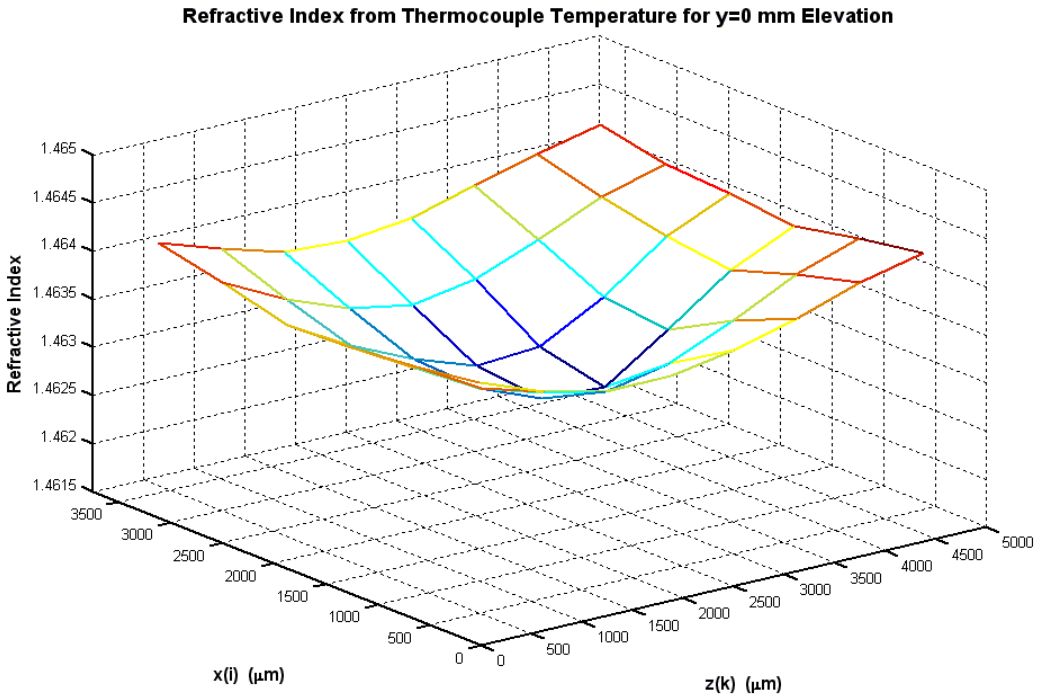

Figure 7.3.2: Index-of-Refraction from Measured Temperature at y=0 mm Elevation

The refractive index profile shows a central minimum which represents the higher temperature of the central region from the heater. The refractive index error from comparing the reconstruction method to the thermocouple measurements is shown in figure 7.3.3 below:

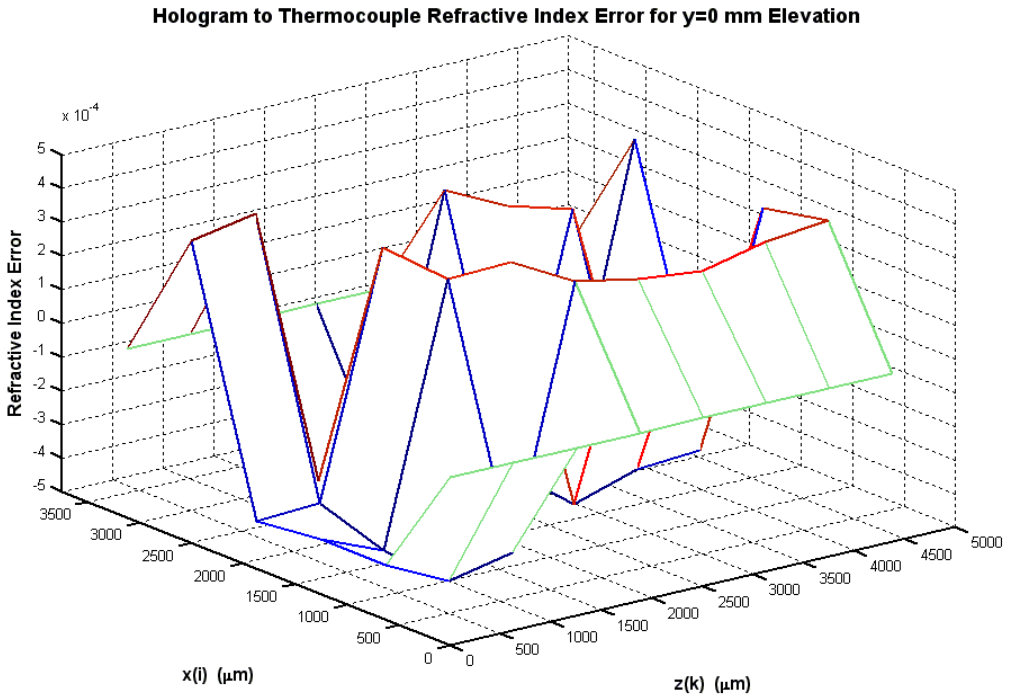

Figure 7.3.3: Reconstructed Index-of-Refraction Error at y=0 mm Elevation

The reconstructed index-of-refraction error is $n_{error} = 0.000371$ 1-σ RMS over the 4x8 interior computational domain array. The BC error was assumed zero and the reconstructed error is mainly due to the hologram measurement error. The error in the measured hologram primarily consists of the phase-shift determination error as there is a varying fringe contrast across the beam overlap region. The reconstructed temperature error Δ*T* (1-σ RMS) was determined from the refractive index to temperature slope of the fluid, which is given as $dn/dT = -3.65 \times 10^{-4}\, 1/°C$.

The temperature error is given as $\Delta T\,(°C) = \dfrac{\Delta n}{|dn/dT|} = \dfrac{0.000371}{0.000365} = 1.02\,°C$ (7.3.1)

The reconstruction error procedure as shown above was repeated for the other elevation planes. Table 7.3.4 below shows the cumulative RMS reconstructed refractive index error and the reconstructed temperature error as calculated from the equation above. The cumulative RMS refractive index error and temperature error for each of the scan plane elevations in the fluid-cell are given in table 7.3.4 below:

Elevation y (mm)	Reconstructed Refractive Index Error	Temperature Error (ºC)
0.0	0.000371	1.02
0.6	0.000301	0.82
1.2	0.000307	0.84
1.8	0.000300	0.82

Table 7.3.4: RMS Reconstructed Refractive Index and Temperature Error at each Elevation Plane

The RMS temperature variation from sample-to-sample appears to represent the peak error of 0.9 to 1.0°C that converts to a refractive index error of 3.6×10^{-4}. The thermocouple measurement error is from ±0.05 to ±0.1°C using custom designed low noise electronic circuits with high-order analog filtering and digital filtering with LabVIEW to minimize the measurement error. A fringe-shift measurement resolution of $\lambda/70\,waves$ will equate to a temperature resolution of ±0.01°C given a refractive index to phase-shift sensitivity of $\frac{dn}{d\phi}=-2.6\times10^{-4}\,1/\,wave$ or a phase-shift to temperature sensitivity of $\frac{d\phi}{dT}=+1.4\,waves/°C$.

In general, holography can resolve a temperature difference of ±0.02°C or a change in refractive index of approximately 7.3×10^{-6}. Due to the optical aberrations from low f/# short focal length optics along with the scanning errors for multiple hologram data collection the resultant error significantly increases by two of orders of magnitude.

7.4 CSLH Microscope Reconstruction Experiment

The CSLH microscope uses the Beam Steering Mirrors (BSMs) to scan in the *xy*-axis and a translation stage to move the telecentric lens for scanning in the *z*-axis. An additional *xy*-axis translation stage is used to move the pinhole apertures in the confocal lens and track the movement of the focused object beam and reference beam onto the pinholes. Translation of the pinhole apertures along the *x*-axis was negligible, but tracking the focal point of the beam in the *y*-axis was over 500 µm/step. Tracking the focal point is more significant in the *y*-axis than the *x*-axis due to the alignment discrepancies of the periscope lens pupil planes in the BSM section for both the forward and reverse propagating beams.

Scanning was done for 8 scan positions along the optical propagation *z*-axis, 2 scan positions in the horizontal *x*-axis, and 4 scan positions in the vertical *y*-axis producing 64 holograms that were recorded by the line scan camera. The scanning order is along the *zxy*-axis coordinates. The phase-shifts at the marginal ray regions of a hologram were determined using the Fourier Transform Method. The phase-shifts from the holograms and refractive index Boundary Conditions (BCs) are used by the "wily" matrix reconstruction algorithm to determine the interior three-dimensional index-of-refraction within the fluid-cell.

The CSLH holograms are quite similar to the holograms produced by the STLH microscope. The main differences are: 1) The beam size is smaller at the output of the confocal lens due to a slight de-magnification of <1 that cannot be corrected by alignment and 2) There are two beams appearing at each pinhole aperture due to the forward and reverse beam propagation through the optical loop. The reverse propagation in the optical loop was mitigated by inserting a half-wave plate and a polarizing lens, which provided one focused beam spot per pinhole.

The phase-shift at the marginal rays was obtained using the Fourier transform method for each scan position. There are two phase-shift measurements for each scan position that are required for the "wily" matrix reconstruction algorithm. One phase-shift represents the positive slope marginal rays and the other phase-shift represents the negative slope marginal rays.

The reconstructed index-of-refraction was compared to the index-of-refraction that was calculated from the thermocouple temperature measurements. The reference fluid refractive index to temperature specification provided the conversion of a measured temperature to an index-of-refraction. At each of the four elevation planes there are 16 measured holograms and 16 boundary conditions that are used as input parameters to the "wily" matrix reconstruction algorithm. The reconstruction error is the reconstructed refractive index relative to the index-of-refraction that is based on the thermocouple temperature. The 1-σ RMS reconstruction error is determined from the 4x8 interior computational domain array at each elevation plane.

The RMS error is based on the reconstructed index-of-refraction array of $i = 1\ to\ 4$ and $k = 1\ to\ 8$ or a 4x8 array for each of the 4 vertical *y*-axis planes.

The reconstructed index-of-refraction (n_{rec}) from phase-shift measurement (ϕ_{obj}) data is

$$n_{rec} = [wily]^{-1} \times (\lambda\phi_{obj} - OPL_{BC}) \quad \text{(see section 4.1)} \tag{7.4.1}$$

Factoring the reference hologram the reconstructed index-of-refraction becomes:

$$\Delta n_{rec} = [wily]^{-1} \times (\lambda(\phi_{obj} - \phi_{ref}) - OPL_{BC}) \tag{7.4.2}$$

$$\Delta n_{rec} = n_{obj} - n_{ref} \quad \text{from the object and reference holograms} \tag{7.4.3}$$

The resolution of the microscope is based on the reconstruction error. The temperature is determined from the reconstructed index-of-refraction. Reconstruction is performed in the *xz*-plane at a constant *y*-axis vertical height or elevation. Holograms provide the phase-shift data for the "wily" matrix reconstruction algorithm. An example of a hologram imaged by the line scan camera is shown in figure 7.4.1 below:

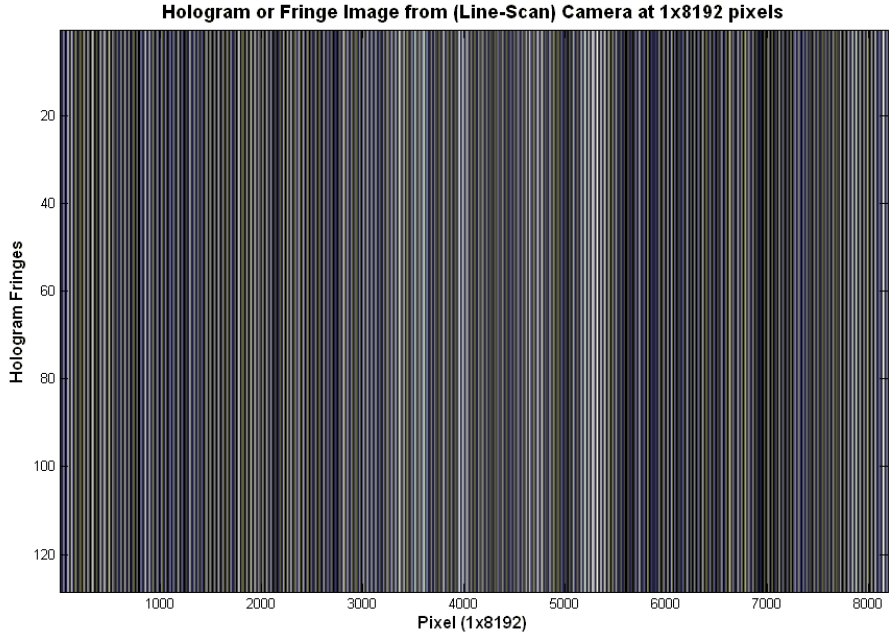

Figure 7.4.1: A single frame hologram from the Dalsa Piranha P2-23-08k40 Line Scan Camera

The vertical axis shows a copy of the sampled line image for 128 lines. The line scan camera has a detector width of 57 mm (8192 pixels at 7 µm/pixel) to accommodate the overlapped beams. The Left-Hand Side (LHS) and Right-Hand Side (RHS) of the hologram is where the marginal rays from the coincident object and reference beams overlap. Detail on the LHS of the hologram is shown in figure 7.4.2 below:

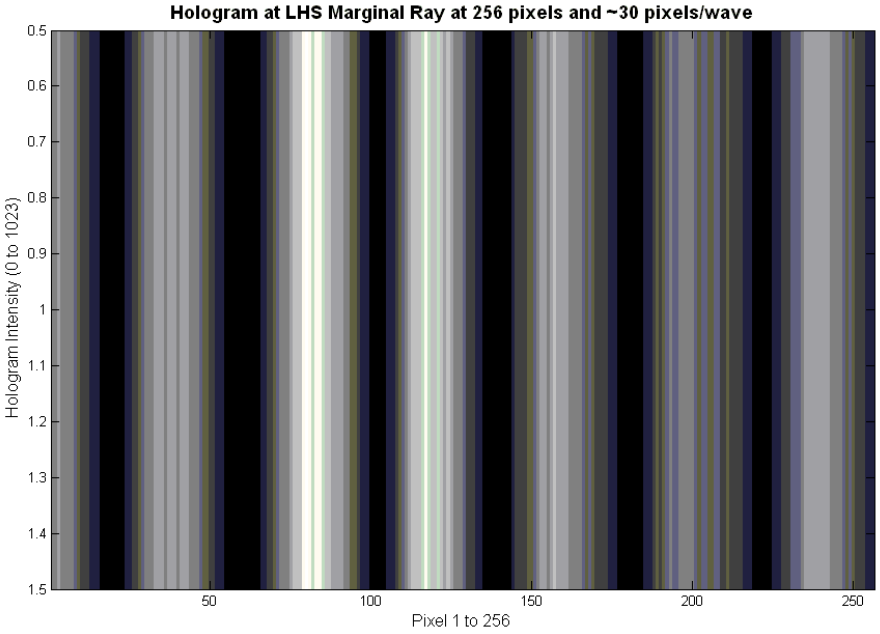

Figure 7.4.2: Hologram at the Left-Hand Side of the Camera for 256 samples

The LHS starting point is pixel #2 for 256 samples that contain approximately 6 fringes. This hologram shows constant fringe spacing that produces a dominant spatial frequency in the power spectrum. The phase-shift at the LHS starting point is determined by the Fourier Transform Method. A similar hologram occurs on the RHS at starting pixel #7935 which represents the marginal ray location for 256 samples. The hologram data from the camera was transferred to Matlab to determine phase-shift and reconstruct the refractive index. The sampled data points for the LHS hologram are more clearly seen in figure 7.4.3 below:

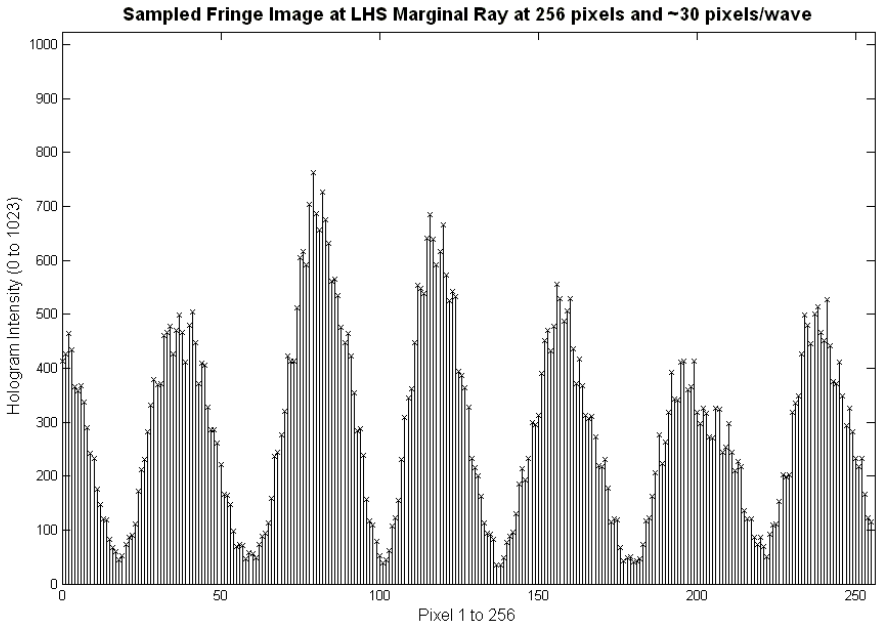

Figure 7.4.3: Left Hand Side Sampled Fringe Image Waveform

The LHS hologram figure above shows a phase-shift of approximately 90° or 1/4 wave. Calculations estimate 30 samples/fringe, which was adequate to accurately determine the phase-shift. The reason for such high spatial sampling is because a very shallow angle 0.5° optical wedge was used to overlap the object beam onto the reference beam. Identical sampling occurs at the RHS marginal ray point on the camera. The Fourier transform of the sampled data is then converted to a power spectrum for the LHS marginal rays as shown in figure 7.4.4 below:

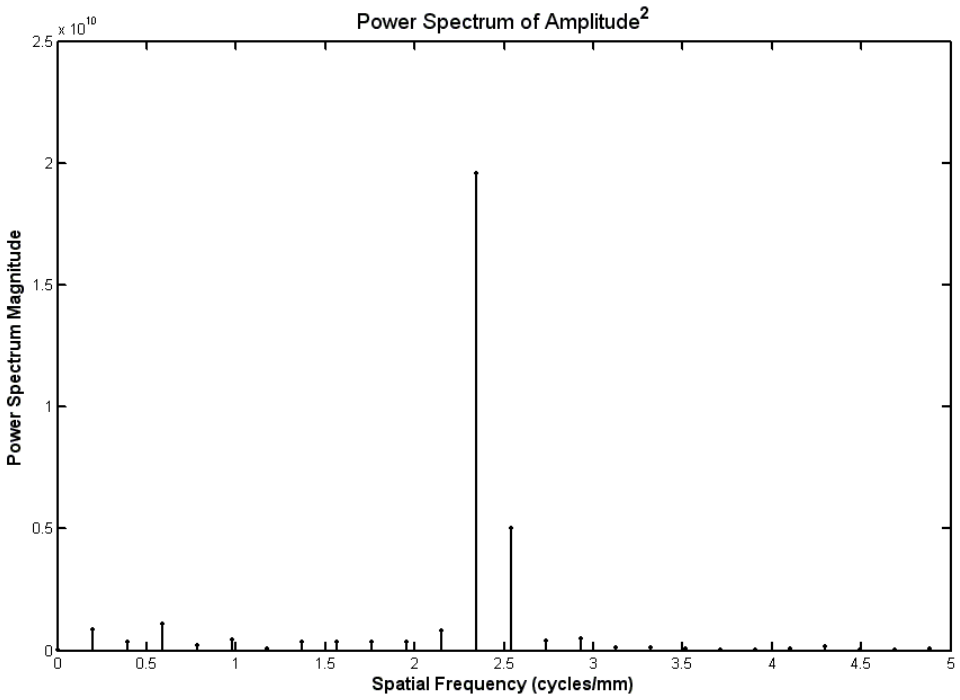

Figure 7.4.4: Left Hand Side Power Spectrum

The power spectrum shows a dominant spatial frequency from the fringes in the hologram, representing the carrier frequency. The object and reference beams are slightly divergent and spatial sampling is approximately 40 samples/fringe at the camera. This is well above the absolute minimum requirement of 8 samples/fringe and is primarily due to the 0.5° shallow wedge angle of the prism that overlaps the beams and the slightly diverging or de-collimating object and reference beams from the telecentric lens. The beam path to achieve complete beam overlap is quite long at 9 meters. The relatively constant fringe spacing produces a peak in the power spectrum where the phase-shift information is contained. The phase-shift is determined from the Fourier transform at the spatial carrier frequency (or frequency at the power spectrum peak). The phase-shift is the arc-tangent of the imaginary part to the real part ratio. The spatial carrier frequency or the frequency at peak of the power spectrum is 2.3 cycles/mm. The Fourier Transform Method produces a phase-shift of +65.66º given 2x256=512 samples over 6 fringes.

No data window or apodization function or tapering function was used prior to the Fourier transform because it was found to introduce an algorithm based phase-shift. Data windowing is unnecessary if the phase-shift at the carrier frequency only is required. The spatial carrier frequency happens to be substantially lower than the

Nyquist frequency limit as seen in the power spectrum, which means that a window is an unnecessary signal processing function. The Fourier Transform Method produces a phase-shift of -69.80° given 2x256=512 samples over 6 fringes.

The Fringe-Spacing $fs = 1/(3.35 \times 0.007) = 43\ pixels\ /\ fringe$ given a detector spacing of $7\ \mu m\ /\ pixel\ = 0.007\ mm\ /\ pixel$.

Reconstruction is performed in the *xz*-plane at a constant *y*-axis vertical height. The *y*-axis dimension is represented by the vertical distance from the heater to the focal point of the object beam in the fluid-cell. Given a coordinate system origin at near the top-left-back of the fluid-cell the vertical distance to the heater for various *y*-values is shown in table 7.4.1 below:

Elevation y (mm)	Vertical Distance To Heater (mm)
0.0	2.3
0.6	1.7
1.2	1.1
1.8	0.5

Table 7.4.1: Elevation Displacements along the Vertical *y*-axis

The elevation column is represented by a unit vector pointing in the downward direction and the vertical distance from focal point to heater decreases as *y*-elevation increases. Three-dimensional reconstruction is determined for each *xz*-plane along the *y*-axis elevation planes. Reconstruction at elevation *y*=0 mm is as follows:

Elevation at y=0 mm (Furthest distance from focal point to heater)

The measured phase-shift $\phi_{meas}(sp, r)$ that is indexed to a reference scan position (*sp*) and slope (*r*) shows the number of waves relative to a specific cell. This measured relative phase-shift at *y*=0 mm elevation is shown in table 7.4.2 below:

Measured Phase-Shift (waves)	
1.500	-2.192
-0.666	-1.528
-3.495	-0.750
-5.657	0.268
-6.890	1.291
-7.654	2.113
-7.377	1.512
-6.701	0.000
-6.347	-1.139
-4.988	-1.926
-3.752	-1.778
-3.310	-2.281
-2.992	-3.887
-2.205	-5.053
-0.708	-5.393
0.000	-4.182

Table 7.4.2: Phase-Shift from Hologram at *y*=0 mm Elevation

Table 7.4.2 above shows 16 scan position (*sp*) rows and 2 slope (*r*) condition columns. The column (*r*=1) represents marginal rays with negative slope and column (*r*=2) represents marginal rays with positive slope. A reference point for the marginal ray that passes through the most number of boundary condition cells is at scan position (*sp*=16) for a negative slope (*r*=1) ray and scan position (*sp*=8) for a positive slope (*r*=2) ray. The phase-shift at the negative and positive slope reference points is defined as zero. The measured phase-shift data array is shifted to zero at these reference points. This definition for a scan position and slope reference point produces minimal reconstruction error since the number of boundary condition (BC) cells is maximum and the unknown cells in the computational domain is minimum. These scan position and slope reference points are also used to estimate the reference Optical Path Length (*OPL*) for the respective rays. The phase-shift reference points that set the reference hologram conditions are also indexed to the marginal ray left-hand side and right-hand side points in the hologram. The reconstructed (interior 4x8 computational domain array) index-of-refraction from the measured hologram phase-shift data is shown in figure 7.4.5 below:

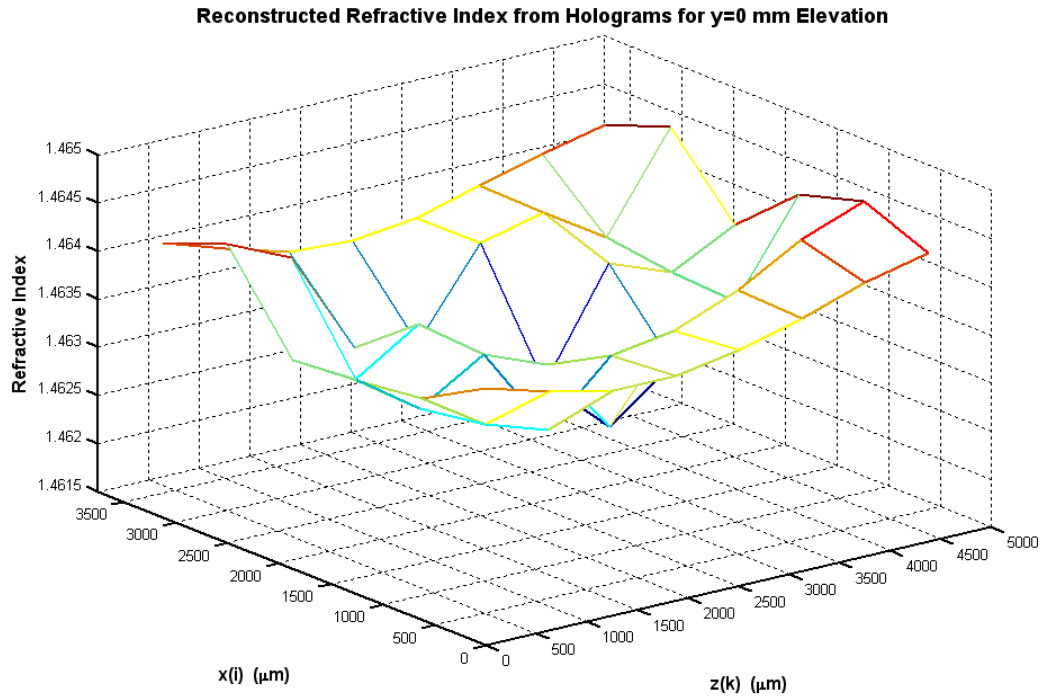

Figure 7.4.5: Reconstructed Index-of-Refraction for y=0 mm Elevation

The refractive index profile shows a central minimum which represents the higher temperature from the heater. This refractive index distribution is a 6x8 array that includes the Boundary Conditions (BCs). The boundary conditions are along the edges for x=0 from z=0 to 5000 mm and for x=3750 mm from z=0 to 5000 mm. The 2x8 array boundary conditions are assumed to have no error for reconstruction. The index-of-refraction range is from 1.4620 to 1.4645.

The calculated refractive index from the measured thermocouple temperatures along the *xz*-plane in the fluid-cell is shown in table 7.4.3 below:

Index-of-Refraction							
1.45607	**1.45589**	**1.45574**	**1.45574**	**1.45585**	**1.45604**	**1.45625**	**1.45640**
1.45604	**1.45571**	**1.45545**	**1.45531**	**1.45545**	**1.45574**	**1.45607**	**1.45629**
1.45596	**1.45560**	**1.45523**	**1.45498**	**1.45494**	**1.45538**	**1.45585**	**1.45615**
1.45593	**1.45556**	**1.45527**	**1.45505**	**1.45509**	**1.45545**	**1.45593**	**1.45622**
1.45611	**1.45578**	**1.45552**	**1.45542**	**1.45552**	**1.45578**	**1.45607**	**1.45625**
1.45625	**1.45604**	**1.45585**	**1.45582**	**1.45589**	**1.45607**	**1.45625**	**1.45640**

Table 7.4.3: Index-of-Refraction Based on Thermocouple Measurements that Includes the Boundary Conditions

The reason for showing the index-of-refraction from thermocouple measurements is to compare the thermocouple measurements to the reconstruction method. The index-

of-refraction in table 7.4.3 above is a 6x8 array that includes the boundary condition cells. A mesh plot of the index-of-refraction over the *xz*-plane in the fluid-cell is shown in figure 7.4.6 below:

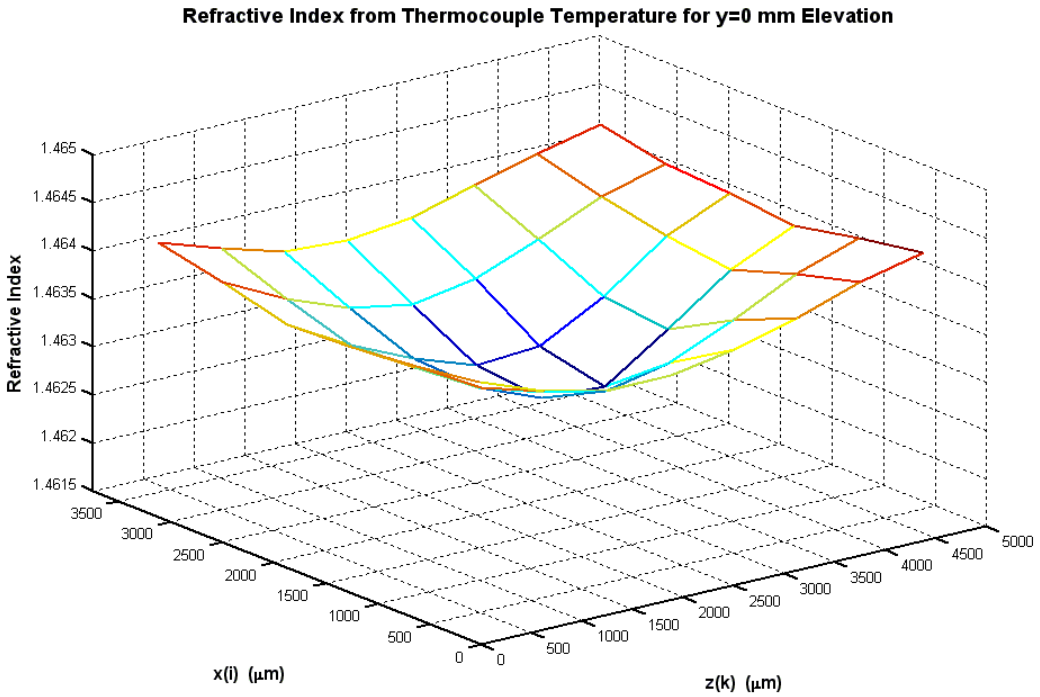

Figure 7.4.6: Index-of-Refraction from Measured Temperature at y=0 mm Elevation

The refractive index profile shows a central minimum which represents the higher temperature of the central region from the heater. The refractive index that is calculated from the thermocouple temperature measurements has less variation than the reconstructed index-of-refraction from the holograms and boundary conditions. A fringe-shift measurement in a hologram can measure a temperature more accurately than a thermocouple. Reconstructing a hologram in the *xz*-axis for each vertical plane requires 16 holograms for 32 phase-shifts and 16 boundary conditions. The cumulative measurement errors produce a reconstruction resolution that is less than the thermocouple resolution, which is a point-to-point scanned measurement. The refractive index error from comparing the reconstruction method to the thermocouple measurements is shown in figure 7.4.7 below:

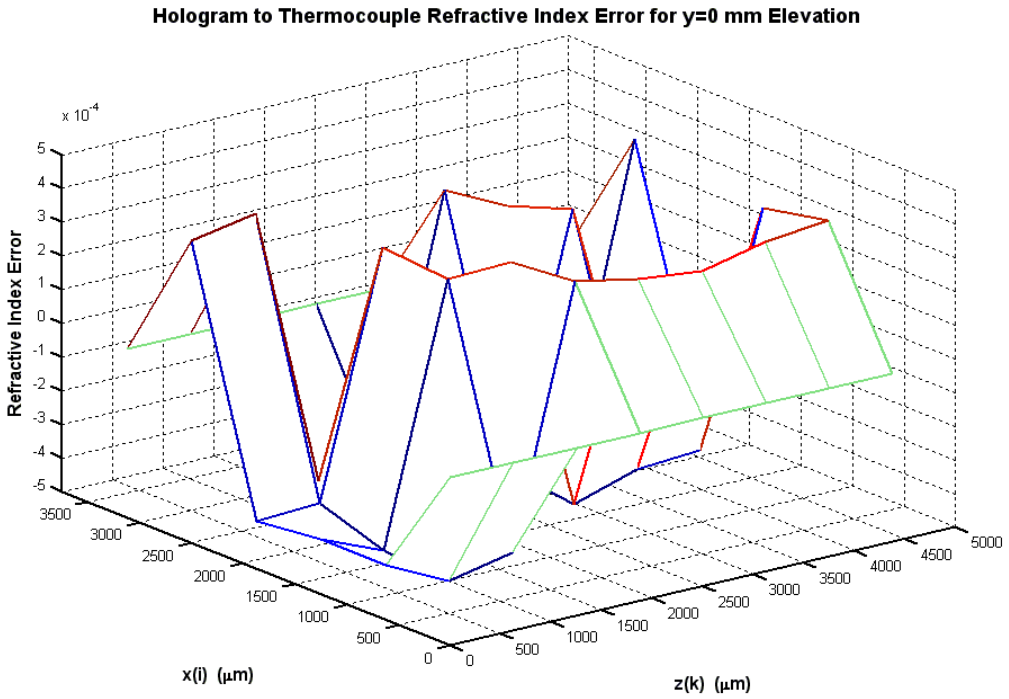

Figure 7.4.7: Reconstructed Index-of-Refraction Error at y=0 mm Elevation

The reconstructed index-of-refraction relative error is $n_{error} = 0.000535$ 1-σ RMS over the 4x8 interior computational domain array. The BC error was assumed zero and the reconstructed error is mainly due to the hologram measurement error. The error in the measured hologram primarily consists of the phase-shift determination error as there is a varying fringe contrast across the beam overlap region.

The data and figures for the other elevations as the scan beam approaches the heater are shown below. As *y* increases the vertical distance to the heater decreases which is shown by an increasing size of the peak in the negative direction for the index-of-refraction. As the scan position approaches the heater the thermal gradient increases and the index-of-refraction gradient also increases as a negative value. The reconstructed index-of-refraction and the reconstruction error figures appear similar for all of the elevations. Even though there are small differences in the figures this does show the scanning and reconstruction in three-dimensions for the three additional discrete elevation planes that are separated by 625 µm along the *y*-axis.

Elevation at y=0.6mm

The measured phase-shift $\phi_{meas}(sp,r)$ that was indexed to a reference scan position (*sp*) and slope (*r*) shows the number of waves relative to a specific cell. This measured relative phase-shift at y=0.6 mm Elevation is shown in table 7.4.4 below:

Measured Phase-Shift (waves)	
-0.430	-5.428
-1.151	-4.346
-2.511	-3.595
-2.646	-3.783
-3.852	-2.480
-4.514	-2.074
-4.772	-1.314
-5.979	0.000
-6.786	-0.851
-6.762	-2.735
-5.507	-4.092
-3.624	-5.485
-1.855	-6.589
-0.894	-6.700
-0.122	-7.141
0.000	-6.255

Table 7.4.4: Phase-Shift from Hologram at *y*=0.6 mm Elevation

The reconstructed index-of-refraction from the measured hologram phase-shift data is shown in figure 7.4.8 below:

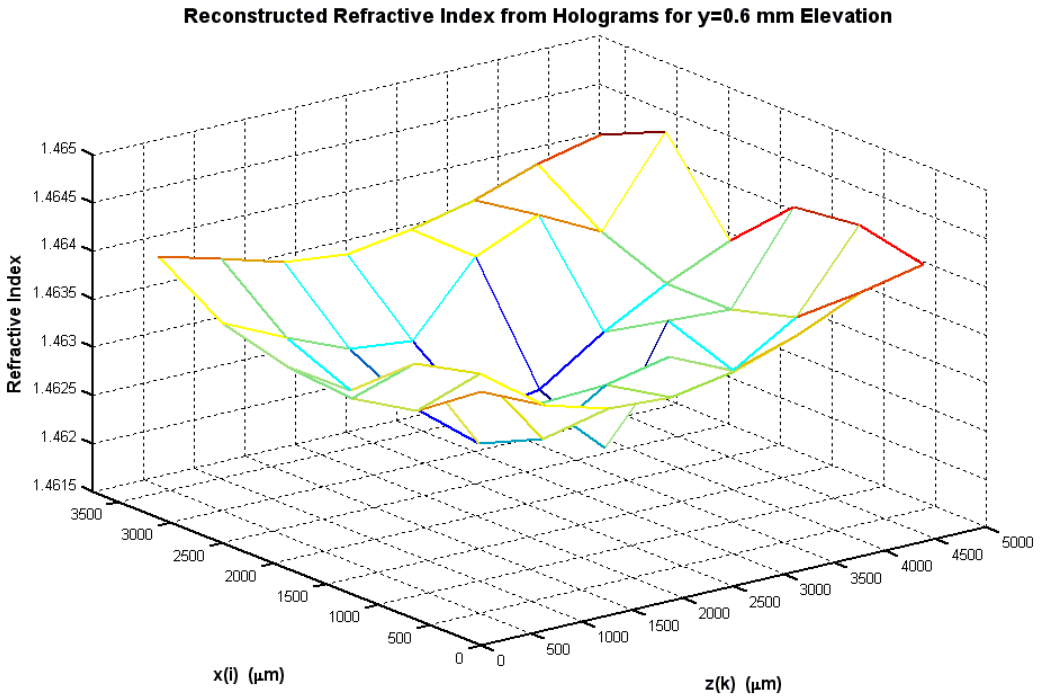

Figure 7.4.8: Reconstructed Index-of-Refraction for y=0.6 mm Elevation

The refractive index that is calculated from the measured thermocouple temperature profile is shown in table 7.4.5 below for y=0.6 mm Elevation.

Index-of-Refraction							
1.45604	1.45574	1.45556	1.45552	1.45563	1.45585	1.45615	1.45629
1.45589	1.45552	1.45523	1.45509	1.45520	1.45556	1.45593	1.45618
1.45574	1.45534	1.45498	1.45465	1.45458	1.45516	1.45574	1.45607
1.45582	1.45538	1.45505	1.45483	1.45494	1.45538	1.45578	1.45607
1.45596	1.45563	1.45538	1.45534	1.45545	1.45571	1.45600	1.45625
1.45611	1.45593	1.45574	1.45567	1.45578	1.45593	1.45615	1.45629

Table 7.4.5: Index-of-Refraction Based on Thermocouple Measurements that Includes the Boundary Conditions

A mesh plot of the index-of-refraction is shown in figure 7.4.9 below:

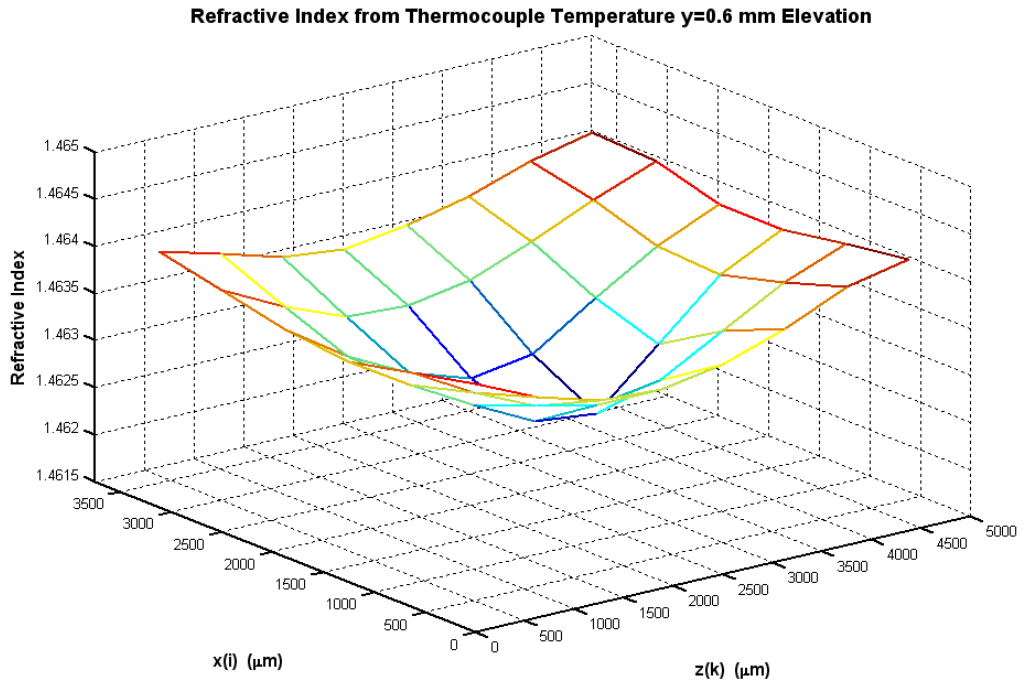

Figure 7.4.9: Index-of-Refraction from Measured Temperature at y=0.6 mm Elevation

The reconstructed refractive index error with respect to thermocouple measurements is shown in figure 7.4.10 below:

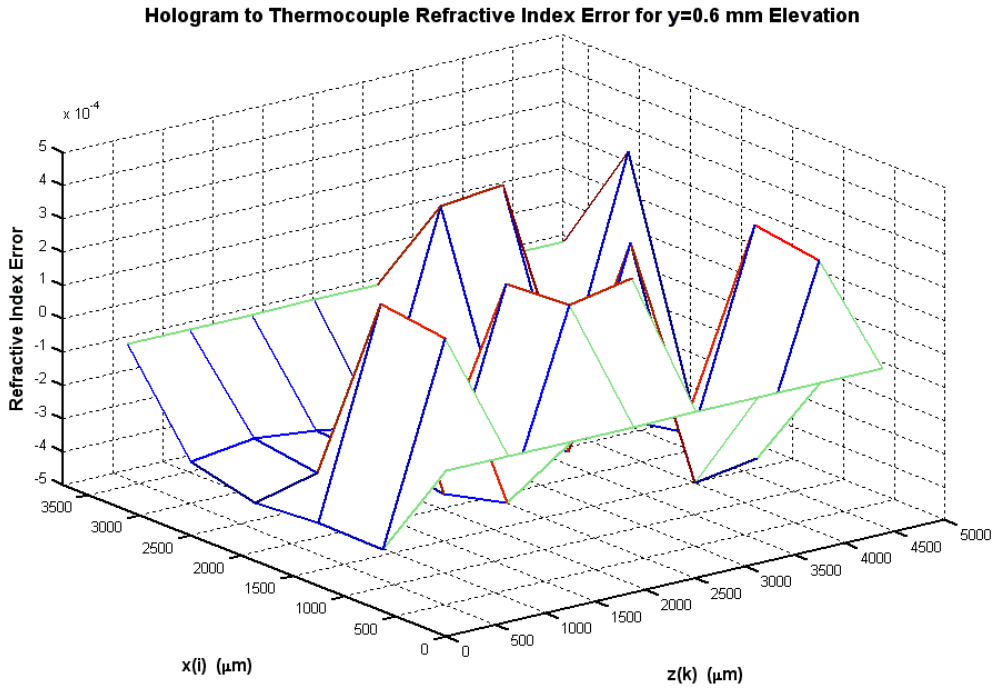

Figure 7.4.10: Reconstructed Index-of-Refraction Error at y=0.6 mm

The reconstructed index-of-refraction relative error is $n_{error} = 0.000452$ 1-σ RMS over the 4x8 interior computational domain array.

Elevation at y=1.2mm

The measured phase-shift $\phi_{meas}(sp, r)$ that was indexed to a reference scan position (*sp*) and slope (*r*) shows the number of waves relative to a specific cell. This measured relative phase-shift at y=1.2 mm Elevation is shown in table 7.4.6 below:

Measured Phase-Shift (waves)	
-6.338	-0.693
-5.851	-2.183
-5.289	-3.530
-4.723	-5.044
-4.984	-4.885
-6.848	-3.253
-8.700	-1.913
-8.812	0.000
-7.921	3.646
-6.667	2.877
-4.940	2.115
-2.677	1.378
-2.102	1.637
-1.322	1.723
0.000	1.926
0.000	1.366

Table 7.4.6: Phase-Shift from Hologram at *y*=0.6 mm Elevation

The reconstructed index-of-refraction from the measured hologram phase-shift data is shown in figure 7.4.11 below:

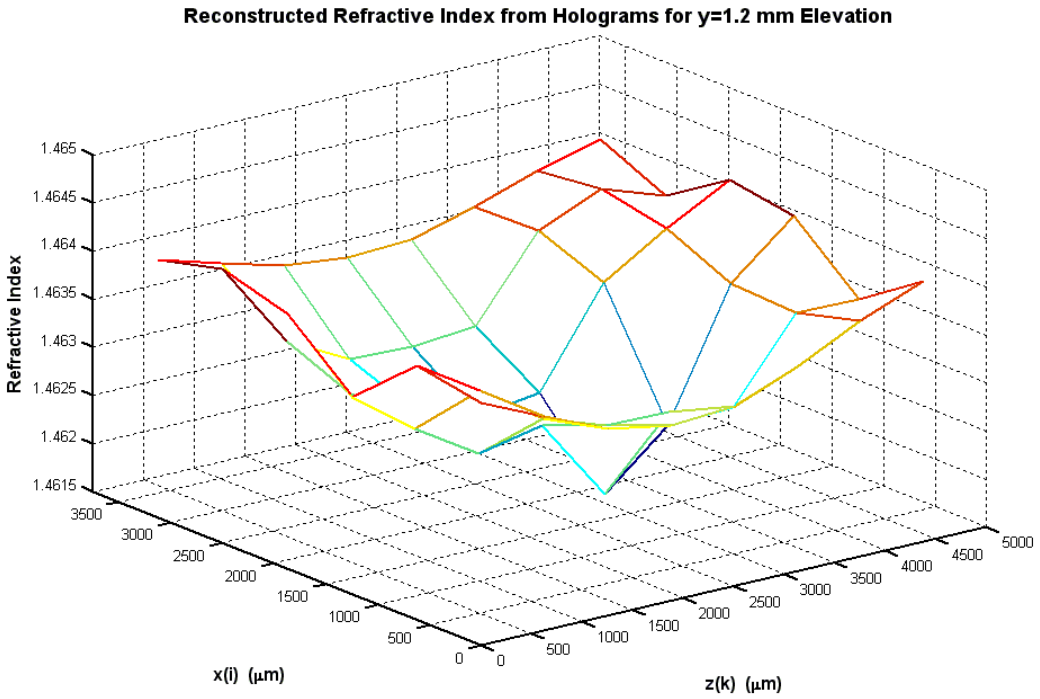

Figure 7.4.11: Reconstructed Index-of-Refraction for y=1.2 mm Elevation

The refractive index that is calculated from the measured thermocouple temperature profile is shown in the table 7.4.7 below for y=1.2 mm Elevation.

Index-of-Refraction							
1.45593	1.45563	1.45534	1.45523	1.45527	1.45552	1.45585	1.45611
1.45574	1.45531	1.45490	1.45461	1.45465	1.45512	1.45560	1.45600
1.45574	1.45531	1.45487	1.45439	1.45414	1.45472	1.45545	1.45593
1.45578	1.45538	1.45501	1.45479	1.45490	1.45527	1.45571	1.45604
1.45596	1.45563	1.45538	1.45527	1.45534	1.45556	1.45589	1.45618
1.45607	1.45589	1.45571	1.45563	1.45567	1.45585	1.45607	1.45625

Table 7.4.7: Index-of-Refraction Based on Thermocouple Measurements that Includes the Boundary Conditions

A mesh plot of the index-of-refraction is shown in figure 7.4.12 below:

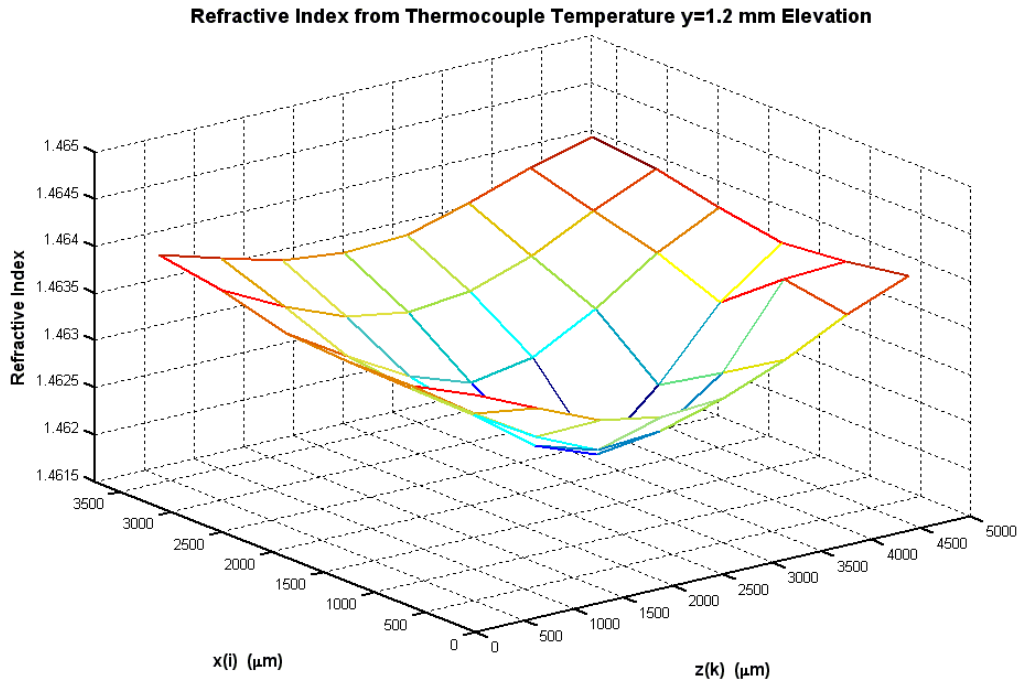

Figure 7.4.12: Index-of-Refraction from Measured Temperature at y=1.2 mm Elevation

The reconstructed refractive index error measurement is shown in figure 7.4.13 below:

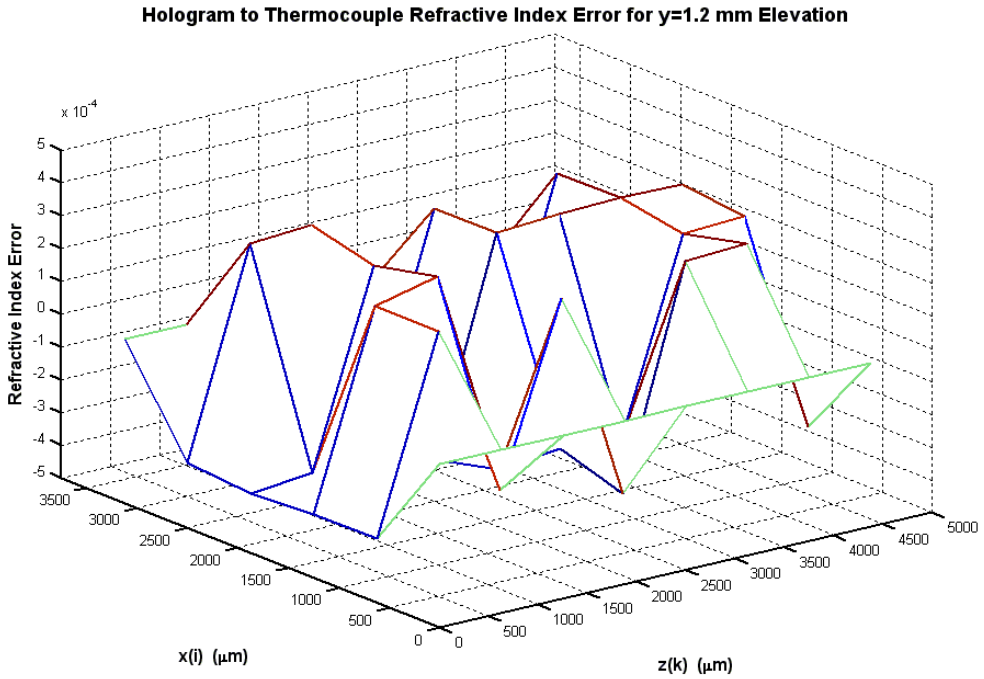

Figure 7.4.13: Reconstructed Index-of-Refraction Error at y=1.2 mm

The reconstructed index-of-refraction relative error is $n_{error} = 0.000434$ 1-σ RMS over the 4x8 interior computational domain array.

Elevation at y=1.8mm

The measured phase-shift $\phi_{meas}(sp, r)$ that was indexed to a reference scan position (*sp*) and slope (*r*) shows the number of waves relative to a specific cell. This measured relative phase-shift at y=1.8 mm Elevation is shown in table 7.4.8 below:

Measured Phase-Shift (waves)	
-7.887	0.432
-8.889	-1.877
-8.234	-3.729
-8.682	-3.865
-9.989	-2.583
-11.390	-1.308
-12.600	-0.062
-11.527	0.000
-9.004	6.198
-5.526	4.621
-2.902	3.033
-1.656	2.110
-0.208	0.894
0.175	1.251
-0.218	1.767
0.000	1.572

Table 7.4.8: Phase-Shift from Hologram at *y*=1.8 mm Elevation

The reconstructed index-of-refraction from the measured hologram phase-shift data is shown in figure 7.4.14 below:

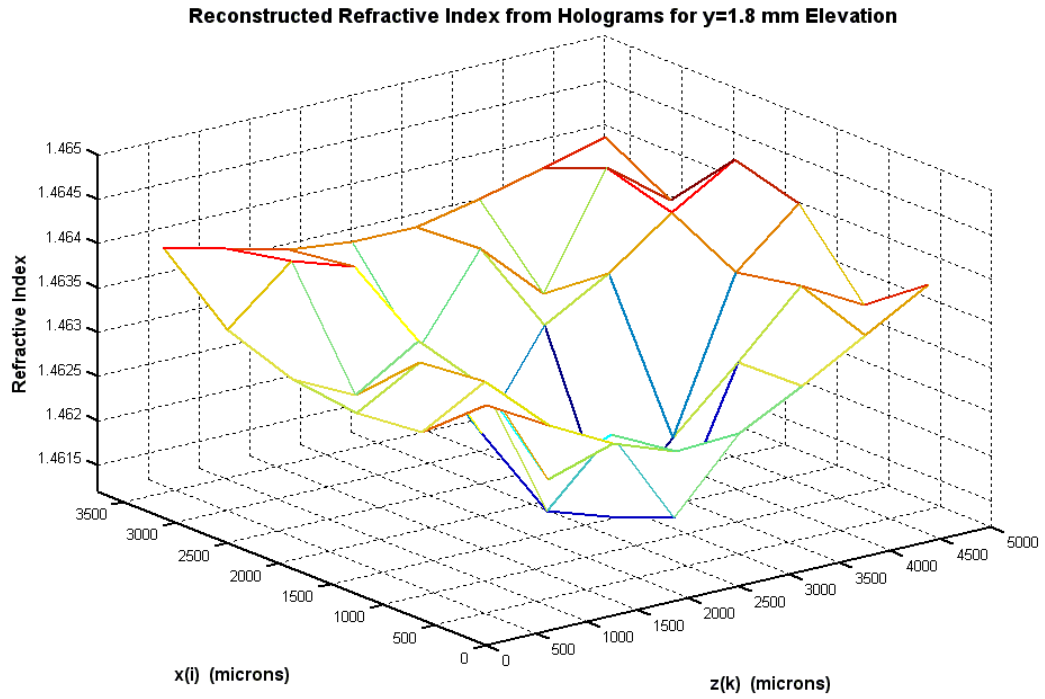

Figure 7.4.14: Reconstructed Index-of-Refraction for y=1.8 mm Elevation

The refractive index that is calculated from the measured thermocouple temperature profile is shown in table 7.4.9 below for y=1.8 mm Elevation.

Index-of-Refraction							
1.45582	1.45542	1.45505	1.45479	1.45483	1.45520	1.45560	1.45600
1.45567	1.45520	1.45472	1.45425	1.45410	1.45469	1.45538	1.45589
1.45560	1.45512	1.45461	1.45399	1.45374	1.45447	1.45531	1.45589
1.45571	1.45534	1.45490	1.45465	1.45472	1.45512	1.45563	1.45607
1.45596	1.45563	1.45538	1.45523	1.45531	1.45552	1.45585	1.45618
1.45615	1.45596	1.45578	1.45571	1.45571	1.45585	1.45604	1.45622

Table 7.4.9: Index-of-Refraction Based on Thermocouple Measurements that Includes the Boundary Conditions

A mesh plot of the index-of-refraction is shown in figure 7.4.15 below:

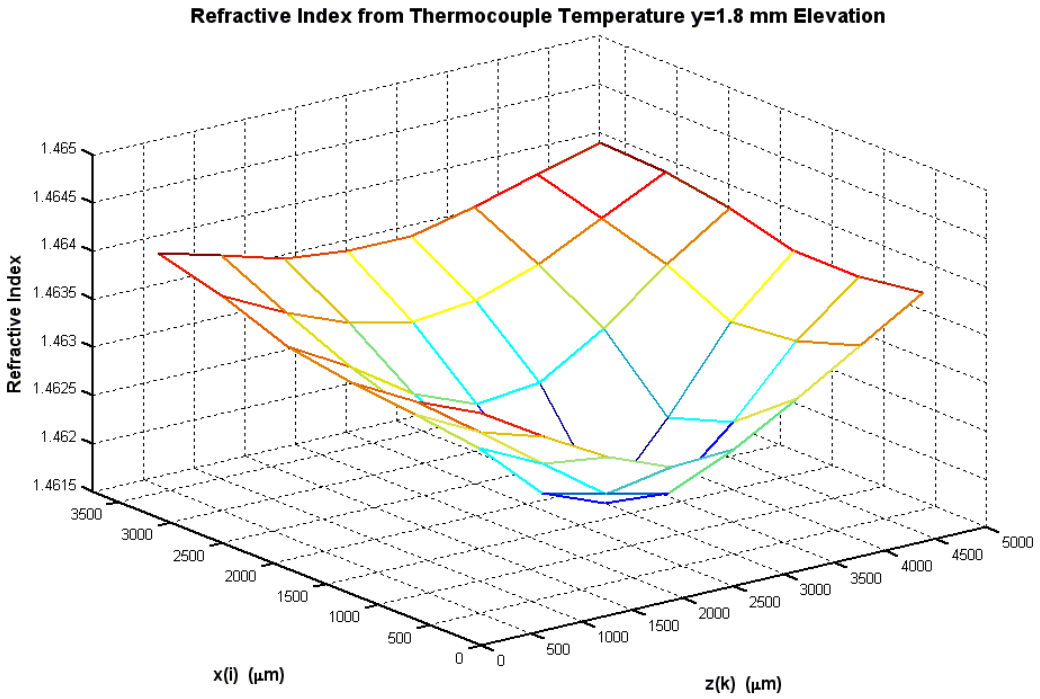

Figure 7.4.15: Index-of-Refraction from Measured Temperature at y=1.8 mm Elevation

The reconstructed refractive index error is shown in figure 7.4.16 below:

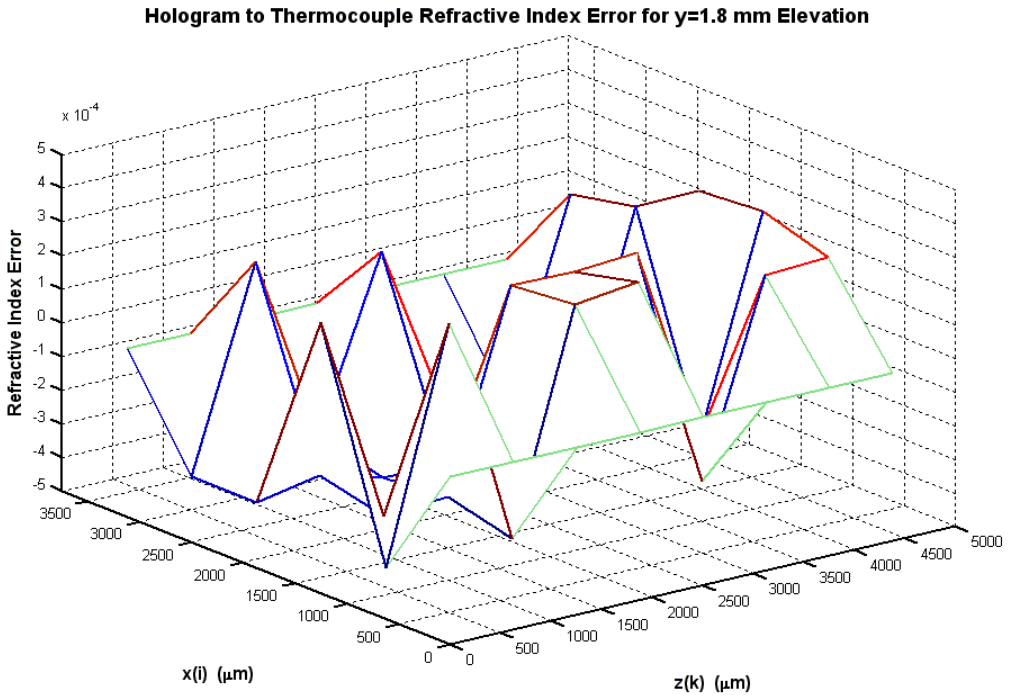

Figure 7.4.16: Reconstructed Index-of-Refraction Error at y=1.8 mm

The reconstructed index-of-refraction relative error is $n_{error} = 0.000478$ 1-σ RMS over the 4x8 interior computational domain array. The BC error was assumed zero and the reconstructed error is mainly due to the hologram measurement error. The error in the measured hologram primarily consists of the phase-shift determination error as there is a varying fringe contrast across the beam overlap region. The reconstructed temperature error Δ*T* (1-σ RMS) was determined from the refractive index to temperature slope of the fluid, which is given as $dn/dT = -3.65 \times 10^{-4} 1/°C$.

The temperature error is given as $\Delta T\,(°C) = \dfrac{\Delta n}{|dn/dT|} = \dfrac{0.000478}{0.000365} = 1.31°C$ (7.4.4)

Table 7.4.10 below shows the reconstructed refractive index error and the reconstructed temperature error. The estimated errors assume no error in the measured boundary conditions. The RMS cumulative error is for the scan planes at each elevation plane in the fluid-cell.

Elevation y (mm)	Reconstructed Refractive Index RMS Error	RMS Temperature Error (ºC)
0.0	0.000535	1.47
0.6	0.000452	1.24
1.2	0.000434	1.19
1.8	0.000478	1.31

Table 7.4.10: RMS Reconstructed Refractive Index Error and Temperature Error for the Four Elevation Planes

The thermocouple measurement error is from ±0.05 to ±0.1 °C. Typical thermocouple measurement error in terms of repeatability and precision is ±1°C using an industry standard cold junction reference and amplifier. Designing an ultra-low noise instrumentation amplifier circuit with low-pass noise filtering reduced the precision error from ±1ºC to ±0.05ºC. The RMS temperature variation from sample-to-sample appears to represent the peak error of 1.2 to 1.5°C that converts to a refractive index error of 5.5×10^{-4}. The thermocouple measurement error is from ±0.05 to ±0.1 °C. A fringe-shift measurement resolution of $\lambda / 70\, waves$ will equate to a temperature resolution of ±0.01°C given a refractive index to phase-shift sensitivity of $\dfrac{dn}{d\phi} = -2.6 \times 10^{-4} 1/wave$

or a phase-shift to temperature sensitivity of $\dfrac{d\phi}{dT} = +1.4\, waves/°C$

8 Characterization and Performance Specifications

The characteristics and limitations of the CSLH microscope are described in this section. The overall reconstruction performance of the STLH microscope was compared the CSLH microscope since the STLH microscope is considered to be a simplified benchmark version of the CSLH microscope. The original intention of using the CSLH microscope in a space experiment for the study of Marangoni convection and fluid flow at low Reynolds number and high Prandtl number can be accomplished. The performance of the microscope was assessed to meet general specifications for the non-intrusive three-dimensional temperature measurements of steady-state heat transfer. The restriction that limited scanning to a single viewing window placed the burden of feasibility on the three-dimensional reconstruction algorithm. A unique method for reconstruction was derived for the CSLH microscope, named the “wily” matrix reconstruction algorithm. Ideas to improve the performance of the CSLH microscope in order to approach the theoretical limits and overcome optical aberrations and mechanical vibrations are suggested in this section. Increasing camera sensitivity, scan rate, and LabVIEW loop refresh rate will allow the microscope to measure temperatures under dynamic flow conditions. A discussion of the error sources for the CSLH microscope and its sensitivity to various parameters is also presented in this section. Some applications are proposed below for situations involving phase-shift measurement of coherent beams.

8.1 Characterization and Performance of the STLH & CSLH Microscopes

The refractive index in the specimen produces changes in the optical path length, which creates a shift in the fringes of the hologram. The spacing between scan positions is defined by the “wily” matrix reconstruction method and the size of the fluid-cell; thus, certain physical and operational parameters must be defined for the reconstruction to operate optimally with minimal error. The operational parameters are: 1) the scanning geometry that evenly distributes the scan positions of the focused probe beam within the specimen, 2) the boundary condition temperatures along the side-to-side walls of the fluid-cell, and 3) the optical properties of the fluid that provides the conversion from refractive index to temperature.

The fringes are constantly spaced, which produces a single carrier frequency. The fringe spacing is primarily due to the wavelength of the laser and the convergence angle

of the overlapping beams. The phase-shift is determined from the hologram by taking a Fourier transform and determining the real and complex variable phase at the carrier frequency. The phase-shift array from the experiment holograms and reference holograms plus the boundary condition refractive index array are input variables to the "wily" matrix reconstruction algorithm. The output of the "wily" reconstruction algorithm is the index-of-refraction array along the *xz*-axis for a horizontal plane or slice at constant elevation from the heater in the fluid-cell. Scanning along the *y*-axis completes the three-dimensional profile for the interior temperature. The index-of-refraction is then converted to temperature using a linear equation.

The STLH is similar to the CSLH except that the confocal feature is removed along with the optics that support the confocal feature. The STLH microscope has a shorter path length than the CSLH microscope and the fluid-cell is moved with *xy*-axis translation stages instead of *xy*-axis scanning with the beam steering mirrors. The cumulative RMS temperature error at each elevation plane in the fluid-cell is shown in table 8.1.1 below:

		STLH Microscope		**CSLH Microscope**	
Elevation y (mm)	**Vertical Distance to Heater (mm)**	**Reconstructed RMS Refractive Index Error**	**RMS Temperature Error (°C)**	**Reconstructed RMS Refractive Index Error**	**RMS Temperature Error (°C)**
0	2.3	0.000371	1.02	0.000535	1.47
0.6	1.7	0.000301	0.82	0.000452	1.24
1.2	1.1	0.000307	0.84	0.000434	1.19
1.8	0.5	0.000300	0.82	0.000478	1.31

Table 8.1.1: Comparison of STLH to CSLH Microscope Reconstruction Error

The CSLH microscope error is approximately 1.49 times greater than the STLH microscope. This is most likely due to the additional optical components and the longer path length that degrades the beam shape. The additional optical components of the CSLH microscope include the optical loop, scanning mirrors, periscope lenses, and the confocal lens. The added complexity makes alignment more difficult and critical. The CSLH microscope optical performance can be improved by incorporating precision custom lenses and obtaining a camera with greater radiometric sensitivity. The STLH microscope produces lower optical aberrations than the CSLH microscope due to fewer lenses. The confocal lens and pinhole apertures reduce optical aberrations and the rays

that pass through the pinhole aperture are optically conjugated to the focal point in the fluid-cell specimen.

The CSLH microscope temperature resolution is 0.02°C or ±0.01°C from hologram-to-hologram at λ/20 waves RMS wavefront error. This temperature error is represented by a minute change in refractive index of $\pm 3.5 \times 10^{-6}$. The CSLH microscope reconstructed temperature resolution is 0.5°C to 1.0°C for 64 holograms and 64 boundary conditions at λ/20 waves RMS wavefront error. The "wily" reconstruction algorithm error is negligible, so the significant increase of reconstruction error to a single hologram measurement error is primarily due to the accumulated measurement error of the 16 holograms and the 16 boundary conditions for each of the 4 elevation planes. The holograms and boundary conditions are obtained from the *xyz*-scanning steps of 2x4x8 respectively. The main contributors to the phase-shift measurement error are the optical aberrations from low f/# short focal length optics and the scanning positional errors for multiple hologram data collection relative to the reference holograms. The accumulated error from multiple holograms and boundary conditions increases the error by two orders of magnitude for reconstruction.

8.2 Trade-Off Issues

The CSLH microscope design incorporated trade-off parameters to optimize optical resolution along with image acquisition resolution in order to provide a measurement displacement accuracy of ~1/200 x fringe-space which is slightly larger than the wavelength of light. The possibility of increasing fringe stability by using sensor feedback control to reduce the effects of mechanical vibrations was considered. Passive vibration reduction was chosen over active vibration isolation due to complexity and the cost of controllers. The approach to passive vibration isolation was to use sensitive accelerometers to measure floor vibrations in various laboratory rooms and then select one of the quietest rooms available. The accelerometers are sensitive enough to detect engine vibrations from a truck in a parking lot approximately 100 feet away. The vibration level at the laboratory room for the CSLH microscope is as benign as the nearby laboratory that is used for one of the highest resolution electron microscopes in the world. Ground vibrations are further reduced by the pneumatic support legs on the Newport optics table. An air damper on the pneumatic chambers means that the table isolates the floor vibrations as a low-pass filter. Air flow from the Heating Ventilation and Air-Conditioning (HVAC) in the room was significantly reduced by suspending fabric

sheeting approximately 4 inches from the ceiling covering the entire ceiling area. Furthermore, cooling fans on power supplies and lasers were replaced with an extremely quiet laminar flow and balanced blade fans to reduce vibrations from rotating imbalance and turbulence induced vibrations. The changes made to the laboratory and the microscope passively reduce vibrations and improve fringe stability on a hologram. The trade-off decision was to exploit passive vibration isolation methods as much as possible and accept the vibrations induced from the actuators. The beam steering mirrors are driven by electro-magnets and the translation stages are driven by a DC motor and worm drive gearbox. The Cambridge Technology galvanometer beam steering mirrors at 2 µrad resolution are the most precise on the market and the Newport translation stages with PID control have a 0.1 µm resolution.

A few of the optical design trade-off parameters are considered as follows:
1) A trade-off compromise is drawn because, as the cone angle of the object beam increases the reconstruction error will decrease, but as the cone angle increases the optical aberrations will increase. In a similar manner, shortening the focal length will decrease the path length, but the blur spot size at the focal point in the specimen will consequently increase along with an increase in the optical aberrations. In general, laser beams cannot be perfectly re-collimated. The f-number of the probe beam in the fluid-cell specimen is f/2, which is a compromise between optical aberrations in the hologram and reconstruction error. The focused beam blur spot size in the fluid-cell specimen is 140 µm RMS radius as determined by Zemax for the telecentric lens. The positional resolution relationship to scanning is that the scan position step size is 625 µm with a Newport translation stage positional resolution of 0.1 µm. Along the optical *z*-axis scanning is for 8 scan positions at 625 µm/step over the depth of the fluid-cell at 5 mm. The number of scan steps in the *xyz*-axis is represented by a 2x4x8 array respectively. The number of computational cells in a single plane along the *y*-axis is represented by a 4x8 array while the BC cells are represented by a 2x8 array. The total number of computational and BC cells in a single plane along the *y*-axis is a 6x8 array.

2) Another trade-off consideration is that as the path length increases the fringe-spacing will also increase, but the wavefront error will increase and the fringe contrast will decrease due to the degraded wavefront. At the coherence length of the laser the fringes become indiscernible and the fringe contrast reduces to less than 50% due to the

wavefront error, which is an acceptable fringe contrast for recording holograms. The minimum spatial sampling rate at the line scan camera is 8 pixels/wave of a fringe given uniform amplitude. The fringe peaks across the hologram forms a parabolic dish shaped curve instead of an ideal straight horizontal line. The dish shape of the hologram can be due to the spherical aberrations of the lenses that phase-shift retard the central rays more than the perimeter edge rays of the lens. The dish shape of the hologram can also be due to non-uniform aperture illumination of the microscope optics as well as the background illumination source to DC-offset or bias the fringe intensity on the hologram. Biasing the fringe intensity prevents low level clipping of the fringe valleys on the hologram. The minimum spatial sampling rate at the line scan camera is 16 pixels/wave of a fringe since the fringe peaks vary in a parabolic curve shape in order to accurately determine the phase-shift. The spatial sampling rate is a compromise between phase-shift resolution and path length such that the object beam completely overlaps the reference beam at the hologram image plane.

3) The distortions in the hologram are primarily due to the aberrations of the optics. The distortions are compensated for by taking a reference hologram. The reference hologram is produced by scanning the fluid-cell at constant temperature. Taking a reference hologram for every scan position occurs at constant temperature and scanning at elevated temperature occurs at a later point in time. The relative position of a point in the fluid-cell to the thermocouple in comparison to a scan point for the focused laser probe beam in the fluid-cell specimen is considered negligible in error. This is because the translation resolution of the focal point in the specimen is 0.1 μm and the grid-cell size is 625μm per side of the grid-mesh cube. Similarly, the scan point at the elevated temperature during experiments in comparison to a scan point for the reference hologram is also assumed to be a negligible error because of the translation stage resolution and beam steering mirror accuracy. The position error of the object beam focal point scan position has a negligible effect on reconstruction error because of the confocal feature that places a virtual aperture over the focal point in the fluid specimen. The reference hologram compensates for the optical aberration errors that affect the determination of a phase-shift, but then introduce a potential positional error as the scanning must track the same scan positions in the fluid-cell.

4) If the temperature gradient is high then the phase-shift is high (strong phase object with high refractive index gradient) between scan positions and if the temperature gradient is low the smallest discernable fringe-shift becomes a resolution issue.

5) There are also positioning errors associated with scanning using translation stages and the beam steering mirrors that also contribute to the overall reconstruction error. Scanning with the beam steering mirrors translates the beam across the lens and an ideal lens will provide a stationary focal point. The spherical aberrations of a lens will cause the focal point to shift as shown in figure 8.2.1 below.

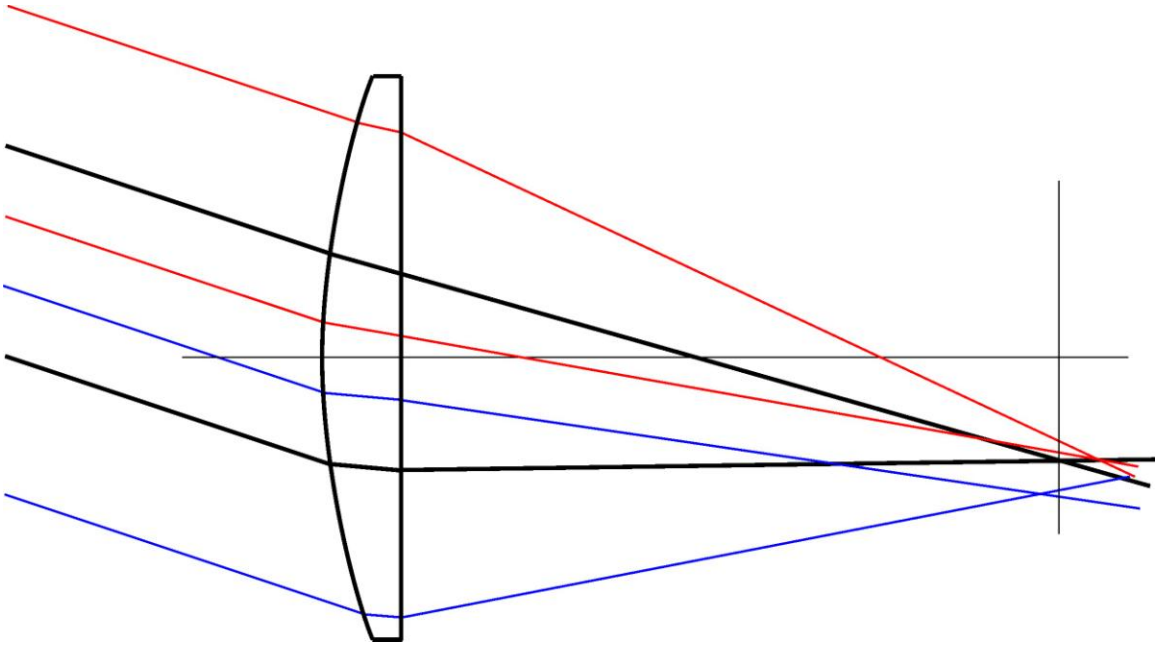

Figure 8.2.1: Focal Point Shift due to Pupil Translation on a Standard Lens

The oblique rays produce off-axis coma as the focal point varies along optical propagation axis and the focal plane. This produces error in re-collimation and stationary pupil plane relay. The optical solution is to design lenses with significantly lower spherical aberrations and coma such as the Wollaston landscape lens design or meniscus type of lens design.

8.3 Configuration Limits

The CSLH microscope requires less than one wave of phase-shift between measurement points. The reference optical path length must be measured or estimated accurately to within a fraction of a wave. If a phase-shift gradient is high (strong phase object) compared to a weak phase object then the scan position step size needs to be

reduced so that the phase-shift between sample steps is less than one wave. A weak-phase shift specimen with a phase-shift range from λ/20 to λ/1 waves between scan position steps or measurement points is required for both microscopes.

The phase-shift cannot exceed 1 fringe-shift spacing from scan point to scan point because the number of waves (*n*) cannot be determined using a single laser. A strong-phase object has a phase-shift that is represented by the following equation: $\phi = 2\pi \cdot n + \Delta\phi$ where *n*=0,1,2,3,… A weak-phase object, such as the fluid-cell in the CSLH microscope, is the case where *n*=0. The effective phase-shift resolution and range is from λ/20 to λ/1 waves between scan positions. This dynamic range of 20:1 is relatively small, but over 50 scan positions in a single axis it can be as high as 1000:1.

8.4 Characterization and Performance Specifications

The characterization specifies general operating parameters for the CSLH microscope experiments. The operational parameters are given as follows:
Ambient Room Temperature: 23.8ºC
Constant Temperature in Fluid-Cell: 30.8ºC
(Constant fluid temperature over a few hours to reach equilibrium temperature)
Heated Fluid-Cell Temperature: 31.8ºC Minimum
Heated Fluid-Cell Temperature: 38.6ºC Maximum
Temperature Range: ΔT = 38.6-31.8 = 6.8ºC
Scan Position Step Size: Δz = 625 μm/step
Probe Beam Diameter or Blur Spot Diameter in the Specimen: $D_{PSF} = 350\mu m$
(Point Spread Function (*PSF*))
Heated Fluid-Cell Scan-to-Scan Phase-Shift: Δφ = 0.88 waves Maximum
Phase-Shift to Temperature Sensitivity: $\frac{d\phi}{dT} = +1.4\, waves/°C$ for Heating Up Fluid
Phase-Shift to Temperature Sensitivity: $\frac{d\phi}{dT} = -4.2\, waves/°C$ for Cooling Down Fluid

Temperature resolution following “wily” reconstruction with Boundary Conditions (BCs) is within 1°C RMS. The “wily” reconstruction method is based on phase-shift determination using the Fourier transform method from the measured holograms.

The thermocouple measurement error is from ±0.05 to ±0.1°C. Typical thermocouple measurement error in terms of repeatability and precision is ±1°C using an industry

standard cold junction reference and an amplifier. Designing an ultra-low noise instrumentation amplifier circuit with low-pass noise filtering reduced the precision error from ±1ºC to ±0.05ºC. See the appendix for more information on thermocouple calibration and temperature measurements in the fluid-cell. Theoretically, a fringe-shift measurement resolution of $\lambda / 50\, waves$ will equate to a temperature resolution of ±0.01°C given a refractive index to phase-shift sensitivity of $\frac{dn}{d\phi} = -7.3 \times 10^{-5}\, 1/wave$ of a fringe. Reconstructing a single elevation plane in the fluid-cell requires 32 phase-shifts from 16 holograms and16 boundary conditions. Included with the measurement errors are optical aberrations, off-axis coma from BSM scanning, and alignment errors. The ±0.01°C temperature resolution due to a phase-shift degrades to approximately ±1°C when applying three-dimensional reconstruction. The RMS temperature variation from sample-to-sample appears to represent the peak error of 0.9 to 1.0°C, which converts to a refractive index error of 3.6×10^{-4}.

8.5 Vibrations and Step-Stare Frame Grabbing

Fringe stability is based on the resolution of the camera and the frame rate as a Fourier transform algorithm is used to determine the phase-shift in the hologram. A phase-shift error of a fringe line is also based on the mechanical vibrations, acoustic microphonic vibrations, and spatial beam coherence of the laser. The coherence length of the laser relates to the wavefront error, which has both a static and dynamic value. Optical resolution and line-of-sight jitter from angular deflections of the beams also affects fringe stability.

Mechanical vibrations are primarily caused by ground vibrations that are damped out by the pneumatic support legs on the Newport optics table. Other mechanical vibrations are caused by microphonics. For example, speaking in the room causes the fringes in a hologram to vibrate or jitter in some circumstances; therefore, power supplies and power supplies with fans have been placed beneath the optics table. Transformers on power supplies can produce mechanical vibrations from the current in the coils and the electrical load. The fan mounted on the laser was replaced with a low noise balanced upgrade from the Melles-Griot factory supplied fan, which is more turbulent and noisy. The microscope does not have an optical jitter sensor to correct the mechanical vibrations that affect fringe stability because: 1) a feedback controller from camera data would need to be real-time which would be a complicated and expensive controller to

design and incorporate, and 2) the feedback controller would only be responsive to low order mode shapes from a single location on the optics table. The mode shapes vary on the optics table and the vibrations travel to individual optical components at their mounting bases. The multiple modes at various locations means that the residual optical jitter from the feedback controller would be relatively high. Converting from passive vibration isolation to active vibration isolation may not significantly reduce the vibration effects on a hologram.

Both the STLH and CSLH microscopes translate the telecentric lens along the optical *z*-axis for scanning. The CSLH microscope uses beam steering mirrors to scan in the *xy*-axis as the fluid-cell specimen does not move. The STLH uses an *xy*-translation stage to move the fluid-cell specimen for scanning. A vibration induced by scan steps occurring from the *xy*-translation stages was a concern. The *z*-axis telecentric lens is stepped in 500 msec intervals. At the end of 8 steps the telecentric lens is slewed back to its start position along with the *x*-axis advancing to the new position. At the end of this stroke both the *z*-axis and *x*-axis translators are returned to their start positions while the *y*-axis translator is advanced to the new position. The effect of vibrations due to translator motion in terms of settling time was considered. Increasing the step-stare image grab loop delay from 500 msec to 1500 msec did not measurably reduce fringe line jitter and reconstruction error.

The step-stare approach to image acquisition was preferred over acquiring images at constant velocity scanning because the irradiance level at the detector is higher due to the longer exposure dwell time which improves the SNR at the camera.

9 Conclusions

The conclusions summarize the discoveries, accomplishments, and results of the research on the proof-of concept CSLH microscope.

9.1 Conclusions

The CSLH microscope is a unique design that combines the features of a confocal microscope with holography. Instead of incrementing an existing technology this research project pioneers a new methodology for non-intrusive three-dimensional measurement of the internal temperature of a fluid. The CSLH microscope proves that the temperature can be measured in three-dimensions using a fixed position non-intrusive laser and a 28° viewing angle or scan angle to probe a specimen.

The scanning geometry is limited to a 28° viewing angle, which is the angle of the cone beam that probes the specimen, instead of the typical 180° to 360° scanning angle that is used in many tomography applications. The reconstruction of the three-dimensional internal temperature of a fluid specimen, while the CSLH microscope was in transmission mode, was achieved in this research.

A hologram is a measurement of the cumulative effects of refractive index as the laser propagates through the specimen. A phase-shift in a hologram is due to a change in refractive index, which affects the wave velocity in the medium or specimen. The phase-shift is represented by a fringe translation in the hologram, which is sensitive to a change in refractive index or temperature. The refractive index is converted to temperature based on the optical properties of the fluid. Accurately determining the phase-shifts in the measured holograms and reconstructing the three-dimensional temperature was one of the main challenges of this research.

The experiments in this thesis demonstrate the ability to reconstruct a property, such as the internal temperature of a specimen, in three-dimensions given a single view port window. The optical propagation axis remaining perpendicular to the viewing window of the specimen is the single view port window. The main elements required for reconstruction are: 1) A focused probe beam, 2) Boundary conditions, and 3) The “wily” reconstruction algorithm.

The microscope shows sufficient sensitivity to a small change in temperature or a minute change in refractive index to produce a discernable fringe-shift in the hologram. The measurable temperature range is limited by a phase-shift that is less than one fringe between scan positions, which is a weak phase specimen. A weak phase specimen has

a relatively low temperature gradient, such as the heated fluid used in the CSLH experiments. Two lasers operating at slightly different wavelengths are required for the phase unwrapping of a strong phase object when the phase-shift exceeds one fringe spacing between scan positions. Phase unwrapping is not required for a weak phase object, which is the case for the CSLH microscope configuration due to the relatively low temperature gradients in the fluid-cell.

The microscope provides high resolution magnification of the needle point on the micro-probe thermocouple in imaging mode. Imaging mode is achieved by blocking out the reference beam. High quality imaging is important to produce a hologram with greater resolution to determine the fringe-shift.

The angular scanning restriction means that the CSLH microscope has applications in space experiments. Movement and vibrations of the specimen must be held to an absolute minimum for the study of heat transfer and Marangoni convection of a fluid in a micro-gravity space experiment [2,3,31,32].

Since rotational scanning is restricted to the cone angle of the focused beam within the specimen, the burden of reducing the reconstructed temperature error is placed on the reconstruction algorithm. This scanning configuration was thought impossible to solve due to an ill-posed scanning problem that produced a singular or ill-conditioned reconstruction matrix. This research proves that a solution has been found to accurately reconstruct the temperature from the phase-shifts in the holograms by using the “wily” reconstruction algorithm.

The CSLH microscope, conceived by Herring [1] was based on the Dixon [17] Confocal Scanning Laser Microscope (CSLM) which is an imaging microscope. The CSLH microscope uses optical biprisms to separate the laser source into an object beam and a reference beam which are propagated through a beam steering mirror section, an optical loop containing a specimen section, a confocal optics and projector optics section, and hologram formation to image the fringes onto a camera section. The major difference between the CSLM and the CSLH microscope is that the CSLH microscope uses wavefront splitting of the laser beam into an object and reference beam along with telecentric optics for both the specimen and the confocal pinhole apertures.

The reverse beam propagation from the output of the optical loop back through the beam steering mirror section provides a focal point that is stationary on the pinhole apertures during scanning. This worked well for scanning along the horizontal axis, but not the vertical axis. The focal point translation on the pinhole aperture is due to

alignment error of the pupil planes, which increases with scan angle or field angle off the optical axis centerline. The *xy*-axis galvanometer beam steering mirrors are separate units that are spaced about 400 mm from one another with a periscope lens in between them in order to minimize beam walk on the lenses and mirrors during scanning. This configuration allows for accurate pupil alignment and negligible focal point translation on the confocal pinhole apertures in one axis, but not both axes.

A Zemax simulation using standard commercial lenses showed the pupil plane offset due to a ±5° scan angle on the symmetrical optics periscope lens, which was unanticipated. The Zemax simulations showed no movement of the focal point on the pinhole apertures but the experiments did. The output pupil plane translates along the optical propagation axis and tilts as a function of field angle or scan angle of the beam. The translation and tilt of the pupil plane causes the focal point to move on the pinhole apertures during scanning.

Lenses such as the telecentric lens, confocal optics lens, periscope lens, wavefront splitter, beam expander, and beam convergence prism were individually designed in sequential mode using Zemax. The CSLH microscope is a combination of all the lenses and was simulated with Zemax in non-sequential mode. Non-sequential mode allows reverse ray propagation through lenses and optical components, which is important for the beam steering mirror section where reverse beam propagation occurs. The non-sequential mode simulations showed minor aberrations at the focal points of the beam as well as negligible movement of the focal point at the pinhole apertures, caused by tilting the beam steering mirrors. Negligible translation of the focal point at the pinhole apertures was due to the custom designed periscope and telecentric lenses, along with the ideal alignment of the optical components, which were used in the Zemax simulation. Standard commercial lenses were used for the periscope optics and the telecentric lenses in the experiments, which produced a noticeable pupil plane shift and focal point translation on the pinhole apertures when scanning.

A silicone oil based fluid specimen with known optical properties was used in the experiments. The homogeneous fluid provided a means to analyze the performance of the microscope by accurately determining the three-dimensional reconstructed temperature of a heated fluid to compare to thermocouple measurements. A point source heater with steady-state heat transfer and minimal convection currents was configured to produce constant thermal gradients in the fluid-cell. The temperature

difference of 6° C from the heater to the outside wall temperature provided constant thermal gradients in the fluid-cell for a 20 minute time period.

I derived a unique “wily” reconstruction algorithm from the scanned holograms for the microscope given a restricted scanning angle. Tomographic reconstruction typically involves rotational scanning, but in this configuration the focal point of the object beam is raster scanned in three-dimensions within the specimen instead. A three-dimensional computational domain grid-mesh is specified for the specimen where phase-shift, index-of-refraction, and temperature are assumed constant for each computational cell within the grid-mesh. The reconstruction error is primarily due to the boundary condition error and phase-shift measurement error from the holograms using the Fourier Transform Method.

The primary trade-off relationship to consider when seeking optimal results is the resolution or blur spot size of the object beam focal point in the specimen and the reconstruction error. As the cone angle of the beam is increased the reconstruction error will decrease because the marginal rays will subtend more grid-cells within the computational domain volume. The increased cone angle of the beam will increase optical aberrations however, as well as the blur spot size of the focal point in the specimen.

The secondary trade-off to consider is the spatial resolution of a fringe at the camera and the wavefront error affecting the hologram. As the beam convergence angle is decreased the fringe spacing increases and the distance to the camera also increases so that the beams can completely overlap one another at the camera. Increased fringe spacing increases the spatial resolution of a fringe, which will decrease the error in determining a fringe-shift or phase-shift. As the path length to the camera increases so will the wavefront error increase, which will decrease the fringe contrast at the hologram.

Beam convergence is accomplished with a 0.5° or 1.0°optical wedge, or a 10° Fresnel biprism in these experiments. The best results were obtained using a 0.5° optical wedge, which set a 500 cm path length to converge and completely overlap the beams at the camera.

A reference hologram compensated the effect of optical aberrations and wavefront error on the hologram. The reference hologram provides a measurement of the optical aberrations and wavefront error with the fluid-cell at constant room temperature since the optical aberrations are constant for any temperature of the fluid-cell.

The CSLH microscope combines many physics and engineering disciplines such as traditional ray optics, wave optics, interferometry and holography, sensors and sensor electronics, feedback controls, sampled data digital signal processing, mechanical design, vibration isolation, data acquisition and computer control, and digital image processing. This proof-of-concept CSLH microscope opens up possibilities for extended research in refractive index measurement and three-dimensional reconstruction along with the applications proposed in the following section.

10 Recommendations and Applications

These recommendations are a review of how methods could be improved given increased knowledge and the accomplishments within this research. The applications are a examination of possible uses of the CSLH microscope in fluid science studies and practical applications in society.

10.1 Recommended Changes to Improve the Microscope

The recommended improvements to the CSLH microscope are:

1) Increased vibration isolation to stabilize the fringes to within < 3º phase-shift.
2) Improve peak-to-valley fringe uniformity in the hologram by designing an optical phase corrector plate to compensate for the optical aberrations produced by the beam expander, telecentric lens, confocal lens, and periscope lenses.
3) More accurately determine the reference Optical Path Length (*OPL*) through the specimen with either a frequency counter or a mathematical estimator using ray tracing that utilizes as many boundary condition cells as possible.
4) Isolate the spatial frequency of the fringes using an optimized band-pass filter.
5) Obtain a more (radiometrically) sensitive line scan camera that does not require a uniform background illumination source.
6) Decrease the 150 μm radius probe beam size in the specimen by using custom precision lenses in the telecentric and confocal lenses.
7) Place a half-wave plate and a polarizing lens in the optical loop to eliminate reverse beam propagation in the optical loop, which will also eliminate the additional images at the confocal lens.
8) Flush mount thermocouples to the walls of the fluid-cell to minimize boundary condition intrusion.

The CSLH microscope is particularly sensitive to pupil placement since there are both forward and reverse propagating beams in the beam steering mirror section. A slight misalignment of the pupil planes through the optical loop and the periscope lenses up to the confocal lens means that the focal point on the confocal apertures will move during scanning. A method to establish a coincident pupil plane on the second cube beam splitter of the optical loop is shown in figure 10.1.1 below:

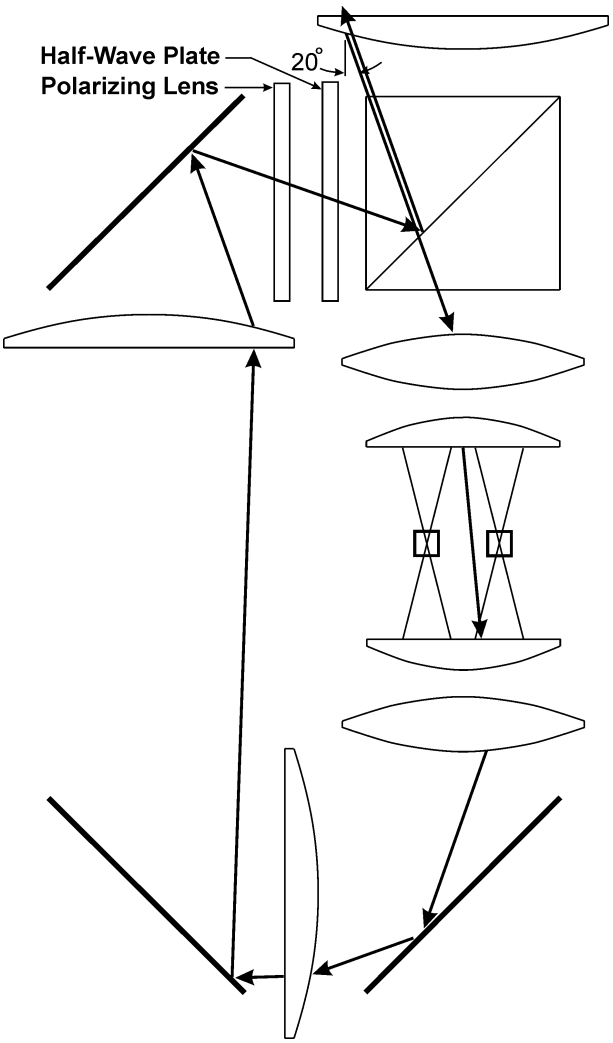

Figure 10.1.1: Suggested Improvements to the Optical Loop

The periscope lens was re-oriented by placing a folding mirror between the two lenses. This provided a shorter pupil distance that minimizes beam translation of the outgoing beam relative to the incoming beam. The ray tracing shows the pupil position for the chief ray where the marginal rays may extend beyond the edges of the optical components. If the beam steering mirror is tilted by 10° however, it produces a 20° incident beam into the specimen for example, which more clearly shows the effect of pupil plane misalignment or alignment error at the optical loop input-output. Given an 80 mm focal length of the telecentric lens the beam translation in the specimen would be ±30 mm. The required amount is ±1.6 mm or a ±1.1° scan angle in the specimen. The pupil plane distances are relatively short in relation to the focal length of the periscope lens, which is larger than the telecentric lens. A half-waveplate and polarizing lens is inserted into the optical loop to prevent reverse beam propagation. The forward propagation is in the direction of the arrows in the diagram. Reverse beam propagation

produces four beams at the projector lens instead of the desired two beams. The introduction of the half-wave plate and the polarizing lens introduces some transmission beam loss or beam attenuation, which affects camera detection and reduces SNR. This signal loss or SNR reduction is acceptable for hologram detection at the line scan camera.

One of the issues discovered with the Dixon CSLM design [17] was that a stationary focal point on the confocal apertures was possible in one axis of the scan mirror *xy*-axis but not both. This is because the beam steering mirrors establish a pupil plane for each axis of rotation and only one of the conjugate pupil planes can be placed at the entrance of the confocal lens using the periscope lens. Both *xy*-axis pupil planes cannot be co-located at the confocal lens since the distance from the steering mirror to the respective periscope lens establishes the entrance and exit pupil distance. The focal point at the confocal lens pinhole aperture can therefore remain stationary for only one beam steering mirror scanning axis. The solution is to translate the confocal pinhole apertures in the *y*-axis. The CSLH microscope requires only one scan step in the *x*-axis for upper and lower scanning lines down the fluid-cell in order to provide sufficient holograms for reconstruction. A single scan step of 1250 μm in the fluid-cell along the *x*-axis provides minimal translation of the focal point on the confocal apertures since the scanning is not over the 5000 μm width of the fluid-cell.

The final assessment of the CSLH microscope design was to understand why the focal points moved on the pinhole apertures of the confocal lenses since they are supposed to be stationary. The optical loop was carefully aligned as accurately as possible so that the entrance and exit pupils were co-located and stationary at the cube beam splitter of the optical loop. The telecentric lens was designed with an entrance pupil 30 mm to the first bi-convex lens. A 30 mm entrance pupil is too short because of component separation on rail carriers and micrometer translation stages. The periscope lens consisting of two 200 mm focal length plano-convex lenses was assessed with an independent Zemax simulation. The Melles-Griot 01LPX281 200 mm FL x 130 mm diameter lenses were given an entrance pupil of 150 mm, which represents the distance of the beam steering mirror to the lens. The exit pupil was found to be between 195 to 220 mm depending on the selected marginal ray. This shifting exit pupil was from a 5° incident field angle and the effects of geometric optics caused the exit pupil to shift +57.5 mm from the 150 mm entrance pupil distance. Zemax also shows the exit pupil to extend over 25 mm along the optical propagation *z*-axis from the marginal ray crossing

difference even though relatively long focal length lenses are used. The Zemax periscope lens design is shown in figure 10.1.2 below:

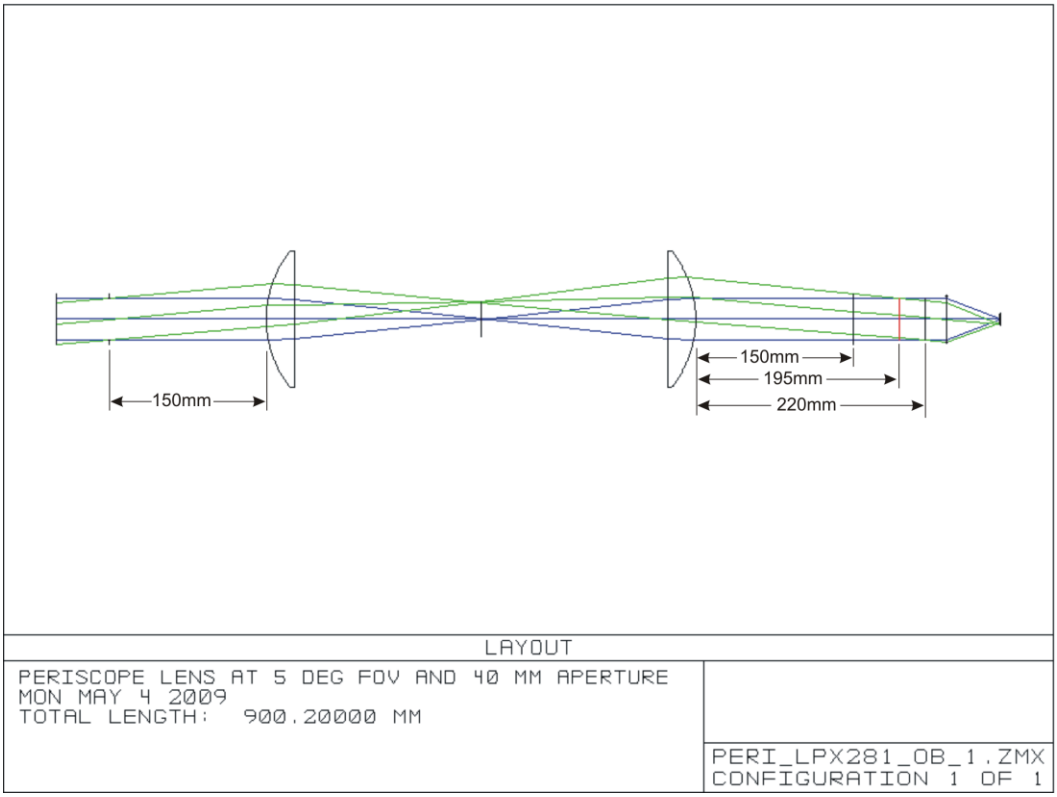

Figure 10.1.2: Zemax Layout for Periscope Lens with 5° Field Angle and On-Axis

This shift in pupil plane distance from entrance to exit pupil presents a problem for the forward and back propagating beams in the beam steering mirror section. A shift in the pupil plane will cause a slight shift in the focal point of the periscope lenses as well as the confocal lens. A more stable relatively fixed exit pupil plane could be achieved by designing a more complex periscope lens with additional lenses. A more complex periscope lens design would also be more difficult to align having many more degrees-of-freedom.

At the time of designing the optics with Zemax the CSLH microscope simulation showed no problems with scanning ±2° in the *x*-axis using non-sequential ray tracing mode. There were problems with ray reflection in the cube beam splitters and the polarizing lenses, but these reflections did not significantly affect the hologram. Zemax did not simulate scanning in the *y*-axis due to vignetting conflicts. Attention to pupil planes was not considered by Zemax experts who provided assistance with modeling and design at the early stages of the research. The design was assumed to work as theoretically proposed as long as the back propagating beam angles matched the

forward propagating beam angles at the entrance and exit of the optical loop. The pupil planes must be stationary and coincident however, for the forward and reverse propagating beam interfaces. The A.E. Dixon Confocal Scanning Laser Microscope (CSLM) [17] has a similar optical loop and beam steering mirror section with beam splitting to the confocal lens optics section. Dixon's CSLM publication in "Nature" points out the critical entrance and exit pupil plane alignment for the optical loop. Dixon states that the optical loop entrance and exit pupils are at the same position and stationary during scanning. Dixon also states that the first periscope lens in the beam steering mirror section is used to place a stationary pupil on the second beam steering mirror and the second periscope lens in the beam steering mirror section places a pupil plane at the focusing lens (or the telecentric lens for the CSLH microscope) in the optical loop. Even with the higher quality optics of the periscope lenses used on the CSLH microscope, the non-equal entrance to exit pupil distances was present. Correction would require a periscope lens to have the same entrance and exit pupil distances along with high quality optics to minimize the shift in exit pupil plane across the aperture from chief rays to marginal rays. The solution for the CSLH microscope setup was to establish a stationary focal point on the confocal pinhole apertures for *x*-axis scanning and then translate the pinhole apertures in the *y*-axis to track the vertical movement of the focal point on the pinhole aperture. This configuration produced acceptable holograms at the camera.

Contrary to the Dixon CSLM design the CSLH microscope uses a retro-reflector instead of a mirror in reflection mode configuration. A mirror reflects back a negative angle that will be opposite in direction to the incident ray. The negative angle reverse propagating beam will cause problems when attempting to maintain a stationary focal point on the confocal lens pinhole apertures.

The CSLH microscope in reflection mode operation is shown in figure 10.1.3 below:

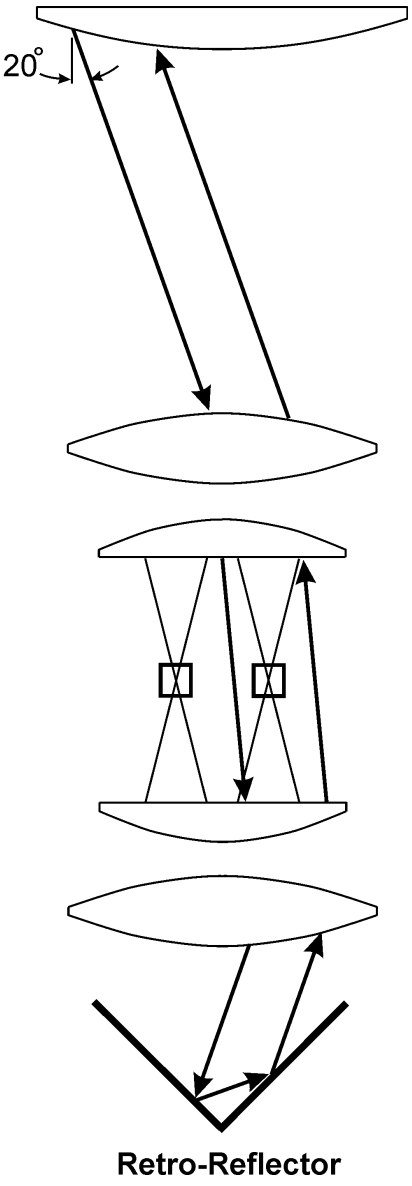

Figure 10.1.3: CSLH Microscope in Reflection Mode with a Retro-Reflector

The ray tracing diagram shows an incident beam refracting through the telecentric lens and reflecting back using a retro-reflector. The entrance and exit angles to the telecentric lens are the same, which is desired. Reflection mode will also work with a mirror placed near the focal point of the object and reference beams in the specimen. In this experiment the mirror would have to be placed inside the fluid-cell then have to be translated along the optical propagation *z*-axis for three-dimensional scanning. The displacement of the beam by the retro-reflector shifts the output pupil, which could also present some problems with maintaining a stationary focal point at the pinhole apertures.

10.2 Applications for the CSLH Microscope

Possible applications for the CSLH microscope are listed below. The experiments and research of this thesis did not venture beyond proof-of-concept principal so further work is needed to determine the feasibility, effectiveness, and cost of these applications.

1) Space based microgravity fluid dynamics experiments where the specimen cannot be moved or the scan mechanism rotated [2,3,31,32].
2) Transfer from optical microscope to acoustic wave ultrasound microscope [35].
3) Three-dimensional wind tunnel flow measurements given side-to-side view ports.
4) Determining atmospheric turbulence at various altitudes for observatory telescopes with adaptive optics using laser guide stars.
5) Low reconstruction error for limited viewing angle tomography and CAT scans.
6) Three-dimensional refractometer to measure composition and temperature.
7) Determining sugar concentration (Brix level) profiles in a grape to better understand development and maturation for harvesting in wine production.
8) Determining coherence from a fluoresced specimen and beam scattering.
9) Correlation of coherence and fringe contrast to wavefront error.
10) In transmission mode the microscope can be used to measure the specimen's thickness given the refractive index.
11) In reflection mode the microscope can be used as a profilometer.
12) Measuring the internal temperature of a flame.
13) Sensitivity and characterization of biological specimens for science and medicine.
14) Weather conditions measurement at various altitudes.

In medical applications CAT scanning is not considered fully reliable and surgery is not ordered solely based on CAT images. CAT scanning can either introduce artifacts that are not present or remove an artifact that that is important for an accurate diagnosis. The rotations of reference coordinate frames and superimposing images by filtered back-plane projection can present a challenge to the reconstruction algorithm. The high-frequency detail found in the edges of an object can be lost or distorted due to the sampling resolution on the detector, phase-shift across the spectral band, and digital signal processing. The signal processing consists of Fourier Transforms, Fourier Transform windows, and anti-aliasing low-pass filters. The perspective effect along the edges can be produced, but sufficient error exists in the reconstruction algorithm that

medical diagnosis can be in error. Surgery can prove an error in the CAT scan when nothing is found in the patient or when something is found in the patient that the CAT scan missed. The predominant error of CAT scanning is producing artifacts that are not actually present. The “wily’ matrix algorithm may be able to reduce the image processing errors found in tomography.

10.3 Further Research and Exploration of the CSLH Microscope

Further research addresses technical issues that were discovered and unresolved issues. Exploration of the CSLH microscope provides suggested continuation and experiments for the microscope. Fundamental insight into other fields is accomplished by applications where this microscope can provide a measurement that is not otherwise possible.

Experiments using various specimens to characterize the CSLH microscope are suggested below:

1) Determination of the microscope phenomenology, sensitivity, and diagnostics capability of various specimens such as fluids, solids, plasmas, and biological samples.
2) Measurement of the coherence found in fluorescent objects. In general, fluorescence is considered incoherent emission and to measure the amount of coherence would be useful for biological research.
3) Measurement of refractive index in protein and living cells.

11 References

1) Herring, R.A., “Confocal scanning laser holography and an associated microscope: A proposal”, *Optik*, Vol 105, No 2, pgs 65-68, April 1997.

2) Jacquemin, P.B., McLeod, R., Laurin, D., Lai, S., and Herring, R.A., “Design of a confocal holography microscope for three-dimensional temperature measurements of fluids in microgravity”, *Microgravity Science and Technology*, Vol 17-4, pgs 36-40, 2005.

3) Jacquemin, P.B., Laurin, D., Atalick, S., McLeod, R., and Herring, R.A., “Non-intrusive three-dimensional temperature and composition measurements inside fluid cells in microgravity using a confocal holography microscope”, *Acta-Astronautica*, Vol 60, Issues 8-9, pgs 723-727, April-May 2007.

4) McLeod, R.A., Jacquemin, P.B., Lai, S., and Herring, R.A., “Confocal holography: Improved resolution through object scanning”, Honolulu, HI, *Proceedings of Microscopy & Microanalysis* Vol 11 (Suppl 2), pgs 784-785, August 2005.

5) Lai, S., McLeod, R.A., Jacquemin, P.B., Atalick, S., and Herring, R.A., “An algorithm for 3-D refractive index measurement in holographic confocal microscopy”, *Ultra-Microscopy*, Vol 107, Issues 2-3, pgs 196-201, doi:10.1016/j.ultramic.2006.07.002, July 2006.

6) Sheard, S., Suhara, T., Nishihara, H., "Integrated-optic implemenation of a confocal scanning optical microscope", *Journal of Lightwave Technology*, Vol 11, Issue 8, pgs 1400-1403, doi:10.1109/50.254101, August 1993.

7) Kak, A.C. and Slaney, M., “Principles of computerized tomographic imaging”, *IEEE Press*, 1988.

8) Gabor, D., *Nature*, Vol 161:777, 1948.

9) Gabor, D., “Microscopy by Reconstructed Wavefronts: I”, *Proceedings of the Royal Society of London*, Section A, Vol 197(1051), pgs 454-487, July 1949.

10) Gabor, D., “Microscopy by Reconstructed Wavefronts: II”, *Proceedings of the Royal Society of London*, Section B, Vol 64(6), pgs 449-469, June 1951.

11) An Interview with “The Father of Holography: D. Gabor”, *In: Optical Spectra*, pg 32, Oct 1970.

12) Rogers, Gordon L., “Gabor diffraction microscopy: The hologram as a generalized zone-plate”, *Nature*, Vol 166, pgs 237-238, 1950.

13) Rogers, Gordon L., “Experiments in diffraction microscopy”, *Proceedings of the Royal Society (Edinburgh)*, Vol A63, pg 193, 1952.
14) Zernike, F., “Phase-contrast: A new method for microscope observation of transparent objects. Part I”, *Physica*, Vol 9, pgs 686-698, 1942.
15) Zernike, F., “Phase-contrast: A new method for microscope observation of transparent objects. Part II”, *Physica*, Vol 9, pgs 974-986, 1942.
16) Zernike, F., “How I discovered phase contrast”, *Science*, Vol 121, pgs 345-349, 1955.
17) Dixon, A.E., Damaskinos, S., and Atkinson, M.R., “A scanning confocal microscope for transmission and reflection imaging”, *Nature*, Vol 351, pgs 551-553, June 1991.
18) Francon, M., “Holography”, *Academic Press*, 1974.
19) Ostrovsky, Y.I. and Leib, G., “Holography and Its Application”, *Mir Publishers*, Moscow, 1977.
20) Tonomura, A., “Electron Holography: Progress in Optics”, Vol. XXIII, pg183, Ed. E. Wolf, North-Holland, Amsterdam, 1986.
21) Tonomura, A., “Electron Holography”, *Springer-Verlag Series in Optical Sciences*, Vol 70, Springer-Verlag, Berlin 1993.
22) Urata, Kenya, Ishizuka, Kazuo, Tanji, Takayoshi, and Tonomura, Akira, “An Application of Digital Filtering in Electron Holography at Atomic Resolution”, *Journal of Electron Microscopy* 42(2): pgs. 88-93, 1993.
23) Lai, G., Hirayama, T., Ishizuka, K., Tanji, T., and Tonomura, A., “Three-dimensional reconstruction of electric-potential distribution in electron-holographic interferometry”, *Applied Optics*, Vol 33, No 5, pgs 829-833, February 1994.
24) Lichte, Hannes, “Optimum focus for taking electron holograms”. *Ultramicroscopy* 38(1): 13-22. doi:10.1016/0304-3991(91)90105-F, 1991.
25) Lichte, Hannes, “Electron holography: performance and performance limits”, *EMC 2008: 14th European Microscopy Congress 1-5 September 2008*, Aachen, Germany, Springer Berlin Heidelberg, pgs. 265-266 doi:10.1007/978-3-540-85156-1.
26) Rowley, P. D., “Quantitative interpretation of three-dimensional weakly refractive phase objects using holographic interferometry”, Journal of the Optical Society of America, Vol 59B, pgs 1496-1498, November 1969.
27) Xu, X. F., Cai, L. Z., Wang, Y. R., Meng, X. F., Zhang, H., Dong, G. Y., and Shen X. X., “Blind phase shift extraction and wavefront retrieval by two-frame phase-shifting interferometry with an unknown phase shift”, *Optics Communications*, *Elsevier*,

www.elsevier.com/locate/optcom, doi:10.1016/j.optcom.2006.12.033, December 2006.

28) Abe, Y. and Iwasaki, I., “Observation of a vapor bubble of non-azeotropic binary mixture in microgravity with a two-wavelength interferometer”, *Proceedings of the 5th ASME/JSME Joint Thermal Engineering Conference*, San Diego, Jul. 1999, AJTE99-6418.

29) Antar, B.N. and Nuotio-Antar, V.S., “Fundamentals of low gravity fluid dynamics and heat transfer”, *CRC press Boca Raton*, pub text 1993, 1st ed 1994.

30) Abbott, M.B. and Basco, D.R., “Computational fluid dynamics: An introduction for engineers”, *Longman Scientific & Technical* and co-publisher *John Wiley & Sons*, 1989.

31) Herring, R.A. and Laurin D., “A confocal holography microscope for microgravity experiments”, *World Space Congress*, Houston, Texas, IAC-02-J.5.01, October 2002.

32) Tryggvason, B.V., Redden, R.F., Herring, R. A., Duval, W.M.B., Smith, R.W., Rezkellah, K.S., and Varma, S., “The vibration environment on the international space station: Its significance to fluid based experiments”, *Acta Astronautica* vol. 48, pg 59, March 2001.

33) McLeod, R.A., Jacquemin, P.B., Laurin, D., and Herring, R.A., “A viable confocal holography microscope and method for high-level research measurements”, Savannah, GA, *Microscopy and Microanalysis* 10 (Suppl 2): 1246-1247CD Cambridge University Press, Microscopy *Society of America* doi:10.1017/S1431927604885210, pg 1246, August 2004.

34) McLeod, R.A., Jacquemin, P.B., Lai, S., and Herring, R.A., “Confocal holography: A tool for non-invasive internal measurement”, *Microscopy Today* 13, pgs 30-31, January 2005.

35) Herring, R.A., Jacquemin, P.B., Sawicka, B.D., Atalick, S., “Developing a confocal acoustic holography microscope for non-invasive 3D temperature and composition measurements”, *Ultramicroscopy* vol. 109, pgs. 830-836, doi:10.1016/j.ultramic.2009.03.027, March 2009.

36) Atalick, S. “The confocal scanning laser holography microscope”, Coop Student Report to the Canadian Space Agency, May 2002.

37) Tieng, S. and Chen H., "Holographic tomography by SART and it's application to reconstruction of 3D temperature distribution", *Heat and Mass Transfer*, Vol 26, Number 1, pgs 49-56, Jan 1991, doi:10.1007/BF01589903

38) Rantala, M., Vanska, S., Jarvenpaa, S., Kalke, M., Lassas, M., Moberg, J., Siltanen, S., "Wavelet-based reconstruction for limited-angle X-ray tomography", *IEEE Transactions on Medical Imaging*, Vol 25, Issue 2, pgs 210-217, Feb. 2006, doi:10.1109/TMI.2005.862206

39) Verhoeven, Dean, "Limited-data computed tomography algorithms for the physical sciences", *Applied Optics*, Vol 32, Issue 20, pgs 3736-3754, 1993 doi:10.1364/AO.32.003736

40) Hiroyuki, Kudo, Tsuneo, Saito, "A tomographic image reconstruction from limited view angle projection data", *Systems and Computers in Japan*, Vol 19, Issue 7, pgs 56-64, Sep. 2007, doi:10.1002/scj.4690190706

41) Hecht, E., Zajac, A. “Optics 4th Edition”, *Addison-Wesley Publishing*, pgs 564-571, 2002

12 Appendix

TABLE OF CONTENTS

PAGE NUMBER

Digital Band-Pass Filter (BPF) Algorithms to Improve Phase-Shift Detection

The fringes on a hologram have constant spacing that produces a constant spatial frequency. A Band-Pass Filter (BPF) can reduce the interference of other frequencies that could be introduced by Fresnel near-field sources, diffraction far-field sources, internal reflections in optical components, and optical aberrations. A BPF isolates the frequency of interest and attenuates the out-of-band interfering frequencies. A feature of the BPF is the introduction of minimal phase-shift and sometimes no phase-shift at the band-pass frequency. A second-order filter is evaluated since it offers higher roll-off slope than a first-order filter and this will attenuate the signal at -12dB/octave. This means that a frequency that is 2x the BP frequency and a frequency that is 1/2x the BP frequency will be attenuated by -12dB or x1/16 reduction at 1 octave band on either side of the band-pass frequency. The digital BPF exhibits different characteristics from low frequency to high frequency attenuation due to the conversion from a continuous system to a sampled data system.

The conditions for evaluating various BPF configurations are as follows:
Low Frequency: 16 samples/wave
BP Frequency: 8 samples/wave
High Frequency: 4 samples/wave
Nyquist Frequency Limit: 2 samples/wave

The 2x Over Sampling using Linear Interpolation producing:
Low Frequency: 32 samples/wave
BP Frequency: 16 samples/wave
High Frequency: 8 samples/wave
Nyquist Frequency Limit: 2 samples/wave

The attenuation gain (A_p) to dB relationship is given by:

$$dB = 10\log(A_p) = 10\log(A_x^2) = 20\log(A_x)$$

Power Attenuation or Intensity Gain: $A_p = A_x^2 = 10^{dB/10} = 10^{-12/10} = 1/16$

Amplitude Attenuation or Gain: $A_x = \frac{X(s)}{X_i(s)} = \sqrt{A_p}$

A 4 samples/cycle waveform with no phase-shift is shown in the figure below:

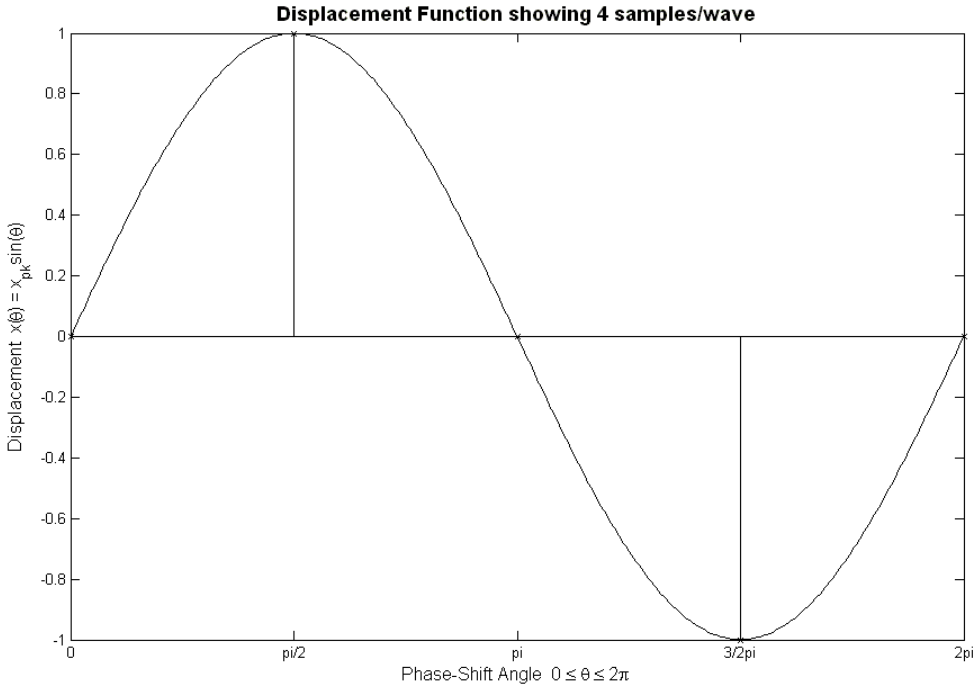

Figure 1 Waveform at 4 samples/wave Sampling and No Phase-Shift

The same sampled waveform with 20º phase-shift is shown in the figure below:

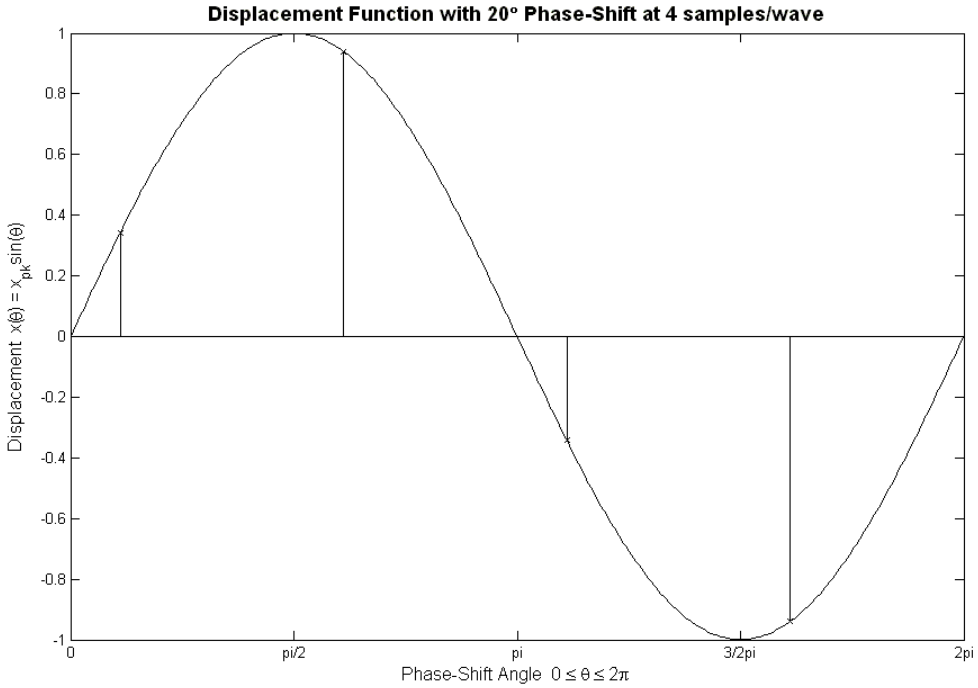

Figure 2 Waveform at 4 samples/wave Sampling and 20º Phase-Shift

Now there are only 4 sample points along the wave instead of 5 sample points for the zero phase-shift case. This represents the sparse sampling condition at high frequency where the velocity error can be determined from a reference waveform. The reference waveform is given as follows:

Displacement: $x_{ref}(t) = x_{pk}\sin(2\pi f \cdot t + \phi)$

Velocity: $\dot{x}_{ref}(t) = 2\pi f x_{pk}\cos(2\pi f \cdot t + \phi)$

Given:

Wave Peak: $x_{pk} = 1$

Frequency: $f = 25$ cycles/sec

Sample Time: $\Delta t = \frac{1}{4f} = 0.01$ sec/sample or mm/sample

Phase-Shift Angle: ϕ

The velocity is the derivative of the displacement function is shown in the figure below:

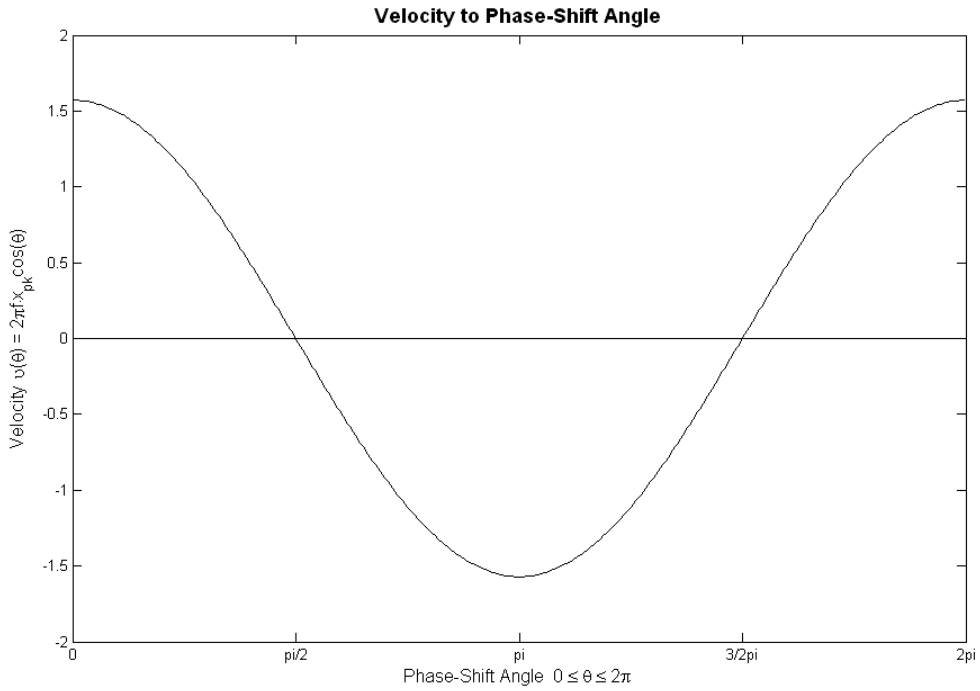

Figure 3 Velocity as Derived from the Displacement Function

The velocity is phase-shifted from the displacement function by 90º.

The finite difference equations for velocity and acceleration are derived from either a polynomial path function or the bi-linear z-transform.

The polynomial path function is given by:

$$x(t) = a_1 + a_2 x(t) + a_3 x(t)^2 + a_4 x(t)^3 + a_5 x(t)^4 + \cdots$$

The velocity $\dot{x}(t)$ is the first derivative of $x(t)$.

$$\dot{x}(t) = a_2 + 2a_3 x(t) + 3a_4 x(t)^2 + 4a_5 x(t)^3 + \cdots$$

The acceleration $\ddot{x}(t)$ is the second derivative of $x(t)$.

$$\ddot{x}(t) = 2a_3 + 6a_4 x(t) + 12a_5 x(t)^2 + \cdots$$

The Bi-Linear z-Transform is given by: $s = \frac{n}{\Delta t}\frac{1 - z^{-1}}{1 + z^{-1}}\frac{X(z)}{X(s)}$ where

$n = 1, \sqrt{2}, 2$ depending on the method of derivation from sampling theory.

The finite difference equations are derived from first principles mathematics and are shown as:

Velocity derived by First-Difference Equation:

$$\dot{x}(t) = \frac{1}{\Delta t}(x(t) - x(t - \Delta t))$$

Velocity derived from the z-Transform or the Path Function that is Second-Order Central-Difference Accurate:

$$\dot{x}(t) = \frac{1}{2 \cdot \Delta t}(x(t) - x(t - 2 \cdot \Delta t))$$

Velocity derived from a Second-Order Finite Difference or the Second-Order Path Function (3-terms):

$$\dot{x}(t) = \frac{1}{2 \cdot \Delta t}(3x(t) - 4x(t - \Delta t) + x(t - 2 \cdot \Delta t))$$

Velocity derived from a Third-Order Path Function

$$\dot{x}(t) = \frac{1}{6 \cdot \Delta t}(11x(t) - 18x(t - \Delta t) + 9x(t - 2 \cdot \Delta t) - 2x(t - 3 \cdot \Delta t))$$

Velocity derived from a Fourth-Order Path Function

$$\dot{x}(t) = \frac{1}{12 \cdot \Delta t}(25x(t) - 48x(t - \Delta t) + 36x(t - 2 \cdot \Delta t) - 16x(t - 3 \cdot \Delta t) + 3x(t - 4 \cdot \Delta t))$$

Substituting for $x(t)$ in the finite-difference equations

$$x(t) = \sin(2\pi f \cdot t + \phi)$$

Then the velocity error for all the finite-difference equations is

$$\Delta \upsilon = \left| \dot{x}(t) - \dot{x}_{ref}(t) \right|$$

The velocity error is shown in the figure below:

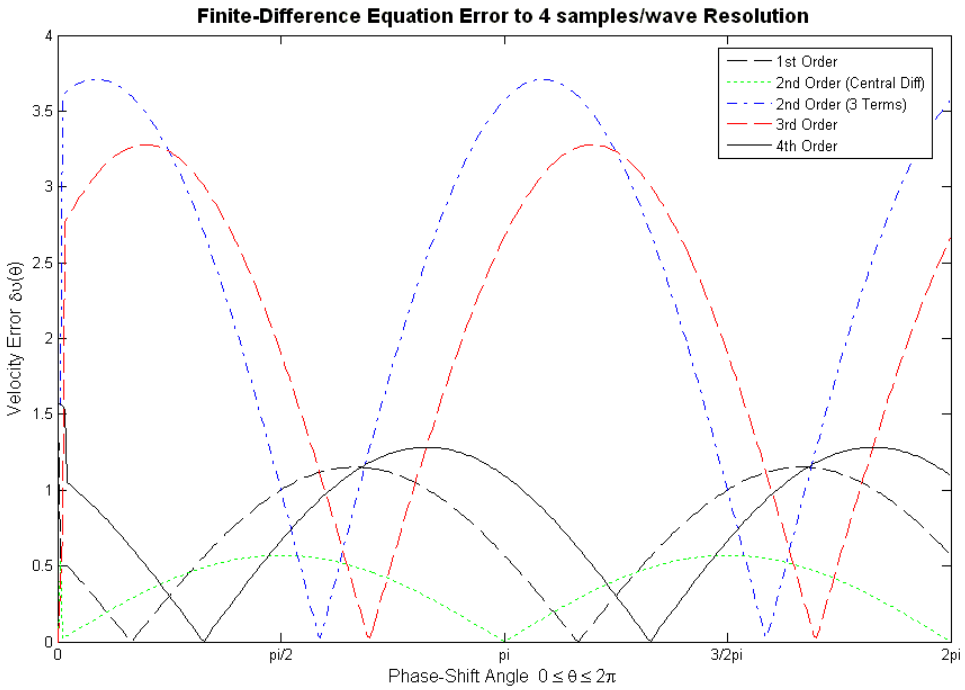

Figure 4 Velocity Error at 4 samples/cycle of the Waveform

The filters show a transient response and convergence to the steady-state conditions from the input waveform. The velocity error peaks is due to the phase-shift angle as the input waveform is sampled. The peaks vary radically from function to function. The

lowest velocity error occurs from the second-order central difference equation, which is derived from a second-order path function or the bi-linear z-transformation. This is the Second-Order Central Difference equation:

$\dot{x}(t) = \frac{1}{2 \cdot \Delta t}(x(t) - x(t - 2 \cdot \Delta t))$ which will be used for evaluating different BPF formulations and designs.

Let $n = 1$ octave-band

Low Frequency: $\omega_{low} = 2\pi f_{low}$

Band-pass (BP) Frequency: $\omega_{bp} = 2\pi f_{bp}$

High Frequency: $\omega_{high} = 2\pi f_{high}$

$$\frac{f_{bp}}{f_{low}} = \frac{f_{high}}{f_{bp}} = 2^n = 2$$

$$\frac{\omega_{bp}}{\omega_{low}} = \frac{\omega_{high}}{\omega_{bp}} = 2$$

The bi-linear z-transform is the standard method used to convert from continuous s-frequency domain to discrete sampling time domain. This is handy since filters are typically derived and expressed in the continuous frequency domain.

The continuous BPF transfer function is given as:

$$\frac{X(s)}{X_i(s)} = \frac{2\zeta\omega_n s}{s^2 + 2\zeta\omega_n s + \omega_n^2} = \frac{2\zeta(\omega/\omega_n)}{\left(1-(\omega/\omega_n)^2\right)^2 + \left(2\zeta(\omega/\omega_n)\right)^2}\left(2\zeta(\omega/\omega_n) + j\left(1-(\omega/\omega_n)^2\right)\right)$$

Given $s = j\omega$

Phase-Shift $\phi(\omega) = \tan^{-1}\left(\frac{1-(\omega/\omega_n)^2}{2\zeta(\omega/\omega_n)}\right)$

At the BP frequency $\omega_{bp} = \omega_n = \omega$

Phase-Shift $\phi(\omega_{bp}) = 0$

So, the BPF introduces no phase-shift at the BP frequency.

Amplitude Attenuation or Gain:

$$A_x = \left| \frac{X(s)}{X_i(s)} \right| = \frac{2\zeta(\omega/\omega_n)}{\sqrt{\left(1-(\omega/\omega_n)^2\right)^2 + (2\zeta(\omega/\omega_n))^2}}$$

At BP Frequency: $\omega/\omega_n = \omega_{bp}/\omega_{bp} = 1$

$A_x = 1$ for any value of ζ

Power Attenuation or Intensity Gain: $A_p = A_x^2 = 1$

At Low Frequency: $\omega/\omega_n = \omega_{low}/\omega_{bp} = 1/2$

Given: $\zeta = 1/2$

$$A_x = \frac{1}{\sqrt{13}/2} = \frac{1}{1.80}$$

Power Attenuation or Intensity Gain: $A_p = A_x^2 = \frac{1}{13/4} = \frac{1}{3.25}$

Also

$$s^2 X(s) + 2\zeta\omega_n s X(s) + \omega_n^2 X(s) = 2\zeta\omega_n s X_i(s)$$

Where:

$X(s)$ Displacement Response

$X_i(s)$ Input (Forcing Function) Displacement

$\zeta = 1/2$ Damping Factor where under-damping will increase the out-of-band frequency rejection. Range is $0 \le \zeta \le 1$

$\omega_n = 2\pi \cdot f_{bpf}$ Natural Frequency

$f_{bpf} = 12.5$ cycles/sec or cycles/mm BP frequency that represents 8 samples/wave at 1x Sampling Rate

Converting from the continuous frequency domain to differential equations is straightforward by substituting $s^2 X(s) = \ddot{x}$, $sX(s) = \dot{x}$, and $X(s) = x$.

This BPF equation is as follows:

$$\ddot{x} + 2\zeta\omega_n \dot{x} + \omega_n^2 x = 2\zeta\omega_n \dot{x}_i$$

The differential equation is represented by the finite difference of the discrete sampled time data. Substituting the bi-linear z-transform into the continuous BPF transfer function produces the following terms:

$$x = x(t) + 2x(t-\Delta t) + x(t-2\cdot\Delta t) = (1+z^{-1})^2 X(z)$$

$$\dot{x} = \frac{n}{\Delta t}(x(t) - x(t-2\cdot\Delta t)) = \frac{n}{\Delta t}(1-z^{-2})X(z)$$

$$\ddot{x} = \left(\frac{n}{\Delta t}\right)^2 (x(t) - 2x(t-\Delta t) + x(t-2\cdot\Delta t)) = \left(\frac{n}{\Delta t}\right)^2 (1-z^{-1})^2 X(z)$$

Where:

$$s = \frac{n}{\Delta t}\frac{1-z^{-1}}{1+z^{-1}}\frac{X(z)}{X(s)}$$

And

$$n = 1, \sqrt{2}, 2$$

The bi-linear z-transform BPF equation is derived as

$$x(t) = \frac{1}{(\omega_n\cdot\Delta t)^2 + 2n\zeta(\omega_n\cdot\Delta t) + n^2}\left\{\begin{array}{l} 2n\zeta(\omega_n\cdot\Delta t)(x_i(t) - x_i(t-2\cdot\Delta t)) \\ +2(n^2 - (\omega_n\cdot\Delta t)^2)x(t-\Delta t) \\ -(n^2 - 2n\zeta(\omega_n\cdot\Delta t) + (\omega_n\cdot\Delta t)^2)x(t-2\cdot\Delta t)\end{array}\right\}$$

Substituting the second-order path function polynomial terms into the discrete BPF function produces the following terms:

$$x = ax(t) + bx(t-\Delta t) = (a+bz^{-1})X(z)$$

$$\dot{x} = \frac{1}{2\cdot\Delta t}(x(t) - x(t-2\cdot\Delta t)) = \frac{1}{2\cdot\Delta t}(1-z^{-2})X(z)$$

$$\ddot{x} = \frac{1}{\Delta t^2}(x(t) - 2x(t-\Delta t) + x(t-2\cdot\Delta t)) = \frac{1}{\Delta t^2}(1-z^{-1})^2 X(z)$$

Given constants

a	b
1	0
0	1
1/2	1/2

The polynomial path function BPF equation is derived as

$$x(t) = \frac{1}{a(\omega_n \cdot \Delta t)^2 + \zeta(\omega_n \cdot \Delta t) + 1} \begin{Bmatrix} \zeta(\omega_n \cdot \Delta t)(x_i(t) - x_i(t - 2 \cdot \Delta t)) \\ + (2 - b(\omega_n \cdot \Delta t)^2) x(t - \Delta t) \\ - (1 - \zeta(\omega_n \cdot \Delta t)) x(t - 2 \cdot \Delta t) \end{Bmatrix}$$

The BPFs are evaluated using the Fourier transform and the power spectrum to determine the overall performance using a high and low frequency.

Low Frequency: $f_{low} = \frac{1}{2} f_{bpf}$ An octave band below f_{bpf}

BP Frequency: f_{bpf}

High Frequency: $f_{high} = 2 f_{bpf}$ An octave band above f_{bpf}

The waveform equation for the discrete frequencies is given as:

$$x(t) = x_{bias} + x_{pk1} \sin(2\pi f_{low} \cdot t + \phi) + x_{pk2} \sin(2\pi f_{bpf} \cdot t + \phi) + x_{pk3} \sin(2\pi f_{high} \cdot t + \phi)$$

Where:

$x_{bias} = 0$

$x_{pk1} = x_{pk2} = x_{pk3} = 1$

$\phi = 0$

The waveform equation is plotted below:

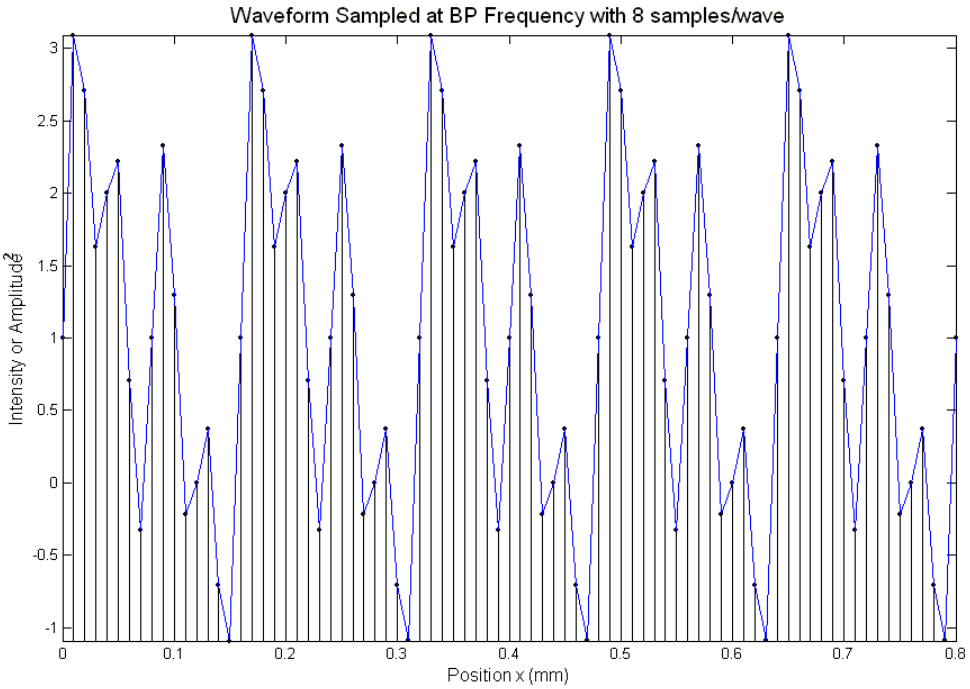

Figure 5 1x Sampled Data Waveform with the BP Frequency sampled at 8 samples/cycle

The high frequency is sampled at 4 samples/cycle and the low frequency is sampled at 16 samples/cycle.

The waveform is then 2x Over-Sampled using linear interpolation so that the number of samples per cycle will double at the discrete frequencies (f_{low} , f_{bpf} , f_{high}). This interpolated waveform is shown in the figure below:

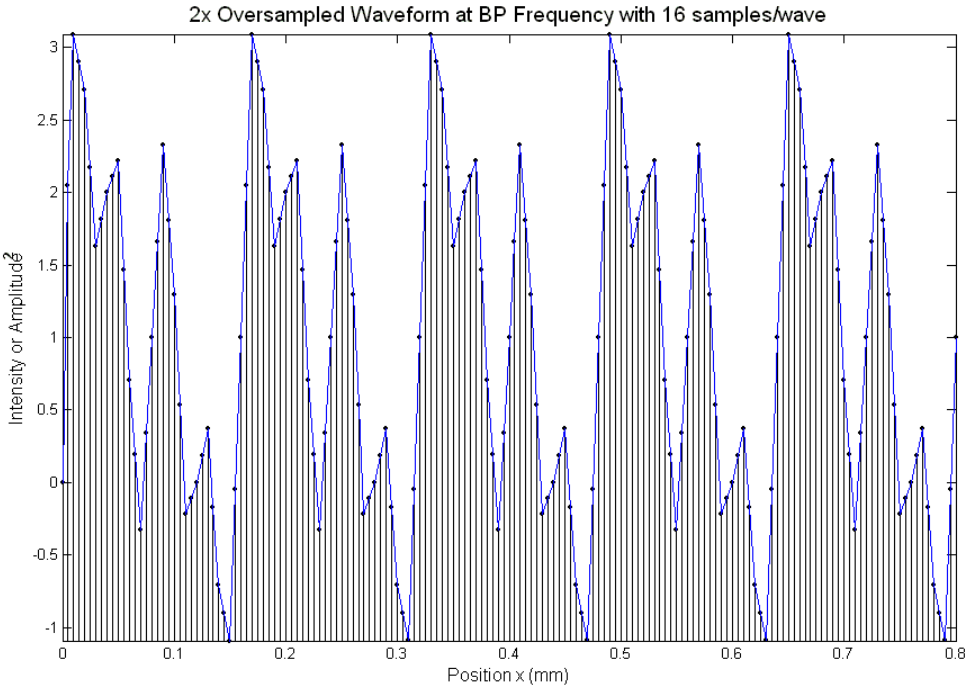

Figure 6 2x Over-Sampling with the BP Frequency sampled at 16 samples/cycle

The 2x Over-Sampled waveform is normalized before the data enters the filter. The normalization factors are determined from the waveform bias and peak intensity levels. The waveform is then scaled back to its original size at the output of the filter. Running the 2x Over-Sampled waveform signal through any of the digital BPFs produces BPF response plots where all of them look similar.

An example of the input signal waveform and the BPF response is shown in the figure below.

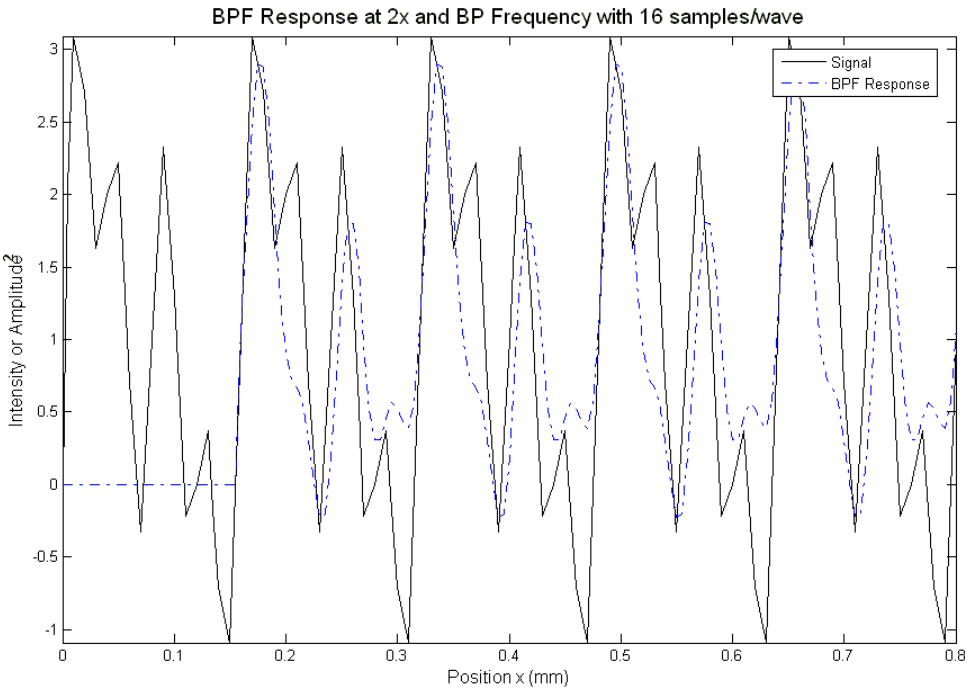

Figure 7 Waveform of the Input Signal and Typical BPF Response for any of the Filter Configurations

The filter output is set to zero for 1 cycle or 1 wave of the low frequency. This eliminates the transient response of the filter, which converges to a steady-state condition and also sets the waveform intensity to zero for initial condition data input to the Fourier transform. The Fourier transform for all the filter configurations will show the power spectrum for the input waveform along with the BPF response.

The power spectrum of the Bi-Linear z-Transform with $n=1$ is shown in the figure below:

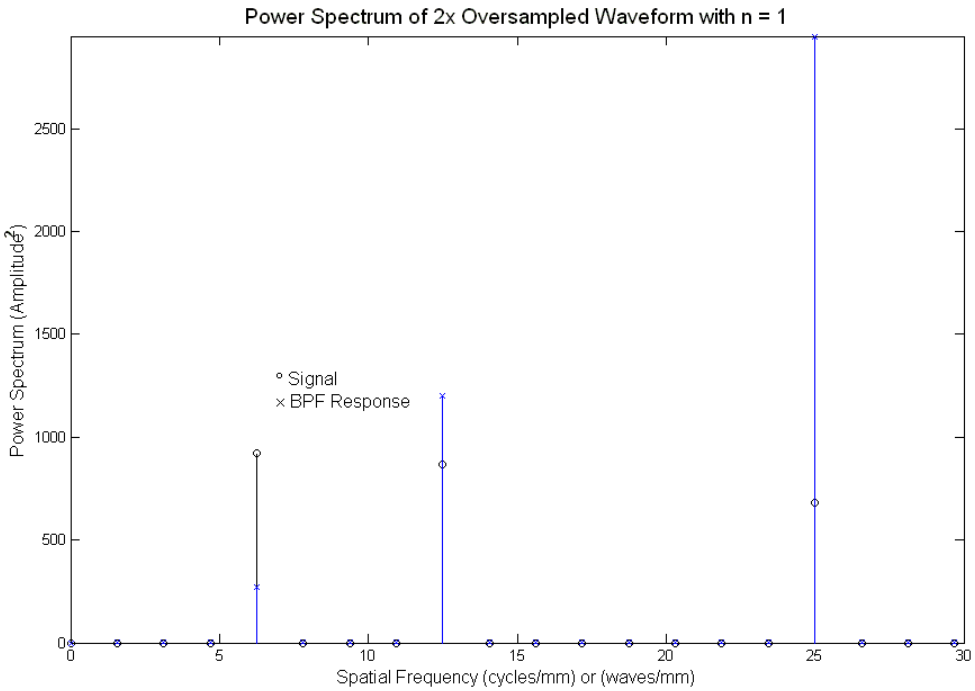

Figure 8 Bi-Linear Transform Power Spectrum at $n=1$

The BPF response at the high frequency is too large and possibly divergent. The power spectrum of the Bi-Linear z-Transform with $n = \sqrt{2}$ is shown in the figure below:

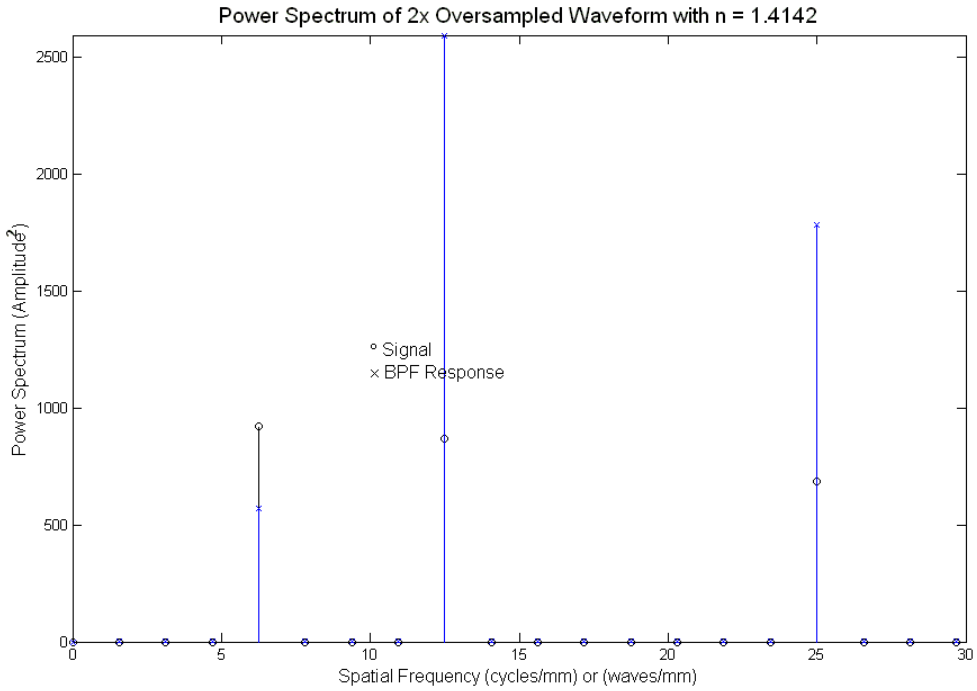

Figure 9 Bi-Linear Transform Power Spectrum at $n = \sqrt{2}$

This figure shows greater attenuation of the low frequency in relation to the high frequency.

The power spectrum of the Bi-Linear z-transform with $n = 2$ is shown in the figure below:

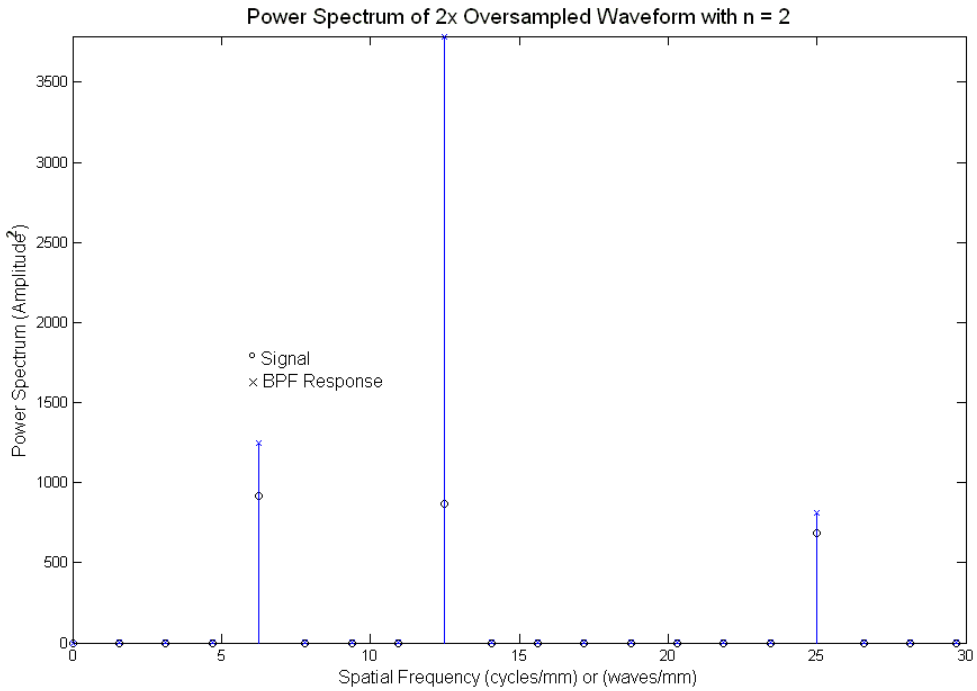

Figure 10 Bi-Linear Transform Power Spectrum at $n = 2$

This figure shows an appropriate balance of the attenuation of the low frequency and the high frequency.

The power spectrum of the Path Function with $a = 1$ and $b = 0$ is shown in the figure below:

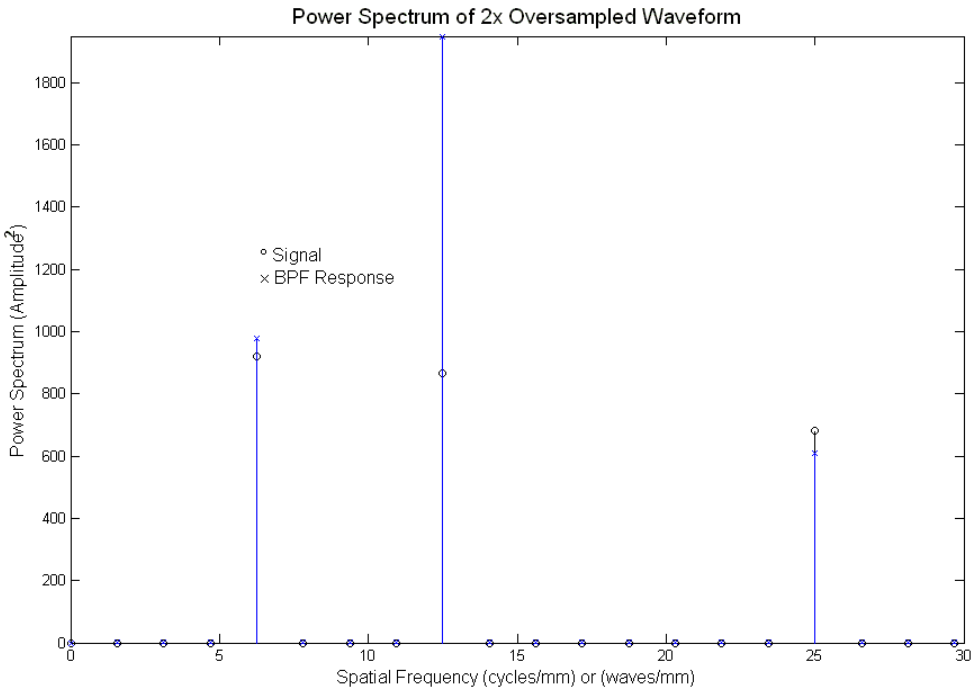

Figure 11 Path Function Power Spectrum at with $a = 1$ and $b = 0$

The BPF response at both the low and high frequencies show minimal error with respect to the input signal.

The power spectrum of the Path Function with $a = 0$ and $b = 1$ is shown in the figure below:

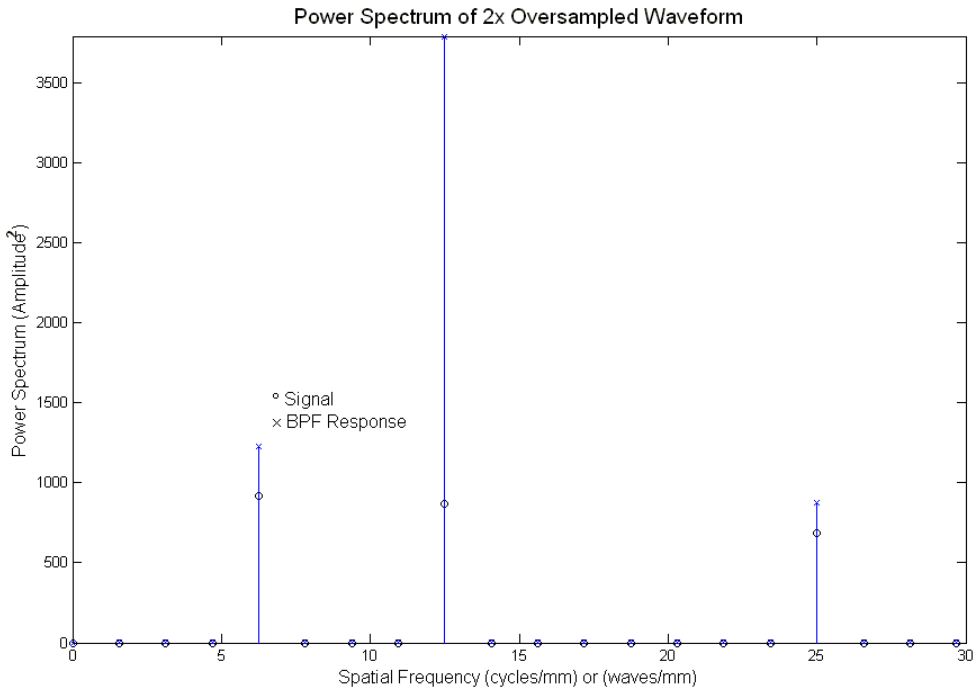

Figure 12 Path Function Power Spectrum at with $a = 0$ and $b = 1$

This plot shows the power spectrum to be larger than the previous figure at the BP frequency of 12.5 cycles/mm or cycles/sec.

The power spectrum of the Path Function with $a = 1/2$ and $b = 1/2$ is shown in the figure below:

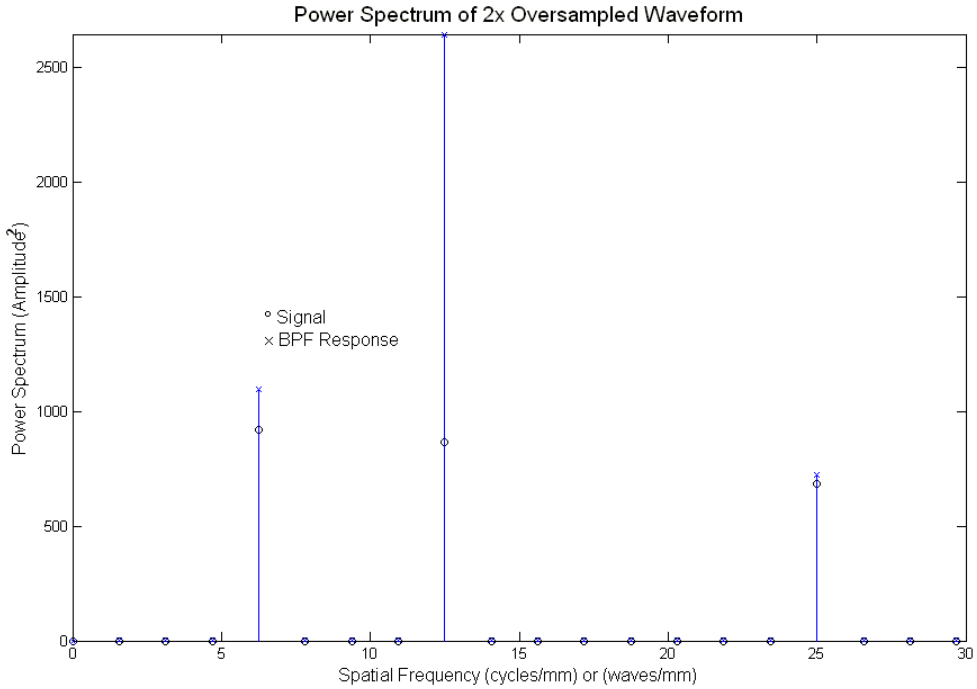

Figure 13 Path Function Power Spectrum at with $a = 1/2$ and $b = 1/2$

The overall best performance showing maximum peak at the BP frequency with balanced attenuation of the low and high frequencies are found in the Bi-Linear z-Transform with $n = 2$ and the Path Function with $a = 0$ and $b = 1$. The attenuation of the Bi-Linear z-Transform and the Path Function is $\times \frac{800}{4000} = \times \frac{1}{5}$, which is slightly less than the calculated Power Attenuation or Intensity Gain of $\times \frac{1}{3.25}$. This is due to the damping factor $\zeta = 0.5$ that sharpens the peak from the nominal setting of $\zeta = 1$. Further reduction of the damping factor will sharpen the peak at the risk of numerical instability. The sharpened peak will furthermore reduce or attenuate signals that are close to the BP frequency.

Set $\zeta = 0$

The Bi-Linear z-Transform BPF with $n = 2$ produces the following waveform filtering as shown in the figure below:

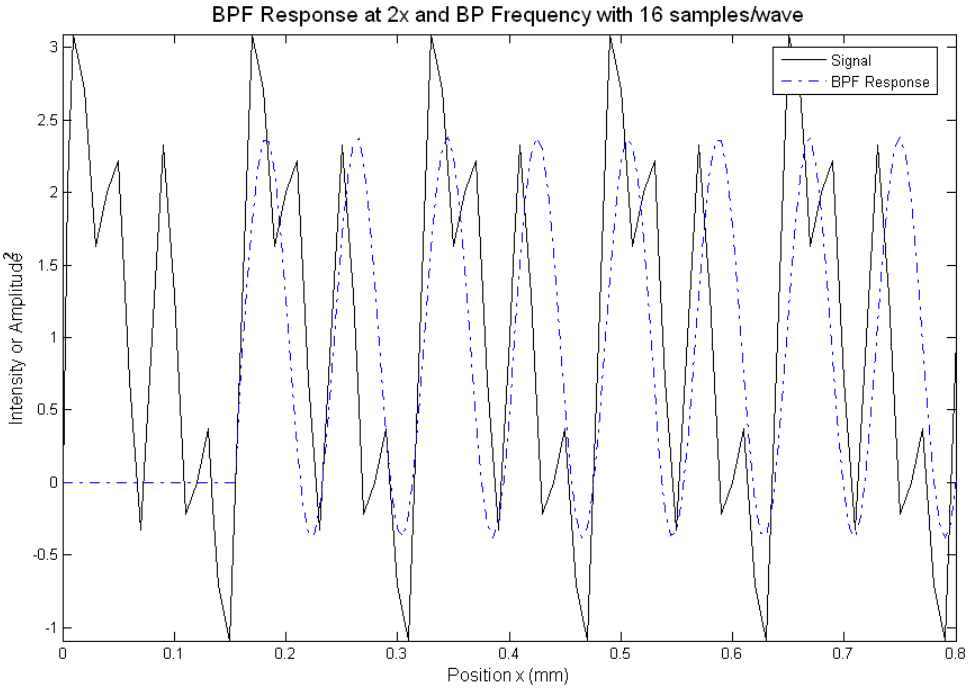

Figure 14 Waveform of Input Signal and BPF Response of the Bi-Linear z-Transform BPF with $n = 2$

The power spectrum of the input signal and the BPF response is shown in the figure below:

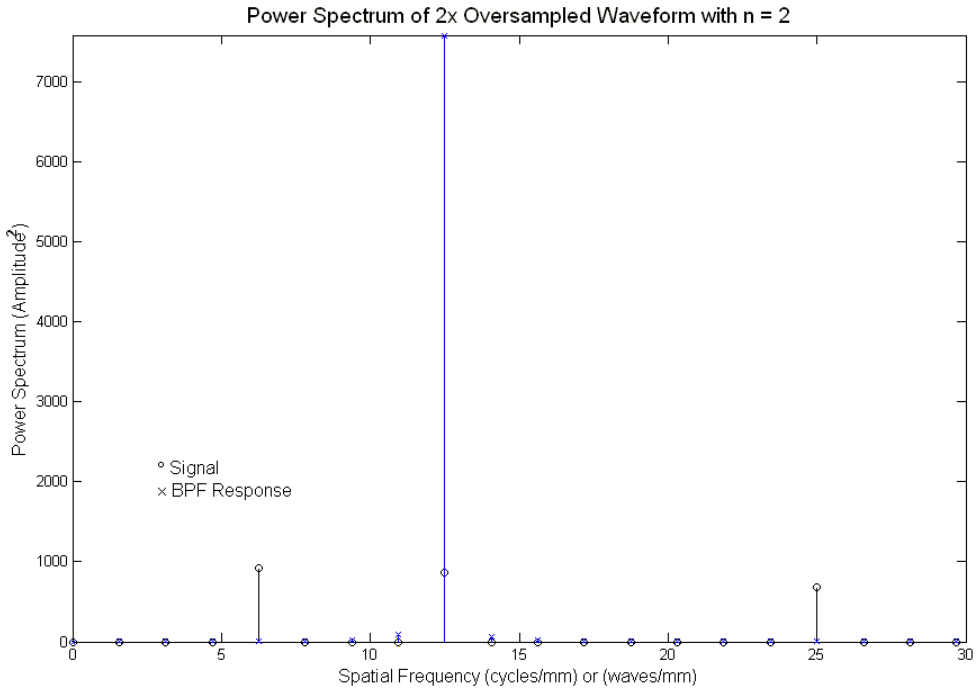

Figure 15 Bi-Linear z-Transform BPF Power Spectrum with $\zeta = 0$ and $n = 2$

This power spectrum shows an attenuation $\times \frac{4.8}{7586} = \times \frac{1}{1580}$ of the BP frequency with respect to the low frequency.

The Path Function BPF with $\zeta = 0$ and $a = 0$ and $b = 1$ produces the following waveform filtering as shown in the figure below:

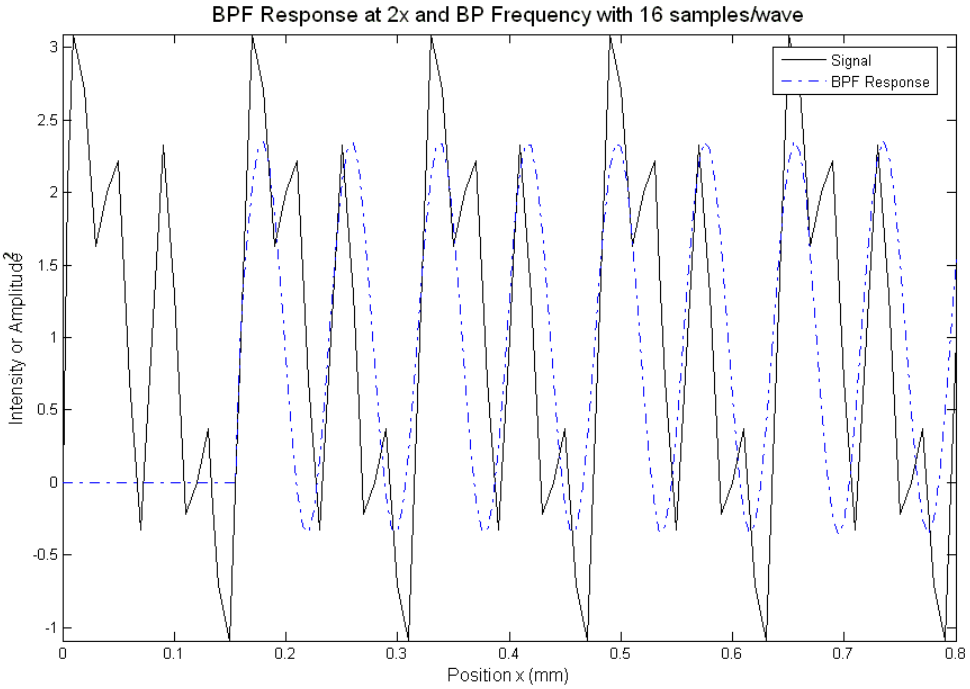

Figure 16 Waveform of Input Signal and BPF Response of the Path Function BPF with $\zeta = 0$ and $a = 0$ and $b = 1$

The figure above shows the filter response to be better phase aligned with respect to the input waveform than is seen in the filter response of figure 14 above.

The power spectrum of the input signal and the BPF response is shown in the figure below:

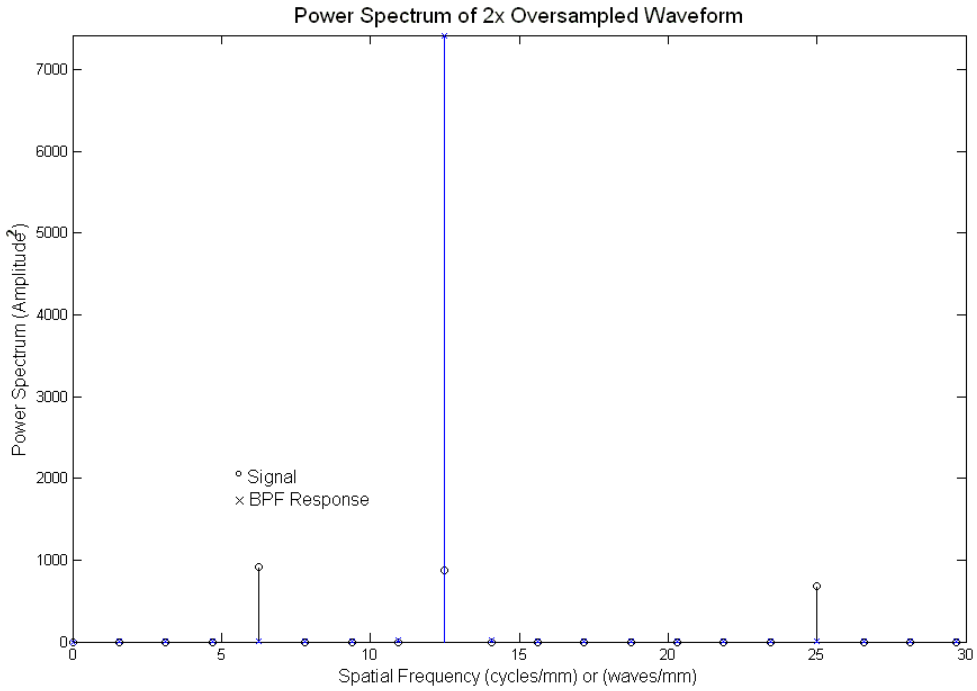

Figure 17 Path Function BPF with $\zeta = 0$ and $a = 0$ and $b = 1$

This power spectrum shows an attenuation $\times \frac{0.55}{7423} = \times \frac{1}{13{,}500}$ of the BP frequency with respect to the low frequency, therefore, the BPF with the highest sideband frequency rejection is the Path Function BPF with $\zeta = 0$ and $a = 0$ and $b = 1$.

Another approach to filtering is by the direct solution of the differential equation as follows:

$$\ddot{x} + 2\zeta\omega_n\dot{x} + \omega_n^2 x = 2\zeta\omega_n\dot{x}_i$$

Given Input (Forcing Function) Rate: $\dot{x}_i = \frac{1}{2 \cdot \Delta t}(x_i(t) - x_i(t - 2 \cdot \Delta t))$ Central-Difference

The input rate is the waveform containing the three discrete frequencies.

This equation can be spilt into coupled single-order differential equations as follows:

State-Space Matrix

$$\begin{bmatrix} \dot{x}_1 \\ \dot{x}_2 \end{bmatrix} = \begin{bmatrix} 0 & 1 \\ -\omega_n^2 & -2\zeta\omega_n \end{bmatrix} \cdot \begin{bmatrix} x_1 \\ x_2 \end{bmatrix} + \begin{bmatrix} 0 \\ 2\zeta\omega_n x_i \end{bmatrix}$$

With Initial Conditions (ICs)

$$\begin{bmatrix} x_1(0) \\ x_2(0) \end{bmatrix} = \begin{bmatrix} x_1(0) \\ \dot{x}_1(0) \end{bmatrix} = \begin{bmatrix} 0 \\ 0 \end{bmatrix}$$

Then Integrating the Output Rates

$$x(t) = x(t - \Delta t) + \int_{t-\Delta t}^{t} \dot{x}(t)dt$$

Where:

$x_{bpf} = x_1$ BPF Response

$x_2 = \dot{x}_1$ BPF Rate or Velocity

A modified Runge-Kutta integrator with constant step-size intervals at 20 step increments between the Δt time steps was programmed into the BPF response simulation.

where $dt = \Delta t / 20$ is the differential time integration step-size.

Running the simulation at $\zeta = 0.5$ with the same input waveform produces the BPF response plot in the figure below:

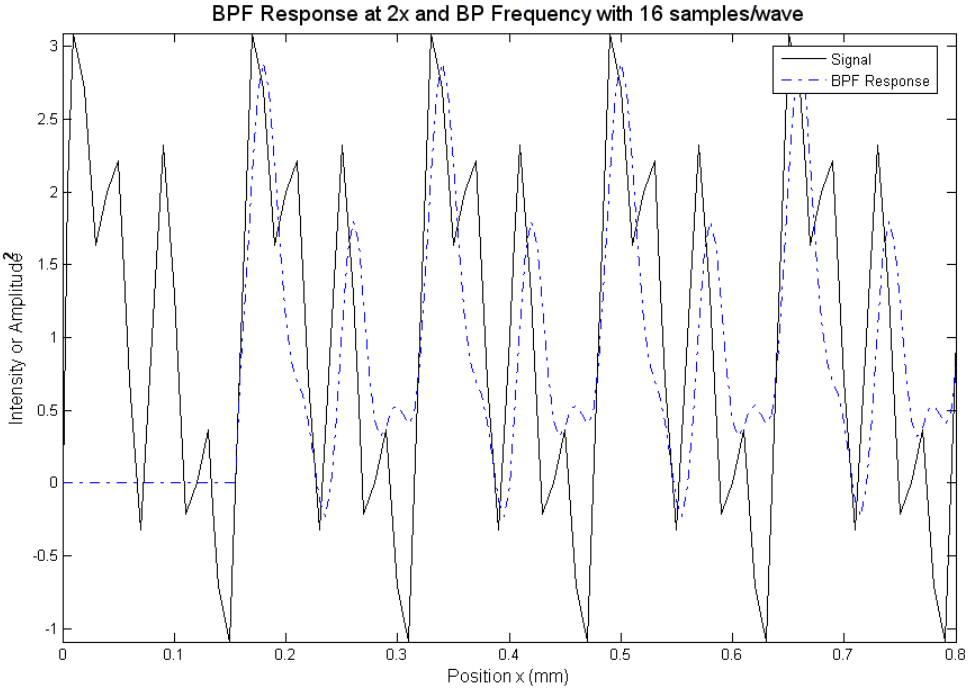

Figure 18 Input Waveform and State-Space BPF Response with $\zeta = 0.5$

The Fourier transform and the power spectrum of the input waveform and the BPF response is shown in the figure below:

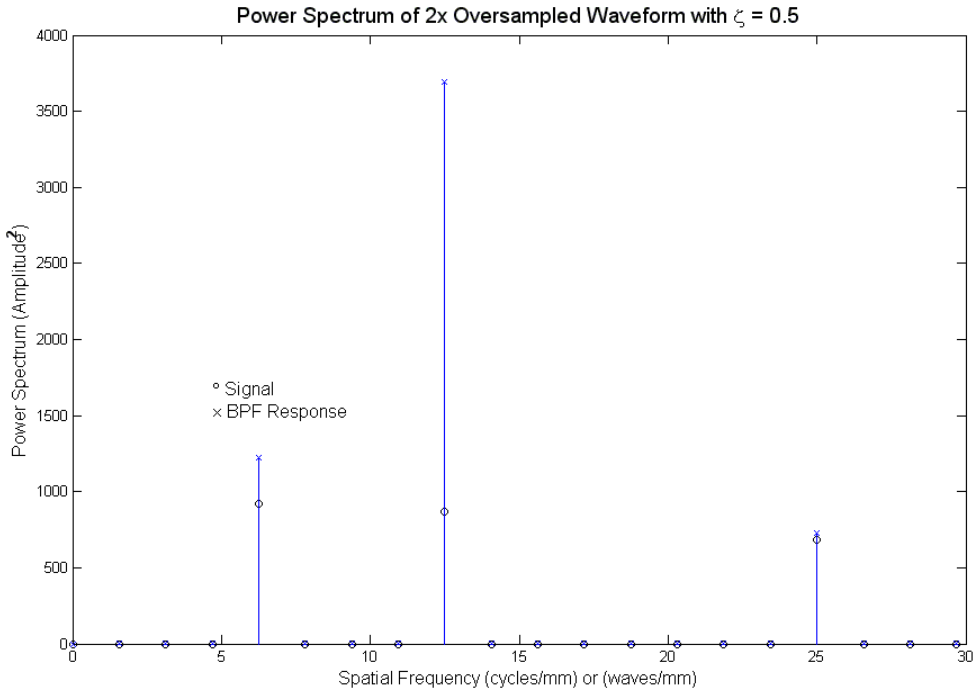

Figure 19 Input Waveform and State-Space BPF Response Power Spectrum

This power spectrum shows an attenuation $\times\frac{1225}{3693}=\times\frac{1}{3}$ of the BP frequency with respect to the low frequency. This is close to the calculated Power Attenuation or Intensity Gain of $\times\frac{1}{3.25}$ for $\zeta=0.5$ at the BP frequency.

Now reduce the damping factor to $\zeta=0.1$

Running the simulation at $\zeta = 0.1$ with the same input waveform produces the BPF response plot in the figure below:

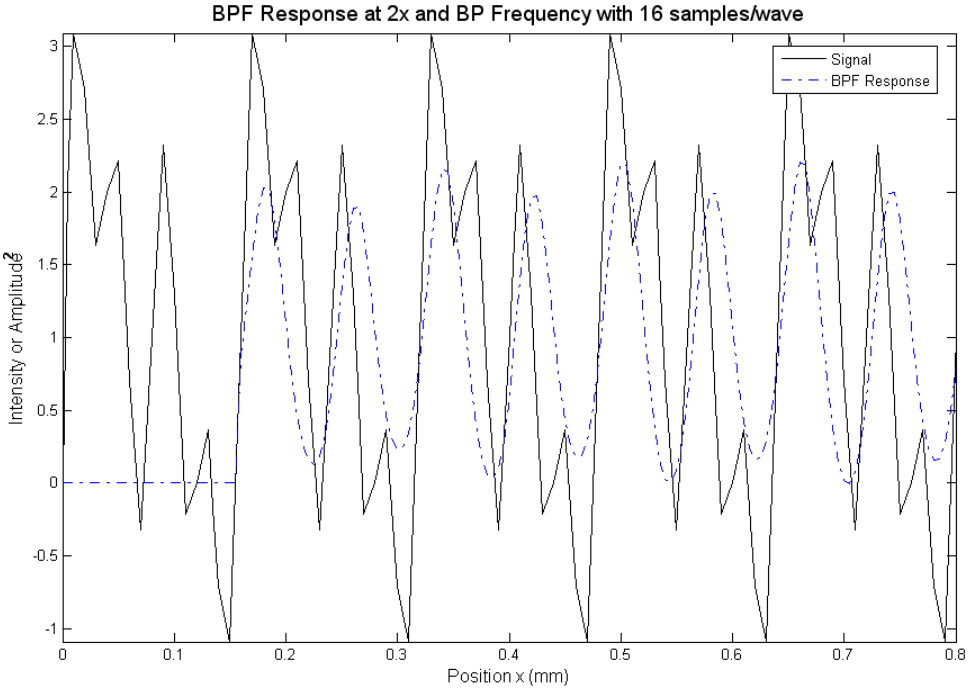

Figure 20 Input Waveform and State-Space BPF Response with $\zeta = 0.1$

The Fourier transform and the power spectrum of the input waveform and the BPF response is shown in the figure below:

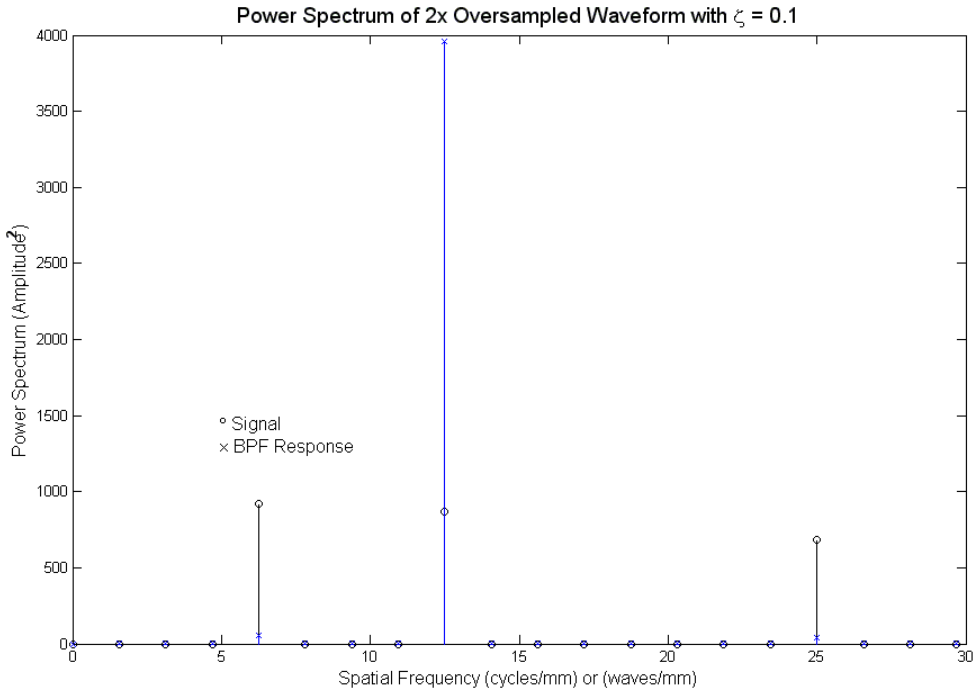

Figure 21 Input Waveform and State-Space BPF Response Power Spectrum

This power spectrum shows an attenuation $\times\frac{58}{3958}=\times\frac{1}{68}$ of the BP frequency with respect to the low frequency.

Reducing the damping factor to $\zeta=0$ significantly attenuates the BPF response, which results in an unacceptable filter design.

The advantages of the State-Space BPF are as follows:

1. Over-sampling is incorporated in the Runge-Kutta integrator that improves response accuracy. The simulation used x20 Over-sampling with interpolation of the forcing function signal. The other BPFs used x2 Over-sampling with interpolation.

2. The State-Space BPF converges within one Δt sample step as opposed to the other filters that converge within 1.5 waves of the lowest frequency in the signal.

Conclusions

The bilinear transform: $s = \frac{n}{\Delta t}\frac{1-z^{-1}}{1+z^{-1}}\frac{X(z)}{X(s)}$ is divergent when $x(t)+x(t-\Delta t)=0$ and then the estimate in velocity goes to infinity. An optimal estimate for the velocity has recently been derived, but not analyzed with BPF simulation. This velocity estimate is as follows:

$$\dot{x} = sX(s) = \frac{2}{3}\times\frac{1}{2\cdot\Delta t}(x(t)-x(t-2\cdot\Delta t))+\frac{1}{3}\times\frac{1}{\Delta t}(x(t)-x(t-\Delta t))$$

$$\dot{x} = sX(s) = \frac{1}{3\cdot\Delta t}(2x(t)-x(t-\Delta t)-x(t-2\cdot\Delta t))$$

$$\dot{x} = sX(s) = \frac{1}{3\cdot\Delta t}(2-z^{-1}-z^{-2})X(z) = \frac{1}{3\cdot\Delta t}(2+z^{-1})(1-z^{-1})X(z)$$

Thus, $s = \frac{1}{3\cdot\Delta t}(2+z^{-1})(1-z^{-1})\frac{X(z)}{X(s)}$

And the estimate for the acceleration is as follows:

$$\ddot{x} = s^2X(s) = \frac{1}{\Delta t^2}(x(t)-2x(t-\Delta t)+x(t-2\cdot\Delta t))$$

$$\ddot{x} = s^2X(s) = \frac{1}{\Delta t^2}(1-2z^{-1}+z^{-2})X(z) = \frac{1}{\Delta t^2}(1-z^{-1})^2X(z)$$

Thus, $s^2 = \left(\frac{1}{\Delta t}(1-z^{-1})\right)^2\frac{X(z)}{X(s)}$

The equations for $\dot{x}\ and\ \ddot{x}$ or $s\ and\ s^2$ can be substituted into the differential equation for the BPF and a digital BPF function can be derived as follows.

$$\ddot{x}+2\zeta\omega_n\dot{x}+\omega_n^2x = 2\zeta\omega_n\dot{x}_i$$

Substituting $\dot{x}$ and $\ddot{x}$ and then re-arranging:

$$x(t) = \frac{1}{3(\omega_n\cdot\Delta t)^2+4\zeta(\omega_n\cdot\Delta t)+3}\begin{Bmatrix}2\zeta(\omega_n\cdot\Delta t)\cdot(2x_i(t)-x_i(t-\Delta t)-x_i(t-2\cdot\Delta t)\\+2(\zeta(\omega_n\cdot\Delta t)+3)\cdot x(t-\Delta t)\\+(2\zeta(\omega_n\cdot\Delta t)-3)\cdot x(t-2\cdot\Delta t)\end{Bmatrix}$$

Further attenuation and sideband frequency rejection can be achieved by cascading multiple BPFs in order to increase the roll-off slope or the order of the filter. This would also increase the response time delay due to the effective addition of the multiple delay taps. A BPF can be designed to produce zero phase-shift at the peak of the band-pass Power Spectrum. Cascading multiple BPFs may well introduce an unsuspected phase-

shift due to tolerances and sensitive parameters in the filter. The Path Function BPF with $\zeta = 0$ and $a = 0$ and $b = 1$ may prove to be useful in isolating the desired fringe spatial frequency in the hologram since it shows the highest sideband frequency rejection. The optimal velocity and acceleration derivations are also attractive for a discrete BPF design since preliminary calculations show minimal phase-shift error. Finally, the State-Space BPF deserves high consideration since the modified Runge-Kutta integrator at a high over-sampling rate of about 5x that is coupled to a recursive quadratic polynomial function for interpolation gives the filter accurate response along with quick convergence. The simultaneous integration of $\dot{x}$ and $\ddot{x}$ produces minimum filter lag. The recursive quadratic polynomial for interpolation will reduce the change in amplitude between sampled steps that would otherwise reduce numerical stability using linear interpolation or no interpolation.

These optimized digital band-pass filters can be easily converted to low-pass, high-pass, and notch filters. Applications for these filters can be lead-lag compensation for feedback controllers, image processing, and sensor signal processors. There are no references as the filter equations were derived from fundamental principles and basic theory as shown in the text.

Computational Fluid Dynamics (CFD) and Heat Transfer Analysis of the Fluid-Cell

Introduction

The comparison of 2D to 3D Computational Fluid Dynamics (CFD) modeling consists of the governing equations, namely the Navier-Stokes equations for continuity, momentum, and energy, and the assumptions. Solutions to these non-linear equations consist of either direct exact methods and the simplifying assumptions or numerical methods that require the discretization of the continuous system of governing equations. The numerical method approaches are finite difference, finite element, finite volume, and spectral where accuracy, stability, and consistency are trade-off considerations for performance and application. Finite difference uses the Taylor Series expansion approximation of the equations and has the advantages of simplicity with truncation error and does not ensure conservation at the boundaries. The application of Trapezoidal Rule to finite differences provides a single step propagation formula that is not restricted

to uniform intervals at the expense of accuracy. Finite element methods use interpolation of weighted elements and are very flexible for complicated problems. Finite volume uses Simpson's Rule for integration for fitting a 3-point parabola. The advantages are accuracy and simplicity at the expense of equal intervals and 2-step propagation. Spectral methods require a function that has infinite derivatives and is continuous. Converting the governing equations to frequency space by Laplace Equations or Fourier Equations permits algebraic operations of linear systems. It is the inverse of this equation that is complex and requires a numerical approach. Some of these methods will be explored with regards to the application, which in this case is a fluid-cell.

The fluid-cell is a test chamber for a laser to measure the change in index-of-refraction that results from pressure gradients. The laser passing through this chamber is combined with a reference beam laser to produce an interference pattern on a camera. This interference pattern is sensitive to phase-shift in the optical propagation of a wave. This Optical Phase Difference (OPD) relates back to the index-of-refraction in the fluid-cell. This experiment is different from other systems, such as optical tomography, confocal holography, and cross-beam correlation that use a collimated laser beam instead of a focused beam. The figure below shows the difference between a collimated laser (constant diameter) beam to a focused laser beam, where the focusing cone angle is f/2 (f/# = Focal Length/Diameter), in this situation.

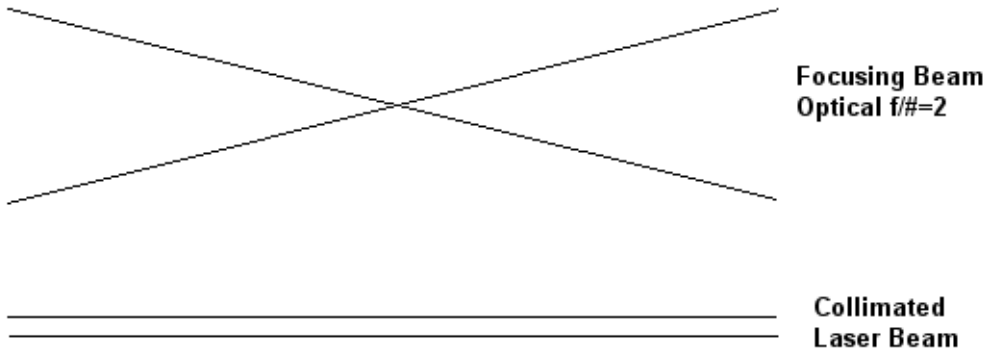

Figure 1 Focusing Laser Beam to Parallel Ray Collimated Laser Beam

In this application a focused laser beam is used to scan through the specimen and the collection of phase information can be used to determine the index-of-refraction at the focal point in the specimen rather than obtain the integrated value of index-of-refraction as the laser propagates all the way through the specimen. This feature is unique where 3-Dimensional measurements are obtained. The pressure gradients that

affect index-of-refraction can be modeled through CFD. The interface of ray propagation, optical path length, refraction, and optical phase difference for holography can be integrated into a 3-D CFD simulation model. Computer code for the determination of index-of-refraction from the detected phase difference interference is being developed in the University of Victoria department of mechanical engineering by Dr. Lai. A similar approach is proposed for the integration of CFD models to optical wave propagation models, and this is why commercial CFD software packages such as Fluent, FEMLAB, and ANSYS, were not considered at this time. Therefore, 2-D to 3-D CFD simulation models will be compared using code developed on Matlab and in the future on C++ compilers.

The fluid-cell specimen chamber is a rectangular volume of 10Hx10Wx15D mm where the laser propagates along the axis of depth is shown in the figure below:

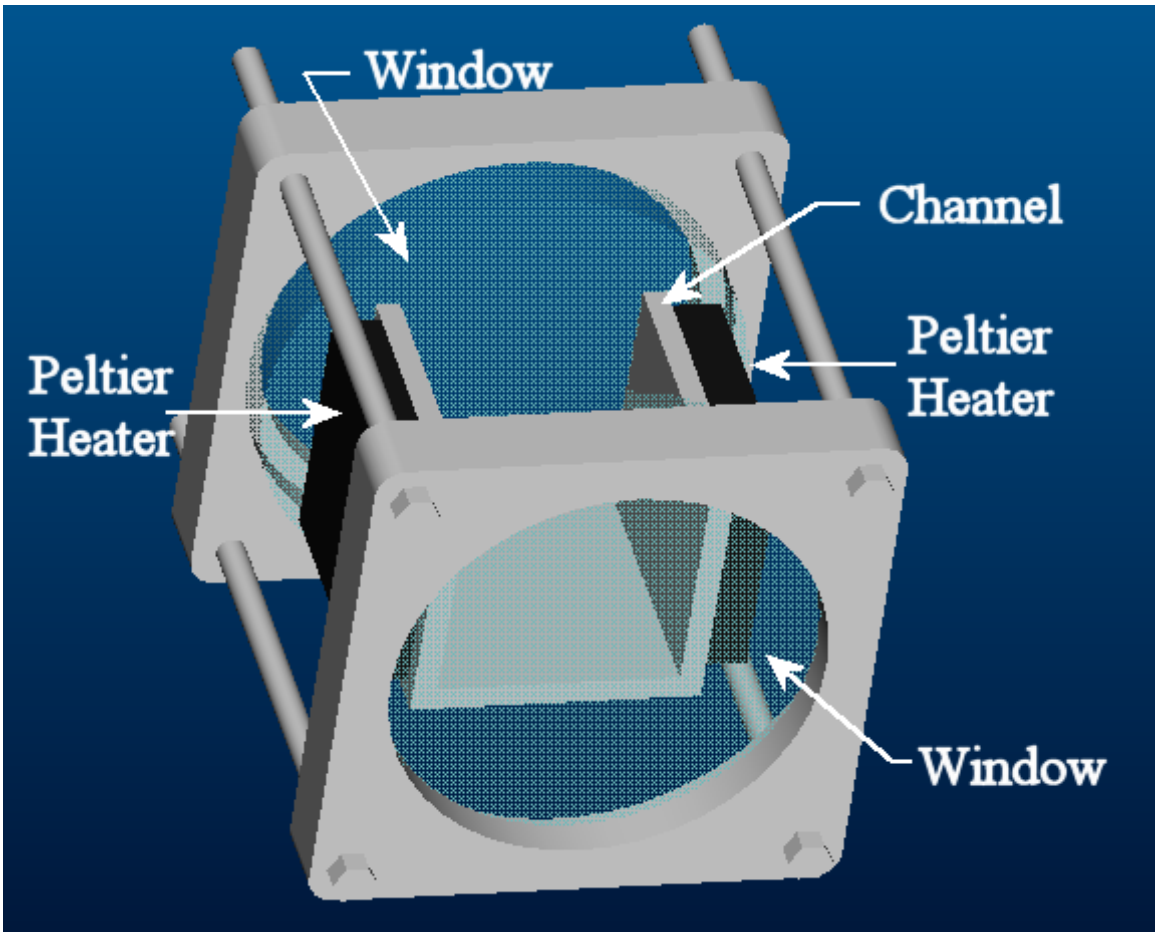

Figure 2 Fluid-Cell with Optical Windows and Peltier Heaters to Induce Convection

Side Peltier heaters provide a thermal gradient across the fluid and induce convection along the *y*-axis. The laser propagates along the *z*-axis from front to back and the thermal gradient properties are constant along this path. Convection and heat transfer properties should therefore be the same for any cross-sectional cutting plane along the *z*-axis. Because of this configuration, 2-D simulation can be fairly compared to 3-D simulation for an *xy*-plane along any point of the *z*-axis. In the future the side-to-side Peltier heaters will be replaced with a central point source heater that will provide a 3-Dimensional thermal gradient. The proposed fluid will be silicone oil with relatively high viscosity. Reynold's number will be kept low to provide laminar flow and possibly a circulation path so that measurements can be made in a steady-state condition with no turbulence. A low Reynold's number means that viscous effects will predominate.

The laser that scans the fluid-cell is over a plus/minus 1 degree field-angle in the *x*-direction and the *y*-direction. Small field-angle or field-of-view preserves high beam quality where the optical aberrations are maintained to a tolerable minimum within this off-axis range.

Objectives

The purpose and objectives are to compare the various methods of solution to the Partial Differential Equations (PDE's) along with the numerical approach of 2-D to 3-D simulation.

Summary

This section discusses the comparison of analytical approaches from the CFD governing equations and the finite difference numerical solution. The coordinate frame axes of the fluid-cell are shown in the figure below before defining the CFD convection equations.

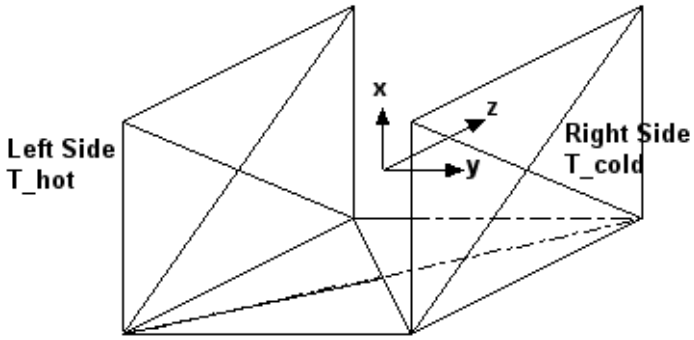

Figure 3 Fluid-Cell Channel Configuration and Coordinate Frame

The coordinate frame is described and defined as follows. The *z*-axis is along the front-to-back optical propagation axes. The *y*-axis is horizontal and is normal to the planes of the heat sources on the sides. The *x*-axis is vertical and the buoyancy driven gravitational forces act in this direction. A cross-sectional cutting plane along the *z*-axis would represent an *xy*-plane, which will be the plane of interest in 2-D modeling.

The non-dimensional parameter (variable) steady-state buoyancy-driven convection Navier-Stokes Boussinesq 3-Dimensional Equations are given as follows:

z-axis Momentum

$$\bar{u}\cdot\nabla w = -\frac{\partial p}{\partial z} + \frac{1}{\mathrm{Re}}\nabla^2 w$$

y-axis Momentum

$$\bar{u}\cdot\nabla v = -\frac{\partial p}{\partial y} + \frac{1}{\mathrm{Re}}\nabla^2 v$$

x-axis Momentum

$$\bar{u}\cdot\nabla u = -\frac{\partial p}{\partial x} + \frac{1}{\mathrm{Re}}\nabla^2 u + \frac{\beta}{Fr}\left(T - T_r\right)$$ Reference temperature: T_r

Energy

$$\bar{u}\cdot\nabla T = \frac{1}{\mathrm{Re}\cdot\mathrm{Pr}}\nabla^2 T$$

Continuity or Conservation-of-Mass

$\frac{\partial u}{\partial x} + \frac{\partial v}{\partial y} + \frac{\partial w}{\partial z} = 0$ Assuming an incompressible fluid with constant density.

Coefficient of Thermal Expansion for Fluid: $\beta = -\frac{1}{\rho}\left(\frac{\partial \rho}{\partial T}\right)_p$

Velocity Vector: $\bar{u} = u \cdot \bar{e}_i + v \cdot \bar{e}_j + w \cdot \bar{e}_k$

$u = u_x \ , \ v = v_y \ , \ w = w_z$

Non-Dimensional Equations

Velocity: U

Length or Displacement: L

Time: $t = t/\tau = \frac{t}{\left(\frac{L}{U}\right)}$

Pressure: $p = \frac{p - p_0}{\left(\frac{\rho U^2}{g_c}\right)}$ $\quad g_c = 32.174 \frac{lbm}{lbf} \frac{ft}{\sec^2}$

Temperature: $T = \frac{T - T_c}{T_h - T_c} = \frac{T - T_c}{\left(\frac{\mu U^2}{k g_c}\right)}$

Reynolds Number: $\mathrm{Re} = \frac{InertiaForce}{ViscousForce} = \frac{\rho \frac{Dv_i}{Dt}}{\mu \nabla^2 v_i} = \frac{UL}{\frac{\mu}{\rho}} = \frac{UL}{\upsilon}$

Prandtl Number: $\mathrm{Pr} = \frac{ViscousDiffusion}{ThermalDiffusion} = \frac{\mu c_p}{k}$

Froude Number: $Fr = \frac{InertiaForce}{BuoyancyForce} = \frac{U^2}{g_i L}$

Kinematic Viscosity: $\upsilon = \mu / \rho$

Boundary Conditions

Bottom Surface

u=v=w=0 No Slip

p=1

T(y)=(T_cold - T_hot) x y + T_hot

Top Surface

u=w=0 Assume No Slip
v(y)=0.2 Left-to-Right Velocity due to Surface Tension
p=0
T(y)=(T_cold - T_hot) x y + T_hot

Left-Side Surface
u=v=w=0 No Slip
p(x)=1 - x
T=T_hot

Right-Side Surface
u=v=w=0 No Slip
p(x)=1 - x
T=T_cold

Front Surface
u=v=w=0 No Slip
p(x)=1 – x
T(y)=(T_cold - T_hot) x y + T_hot

Back Surface
u=v=w=0 No Slip
p(x)=1 – x
T(y)=(T_cold - T_hot) x y + T_hot

Analytical Solutions to PDE's

Parallel flow assumes that the flow over one surface is independent of the other surfaces with no coupling, and that the flow is one direction.

Then from continuity $\frac{\partial u}{\partial x} = 0$, which means that u cannot depend on x.

For parallel flow $u = u(y, z)$ and $v = w = 0$

Furthermore, pressure only depends on x, which implies $\frac{\partial p}{\partial y} = \frac{\partial p}{\partial z} = 0$

Thus, all convective terms vanish in the x-direction and

$$0 = -\frac{\partial p}{\partial x} + \frac{1}{\mathrm{Re}}\left(\frac{\partial^2 u}{\partial x^2} + \frac{\partial^2 u}{\partial y^2}\right)$$

Since, $\frac{\partial u}{\partial x} = 0$ then it follows that $\frac{\partial^2 u}{\partial x^2} = 0$

Thus, $u(y) = 0$ since flow is in a single direction and y is perpendicular to the direction of flow or the plane surface.

The equations of motion reduce to $\frac{\partial^2 u}{\partial y^2} = 0$ with Pressure *p*=constant.

Under the no-slip condition $u(y)=0$ at $y=0$

Shear Stress at the Wall: $\tau_w = \mu\left(\frac{\partial u}{\partial y}\right)_{y=0}$

Velocity: $u = \frac{\tau_w}{\mu} y$ where velocity is a linear function of y

Laplace (elliptic equilibrium) Equation: $\frac{\partial^2 \psi}{\partial x^2} + \frac{\partial^2 \psi}{\partial y^2} = 0$

Poisson (elliptic) Equation: $\frac{\partial^2 \psi}{\partial x^2} + \frac{\partial^2 \psi}{\partial y^2} = \xi$, given $\xi = const.$

The exact analytical solution to the Poisson PDE is given as follows

$$\frac{\partial^2 \psi}{\partial x^2} + \frac{\partial^2 \psi}{\partial y^2} = \xi_{x,y}$$

$$\psi_{x,y} = \sum_{n=1}^{\infty}\sum_{m=0}^{\infty} \frac{-\xi_{m,n}}{\left(m^2+n^2\right)\pi^2} \sin\left(n\pi x\right)\cos\left(m\pi y\right)$$

Given Boundary Conditions (BC's)

$\psi_{x,0} = \psi_{x,1} = 0$ Bottom-Top Surfaces

$\psi_{0,y} = \psi_{1,y} = 0$ Left-Right Sides

The exact analytical solution to the Laplace PDE is given as follows

$$\frac{\partial^2 \psi}{\partial x^2} + \frac{\partial^2 \psi}{\partial y^2} = 0$$

$$\psi_{x,y} = f^0(1-x) + \sum_{n=1}^{\infty} f^n \frac{\sinh\left(n\pi(1-x)\right)}{\sinh\left(n\pi\right)} \cos(n\pi y)$$

Given Boundary Conditions (BC's)

$\psi_{0,y} = f(y)$, $\psi_{1,y} = 0$ Left-Right Sides

$\psi_{x,0} = \psi_{x,1} = 0$ Bottom-Top Surfaces

Finite Volume

The finite volume approach assumes a continuous function solution with a centered point within the boundary of the finite volume. The form of the solution to the differential equation is given as:

$$\phi_i = \frac{1}{\Delta x}\int_{x_{i-1/2}}^{x_{i+1/2}} \frac{\partial \phi(x)}{\partial x}\,dx$$

Typically, the Trapezoidal Rule or Simpson's Rule of Integration can be applied. The advantage of Trapezoidal Rule of Integration is a one-step formula that is not restricted to uniform intervals, and the disadvantage is low accuracy. The advantage of Simpson's Rule of Integration is accuracy over a 3-point fit to a parabola, and the disadvantage is a 2-step increment.

Finite Element

The finite element approach is an application of Calculus of Variations with the solution given as:

$$F(y) = F(y(x)) = \int_a^b f\left(x, y(x), y'(x)\right)dx$$

given $y'' - y' + y - x = 0$, for example

or $\frac{\partial^2 y}{\partial x^2} - \frac{\partial y}{\partial y} + y - x = 0$, can be separated into two coupled first order equations.

The advantage is that this method is very flexible over complicated problems as the solution essentially interpolates over the weighted elements. The disadvantage is that y(x) must be differentiable and the function stationary over an interval such that a minima or maxima is outside the boundary of integration.

Spectral Method

The spectral method requires an infinite number of derivatives or a continuous function. The Fourier Transform or the Laplace Transform is used convert the equations from spatial domain to frequency domain. The Laplace Transform (Ref. 4) is given by:

$$F(s) = \int_0^\infty f(x)e^{-sx}dx$$

The Laplace Transform is useful for solving linear differential equations with constant coefficients along with many boundary value problems.

$\frac{d^2u}{dx^2} = s^2U_x(s) - s\cdot u_x(x_0) - \dot{u}_x(x_0)$ where x_0 are the initial boundary conditions.

Complex variable: $s = j\omega$ with Spatial Frequency: $\omega = \frac{2\pi}{\lambda}$

The damped natural frequency from the characteristic equation is given as:

$\omega_d = \omega_n \sqrt{1-\zeta^2}$ Damping Factor $0 < \zeta < 1$

Converting the function back into the spatial domain is given by the Inverse Laplace Transform:

$$f(x) = \frac{1}{2\pi i} \int_{a-i\infty}^{a+i\infty} F(s) e^{sx} ds$$

The simplest diffusion equation for all physical (microscopic to macroscopic land) scales is given as: $\frac{\partial \phi}{\partial t} = \kappa \frac{\partial^2 \phi}{\partial x^2}$ given Diffusion Coefficient: $\kappa > 0$

A solution for a particular wave number is given as: $\phi(x,t) = \exp(ikx - \kappa k^2 t)$

The wave number: $k = 2\pi \frac{n}{L}$ for any wave number $n = 1,2,3...$

For all wave numbers, the general solution is the Fourier Integral of the form:

$\phi(x, t_0 + \tau) = \int_{-\infty}^{+\infty} w(\varepsilon) \cdot \phi(x + \varepsilon, t_0) \cdot d\varepsilon$, where the weighting function $w(\varepsilon)$ has the nature of a probability distribution

The general Fourier Integral then becomes

$\phi(k) = \int_{-\infty}^{+\infty} w(\varepsilon) \cdot \phi(\varepsilon) \cdot \exp(ik\varepsilon) \cdot d\varepsilon$, where ϕ is a function of spatial frequency (k)

Finite Difference

The finite difference approach handles the non-linear equations, but its accuracy is limited by the Taylor Series expansion truncation error. Spatial resolution of the discrete finite difference Partial Differential Equations (PDEs) impacts the stability of the algorithm since spatially sampled data is an approximation to the continuous PDEs. The Taylor Series expansion is found in many fluid dynamics textbooks for the discretization of PDE's

$$u_{j+1} = u_j + \Delta x \left(\frac{\partial u_j}{\partial x} \right) + \frac{\Delta x^2}{2!} \left(\frac{\partial^2 u_j}{\partial x^2} \right) + \cdots$$

$$u_{j-1} = u_j - \Delta x\left(\frac{\partial u_j}{\partial x}\right) + \frac{\Delta x^2}{2!}\left(\frac{\partial^2 u_j}{\partial x^2}\right) - \cdots$$

Adding the two equations above produces

$$\frac{\partial^2 u_j}{\partial x^2} = \lim_{\Delta x \to 0}\left(\frac{1}{\Delta x^2}\left(u_{j+1} - 2u_j + u_{j-1}\right)\right); \quad \mathrm{O}\left(\Delta x^2\right)$$

The equation above is second-order accurate due to truncation error (Ref. 6).

Reduction from 3-Dimensional to 2-Dimensional Equations:
(assuming constant properties & characteristics along the z-axis)

Momentum Equation for Vorticity: ζ

$$u\frac{\partial \zeta}{\partial x} + v\frac{\partial \zeta}{\partial y} = \frac{1}{\mathrm{Re}}\left(\frac{\partial^2 \zeta}{\partial x^2} + \frac{\partial^2 \zeta}{\partial y^2}\right) - \frac{\beta}{Fr}\frac{\partial T}{\partial y}$$

Energy

$$u\frac{\partial T}{\partial x} + v\frac{\partial T}{\partial y} = \frac{1}{\mathrm{Re}\cdot \mathrm{Pr}}\left(\frac{\partial^2 T}{\partial x^2} + \frac{\partial^2 T}{\partial y^2}\right)$$

Conservation-of-Mass or Continuity

$$\frac{\partial u}{\partial x} + \frac{\partial v}{\partial y} = 0$$

Stream Function (Poisson Equation) and Velocity Relations

$\frac{\partial^2 \psi}{\partial x^2} + \frac{\partial^2 \psi}{\partial y^2} = -\zeta = \frac{\partial u}{\partial y} - \frac{\partial v}{\partial x}$ Poisson Equation for Stream Function: ψ

$u = \frac{\partial \psi}{\partial y}$ $v = -\frac{\partial \psi}{\partial x}$ Velocity Relations

Boundary Conditions for Stream Function: ψ

$\psi_{1,j} = \psi_{m+1,j} = \psi_{i,1} = \psi_{i,n+1} = 0$ for Left, Right, Bottom, and Top Boundaries Respectively

Boundary Conditions for Vorticity (vort or zeta) that are 2nd Order Accurate:

$$\zeta_{i,j} = \frac{\partial v_{i,j}}{\partial x} - \frac{\partial u_{i,j}}{\partial y} \quad \text{given} \quad i = 1, m+1 \quad \text{and} \quad j = 1, n+1$$

$$\zeta_{1,j} = \frac{1}{2\Delta x}\left(-3v_{1,j} + 4v_{2,j} - v_{3,j}\right) - \frac{1}{2\Delta y}\left(u_{1,j+1} - u_{1,j-1}\right) \quad \text{Left Side}$$

$$\zeta_{M+1,j} = \frac{1}{2\Delta x}\left(3v_{M+1,j} - 4v_{M,j} + v_{M-1,j}\right) - \frac{1}{2\Delta y}\left(u_{M+1,j+1} - u_{M+1,j-1}\right) \quad \text{Right Side}$$

$$\zeta_{1,j} = \frac{1}{2\Delta x}\left(v_{i+1,1} - v_{i-1,1}\right) - \frac{1}{2\Delta y}\left(-3u_{i,1} + 4u_{i,2} - u_{i,3}\right) \quad \text{Bottom}$$

$$\zeta_{1,N+1} = \frac{1}{2\Delta x}\left(v_{i+1,N+1} - v_{i-1,N+1}\right) - \frac{1}{2\Delta y}\left(3u_{i,N+1} - 4u_{i,N} + u_{i,N-1}\right) \quad \text{Top}$$

Simulation using the finite difference approach and the Gauss-Seidel (GS) along with the Successive Over-Relaxation (SOR) methods for solutions of the coupled non-linear differential equations. The Gauss-Seidel and SOR formulation of second-order finite difference equations stems from the Poisson equation as follows:

Poisson 3-D Equation:

$$\frac{\partial^2 \psi}{\partial x^2} + \frac{\partial^2 \psi}{\partial y^2} + \frac{\partial^2 \psi}{\partial z^2} = f$$

Gauss-Seidel Formulation:

$$\psi^n_{i,j,k} = \frac{1}{2\left(1 + \left(\frac{\Delta x}{\Delta y}\right)^2 + \left(\frac{\Delta x}{\Delta z}\right)^2\right)}\left(\psi^{n-1}_{i+1,j,k} + \psi^n_{i-1,j,k} + \left(\frac{\Delta x}{\Delta y}\right)^2\left(\psi^{n-1}_{i,j+1,k} + \psi^n_{i,j-1,k}\right) + \left(\frac{\Delta x}{\Delta z}\right)^2\left(\psi^{n-1}_{i,j,k+1} + \psi^n_{i,j,k-1}\right) - f^n_{i,j,k} \cdot \Delta x^2\right)$$

Where n represents the current iteration and n-1 represents the previous iteration.

SOR (Successive Over-Relaxation) Formulation:

$\psi^n_{i,j,k} = (1-\omega)\psi^{n-1}_{i,j,k} + \omega\psi^n_{i,j,k}$, given Relaxation Factor: $0 < \omega < 2$

This equation can improve stability by weighting the previous (n-1) iteration, which is important for the convergence of non-linear equations.

Input Parameters

Re=25 Reynold's Number

Pr=1 Prandtl Number

Fr=1 Froude Number

β=0.1 Coefficient of Thermal Expansion

ω=0.2 Under-Relaxation Factor or Relaxation Factor

L=M=N=20 Number of Grid-Mesh Intervals

u=0.2 Velocity BC at Top Surface

where $\Delta x = (x_{\max} - x_{\min})/L$, $\Delta y = (y_{\max} - y_{\min})/M$, $\Delta z = (z_{\max} - z_{\min})/N$ are the Interval Step Sizes

$$x_{\max} = y_{\max} = z_{\max} = 1$$

$$x_{\min} = y_{\min} = y_{\min} = 0$$

Central-Difference (CD) approach is implemented with Upwind-Downwind features disabled since CPU run time or execution time is reduced from hours to minutes on Matlab. Disabled Upwind-Downwind features lose little in integrity and accuracy since Reynold's number is sufficiently low that turbulence or reverse flow due to high vorticity does not occur.

A simplified flow diagram of the 2-D and 3-D algorithm is shown in the figure below:

Where: Vorticity = vort = zeta

Stream Function = psi

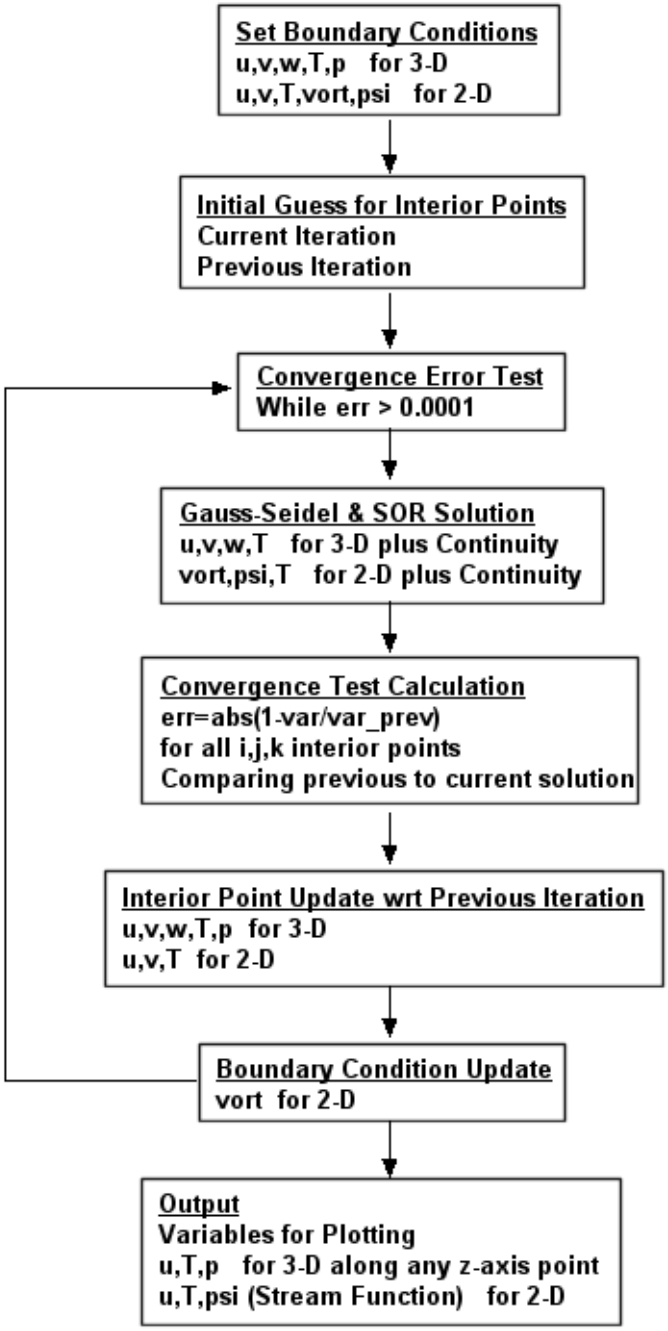

400 Lines of Code for 2-D Simulation
600 Lines of Code for 3-D Simulation

Figure 4 Flow Diagram for 2-D & 3-D Computer Program Simulation

Results

3-D Simulation: Shown below are xy-plane cross-sectional views at $z = z_{ctr}$

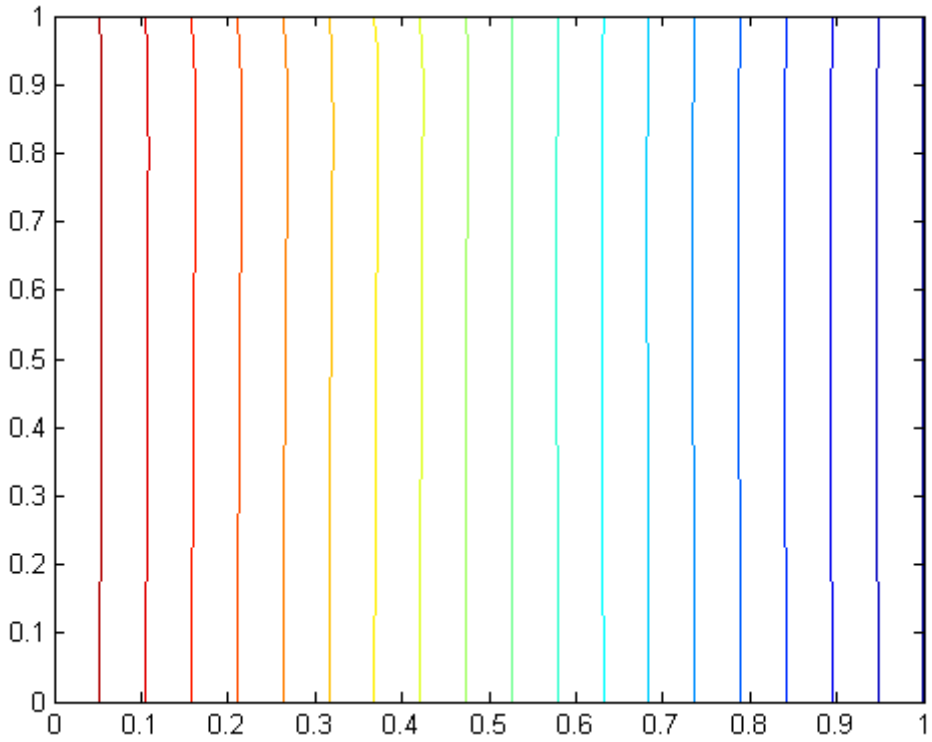

Figure 5 Contour Plot of Temperature

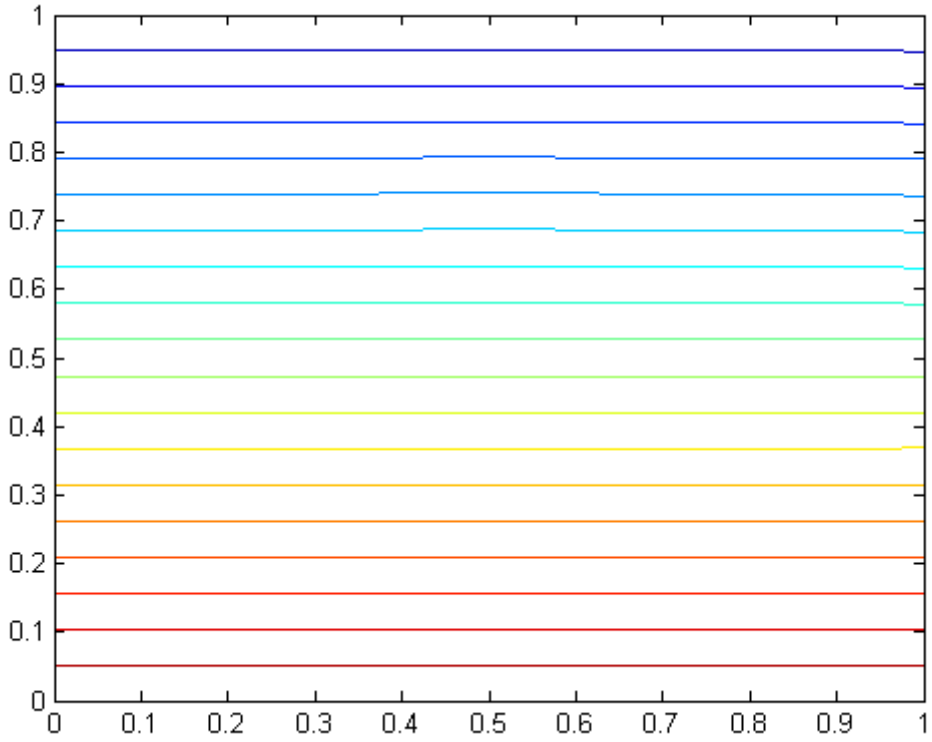

Figure 6 Contour Plot of Pressure

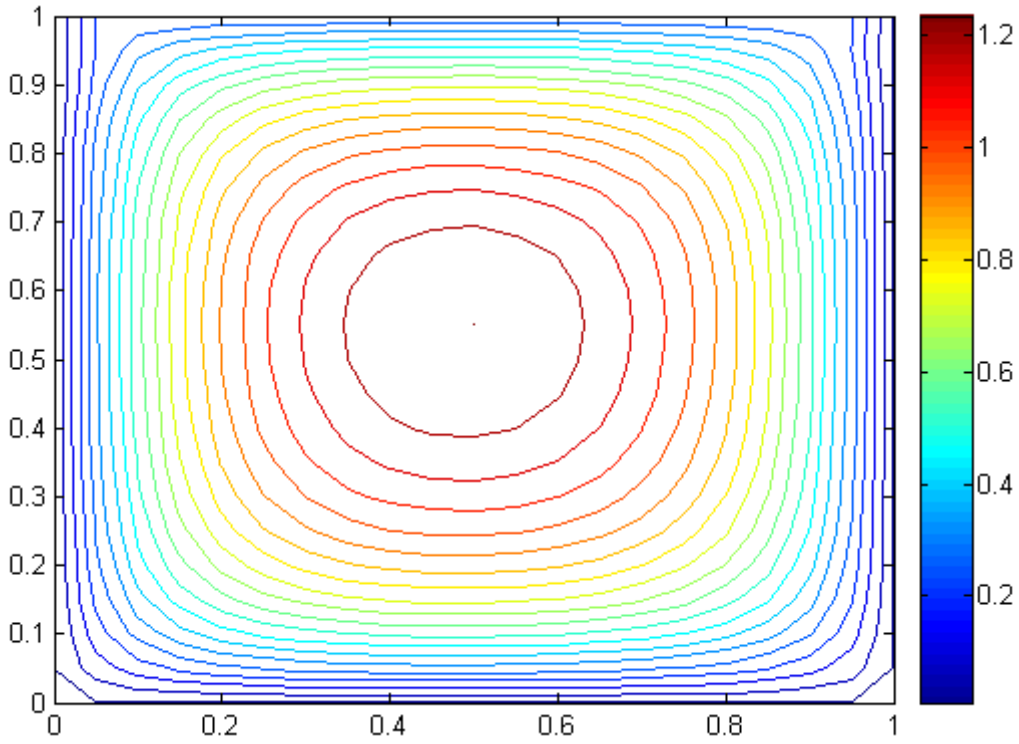

Figure 7 Contour Plot of u-Velocity

2-D Simulation: At xy-plane cross-sectional views through the center $z = z_{ctr}$

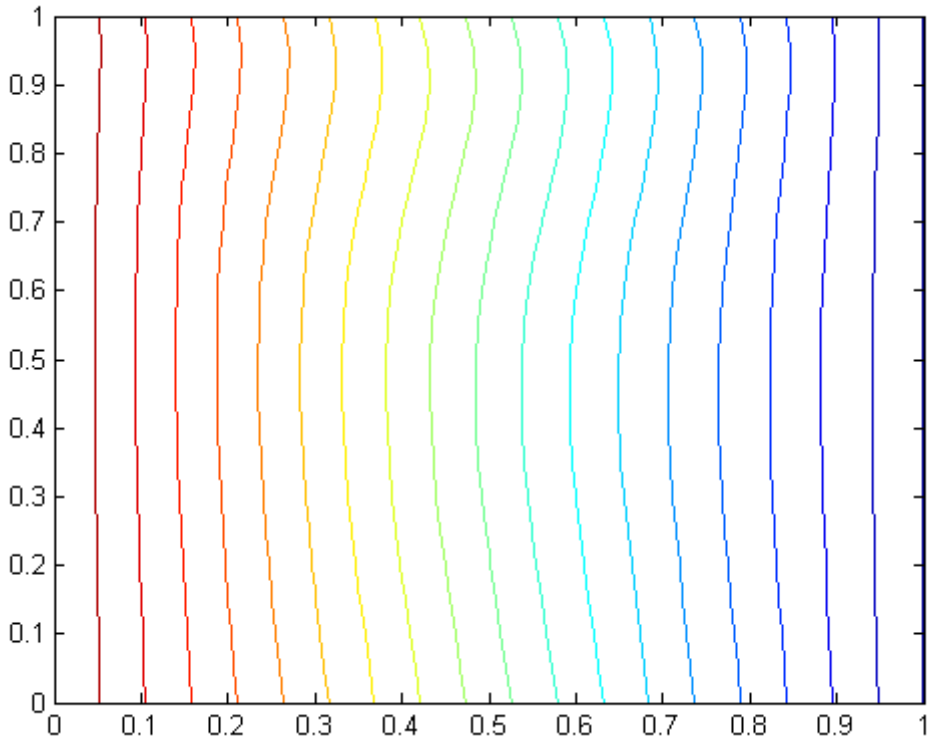

Figure 8 Contour Plot of Temperature

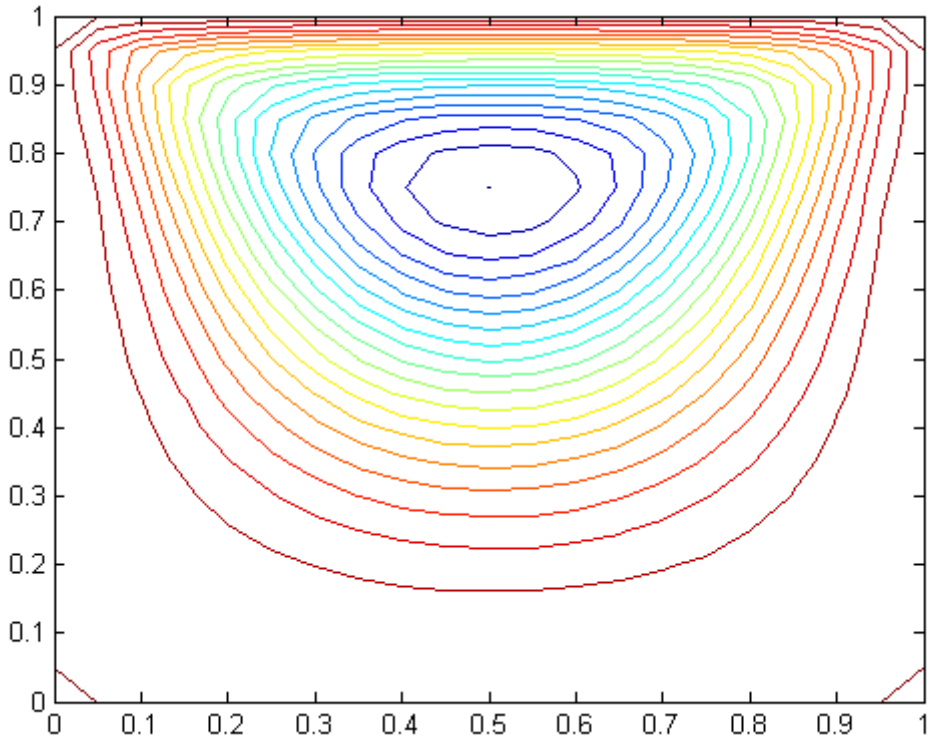

Figure 9 Contour Plot of Stream Function (psi)

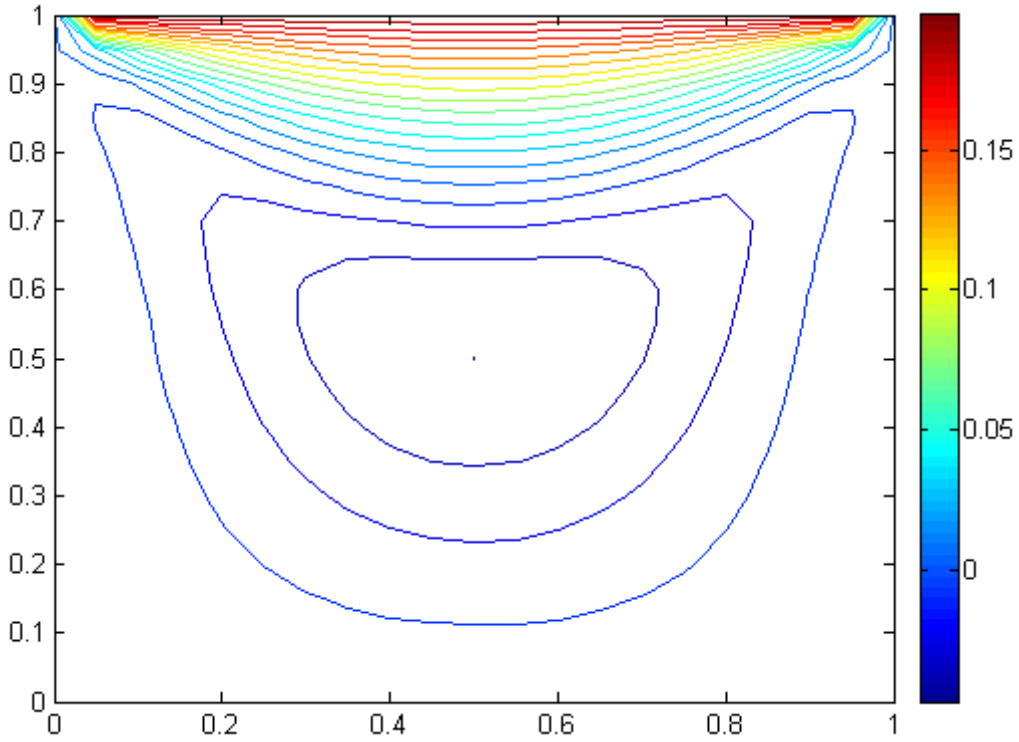

Figure 10 Contour Plot of u-Velocity

Conclusions

Various approaches to solutions of Partial Differential Equations (PDE's) were explored. The spectral methods apply to linear systems where an inverse transform requires the sampling of the continuous system or discretization. Integration of the functions as found in the finite volume and finite element approaches will tend to average or smooth the response and provide algorithm stability. High order polynomial curve-fitting will exhibit oscillation between the grid-mesh points and finite difference approaches require diagonal dominance in order to remain stable. In this solution to the Navier-Stokes non-linear equations, a Gauss-Seidel with SOR finite difference approach was used with under-relaxation to maintain stability during convergence. The comparison from 3-D to 2-D was made with consistent parameters at a point in the center of the fluid-cell $z = z_{ctr}$. The 3-D simulation model with 20x20x20 grid shows absolutely linear temperature and pressure gradients in the cross-sectional viewing plane as shown on Figures 5 and 6. The u-velocity or y-direction horizontal velocity contour plot of Figure 7 shows the boundary condition of 0.2 velocity (shown in blue) along the top surface along with a centered circulation loop. The velocity is shown to

increase (from blue to red) as is possible through the energy equation, which influences the momentum. There are a number of gradients to contend with in the 3-D simulation. For velocity there are 9 gradients, for temperature there are 3 gradients, and for pressure there are 3 gradients. In addition, all variables except for scalar constants (such as *Re, Pr, Fr,* etc.) are indexed to 3-dimensional indices (for example, velocity component $u_{x,y,z}$). All of these variables contribute to longer processing times. By eliminating the upwind-downwind algorithm, the processing time for 3-D was reduced from hours to 190 seconds. Eliminating the upwind-downwind algorithm does not create inaccuracies, since upwind-downwind increases algorithm stability at high Reynold's number (of around *Re* = 200). In this experiment, turbulence is to be avoided and *Re* as well as *Pr* numbers are low.

The 2-Dimensional model with 20x20 grid applies when axis-symmetric flow can be assumed or occurs due to the boundary conditions and properties of the problem. In this application, side-to-side heating in a rectangular channel means that axis-symmetric flow occurs and the properties are consistent or equal along the optical propagation (or z-axis). Holding the parameters and variables constant between the 3-D and 2-D case, the temperature contour plot of Figure 8 shows a small amount of waviness or non-linearity along the upper regions of the plot. The 2-D simulation employs the Poisson equation for Stream-Function with Vorticity as the constant as shown as follows:

$\frac{\partial^2 \psi}{\partial x^2} + \frac{\partial^2 \psi}{\partial y^2} = -\zeta$ Poisson Equation with Stream-Function = ψ and Vorticity = ζ

In this equation, the Vorticity variable is assumed a constant. ζ = constant

The algorithm required 50 iteration loops to stabilize vorticity to a constant before updating the vorticity boundary conditions. Furthermore, the negative vorticity tends to de-stabilize the Gauss-Seidel equation. All this contributes to longer processing times, which in this case is 45 seconds. In addition, finer grid-mesh resolution will reduce algorithm instability. The contour plot of Stream-Function (ψ) shown in Figure 9 depicts non-centered potential lines, which is possibly due to the surface velocity of 0.2 and the addition of heat energy that increases momentum in the upper region and reduces momentum in the lower region. The contour plot of u-Velocity or y-direction velocity in figure 10 shows the boundary condition of 0.2 velocity along the top surface in red. A boundary layer is formed as the velocity gradient decreases along the vertical axis. The dark blue region shows reverse flow as there is a little re-circulation in the lower and

bottom regions as occurs in the 3-D case. The circulation loop is centered as in the 3-D case and there is a little confusion as to the direction of flow in the upper corners. This is possibly due to the requirement that the boundary conditions for Stream-Function and Vorticity be continuous, which may not be the case for the corners or transition from horizontal to vertical directions. The partial differential equation for vorticity that is used at the boundaries is given as: $\zeta = \frac{\partial v}{\partial x} - \frac{\partial u}{\partial y}$ and,

for Stream-Function at the boundaries: $\psi = 0$.

In general, 2-D simulation is great for cutting plane flow visualization and must be regarded or considered to be consistent with the true situation given the underlying assumptions and approximations. Two-Dimensional modeling is significantly faster in processing speed, but for this experiment the 3-D model was pursued so that optical ray and wave propagation models can be integrated into the fluid-dynamics model. This project using Matlab to program the Navier-Stokes equations is a valuable stepping stone to obtaining a valid approach to simulating the fluid dynamics problem of our confocal holography experiment.

Diffraction Limit and the Point Spread Function (PSF)

Ultimate resolution is the diffraction limited resolution that produces the smallest possible blur spot size or Point Spread Function (PSF). The aperture edge, field-stop edge, or entrance pupil edge is a diffraction source that creates interference with the incident wave across the aperture of the pupil plane. Diffraction limited resolution is a function of the aperture diameter and the wavelength of the emission source along with the focal length assuming no lens or optical aberrations. The diffraction limit focal point or PSF from a circular aperture produces a focused spot with a set of concentric rings formed by the intensity or wave energy of the incident beam interfering with the diffracted beam from the edges of the aperture.

Fraunhofer far-field diffraction limit is the in-focus condition where the collimated rays entering the aperture are plane waves with no spherical wavefront. Fraunhofer diffraction has multiple concentric light and dark diffraction rings representing constructive and destructive wave interference. Diffraction limited resolution is the radius from the optical centerline out to the first dark airy disc at the focal plane. The angular extension to the first dark airy disc assumes ideal optics with perfect lenses and is defined as:

Diffraction Limited Resolution Radial Angle: $\theta_r = 1.22\lambda / D$ to the first airy dark ring.

Wavelength range for visible light: $\lambda = 380\ to\ 750\ nm/wave$ from violet to red.

Approximate wavelength for an electron beam: $\lambda \cong 0.1\overset{0}{\text{A}}/wave = 0.01nm/wave$.

Since electron microscopes have a significantly shorter wavelength than optical microscopes then the resolution to measure detail is much greater. The limiting factor for electron microscopes is the aberrations generated by the electro-magnetic lenses.

The ultimate minimum resolution is the diffraction limit which is a function of the wavelength and aperture. Optical components degrade resolution and increase the blur spot size from the diffraction limited condition. Typically, aspheric lens surfaces and long focal lengths are required to image at the diffraction limit. The characteristics of optical diffraction limited resolution is explained below.

Aperture Diameter or Entrance Pupil Diameter or Field-Stop Diameter: D
Note: Marginal rays are located at the perimeter or circumference of the aperture at

$$r = r_{\max} = \frac{1}{2}D$$

Chief rays are central to the optical axis at $r = 0$.

The Nyquist sampling limit is represented by two samples per wave or cycle of a waveform. A fringe can be considered a waveform since it is a repeated sinusoidal pattern. The Nyquist frequency is one-half the sample rate, which represents the transition from complex values to complex conjugate values in the Fourier transform.
1 wave = 1 cycle = 2 pixels = 2 detectors = 2 samples to the Nyquist sampling limit
2 pixels = 1 line pair (Nyquist limit is 1 dark line and 1 light line)
1 fringe = 1 fringe-spacing for a hologram or wave interference pattern
1 wave of a hologram fringe pattern = 1 fringe-spacing

However, the Nyquist limit of two samples per fringe is inadequate to determine a minute phase-shift in the hologram. Small changes in phase-shift, <λ/80 waves, require at least 16 samples per fringe. The convergence angle of the beams to the camera sets the fringe-spacing at the camera. The optical wedge is between 0.5° to 1° and this shallow

convergence angle makes for a long path length to the camera. The long path length also provides for complete beam overlap at the camera.

The airy disc is the smallest possible focal point radius with a perfect circular aperture lens that is limited by the diffraction of light. The diffraction pattern from a uniformly illuminated circular aperture has a bright central region (airy disc) followed by a series of concentric light and dark rings (airy pattern). Fresnel near-field diffraction is the condition for out-of-focus rays that occurs from the interference of waves that have curvature. Ray or wave propagation over a longer path length will transition from a curved spherical wave to a more planar wave. The diffraction limited radial displacement at the focal plane (*fp*) is given as:

Diffraction Limited Resolution Radial Displacement: $r_{fp} = FL \times \tan\theta_r$

Path Length or Focal Length: *FL*

If the *FL* is sufficiently large compared to the radius-of-curvature of the wave at the aperture then the diffraction is far-field Fraunhofer otherwise the diffraction is near-field Fresnel. An optical system that has negligible aberrations will produce a Point Spread Function (PSF) resolution at the image plane that is near the diffraction limit. The Fraunhofer far-field diffraction pattern PSF for a circular aperture with no focusing lens aberrations is shown in the figure below:

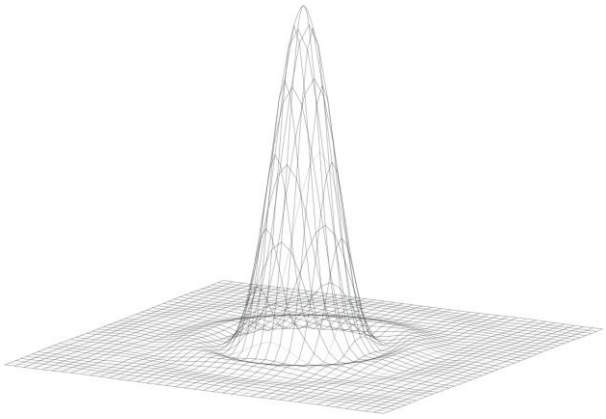

Figure 1: The Airy Disc Point Spread Function (PSF) in the Image Plane for a Circular Aperture

Diffraction limited resolution is the radius out to the first dark ring that contains 83.8% of the encircled energy. The angular subtense from the center out to the first dark ring is $\theta_r = 1.22\lambda / D$ (as above)

The radius at the focal plane (*fp*) is given as: $r_{fp} = FL \times \tan\theta_r$ (as above)

Effective Focal Length of the lens: *FL*

Focal Ratio or Optics f-number: $f/\# = \frac{FL}{D} = \frac{1}{2\tan\theta}$

For example: $f/2 = \frac{8}{4} = 2$

The low-pass filter spatial cut-off frequency (f_{lpf}) for a perfectly corrected optical system is given as: $f_{lpf} = \frac{1}{\lambda \times (f/\#)}$

Numerical Aperture is given as: $NA = n\sin\theta \cong \frac{n}{2}\frac{D}{FL} \cong \frac{n}{2\times(f/\#)}$

Where:

Index-of-Refraction: *n* = 1 for air
Index-of-Refraction: *n*=1.5 for glass

The encircled energy or intensity out to the first airy disc is 83.8%. Converting from a Fraunhofer diffraction limited resolution PSF to a normal Gaussian PSF at the same encircled energy of 83.8% produces a radial standard-deviation of $r_{fp} = 1.91\sigma_r$. The diffraction limited PSF resolution represents the smallest blur spot size at the focal point given ideal aberration free focusing optics. The geometrical aberrations added to the diffraction limited resolution for a Gaussian distributed blur spot size is given as:

Standard-Deviation for Geometrical Aberrations: $\sigma_{geo} = \sqrt{\sigma_{diff}^2 + \sigma_{sph}^2 + \sigma_{dfoc}^2 + \sigma_{coma}^2}$

Where:

Standard-Deviation for Diffraction Limit to Gaussian PSF Conversion: $\sigma_{diff} = 1.91\sigma_r$

Diffraction Limited Resolution PSF Radial Angle subtense: $\sigma_r = 1.22\lambda / D$

Standard-Deviation for Spherical Aberrations: σ_{sph}

Standard-Deviation for De-Focus: σ_{dfoc}

Standard-Deviation for Off-Axis Coma: σ_{coma}

The dominant resolution sources in electron microscopes are the spherical aberrations and de-focus where $\sigma_{sph} > \sigma_{diff}$ and $\sigma_{dfoc} > \sigma_{diff}$. Microscopes that direct the beam off-axis will introduce coma aberrations where $\sigma_{coma} > \sigma_{diff}$.

Aspheric Lens Design for Low f/number and Low Distortions

The initial objective was to provide a low focal ratio f/number to maximize the angle of the cone beam in the specimen region. This would reduce reconstruction error since the angle to the marginal rays is large and more of the rays would intersect the computational grid-mesh cells allocated to the specimen. The field-of-view is ±2º for scanning the probe beam in the *xy*-axis directions. The *xy*-axis is a plane that is perpendicular to the optical propagation *z*-axis. The focused spot size is to be near diffraction limited to minimize the size of the probe beam for scanning resolution. Aspheric optics with focal ratio varying from f/1.5 to f/2 was investigated to produce low aberrations at low focal ratio f/number.

A ray trace program was written in Matlab to study a single aspheric lens as shown in the figure below:

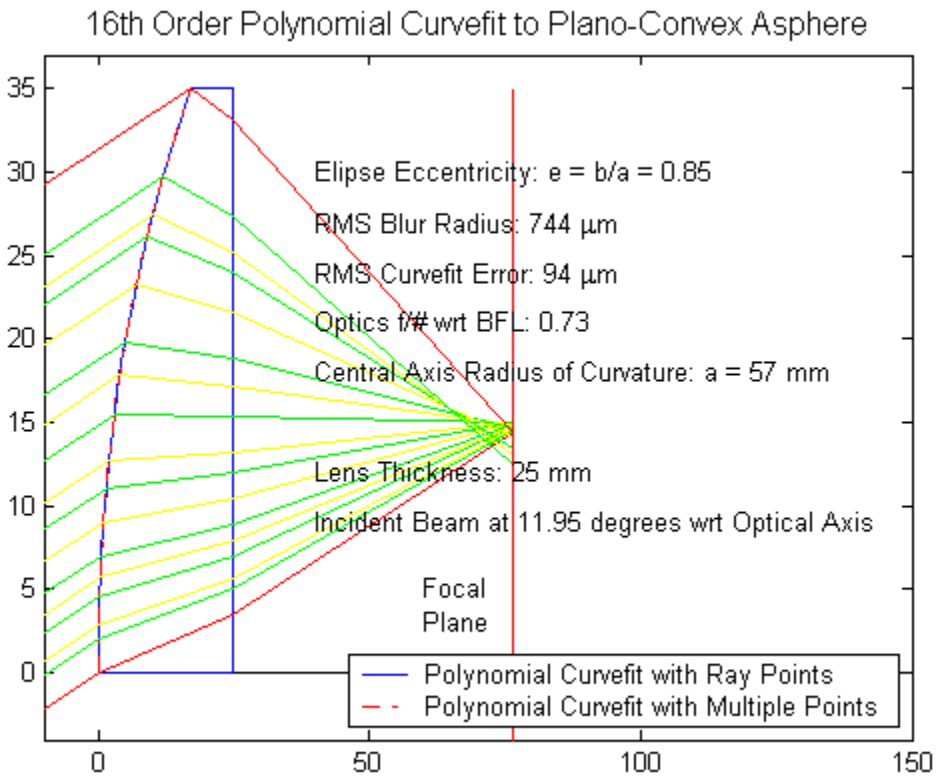

Figure 1 Matlab Ray Trace Program for Aspheric Lens with a 16th Order Polynomial Curvefit

The aspheric lens shape was an ellipsoid with a 16th order polynomial curvefit to input these coefficient terms into Zemax.

An example of an aspheric lens design in Zemax is shown in the figure below.

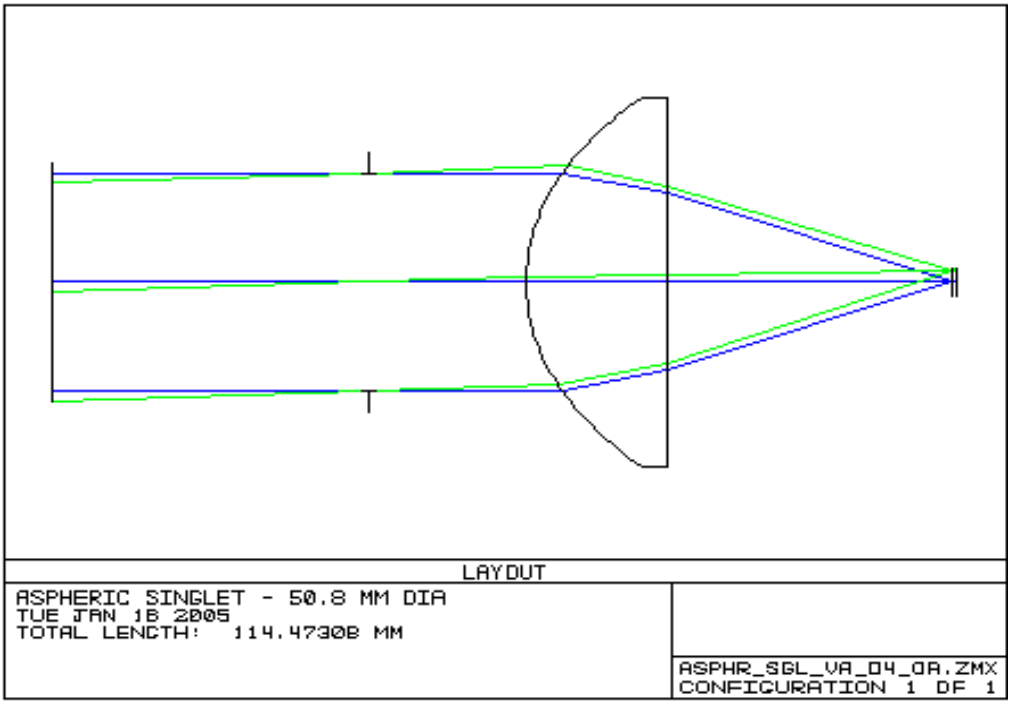

Figure 2 Aspheric Lens Design on Zemax

The single lens design was abandoned because two side-by-side object and reference beams are focused in parallel by a telecentric lens design. The telecentric lens produces geometric aberrations that cannot be corrected by using aspheric surfaces. The result was a lens design using standard spherical surfaces since the improvement in resolution was minimal when designing lenses with custom aspheric surfaces.

Wavefront Error due to Sampling and Optical Aberrations

The wavefront error is represented by the deviation of a fringe line from a straight line. Variations of a fringe line are due to a change in the fringe contrast or intensity in a hologram. The wavefront error is caused primarily by aberrations of the optical lenses and the number of samples per fringe of a fringe pattern waveform or hologram. Vibrations also affect wavefront error, but are considered negligible as compared to the wavefront error produced by spherical aberrations. Phase-shift is represented by a fringe-shift displacement where the fringe spacing is equivalent to 1 wave or 2π radians. The Nyquist sampling criteria is 2 samples/fringe or 2 pixels/wave of a fringe pattern

waveform. The higher the spatial sampling of a waveform or hologram then the lower the wavefront error contribution will be from waveform sampling. Few samples of a fringe or wave means that a sampled data point is less likely to lie at the peak of the wave. The wavefront error is also due to optical aberrations such as spherical, astigmatism, coma, etc. It is not possible to isolate the wavefront error due to sampling from the wavefront error due to optical aberrations. However, it is possible to compensate the effects of a lower spatially sampled wave. A sampling rate compensator algorithm in Matlab pseudo-code that reduces the wavefront error due to sampling is proposed as follows.

1) Collect the Peak Data or Ripple Data given Intensity Data Array (I)

% Intensity Data Array from Hologram: $I = I(x) = I_{bias} + I_{peak}\cos(\omega_x \cdot x + \varphi)$ for the line scan camera

num_smpls = length(I); % Size of array: num_smpls = 8192 pixels or samples

I_{max} = max(I); % Maximum Value in Intensity Array

$I_{min} = I_{max} \cos(1/10 \text{ wave} \times 360 \text{ deg/wave}) = 0.81\ I_{max}$

```
j=1; % Initialization
for i = 1 : num_smpls
   if I(i) > I_min
      I_ripple(j) = I(i); % Peak Ripple Data
       j = j+1; % Counter Update
   end
end
```

I_{ripple}; % Ripple Data Array of Peak Intensity Values

num_ripple_smpls = length($I_{rippple}$); % Number of elements in the Ripple Data Array

2) Smooth the Ripple Data from Sparse Fringe or Wave Sampling

n = input ('Number of Samples per Fringe: Typical (16 or 32) ');

scale_factor = 1 – exp(-n/4.4); % Waveform Sampling Factor

I_{smooth} = scale_factor x I_{ripple}; % Sampled Data Smoothing

n (samples/fringe)	scale_factor
10	0.897
16	0.974
20	0.989
32	0.999

2) Nyquist Sampling Limit:

$$\omega_{nyq} = \frac{2\pi\, rad\,/\,cycle}{1 wave\,/\,cycle} \times \frac{1\dfrac{sample}{pixel}}{2\dfrac{samples}{wave}} \times \frac{1000\,\mu m\,/\,mm}{7\,\mu m\,/\,pixel} = 448.80\, rad\,/\,mm$$

at 7µm/pixel Detector Spacing

The Nyquist sampling limit is 2 samples/wave

The minimum sampling limit to resolve a phase-shift of < λ/20 waves RMS is n = 8 samples/wave or 8 samples/fringe where 1 fringe = 1 wave.

3) Filtering Out Spherical Aberration

Apply a second-order digital High-Pass Filter (HPF) with either a Butterworth, Bessel, or Linkwitz-Riley damping factor.

HPF cut-off frequency:

$$\omega_{hpf} = 10 \times \frac{2\pi\, rad\,/\,cycle}{1 wave\,/\,cycle} \times \frac{1/2\, wave}{1/2 \times (8192)\, pixels} \times \frac{1000\,\mu m\,/\,mm}{7\,\mu m\,/\,pixel} = 1.1 rad\,/\,mm$$

Thus, the wavefront error will be due to the spatial frequency components that are greater than the spherical aberration spatial frequency.

Phase-Shift and Spatial Carrier Frequency Determination from Holograms

There are three methods to determine the phase-shift and the spatial frequency from the wave interference pattern waveform. They are:

1) Direct Waveform Signal Processing Method using the Least-Square Error (LSE) Quadratic Polynomial Curvefit to at least three peaks.
2) Correlation Method by finite phase-shifting a scaled reference waveform until a minimum correlation is found over 2π radians of phase-shift.
3) Fourier Transform Method where the Power Spectrum identifies the spatial frequency from the constant spacing of the fringes. The phase-shift is determined from the arc-tangent of the complex part argument to real part argument ratio from the Fourier transform.

The steps that are common to all three methods are:

1) Define fringe pattern harmonic waveform: $y(x) = X_{offset} + X_{peak}\cos(kx+\phi)$
2) Input the sample rate or the number of samples per wave (default: 8 samples/wave)
3) Input the number of waves (default: 4 waves)
4) Determine the minima and maxima for the number of waves and then normalize the sampled waveform. Estimate the offset and peak values from the waveform minima and maxima values, which can be in error due to the number of samples per wave and the associated phase-shift.
5) Determine the peaks based on zero slope or slope crossing from positive to negative using the first order finite difference
6) Determine the approximate spatial frequency and phase-shift from the waveform peaks

Apply the three different methods:
a) The Direct Waveform Signal Processing Method
    1) Apply Quadratic Polynomial Least-Square Error (LSE) Curvefit to the number of peaks minus one
    2) Calculate the spatial frequency from the multiple peaks
    3) Calculate the phase-shift from the estimated first peak
b) Correlation Method
    1) Create a scaled reference waveform using the calculated waveform minima, maxima, and approximate spatial frequency
    2) Phase-Shift this reference waveform in incremental steps with respect to the sampled data and determine the maximum correlation

3) Phase-Shift occurs at maximum correlation

c) Fourier Transform (FT) Method

1) Peak of Power Spectrum is the spatial carrier frequency of the waveform

2) Phase-Shift of the hologram waveform is the arc-tangent of the FT imaginary to real part ratio at the spatial carrier frequency.

3) Determine the Phase-Shift by taking the arc-cosine of the FT DC component.

The simulation model for the Fringe Interference Pattern Waveform was developed as follows:

Input the Number of Samples per Wave: $num\_smpls\_wave = 8$ (Default)

(Note: 8 samples/wave or 8 samples/fringe is the calculated sampling resolution limit on the camera)

Input the Number of Waves: $num\_waves = 4$ (Default)

Number of Samples: $num\_smpls = num\_smpls\_per\_wave \times num\_waves = 8 \times 4 = 32$

Number of Data Points: $num\_pts = num\_smpls + 1 = 32 + 1 = 33$

Spatial Frequency: $k = 2\pi f = \dfrac{2\pi}{num\_smpls\_per\_wave} = \dfrac{2\pi}{8} rad/sample$

(where: 1 cycle = 1 wave)

Frequency: $f = \dfrac{1}{num\_smpls\_per\_wave} = \dfrac{1}{8} waves/sample$

Nyquist Limit: $nyq = \dfrac{1}{2} num\_smpls = \dfrac{1}{2} 32 = 16\, samples$

Displacement: x_i $(samples)$ $for\, 1 \le i \le num\_pts$

(Where: $x_{i+1} = x_i + \Delta x = x_i + 1\ given\ \Delta x = 1 sample$)

Discrete Fringe Pattern Waveform: $y_i = y(x_i) = X_{offset} + X_{peak} \cos(k \cdot x_i + \phi)$

From the Sampled Data of the Waveform:

$$X_{offset} = \frac{1}{2}(\max(y_i) + \min(y_i))$$

$$X_{peak} = \frac{1}{2}(\max(y_i) - \min(y_i))$$

Optical Aberrations on Holograms

An example of spherical aberration, astigmatism, and coma is shown in the figure below.

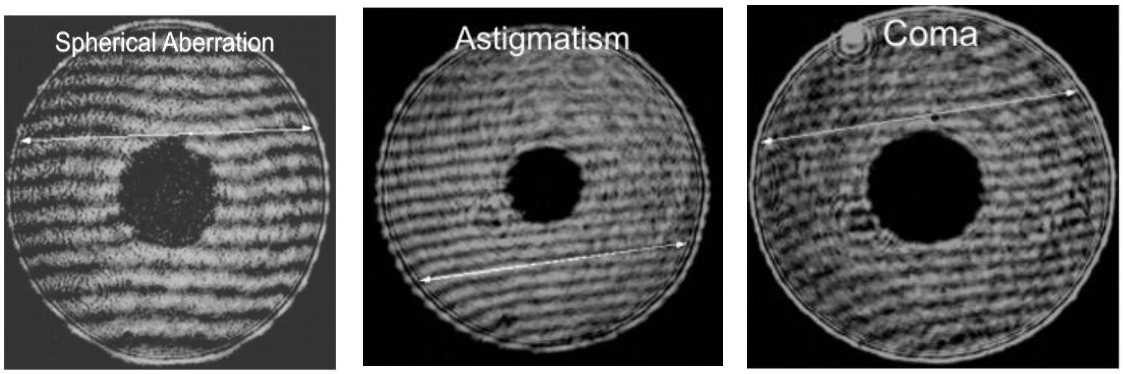

Figure 1: Hologram or Interferogram with Optical Aberrations

Spherical aberrations are represented by the slight gull-wing or dish shape curvature of the fringe lines. Spherical aberrations are due to the on-axis rays propagating through a lens. The blur spot is radially symmetrical since ray propagation is along the optical axis. Since the focusing lens is thicker at the center than at the edges then the phase-shift is greater along the optical centerline. The marginal rays at the edges of the aperture or pupil have a shorter optical path length than the central chief ray and this retards the phase-shift causing a dish shape to the hologram. The phase-shift is the deviation of a fringe line from a straight line. A phase-shift of 1 wave or 2π radians is represented by 1 fringe-spacing. The phase-shift due to spherical aberration along the string line in the figure above is approximately 1/3 wave RMS of a fringe spacing. Astigmatism is represented by a fringe line curvature that is upward on one side and downward on the other side of the central obscuration or annulus. Astigmatism is represented by the rays that propagate in an orthogonal or perpendicular plane have a dissimilar focal point. Coma is represented by serpentine or S-shaped fringe lines. Coma is represented by the aberrations caused by rays propagating through a lens that are off the central axis and they create an asymmetrical blur spot that is greater than the blur spot size for spherical aberration. Beam steering mirrors that tilt the beam incident angle onto optical lenses introduces coma.

Phase-Shift Determination from Fringe Pattern Hologram Measurements

This is the signal-processing algorithm that determines the fringe-shifts at the cone beam marginal rays that produces two holograms for every scan position. The fringe-shift is the phase-shift of the measured hologram at steady-state thermal equilibrium to the reference hologram where there are no dynamic thermal gradients within the fluid-cell. There are three methods to process this signal: 1) Direct Phase Determination from the Waveform, 2) Correlation of the Measured Waveform to a Reference Waveform, and 3) Fourier Transform Method to Determine Phase-Shift.

The method that produces the least error will be used to determine the phase-shift measurements of both the measured and reference holograms as $2\times(16\times 2)\times 4=256$ hologram samples in total. The spatial sampling resolution is limited by 8 detector samples per wave as determined by the shallow angle of the object beam to reference beam overlap. This marginal 8 pixels/wave spatial sampling frequency creates a higher potential error for determining the phase-shift in the hologram. The attributes in favor in this signal-processing situation are: 1) Steady amplitude, 2) Constant spatial frequency, and 3) High fringe contrast ratio. Since the waveform frequency, amplitude, and fringe contrast ratio or fringe dynamic range is easily measured then the only other variable to determine is the phase-shift in respect to a reference edge or origin. A sample hologram is shown in the figure below:

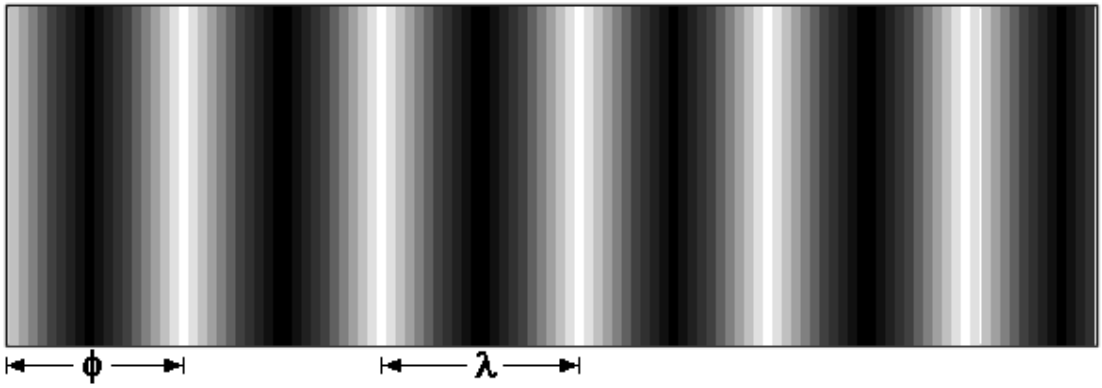

Figure 1 Sample of a Measured Hologram Showing Periodic Intensity Change with Constant Frequency and Amplitude

The Phase-Shift (φ) is the displacement of the waveform from the origin to the amplitude peak. The period or wavelength (λ) of the waveform is determined primarily by the crossing angle of the overlapped object beam onto the reference beam. The discrete

sampling of this 8-bit (0 to 255 scale) resolution waveform is 20 samples per wave as shown by the bar widths on the figure where one wave represents the wavelength.

Matlab simulations were developed to create a discrete sampled waveform and then determine the computed phase-shift from an input phase-shift value. Since the waveform is periodic then the location of the waveform peak can be used to determine the phase-shift.

Method 1: Direct Phase Determination from the Waveform

The most direct method to determine the Phase-Shift is to detect the amplitude peak when the slope transitions from positive to negative. Given an input waveform phase-shift of -60° the computed phase-shift is –45° with 8 samples/wave discrete sampling rate. An example of this sampled waveform is shown in the figure below:

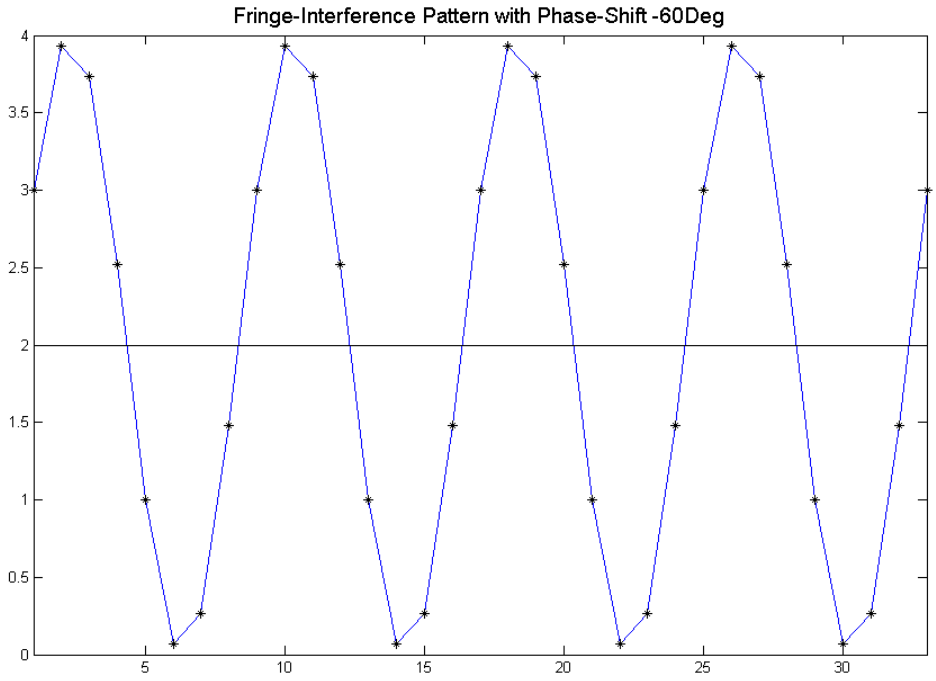

Figure 2 Discretely Sampled Waveform at 8 samples/wave with Marginal Resolution to Determine Phase-Shift

Applying a Least-Square Error (LSE) curvefit to a quadratic polynomial for the amplitude peaks produces a phase-shift of –58.6230°. This error is 60-58.6230=1.377°.

Method 2: Correlation of the Measured Waveform to Reference Waveform

The waveform is scaled so that once an approximate value or the phase-shift is determined then a fine resolution stepping correlation algorithm can be applied to determine the phase-shift. This scaled waveform is shown in the figure below:

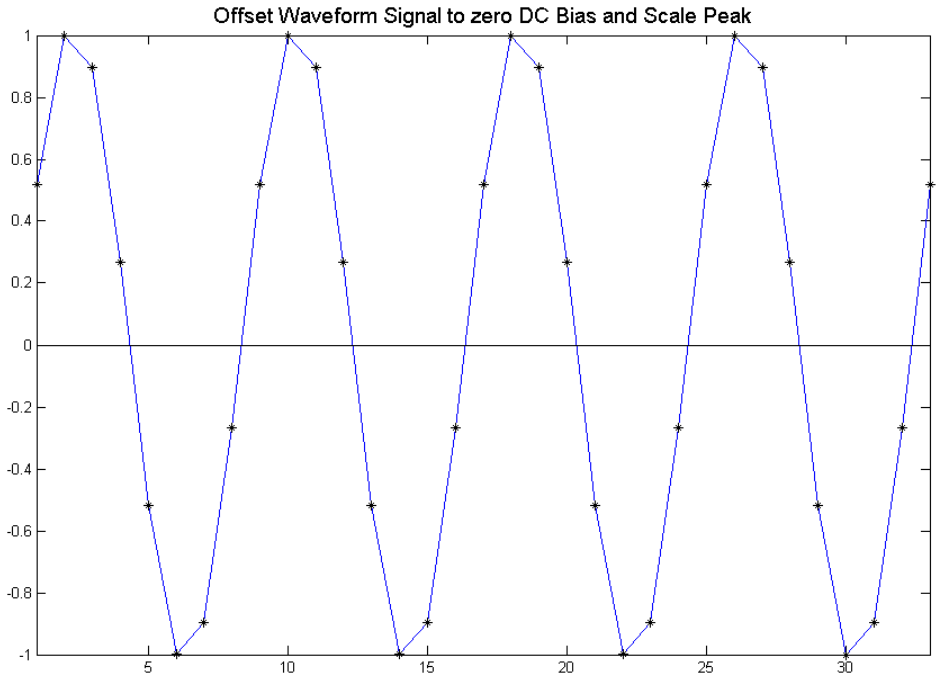

Figure 3 Scaled Waveform within the Desired Domain for Correlation with a Reference Waveform

The Least-Square Error (LSE) correlation method of the scaled waveform to the reference waveform produces a phase-shift error of –60.0230° that has a smaller error than the LSE curvefit error method to a quadratic polynomial method. This error is 60.0230-60=0.0230°.

Method 3: Fourier Transform Method to Determine Fringe-Shift

The Fourier Transform method produces the spatial frequency and phase-shift of the signal directly and no signal filtering or anti-aliasing filters are necessary. The spatial frequency appears as a virtual line frequency with a peak and contrails from the discrete sampling for each wave along with the phase-shift value from the DC component or bias value. The range for determining the phase-shift using the Fourier Transform is between ±90° in contrast to the two other methods that can determine the phase-shift between a ±180° range.

Fringe Image Data Analysis

The camera detects the hologram interference pattern in the form of fringes. The dynamic range of the camera is set to a maximum of 10 bits or a scale of 0 to 1023 for intensity. The neutral density filters and the polarizing wave plate are used to adjust the level of light intensity on the camera. The peaks approach 1023 and are typically around 900 after adjusting the optical attenuators. The valleys are unfortunately truncated at the zero level because the camera is not sensitive to low level light as found with area CCD cameras. The Dalsa Piranha P2-23-08k40 (1x8192 at 7µm/pixel) line scan camera is significantly less sensitive as compared to a typical area scan CCD camera. The RedLake and Point Grey Research 2000x3000 array CCD cameras on FireWire IEEE-1394 links in the lab were significantly more sensitive to light and would saturate on ambient background levels. These more sensitive area scan cameras have issues with frame-to-frame streaking due to problems with electronic and mechanical shutter synchronization. The Dalsa Piranha line scan camera connects to a National Instruments PCI-1428 Frame Grabber with a base mode camera link interface. A uniform flood light source biases the low level intensity slightly above the zero level so that the fringe intensity varies between an average intensity level of 20 to 900 for image acquisition. The CCD array cameras must be operated with the room lights off but the Dalsa line scan camera can be operated with the room lights on. The radiometric sensitivity of the Dalsa line scan camera at 457nm wavelength is 19nJ/cm^2, which is attenuated by 50% from the peak at 720nm wavelength. A simulated cosine waveform shows a typical low level truncation as seen in the data when imaging. This truncation is shown in the figure below at 8 samples/cycle:

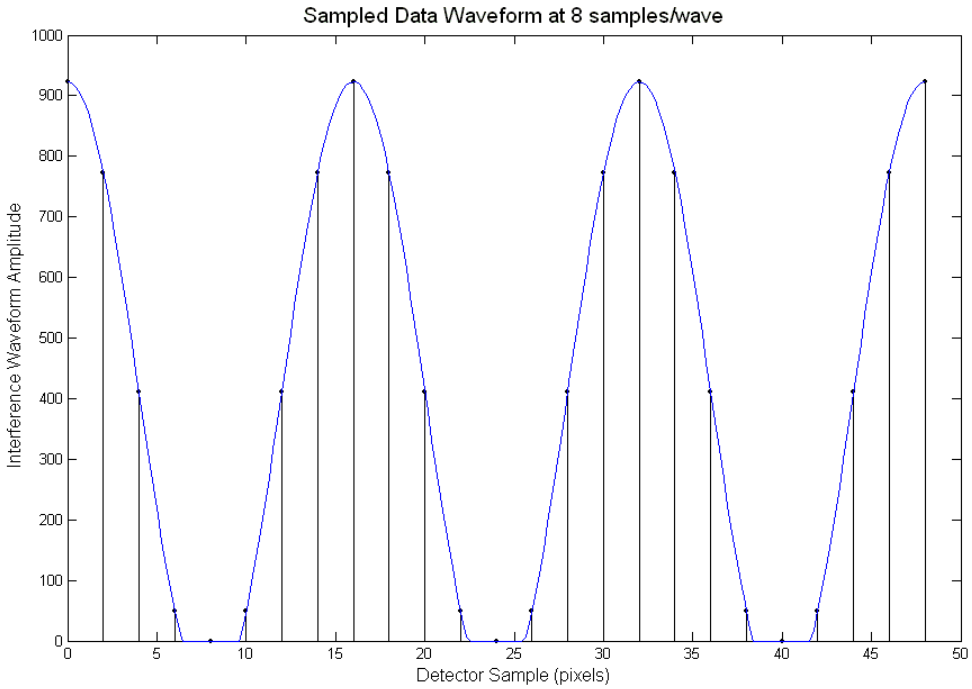

Figure 1 Waveform Clipping at 8 samples/wave

The truncation at 16 samples/cycle is shown in the figure below:

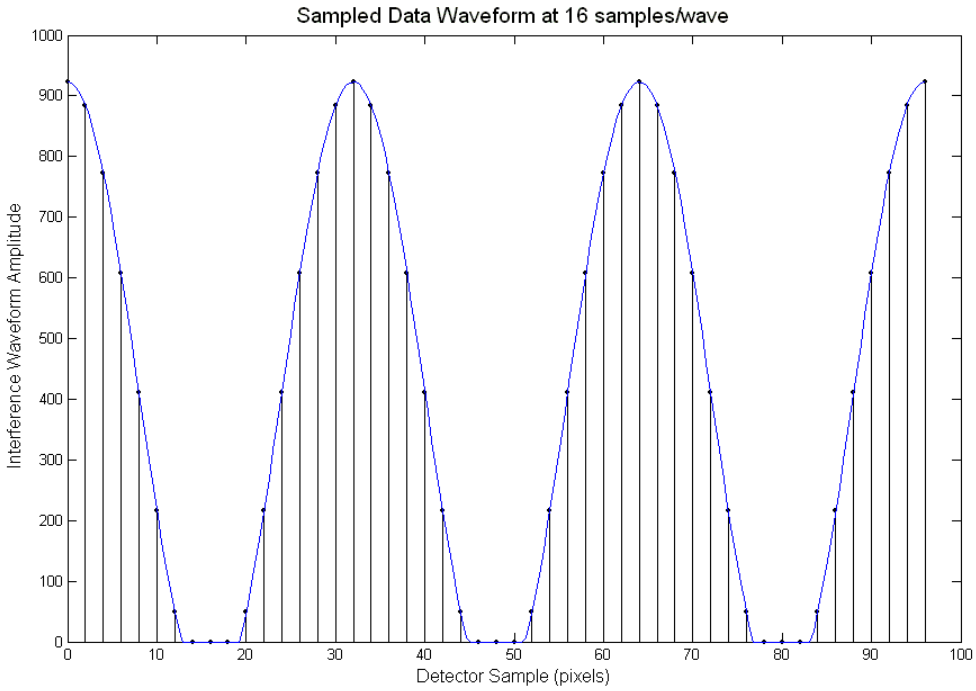

Figure 2 Waveform Clipping at 16 samples/wave

The phase-shift is determined at the origin and in this case is 0 degrees for a cosine wave or 90 degrees for a sine wave. If the truncated region is at the origin then the phase-shift cannot be determined. The Fourier Transform method for determining the phase-shift requires a continuous waveform. Least-Square Error (LSE) polynomial curve fitting is therefore applied to the clipped regions as this should have no impact on phase-shift determination given the constant fringe spatial frequency. LSE polynomial curve fitting uses the data points before and after the truncated region. Second, third, and fourth order polynomial curve fitting methods are examined to find the least error to a cosine wave. The quadratic or second-order polynomial curve fit to 8 samples/cycle is shown in the figure below:

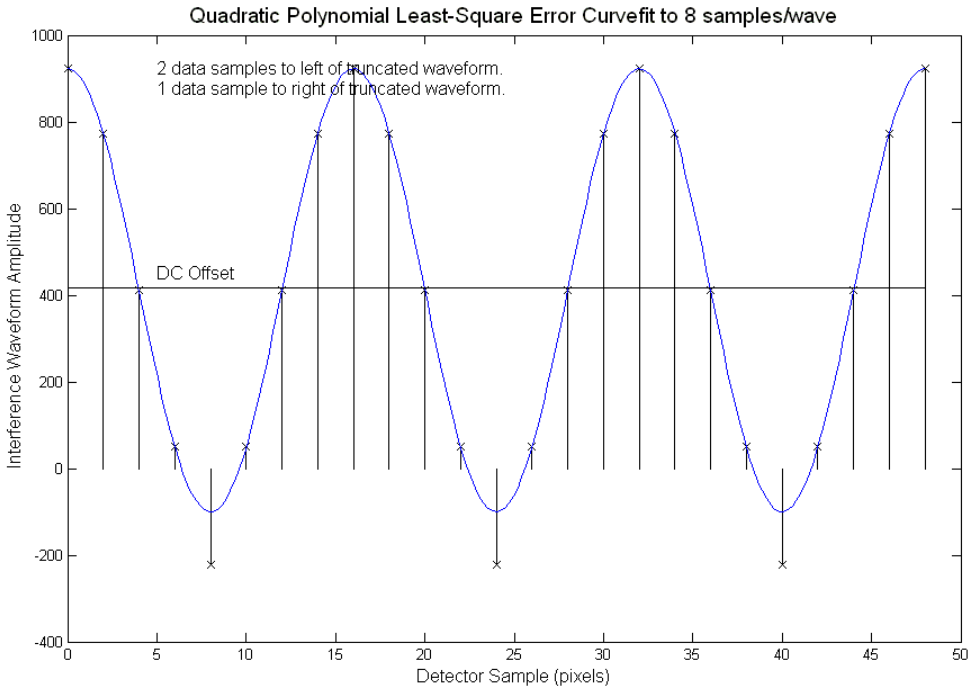

Figure 3 Quadratic Polynomial LSE Curve Fit to 8 samples/wave

The fringe pattern waveform is represented by the continuous curve (blue) line where the x-markers above the zero threshold level represent the sampled data and the x-markers below the zero threshold level represent the interpolated data. The interpolated marker point lies below the continuous curve line because the first-difference slope at the point to the left of the truncated region is greater than the slope defined by the cosine waveform at the same sample point. The quadratic or second-order polynomial curve fit to 16 samples/cycle is shown in the figure below:

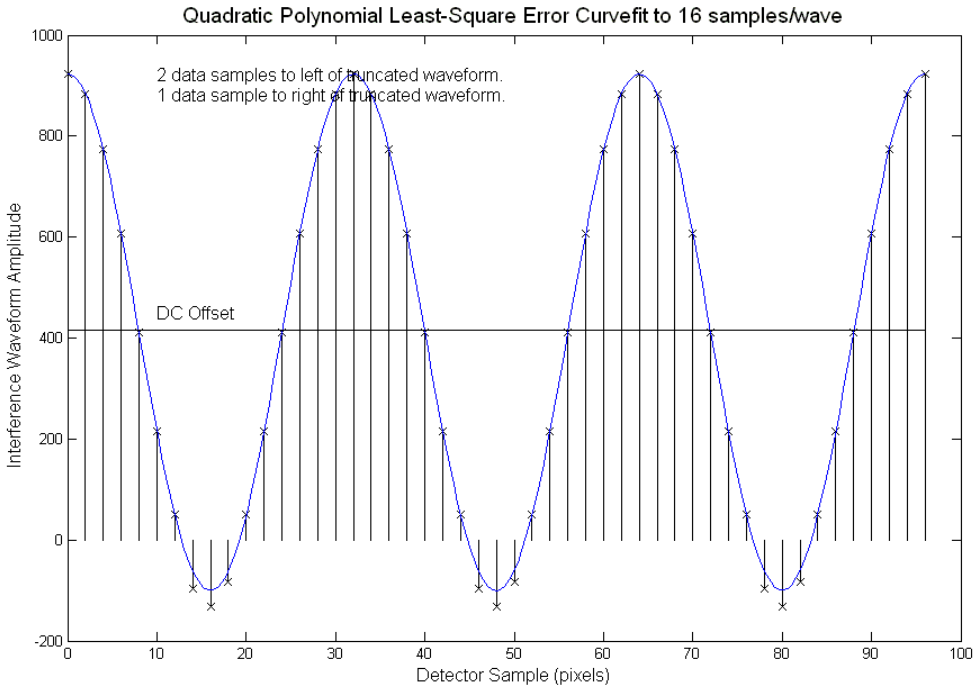

Figure 4 Quadratic Polynomial LSE Curve Fit to 16 samples/wave

The 2x increase in waveform sampling reduces the interpolation error. The cubic or third-order polynomial curve fit to 8 samples/wave is shown in the figure below:

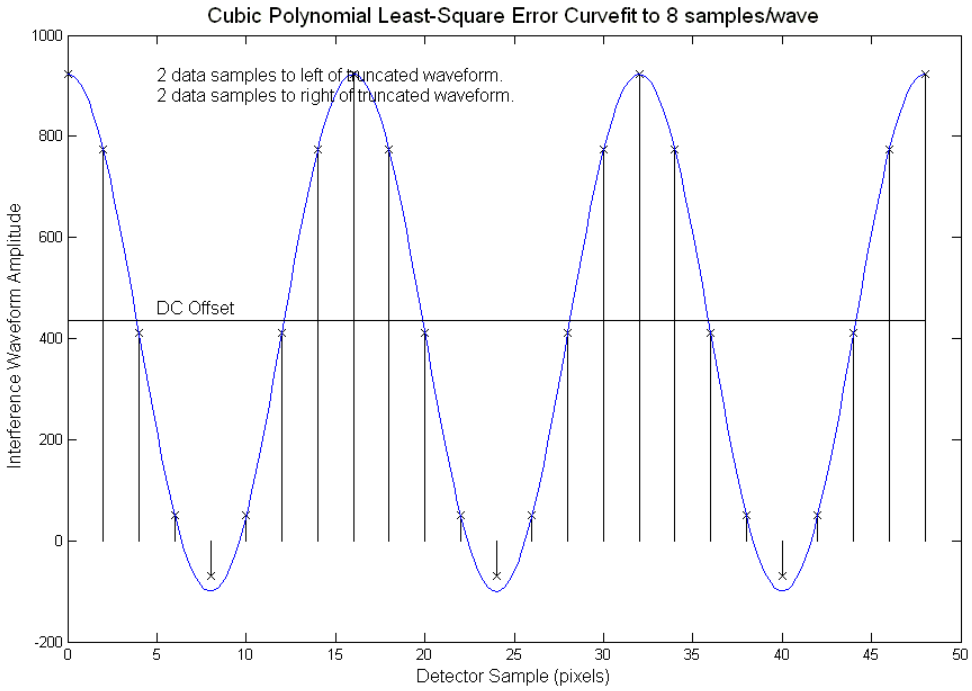

Figure 5 Cubic Polynomial LSE Curve Fit to 8 samples/wave

Using 2 sample points on both the left and right hand sides of the truncated region produces an interpolation point that is less than the waveform. This error is smaller than the error produced by the Quadratic Polynomial LSE Curve Fit. The cubic or third-order polynomial curve fit to 16 samples/wave is shown in the figure below:

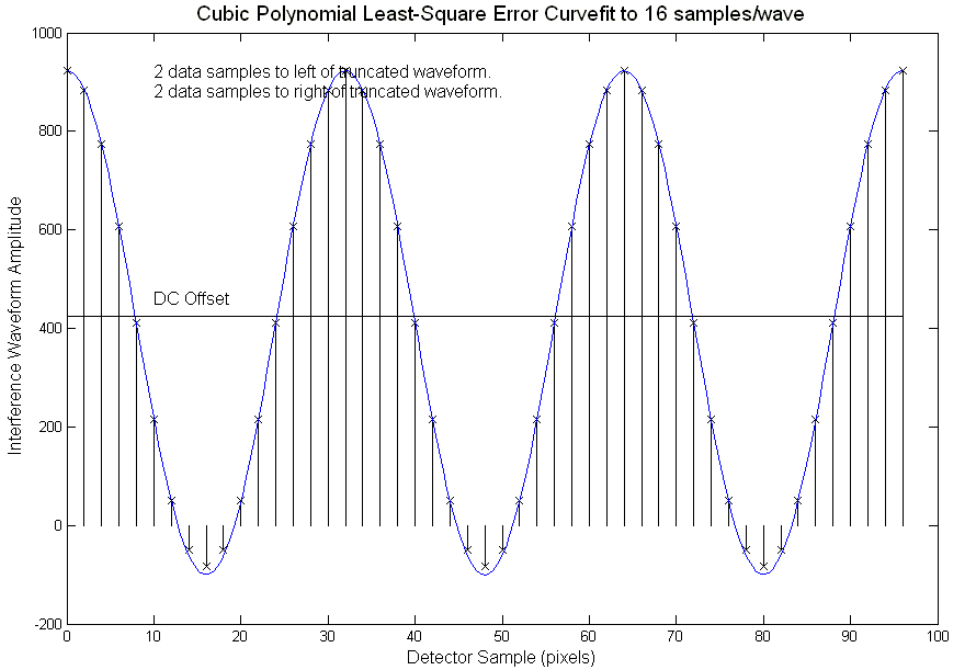

Figure 6 Cubic Polynomial LSE Curve Fit to 16 samples/wave

The curve fit error is reduced to an acceptable level at 16 samples/wave spatial sampling.

The Fourth-Order polynomial curve fit to 8 samples/wave is shown in the figure below:

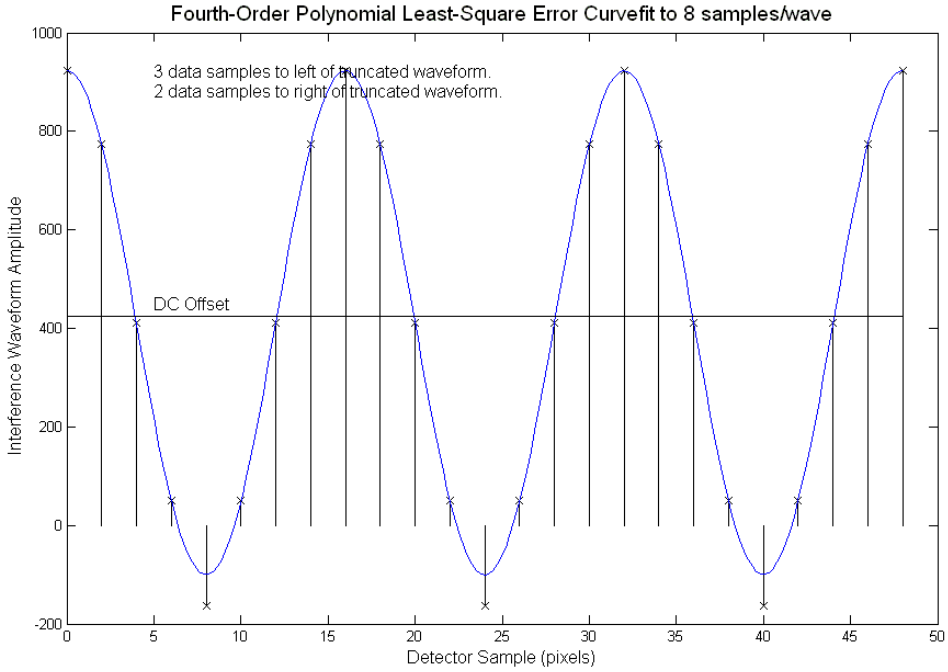

Figure 7 Fourth-Order Polynomial LSE Curve Fit to 8 samples/wave

Three data samples to the left of the truncated region introduces an additional error. This additional error is due to the data point on the far left that is above the DC Offset level or has crossed over into another quadrant of the waveform. This inflection point of the waveform means that the error in sampling for a Fourth-Order Polynomial is unacceptable.

The Fourth-Order polynomial curve fit to 16 samples/wave is shown in the figure below:

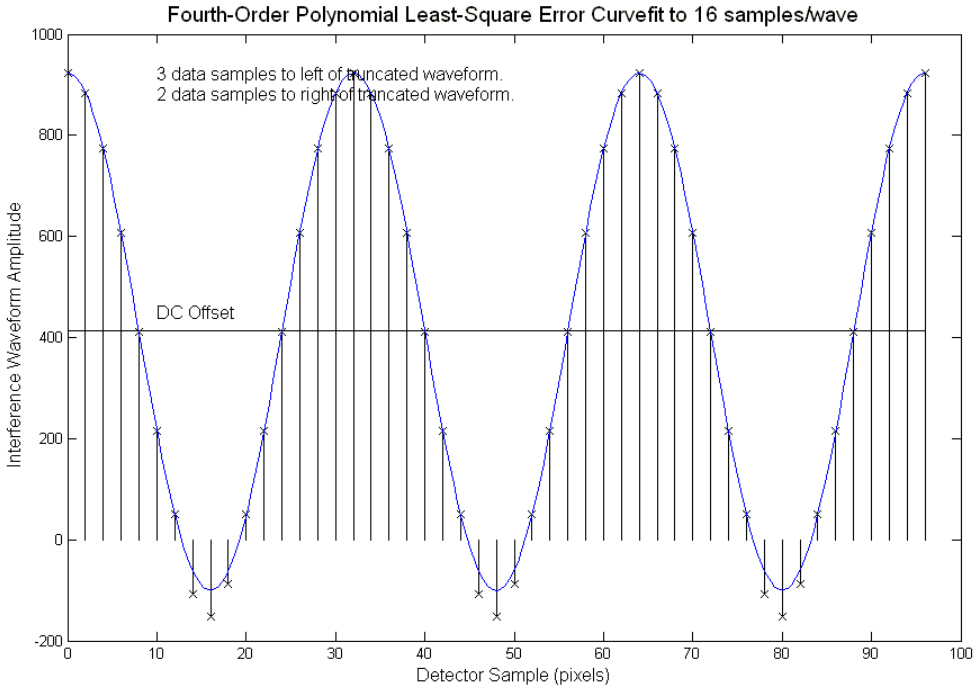

Figure 8 Fourth-Order Polynomial LSE Curve Fit to 16 samples/wave

The cubic polynomial LSE curve fit with 4 data point boundary conditions offers the lowest error and is the selected algorithm to interpolate the truncated data region. The Fourier Transform Method to determine the phase-shift is applied to the 16 samples/wave cosine waveform with truncated data.

The Power Spectrum of the 16 samples/wave cosine waveform with truncated data is shown in the figure below:

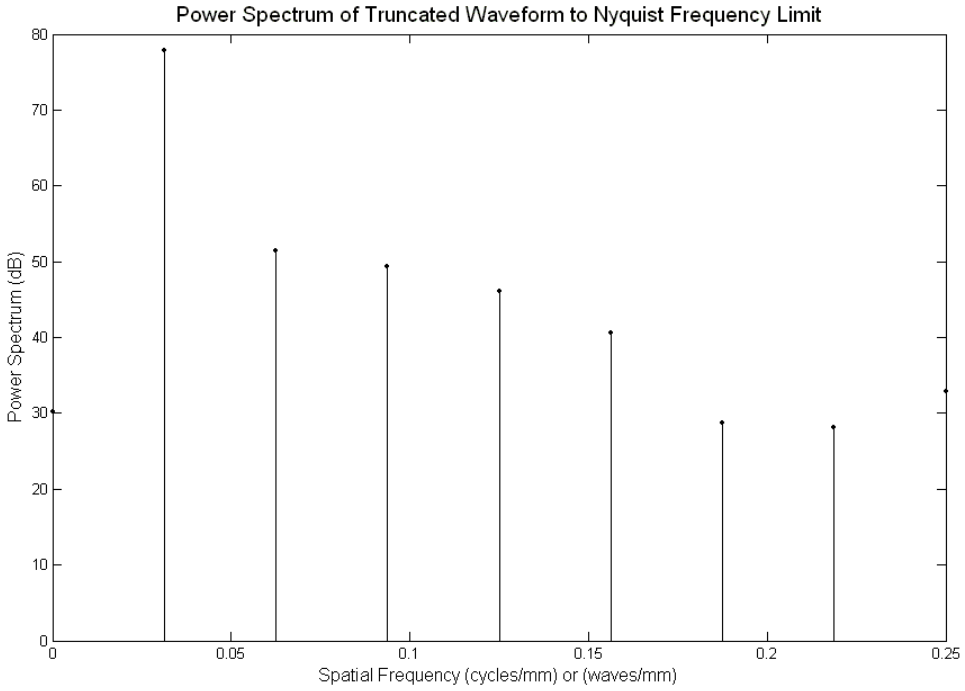

Figure 9 Fourier Transform of Truncated Data at 16 samples/wave

The calculated phase-shift using the Fourier Transform Method at the frequency representing the power spectrum peak is 0.01º for the cosine waveform since a sample point is coincident with the peak of the cosine waveform.

The Fourier Transform Method to determine the phase-shift is applied to the 16 samples/wave cosine waveform with Cubic Polynomial LSE Curve Fit interpolated data.

The Power Spectrum of the 16 samples/wave cosine waveform with Cubic Polynomial LSE Curve Fit interpolated data is shown in the figure below:

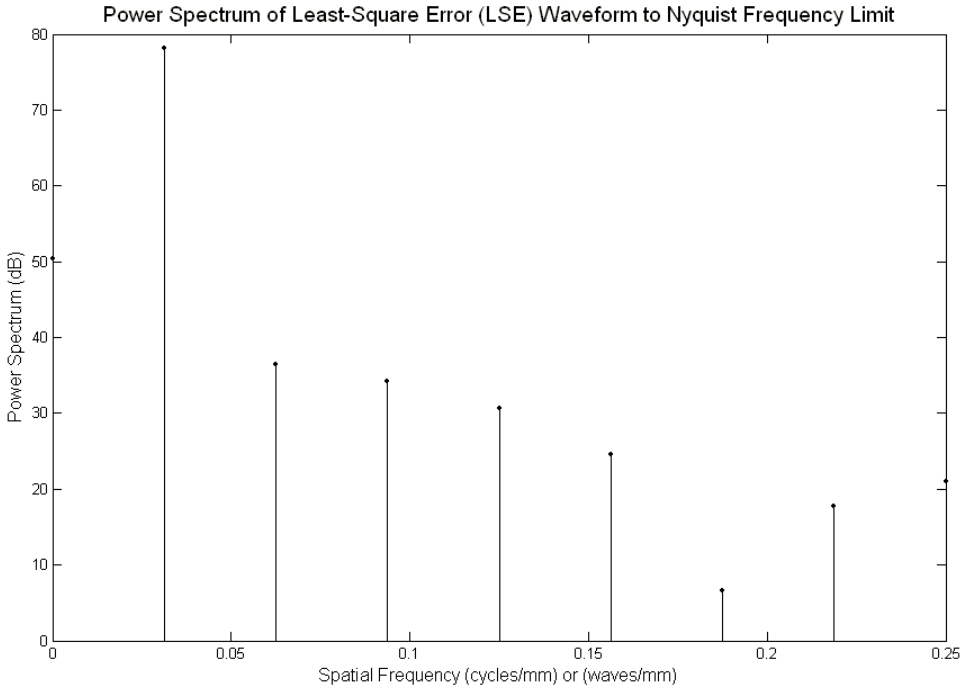

Figure 10 Fourier Transform of Cubic Third-Order Polynomial LSE Curve Fit Smoothed Data at 16 samples/wave

The power spectrum shows a reduction of higher frequency components due to the polynomial curve fitting as opposed to the truncated data. The calculated phase-shift using the Fourier Transform Method at the frequency representing the power spectrum peak is 0.005º for the cosine waveform. The smoothing of the truncated region provides a x2 reduction in error with a more dominant peak in the power spectrum. This dominant peak in the power spectrum represents the waveform spatial frequency of the waveform or the reciprocal of the waveform period. The optimal curve fitting of the truncated region is the Cubic Polynomial LSE Curve Fit with 2 data points to the left of the truncated region and 2 data point to the right of the truncated region.

Characterization: Properties and Specifications for Performance and Capability

The fluid specimen has the following properties:

Cargille Labs Fused Silica Matching Liquid #06350
Index-of-Refraction or Refractive Index: n=1.467 at wavelength λ=0.457μm
The wavelength of the “blue” laser is λ=0.457μm/wave
The wavelength of the “red” laser is λ=0.658μm/wave

Refractive Index sensitivity to a change in temperature is
$dn/dT = -3.65\times10^{-4}/^{\circ}C$ over a 15 to 35°C temperature range

Given a temperature resolution of $\Delta T = 0.1^{\circ}C$ (Very tight and more likely 0.5°C in this experiment) the refractive index resolution becomes:
$dn = dn/dT \times \Delta T = \left|-3.65\times10^{-4}\right| \times 0.1 = 3.65\times10^{-5}$

The central ray path length through the fluid-cell specimen or cuvette is:
$PL_{cntr} = 10mm = 10{,}000\mu m$

The marginal ray path length through the fluid-cell specimen or cuvette is:
$PL_{\text{marg}} = \sqrt{1+m^2} \times PL_{cntr} = \sqrt{1+0.25^2} \times 10{,}000 = 10{,}308\mu m$

Given a focused beam $f/\# = EffectiveFocal\ Length / Diameter = 2.0$
Where Slope: $m = 1/2 \times Diameter / EffectiveFocal\ Length = 1/(2\times f/\#) = 1/4 = 0.25$
Marginal Ray to Central Ray Path Length Difference
$\Delta PL = PL_{\text{marg}} - PL_{cntr} = 10{,}308 - 10{,}000 = 308\mu m$
$\Delta PL = \Delta PL/\lambda = 308/0.457 = 674\ waves$
Therefore, the marginal ray path length is longer than the central ray path length over the depth of the cuvette.

The average temperature is $T = 30^{\circ}C$
The average refractive index change is $\Delta n = dn/dT \times T = \left|-3.65\times10^{-4}\right| \times 30 = 0.01095$
The Optical Path Length (OPL) is $OPL = n \times PL_{cntr} = 1.467 \times 10{,}000 = 14{,}670\mu m$

Since both the object beam (that passes through the specimen) and the reference beam (that passes through a constant refractive index medium or bypasses the specimen) propagate through common optics then the fringe-shift is sensitive to a change in OPL
The OPL resolution is:

$\Delta OPL = 1/10\, waves \times \lambda = 0.10 \times 0.457 = 0.0457\, \mu m = 45.7 nm$

$\Delta OPL = dn \times OPL + n \times dOPL = dn \times OPL$

$\Delta OPL = dn \times OPL = 1/10\, wave \times \lambda$

Re-arranging terms:

$OPL = \lambda \times \Delta OPL / dn = 0.457 \times 0.10 / 3.65 \times 10^{-5} = 1252\, \mu m = 1.25 mm$

$PL_{cntr} = OPL / n = 1252 / 1.467 = 853 \mu m = 0.853 mm$

which is the Path Length at 1/10th wave Resolution

The phase-shift resolution $\Delta\phi = 2\pi \times \Delta OPL = 2\pi \times 0.10\, waves = 0.628\, rad$

The fringe spacing (peak-to-peak) for overlapped object to reference beams is:

$fs = 1/2 \times \lambda / \sin(1/2 \times \theta) = 1/2 \times 0.457 / \sin(1/2 \times 0.5) = 52.4 \mu m / wave$

Given the object to reference beam overlap convergence angle of $\theta = 0.5^{\circ} = 8.73 mrad$

where the detector or pixel size on the camera is $6.8 \times 6.8\, \mu m / pixel$

the spatial sampling resolution is $52.4 / 6.8 = 7.7\ pixels / wave$ (Extremely marginal)

The fringe-shift resolution is:

$\Delta fs = 1/10\, wave = 1/10 \times\ fs = 1/10 \times 52.4 = 5.24 \mu m$

At 1/10th wave resolution

The refractive index sensitivity to a change in wave phase is:

$dn / d\phi = dn / \Delta fs = 3.65 \times 10^{-5} / 0.1 = 3.65 \times 10^{-4} / wave$

which is the refractive index change with respect to a wave-shift on the hologram

The refractive index sensitivity to a fringe-shift displacement on the hologram is:

$dn / d\phi = dn / \Delta fs = 3.65 \times 10^{-5} / 5.24 = 6.97 \times 10^{-6} / \mu m$

which is the refractive index change with respect to a fringe-shift on the hologram

The temperature sensitivity to a phase-shift change on the hologram is:

$dT/d\phi = (dn/d\phi)/(dn/dT) = 6.97\times10^{-6}/-3.65\times10^{-4} = -0.019\ ^{\circ}C/\mu m$

which is the temperature change with respect to a fringe-shift on the hologram

Optical Path Length: $OPL = n \times PL$

Optical Path Length Resolution: $\Delta OPL = \Delta n \times PL + n \times \Delta PL = \Delta n \times PL$

Grid-Mesh Cell Resolution or Path Length (PL) of Cuvette or Fluid-Cell:

$$PL = \frac{1}{8} Cell\ Lgth = \frac{1}{8} \times 10mm \times 1000\,\mu m/mm = 1250\,\mu m$$

Index-of-Refraction or Refractive Index Resolution:

$\Delta n = dn = 3.65\times10^{-5}$ for $\Delta T = 0.1^{\circ}C$ Temperature Resolution

$\Delta OPL = \Delta n \times PL = 3.65\times10^{-5}\times1250 = 0.0456\,\mu m$

Phase-Shift Resolution: $\Delta\phi = \frac{1}{\lambda}\Delta OPL = \frac{1}{0.457}(0.0456) = 0.0998 = \frac{1}{10} waves$

$$\Delta\phi = \frac{1}{10} waves = \frac{180}{10\pi} = \frac{18}{\pi} = 5.7^{\circ} = \pm 2.85^{\circ}$$

The characterization of the microscope will validate the accuracy of these calculations where the spatial sampling resolution (8 pixels/wave) is at the absolute limit of acceptability to accurately determine a phase-shift based on a fine fringe movement of 1/10th wave. Note that the beam overlap convergence angle of 0.5° represents a very long projector optical path length of 610cm (20') that spans two lengths of the optical table. Maintaining a coherent reference and object beam through all of the optical elements of this microscope is challenging.

The wavefront phase properties or the wave properties are typically defined at a pupil plane where *z* is constant and *x* & *y* (independent variables) that are limited to a circular aperture which is given by:

$$I(x,y) = I_0 e^{i(k_x(x-x_0)+k_y(y-y_0)+k_z(z-z_0)-\omega\cdot t+\phi)}$$

$$I(x,y) = I_0 e^{i\theta} = I_0(\cos\theta + i\sin\theta) = \hat{x} + i\hat{y}$$

$\hat{x} = I_0 \cos\theta$

$\hat{y} = I_0 \sin\theta$

Phase: $\theta = \tan^{-1}\left(\frac{\hat{y}}{\hat{x}}\right)$

Circular aperture $(x - x_0)^2 + (y - y_0)^2 = (r - r_0)^2$ where $r - r_0$ is the radius of the aperture at the pupil plane z

k_x, k_y, k_z are the spatial frequencies

ω is the temporal frequency

The wavefront error affects the Point-Spread Function (PSF) at the focal point and the PSF represents the Fourier Transform (FT) of the wavefront at the pupil.

An optical (light imaging) microscope is sensitive to amplitude (opaqueness and translucence) only and the wave equation reduces to:

$I(x, y) = I_0$

Where

$$\left|\cos\theta + i\sin\theta\right| = \sqrt{(\cos\theta + i\sin\theta) \times (\cos\theta + i\sin\theta)^*}$$

$$= \sqrt{(\cos\theta + i\sin\theta) \times (\cos\theta - i\sin\theta)} = \sqrt{\cos^2\theta + \sin^2\theta} = 1$$

Thus, common imaging microscopes are insensitive to the phase property of the wave.

In this experiment the wave equation reduces to $I(x) = I_0 e^{i(k_x(x - x_0) + \phi)}$

Since the spatial frequency (k_x) is constant then the harmonic component can be filtered out and the phase-shift (ϕ) determined from the hologram shown in the figure below:

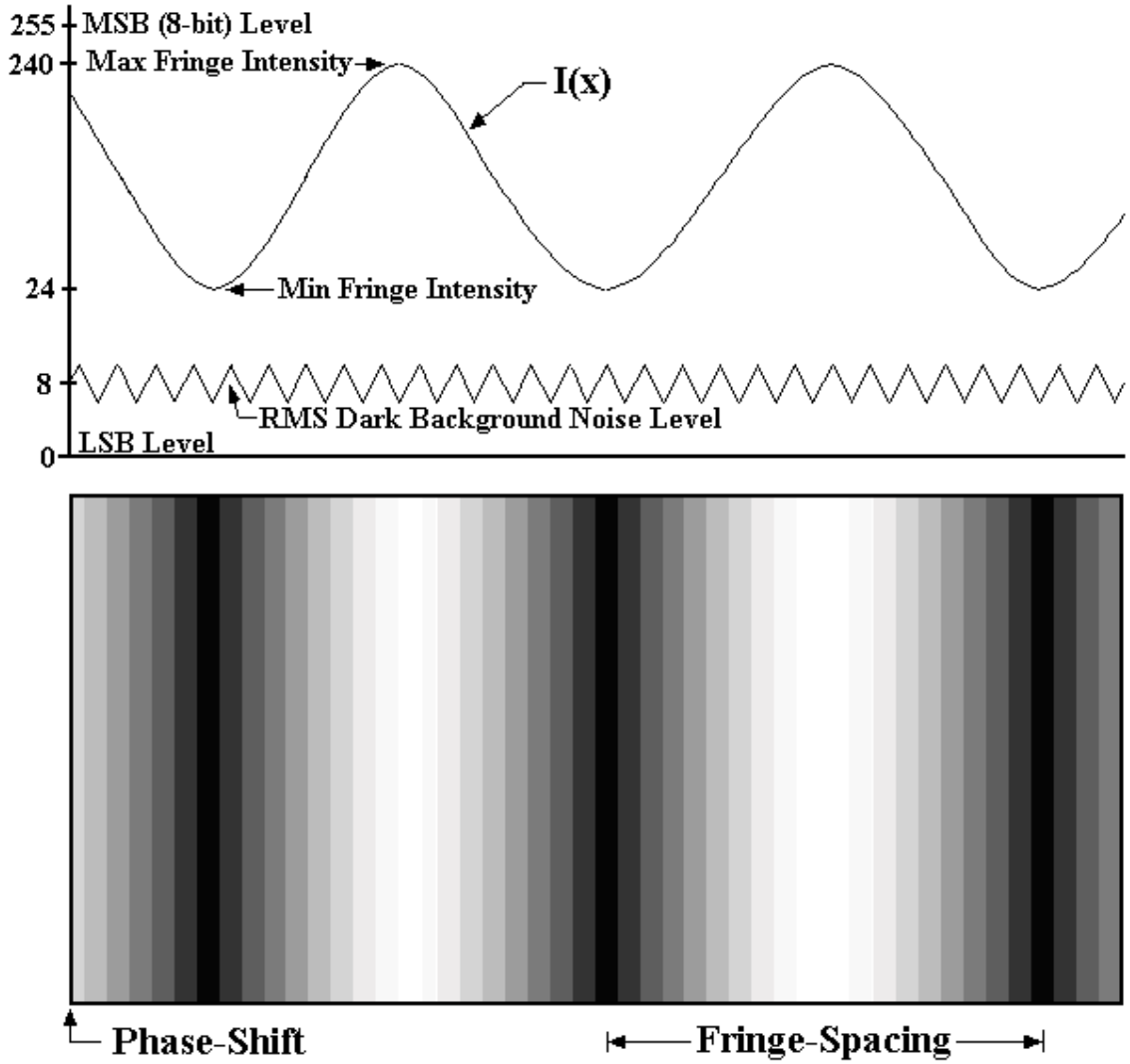

Figure 1 Interference of Object Wave to Reference Wave to Produce a Hologram

This phase-shift (ϕ) represents the change in refractive index due to the effect on Optical Path Length (OPL).

Where: $SpatialFrequency.k_x = 1/FringeSpacing$or

Spatial Frequency: k=1/Fringe-Spacing

The fringe interference pattern energy or Intensity (I) on camera is given as I(x)

The Fringe Contrast Ratio (FCR) or the Fringe Visibility Ratio (FVR) is given by:

$$FVR = \frac{Max\ Intensity - Min\ Intensity}{Max\ Intensity + Min\ Intensity} = \frac{I_{\max} - I_{\min}}{I_{\max} + I_{\min}} = \frac{\frac{I_{\max}}{I_{\min}} - 1}{\frac{I_{\max}}{I_{\min}} + 1} = \frac{n-1}{n+1}$$

Given the Minimum Coherence Length of the Source (FVR=0.50) then the

Intensity Ratio: $n = \frac{I_{\max}}{I_{\min}} = 3$ at FVR=0.50

Given Intensity Ratio: $n = \frac{I_{\max}}{I_{\min}} = 4$ then FVR=0.60

Given Intensity Ratio: $n = \frac{I_{\max}}{I_{\min}} = 10$ then FVR=0.82

Given Signal-to-Background Ratio: $SBR = \frac{Min\,Intensity}{RMS\ Noise} = \frac{I_{\min}}{I_{noise}} = 3$

Given RMS Background Noise Level: $I_{noise} = 8$

Then $I_{\min} = SBR \cdot I_{noise} = 3 \times 8 = 24$

and $I_{\max} = n \cdot I_{\min} = 10 \times 24 = 240$

with 8-bit Resolution the scaling is from 0 (LSB) to 255 (MSB)

Least Significant Bit: $LSB = 0$

Most Significant Bit: $MSB = 2^8 - 1 = 256 - 1 = 255$

Assuming that the Dark Background Noise is a harmonic signal then the Peak Noise from the RMS (Root-Mean-Square) Noise is given as

$I_{peak\_noise} = \sqrt{2} \cdot I_{noise} \cong 1.5 \times I_{noise} = 1.5 \times 8 = 12$

then the Uncertainty in Minimum Fringe Intensity is $\Delta I_{\min} = I_{\min} \pm I_{peak\_noise} = 24 \pm 12$

This is a significant uncertainty for the Minimum Fringe Intensity; therefore, the Dark Background Noise should be significantly smaller by an increase in SBR (Signal-to-Background Ratio) from 3 to 10.

Given SBR=10 then

RMS Dark Background Noise: $I_{noise} = \frac{1}{SBR} I_{\min} = \frac{1}{10} 24 = 2.4$

Peak Dark Background Noise: $I_{peak\_noise} = \sqrt{2} \cdot I_{noise} \cong 1.5 \times I_{noise} = 1.5 \times 2.4 = 3.6 \cong 4$

Uncertainty in Minimum Fringe Intensity: $\Delta I_{\min} = I_{\min} \pm I_{peak\_noise} = 24 \pm 4$

The Dynamic Range: $DR = \frac{I_{\max}}{I_{noise}} = \frac{I_{\min}}{I_{noise}} \frac{I_{\max}}{I_{\min}} = SBR \cdot n = 10 \times 10 = 100$

Logarithmic Dynamic Range: $dB_{dr} = 10\log DR = 10\log 100 = 20\,dB$ for the intensity ratio detection on the camera.

These are the acceptable hologram intensity scaling factor parameters to set up the camera for data acquisition and collection in our experiment.

The RedLake Mega Plus II ES-3200 Camera with 1472x2184 pixels at 6.8μm/pixel.

The dynamic range at 8-bit resolution is $dB_{dr} = 10\log\frac{2^8}{1} = 10\log 256 = 24\,dB$

The dynamic range at 12-bit resolution is $dB_{dr} = 10\log\frac{2^{12}}{1} = 10\log 4096 = 36\,dB$

when the RedLake camera is operated at an 8-bit resolution mode as a limitation on the camera configuration software.

Boundary Conditions (BCs) and Computational Domain Mapping onto the Fluid-Cell

The grid-mesh for the “wily” matrix reconstruction algorithm along a single plane is shown in the figure below:

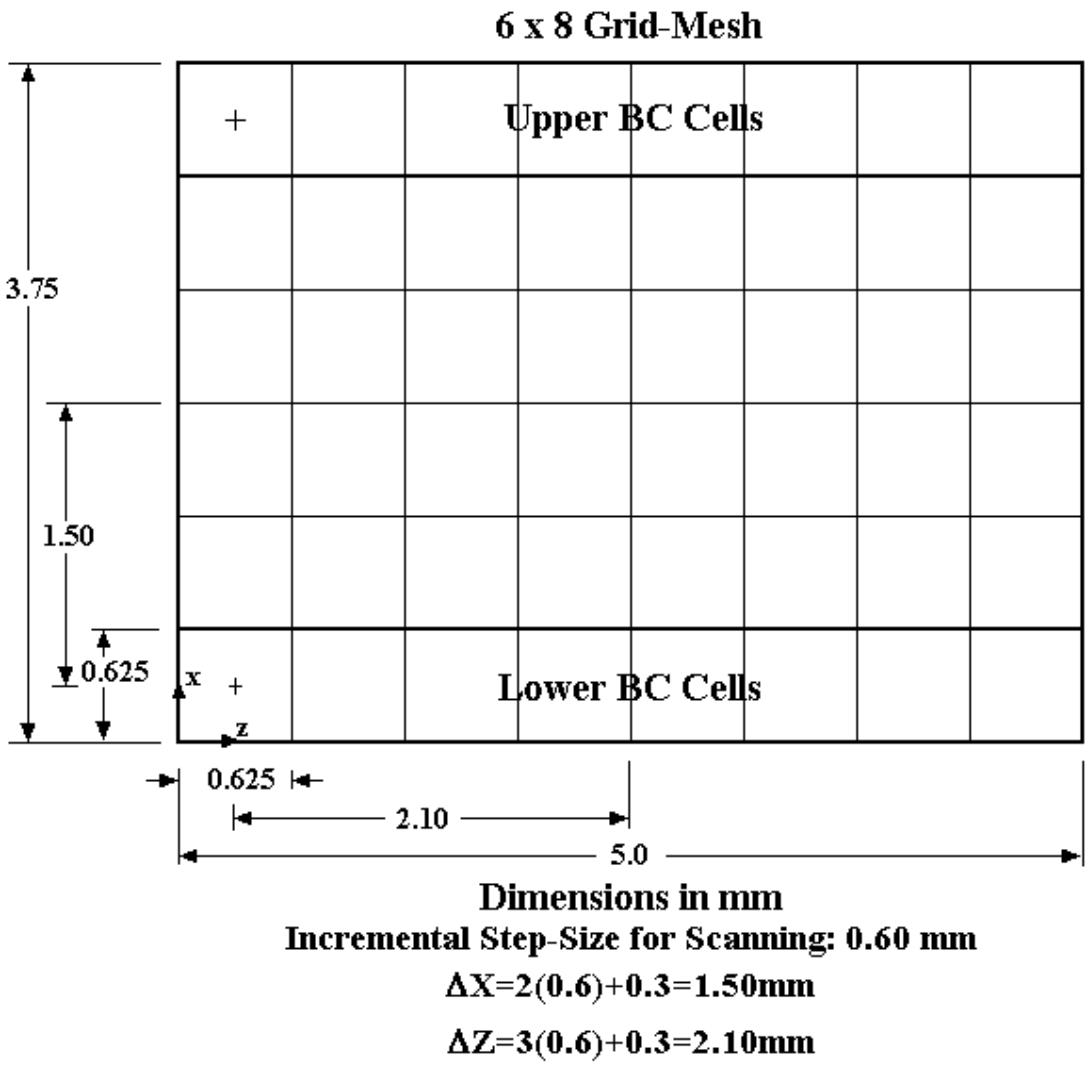

Figure 1 Dimensions and Displacements along the Grid-Mesh

Given the interior cross-sectional dimensions of the fluid-cell cuvette 5 mm deep (*z*-axis) x 5 mm wide (*x*-axis). The mapping of the Boundary Conditions (BCs) and Computational Domain onto the Fluid-Cell is shown in the figure below:

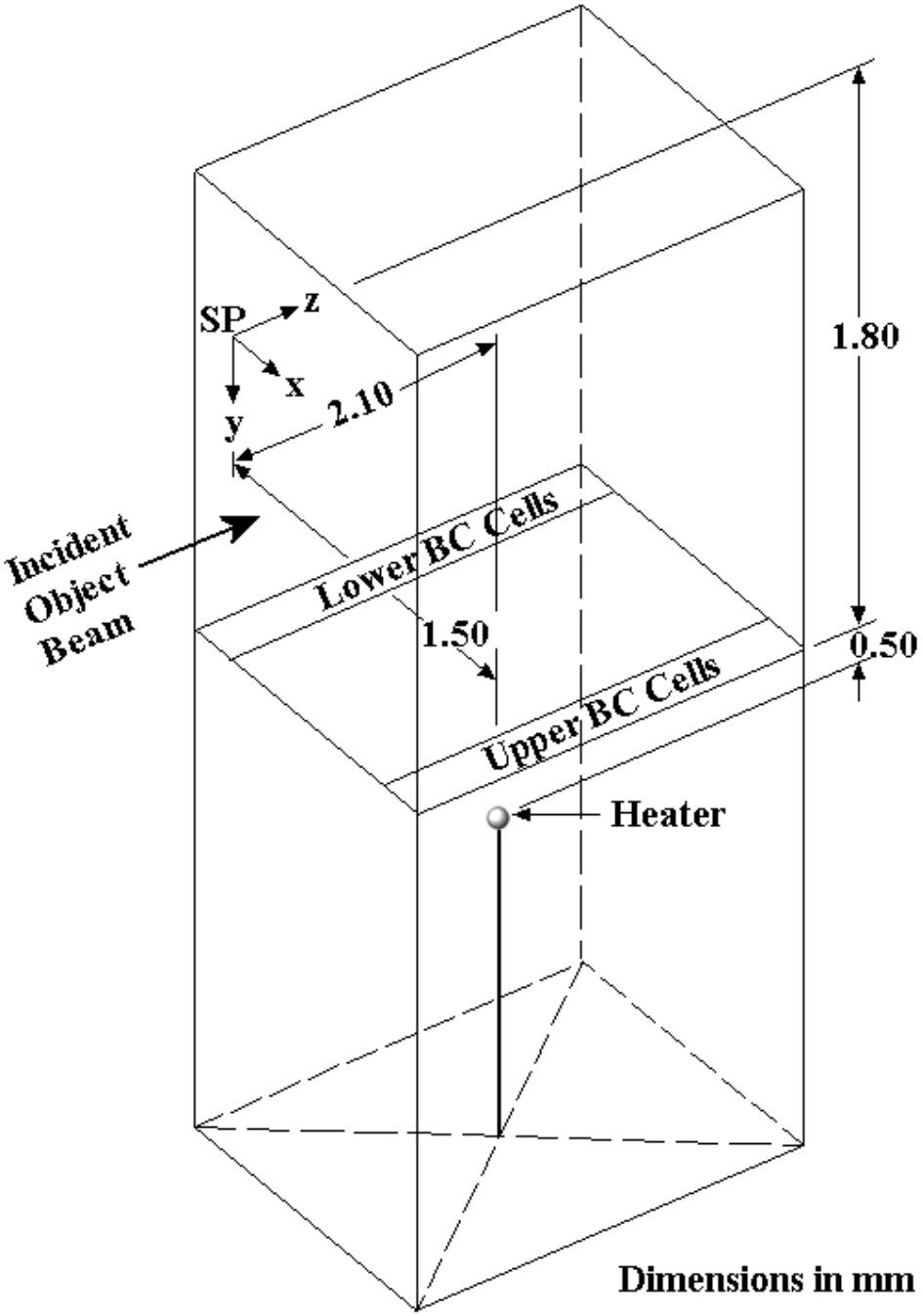

Figure 2 Dimensional Reference Points within the Fluid-Cell Cuvette

The reference is the Heater, which is centered within the 5x5 mm walls of the fluid-cell.

The Start Point (SP) for Scanning is a translation from the heater as follows:

Vertical Up: Δy=1.80+0.50=2.30 mm

Horizontal Back: Δz=2.10 mm or 0.40 mm from wall at Incident Object Beam

Horizontal Left: Δx=1.50 mm or 1.00 mm from LHS wall

The grid-mesh cell dimensions are: $\Delta x = \Delta y = \Delta z = 0.625\,mm$ (cube)

The scanning incremental step-size dimensions are: $\Delta x = \Delta y = \Delta z = 0.625\,mm$ (cube)

The Scan Sequence for Measuring Temperature using the thermocouple is:

1) For every *z*-position along the optical propagation axis at 8-cells deep

2) For every *x*-position from Lower to Upper BCs along the *xz*-plane at 6-cells wide

3) For every *y*-position at 4-cells high

The computational domain is 4-cells high x 4-cells wide x 8-cells deep

The 3D-Temperature plots are:

T(*z,x*) for every *y*-position starting from the furthest distance from the heater along the *y*-axis.

Where the dimensional position vectors are given as:

x_i , $1 \le i \le 6$

y_j , $1 \le j \le 4$

z_k , $1 \le k \le 8$

Laboratory Notes for Experimental Setup and Data Collection

Thermocouple Data Files: Thermocouple 6x8 Meas 11-14

Room Air Temperature: 23.8 deg-C with Data Collected on December 5, 2007

Measurement 11 is Thermocouple at 1.8+0.5=2.3mm above the heater

Measurement 12 is Thermocouple at 1.2+0.5=1.7mm above the heater

Measurement 13 is Thermocouple at 0.6+0.5=1.1mm above the heater

Measurement 14 is Thermocouple at 0.0+0.5=0.5mm above the heater

PhysiTemp Type MT-29/5 Hypodermic Needle Microprobe Thermocouple

Type T Thermocouple (Copper-Constantan)

29 gauge (0.013 inches Dia or 0.33 mm Diameter)

5 cm Long

Response Time Constant: < 1 sec for 1 deg-C Temperature change (ie. Negligible heat capacity or thermal mass)

Thermocouple measurement stability of +/- 0.05 deg-C for over a 10 second Interval using custom built electronic circuits and LabVIEW 8.2 signal processing algorithms for 10-sample averaging. Remarkably stable and accurate since commercial thermocouple amplifiers are accurate to within +/- 1 deg-C and precision accuracy is considered to be within +/- 0.5 deg-C

Time to Collect 8x6x4 = 192 data points using manual micrometer translation stages: 2 hours

Optical Glass Cuvette is 5x5mm in Cross-Section:
Thermocouple Reference Point (RP) is Centered within the Cuvette at 0.5mm vertical clearance directly above the heater.
Coordinate Frame for Scanning the Thermocouple within the Cuvette
+z-axis is along the laser propagation path looking into the cuvette.
+x-axis is horizontal pointing from left-to-right.
+y-axis is vertical pointing downwards with origin furthest from the heater.

Micrometer Stage Scanning Point-by-Point manual adjustment:
Thermocouple Start Point (SP) for Scanning is at the top-front-left hand corner.
Displacement to the Start Point (SP) from the Reference Point (RP) is
delta-z= -2.1mm Back
delta-x= -1.5mm Left
delta-y= -1.8mm Up

Scanning Sequence incremental translation step-size:
delta-z= +0.6mm increments from front-to-back horizontal scans of 8-steps
delta-x= +0.6mm increments from left-to-right horizontal scans of 6-steps
delta-y= +0.6mm increments from top-to-bottom vertical scans of 4-steps as the thermocouple gets closer to the heater.

Initial Conditions (IC's) with Thermocouple at Start Point (SP) of scanning:
Power Off Ambient Temperature: 24.6 deg-C
Steady-State Equilibrium Temperature with Power On: 31.3 deg-C
Time to reach Steady-State Equilibrium Temperature with Power On: 10 minutes

Power to Heater (0402 Surface Mount Resistor at 1/16 Watt): Regulated 7.5 Volts DC into a 470 ohm load:
Green Lead Wires to Heater
Dissipated Power: P = V×V/R = 7.5×7.5/470 = 1/8.3 Watts
Thermocouple Temperature at Point Closest to Heater: 40 deg-C (Approx Maximum)
Maximum Temperature Differential in Fluid-Cell: delta-Temp = 40.0-31.8 = 8.2 deg-C (Max)

Calibration eliminates the bias uncertainties and errors associated with the thermocouple transfer function sensitivity, amplifier gain, cold junction thermocouple effects, and cables. This approach eliminates the numerous variables associated with thermocouple measurement error when relying on the thermocouple transfer function equations or look-up tables that converts from volt to deg-C and the high feedback gain values in the cascaded instrumentation amplifier to the Second-Order analog Low-Pass-Filter (LPF) Operational Amplifier. Noise is further reduced from the LPF by averaging the sampled data to a two second time constant update and using DC batteries in the power supply. Temperature stability is also regulated by the triple insulation of the cold junction thermocouple.

Room Temperature and Ice Bath Calibration points using a laboratory quality mercury bulb thermometer eliminate assumptions associated with sensor amplification and signal processing where the calibration constants are applied to the measurements when running the experiment. Two-Point calibration produces T(V) = mV+b equation that relates Temperature to measured voltage at the National Instruments Data Acquisition Board (NI-DAQmx PCI-6221 (37-pin)).

Thermocouple Calibration

The thermocouple is a PhysiTemp Type MT-29/5 Hypodermic Needle Microprobe with a needle diameter of 29 gauge (0.33 mm) and length of 5 cm as shown in the figure below:

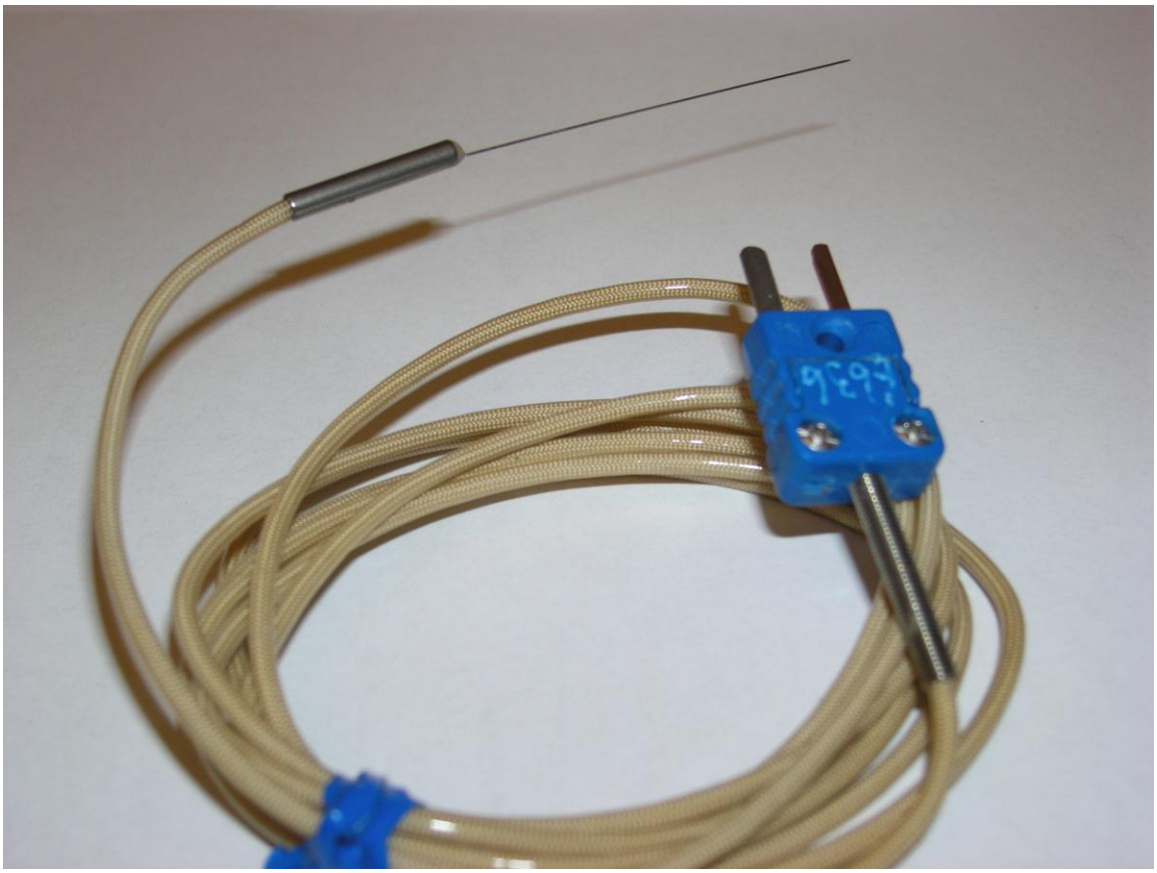

Figure 1 PhysiTemp Type MT-29/5 Hypodermic Needle Microprobe Thermocouple

This thermocouple is a Type T (Copper-Constantan) material. The copper and constantan terminal lugs can be seen on the blue connector. High sensitivity to a small temperature change is required with very high thermal stability and low noise. The temperature measurements must be stable to within ±0.1°C and this is very difficult to obtain since commercial off-the-shelf thermocouple amplifiers typically provide an accuracy to within ±1°C. A custom circuit was therefore designed and built using a PMI AMP-02 Precision Instrumentation Amplifier and a Texas Instruments TI TL-081 Operational Amplifier for the analog Low-Pass Filter (LPF). The thermocouple cold junction is triple insulated to provide a stable reference point. Since this is a high feedback gain configuration for highly sensitive measurements then the polynomial coefficients that transfer type-T thermocouple voltage measurements to temperature along with multiple error sources along the amplification chain become a concern. The decision was made to calibrate the thermocouple output voltages of the LPF amplifier to minimize the cascaded errors of 1) thermocouple cold junction reference, 2) operational amplifier differential input offset voltage error, and 3) feedback gain error. The

cumulative effect of all these errors can be estimated from specifications. However, confidence in an accurate transfer function is uncertain. Two-point calibration was considered as all the bias and offset errors for high gain amplification can be eliminated. This will then leave the error of the reference thermometer accuracy and minor amplifier drift as the only remaining concerns. Temperature stability and thermal drift has turned out to be a non-issue especially since the cold-junction thermocouple was triple insulated to ensure thermal stability. This stability was tested by applying a heat source to the walls of the insulation which resulted in a negligible measurement response.

The two points for calibration are room temperature and an ice bath temperature. The thermometer used was a laboratory grade mercury bulb thermometer with accuracy to approximately 0.1°C to 0.2°C. The absolute accuracy was less of a concern in comparison to the thermal stability throughout the measurements. The schematic diagram for thermocouple amplification and analog Low-Pass Filter (LPF) noise filtering is shown in the figure below along with a list of components and some specifications that address both bias error and thermal stability:

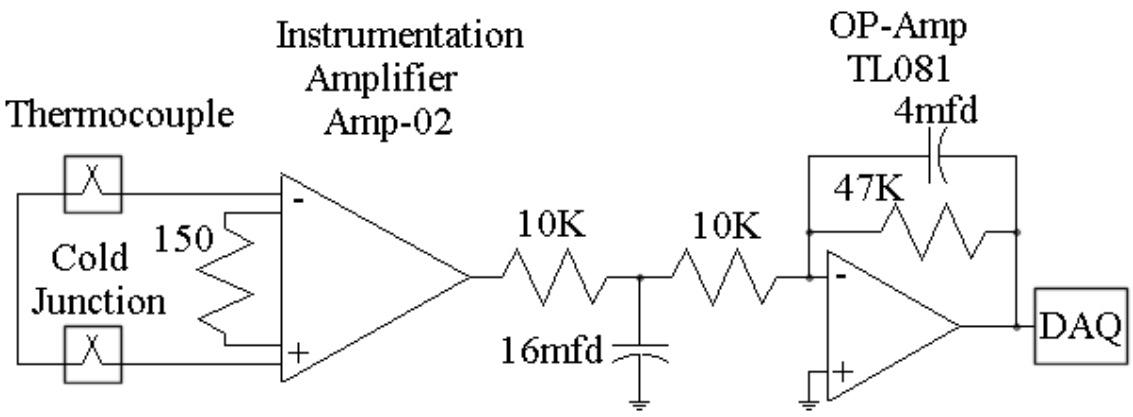

Figure 2 Thermocouple High-Gain Instrumentation Amplifier and Low-Pass Filter to National Instruments Data Acquisition (DAQ) Board in Computer

Micro-Probe T-type (Copper-Constantan) Thermocouple Sensitivity is 25.94°C/mV as obtained from Type-T thermocouple table of polynomial coefficients

Low Noise Instrumentation Amplifier: PMI AMP 02

Input Offset Voltage: 20μV

Input Offset Drift: 0.5μV/°C

Low-Pass Filter (LPF) Operational Amplifier (OP Amp): TI TL081

Input Offset Voltage: 3mV

Input Offset Drift: 18μV/°C

Low Noise Instrumentation Amplifier Gain cascaded with a Low-Pass Filter OP Amp:

Gain: $A_V = \frac{50{,}000\Omega}{150\Omega} + 1 \times \frac{47K\Omega}{20K\Omega} = 334.3 \times 2.35 = 785.7$

Sensitivity to DAQ is $785.7 \times 25.94^{\circ}C/mV = 20{,}381^{\circ}C/mV = 20.4^{\circ}C/\mu V$

Analog Low-Pass Filter (LPF) Noise Reduction Circuit: $f_{LP} = 1Hz$

Data Acquisition (DAQ) Board Least-Significant Bit (LSB) Voltage Resolution is

$$\frac{20Volts}{2^{16}-1} = \frac{20}{65{,}536-1} = 305\mu V$$

for a National Instruments Data Acquisition (NI-DAQmx) PCI-6221 (37-pin) Board with 16-Bit Analog Inputs and LabVIEW 8.2 programs to read the sensor data and provide both data acquisition control along with signal processing functions.

DAQ Over-Sampling Rate Noise Filtering through LabVIEW
LabVIEW Calibration and Temperature Measurement Programs
DAQ Sampling Rate at 10kHz and 10 Samples to calculate the average or mean value and reduce measurement noise effects.

Room Temperature Output Calibration Voltage:
Ice Bath Temperature Output Calibration Voltage:

Thermocouple calibration for room temperature and ice bath temperature is shown in the table below:

Calibration Table

	Temperature (°C)	Output Voltage (Volts)
Room	23.4	-0.110
Ice Bath	0.3	-0.745

with Output voltages as measured with a digital multi-function voltmeter

$T_r = 23.4$ and $V_r = -0.110$

$T_b = 0.3$ and $V_b = -0.745$

Temperature as a function of voltage at the output of the amplifier is given as:

$T(V) = m \times V + b$

Constants m & b are calculated to be:

$$m = \frac{T_r - T_b}{V_r - V_b} = \frac{23.4 - 0.3}{-0.110 - (-0.745)} = 36.378\ ^\circ C/V$$

$$b = T_r - m \times V_r = 23.4 - 36.378 \times (-0.110) = 27.402\ ^\circ C$$

Measured Sensitivity at the Thermocouple is:

$G_{thrcpl} = A_V \times m = 785.7 \times 36.378 = 28{,}582\ ^\circ C/V = 28.58\ ^\circ C/mV$

The Type T Thermocouple Sensitivity from the reference table is $25.94\ ^\circ C/mV$

The LabVIEW program calculates the slope (m) and intercept (b) constants to be:

$m = 36.5164$

$b = 27.466$

where LabVIEW stores these values in a data file for the temperature measurements in the heated fluid-cell using the microprobe thermocouple.

The estimated error due to instrumentation amplifier input offset voltage error is

$V_{os} = A_V \times \Delta V_{os} = 785.7 \times 20\mu V = 15714\mu V = 15.71mV$ at the amplifier output

Temperature error is $\Delta T_{os} = m \times V_{os} = 36.378 \times 0.01571 = 0.57\ ^\circ C$

Where using a two-point calibration scheme with a reference thermometer will eliminate this bias error of the instrumentation amplifier.

The LabVIEW thermocouple calibration program is shown in the three figures below:

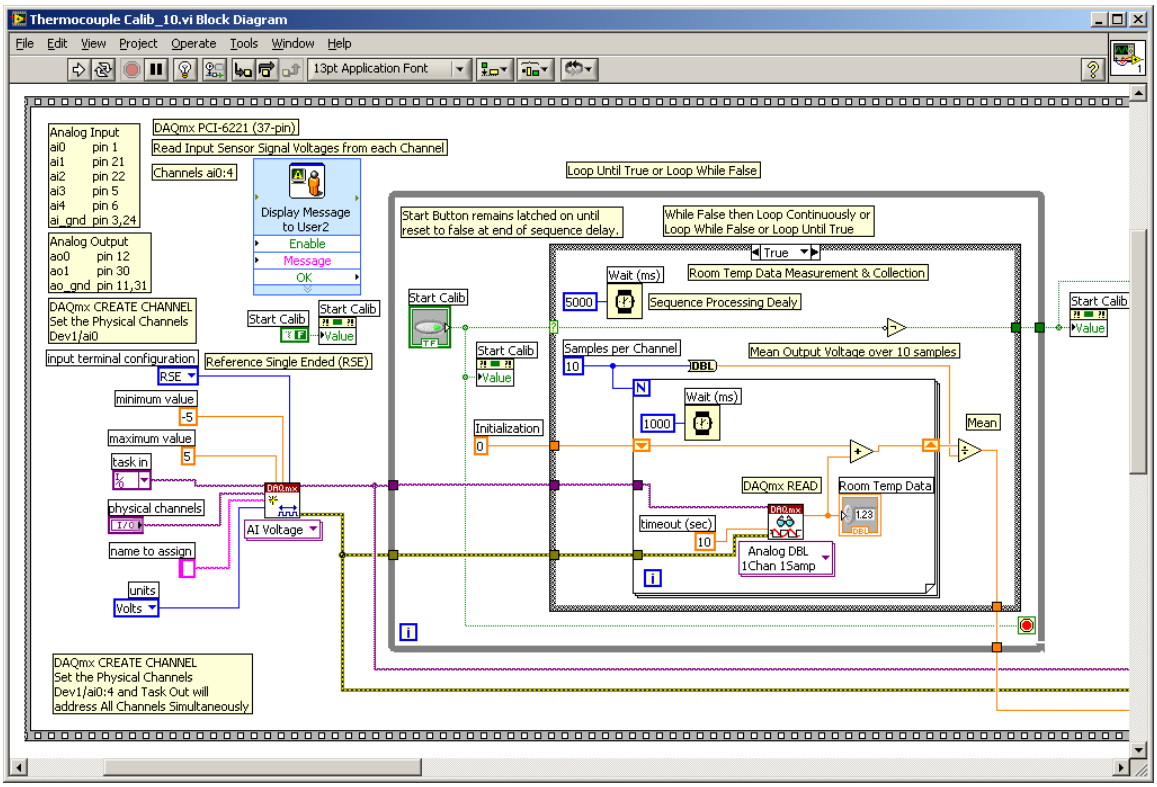

Figure 3 LabVIEW Program for Thermocouple Calibration

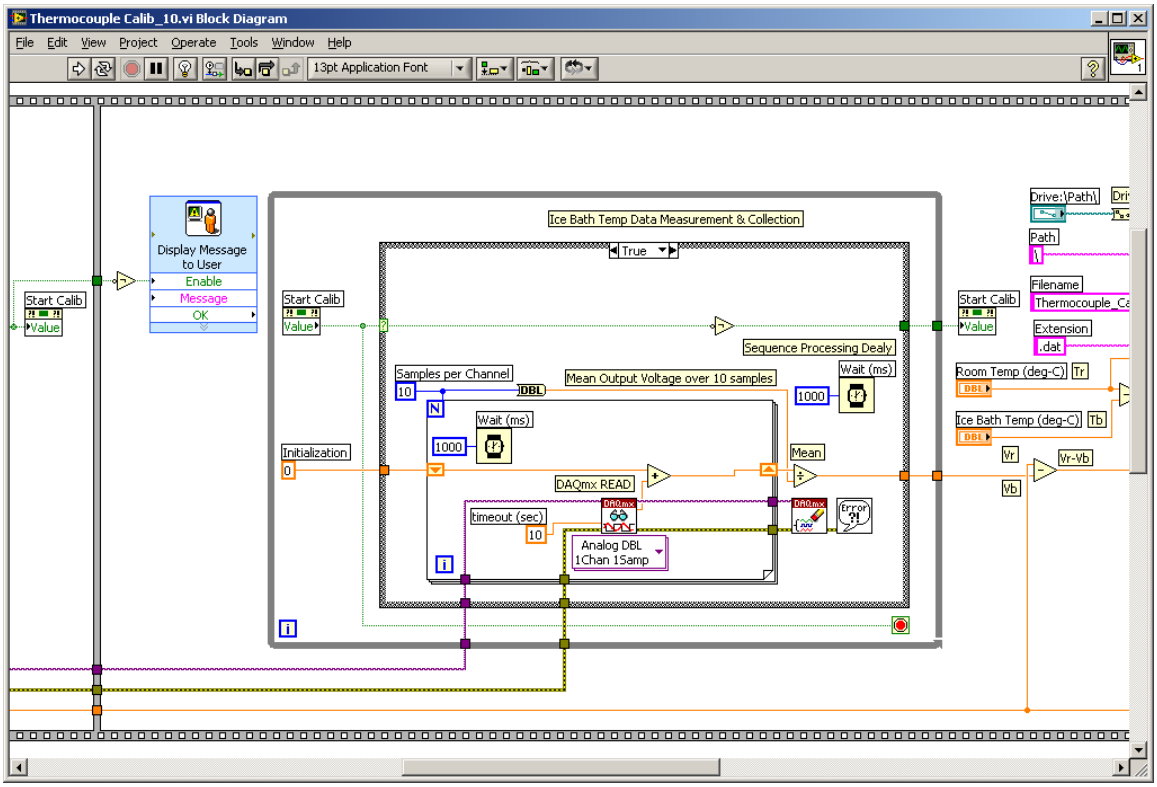

Figure 4 LabVIEW Program for Thermocouple Calibration (continued)

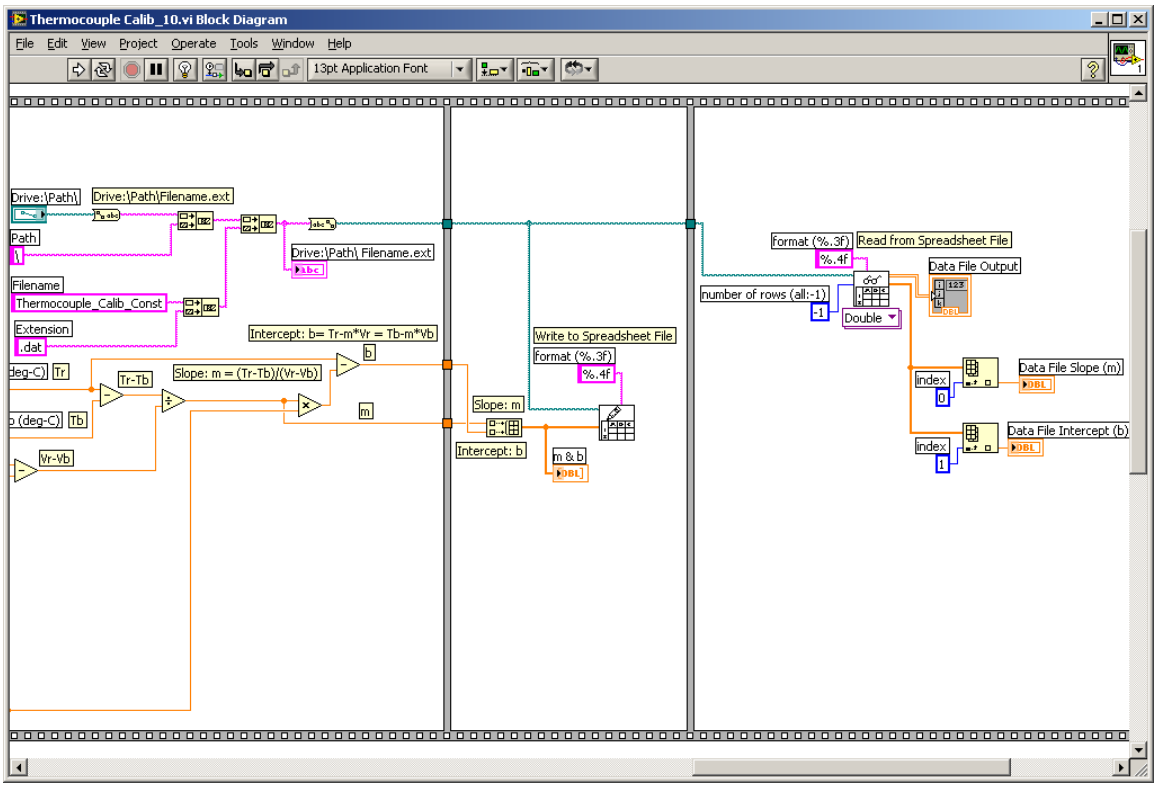

Figure 5 LabVIEW Program for Thermocouple Calibration (continued)

This program features user interface interaction with interrupts and dialog to inform the user to set room temperature conditions to begin the calibration process and then move the thermocouple to the ice bath and resume the second point calibration process. The calibration slope and intercept values are stored in a data file that is used when measuring the temperature profiles in the fluid-cell cuvette.

Thermocouple Measurements of Heated Fluid-Cell Cuvette

The fluid-cell is filled with Cargille Labs Fused Silica Matching Reference Liquid Catalog #19571 and Code 06350. This fluid was selected because of the reference refractive index and the sensitivity to a change in temperature. The fluid with the highest viscosity in this class was selected so that thermal diffusion would dominate with no vortices or convective re-circulation in the flow. Effective thermal equilibrium for steady-state conditions occurs in about 10 minutes following the applying of power to the heater. In about 4 to 5 hours the maximum thermal gradient will shift from the near center of the fluid-cell to the walls. The important properties of this fluid for this experiment are:

Index-of-Refraction: n=1.4587 at 0.5893μm wavelength and 25°C

Refractive Index sensitivity to Temperature: $dn/dT = -3.65\times10^{-4}/^{\circ}C$ from 15 to 35°C

Viscosity: 80 centistokes at 25°C

This viscosity can be compared to another reference fluid that has a viscosity of 19 centistokes at 25°C

The Cauchy Equation relates wavelength to index-of-refraction and is given by the following equation:

Index-of-Refraction: $\mathrm{n} = 1.447193 + 3.833433\mathrm{e}\text{-}3/\lambda^2 + 5.661342\mathrm{e}\text{-}5/\lambda^4$

Given the Laser Wavelength: λ (μm or microns)

Laser Wavelength: $\lambda = 0.457\ \mu m$

$n_{25} = 1.4668$ at $\mathrm{T}_{25} = 25\ ^{\circ}C$ which is the Boundary Condition (BC) to convert from temperature to index-of-refraction as given by the following equation:

$$n(T) = dn/dT \times (T - T_{25}) + n_{25}$$

which is important to transfer the boundary conditions to the “wily” index-of-refraction reconstruction algorithm. The “wily” reconstruction algorithm will then use the fringe-shift measurements to determine the internal temperature profile within the fluid-cell. The heater element electronics and the thermocouple amplification electronics along with the fluid-cell cuvette is shown in the figure below:

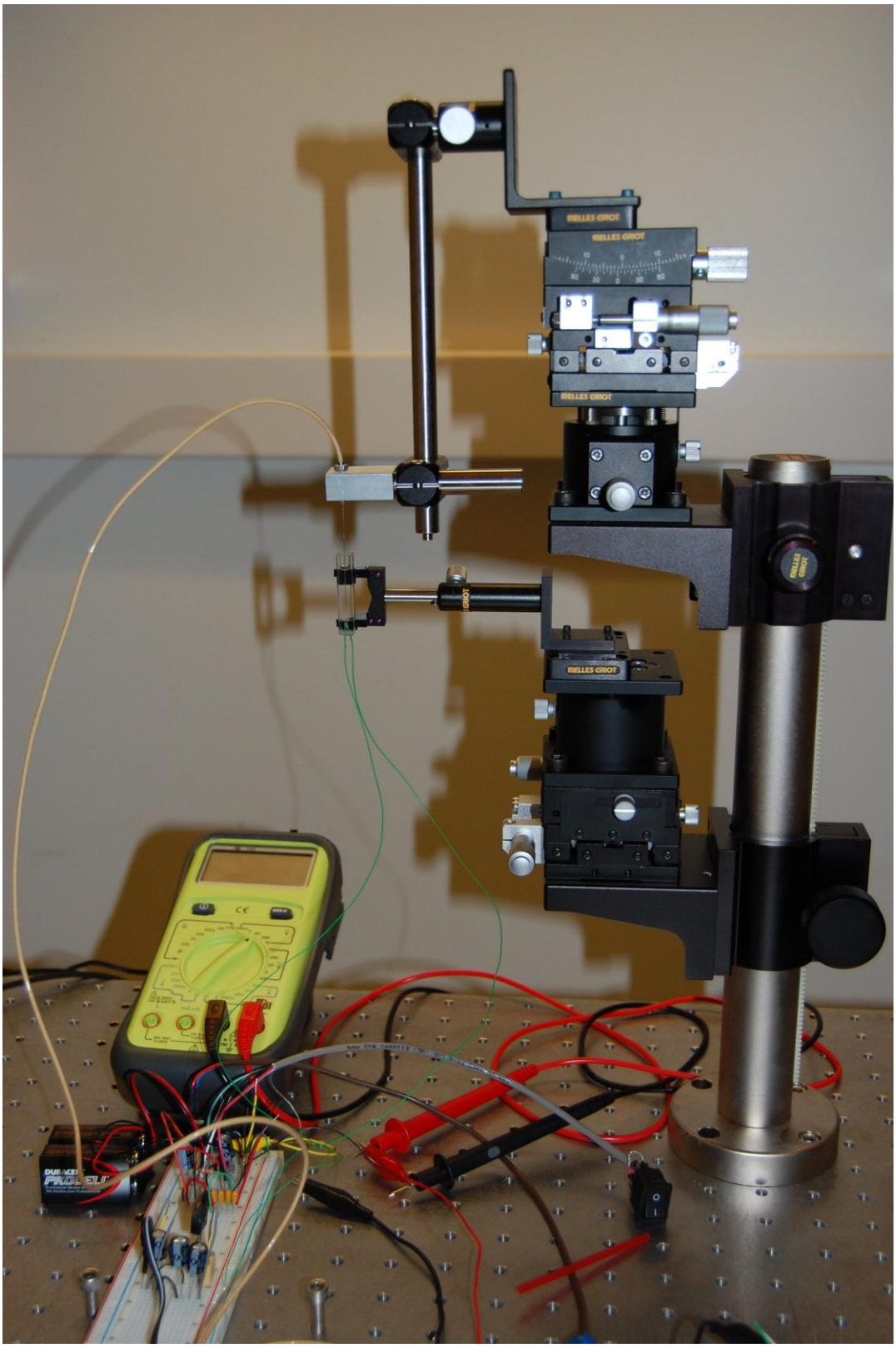

Figure 1 Configuration for Thermocouple Calibration and Measurement

The picture above shows a goniometric stage to align the needle microprobe to be parallel with the walls of the glass fluid-cell in the holder. Multiple translation stages are used to scan the thermocouple within the fluid-cell. The thermocouple amplifier on the upper portion of the breadboard and the voltage regulator for the heater at the bottom of the fluid-cell cuvette occupies the lower portion of the breadboard. The multi-meter is used to monitor the output voltages of the thermocouple amplifier. The picture below shows a close up detail of the thermocouple in the fluid-cell as the thermocouple is immersed in Cargille Labs Fused Silica Matching Liquid Code 06350 Catalog #19571 with a reference index-of-refraction of 1.4571 at 632.8 nm (HeNe) wavelength and 25°C with and Refractive Index to Temperature gradient of dn/dT=-0.000365 /°C $dn/dT = -3.65 \times 10^{-4} / ^{\circ} C$ with range from 15 to 35°C. The index-of-refraction at 457 nm and 25°C is 1.4668 using the Cauchy fourth-order polynomial equation. A close-up view of the inserted thermocouple into the fluid-cell is shown in the figure below:

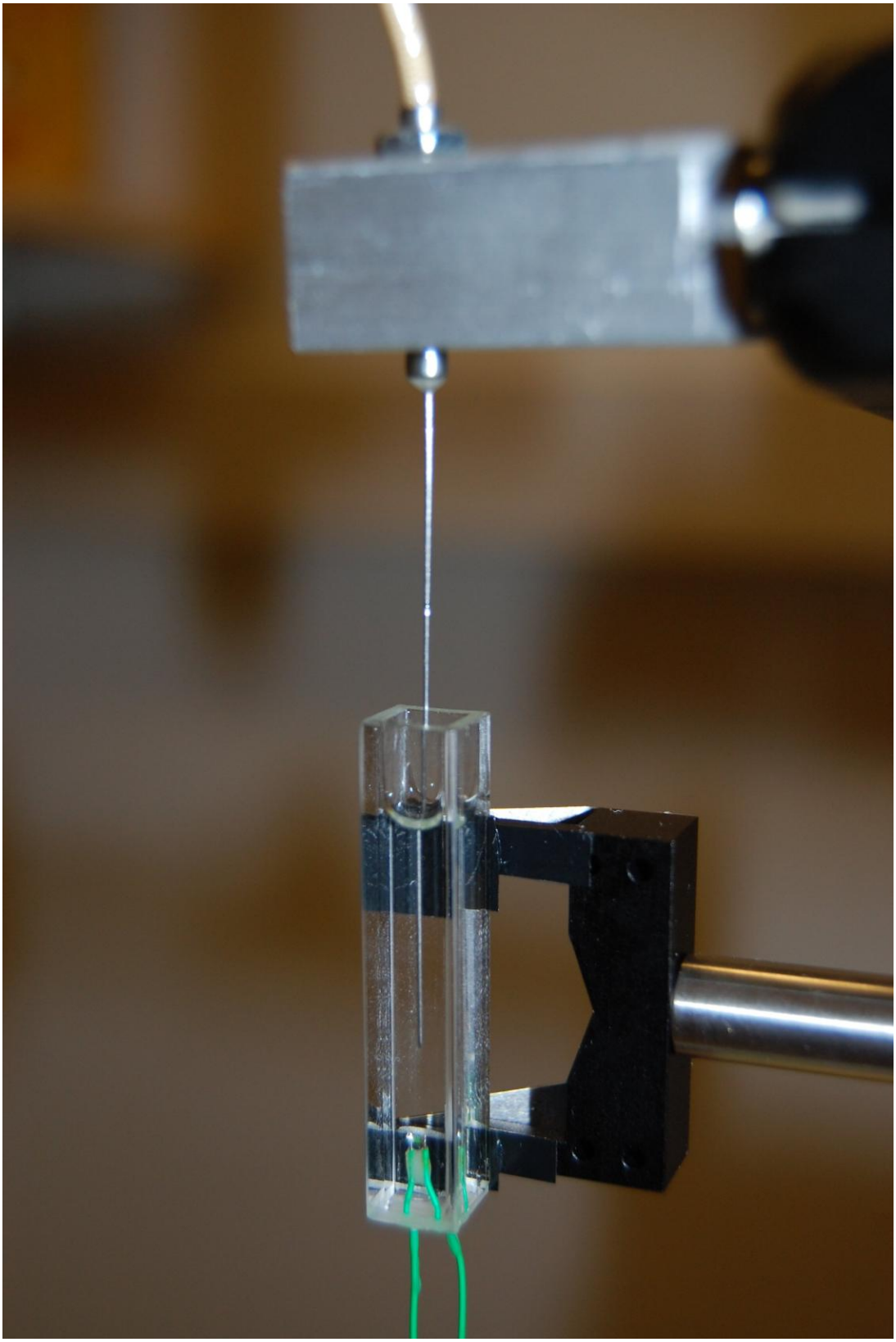

Figure 2 Close-Up of Physi-Temp Needle Probe Thermocouple Immersed in Fluid-Cell with Heater at Bottom Section

A microscope photograph of the smallest surface mount resistor heater element is shown in the figure below:

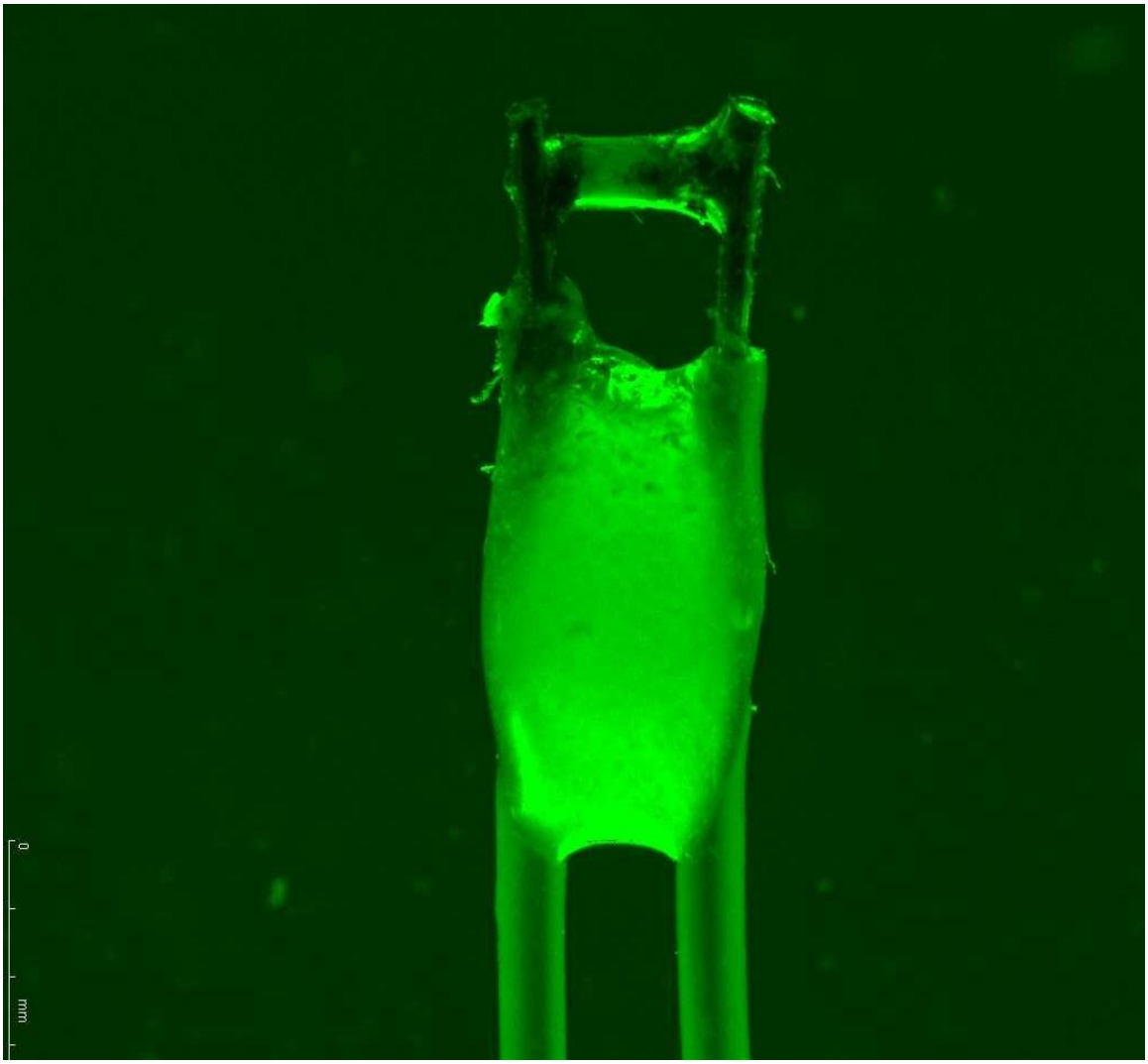

Figure 3 Microscope Photograph of SMT Resistor Heater as attached to Lead Wires

The figure above shows the Surface Mount (SMT) resistor soldered to 30 AWG lead wires. The resistor is relieved from strain by a bulb of epoxy adhesive. The lead wires are then passed through holes drilled into the bottom of the fluid-cell cuvette. When the resistor is aligned and positioned then more epoxy adhesive fixes and seals the attachment of the lead wires to the base of the fluid-cell. The SMT resistor is the smallest available size at (0402) at 1.0L x 0.5H x 0.35T mm and 1/16W at 70°C.

Measured Temperature Profiles in Fluid-Cell

The thermocouple measurements at an elevation of 2.3mm above the heater is shown in the table below:

Measured Temperature Data (°C)

Measurement 11 is Thermocouple at 1.8+0.5=2.3mm above the heater

32.2	32.7	33.1	33.1	32.8	32.3	31.7	31.3
32.3	33.2	33.9	34.3	33.9	33.1	32.2	31.6
32.5	33.5	34.5	35.2	35.3	34.1	32.8	32.0
32.6	33.6	34.4	35.0	34.9	33.9	32.6	31.8
32.1	33.0	33.7	34.0	33.7	33.0	32.2	31.7
31.7	32.3	32.8	32.9	32.7	32.2	31.7	31.3

The following is a plot of the temperature profile:

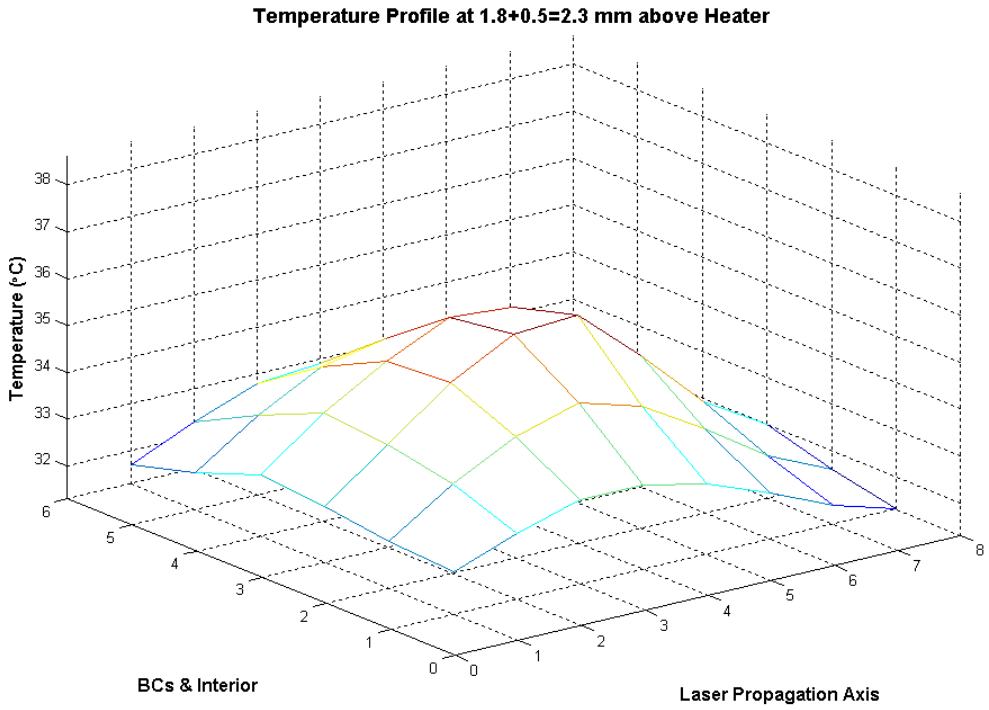

Figure 1 Temperature Profile of BCs and Interior Domain at 2.3mm Elevation

The thermocouple measurements at an elevation of 1.7mm above the heater is shown in the table below:

Measurement 12 is Thermocouple at 1.2+0.5=1.7mm above the heater

32.3	33.1	33.6	33.7	33.4	32.8	32.0	31.6
32.7	33.7	34.5	34.9	34.6	33.6	32.6	31.9
33.1	34.2	35.2	36.1	36.3	34.7	33.1	32.2
32.9	34.1	35.0	35.6	35.3	34.1	33.0	32.2
32.5	33.4	34.1	34.2	33.9	33.2	32.4	31.7
32.1	32.6	33.1	33.3	33.0	32.6	32.0	31.6

The following is a plot of the temperature profile:

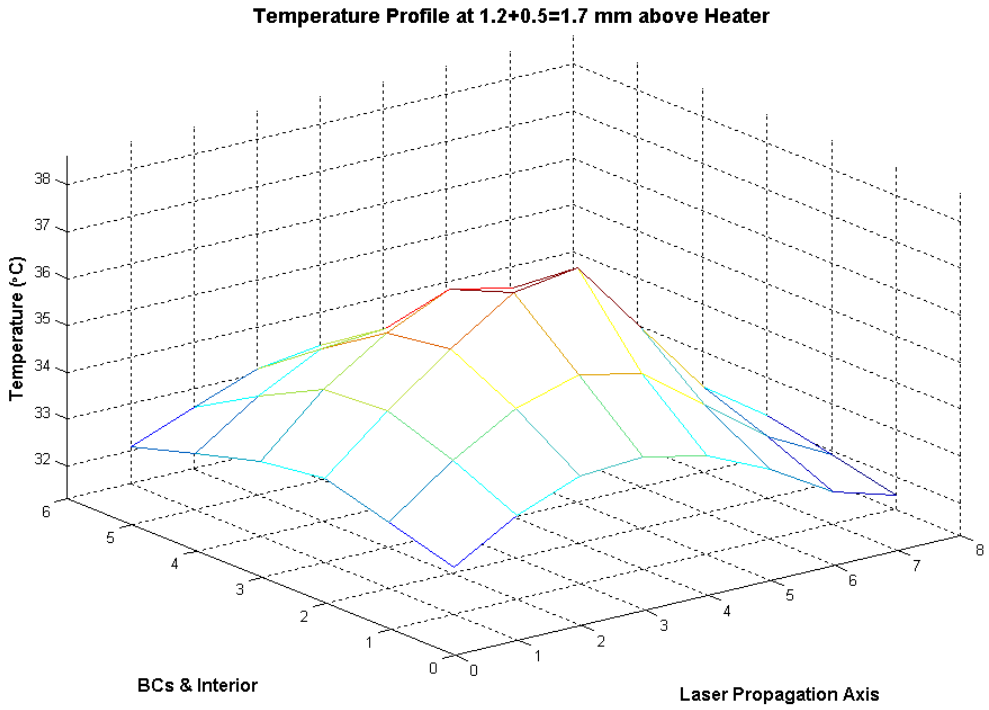

Figure 2 Temperature Profile of BCs and Interior Domain at 1.7mm Elevation

The thermocouple measurements at an elevation of 1.1mm above the heater is shown in the table below:

Measurement 13 is Thermocouple at 0.6+0.5=1.1mm above the heater

32.6	33.4	34.2	34.5	34.4	33.7	32.8	32.1
33.1	34.3	35.4	36.2	36.1	34.8	33.5	32.4
33.1	34.3	35.5	36.8	37.5	35.9	33.9	32.6
33.0	34.1	35.1	35.7	35.4	34.4	33.2	32.3
32.5	33.4	34.1	34.4	34.2	33.6	32.7	31.9
32.2	32.7	33.2	33.4	33.3	32.8	32.2	31.7

The following is a plot of the temperature profile:

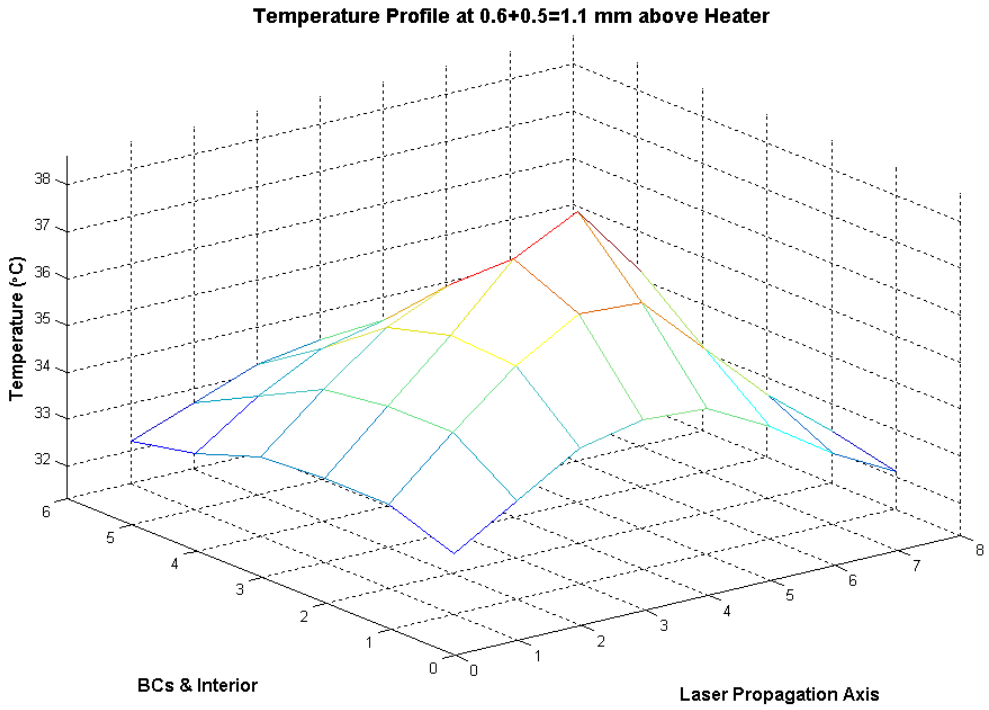

Figure 3 Temperature Profile of BCs and Interior Domain at 1.1mm Elevation

The thermocouple measurements at an elevation of 0.5mm above the heater is shown in the table below:

Measurement 14 is Thermocouple at 0.0+0.5=0.5mm above the heater

32.9	34.0	35.0	35.7	35.6	34.6	33.5	32.4
33.3	34.6	35.9	37.2	37.6	36.0	34.1	32.7
33.5	34.8	36.2	37.9	38.6	36.6	34.3	32.7
33.2	34.2	35.4	36.1	35.9	34.8	33.4	32.2
32.5	33.4	34.1	34.5	34.3	33.7	32.8	31.9
32.0	32.5	33.0	33.2	33.2	32.8	32.3	31.8

The following is a plot of the temperature profile:

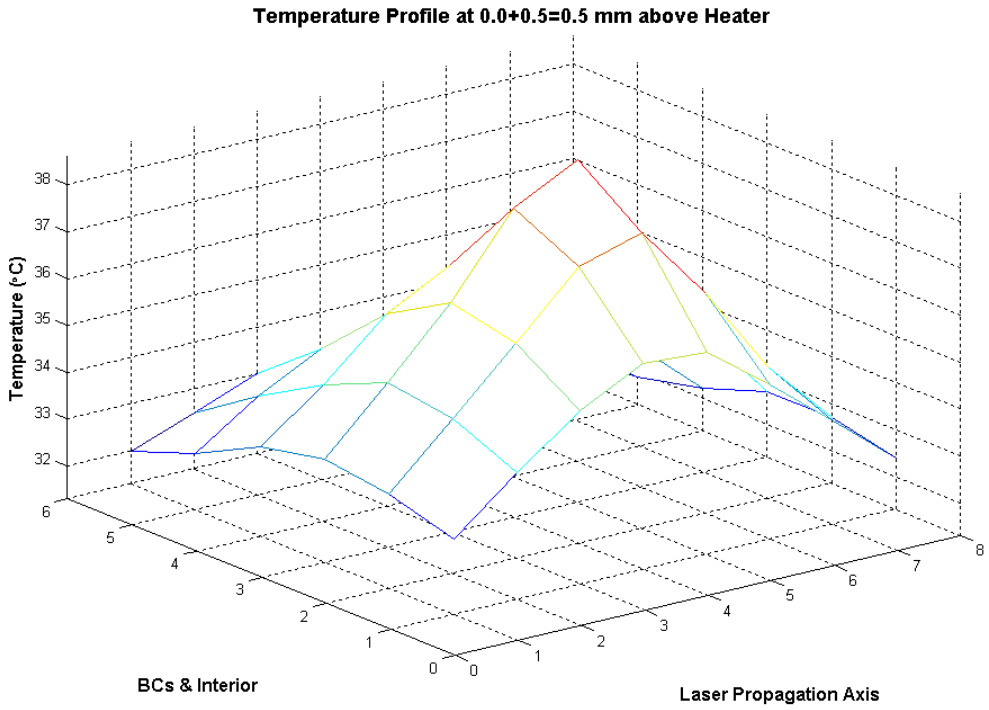

Figure 4 Temperature Profile of BCs and Interior Domain at 0.5mm Elevation

Notice how the off-center peak of the temperature becomes more clearly discernable as the scan plane approaches the proximity of the heater. The heater was positioned to the approximate center of the fluid-cell, but the inaccuracy of this position can be seen upon observation where the offset in the measurements reflects this attribute as well.

The maximum and minimum temperature measurements for all the data are:

$T_{\max} = 38.6\,^{\circ}C$

$T_{\min} = 31.3\,^{\circ}C$

With a maximum temperature difference of:

$\Delta T_{\max} = T_{\max} - T_{\min} = 38.6 - 31.3 = 7.3^{\circ}C$

The Index-of-Refraction that is converted from Temperature measurements is based on: Cargille Labs Fused Silica Matching Reference Fluid Catalog # 19571 Code: 06350

Index-of-Refraction: $n = 1.4587$ at $\lambda = 0.5893\ \mu m$ and $T = 25^{\circ}C$ as specified by Cargille Labs with viscosity of 80 centistokes at 25°C

Refractive Index to Temperature Sensitivity: $\frac{dn}{dT} = -3.65 \times 10^{-4}\ /^{\circ}C$ from 15 to 35°C

Cauchy Equation: $n(\lambda) = 1.447193 + 3.833433 \times 10^{-3}/\lambda^2 + 5.661342 \times 10^{-5}/\lambda^4$

Given Laser Wavelength: $\lambda = 0.457\ \mu$m

Index-of-Refraction: $n_{25} = 1.4668$ at $T_{25} = 25^{\circ}C$

Refractive Index Equation as a function of Temperature: $n(T) = \frac{dn}{dT}(T - T_{25}) + n_{25}$

The index-of-refraction at the discrete elevations in the fluid-cell is shown in the four tables below:

Index-of-Refraction

Measurement 11 is Thermocouple at 1.8+0.5=2.3mm above the heater

1.45607	1.45589	1.45574	1.45574	1.45585	1.45604	1.45625	1.45640
1.45604	1.45571	1.45545	1.45531	1.45545	1.45574	1.45607	1.45629
1.45596	1.45560	1.45523	1.45498	1.45494	1.45538	1.45585	1.45615
1.45593	1.45556	1.45527	1.45505	1.45509	1.45545	1.45593	1.45622
1.45611	1.45578	1.45552	1.45542	1.45552	1.45578	1.45607	1.45625
1.45625	1.45604	1.45585	1.45582	1.45589	1.45607	1.45625	1.45640

Measurement 12 is Thermocouple at 1.2+0.5=1.7mm above the heater

1.45604	1.45574	1.45556	1.45552	1.45563	1.45585	1.45615	1.45629
1.45589	1.45552	1.45523	1.45509	1.45520	1.45556	1.45593	1.45618
1.45574	1.45534	1.45498	1.45465	1.45458	1.45516	1.45574	1.45607
1.45582	1.45538	1.45505	1.45483	1.45494	1.45538	1.45578	1.45607
1.45596	1.45563	1.45538	1.45534	1.45545	1.45571	1.45600	1.45625
1.45611	1.45593	1.45574	1.45567	1.45578	1.45593	1.45615	1.45629

Measurement 13 is Thermocouple at 0.6+0.5=1.1mm above the heater

1.45593	1.45563	1.45534	1.45523	1.45527	1.45552	1.45585	1.45611
1.45574	1.45531	1.45490	1.45461	1.45465	1.45512	1.45560	1.45600
1.45574	1.45531	1.45487	1.45439	1.45414	1.45472	1.45545	1.45593
1.45578	1.45538	1.45501	1.45479	1.45490	1.45527	1.45571	1.45604
1.45596	1.45563	1.45538	1.45527	1.45534	1.45556	1.45589	1.45618
1.45607	1.45589	1.45571	1.45563	1.45567	1.45585	1.45607	1.45625

Measurement 14 is Thermocouple at 0.0+0.5=0.5mm above the heater

1.45582	1.45542	1.45505	1.45479	1.45483	1.45520	1.45560	1.45600
1.45567	1.45520	1.45472	1.45425	1.45410	1.45469	1.45538	1.45589
1.45560	1.45512	1.45461	1.45399	1.45374	1.45447	1.45531	1.45589
1.45571	1.45534	1.45490	1.45465	1.45472	1.45512	1.45563	1.45607
1.45596	1.45563	1.45538	1.45523	1.45531	1.45552	1.45585	1.45618
1.45615	1.45596	1.45578	1.45571	1.45571	1.45585	1.45604	1.45622

The LabVIEW program that reads the calibration coefficients and converts the thermocouple voltage measurements to temperature (°C) is shown in the following five figures:

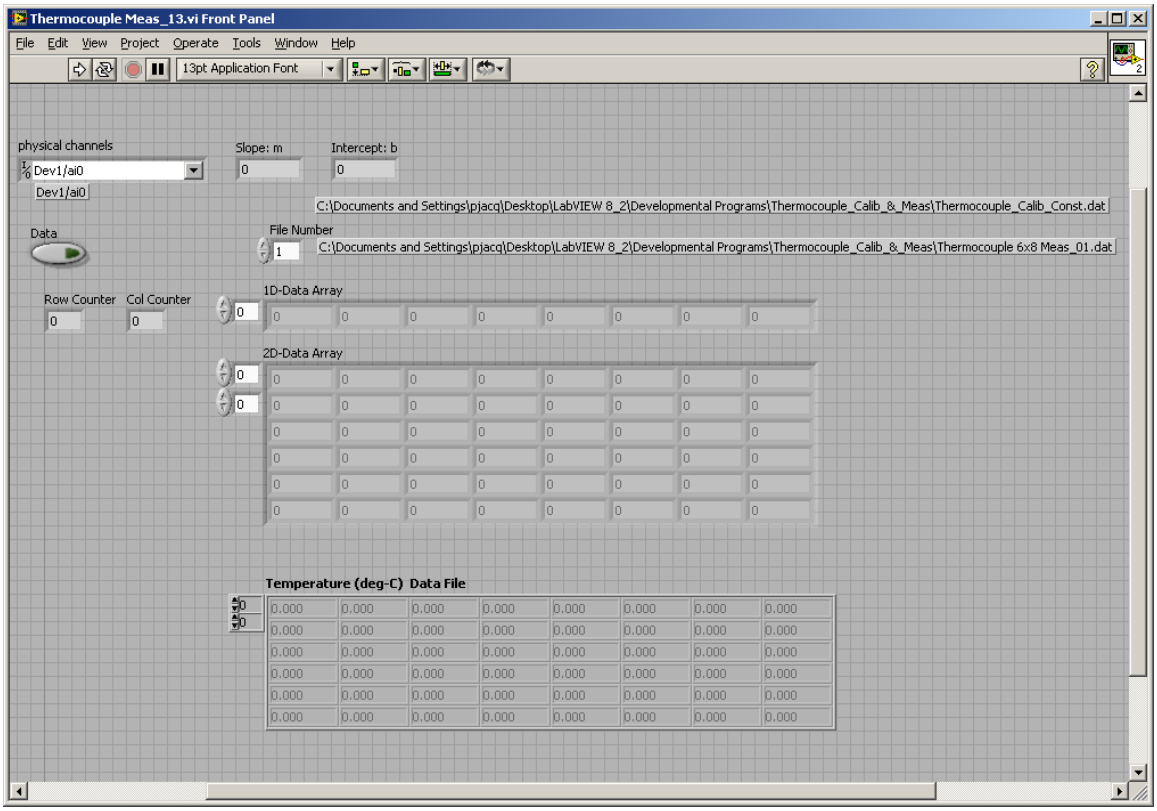

Figure 5 LabVIEW Control Panel Table for Temperature Data Array Entry

The input control Front Panel enters a temperature value for every push of the “Data” button until the 6x8 matrix array is filled term-by-term with values. This array represents a cutting plane in depth and width at a constant elevation from the heater.

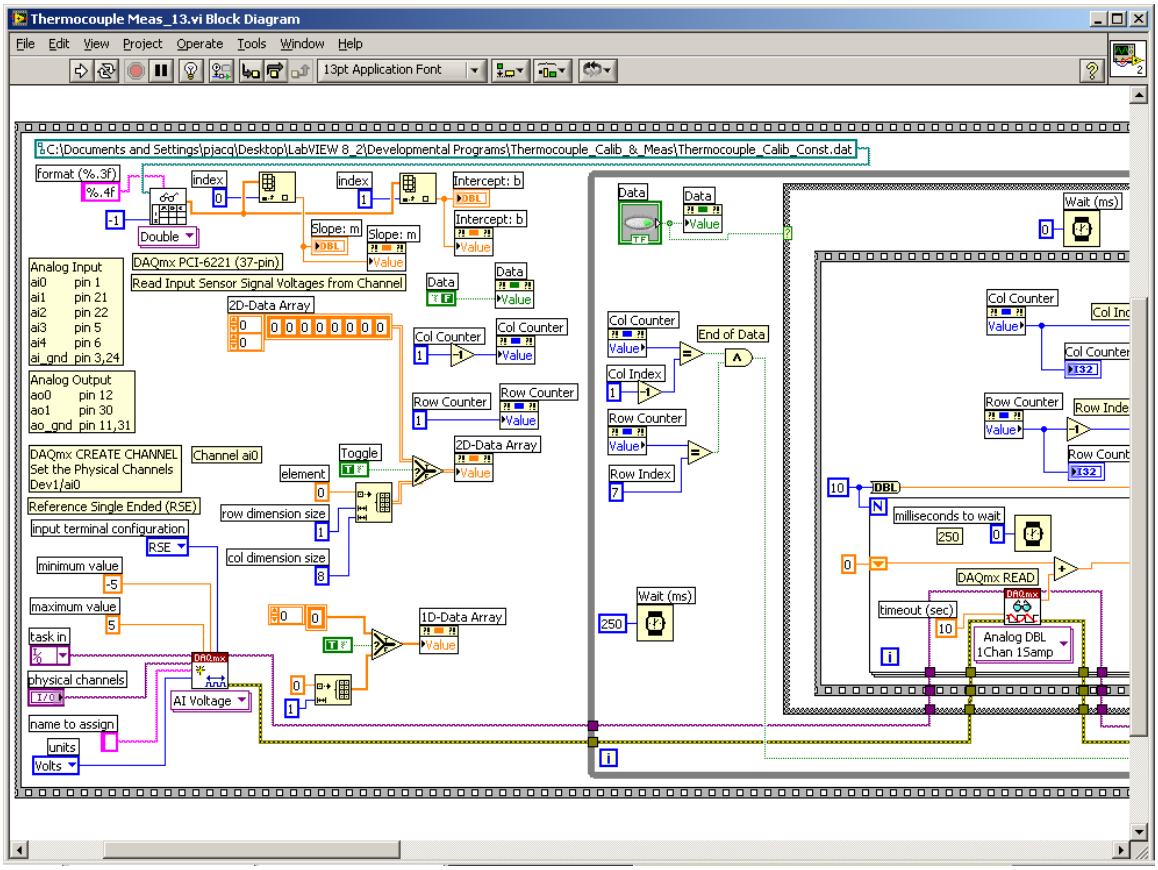

Figure 6 LabVIEW Program for Reading Thermocouple Coefficients and Data Acquisition Measurements

Thermocouple voltages are sampled over 250msec intervals where 10 samples are averaged. The averaged samples are then converted from voltage to temperature. The temperature data is then loaded into an array and stored in a file.

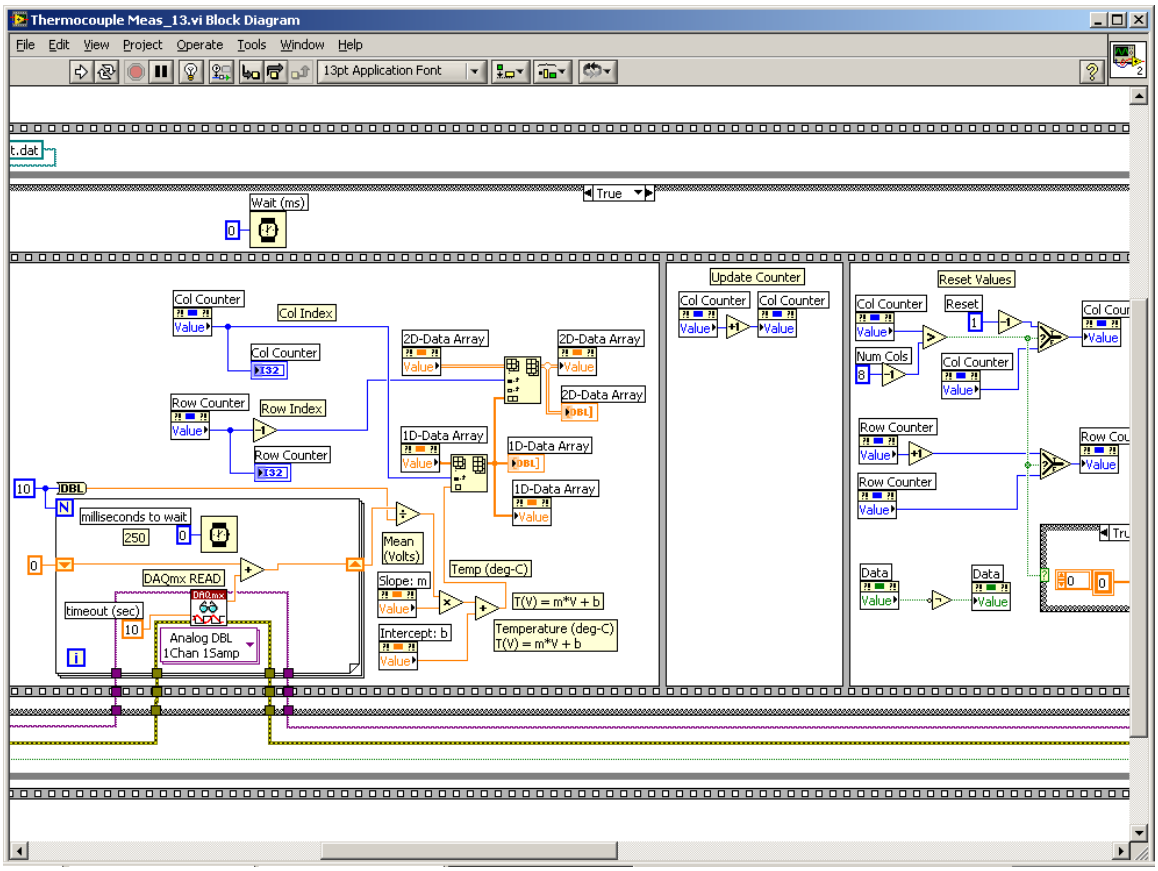

Figure 7 LabVIEW Program for Reading Thermocouple Coefficients and Data Acquisition Measurements (continued)

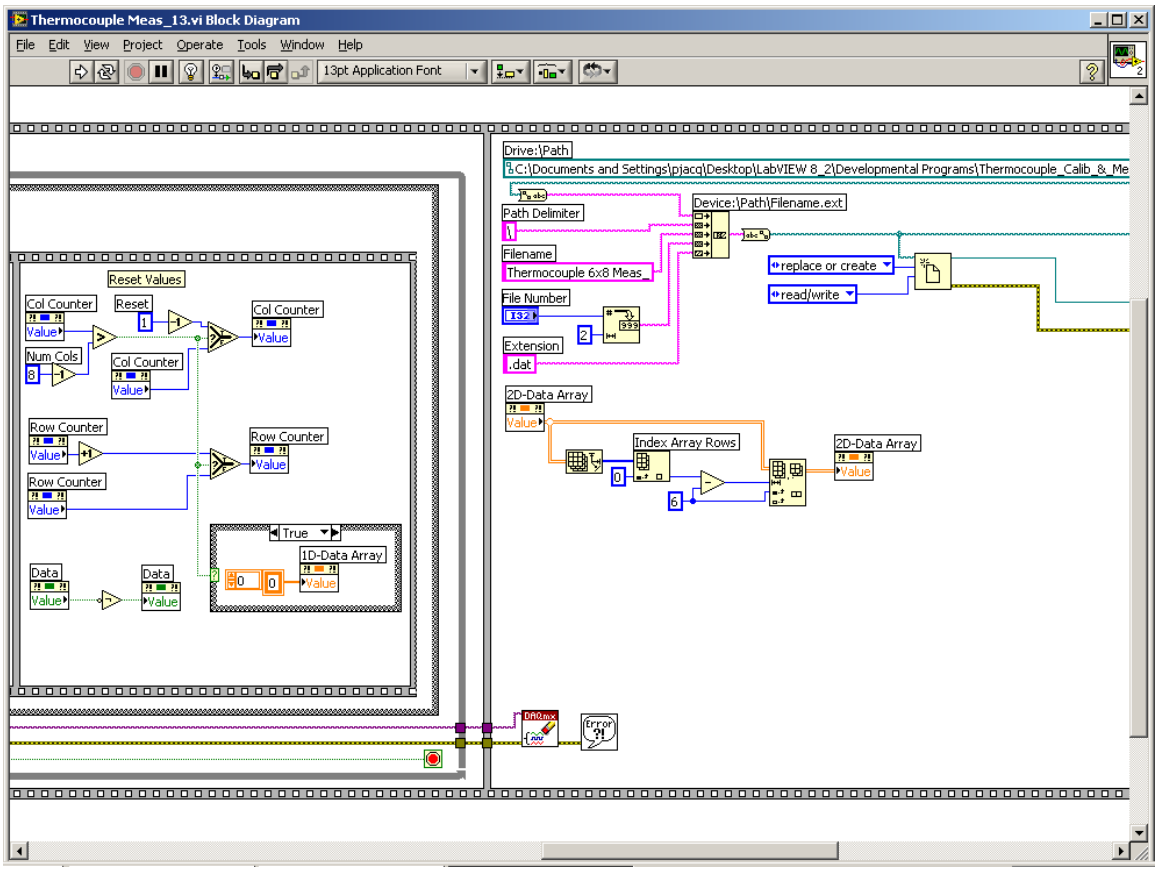

Figure 8 LabVIEW Program for Reading Thermocouple Coefficients and Data Acquisition Measurements (continued)

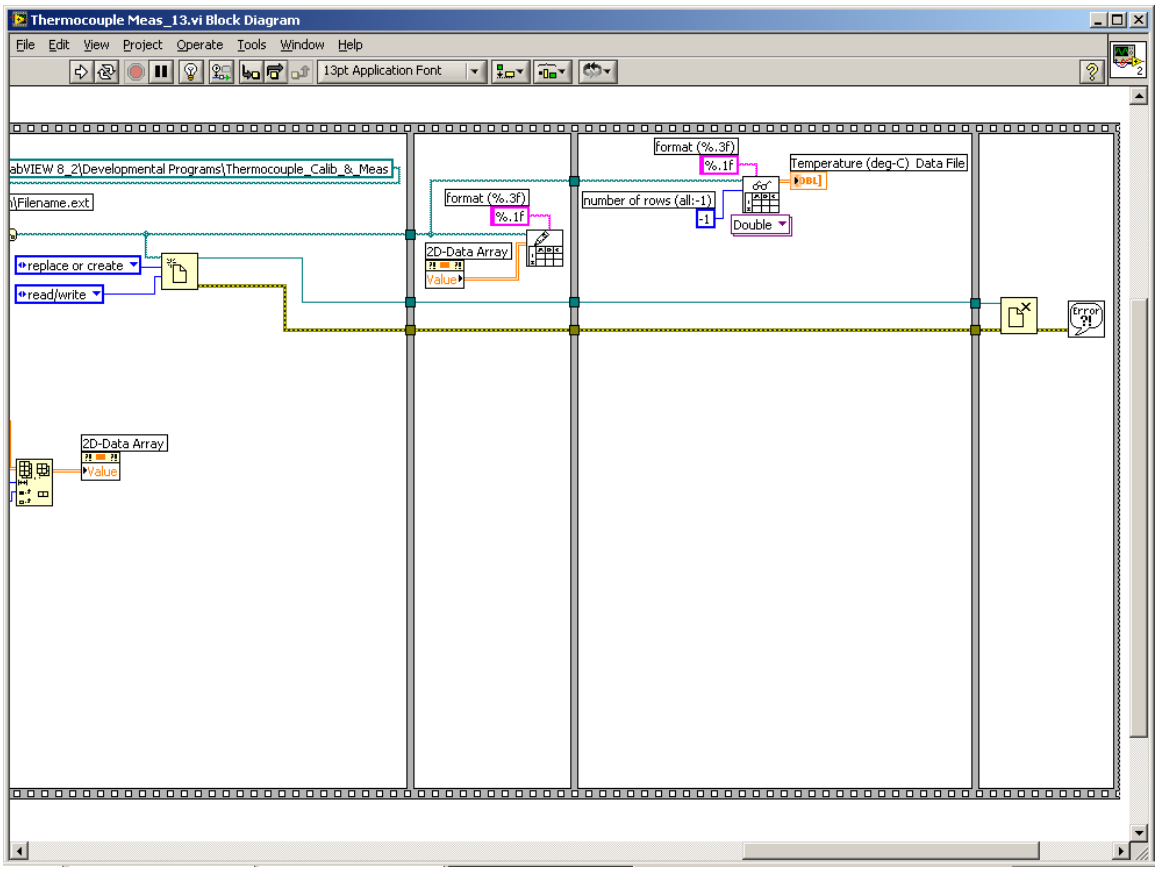

Figure 9 LabVIEW Program for Reading Thermocouple Coefficients and Data Acquisition Measurements

Beam Steering Mirror (BSM) Calibration

Steps for 2-axis Calibration

1) Red & Blue Laser Beam Expansion: Expand laser and collimate output beam for long distance across optical table
2) Setup BSMs and camera with LabVIEW: Focus the laser beam(s) onto the center of camera. Step BSMs with specified gain sensitivity parameter (mV/deg arc angle) and save the image data to a file.
3) Use image-processing software to compress the image data file and determine the centroids. Plot the measured displacement response to commanded BSM voltage.
4) Use least-square-error linear curve-fitting software to determine the slope of the curve and compare the measured gain sensitivity to the gain sensitivity as specified in the BSM operator's manual

Cambridge BSM Specification:

$d\theta_{Shaft}/dV=2.0$ deg/Volt

$$d\theta_{Shaft} / dV = 2.0 \deg / Volt$$

Output Beam

x-axis: $d\theta_x/d\theta_{Shaft}=2$

y-axis: $d\theta_y/d\theta_{Shaft}=2/\sqrt{2}$

x-axis: $d\theta_x / d\theta_{Shaft} = 2$

y-axis: $d\theta_y / d\theta_{Shaft} = 2/\sqrt{2}$

Sensitivity

x-axis: $d\theta_x/dV=d\theta_x/d\theta_{Shaft}$ x $d\theta_{Shaft}/dV$ = 2 x 2 = 4 deg/volt

y-axis: $d\theta_y/dV=d\theta_y/d\theta_{Shaft}$ x $d\theta_{Shaft}/dV$ = $2/\sqrt{2}$ x 2 = $4/\sqrt{2}$ = 2.83 deg/volt

x-axis: $d\theta_x / dV = d\theta_x / d\theta_{Shaft} \times d\theta_{Shaft} / dV = 2 \times 2 = 4 \deg / Volt$

y-axis: $d\theta_y / dV = d\theta_y / d\theta_{Shaft} \times d\theta_{Shaft} / dV = 2 \times 2 / \sqrt{2} = 4 / \sqrt{2} = 2.83 \deg / Volt$

BSM Calibration Procedure**:**

The main controller for the experiment is through LabVIEW, which drives the two-axis BSMs, translation stages, and records the camera images for three-dimensional scanning. A LabVIEW Data Acquisition (DAQ) board is used to measure thermocouple data and send out analog voltages to the each of the BSMs. The calibration process determines the angular displacement of the output beam for an input voltage applied to the BSM. LabVIEW provides the step-stare control and saves the image data file from the camera as a focused laser spot is scanned across the CCD camera. The camera can be thought of as the fluid-cell where the displacement dimensions are ±2.5mm for scanning.

The equipment is as follows:

LabVIEW 8.2 under Microsoft Windows XP

National Instruments PCI-6221 (37-pin) DAQ board

- Melles-Griot 85-BLS-301 100mW x 457nm Wavelength x 0.16mm Dia Beam “Blue” Diode Pumped Solid-State (DPSS) Laser
- Melles-Griot Beam Expander:
- 04 OAS 014 25x Microscope Objective
- 01 LAO 169 Achromat Doublet 180mmFL x 30mmDia
- National Aperture 200μm Pinhole
- Melles-Griot 02 WRM 029 λ/2 x 50mm Dia Half-Wave Retardation Plates or otherwise known as polarizer lenses for Attenuation
- Cambridge Technology Model 6900 Galvanometer Optical Scanners or BSMs
- Cambridge Technology MicroMax Series 671 Single Axis Board Level Mirror Positioning System or Electronic Amplifier Board for BSM Control
- Melles-Griot 02 MPQ 017/023 100mm Dia x λ/10 waves Flat Folding Mirror
- Melles-Griot 01 LPX 281 Plano-Convex Focusing Lens 200mmFL x 130mmDia
- Point-Grey Research (PGR) Grasshopper GRAS-50S5M-C 2448x2048pixels x 3.45μm/pixel Detector Spacing x 8-bit Radiometric Dynamic Range (0-255) Gray-Scale CCD Camera with electronic shutter

Due to a known Windows XP bug for Firewire IEEE-1394 camera interface the limited data throughput reduces the 2448x2048 resolution to 1600x1200 at 3 frames/sec.

The optical layout shown in the figure below depicts the Keplerian pinhole 25x Beam Expander (BE) which produces a 25mm Diameter collimated beam that is truncated with an adjustable iris diaphragm for uniform aperture illumination as shown in the figure below:

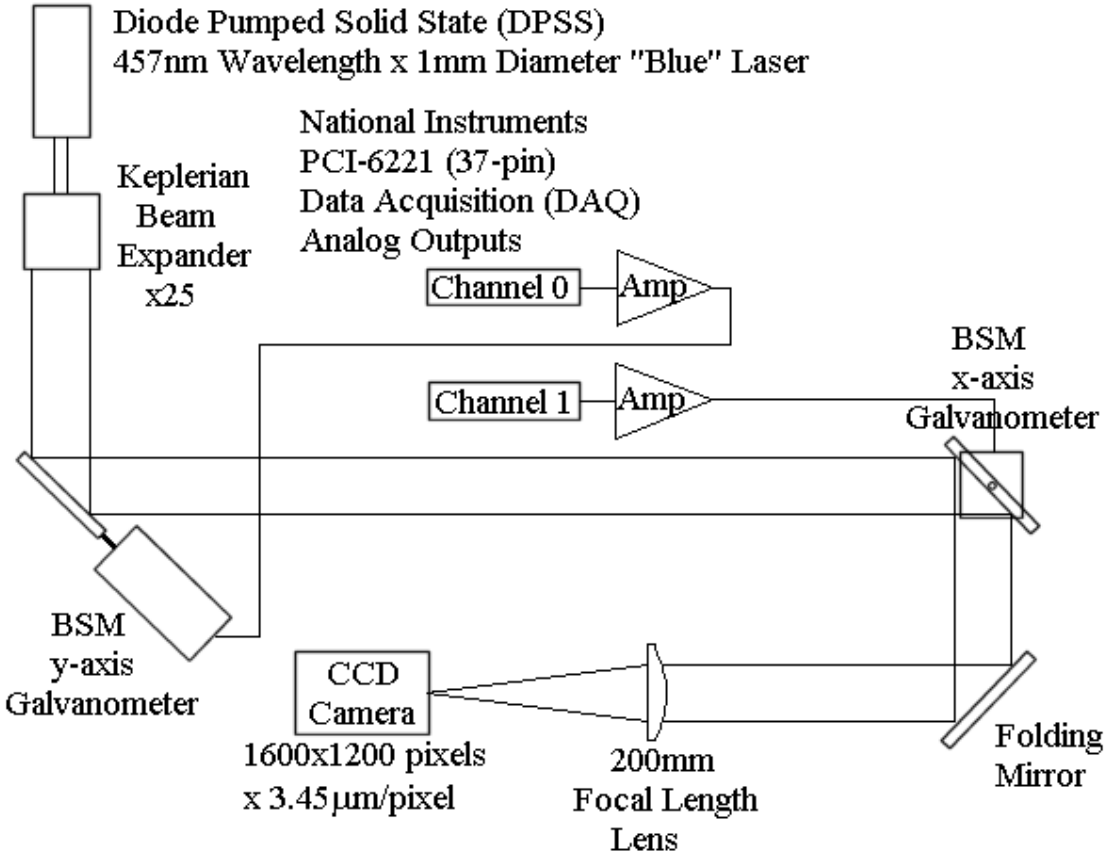

Figure 1 Optical Layout

The laser then propagates through the 45° tilted *y*-axis BSM and afterward through the *x*-axis BSM with the vertical rotation axis. The folding mirror has micrometer adjusters for tilt that is used to center or offset the laser spot position on the CCD camera. The CCD camera is especially sensitive to radiometric intensity. Significant amounts of optical attenuation are required to reduce blooming and overfill saturation. This camera has an electronic shutter rather than a mechanical shutter which makes the camera more susceptible to saturation overfill and blooming to neighboring detectors. The size of the focused spot is not so much a concern as the calibration objective is to track the motion of the spot on the CCD camera as a command signal is applied to rotate the BSMs.

The configuration of the components is shown in the figure below:

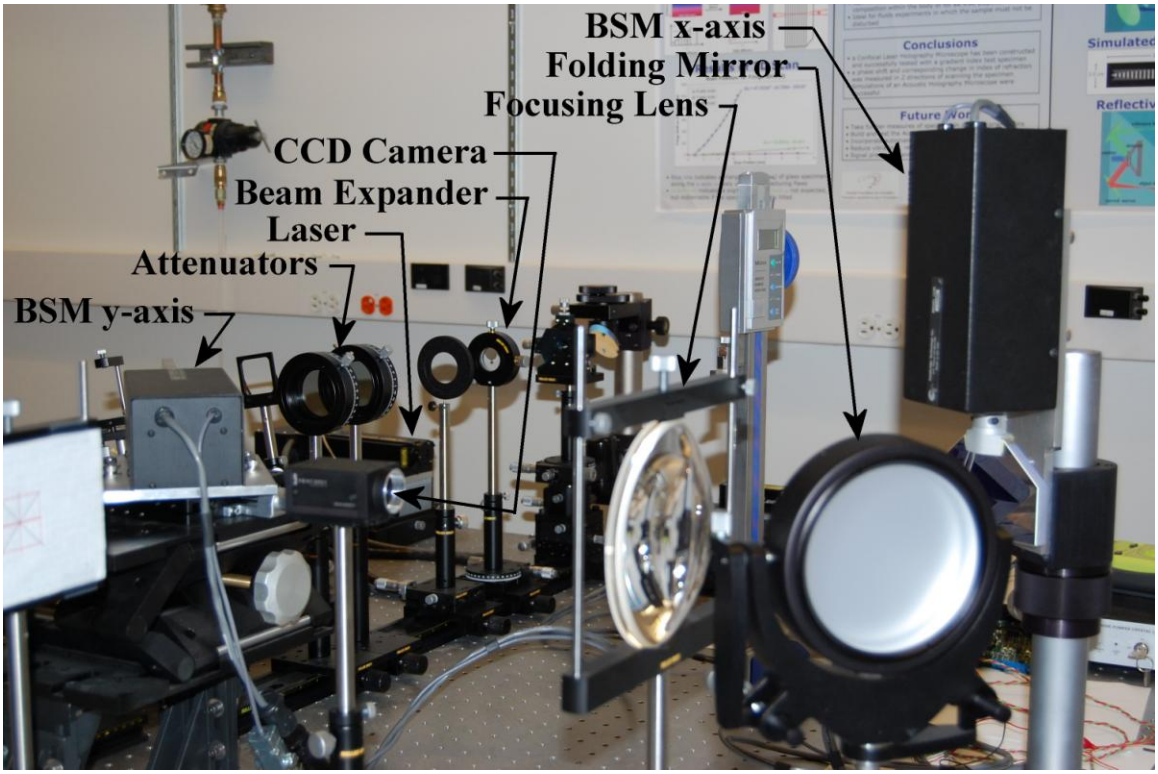

Figure 2 Photograph of Equipment Layout on Optical Bench

The laser optics is in the background and the relatively small Point Grey Research CCD camera is shown in the foreground. Another view with the *y*-axis BSM in the center of the picture is shown in the figure below:

Figure 3 BSM y-axis Galvanometer along with Optical Attenuators and CCD Camera

The reflected image of the BSM electronic amplifier can be seen in the mirror. This circuit board is where the output of the DAQ analog voltage inputs is connected. The focusing lens and the CCD camera with the back surface of the folding mirror in the foreground is shown in the figure below:

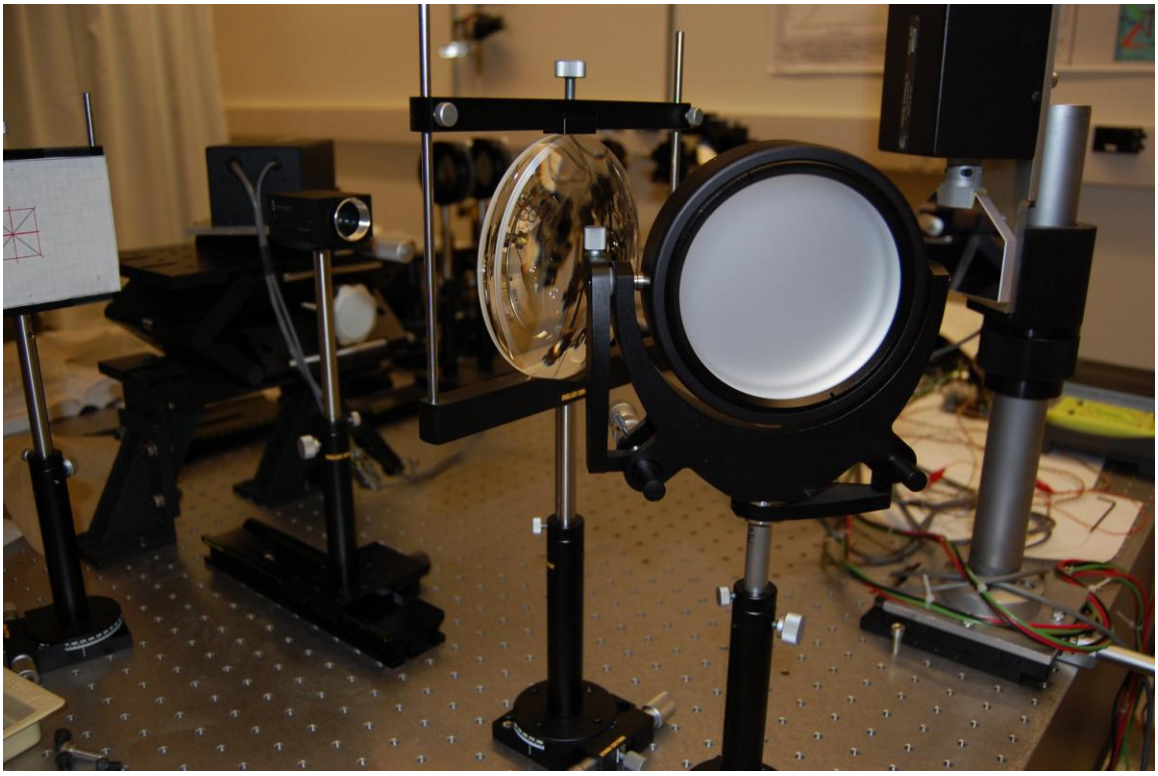

Figure 4 Focusing Lens and Camera Detail

The *x*-axis BSM with a short and wide mirror at the right hand side of the picture is used for scanning along the horizontal direction. The Zemax simulation shows the arrangement of the focusing lens to determine the spot size. The Zemax optical layout is shown in the figure below:

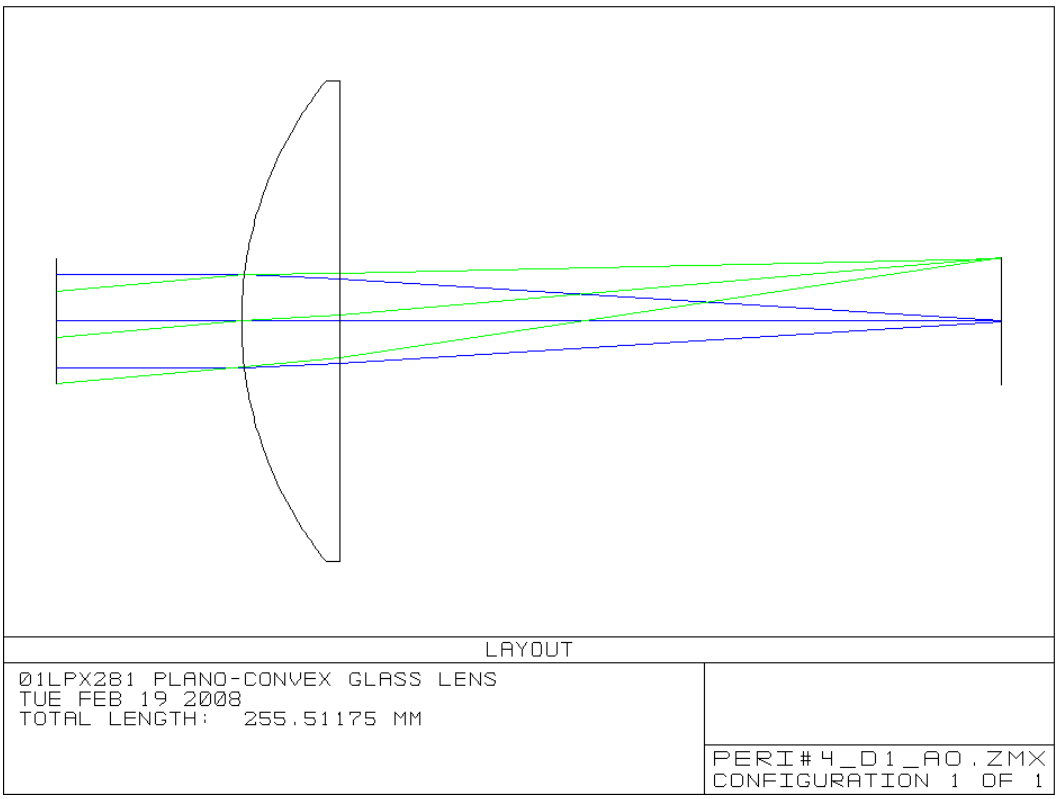

Figure 5 Zemax Layout of Focusing Lens with on-axis and 5° off-axis incident beams.

The Zemax spot diagrams are shown in the figure below:

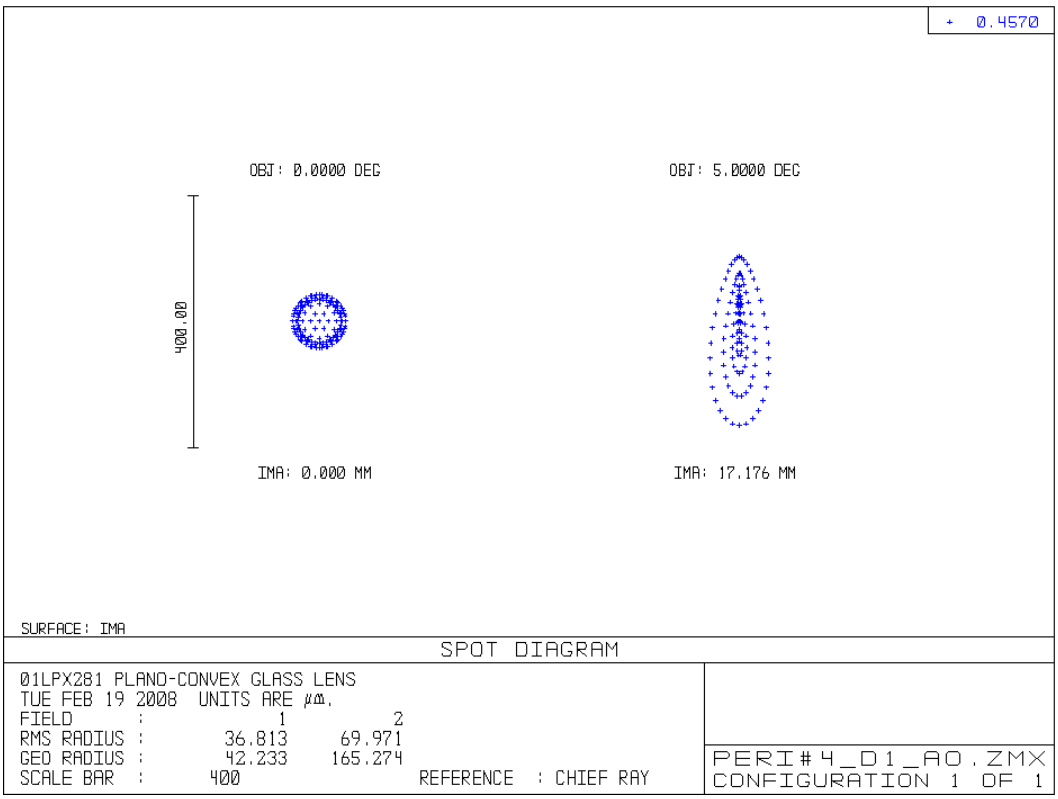

Figure 6 Spot Diagrams in Microns for on-axis and 5° off-axis Beams

The on-axis geometric spot radius is 42μm which is significantly different from the spot radius on the CCD camera, which is around 1200μm. Even though the optical attenuation is set to maximum with the polarizer wave plates the focused beam still saturates the detector at intensity level of 255. This saturation of excessive intensity at the focal point causes the camera saturation to overfill and affect the neighboring detectors. This problem is worse with a camera that uses an electronic shutter instead of a mechanical shutter. The electronic shutter of the Point-Grey Research Grasshopper CCD camera greatly increases the focused beam spot size. Since BSM calibration tracks the motion of the spot for a change in input voltage to the BSM then the size of the spot is not a concern as long as the spot remains within the 1600x1200 frame of the camera. This focused laser spot image on the CCD camera can be seen in the figure below:

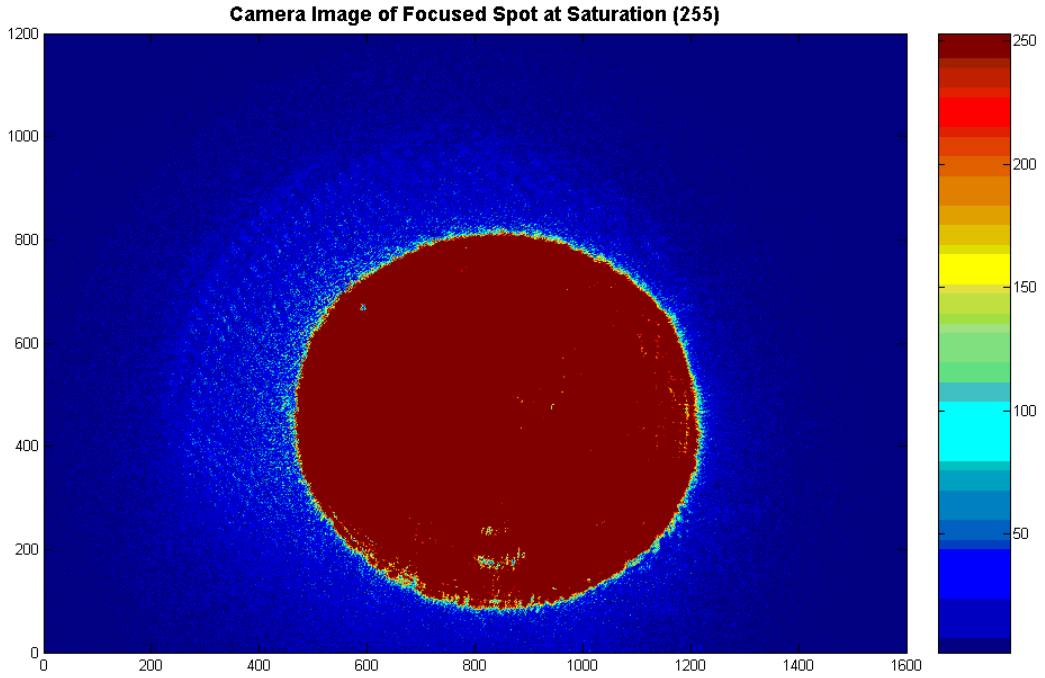

Figure 7 Laser Spot Image of about 700 pixels in Diameter on CCD Camera

This laser spot is initially set near the bottom camera of the viewing frame and as the voltage is increased with constant step-size then the laser spot moves upward for y-axis BSM calibration. The approximate maximum diameter is around line 500 or pixel 500 row. The intensity profile for this cross-section is shown in the figure below:

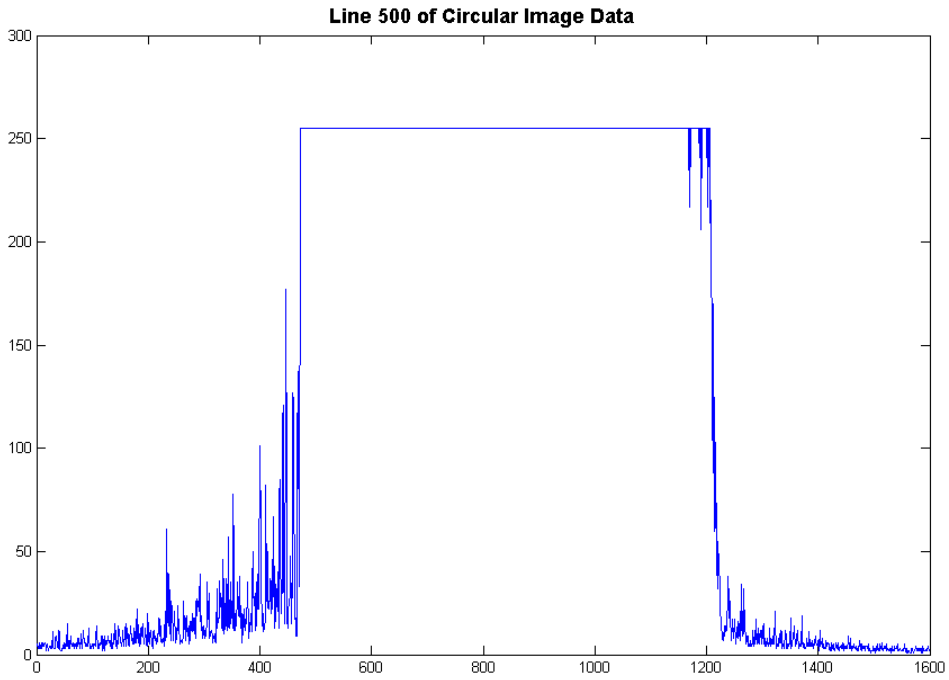

Figure 8 Intensity Profile along Line 500 of the Spot Image

The figure above shows relatively sharp edges to the saturated center where the horizontal centroid is the central point at about column 850 pixel. This centroid marks a constant value since the spot moves upward with increasing input voltage and the vertical y-axis centroid can be calculated for each voltage increment step. The edges of the beam however, are detected by first applying a fourth-order digital low-pass filter and then a second-order high-pass filter to determine the edges of the slope. The application of the digital fourth-order low-pass filter to the figure above is shown in the figure below:

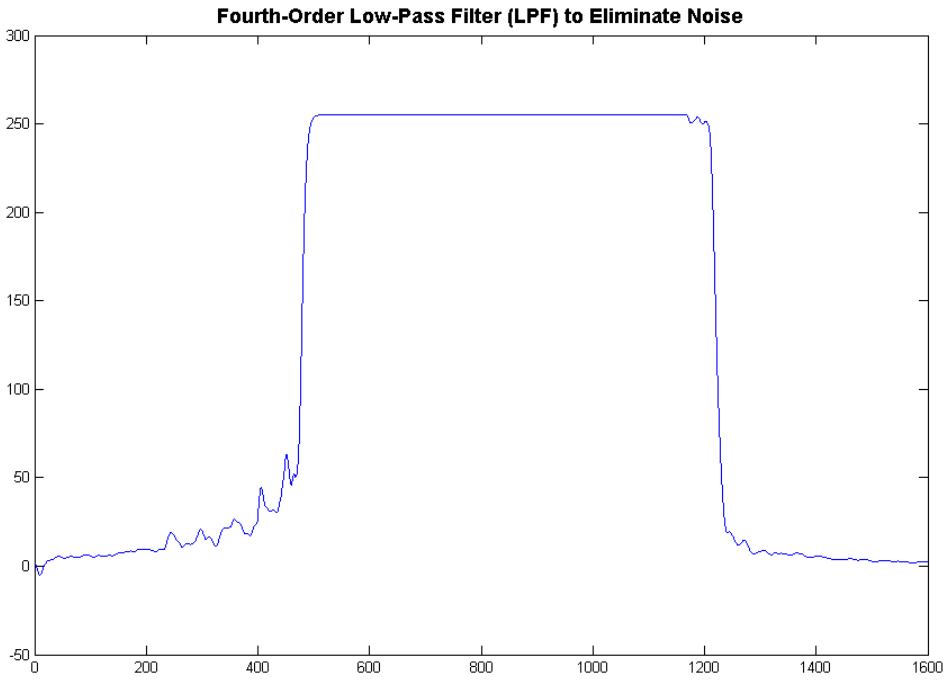

Figure 9 Fourth-Order Low-Pass Filter First-Order Accurate to Taylor Series Expansion

Applying the fourth-order low-pass filter to the focused and saturated spot image on the camera is shown in the figure below:

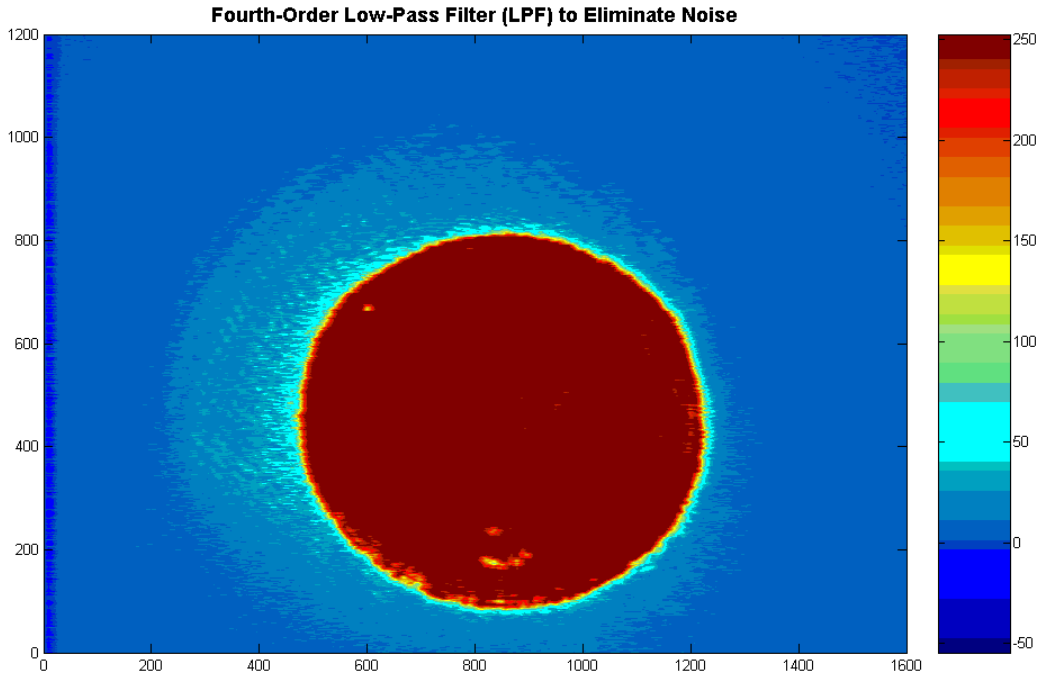

Figure 10 Low-Pass Filter Noise Reduction to Focused Laser Spot Image at Calibration Start Point

The noise is reduced as compared to figure 7 above. The final position of the laser spot for *y*-axis vertical BSM calibration is near the upper edge of the camera frame as shown in the figure below. An increase in *y*-axis input voltage therefore moves the spot upward as shown in the figure below:

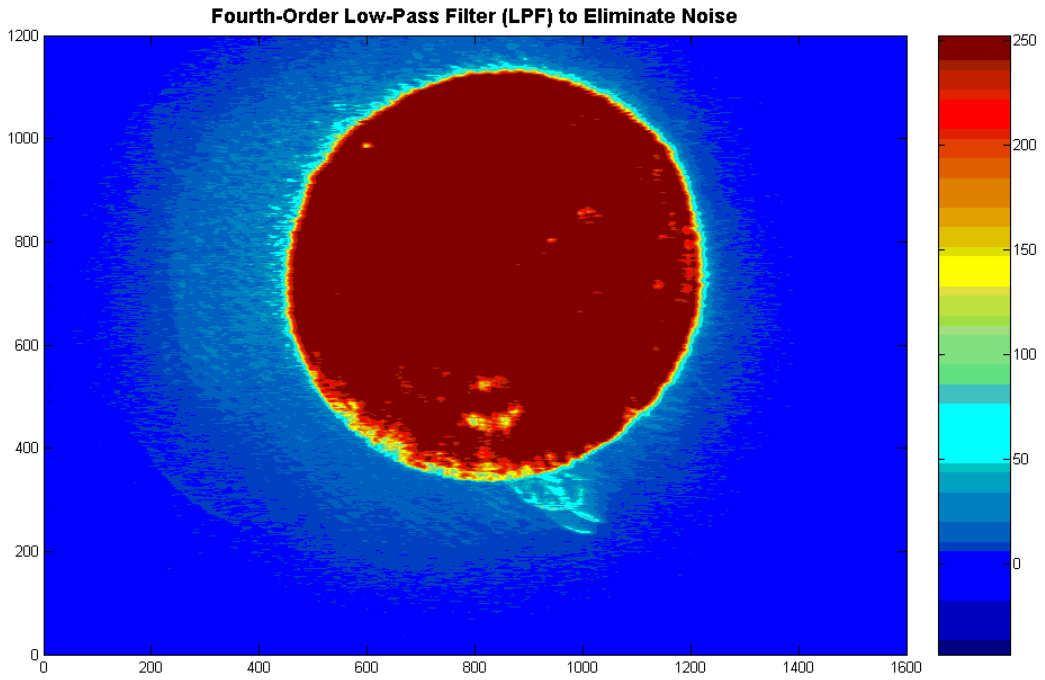

Figure 11 Low-Pass Filter Noise Reduction to Focused Laser Spot Image at Calibration End Point

Applying a digital second-order high-pass filter to detect the edge gradients in figure 9 above is shown in the figure below:

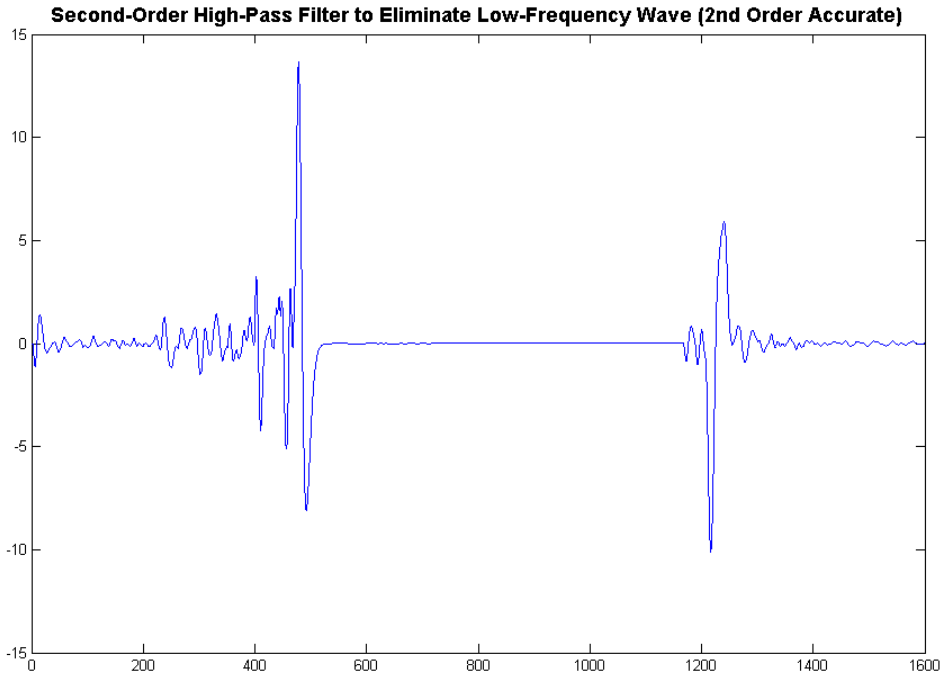

Figure 12 Second-Order High-Pass Filter Second-Order Accurate to Taylor Series Expansion

The left-hand side positive peak and the right-hand side negative peak shows the gradient edge. The central point between these two left-hand side and right-hand side edges is the centroid.

Tracking the centroid, which represents beam deflection for a change in input voltage, along the *y*-axis is shown in the figure below:

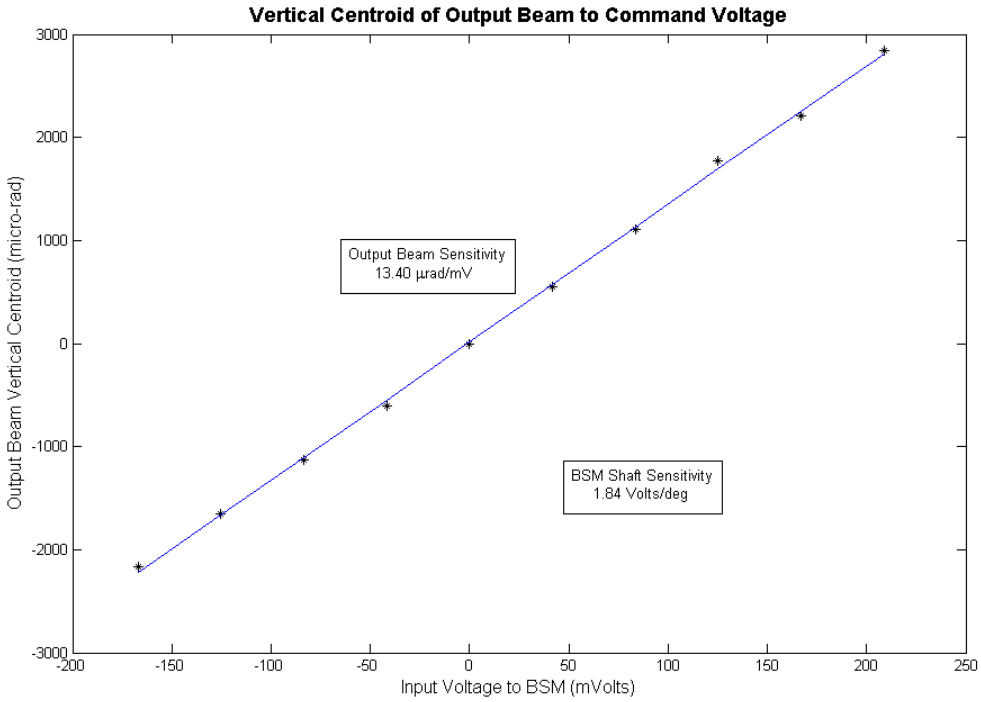

Figure 13 Sensitivity of Output Beam Angular Deflection to Input Voltage to BSM

The vertical *y*-axis output beam sensitivity is 13.40µrad/mV and this figure is converted to the sensitivity of the vertical BSM shaft of 1.84 volts/deg.

Switching from the *y*-vertical axis over to the *x*-horizontal axis the laser spot image propagates from left-to-right for an increase in input BSM voltage. The initial position of the spot on the CCD camera is shown in the figure below:

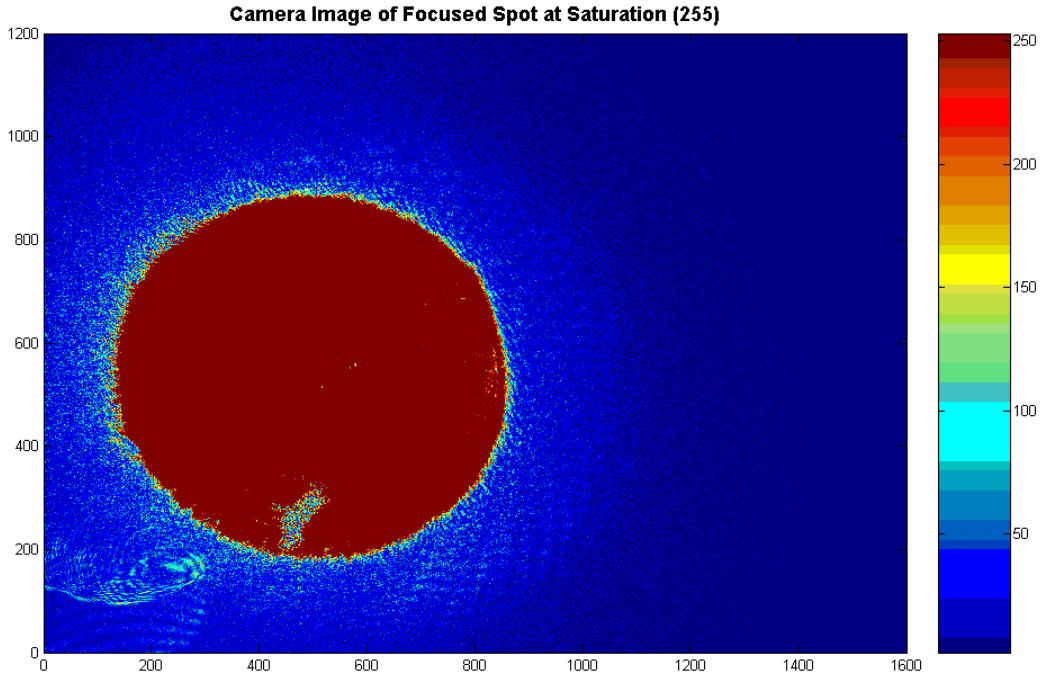

Figure 14 Horizontal *x*-axis BSM Calibration with Spot at Start Point

Applying the fourth-order high-pass filter to the figure above produces the image as shown in the figure below:

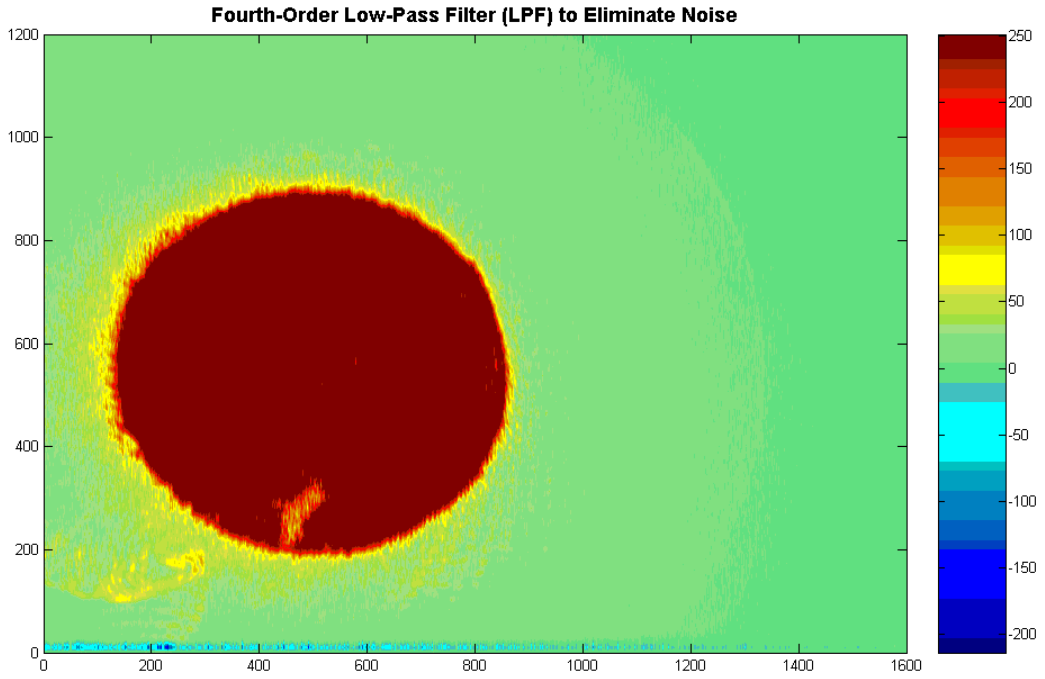

Figure 15 Low-Pass Filter Noise Reduction to Focused Laser Spot Image at Calibration Start Point

Applying the same fourth-order low-pass filter to the spot image at the right-hand side end point is shown in the figure below:

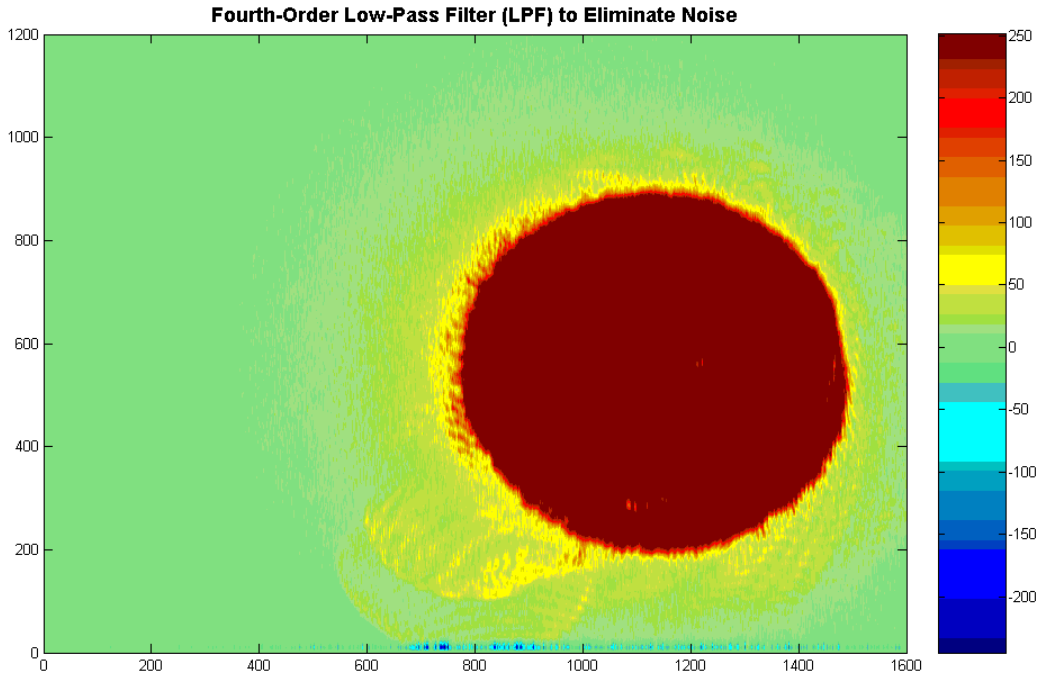

Figure 16 Low-Pass Filter Noise Reduction to Focused Laser Spot Image at Calibration End Point

An increase in *x*-axis input voltage therefore moves the spot to right-hand side.

Tracking the centroid, which represents beam deflection for a change in input voltage, along the *x*-axis is shown in the figure below:

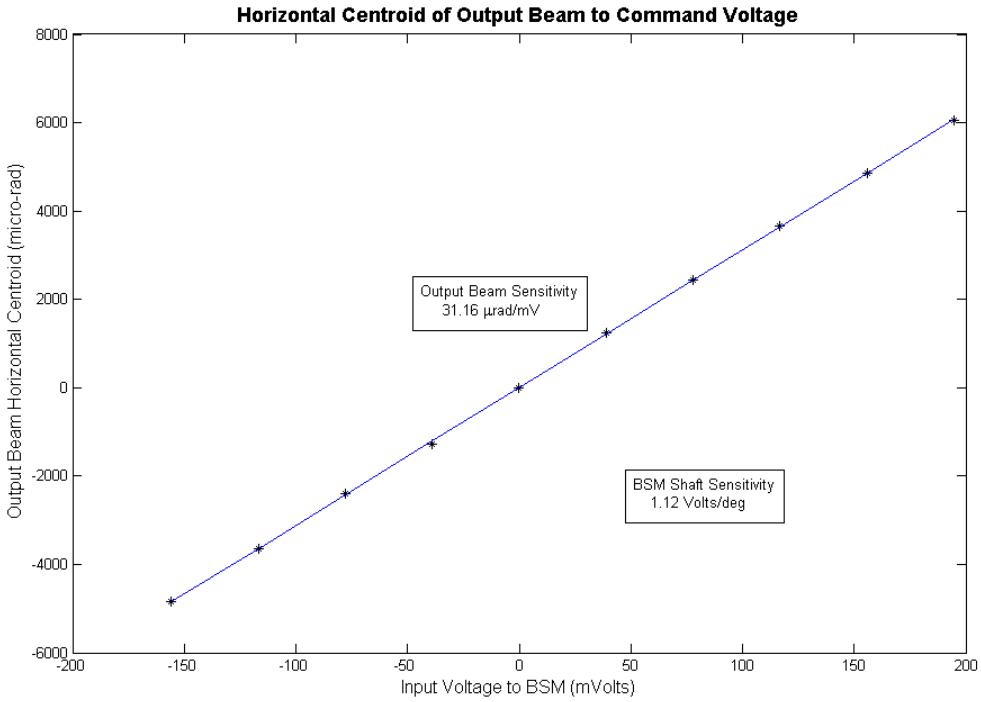

Figure 17 Sensitivity of Output Beam Angular Deflection to Input Voltage to BSM

The vertical *y*-axis output beam sensitivity is 31.16µrad/mV and this figure is converted to the sensitivity of the vertical BSM shaft of 1.12 volts/deg.

The control and image data acquisition is provided by LabVIEW. The control panel to observe the spot image and input the initial start voltages along with the voltage step-size to the BSMs is shown in the figure below:

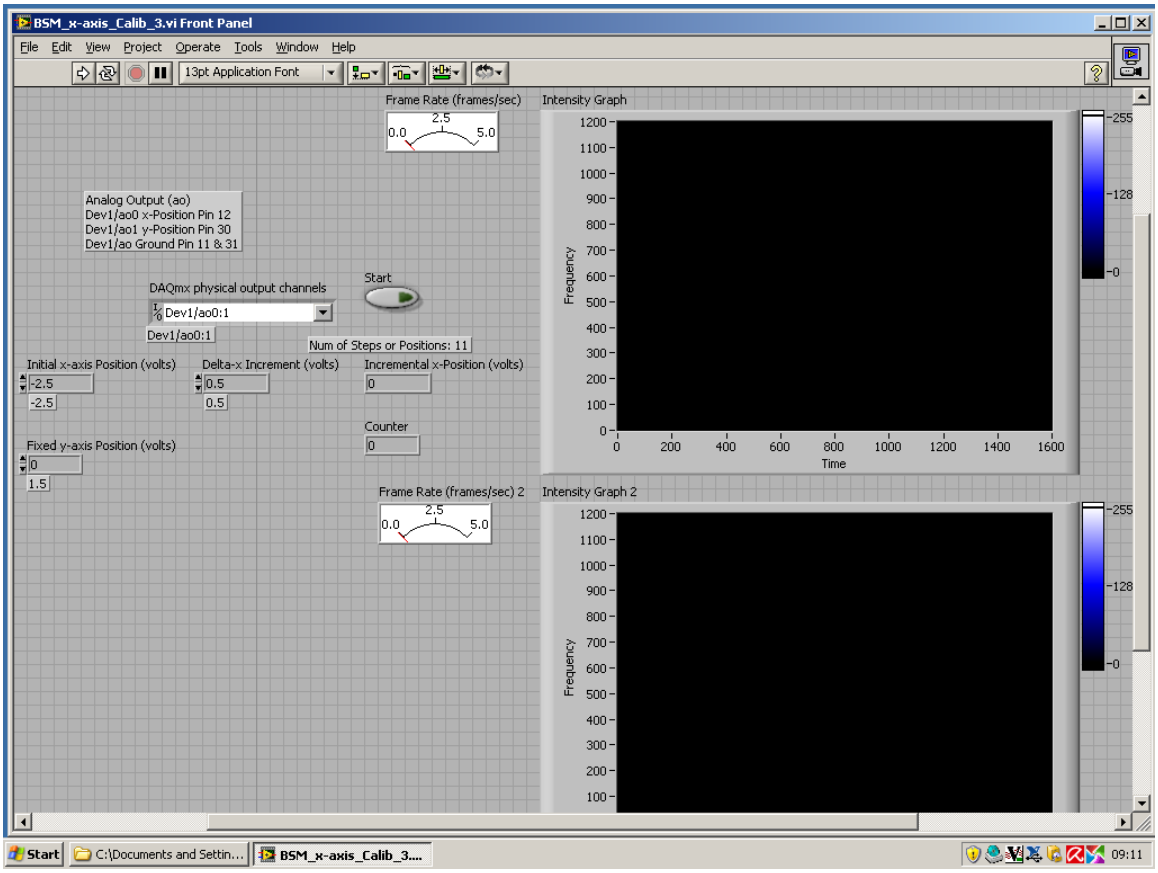

Figure 18 LabVIEW Control Panel to Monitor the Camera Images and Input Voltages to BSMs

The LabVIEW program begins with initializing the parameters to the Data Acquisition (DAQ) board PCI-6221 (37-pin) that provides two-channel analog output voltages as shown in the figure below. Edges of the LabVIEW flat sequence structures and iterative loops are truncated in these screen shot images because reducing the size of the image for screen display was not possible.

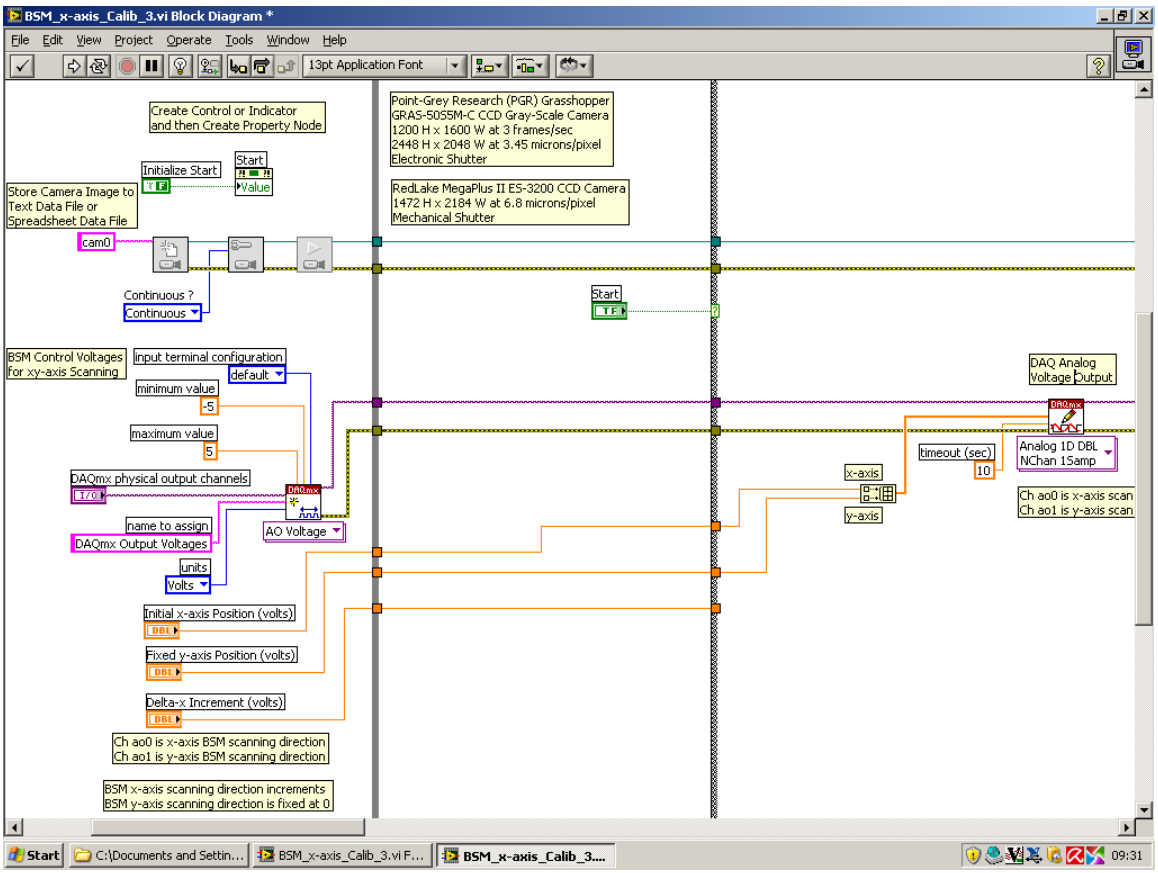

Figure 19 DAQ Configuration Parameters and Output within Loop Structure

The LabVIEW block diagram program continues with camera frame grabbing functions following the configuration for the Point-Grey Research (PGR) camera at 1200 x 1600 frame resolution as shown in the figure below:

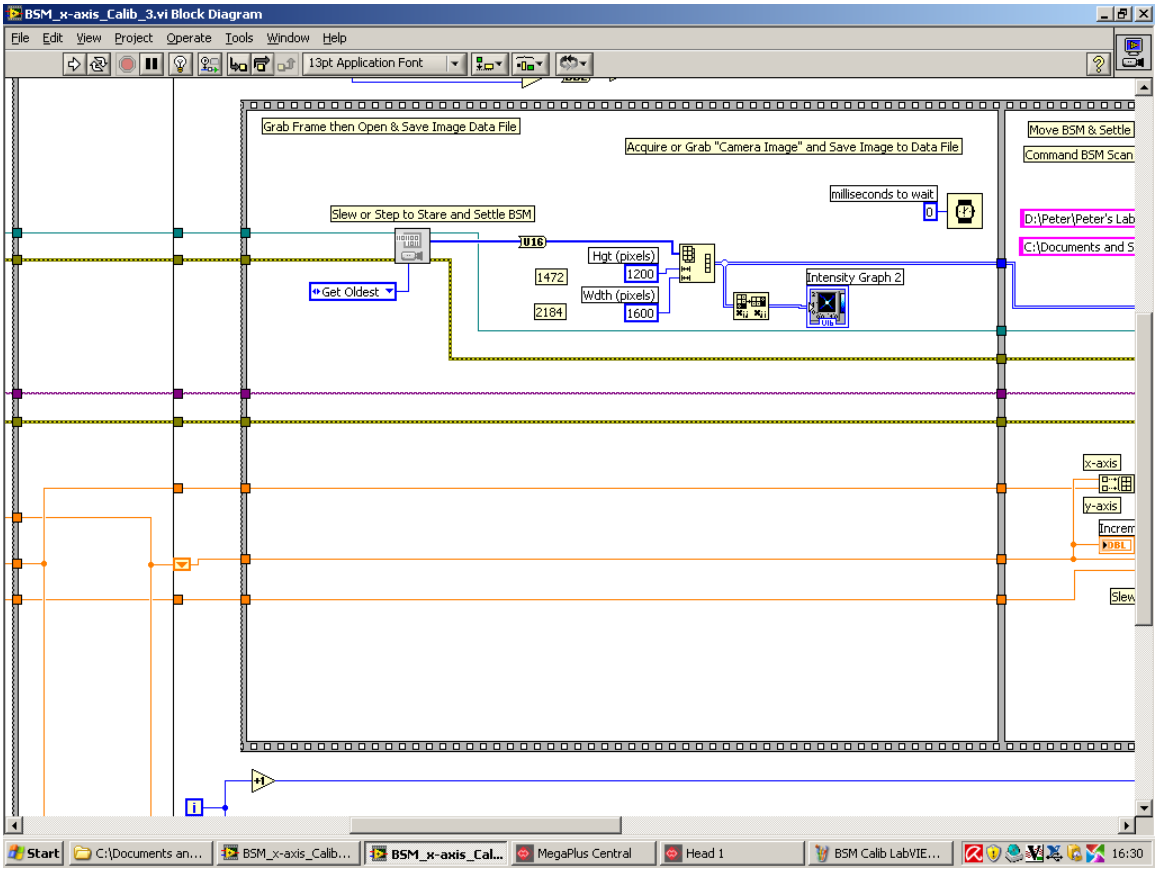

Figure 20 Grabbing Image Data for Display and Sending to File Storage

The step-stare approach to image acquisition is updated and the image files stored to a directory and file as shown in the figure below. In addition, the BSMs are returned to the initial start position at end of scanning when collection of image data is complete.

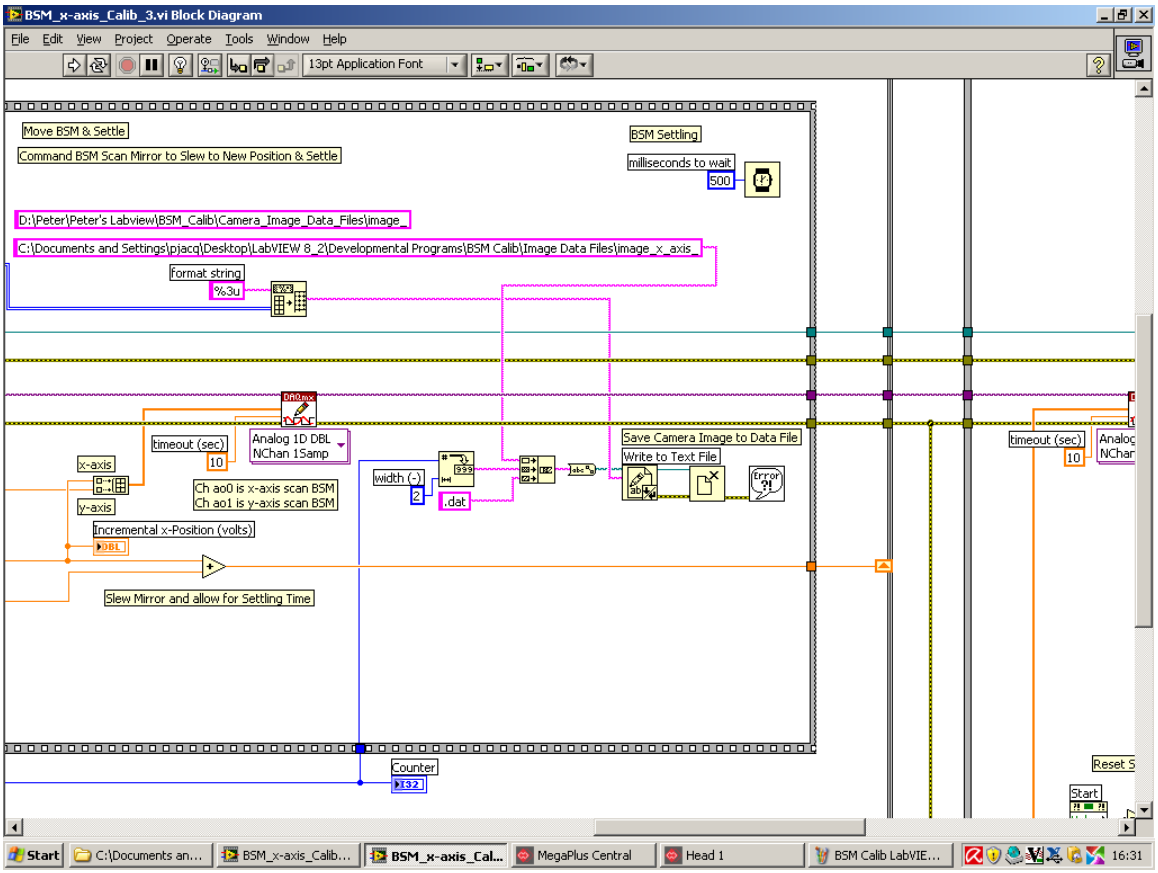

Figure 21 Saving Image Data to a File Number that is Sequenced by a Counter

Closing open devices ends the LabVIEW program as shown in the figure below:

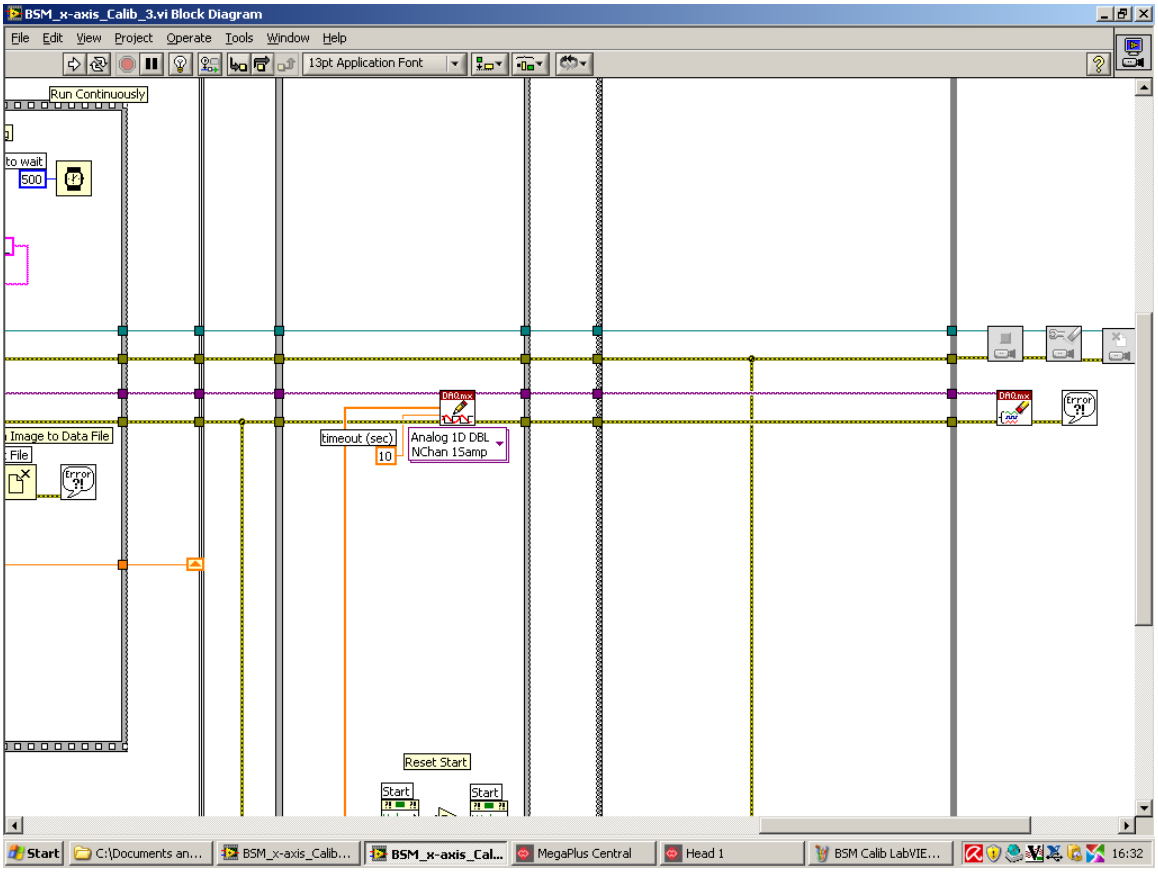

Figure 22 Closing LabVIEW Functions

The vertical *y*-axis and horizontal *x*-axis output beam sensitivity provides an accurate method to scan the focused probe beam within the fluid-cell. The fluid-cell specimen is placed at the focal point of the telecentric lens where an angular change of the incident beam translates the focal point. The output beam deflection of the BSMs is the incident beam to the telecentric lens, which is modeled using Zemax. The optical layout of the telecentric lens given an assumed input Fresnel biprism of 130° is shown in the figure below:

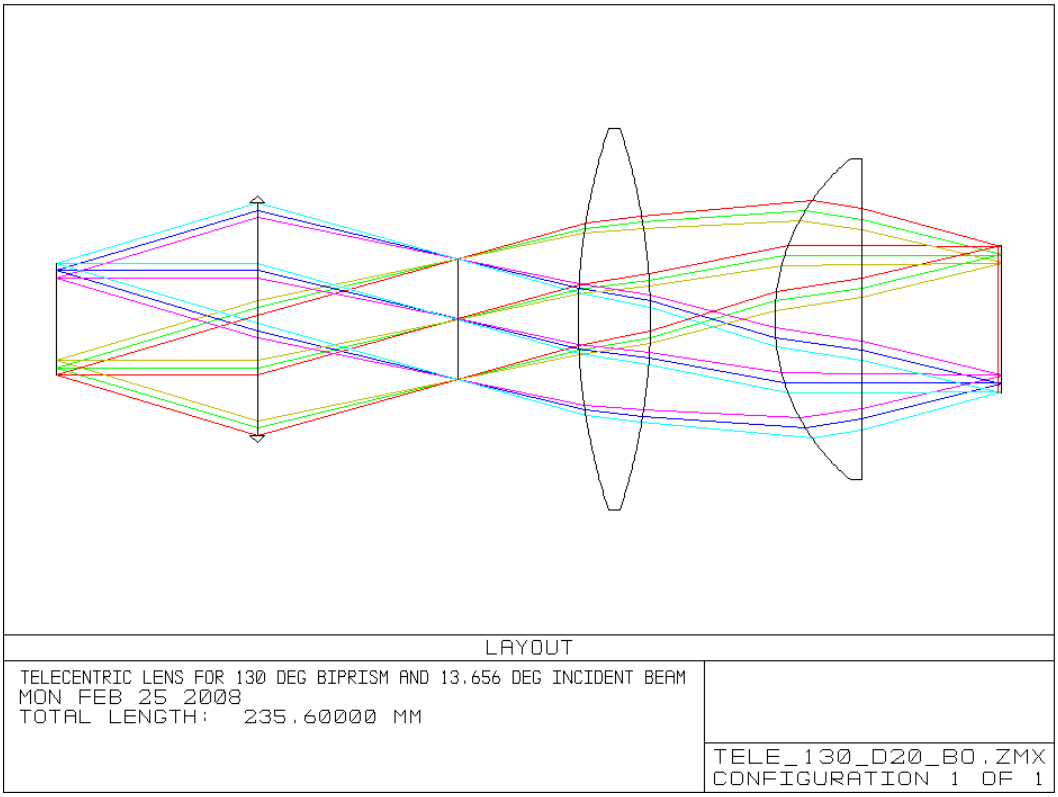

Figure 23 Telecentric Lens with Focused Object Probe Beam and Reference Beam

The focused probe beam scans the specimen where the BSMs provide an angular deflection of ±2° as an input to the telecentric lens. This scan angle displaces the beam ±2.18mm at the focal point, which is sufficient excursion to scan the entire region of the fluid-cell specimen given a cross-sectional internal dimension of 5x5mm. The f/number of the beam probing the fluid-cell specimen is an f/2.1 cone beam that is a close value to the desired f/2 for refractive index reconstruction. The scan sensitivity displacement at the focal point is therefore 2.18/2=1.09mm/deg.

Table Vibrations

Two accelerometers were used to measure floor vibrations as well as the vibrations on the optical table. The optical table is a Newport Research RS4000-48-12 that is 8'L x 4'W x 12"Thk and weighs approximately 1,000 lbs. The support legs are Newport Research I-2000 pneumatic vibration isolators with automatic level control. Laminar flow isolator devices within the legs provide vibration damping. Measurements using the Vibra-Metrics model 1030 accelerometers show the attenuation of vibrations from floor to table to be approximately x10 reduction.

The two accelerometers are connected to two of analog signal amplifiers which interface with a Data Acquisition (DAQ) module. The DAQ converts the analog signal to a digital signal and stores the data in a file as ASCII text data. Matlab programs read the data file and then signal-processing algorithms are applied to the data. A simple configuration diagram is shown in the figure below:

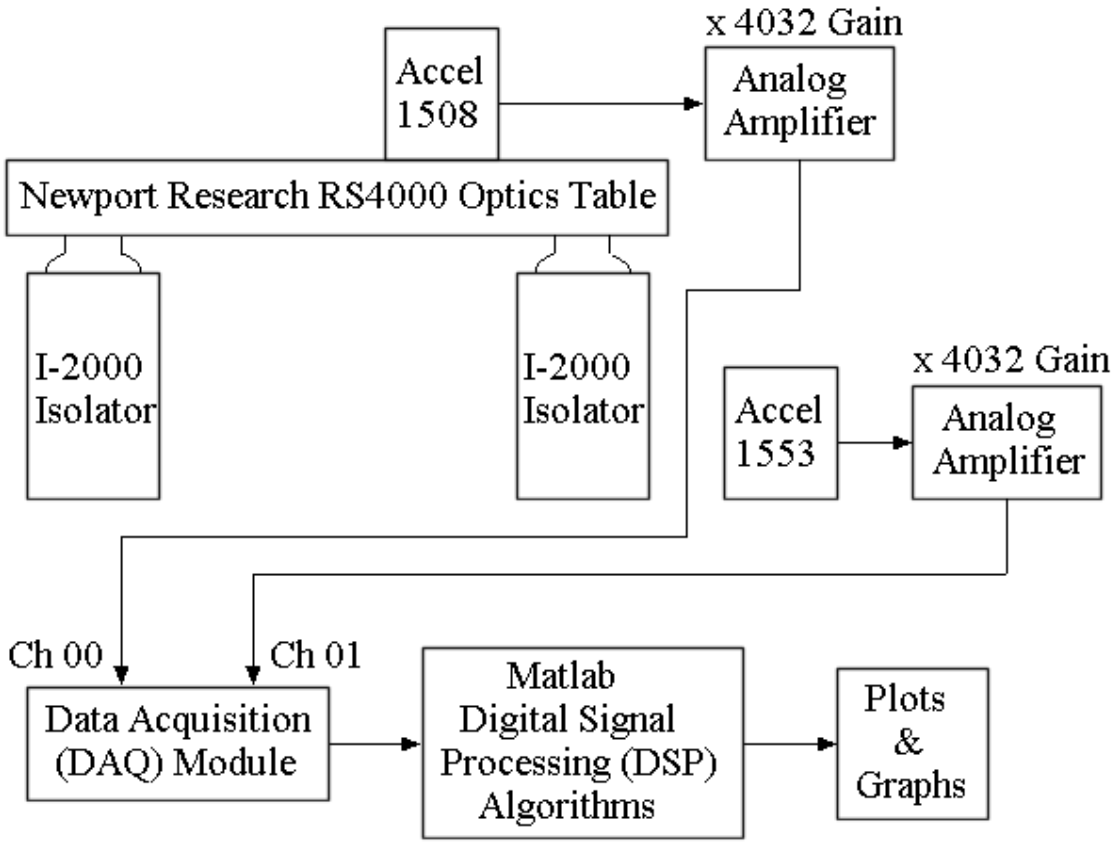

Figure 1 Accelerometer Configuration Diagram

Figure 1 shows accelerometer unit 1508 on the table and unit 1553 on the floor.

The experimental procedure is in three steps:
1) No accelerometer with input terminated by a 130 KΩ resistor to measure the electronics noise without the sensor.
2) Both accelerometers on floor to compare relative sensitivity.
3) Accelerometer 1508 on table and 1553 on floor to assess the vibration suppression afforded by the pneumatic isolators.

Finally, the floor vibrations of the Engineering Lab Wing (ELW-A136) laboratory for the Confocal Scanning Laser Holography (CSLH) microscope were compared to the floor vibrations of a basement laboratory in the Cunningham building. The configurations for data collection are:
1) Amplifier electronic noise with no accelerometers
2) Accelerometer 1508 on floor and 1553 on floor to compare sensitivity
3) Accelerometer 1508 on table and 1553 on floor under steady-state isolation
4) Accelerometer 1508 on table and 1553 on floor with a stomp to the floor

The specifications on the equipment are as follows:

Vibra-Metrics Model 1030 Accelerometer:

Unit 1508 Sensitivity: 7.000 mV/mG
Unit 1553 Sensitivity: 6.778 mV/mG
Noise: 1.0 μG rms at 0.1-180 Hz
Bandwidth: BW=200 Hz
Source Resistance: 620 Ω Output Impedance

Analog Amplifier:
The analog amplifier is a high voltage gain cascaded amplifier as shown in the figure below:

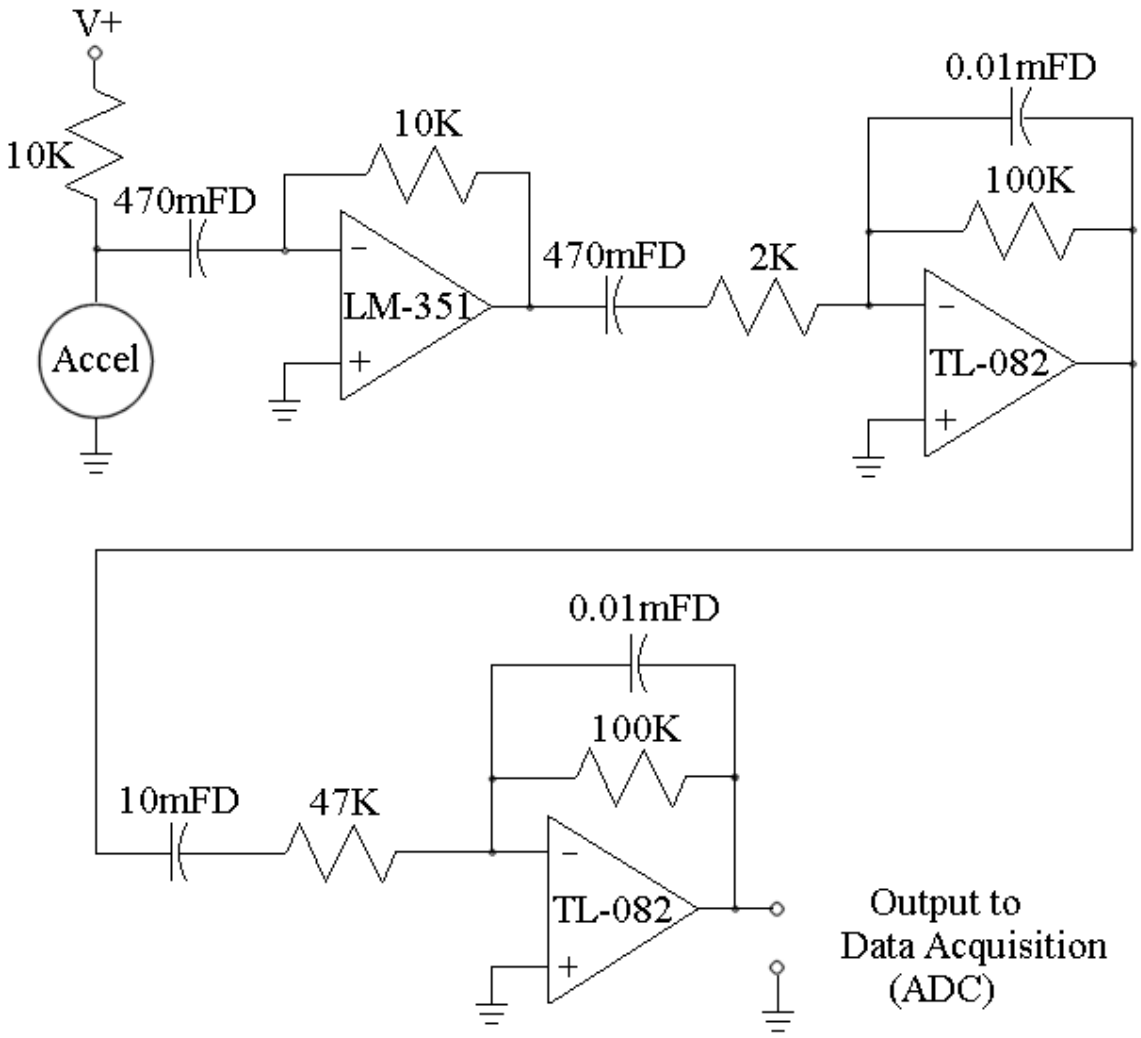

Figure 2 Cascade Sensor Amplifier Interface with Data Acquisition (DAQ) Module

The operational amplifiers are Direct Current (DC) coupled with large value capacitors to provide very low frequency response that is compatible with the response bandwidth or range of the accelerometer. The capacitors across the feedback resistors limit the high frequency response so that aliasing error when sampling the data will be minimized. The power to the operational amplifiers and the accelerometer bias resistor is by 9 Volt batteries so that there is no power supply ripple voltage when using a regulated power supply whose source is 120V through an isolation transformer. Two 9 Volt batteries provide the split rail voltage of ±9 Volts. The circuit above is duplicated so that there is an amplifier for each accelerometer with isolated power supplies and grounds. The input is amplified by x4032 and this output goes to the Data Acquisition (DAQ) module for Analog-to-Digital Conversion (ADC).

Amplifier Voltage Gain: $A_v = \frac{V_{output}}{V_{input}}$

$$A_v = A_{v_1} \cdot A_{v_2} \cdot A_{v_3} = \frac{10K\Omega}{620\Omega} \cdot \frac{100K\Omega}{2K\Omega} \cdot \frac{100K\Omega}{20K\Omega} = 16.13 \times 50 \times 5 = 4032$$

High-Pass Cut-Off Frequency: 0.3 Hz

Low-Pass Cut-Off Frequency: 170 Hz

Bandpass Frequency Range: 0.3-170 Hz

Input Amplifier LF-351 Noise: $e_{noise} = 25nV/\sqrt{Hz}$

Input Noise: $e_n = e_{noise} \times \sqrt{BW} = 25 \times \sqrt{200} = 353nV = 0.353\mu V$

Converting from Voltage (Volts) to Acceleration (G)

Noise: $\frac{0.353\mu V}{7.00 mV/mG} \times \frac{1000\mu G/mG}{1000\mu V/mV} = 0.0504\mu G$ rms

Data Translation DT9802 Data Acquisition (DAQ) Module:

±10 Volt Range at 12-bit Resolution

11-bit Range with 1-bit for sign

Set to 1 KHz Sample Rate and 4 sec Data Collection

Channel 00 to Accelerometer 1508

Channel 01 to Accelerometer 1553

Least Significant Bit (LSB) Resolution: $LSB = \frac{10V}{2^{11}} = \frac{10V}{2048} = 0.00488\,V$

Convert from Voltage (Volts) to Acceleration (G)

$$LSB\ Resolution = 0.00488\,V \times \frac{1}{4032} \times \frac{1000\mu G/mG}{0.0070\,V/mG} = 0.173\,\mu G$$

Therefore;

Amplifier Electronic Noise < LSB Resolution < Accelerometer Noise

0.050 µG < 0.173 µG < 1.0 µG

Measuring electronic noise with no accelerometers and the input terminated with a 130 KΩ Resistor shows no output where the output is less than the LSB resolution of the DAQ Analog-to-Digital Conversion (ADC). This confirms the calculated estimate above.

The Digital Signal Processing (DSP) processing algorithm windows the data and applies a digital Low-Pass Filter (LPF) of second-order. A Fourier Transform is then applied to determine the Power Spectrum of the signal and the dominant frequencies. By utilizing a digital LPF the aliasing error due to sampling of the data is minimized and the discrete sampling and digitizing process will not corrupt the measured signal. The DSP functions are shown in the figure below:

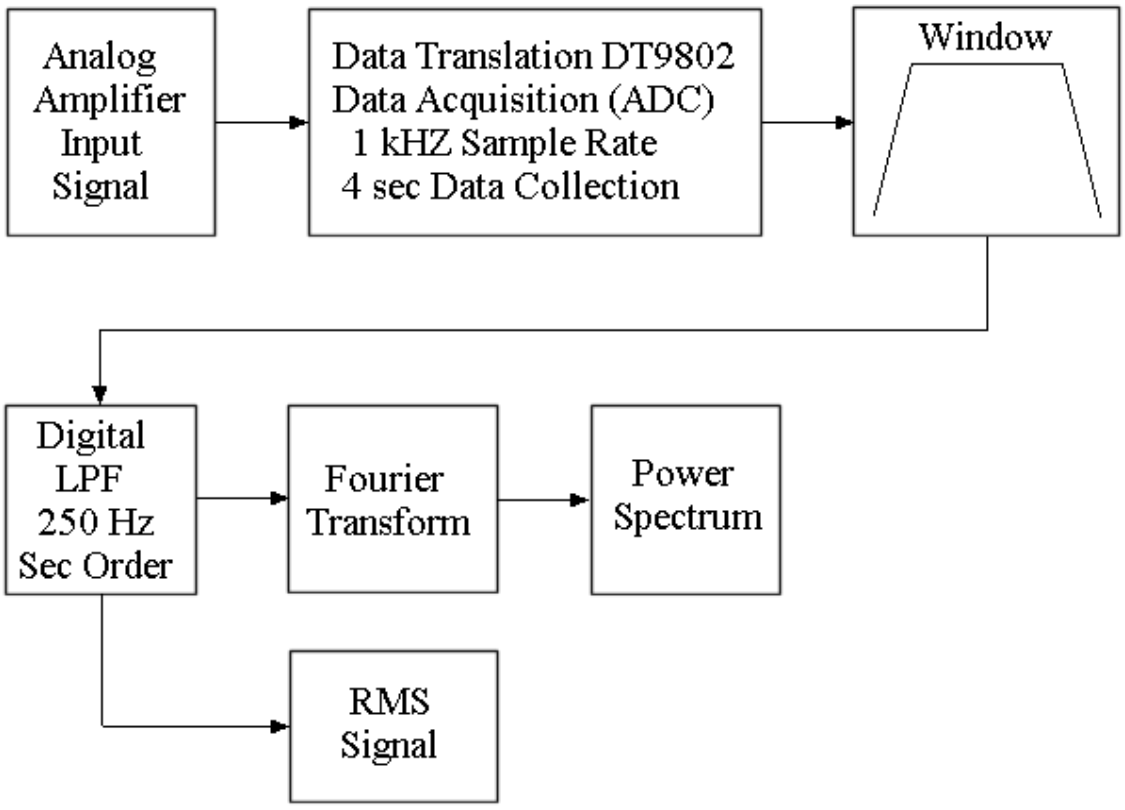

Figure 3 Digital Signal Processing (DSP) Flow Diagram

The ASCII data files produced by the DAQ are imported into Matlab for digital signal processing. All the algorithms are tested and verified with simple harmonic signals to verify the code. A user specified window slope reduces Fourier transform anomalies with respect to the data stream transient. The user can specify the LPF cut-off frequency - 250 Hz was found to be optimum. The 250 Hz LPF cut-off frequency is one-fourth the sampling rate or one-half the Nyquist frequency. The application of a digital LPF introduces a phase–shift at the LPF cut-off frequency. For a second-order filter this phase-shift is –90˚ or a 90˚ phase-lag at the cut-off frequency. Analyzing a simple

harmonic waveform shows the transient response to introduce a low frequency wave as the LPF settles to steady-state response in about one and a half cycles of the cut-off frequency. This low frequency wave is a concern over a few cycles, but becomes negligible over the many cycles that are sampled. The second-order digital LPF is applied to a 100 Hz sinusoid signal that is sampled 16x per cycle. The response to this filter is shown in the figure below:

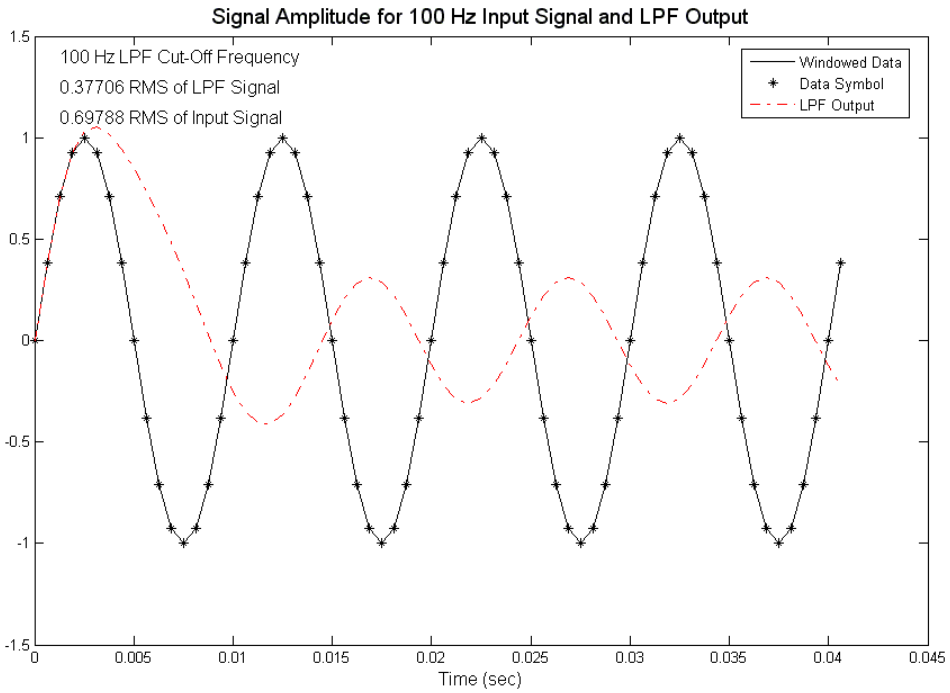

Figure 4 LPF Response to a Single Frequency Waveform

The LPF cut-off frequency is set to 100 Hz and the damping factor to 0.707. The phase-lag in the response occurs over the first one and a half cycles of the cut-off frequency, producing a low frequency error. The result of this low frequency artifact can be seen in the power spectrum of the signal.

The power spectrum for the harmonic input signal and the LPF output signal can be seen in the figure below:

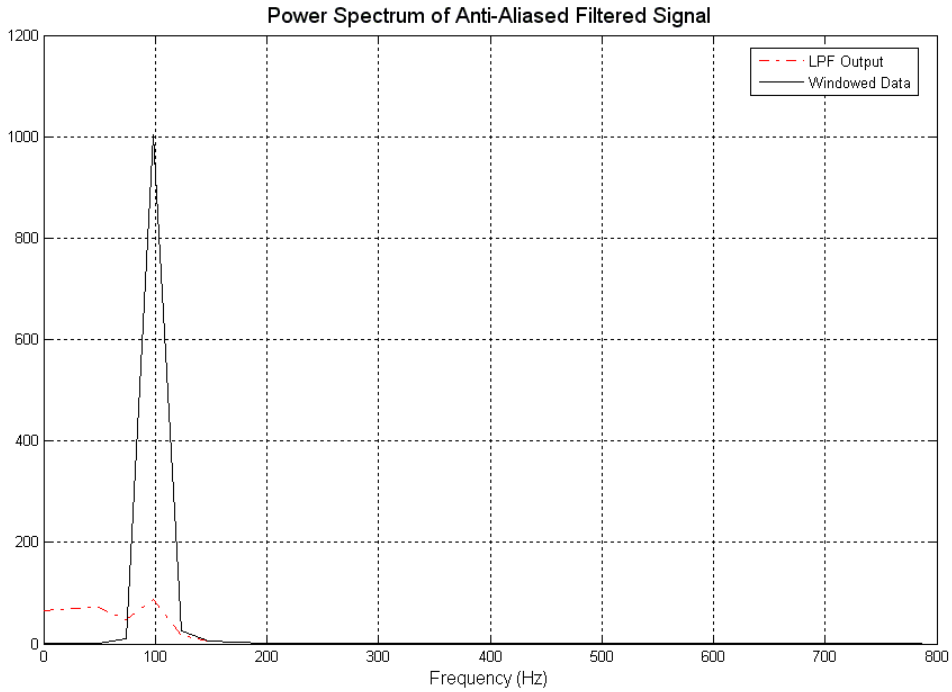

Figure 5 Power Spectrum for 16x Sampled Harmonic Waveform and the LPF Output Signal

The power spectrum shows the low frequency error where the means to eliminate this error is to truncate the transient response data of the LPF. Over many cycles of the waveform the transient response of the LPF can become negligible, which is the case for the 250 Hz LPF cut-off frequency and the 4 sec duration to collect data. The number of cycles at 250 Hz within a 4 sec duration is 4x250=1000 cycles or waves.

The two accelerometers are placed on the floor to compare the relative sensitivity since data is collected simultaneously on two channels then the floor vibrations to each accelerometer is assumed the same. The Matlab program converts the sampled data voltage acceleration and then a window is applied with constant slope edges.

The windowed data and the LPF output data for accelerometer 1508 is shown in the figure below:

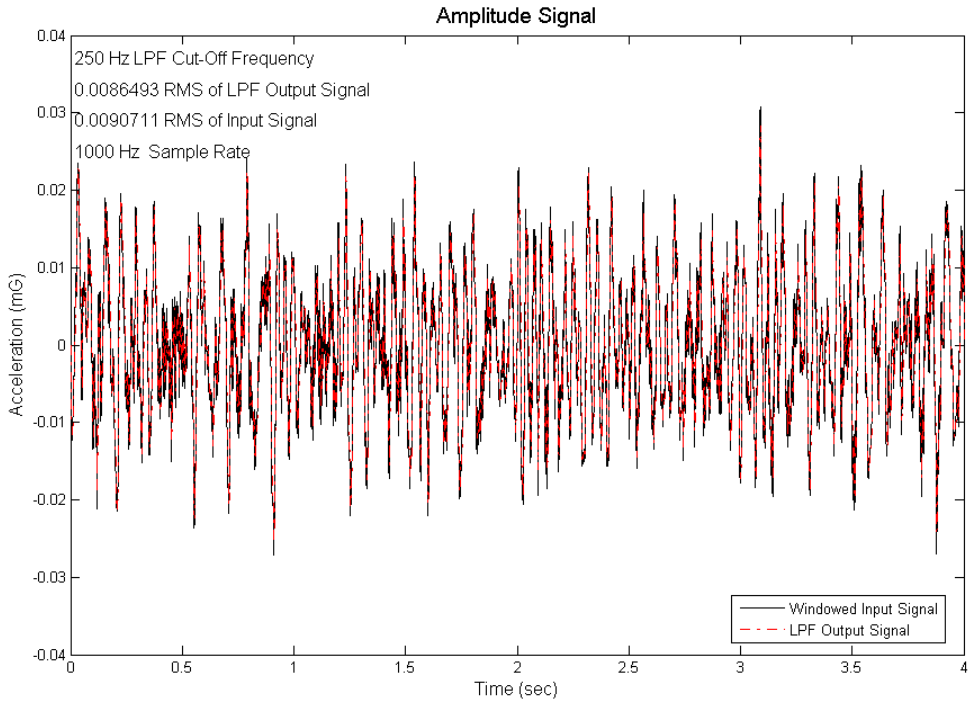

Figure 6 Unfiltered and Filtered Accelerometer 1508 Signal on Floor

The LPF Output Signal is 0.0086493 mG RMS.

The windowed data and the LPF output data for accelerometer 1553 is shown in the figure below:

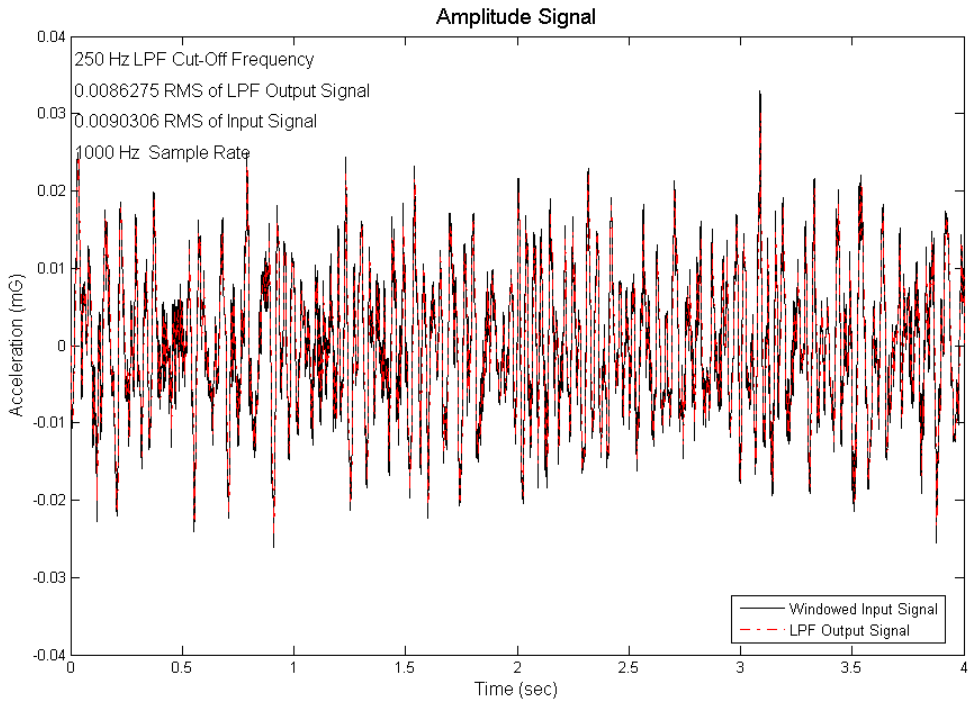

Figure 7 Unfiltered and Filtered Accelerometer 1553 Signal on Floor

The LPF Output Signal is 0.0086275 mG RMS.

The difference error of the two output signals is $100 \times \frac{0.0086493 - 0.0086275}{0.0086493} = 0.25\%$ which is negligible so the sensitivity of the two accelerometers is considered to be the same.

Accelerometer 1508 is moved to the table to measure the amount of vibration isolation in comparison to the accelerometer 1553 on the floor.

Accelerometer 1553 voltage data from the DAQ is converted to acceleration shown in the figure below:

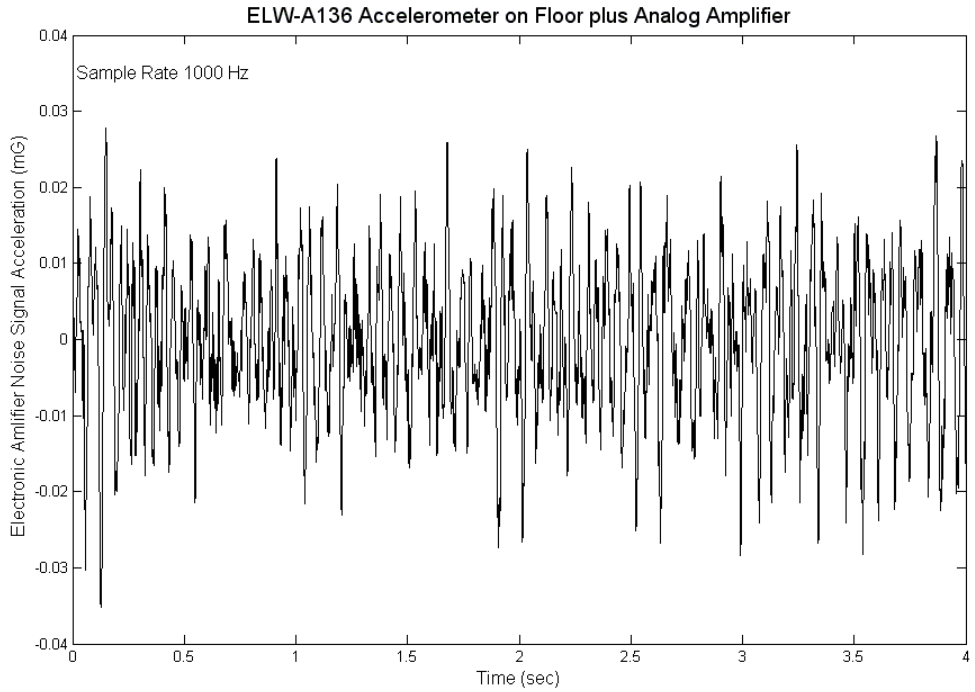

Figure 8 Accelerometer 1553 on Floor Signal from DAQ

The windowed data and the LPF output data for accelerometer 1553 is shown in the figure below:

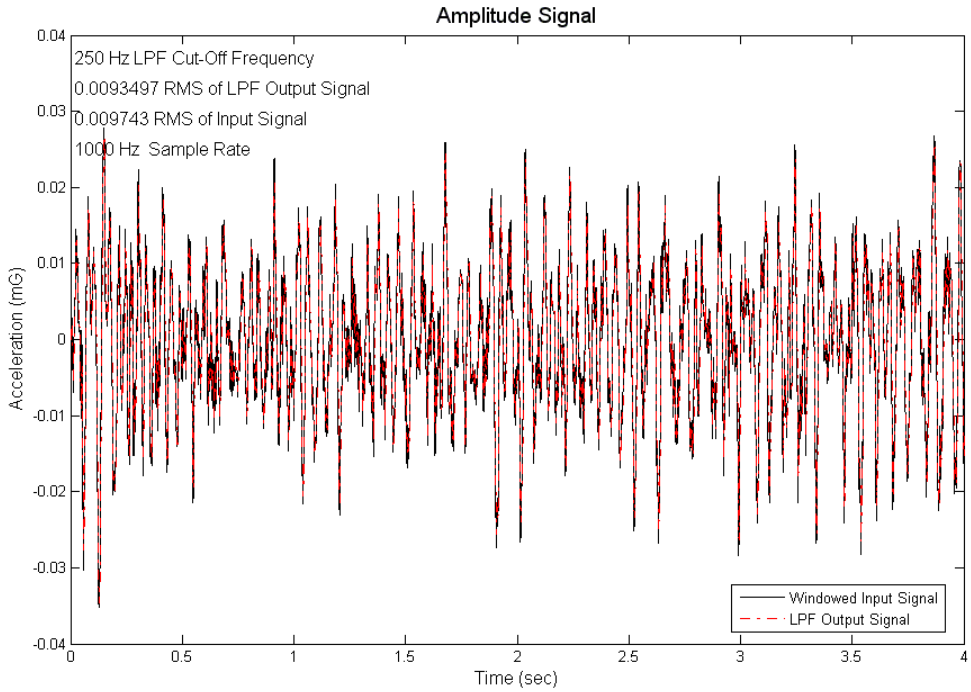

Figure 9 Accelerometer 1553 Windowed Data and LPF Output Data

The LPF Output Signal is 0.0093497 mG RMS for accelerometer 1553. The power spectrum for accelerometer 1553 is shown in the figure below:

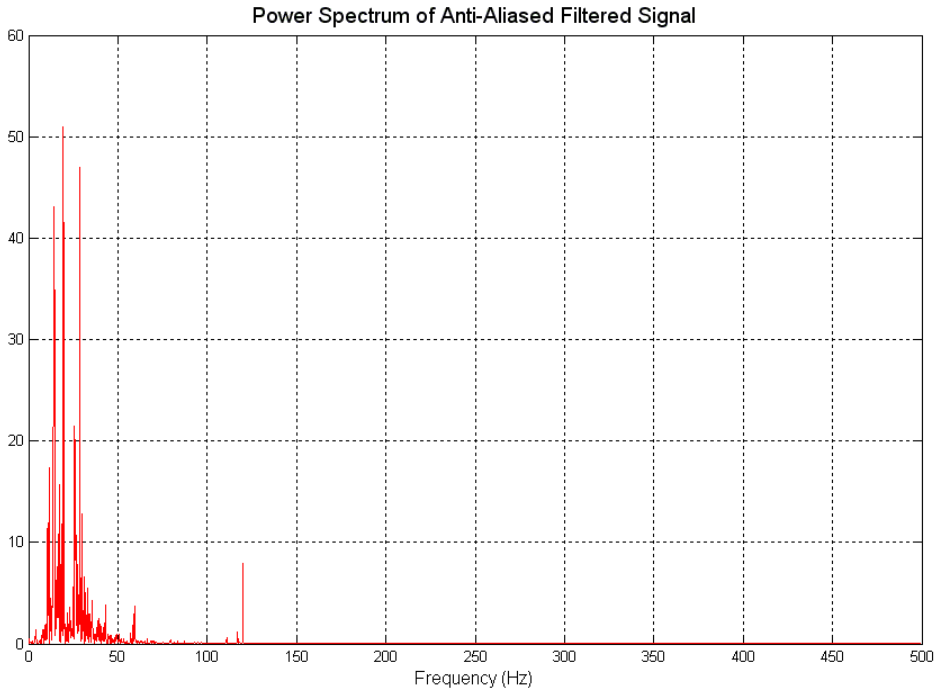

Figure 10 Power Spectrum for Accelerometer 1553 LPF Output

The dominant frequencies for the floor are: 15, 20, 30 Hz.

Accelerometer 1508 voltage data from the DAQ is converted to acceleration shown in the figure below:

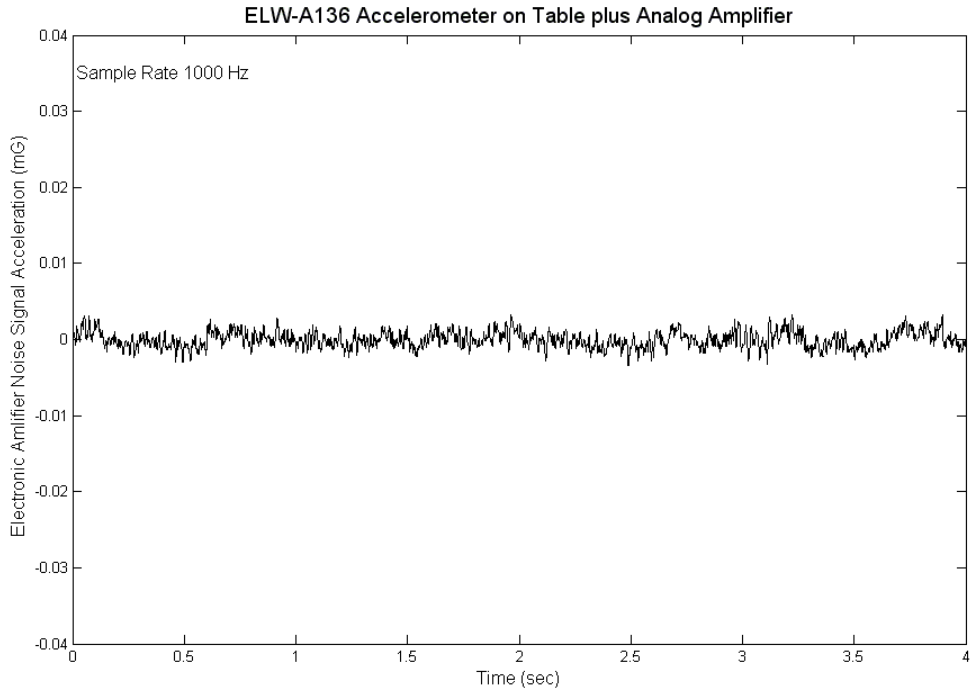

Figure 11 Accelerometer 1508 on Table Signal from DAQ

The windowed data and the LPF output data for accelerometer 1508 is shown in the figure below:

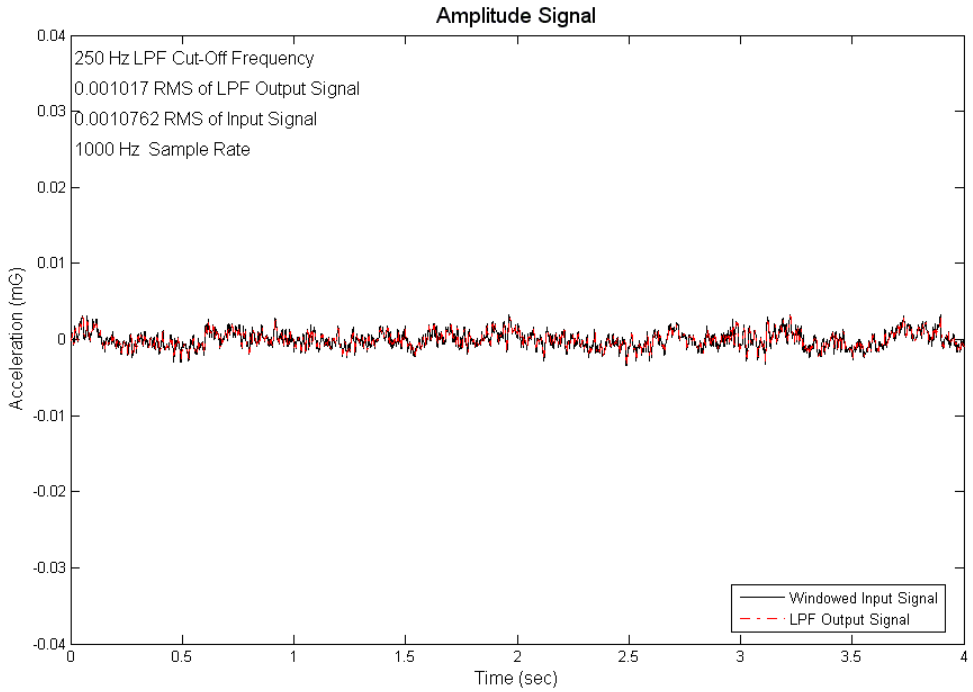

Figure 12 Accelerometer 1508 Windowed Data and LPF Output Data

The LPF Output Signal is 0.001017 mG RMS for accelerometer 1508. The signal attenuation for steady-state vibration isolation system is $\frac{1}{\frac{0.0093497\ \text{mG}}{0.001017\ \text{mG}}} = \times \frac{1}{9.2}$

Accelerometer 1508 on the table LPF output signal is 0.001017 mG RMS = 1.0 µG This is equivalent to the accelerometer noise level in the specification.

The power spectrum for accelerometer 1508 is shown in the figure below:

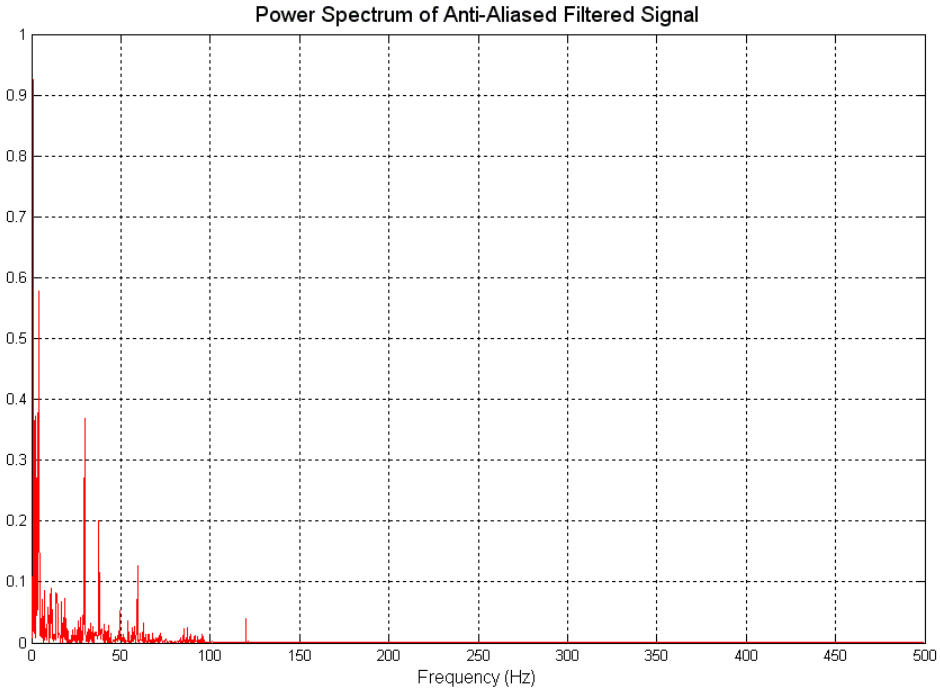

Figure 13 Power Spectrum for Accelerometer 1508 LPF Output

The dominant frequencies for the isolated vibrations on the table are: 5, 30, 40 Hz

The mass inertia of the table and compliant isolation system has shifted the energy spectrum to lower frequencies. A low frequency of 5 Hz will tend to be more of a rigid body floating excitation than a flexure resonance mode. The next step is to repeat the same measurement and include a stomp to the floor to determine the amount of isolation to an impulse.

Accelerometer 1553 voltage data from the DAQ is converted to acceleration shown in the figure below:

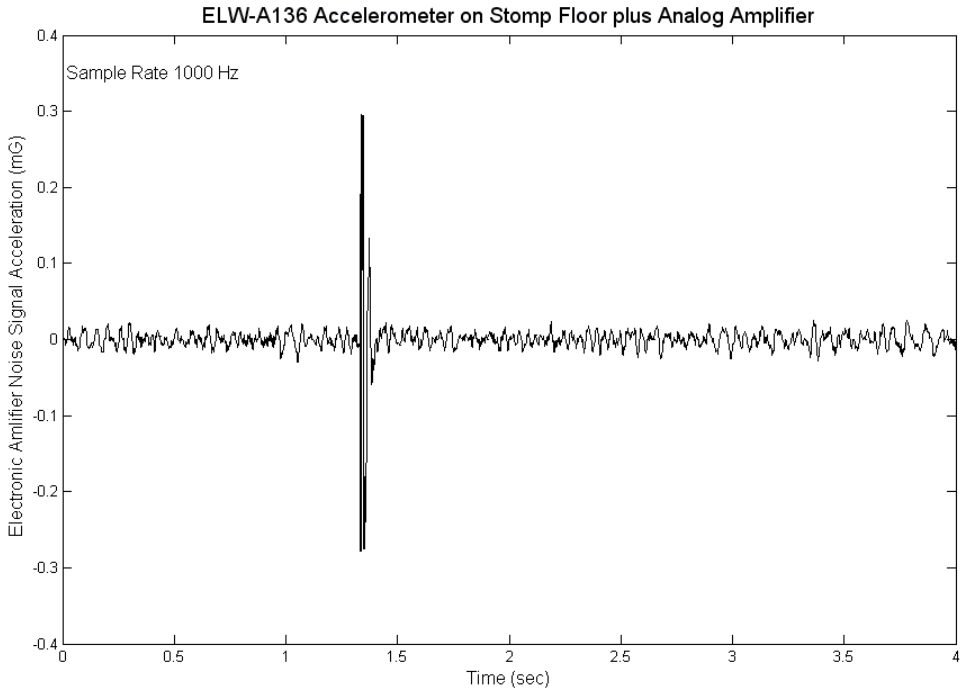

Figure 14 Accelerometer 1553 on Floor Signal from DAQ

The windowed data and the LPF output data for accelerometer 1553 is shown in the figure below:

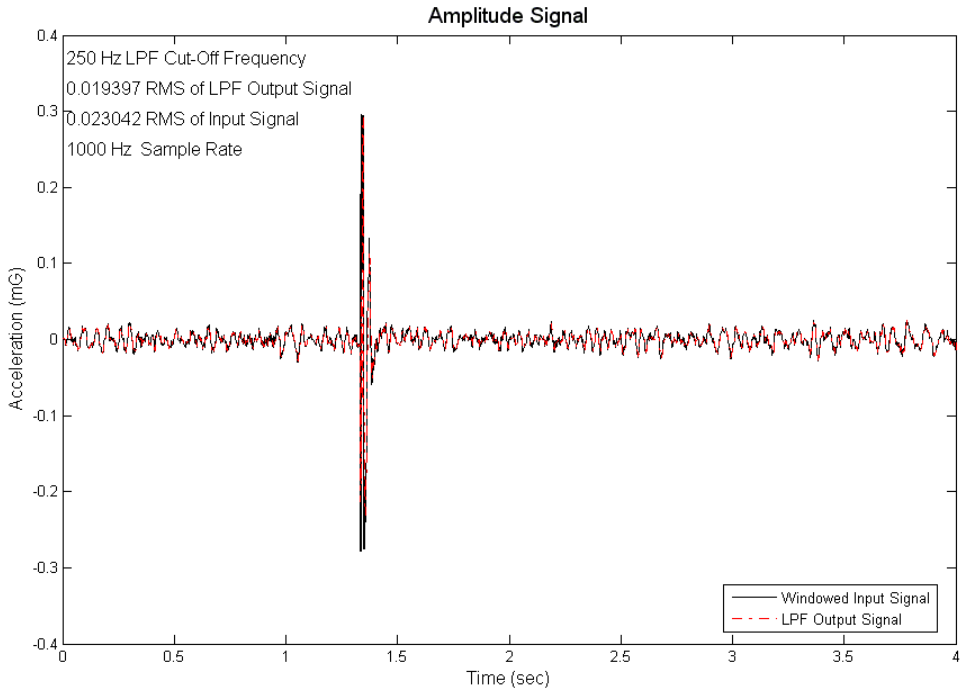

Figure 15 Accelerometer 1553 Windowed Data and LPF Output Data

The LPF Output Signal is 0.019397 mG RMS for accelerometer 1553. The peak signal output is 0.296 mG for accelerometer 1553.

The power spectrum for accelerometer 1553 is shown in the figure below:

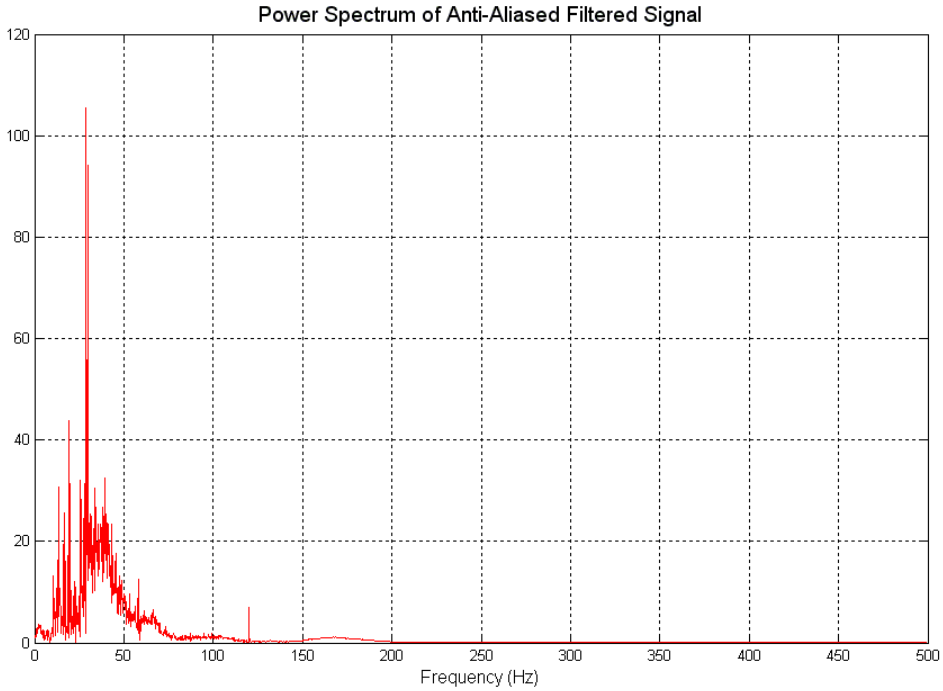

Figure 16 Power Spectrum for Accelerometer 1553 LPF Output

The dominant frequencies for the floor are: 10, 20, 30, 40 Hz.

Accelerometer 1508 voltage data from the DAQ is converted to acceleration shown in the figure below:

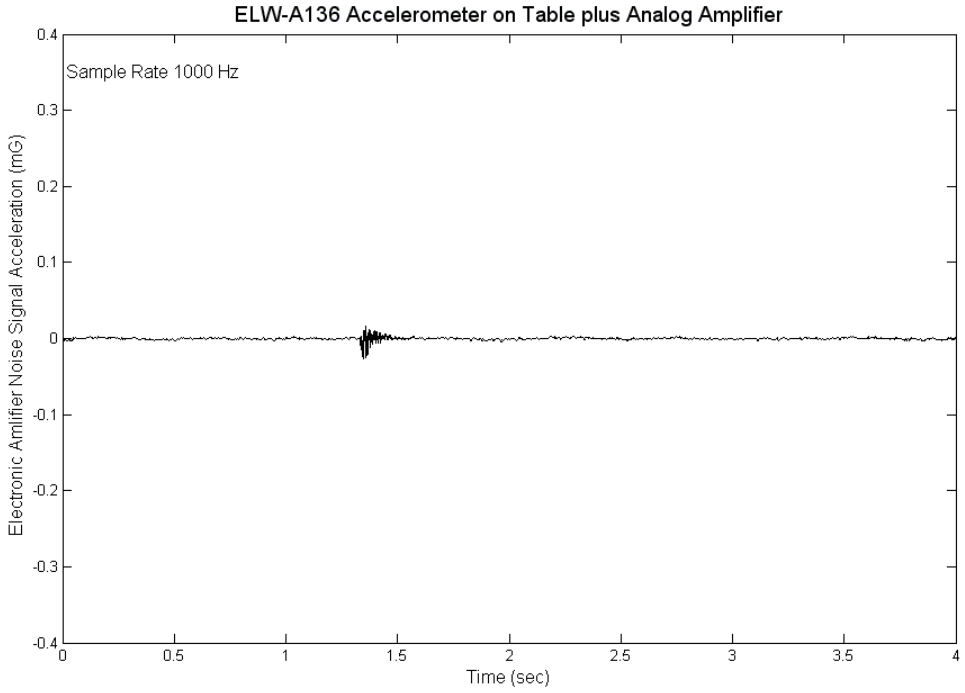

Figure 17 Accelerometer 1508 on Table Signal from DAQ

The windowed data and the LPF output data for accelerometer 1508 is shown in the figure below:

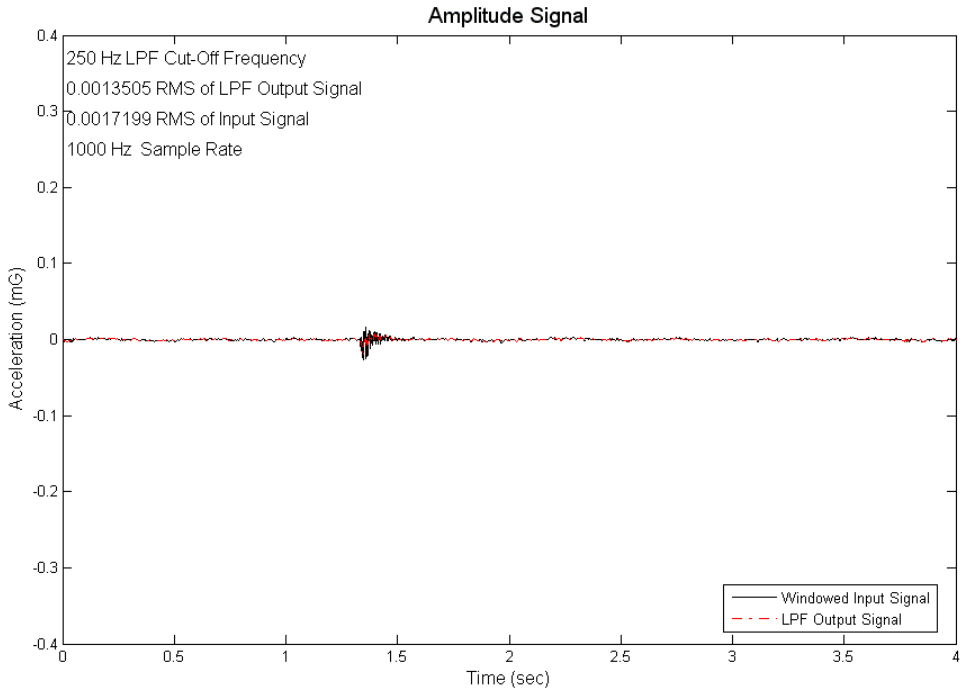

Figure 18 Accelerometer 1508 Windowed Data and LPF Output Data

The LPF Output Signal is 0.0013505 mG RMS for accelerometer 1508. The peak signal output is 0.0273 mG for accelerometer 1508. The signal attenuation for peak vibration isolation system is $\frac{1}{\frac{0.296\,mG}{0.0273\,mG}} = \times \frac{1}{10.8}$

The power spectrum for accelerometer 1508 is shown in the figure below:

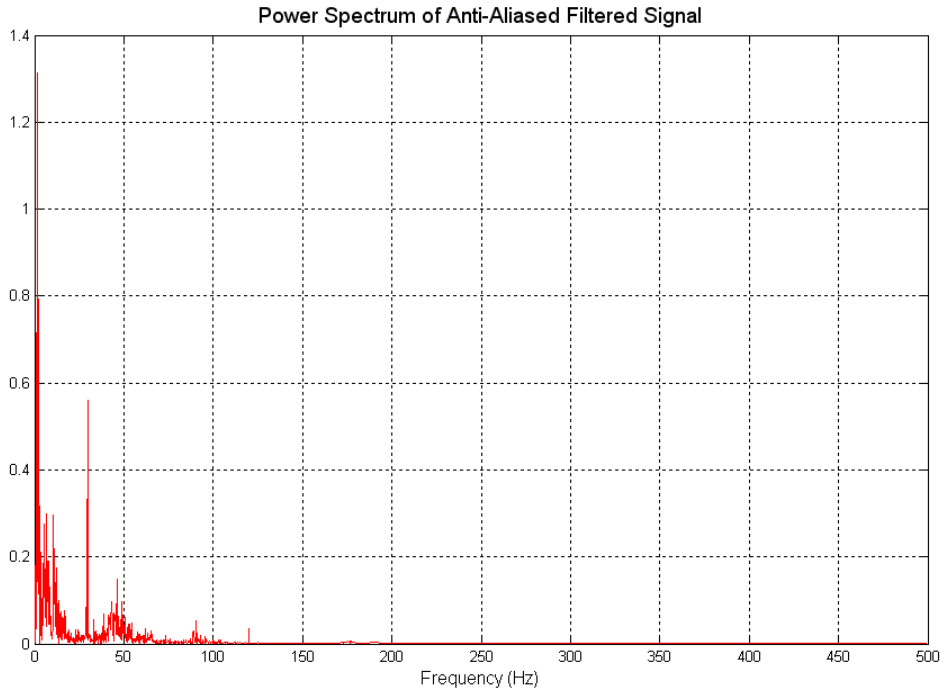

Figure 19 Power Spectrum for Accelerometer 1508 LPF Output

The dominant frequencies for the isolated vibrations on the table are: 1, 10, 30 Hz
Again the isolation system has shifted the spectrum energy to lower frequencies, which is desirable.

The attenuation for the table is:

For Steady-State Vibration $\times\frac{1}{9.2}$

For Peak Suppression $\times\frac{1}{10.8}$

The ELW floor vibrations are sufficiently low that the accelerometer on the table produces an output of 1μG RMS that is equivalent to the specified noise level for the accelerometer. Finally, the benign ELW floor vibration level has been compared to other lab places in the Engineering Lab Wing (ELW) and the Cunningham building nearby.

Recent measurements taken at the Cunningham basement laboratory show the LPF RMS output signal level ratio to be:

ELW/Cunningham Ratio $\frac{1}{\frac{0.0680\ mG\ RMS\ Cunningham}{0.0110\ mG\ RMS\ ELW}} = \times \frac{1}{6.2}$

In other words the ELW is 6x more quiet than the Cunningham building laboratory.

Table Vibrations & Fringe Stability

The fringe stability is the straightness of the fringes due to both low and high frequency environmental vibrations. Movement or jitter of the fringes represents an error to the measurements that cannot be compensated or cancelled. A stable fringe thus defines the resolution of the microscope. The Newport 8'L x 5' W x 1' T optics table is supported on pneumatic lifters to isolate ground vibrations. The resonant frequency of the suspended table is approximately 1 Hz which attenuates a significant amount of low frequency ground disturbance vibrations. The fringe stability can be disturbed with a light tapping to the table and by conversation in the room. The Dalsa Piranha 1x8192 pixels line scan camera scans at 9,000 lines/sec. Displaying 512 lines/frame will show a lowest frequency wave of 0.5x9000/512 = 9 Hz to one-half wave. The expected result on the camera display would show a gradual wave from top to bottom of the fringe.

The figure below is a camera picture with the table grounded or the no float condition:

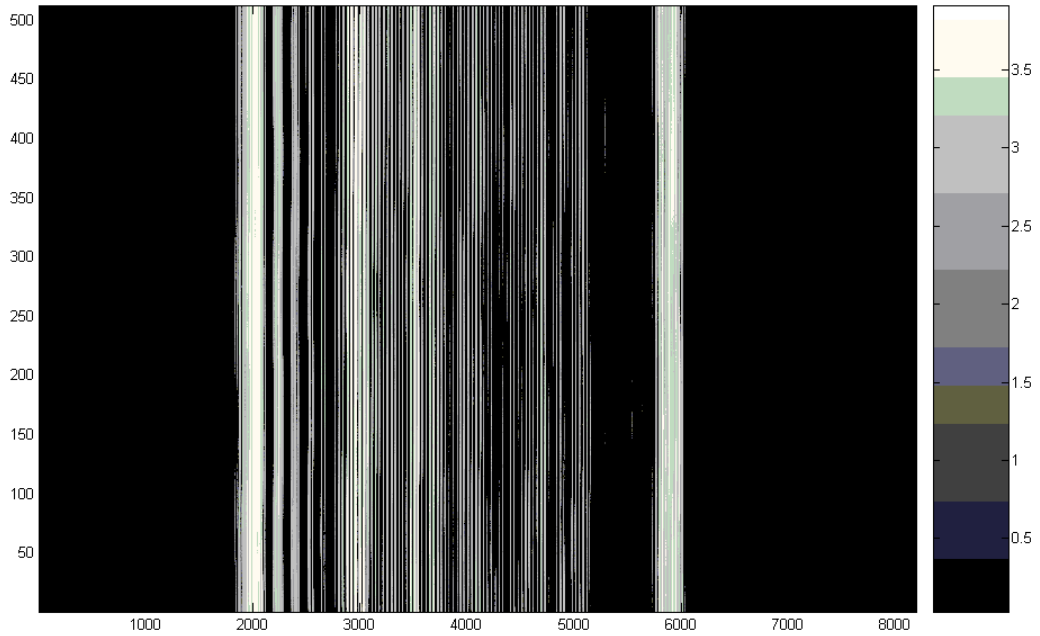

Figure 1 Table Supported by Ground

The ground vibration isolated table camera picture is shown in the figure below:

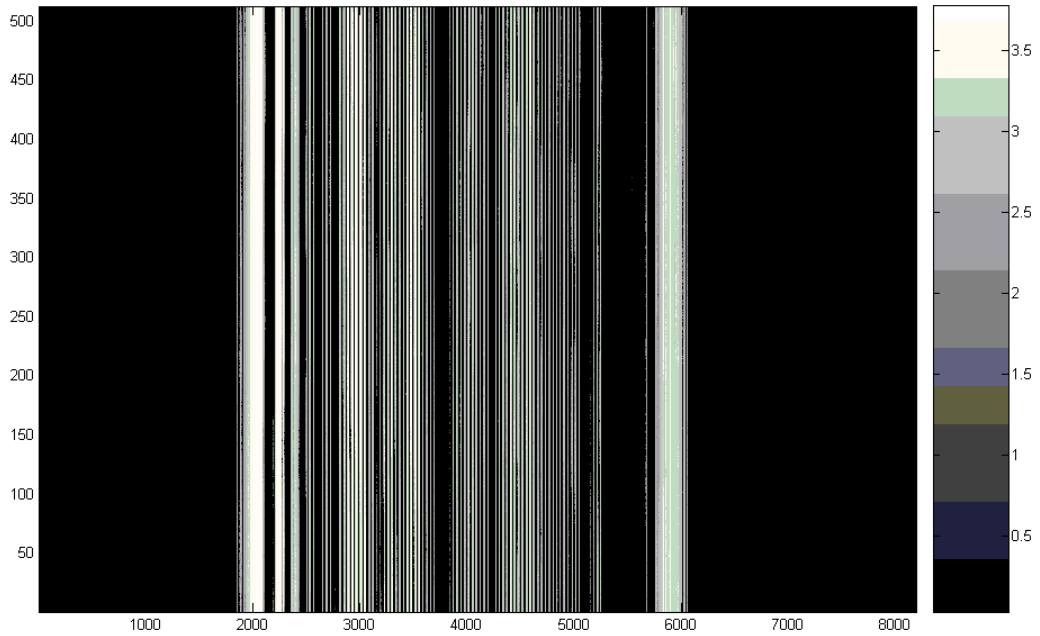

Figure 2 Table Supported by Pneumatic Lifters

The original display graphics show the fringes to be ruler straight whether the table is floated or not even, though the floated table shows straighter lines than the non-floated table. In general, vibration measurements in various laboratories and buildings on campus show this particular placement to be very quiet. In fact the accelerometers and the fringe interference patterns will pick up the vibrations of a truck idling in the parking lot, but this disturbance has no effect when the table is floated. The primary concern is the ability to measure a fringe-shift to approximately λ/10 waves which is possible with the kind of vibration isolation that the pneumatic lifters provide.

A cross-sectional view at the midpoint of the figure above will show the fringe hologram waveform. This waveform of wave interference is shown in the figure below where the object beam and the reference beams are completely overlapped.

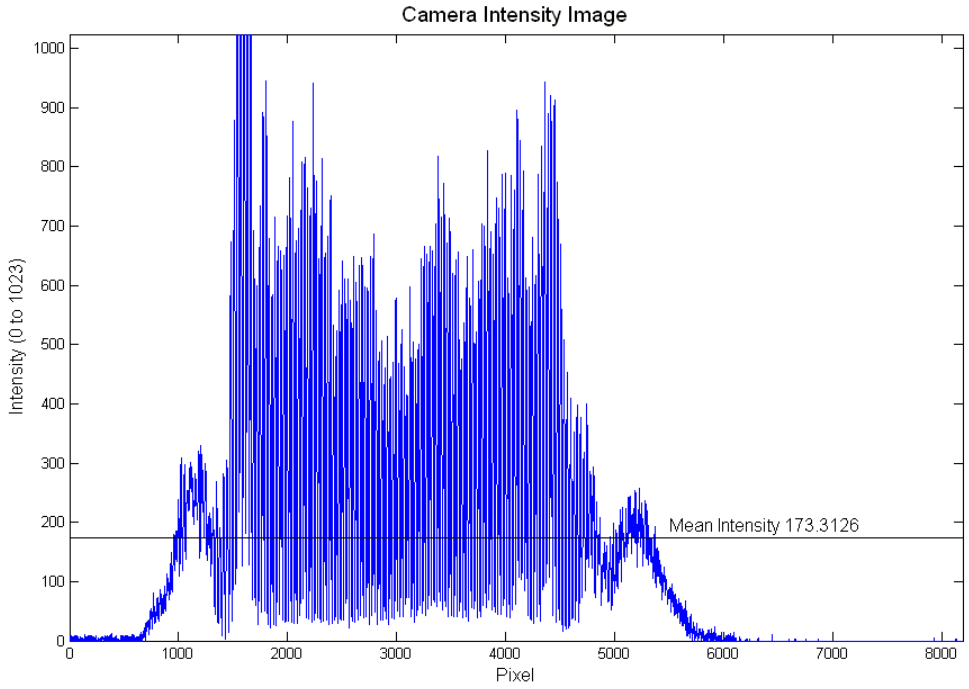

Figure 3 No Float Table Fringe Hologram across the 1x8192 pixel Line Scan Camera

A detail of fringe hologram around pixel 2000 to examine high frequency content is shown in the figure below:

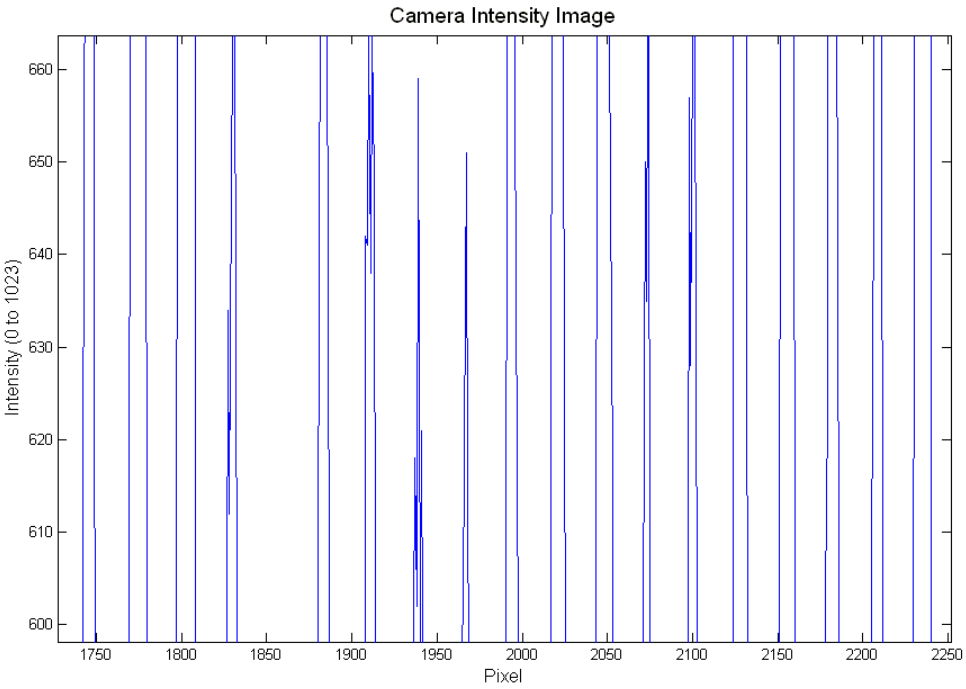

Figure 4 No Float Table Detail of Fringe Hologram

The power spectrum in this same region for 512 samples to the Fourier Transform is shown in the figure below:

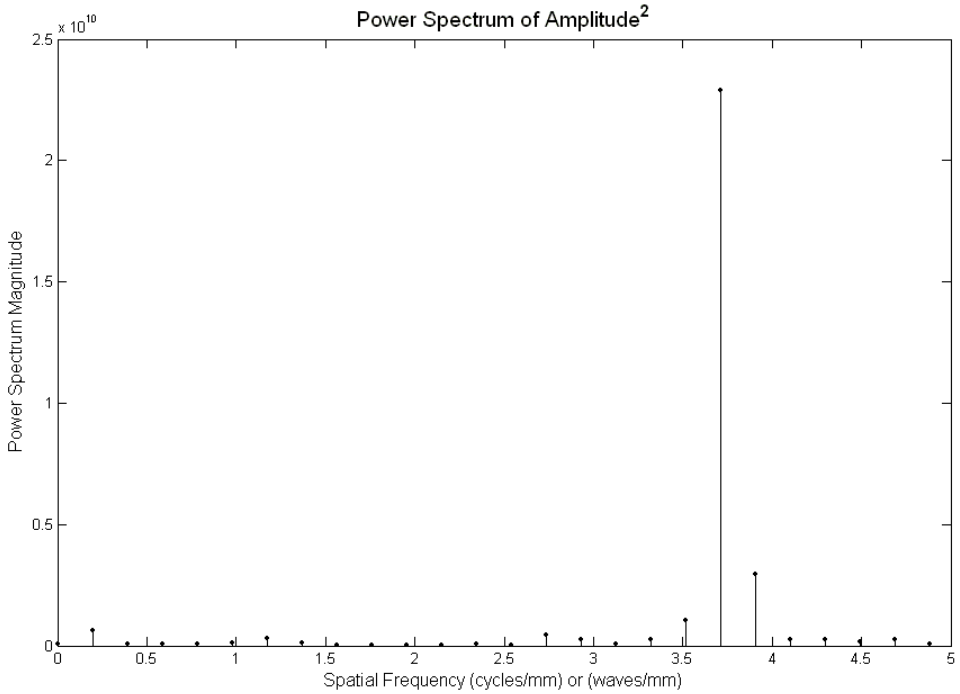

Figure 5 No Float Table Power Spectrum

The dominant line frequency is 3.7 waves/mm, which is expected given a pixel spacing of 7 microns/pixel and 53.9 samples/wave as determined from data analysis of the power spectrum. The fringe hologram is 2x Oversampled using linear interpolation where the detected number of samples per wave is 53.9/2=26.95 samples/wave. The calculated number of samples per wave is 16 samples/wave given an object-to-reference beam convergence angle of 0.5° and a detector spacing of 7 microns. The detected 26.95 samples/wave provides higher spatial resolution than expected and greater accuracy in measuring small changes in phase-shift. The detail of the fringe hologram with the floated table is shown in the figure below:

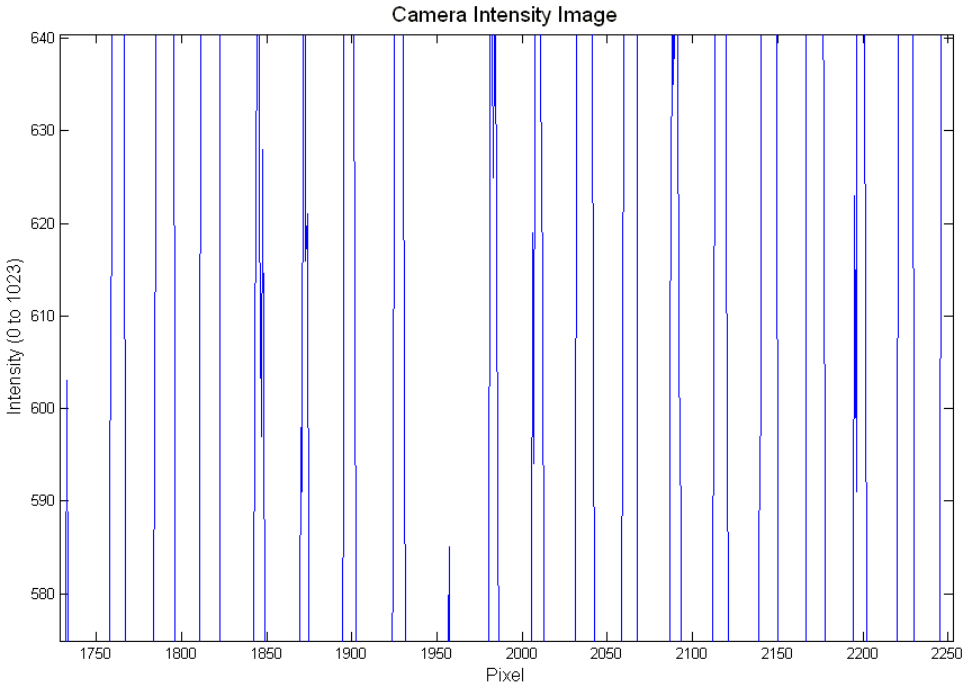

Figure 6 Floated Table Detail of Fringe Hologram

The discrete sampling edges in the figure above appear to be identical to that of the no float condition. The quantization sampling noise reduces over longer running times of the laser when 30 minutes will stabilize the high frequency noise. The close up detail will not show the low frequency effects of a floated to non-floated table. The pneumatic vibration isolators have a resonant frequency of 1 Hz to isolate frequencies up to around 50 Hz. Above these frequencies the fringes are sensitive to micro-phonics and vibro-acoustics and speaking in the room can be observed in the holograms.

The power spectrum of the floated table is shown in the figure below:

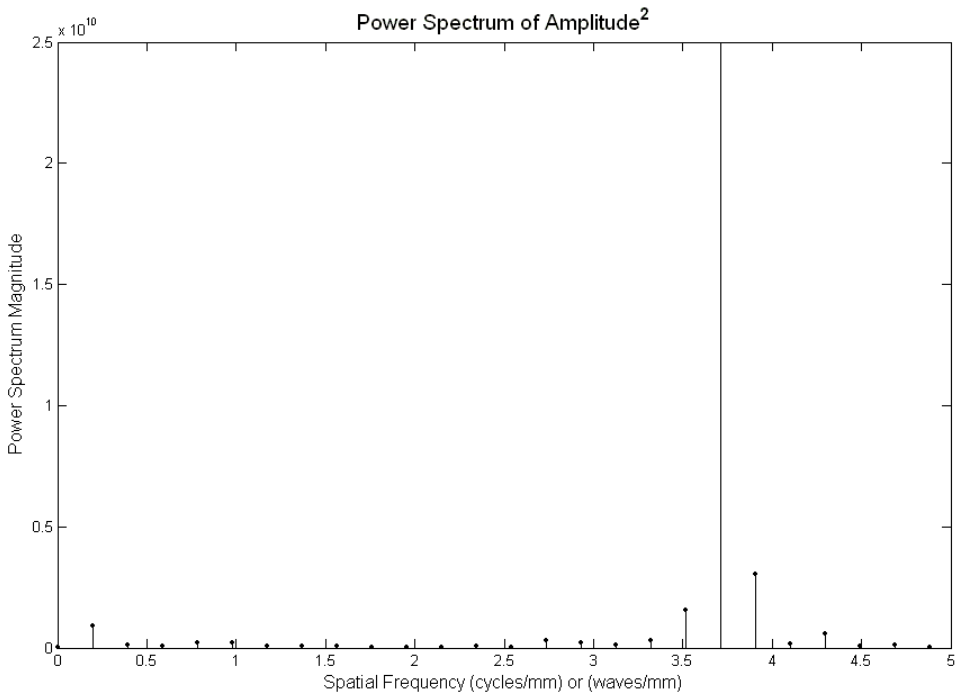

Figure 7 Floated Table Power Spectrum

The distribution of the discrete frequencies remains virtually identical; however, the main fringe frequency is now off the vertical scale. This situation shows a capability to accurately determine a phase-shift with little error due to sideband frequencies. If more phase-shift resolution is required then a high-order band-pass filter (BPF) can be implemented which will introduce a constant phase-shift. For example, a band-pass filter with 24dB/octave slopes will introduce a constant phase-shift of –π radians and a band-pass filter with 12dB/octave slopes will introduce a constant phase-shift of –π/2 radians. The 12dB/octave digital BPF is more numerically stable than the 8^{th} order differential equation solution to the 24dB/octave digital BPF. In addition, the 12dB/octave BPF converges from initial conditions in 1.5 waves and the 24dB/octave BPF converges from initial conditions in 2.5 waves, which reflects marginal stability. Signal processing of the waveform using a digital BPF does reduce the sideband frequencies to a greater extent than floating the table. Even though great efforts to improve beam quality at the laser source and beam expander optics was implemented the off-axis reflections and background radiation was also reduced to provide stable fringes as seen above. The resolution of the microscope to measure a minute fringe-shift based on the number of samples per fringe or number of samples per wave will be examined further in another section.

The images were obtained through a LabVIEW data acquisition program and Matlab data analysis programs. The LabVIEW program is shown below. The LabVIEW program displays a fringe hologram image when running and will save the acquired image to a file when the “Data” button is pressed. Matlab is then used to open the file and display the hologram with 2x Oversampling as well as determine the power spectrum of the hologram. A LabVIEW program to save a hologram or interference pattern image file is shown in the figures below:

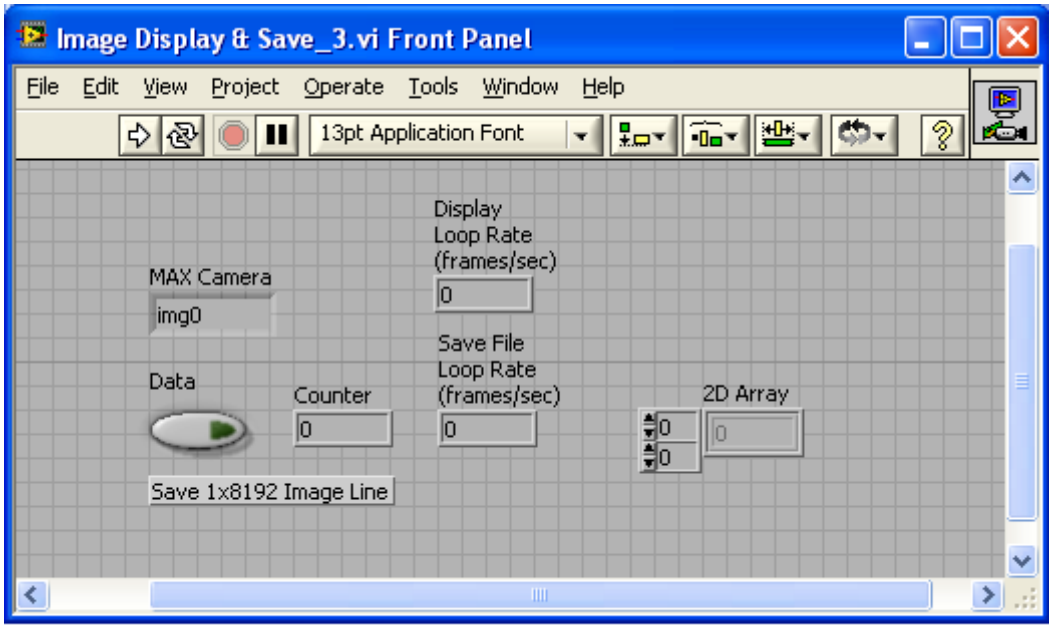

Figure 8 LabVIEW Control and Display Panel to Save an Image File

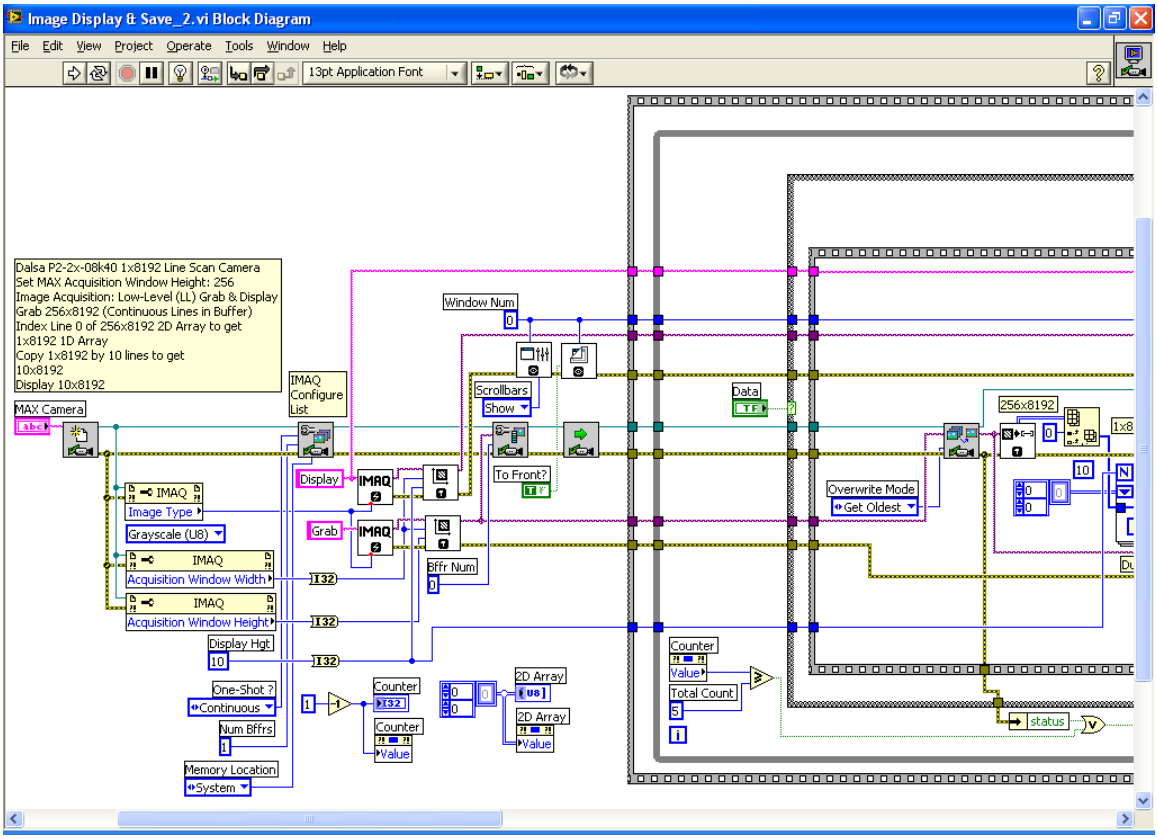

Figure 9 LabVIEW Block Diagram Program

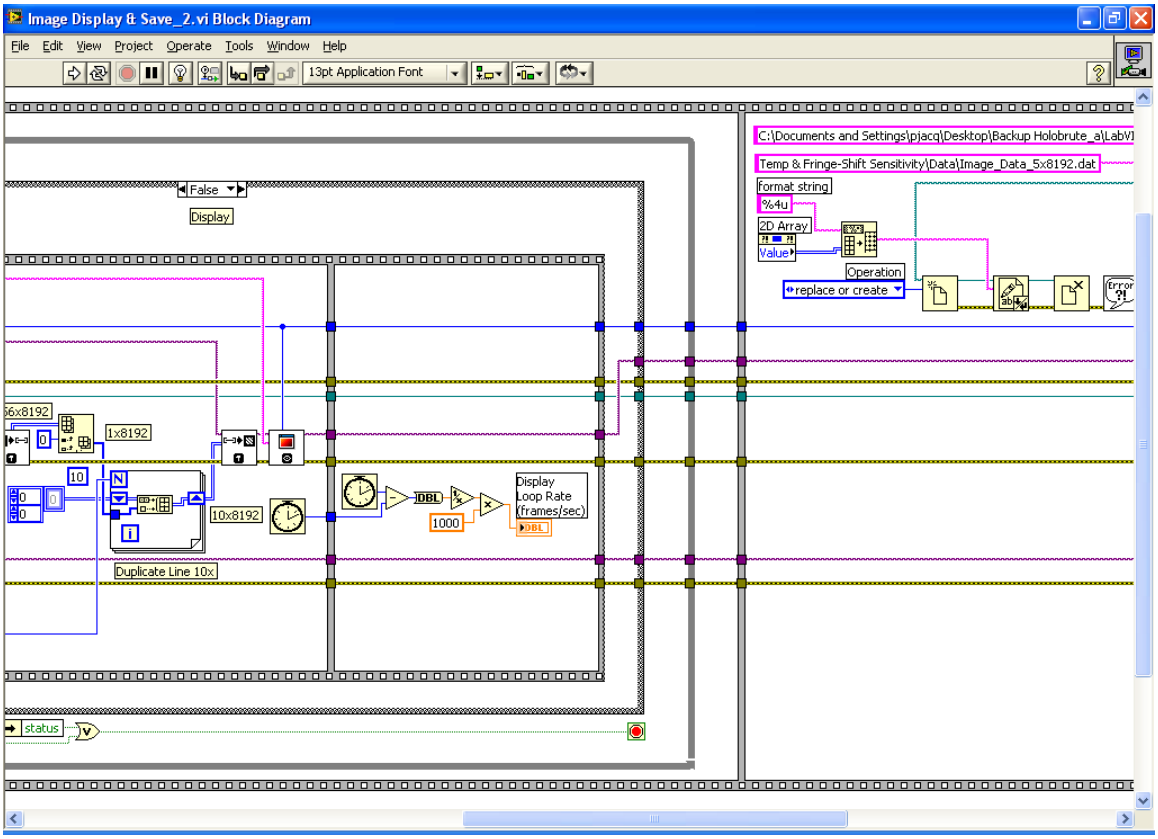

Figure 10 LabVIEW Block Diagram Program (continued)

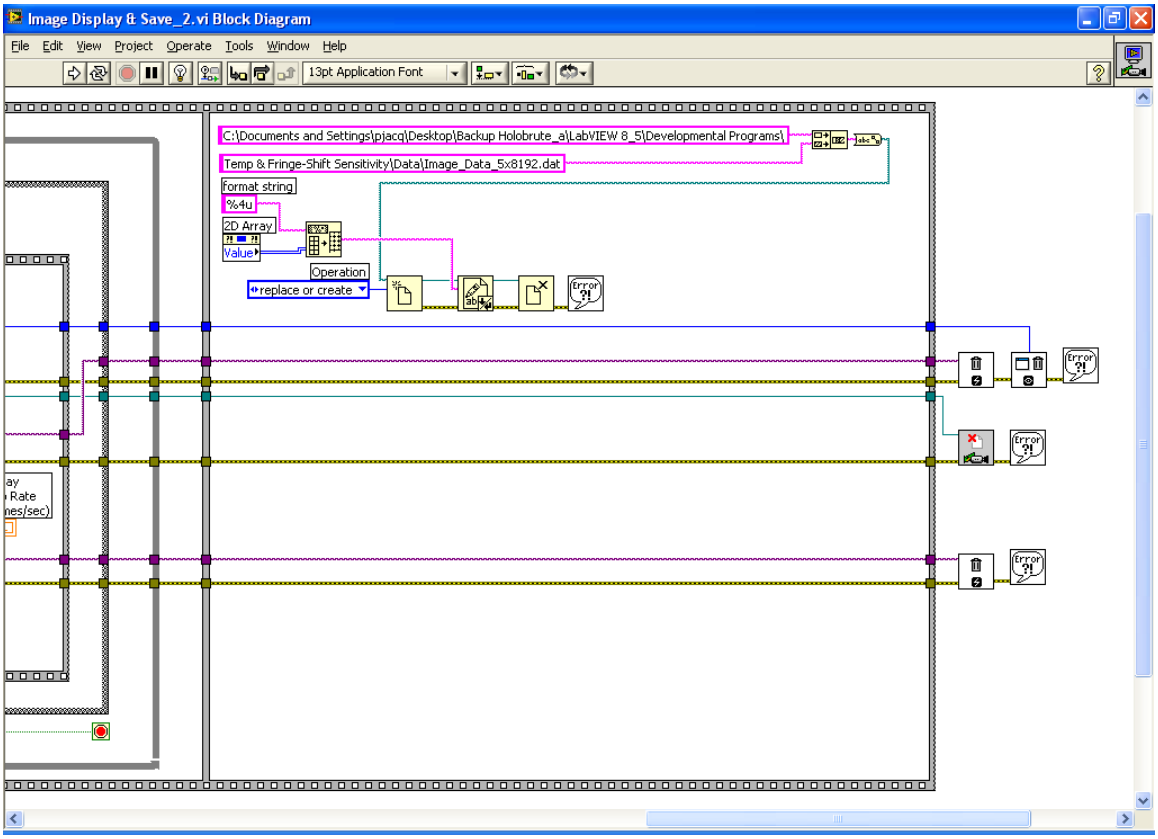

Figure 11 LabVIEW Block Diagram Program (continued)

Analogy to the Principles of Holography and Sensitivity to Index-of-Refraction

In this section a practical example is given to explain in simple terms the principle of the CLSH operation. Imagine a fish swimming in a tank and the fish representing a specimen and the tank representing a fluid-cell cuvette. The fish swims along and then rises up suddenly and then comes back down. I observed this happening and suspected that there was a jet stream from a hose that caused the fish to rise and noticed a very small black tube on the bottom of the tank that was directed upward. I examined the hose carefully to see if it was the source and looked for air bubbles, which did not occur. The fish passed through the same region over and over. After ten minutes of watching I finally saw a tiny deflection on one the fins. At that point I concluded that there was a jet stream in the tank that I could not optically perceive, but could only perceive through the reaction of the fish.

If a traditional imaging microscope were focused on this jet stream then nothing would be seen because the jet stream does not refract a sufficient number of rays to create an optical distortion. The jet stream also does not change the opaqueness or translucence of the water. The jet stream produces minute changes in index-of-refraction where ray bending due to Snell's Law ($n_1 \cdot \sin\theta_1 = n_2 \cdot \sin\theta_2$) is virtually imperceptible.

When looking at the leading of the wing of an airplane, optical distortions of the ground below near the point of highest pressure can be seen. In this case, the high pressure causes a significant change in the refractive index such that the rays are bent or refracted most in the region of highest pressure nearby the stagnation point. Significant changes in refractive index affect standard optical imaging microscopes in a manner of optical focus resolution, depth-of-focus, clarity, maintaining accurate color distribution over a large intensity range, spectral range, and contrast dynamic range. The minute changes in index-of-refraction are detectable with interferometers, which are used to measure the wavefront error and optical quality of precision optical components. For example, our holography microscope has 100mm diameter precision mirrors with a wavefront error of less than λ/50 waves RMS (Root Mean-Square) error. This wavefront error takes into account all the optical distortions and aberrations, such as spherical, geometric, coma, and astigmatism to provide near ideal diffraction limited performance.

This CSLH microscope would be able to detect this jet stream in the water tank because the velocity changes the index-of-refraction and this makes for minute changes in the optical path length that are less than the wavelength of light. The change in optical path length produces a fringe-shift in the hologram that we are measuring. This experiment non-obtrusively measures the internal temperature profile in a fluid-cell specimen given the sensitivity to a change in index-of-refraction and the measurement accuracy of a fringe-shift on the hologram. In a particular way the phase coherent holography microscope can measure properties that a regular optical imaging microscope is insensitive to and this can provide a means to explore some very interesting science and discover new phenomena.

The CSLH Microscope Layout

The CSLH microscope layout is shown in the following photographs of the optical sections. The microscope occupies the entire 5x8 foot (or 1.5x2.4 meter) optics table. The optical path includes the laser source, beam expander, wavefront splitter, beam

steering mirror section, optical loop with telecentric lens, confocal lens, projector lens, and camera. The blue 457nm wavelength laser is used to determine the temperature profile in the fluid-cell specimen.

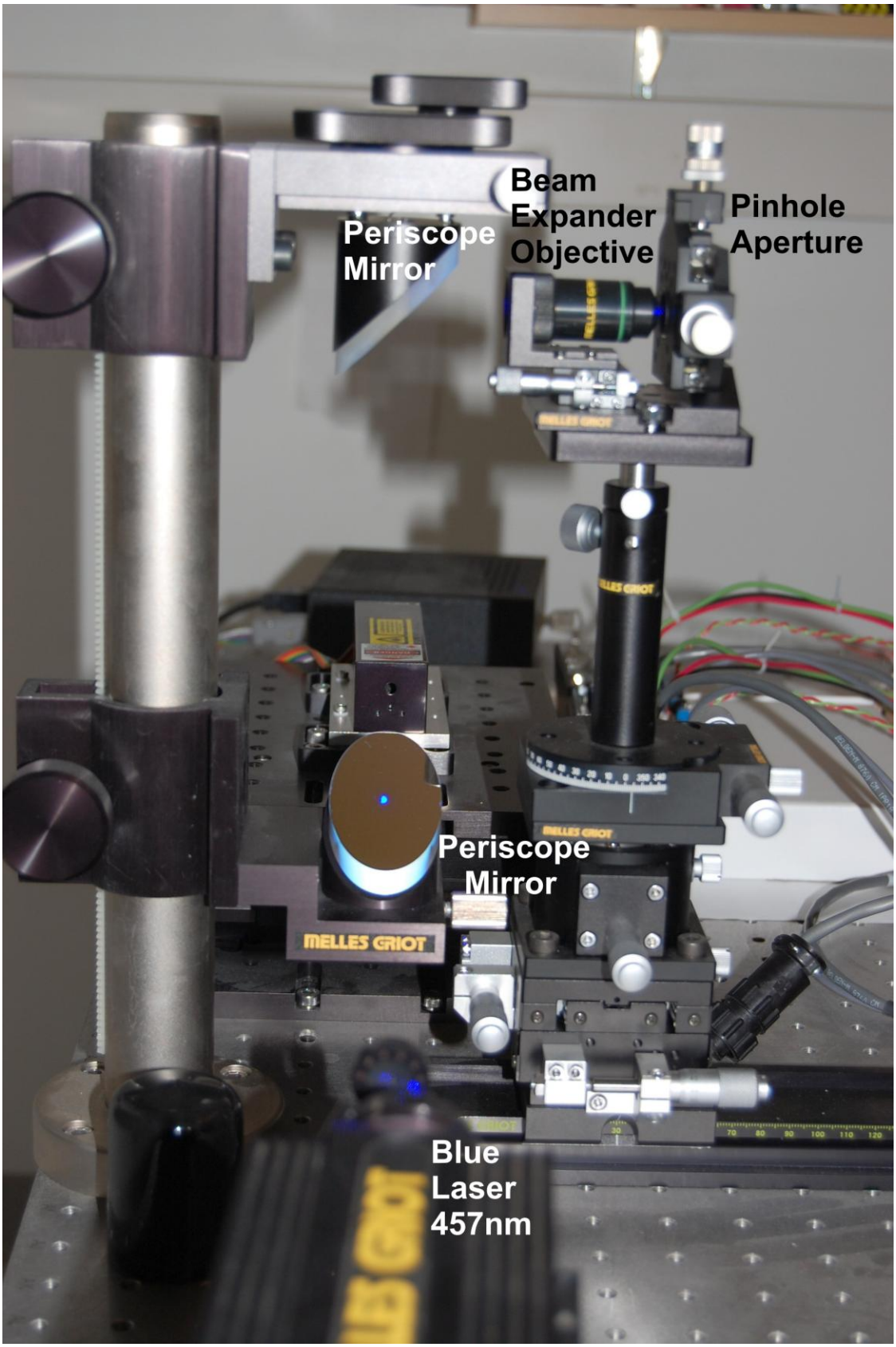

Figure 1 Laser to Periscope Mirrors for Beam Elevation

The output of the laser is elevated to 300mm above the optics table with the two elliptical periscope mirrors as shown in the figure above. The Melles-Griot laser passes through a small iris diaphragm to eliminate stray rays and is then reflected by the two periscope mirrors that elevate the beam. The beam then enters a microscope objective lens with a 10.8mm focal length. The beam is focused at a 100µm pinhole aperture, which reduces aberrations. The expanding beam then propagates off of the right-hand side of the figure. The beam expander is shown in the figure below:

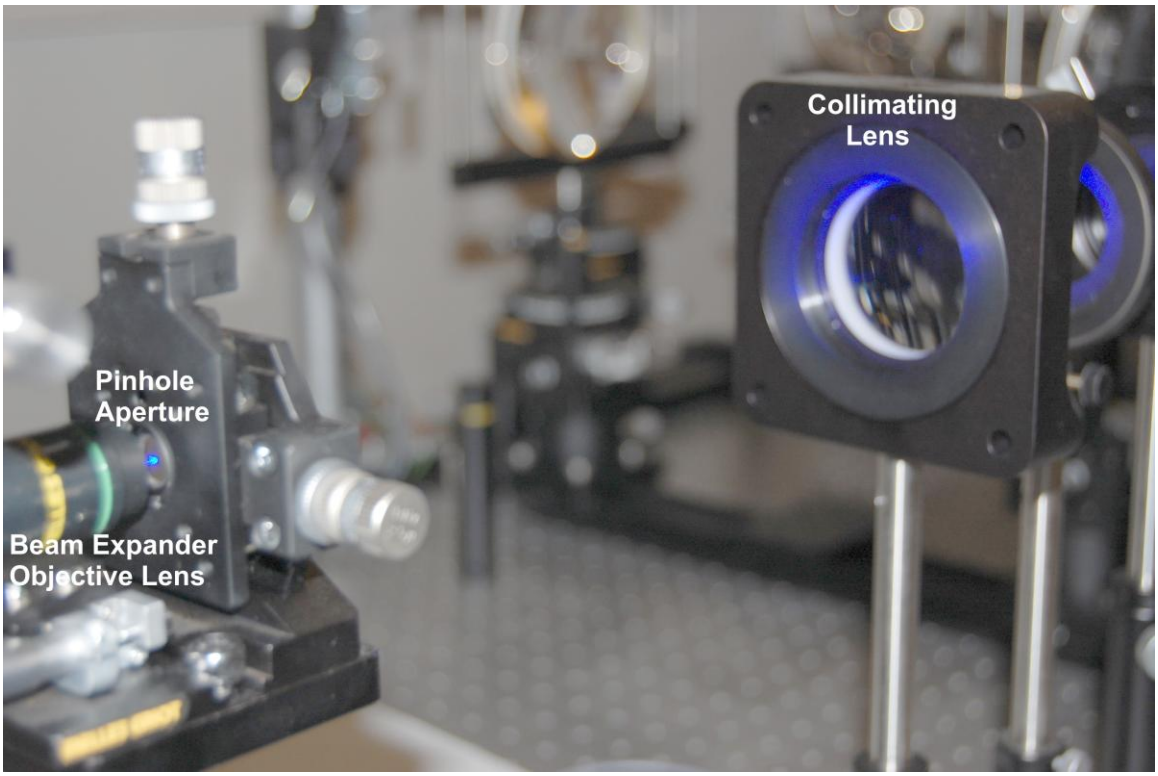

Figure 2 Beam Expander

The Keplerian beam expander consists of the Melles-Griot microscope objective lens and a pinhole aperture to pass the focused laser beam. The expanded beam is collimated by an achromatic doublet lens and is followed by an iris diaphragm that truncates the beam for uniform aperture illumination at 35mm in diameter. This 35mm beam is quite uniform in aperture illumination, but also showed some small spots on the image. The spots primarily show up on the bottom area of the beam. The beam expander image just past the iris diaphragm is shown in the figure below:

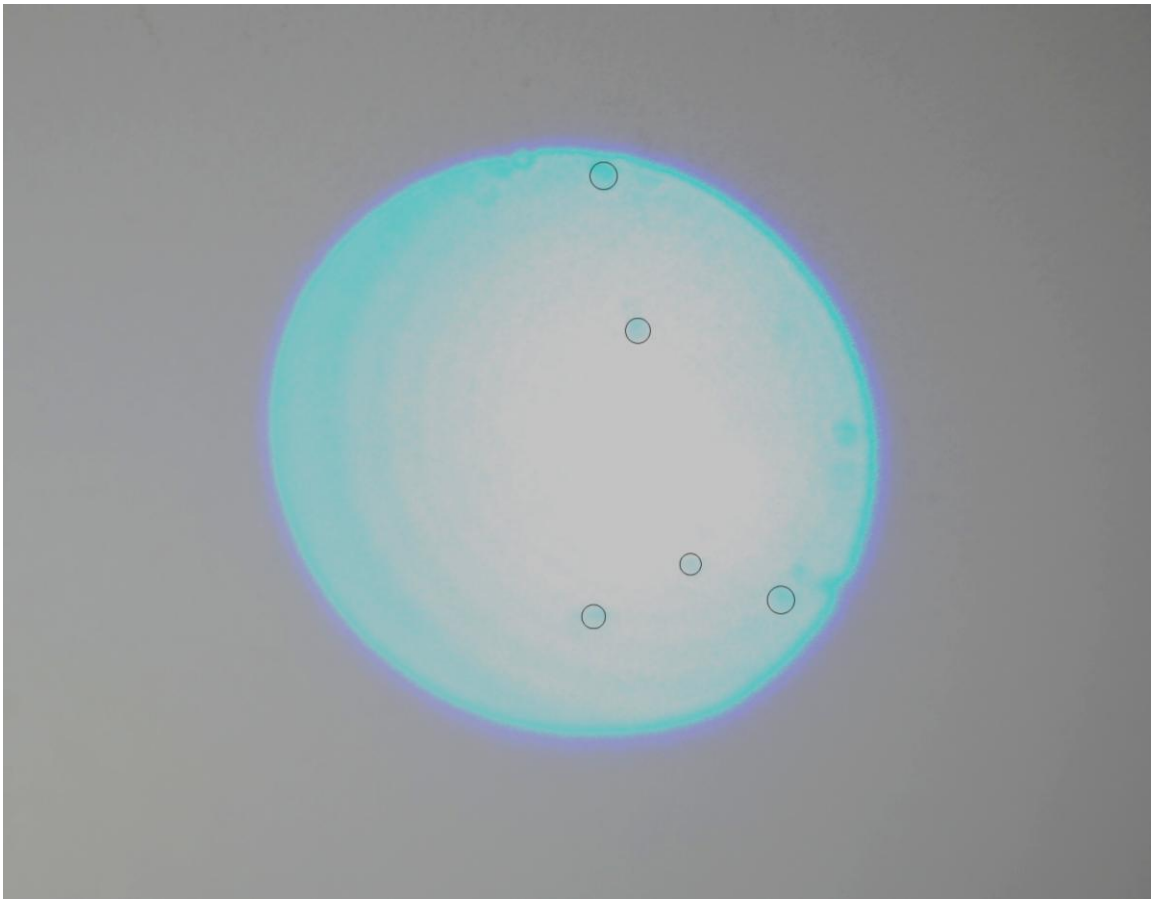

Figure 3 Collimated 30mm Diameter Laser Beam with Circled Spots

Two different Galilean beam expanders of different focal lengths were used in an attempt to reduce the small spots in the figure above. The result was only a small difference in aperture illumination uniformity. The circled areas do not show microstructure and detail of the tiny spots that are clearly imaged. The source of the spots is primarily due to the laser and partially due to the periscope mirrors that reflect a beam that is less than 1mm in diameter. The small spots do not necessarily mean a perturbation in wavefront as this would adversely affect our hologram measurements. After following many optics configurations and adjustments it was found that this was the best beam expander wavefront quality that could be achieved with the available optical components. Many days were spent in reducing aberrations and refining the alignment.

The expanded beam then propagates to the wavefront splitter as shown in the figure below:

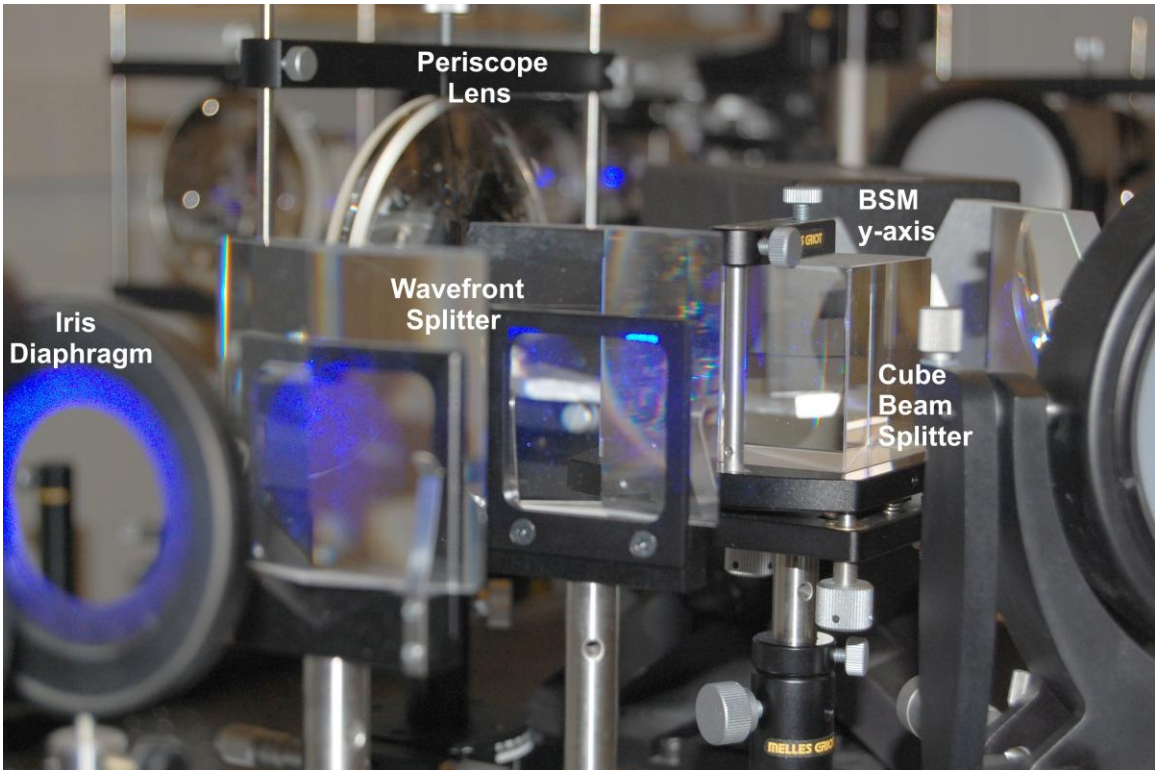

Figure 4 Wavefront Splitter

The wavefront splitter consists of a pair of back-to-back Fresnel biprisms that split the circular shaped beam into two back-to-back “D-shaped” beams. The iris diaphragm is followed by a pair of Fresnel biprisms that wavefront split the beam. The beam that passes through the specimen is designated as the object beam and the beam that bypasses the specimen region is designated as the reference beam. The object and reference beams then propagate to the first cube beam splitter. The beam transmitted through the beam splitter is reflected by the *y*-axis Beam Steering Mirror (BSM) as shown in the background. The reverse propagating beam is reflected by the beam splitter and this beam propagates to the folding mirror as shown on the far right-hand side. The folding mirror sends the beams to the projector optics.

The reflected beams from the *y*-axis BSM sends the beams to the *x*-axis BSM as shown in the figure below:

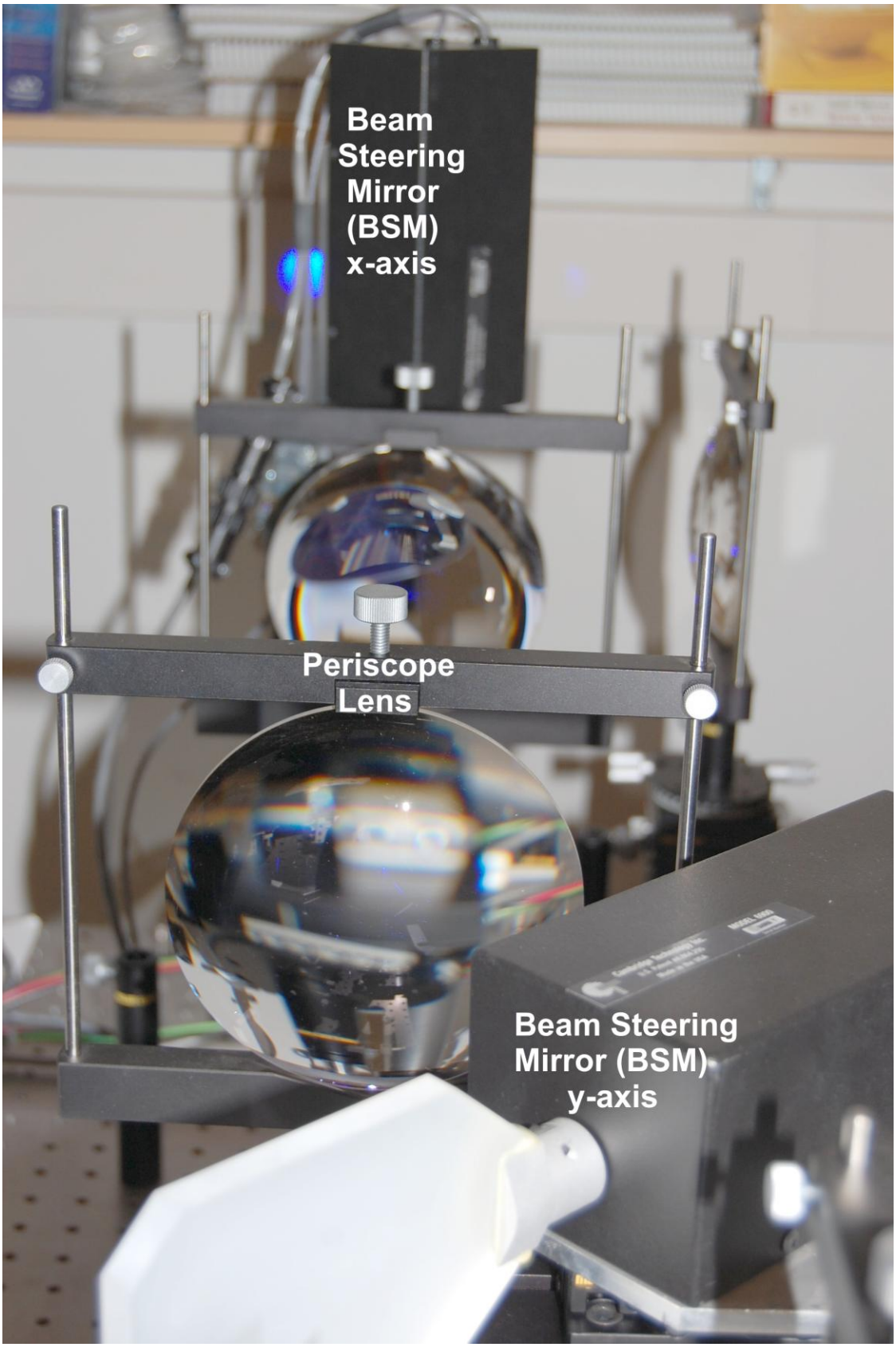

Figure 5 Beam Relay from *y*-axis BSM to *x*-axis BSM

The reflected beams off the *y*-axis BSM propagate through a periscope lens to the *x*-axis BSM. The periscope lens reduces beam translation or beam walk on the first and second cube beam splitters. The BSMs and two periscope lenses are placed between the two cube beam splitters. The periscope lenses also invert the beams for proper orientation as the beams propagate both forward and backwards between the cube beam splitters. The beams that are reflected off the *x*-axis BSM then pass through a periscope lens as seen on the far right-hand side of the figure below:

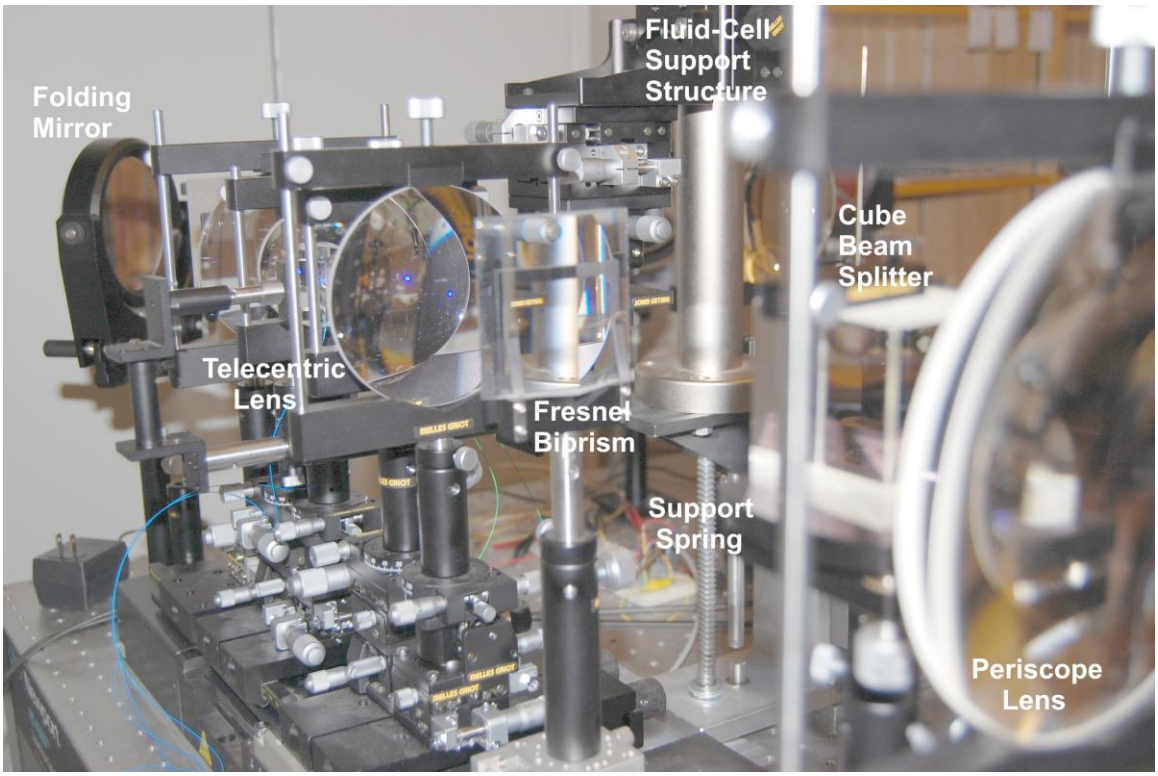

Figure 6 Beam Propagation from the BSMs to the Second Cube Beam Splitter

The periscope lens re-collimates the beams and transmits them to the second cube beam splitter. The second cube beam splitter creates the entrance and exit for an optical loop. The beams that pass through the cube beam splitter enter the telecentric lens. The pupil of the periscope lens is near the Fresnel biprism to maximize the field angle or field-of-view of the scanning optics. The back corner of the optics table shows a folding mirror that forms a part of the optical loop. The telecentric lens focuses the object and reference beams into the specimen fluid-cell and the constant refractive index cuvette. A support spring reduces the load on the vertical translation stage as the fluid-cell support

structure is quite heavy and causes the stalling of the translation stage. The fluid-cell cuvettes in the middle of the telecentric lens are shown in the figure below:

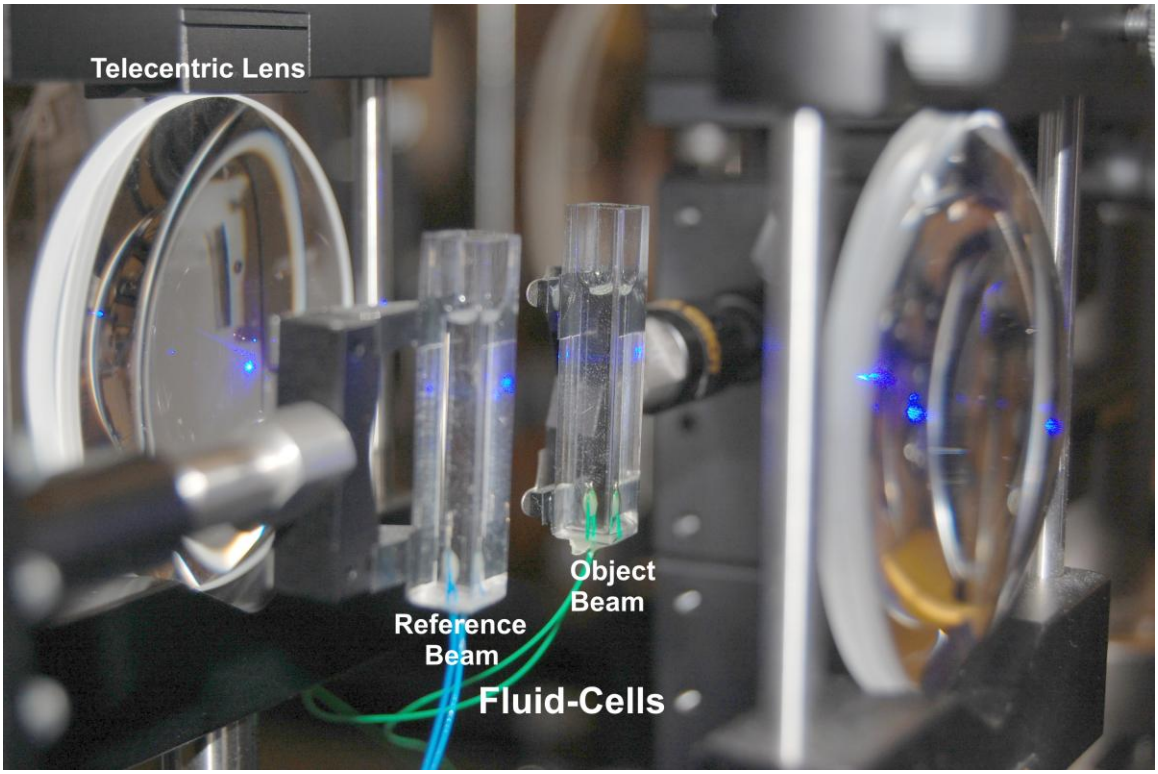

Figure 7 Object Beam Fluid-Cell and Reference Beam Cuvette

The object beam is focused inside the heated fluid-cell and the reference beam is focused inside the constant temperature cuvette. The constant temperature cuvette provides an equivalent focal point to the object beam. The symmetrical optics of the telecentric lens re-collimates the object and reference beams. The equivalent focal points also maintain the same beam size at re-collimation. This is important as the telecentric lens is designed to re-collimate the beams with no magnification and a relative beam size will produce an error when overlapping the beams at the camera.

The telecentric lens transmits the beams to two folding mirrors that form the optical loop as shown in the figure below:

Figure 8 Folding Mirrors of Optical Loop at End of Optics Table

The re-collimated beams that exit the telecentric lens are reflected by two folding mirrors. The beams then pass through a third periscope lens.

A rear view of the optical loop is shown in the figure below:

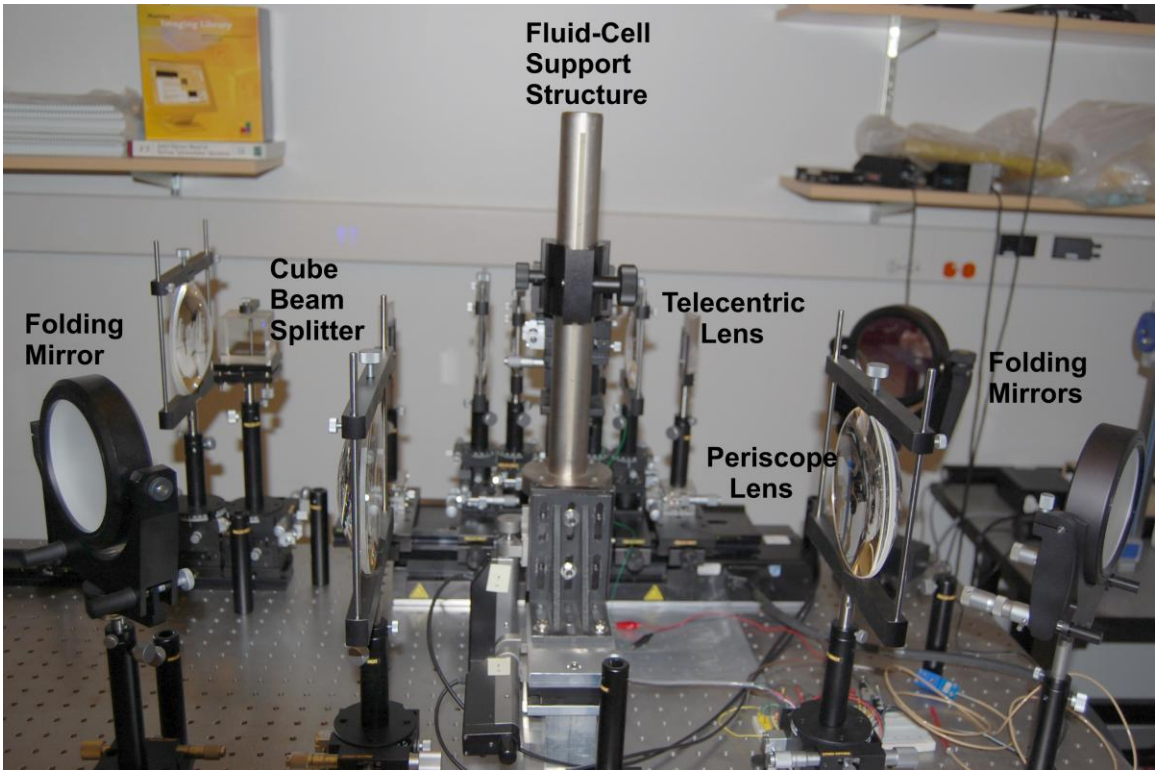

Figure 9 Rear View of Optical Loop Containing the Telecentric Lens and the Periscope Lens

The rear view of the optical loop shows all three folding mirrors that form the optical loop and the second cube beam splitter that reflects the beams for reverse propagation back through the BSMs. In the center of the figure the support structure consisting of a large diameter post for the fluid-cells can be seen. Beneath the post are support brackets and *xy*-translation stages.

Another view of the translation stages for the fluid-cells is shown in the figure below:

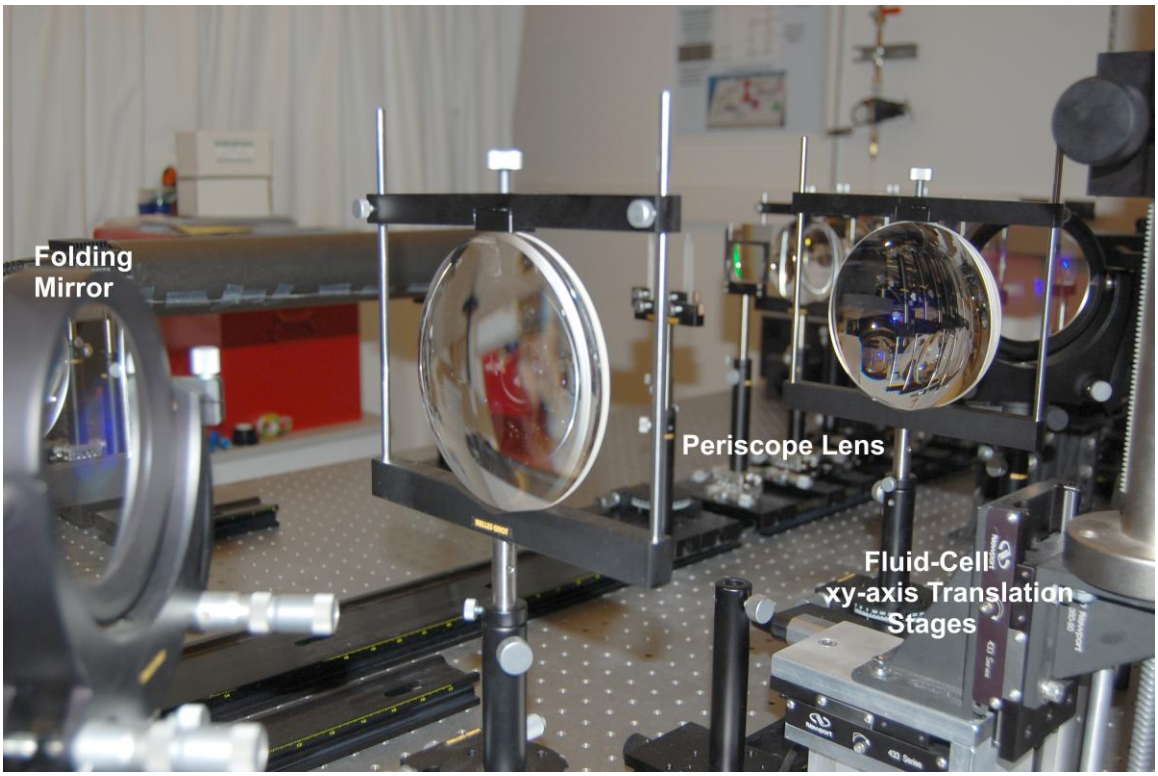

Figure 10 Optical Loop and Translation Stages to Move the Fluid-Cells within the Telecentric Lens

The optical loop also has a reverse optical path as the entering beams are not only transmitted through the beam splitter, but also reflected off the beam splitter. Thus the reflected beam reverse propagates through the periscope lens and the telecentric lens and exits the loop by passing through the beam splitter. This produces four beams at the projector optics instead of an expected two beams.

The beams then reverse propagate back through the BSMs and the periscope lenses from the second beam splitter to the first beam splitter as shown in the figure below:

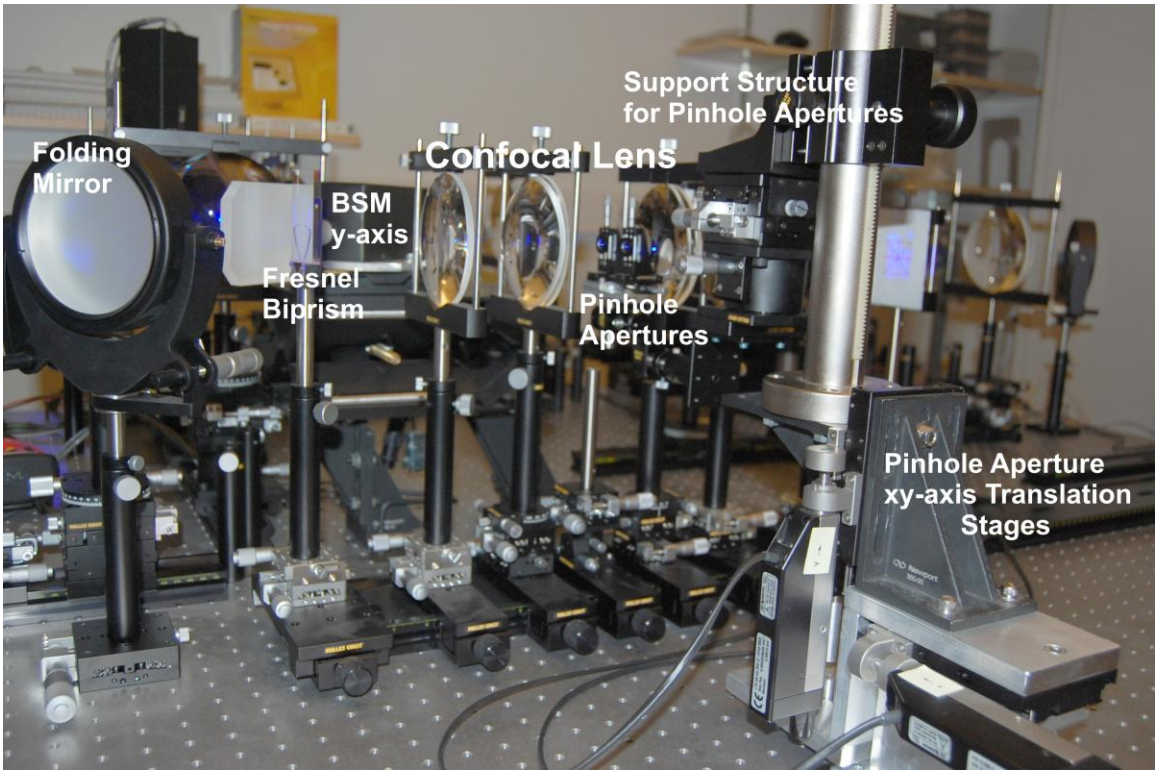

Figure 11 Back Propagation Path from the Optical Loop to the First Cube Beam Splitter

In this figure the back propagating beam is reflected off the *y*-axis BSM to the first cube beam splitter that is behind the folding mirror. The beams that are reflected off the first cube beam splitter are also reflected off the folding mirror and enter the confocal lens. The confocal lens is a modified telecentric lens with pinhole apertures replacing the fluid-cell cuvettes. The lens shapes of the confocal lens are different from the telecentric lens in order to accommodate the separation of the pinhole holders and micrometer adjustment knobs. The pinhole aperture *xy*-axis translation stage provides tracking of the focused beam movement so that the pinholes remain aligned to the focused beams.

A close-up of the pinhole apertures in the confocal lens is shown in the figure below:

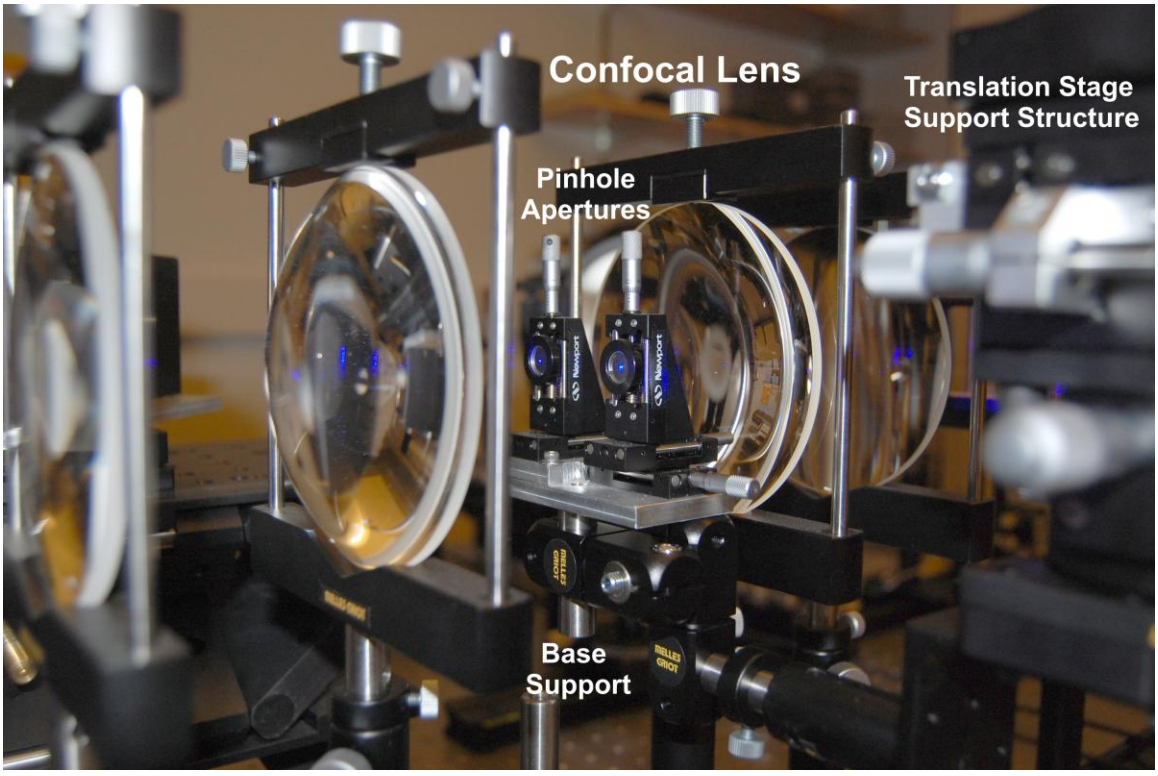

Figure 12 Confocal Lens Pinhole Apertures

The confocal lens is symmetrical about the focal point of the pinhole apertures just as the telecentric lens is symmetrical about the focal point within the fluid-cells. The small amount of blue light in the center of the pinhole apertures shows the reduction of aberrations as this is reflected back off of the stainless steel of the pinhole disc. The 400µm pinholes are sized to accommodate the beam translation during scanning. The lenses past the pinhole apertures recollimate the beams and the Fresnel biprism at the end directs the beams in a parallel direction.

The beams then exit the confocal optics and enter the projector lens as shown in the figure below:

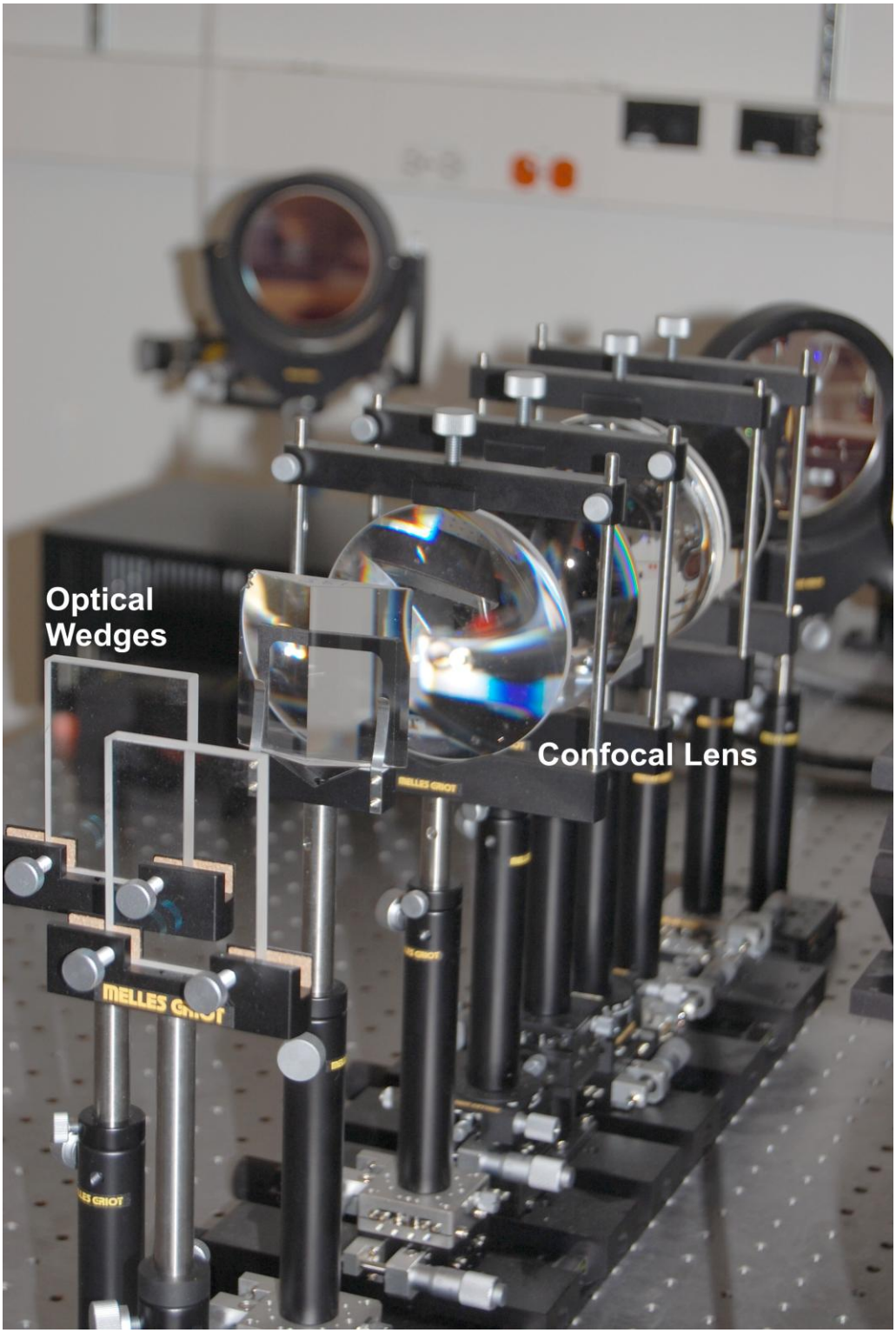

Figure 13 Projector Lens Optics

The projector lens is a simple design consisting of a pair of optical wedges. Any combination of optical wedges can be used where the wedges are 0.5° and 1.0°. These small angle optical wedges can provide the desired fringe spacing at the camera. The required number of camera pixels per fringe is > 16 for accurate determination of the phase-shift.

The optical wedges converge the object and reference beams for complete overlap at the camera. The path length is long with folding mirrors at each end of the table so that the fringe-spacing can be > 112µm. The Dalsa Piranha P2-23-08k40 line scan camera has 1x8192 pixels at 7µm/pixel. One of the folding mirrors and the camera is shown in the figure below:

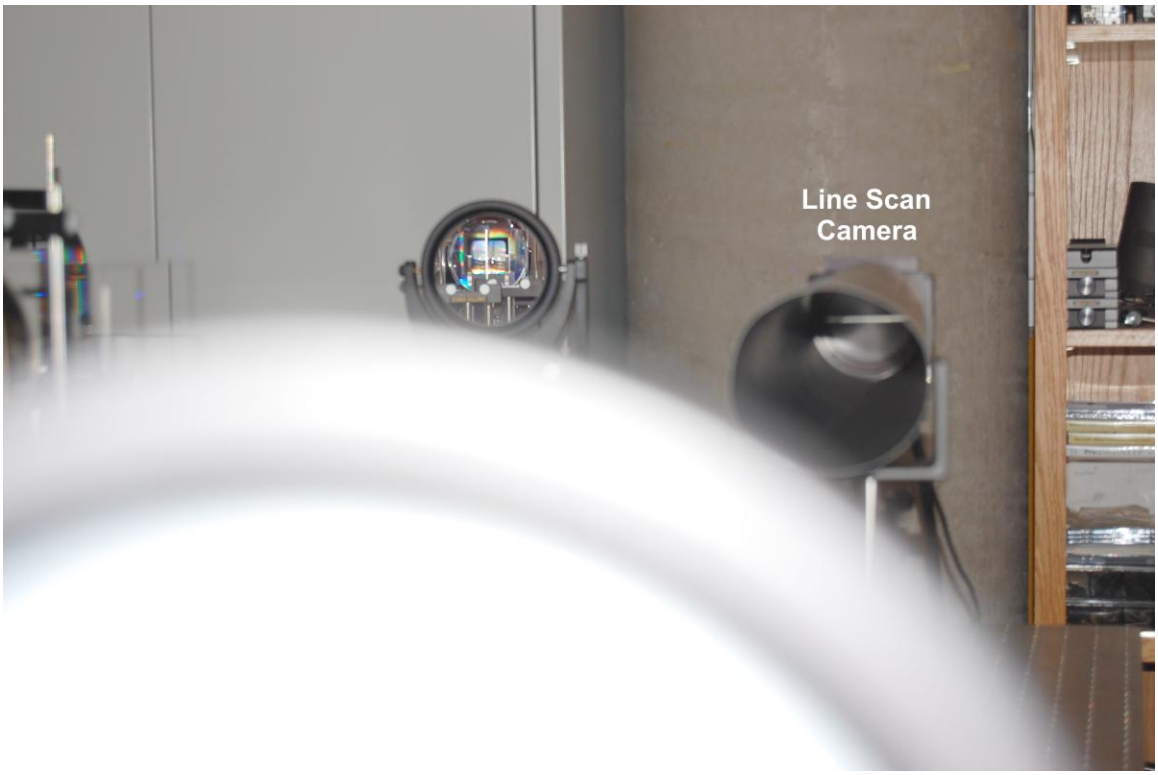

Figure 14 Line Scan Camera with Tube Shroud

The foreground shows the back of one of the folding mirrors and the background shows another folding mirror at the end of the table. The image in the folding mirror shows the optical wedges and the confocal lens. The silver line on the camera shows the 57mm wide set of detector elements.

The object and reference beams at the output of the optical wedges are shown in the figure below:

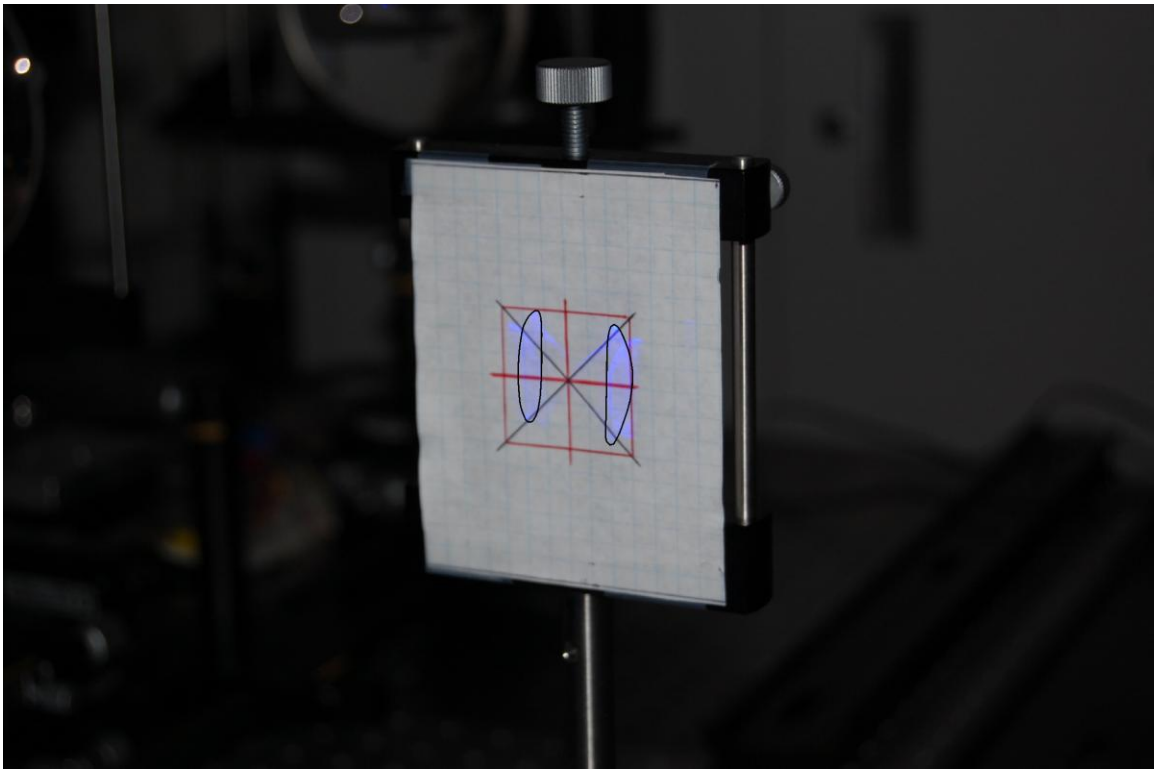

Figure 15 Beams at the Output of the Optical Wedges

These are the beams that have back propagated from the optical loop through the BSM section and are split off at the first cube beam splitter. The beams then propagate through the confocal lens and then through the optical wedges. The beam splitters attenuate the beams along with the optical components along the optical path. A significant stray reflection also occurs at each Fresnel biprism. There are two biprisms for the wavefront splitter, two biprisms for the telecentric lens, and two biprisms for the confocal lens. The beam intensity is sufficiently reduced that very little attenuation by neutral density filters and a polarizing lens is required to produce an adequate hologram or fringe pattern intensity on the camera.

The two beams are outlined in the figure and the optical wedges will converge the beams until they completely overlap one another. The vertical misalignment of the two beams is due to the relative angle of the fluid-cell cuvetttes and can easily be corrected with an adjustment of a tilt angle off of the vertical.

The additional shadowy images are an additional set of “D-shaped” beams that occur due to a reverse propagation of the beams in the optical loop. These additional beams are coincident with the forward propagating beams in the optical loop and pass through the pinhole apertures of the confocal lens. Placing a half-wave plate or phase-shifter followed by a polarizing lens in the optical loop will eliminate the reverse propagation beams. This situation was unanticipated and introducing a half-wave plate along with a polarizing lens will introduce further beam attenuation for the forward propagating beams within the optical loop. A half-wave plate is a component that was not available and the additional beams are slightly off-axis from the main beams. Over the long path length to the camera the additional beams translate off the edges of the camera.

LabVIEW Programs for the STLH and CSLH Microscopes

Sensitivity of a Fringe-Shift with respect to Temperature Measurement

STLH Microscope Reconstruction Experiment

CSLH Microscope Reconstruction Experiment

Sensitivity of a Fringe-Shift with respect to Temperature Measurement

A LabVIEW program for data acquisition of thermal couple measurements and image acquisition of the line scan camera is shown in the figures below:

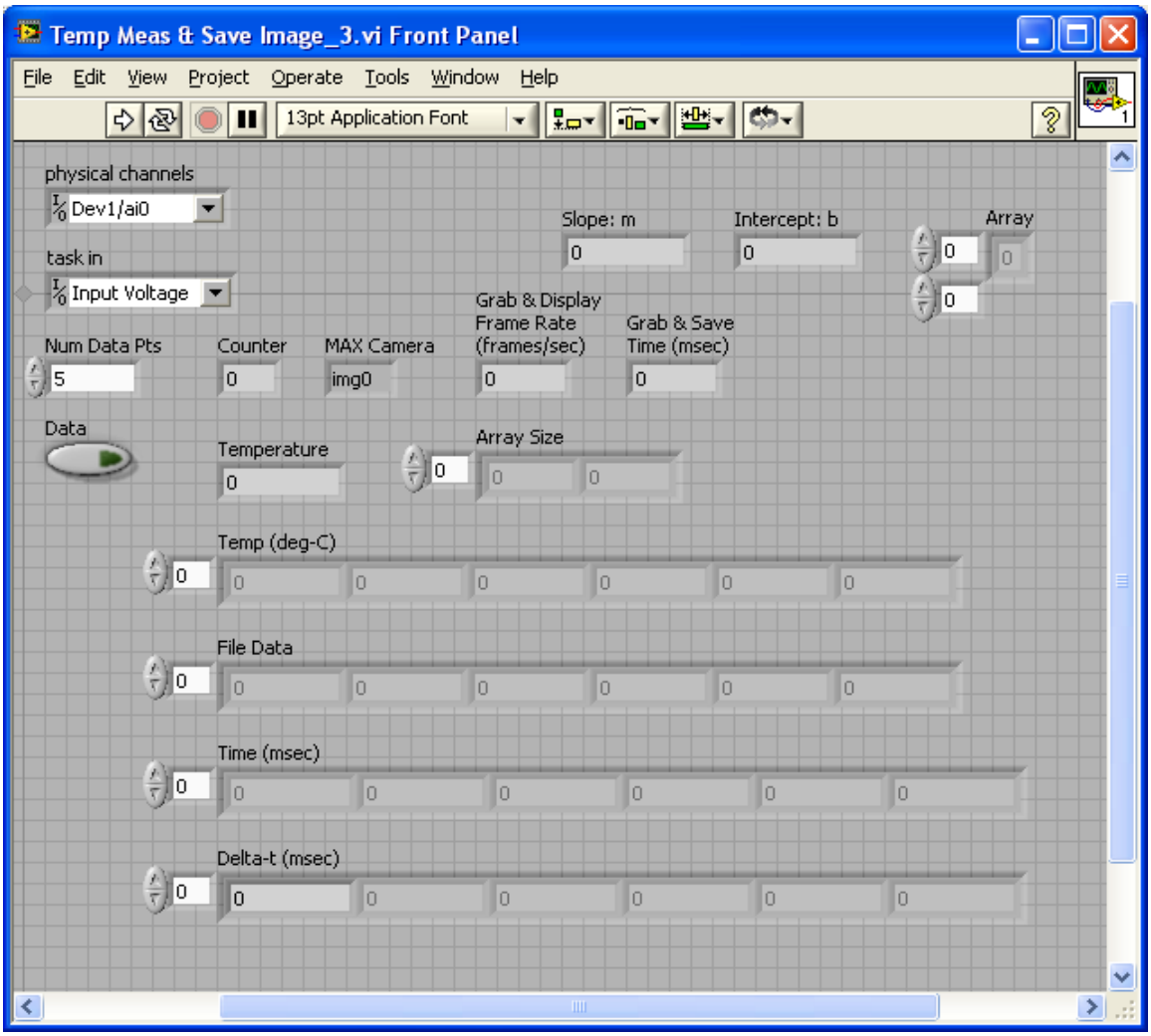

Figure 1 LabVIEW Data and Image Acquisition Showing Control Panel and Program Flow

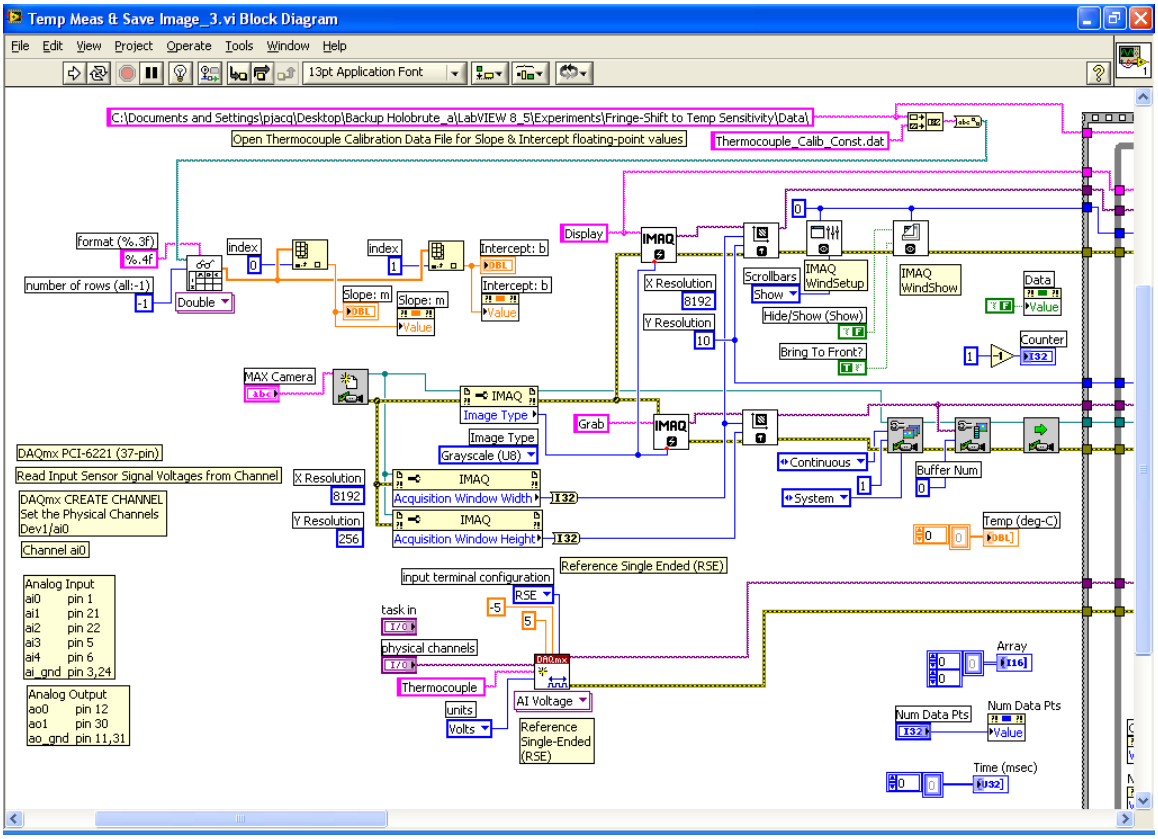

Figure 2 LabVIEW Data and Image Acquisition Block Diagram Program

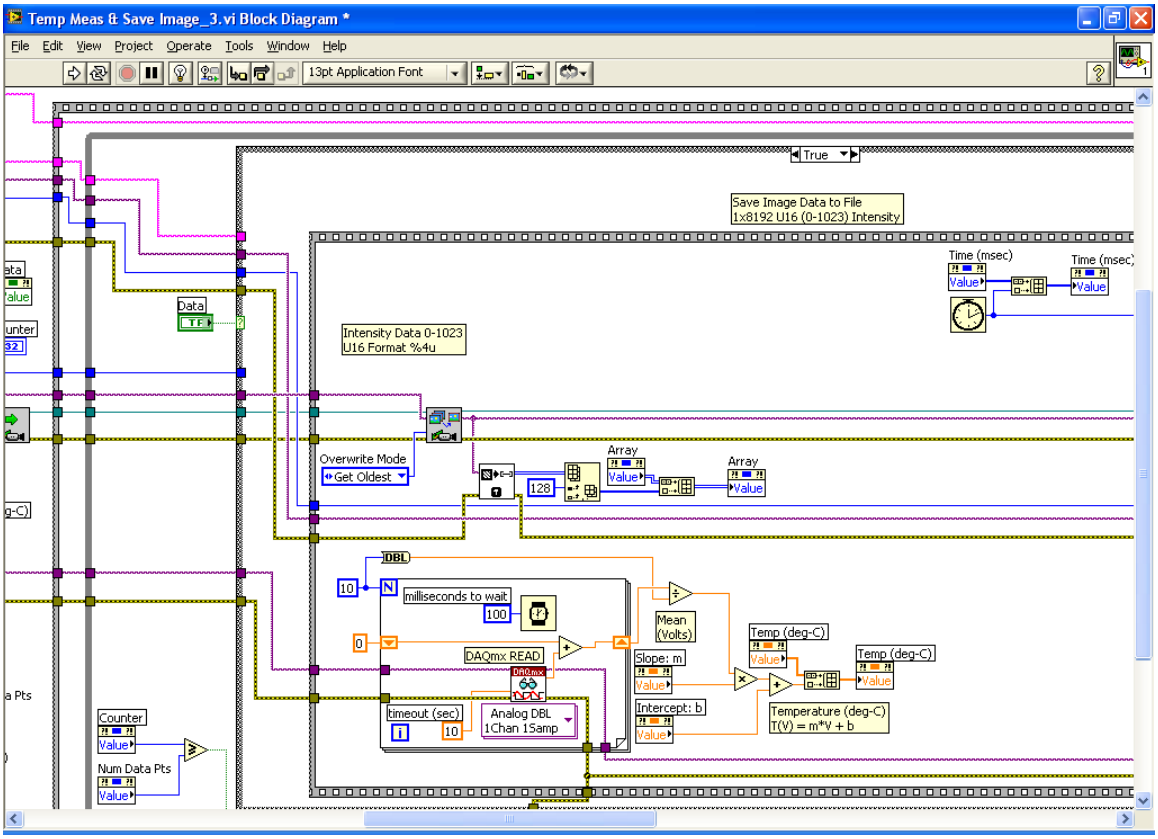

Figure 3 LabVIEW Data and Image Acquisition Block Diagram Program

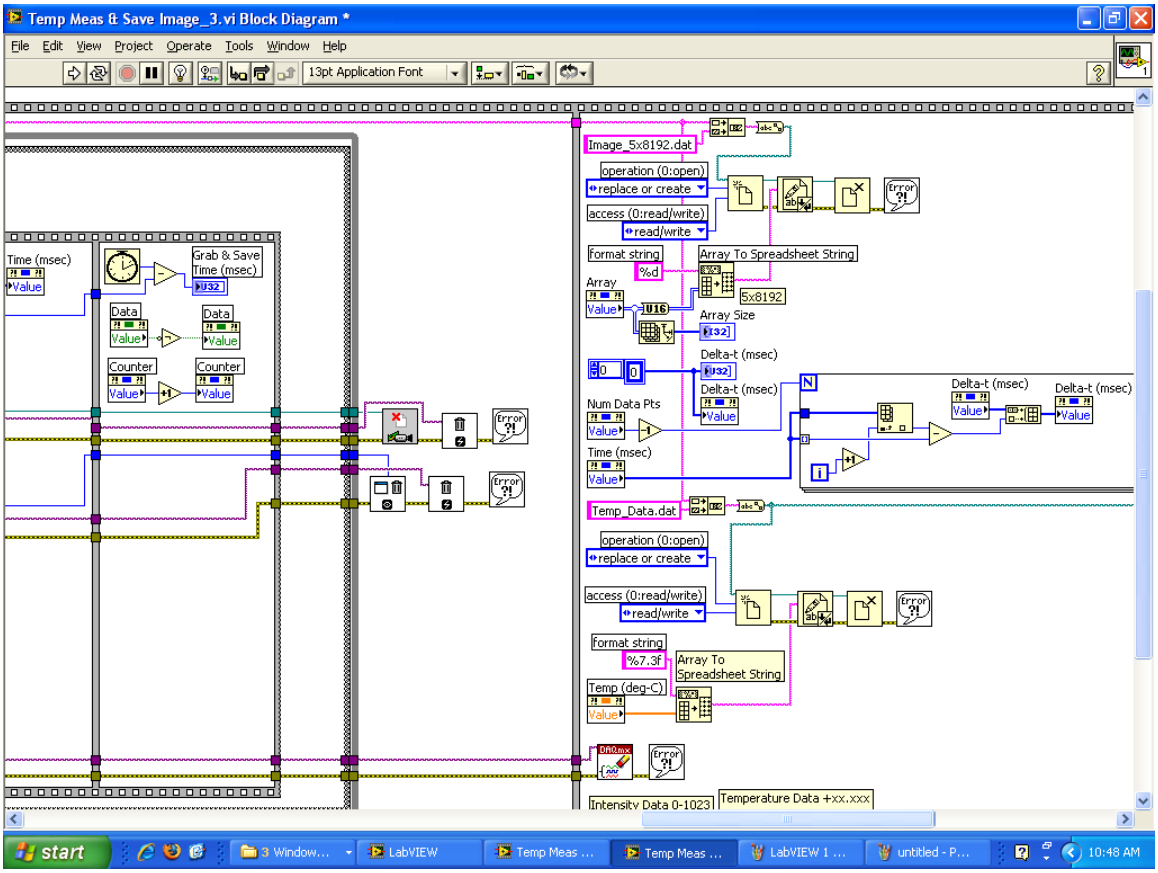

Figure 4 LabVIEW Data and Image Acquisition Block Diagram Program

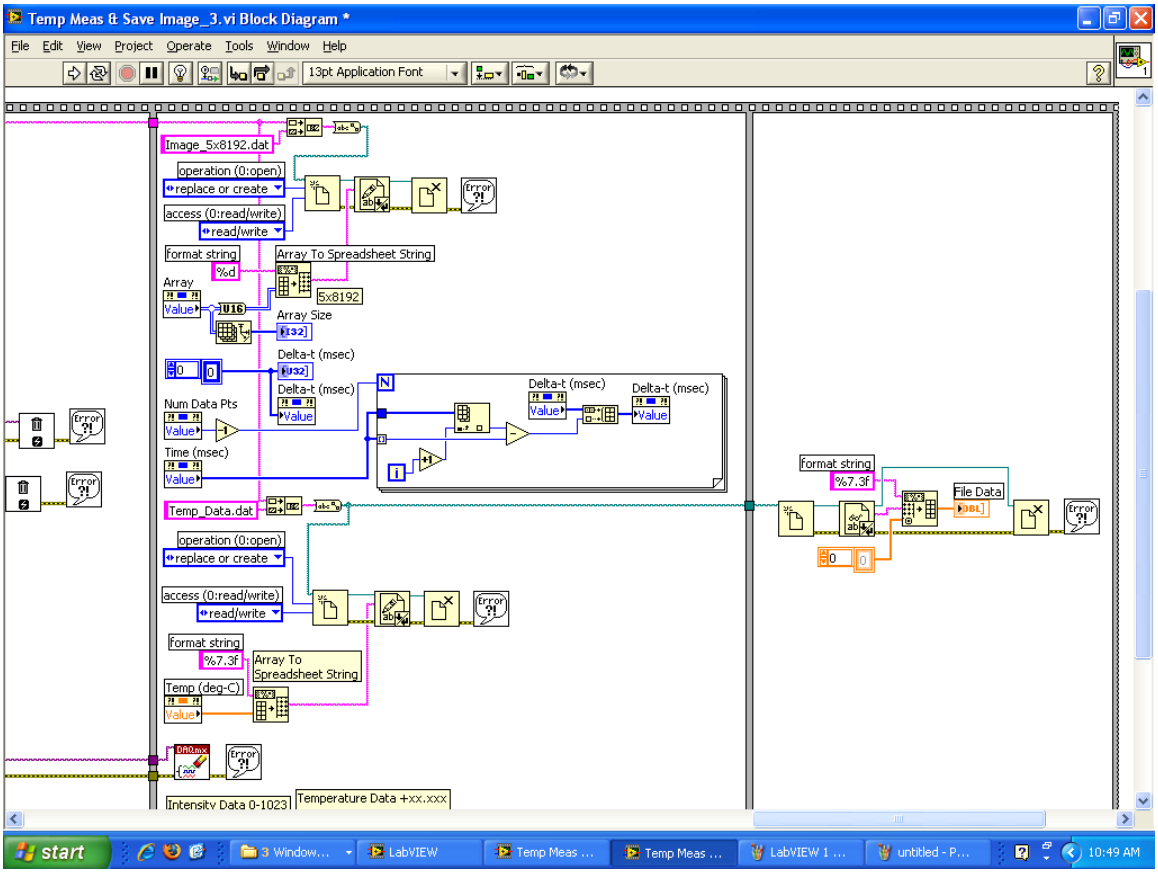

Figure 5 LabVIEW Data and Image Acquisition Block Diagram Program

STLH Microscope Reconstruction Experiment

The LabVIEW program to collect, display and save a few sample images is shown in the figures below:

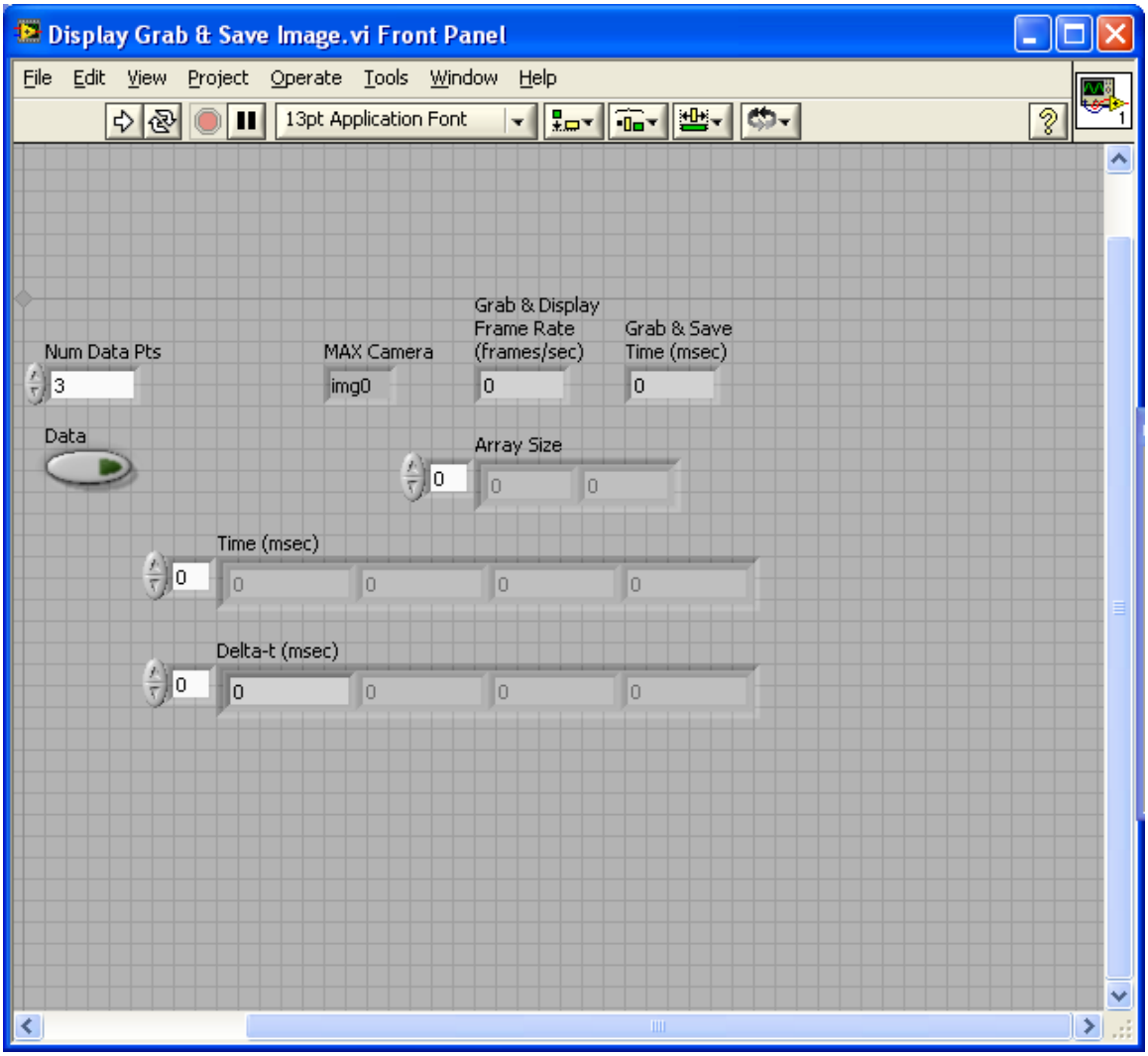

Figure 6 LabVIEW Control Panel to Examine Image Data

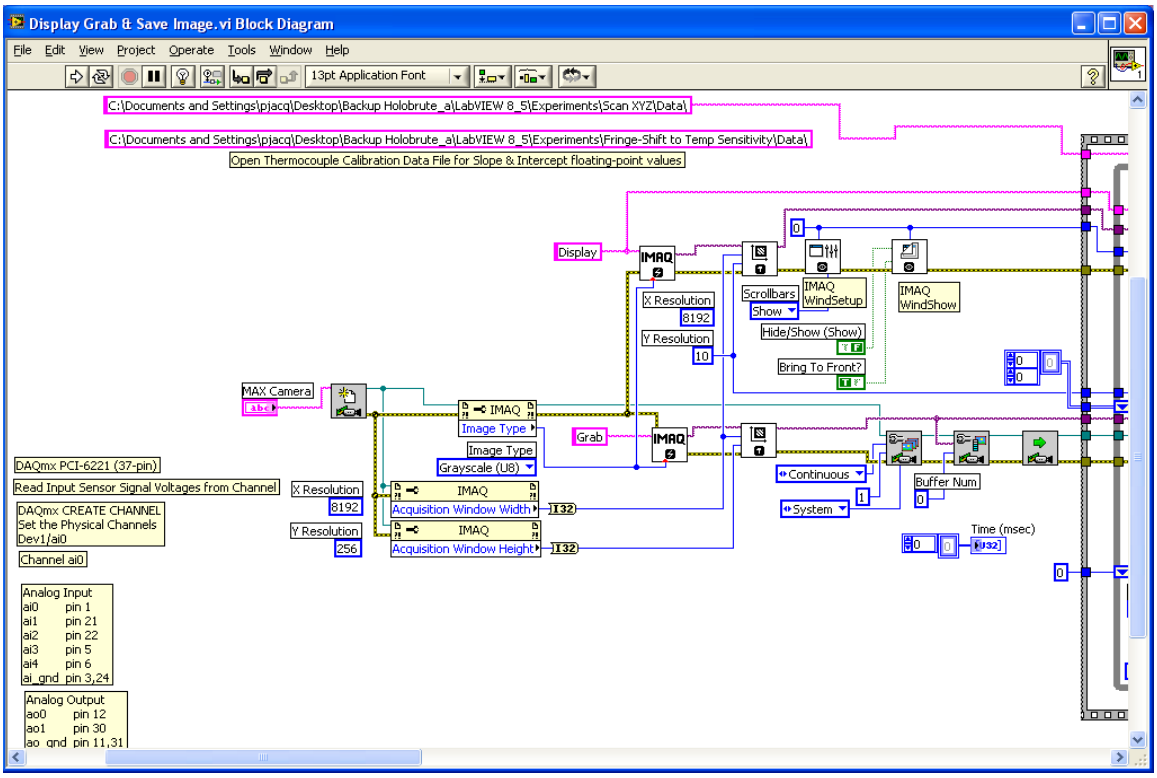

Figure 7 LabVIEW Block Diagram to Examine Image Data

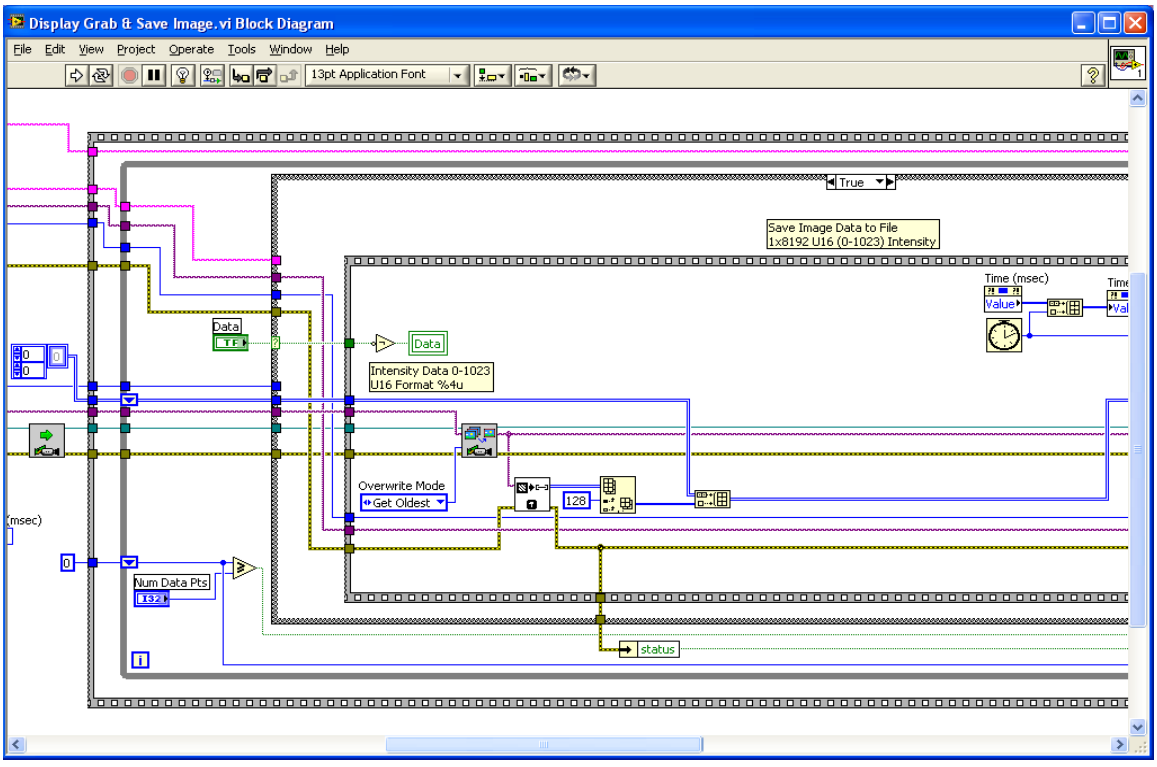

Figure 8 LabVIEW Block Diagram to Examine Image Data

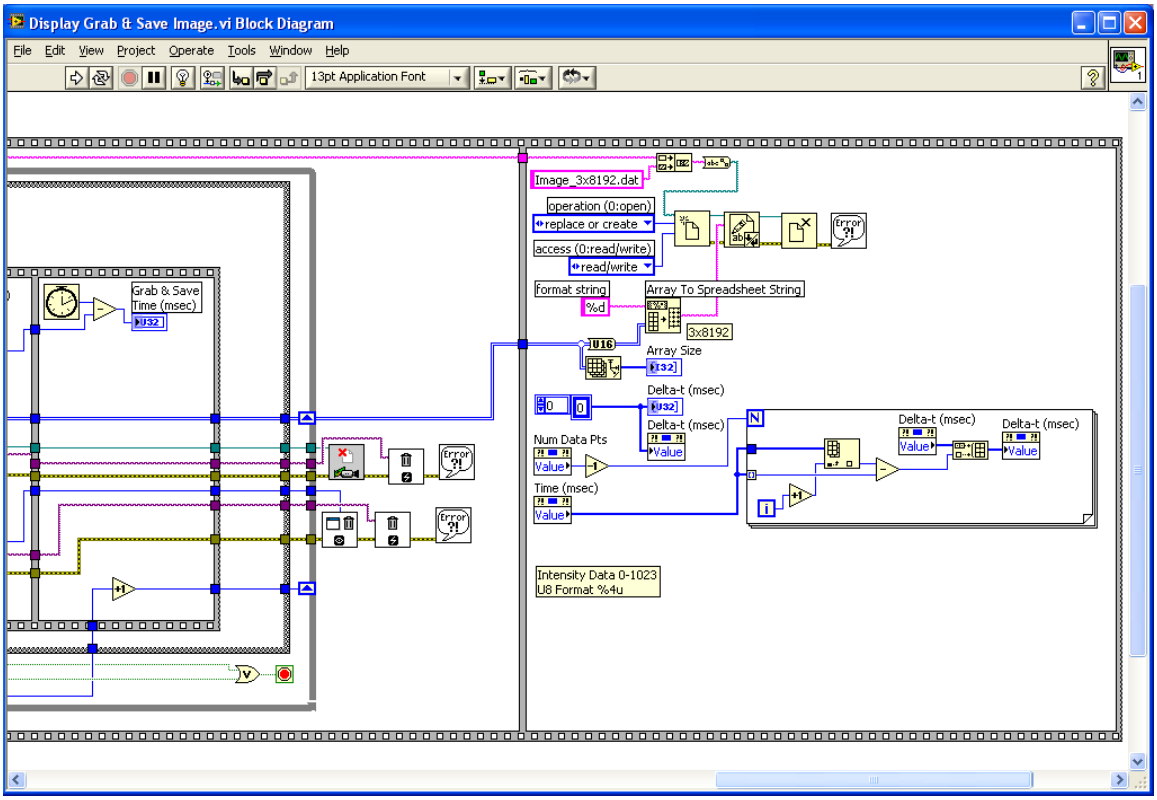

Figure 9 LabVIEW Block Diagram to Examine Image Data

The LabVIEW program named *xyz*-scan which performs step-stare and image grabbing to collect hologram image data is shown in the figures below:

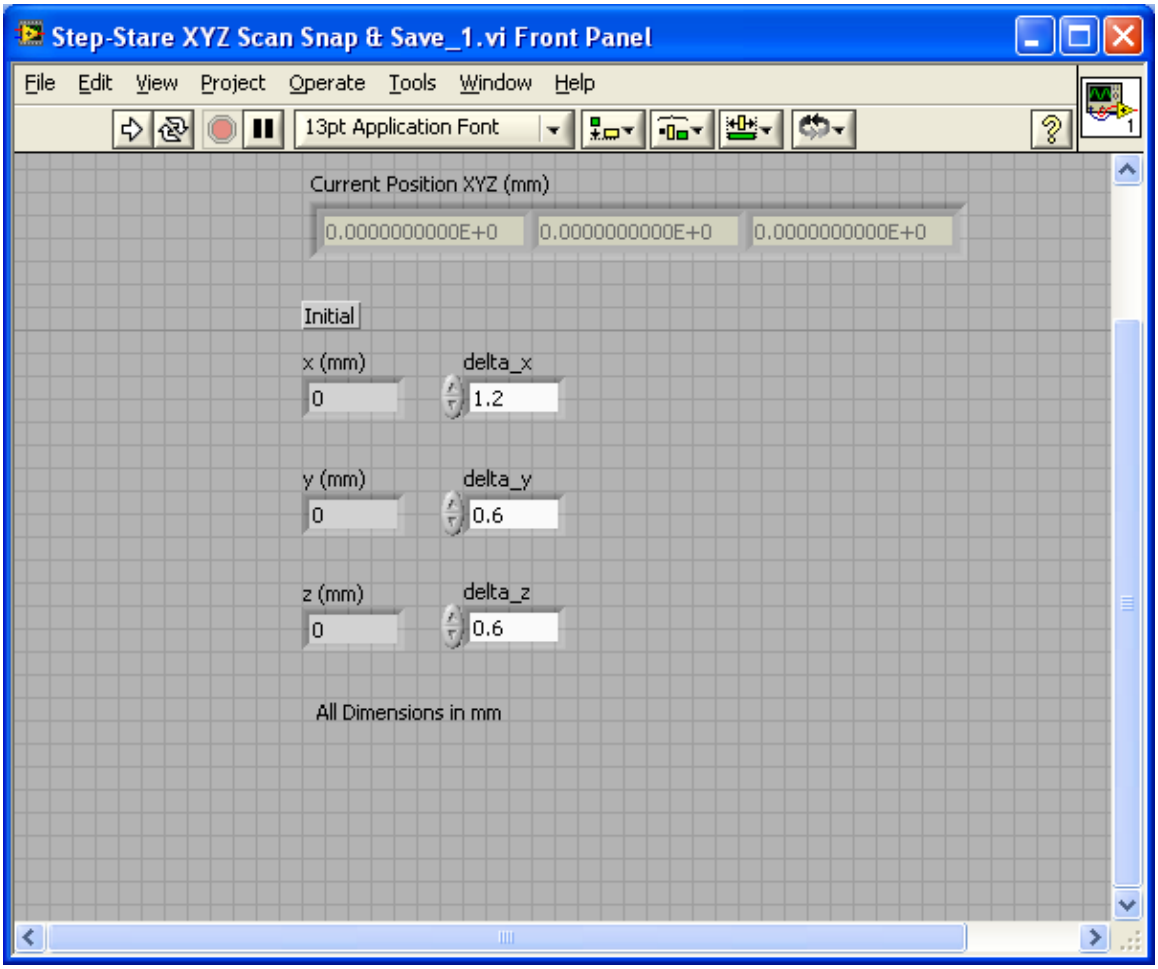

Figure 10 LabVIEW Control Panel to Step-Stare and Collect Scanned Image Data

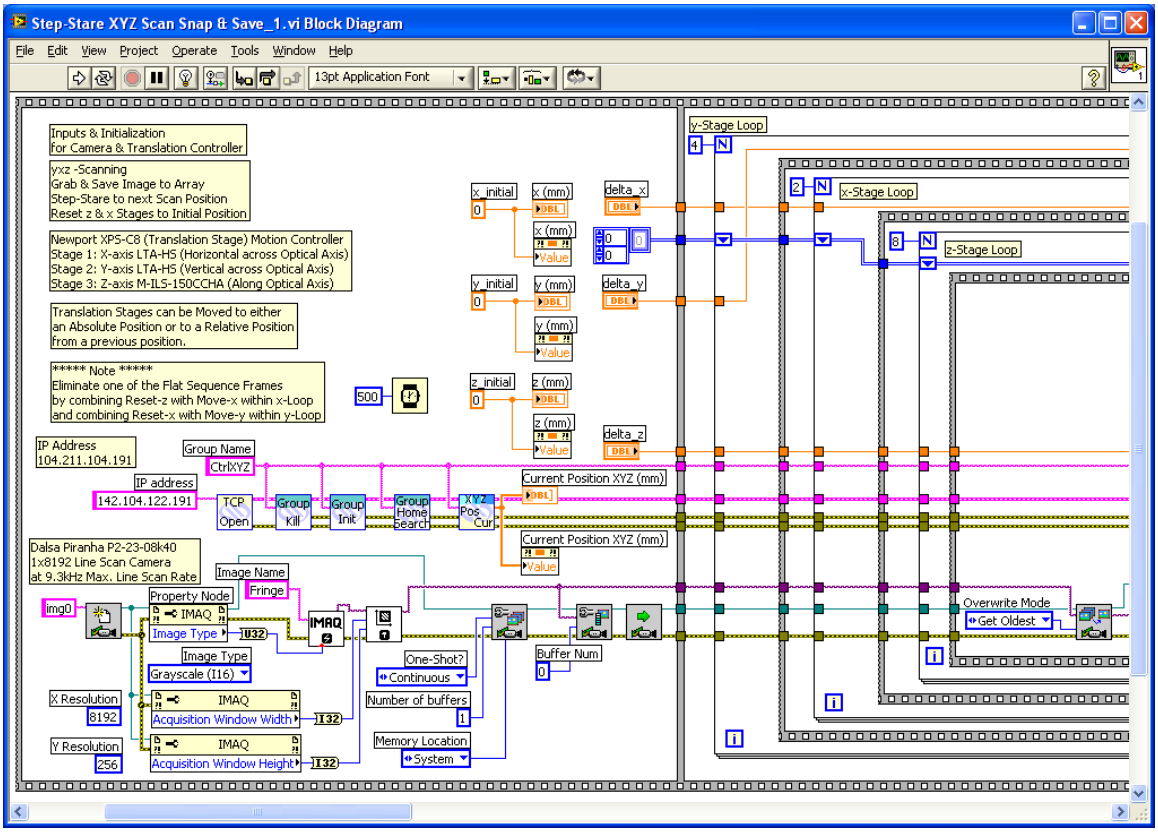

Figure 11 LabVIEW Block Diagram to Step-Stare and Collect Scanned Image Data

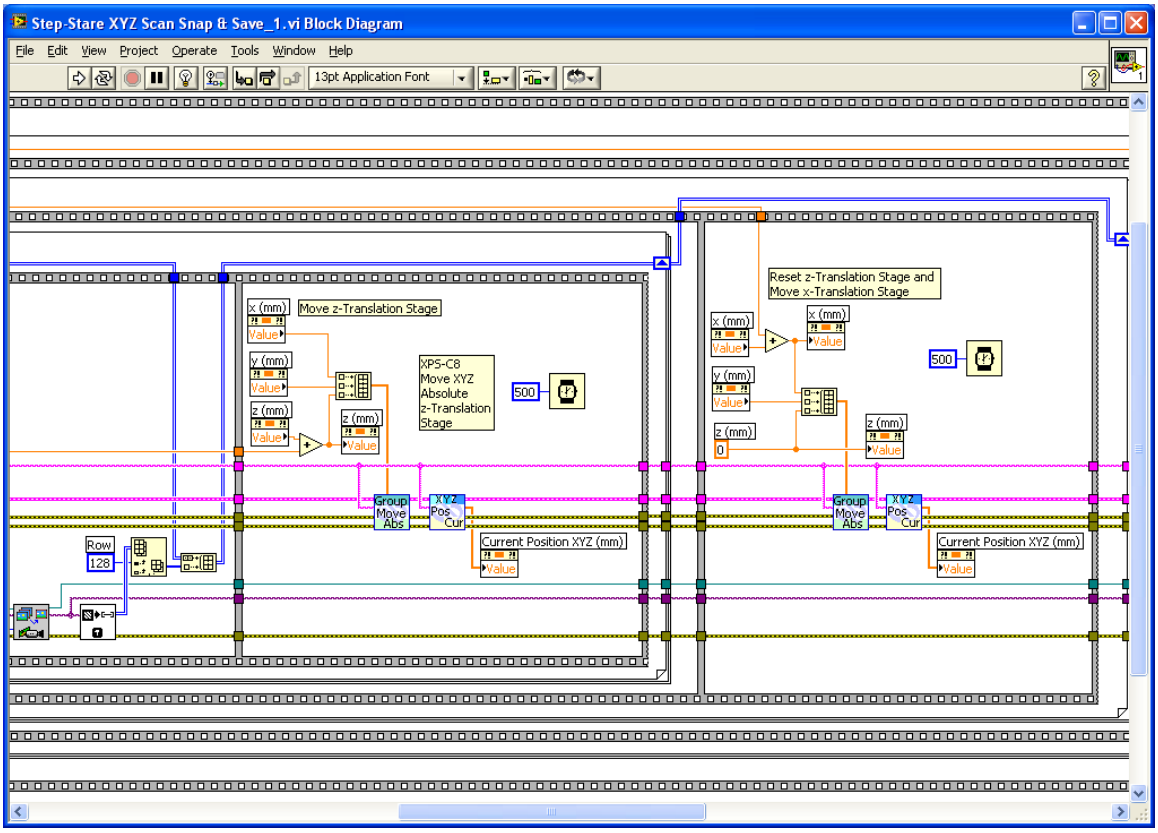

Figure 12 LabVIEW Block Diagram to Step-Stare and Collect Scanned Image Data

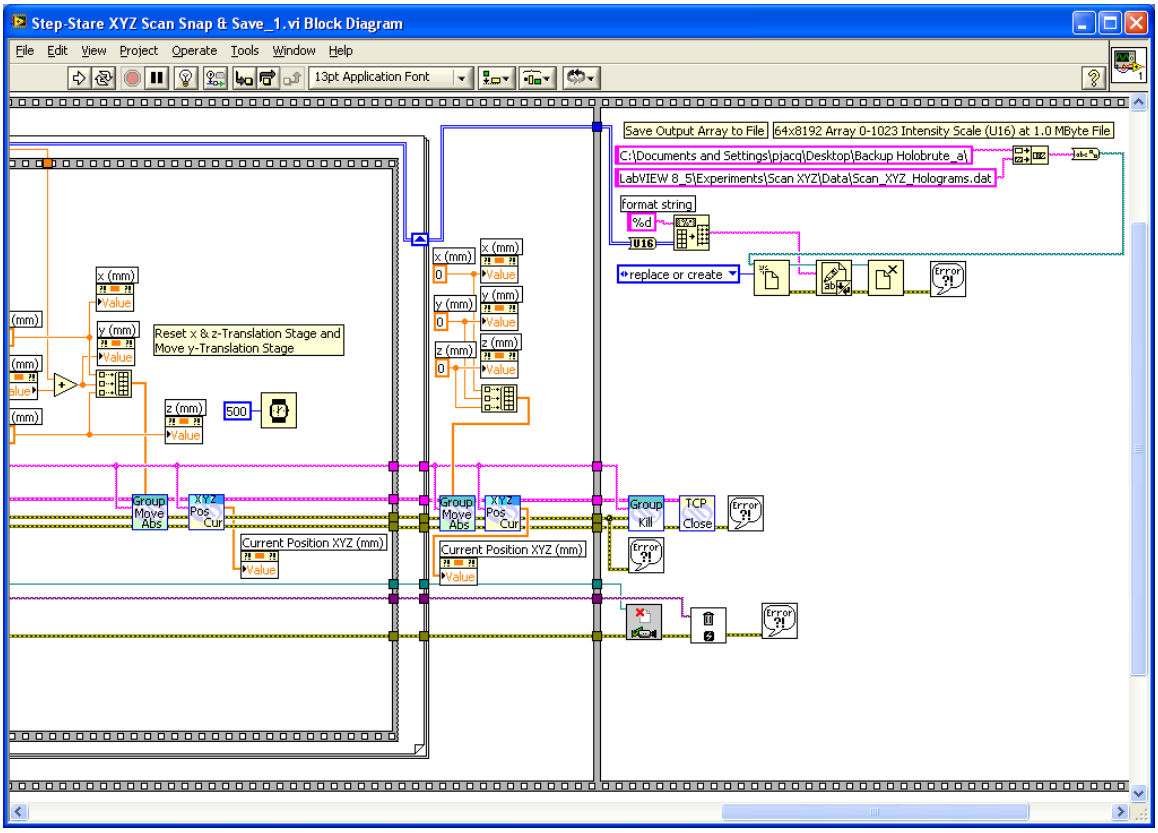

Figure 13 LabVIEW Block Diagram to Step-Stare and Collect Scanned Image Data

CSLH Microscope Reconstruction Experiment

The LabVIEW program to controls the telecentric lens translation stage, BSMs, and confocal aperture translation stages and also to display, acquire, and save a images is shown in the figures below:

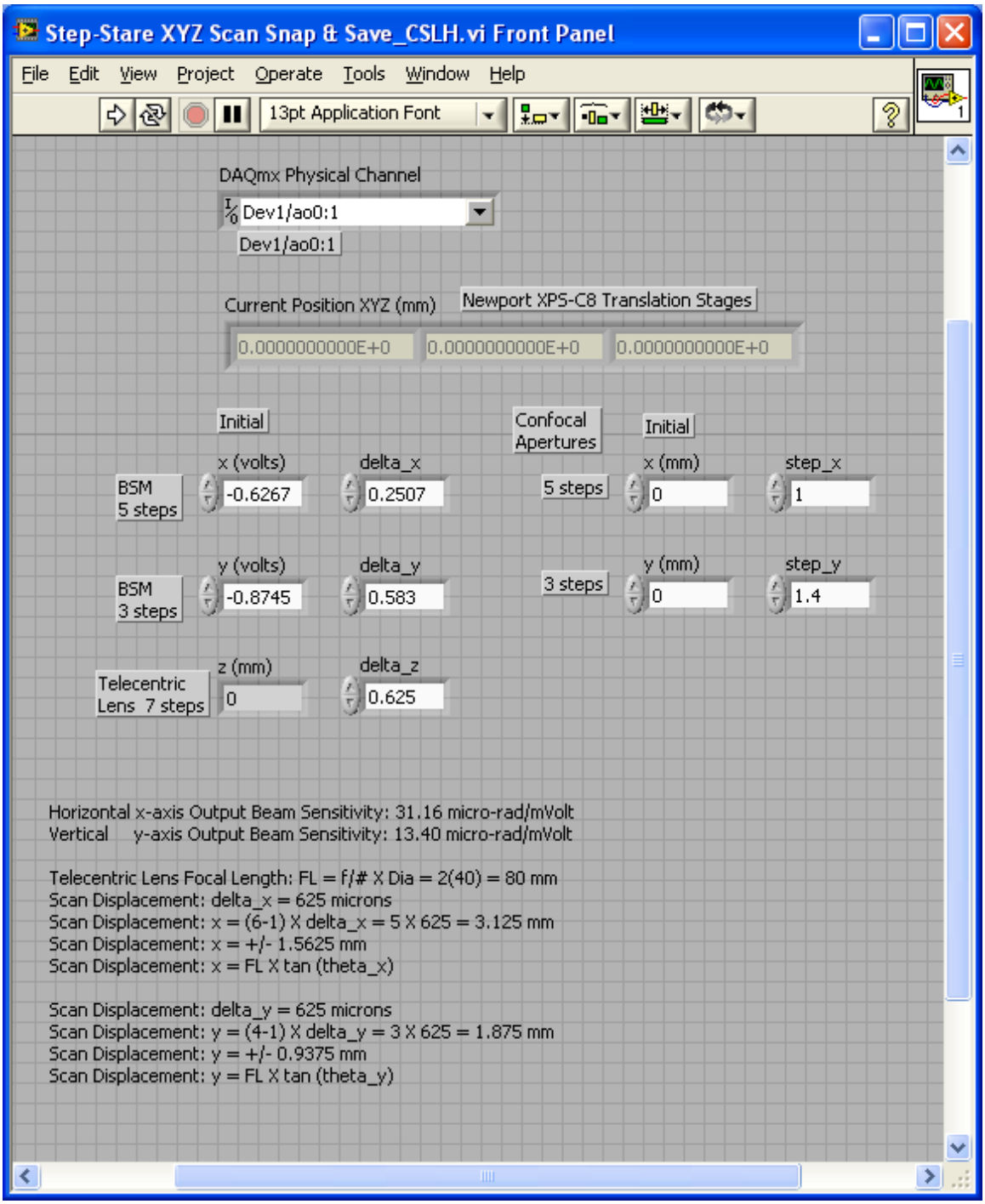

Figure 14 Control Panel and Initial Conditions for the Translation Stages, Mirror Rotation Actuators, and Camera Frame Grabbing

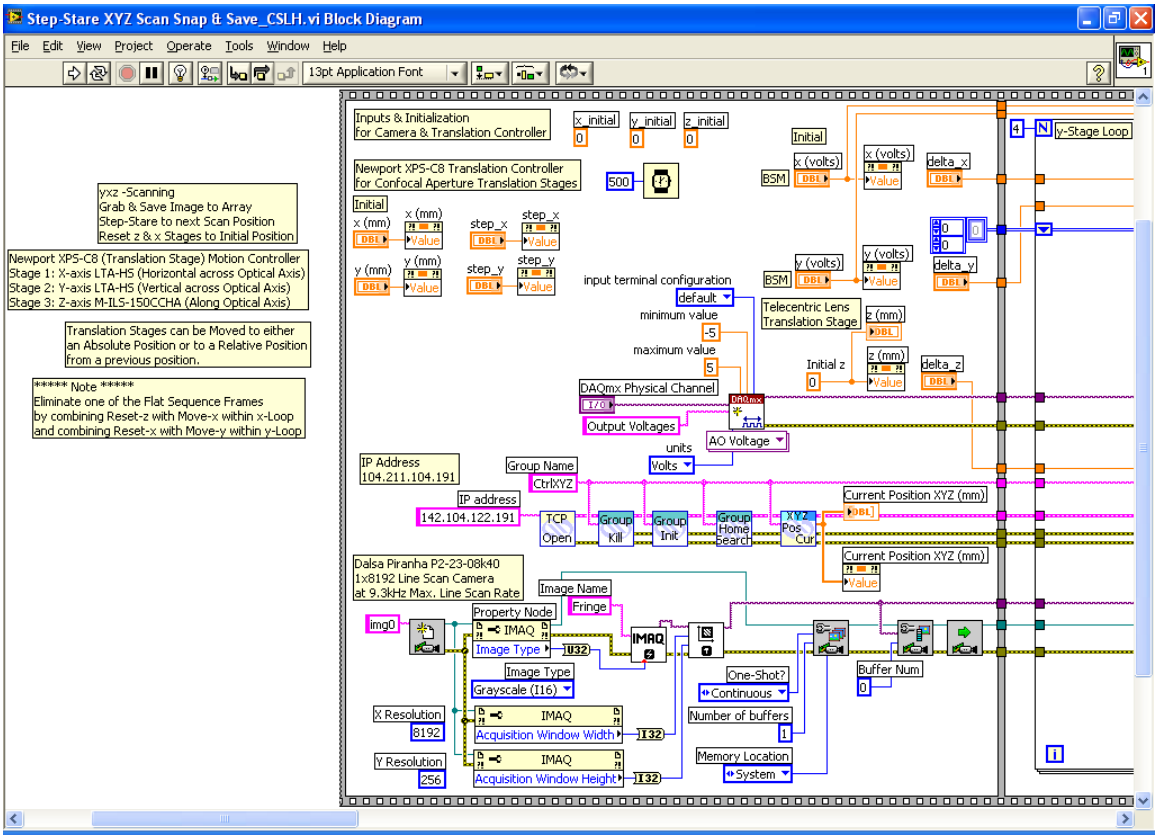

Figure 15 LabVIEW Block Diagram Control, Image Acquisition, and 64x8192 Hologram Array Image Storage

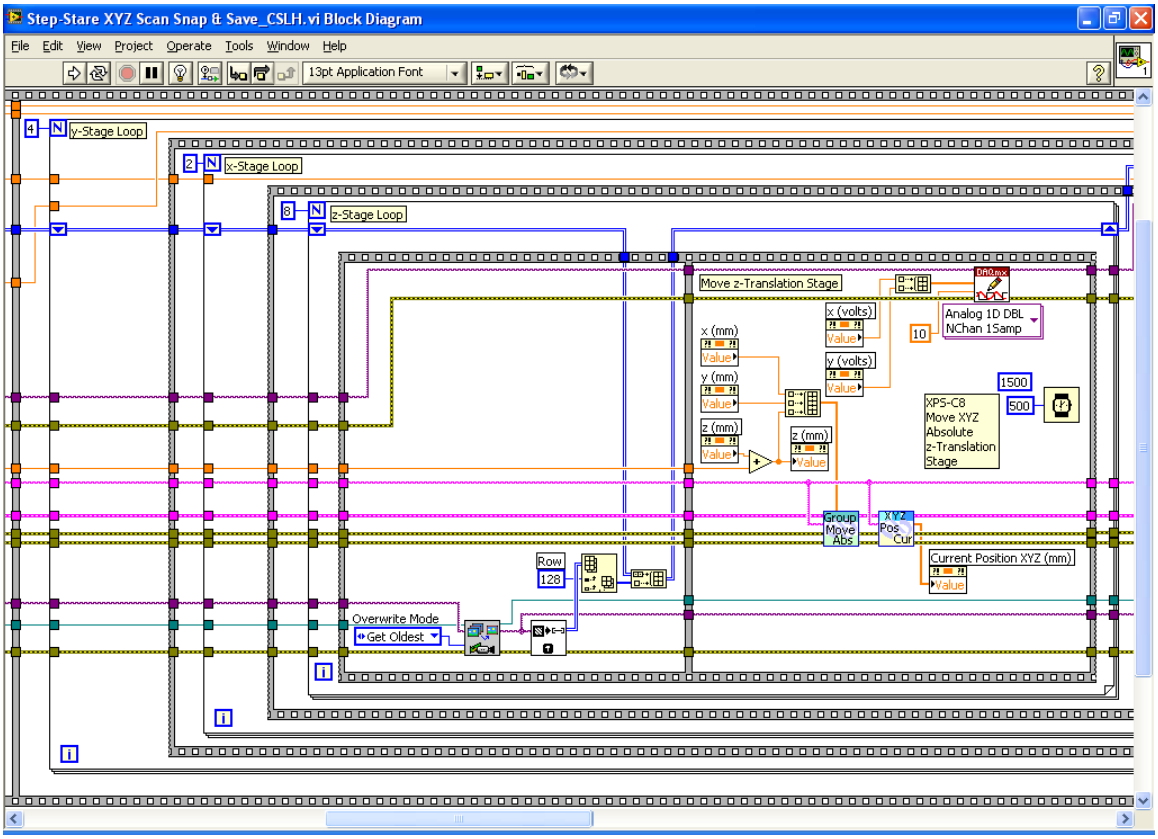

Figure 16 LabVIEW Block Diagram (continued)

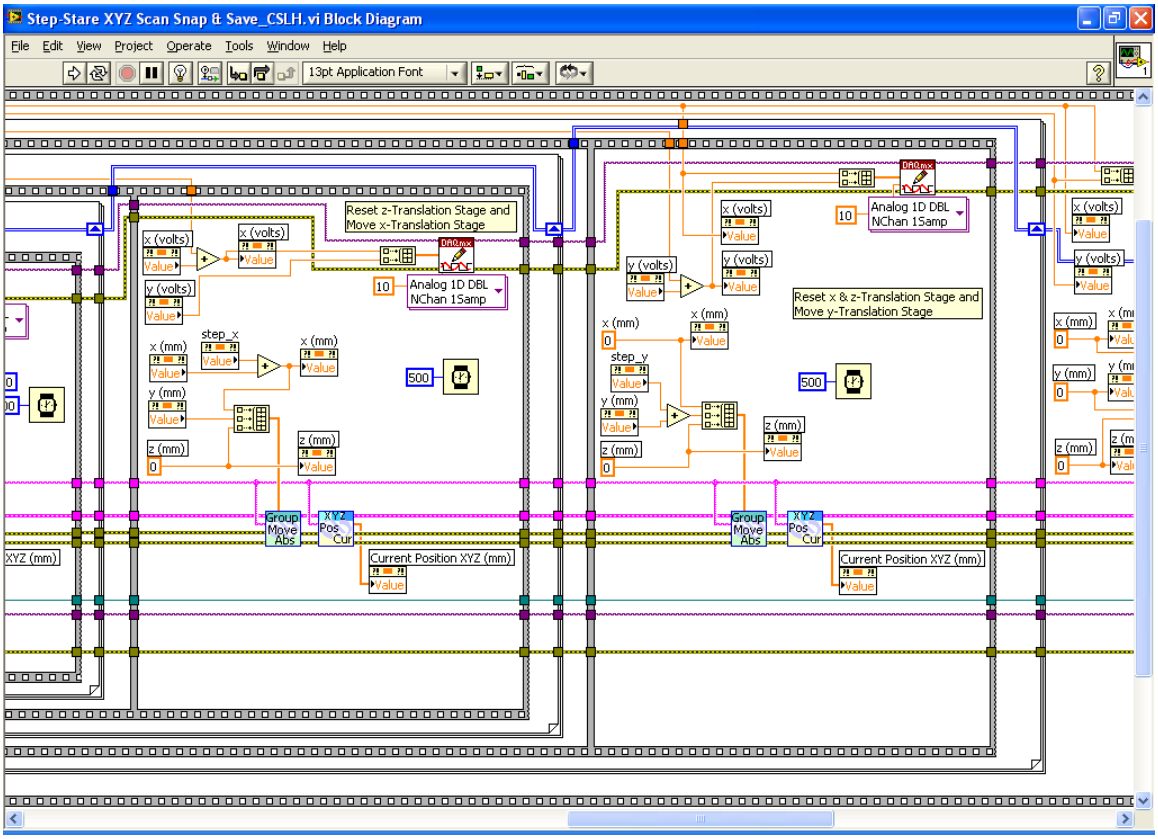

Figure 17 LabVIEW Block Diagram (continued)

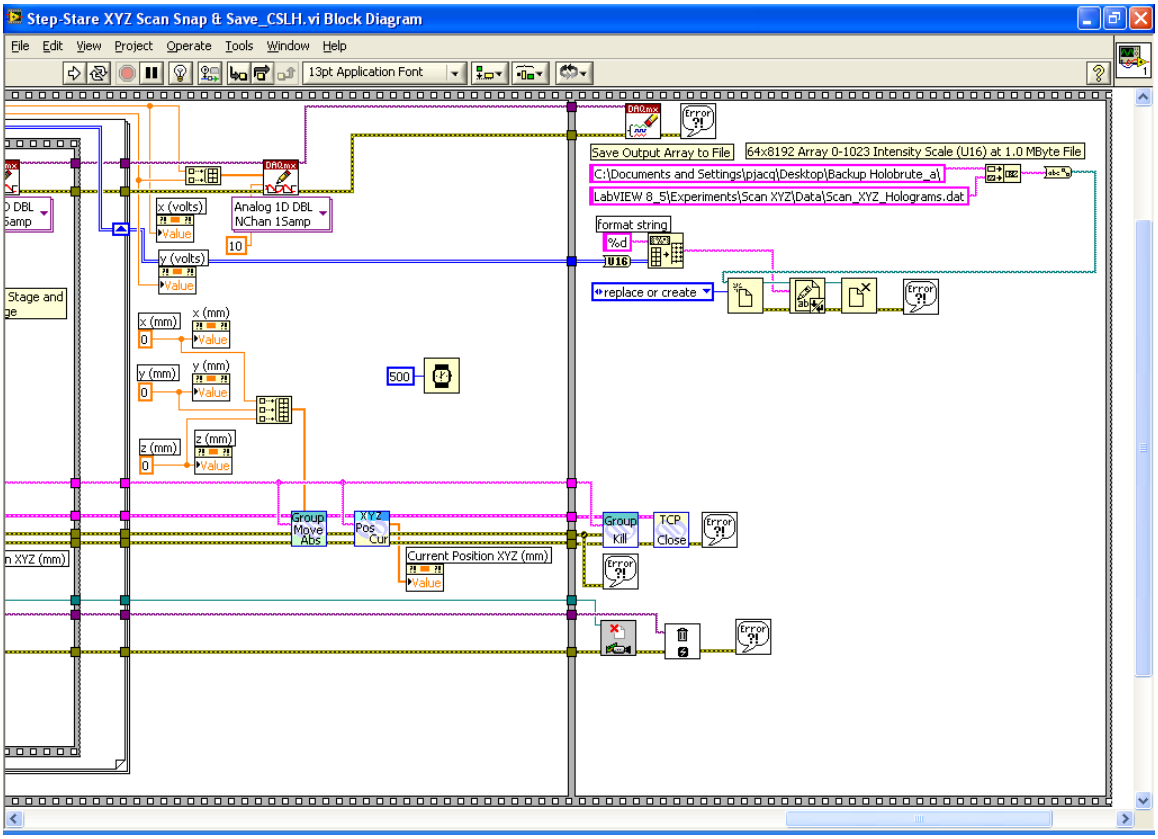

Figure 18 LabVIEW Block Diagram (continued)